RISK-BASED
CRASHWORTHY DESIGNS
TO ENHANCE SHIP DAMAGE STABILITY

By

Hongseok Bae

PhD Thesis

Maritime Safety Research Centre

Department of Naval Architecture, Ocean and Marine Engineering

University of Strathclyde

Glasgow, 2022

COPYRIGHT STATEMENT

Signed: Hongseok Bae 

Date: 06.12.2022

ABSTRACT

SOLAS damage stability regulations have been continuously developed, strengthening a level of ship safety at sea. Nevertheless, many casualties from ship collisions and groundings are still occurring even these days. However, the current SOLAS regulations for passenger ships are not still enough to prevent the current risks. The fundamental problems are that design improvements with new materials and arrangements have been restricted, that individual ship sizes and operational profiles have been disregarded, and that solutions to design issues have been limited. Even though SOLAS opens a door for new designs through “New Technology Qualification (NQT)” procedures and the approval process of “Alternative Design and Arrangements (AD&A)”, they are too time-consuming as well as require expertise. Thus, they are not widely available in the market, stifling developments in this area. Hence, novel approaches and ideas are required to continue improving the stability of passenger ships in general. By addressing this problem conceptually, procedurally and methodologically, this thesis aims to suggest a new methodology with a quantitative risk assessment platform to facilitate and nurture developments in this direction. The method begins by selecting target subdivision zones with high risk via a vulnerability assessment, and several feasible risk control options (RCOs) are applied to these zones. Collision simulations of the region in question using crashworthiness analysis are carried out to determine damage severity in worst-case collision scenarios. The collision speed of a striking ship is derived from a series of pre-simulations, and the speed generating B/2 penetration is employed to fulfil the current SOLAS criteria. Given the penetration results, each RCOs’ cost, and the design change effects of each RCO on the target ship, a cost-benefit analysis is performed to find an optimum solution. The final RCO can be approved and reflected in ship design as an alternative solution by the relevant Administration according to the Approval Process of Alternative Design and Arrangements defined in the IMO. The proposed quantitative risk analysis is applied to a case study with a 65,000 GT medium size cruise ship. The relative collision speed of 10.14 knots from pre-simulations and a vulnerable Zone 15 are identified from the proposed methodology. A total of 26 passive-type RCOs are investigated, including single or double longitudinal subdivisions, different hull thicknesses and permanent foam void-filling measures. The nonlinear finite element method is employed to obtain the maximum penetrations of the stuck ship for all RCOs. Based on the cost and potential loss of life (PLL) of each RCO, the Gross Cost of Averting a Fatality (GCAF) is calculated, and the final three RCOs among all 26 RCOs are successfully

identified as optimum solutions. It is also interesting to examine various simulation parameters' effects from a sensitivity study. The results prove that this methodology gives reliable outcomes regardless of different parameter values with a recommendation of 5% and 10% design margins for longitudinal subdivisions and hull thickness RCOs, respectively. The proposed methodology complements the current problems of SOLAS damage stability regulations, especially for p-factor, providing successful quantitative risk analysis for evaluating various crashworthy RCOs. Thus, this proposed methodology can be used as an alternative design solution for risk prevention or mitigation purposes, finally leading to customised safety designs for individual vessels based on their operating areas and profiles.

ACKNOWLEDGEMENTS

It has been five years since I decided to open a new chapter in my life and left my job in the marine industry after 14 years of work. Since then, I finished my MSc course at the University of Southampton and finally achieved PhD degree at Strathclyde University. Above all, I would like to thank my supervisors, Professor Dracos Vassalos and Professor Evangelos Boulougouris. who guided me in the right direction with support, advice and encouragement. I also appreciate Royal Caribbean Cruise Line company(RCCL) who fully financially supported my PhD research for three years. I hope my research contributes to your innovative ship designs.

Without the support and understanding of my family, I could not have achieved this result in this very short time, going through the COVID pandemic. Thank my parents and parents-in-law for their sincere support and love for me. Finally, I would like to deliver my sincere appreciation to my beloved family: my wife Jinny, my son Minjae Jay, my daughter Minsol Flora and my dog skye. I love you so much!

December 2022 in Glasgow, Scotland UK

ACKNOWLEDGEMENTS

한국에서의 안정된 14 년간의 회사생활을 뒤로하고, 새로운 인생의 길을 선택한지 5 년이라는 시간이 지났습니다. 그 동안 사우스햄튼 대학에서 석사를 마쳤으며, 이곳 스트라스클라이드 대학에서 마침내 박사학위를 취득하였습니다. 한국을 떠날 때, 2 살이던 민솔이는 어느덧 8 살 P4 가 되었고, 민재는 내년에 Secondary school 을 가는 나이가 되었습니다. 나의 인생의 반려자이자 친구인 아내 소진이는 작년 갑자기 찾아온 병으로 힘들었던 시기를 잘 이겨내고, 올해 우리 가족이 된 반려견 스카이의 엄마가 되었습니다.

어찌보면, 영국에서의 시간도 한국과 별 다를게 없이 참 빠르게 흘러가는 것 같습니다. 하지만, 그런 시간 가운데, 가족과 함께 한 행복하고 즐겁고 웃음 가득한 순간들이 더 많이 기억이 되는 걸 보니, 우리의 선택이 틀리지 않았음에 감사합니다. 언제나 밝고 웃음 가득한 우리 아이들 민재, 민솔이에게 고맙고 사랑한다는 말을 전하고 싶습니다. 그리고, 무엇보다도, 아내 소진이가 없었다면, 나에게 이런 인생은 존재하지 않았을 겁니다. 1999 년 그녀를 처음 만났을 때부터 지금까지도 그랬고, 그리고, 앞으로의 시간도 그녀와 함께 한다고 생각나니 기쁘고, 설레여서 힘이 난다고 전하고 싶습니다. 마지막으로, 어려운 시간을 잘 이겨내고, 훌륭히 목표를 잘 이룬 저 자신에게도 감사하고, 사랑한다고, 고생했다고 다독여봅니다.

앞으로도 살아갈 남은 인생에 많은 고민도 함께 하겠지만, 나와 내 가족이 행복 할 수 있는 방향을 선택을 할 것이라는 것은 변함이 없을 것 입니다. 그리고, 우리 가족 안에 나의 자리가 있어서 기쁘고 감사합니다.

하느님 감사합니다. 앞으로의 인생도 제 뜻이아닌, 주님의 뜻대로 살게 해주소서.

Thanks be to God.
Yet not my will, but yours be done.

2022 년 12 월 스코틀랜드 글라스고에서

CONTENTS

LIST OF FIGURES

LIST OF TABLES

NOMENCLATURE

A	Attained Subdivision Index or amount spent initially or; Area of midsurface
A_g	Maximum uniform strain
A_l	Attained Index calculated for the draughts d_l
A_p	Attained Index calculated for the draughts d_p
A_s	Attained Index calculated for the draughts d_s
B	Breadth of Hull
b	Penetration depth or plate breadth between support members
D	Damage evolution
D_{SHEAR}	Damage parameter
d	Draught of the ship
d	Deformation
d_l	Lightest service draught
d_p	Partial subdivision draught
d_s	Deepest subdivision draught
E	Young's modulus or absorbed energy
E_s	Deformation energy of strengthened design
e_i	Unit vector
F_C	Contact force
F_H	Restoring force

F_V	Viscous force
F_W	Wave damping force
f_{ext}	External forces
f_{int}	Internal forces
G	Skew-symmetrical gyroscopic matrix
H	Height of each horizontal subdivision measured from a keel
H_m	Uppermost horizontal subdivision of the ship
I_R	Rupture Index
J	Transfromation matrix
J	Nondimensional length of a compartment
K	Hardening coefficient or coefficient associated with a final equilibrium angle (θ_e), a minimum (θ_{min}) or; Roll moment or; Stiffness
L	Length of damage
L_s	Subdivision ship length
l_e	Element length
M	Mass matrix or Pitch moment
M_A	Constant added mass for infinite frequency
M_{RB}	Structural mass of ship
m	Ship displacement
N	Yaw moment
N_1	Number of persons for whom lifeboats are provided or shape functions
N_2	Number of persons, including officers and crew, that the ship is permitted to carry in excess of N_1 or shape functions

n	Strain hardening exponent
P	Depth of damage
p	Longitudinal damage occurrence probability
p_i	Probability that only the compartment or group of compartments under consideration may be flooded
R	Required Subdivision Index
R^*	Rotation matrix from the reference water plane
r	Transverse damage occurrence probability or reduction factor
r_ε	principal strain ratio between major and minor strains ($\varepsilon_1/\varepsilon_2$)
$Range$	Range of positive righting levers, in degrees, measured from the equilibrium heel angle in any stage of flooding
R_T	Resistance factor
s_{final_i}	Probability of survival at a final state
s_i	Probability of survival after flooding the compartment or group of compartments under consideration
$s_{intermediate_i}$	Probability of survival at intermediate state
s_{moment_i}	Probability of survival with maximum heeling moments
T	Draught or gauge thickness of the specimen
t	Thickness of damage
u	Nodal displacement
$\dot{u}$	Nodal velocity
$\ddot{u}$	Nodal acceleration
V	Collision speed
v	Vertical damage occurrence probability or velocity
v^m	Velocity of midsurface

W	Gauge width and the thickness of the specimen
X	Cost of RCO
X	Force in x-direction
x^m	Element coordinate of midsurface
Y	Force in y-direction
Z	Force in z-direction
Δ	Ship displacement mass (tonnes)
δ	Magnitude depending on strain magnitude
η	Local coordinate system in midsurface (i.g., $(\xi, \eta)= (0,0)$ at the centre of the element)
$\dot{\varepsilon}$	Maximum strain rate value
ε_0	Critical fracture strain from uniaxial tensile conditions
ε_1	Major principal strain
ε_2	Minor principal strain
$\widehat{\varepsilon_1}$	Critical strain
ε_c	Critical fracture strain
ε_{cr}	Critical equivalent true plastic strain
ε_e	Necking strain
ε_f	Stain at rupture in static conditions
ε_{fd}	fracture strain in the dynamic
ε_g	Uniform strain
ε_m	Highly deformed strain in the necking area
ε_n	Through thickness necking strain
ε_{true}	True strain

ε_u	Uniform strain
ε_V	Maximum effective strain
η_a	Average stress triaxiality
θ	Pitching angle
θ_e	Final equilibrium angle
$\boldsymbol{\theta_m}$	Angular velocity at midsurface
θ_{max}	Maximum heeling angle
θ_{min}	Minimum heeling angle
μ	Friction coefficient
ν	Poisson's ratio coefficient
ξ	Local coordinate system in midsurface (i.g., (ξ, η)= $(0,0)$ at the centre of the element)
ρ	Density of sea water
$\overline{\sigma}$	Equivalent Von Mises stresses
$\widetilde{\sigma}$	Flow stress for the damage evolution beyond critical damage initiation
$\hat{\sigma}$	Local stress
σ_{1f}	Principal stress at the onset of necking
σ_{true}	True stress
σ_m	Mean of principal stresses
σ_Y	Static yield stresses
σ_{Yd}	Dynamic yield stresses
Ψ	Yawing angle
ϕ	rolling angle
ω	Angular velocity vector

ABBREVIATIONS

A.P.	After Perpendicular
AIS	Automatic Identification System
BM	Metacentric Radius, distance between the Center of Buoyancy and the Metacenter
BSRA	British Ship Research Association
BV	Bureau Veritas
CAPEX	Capital Expenditures
CDF	Cumulative Distribution Function
CDF	Cumulative Distribution Function
COG	Centre of Gravity
COV	Coefficient of Variation
DG-MOVE	Directorate-General for Mobility and Transport
DOF	Degree of Freedom
DWT	Dead Weight Tonnage
DWT	Deadweight Tonnage
EC	European Commission
EMCIP	European Marine Casualty Information Platform
EMSA	European Maritime Safety Agency
eSAFE	enhanced Stability After Flooding Event
F.P.	Forward Perpendicular
FE	Finite Element
FLARE	FLooding Accident REsponse
FLD	Forming Limit Diagram

FLOODSTAND	Integrated FLOODing control and STANDard for stability
FLSD	Stress-based forming limit curve criterion
FR	Friction Coefficient
FS	Failure Strain
FSA	Formal Safety Assessment
GCAF	Gross Cost to Avert a Fatality
GL	Germanischer Lloyd
GM	Metacentric height
GOALDS	GOAL based Damage Stability
GT	Gross Tonnage
GZ	Righting lever
HARDER	HARmonisation of DEsign Rationale
HAVC	Heating, Ventilation, and Air Conditioning
HAZID	Hazard Identification
HFO	Heavy fuel oil
HY	high-yield steel
IACS	International Association of Classification Societies
IGC	International Gas Carrier Code
IMO	International Maritime Organization
ISSC	International Ship and Offshore Structure Committee
ITTC	International Towing Tank Conference
KG	Vertical centre of Gravity from keel
LBHD	Longitudinal Bulkhead
LCG	Longitudinal centre of Gravity

LEPP	Linear elastic-perfectly plastic model
LFO	Light Fuel Oil
LNG	Liquified Natural Gas
LPG	Liquified Petroleum Gas
LPP	Length between Perpendiculars
LSA	Life Saving Appliances
MARIN	Maritime Research Institute Netherlands
MARPOL	The International Convention for the Prevention of Pollution from Ships
MEPC	Marine Environment Protection Committee
MSC	Maritime Safety Committee
MSRC	Marin Safety Research Centre at the University of Strathclyde
MTSS	Modified True Stress True Strain Curve
NCAF	Net Cost to Avert a Fatality
NLFEM	Nonlinear Finite Element Method
NPV	Net Present Value
OPEX	Operational Expenditure
PDF	Probability Distribution Function
PLL	Potential Loss of Life
POB	Person on Board
RCCL	Royal Caribbean Cruise Line
RCO	Risk Control Option
RoPax	Roll-on/Roll-off Passenger Vessel
Ro-Ro	Roll-on/Roll-off Vessel
SAFEDOR	Design, Operation and Regulation for SAFEty

SDC	The Sub-Committee on Ship Design and Construction
SLF	Sub-Committee on Stability and Load Lines and on Fishing Vessels' Safety
SOLAS	Safety Of Life At Sea
SRtP	Safe Return to Port
SWT	Semi-Watertight
TEU	Twenty Equipment Unit (20-foot container)
UNCLOS	United Nations Convention on the Law of the Sea
USD	US Dollar
VCG	Vertical Centre of Gravity
VTS	Vessel Traffic Service
WT	Watertight

Chapter 1

Introduction

1 INTRODUCTION

1.1 Overview

On the 7th of October 2018, the 160m Ro-Ro vessel *ULYSSE* was heading to *Rades* in Tunisia at dawn, following her usual courses through Corsica Channel TSS. At 07:02 in the morning, ULYSSE violently collied at 19 knots with 5000 TEU container ship *CSL VIRGINIA* which was anchoring at 11 nautical miles from the entrance of the Corsica Channel TSS precautionary area and at 16.5 nautical miles from the TSS entrance on the western route in Figure 1.1(a). The entire forepart of *ULYSSE* penetrated the starboard of *CSL VIRGINIA* almost perpendicularly. As a consequence of this collision, fuel oil tanks of *CSL VIRGINIA* were damaged with a 520 cubic metres oil spill, but no fatalities or injuries occurred (BEAmer, 2018).

(a) (b)

Figure 1.1 Collision accident between Ulysee and CSL Virginia in 2018 (a) Collision scene of both ships and (b) Damages

On the 13th of January 2012, the 114,000 GT *Costa Concordia* was in navigation from Civitavecchia to Savona near the Italian coastline in the Tyrrhenian Sea of the Mediterranean Sea, carrying 4229 persons onboard, including 3206 passengers and 1023 crew. At 9:45 at night time, the vessel suddenly struck at 15.5 knots with the “Scole Rocks” at Giglio Island and immediately lost propulsion resulting in a black-out. The grounding led to a 53 metres long breach, with five-watertight compartments damaged on the side bottom hull on her starboard side. The vessel finally capsized and sank into the shallow water with an 80° heeling angle after two hours later in Figure 1.2. As a consequence of this grounding, 32 persons on board lost their lives with 157 injuries, and 2042.5 cubic metres of oil spilt into the sea (MIT, 2012).

(a) (b)

Figure 1.2 Grounding accident of Costa Concordia in 2012 (a) Grounding scene (b) Damages

Most modern vessels are well equipped with high-technology radar and communication systems for safe navigation. They are also under control by Vessel Traffic Service System (VTS), especially in the areas where heavy marine traffics exist. However, as described above, a significant number of navigational accidents are still occurring these days.

According to the European Maritime Safety Agency (EMSA, 2021a, EMSA, 2014a), a total of 19,500 casualties occurred from 2011 to 2020, which involved ships flying a flag of one of the EU Member States or occurred within EU Member States' territorial sea or internal waters as defined in UNCLOS based on the EU database of maritime incidents EMCIP (European Marine Casualty Information Platform). Among them, navigational accidents such as collision, contact, grounding and stranding account for 46 % of the total casualties (see Figure 1.3).

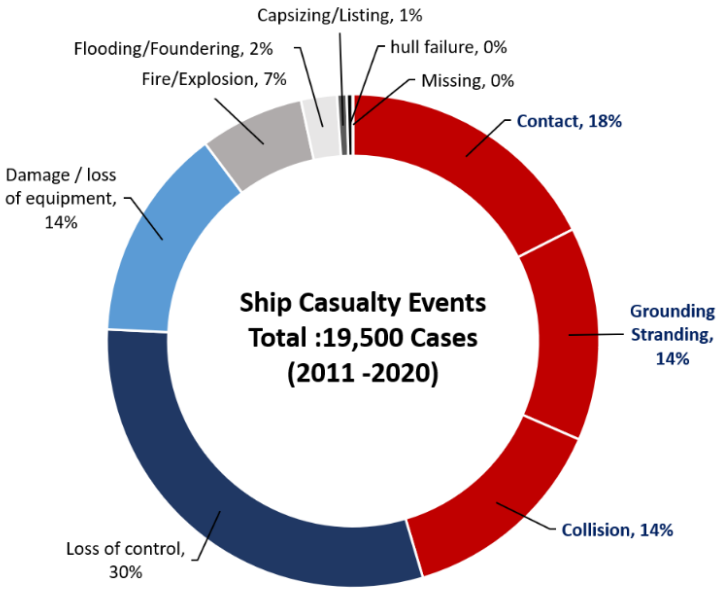

Figure 1.3 Casualty events of ships associated with EU from 2014 to 2020 (EMSA, 2021b)

Furthermore, not only commercial vessels, such as containers, tankers and car carriers, but also passenger ships like cruise ships and Ro-Pax have grown more prominent in capacity over the last two decades as shipping companies seek economies of scale and fuel efficiency. This trend is likely to continue with climate change and the introduction of greenhouse gas emissions reduction for the industry. Despite the recent Covid-19 pandemic, ever-larger vessels are on order, especially for container ships. Figure 1.4 shows the ship capacity changes of both cruise ships and container ships. For example, cruise ships operated by RCL have increased their ship size by approximately 500 % from 1990, while the largest container ship in 2021 can carry approximately 400 % more containers than the ship in 1996. In particular, for cruise ships, the ocean cruise industry has gradually developed with a growth rate of 6.6 % before the Covid19 pandemic in Figure 1.5(a). Due to the increase in these demands, more new cruise vessels have been built with significantly enlarged ship capacity. The maximum passenger capacity of the largest cruise ships each year has soared dramatically by approximately 370 % to 9,000 in 2022 compared to 2,440 in 1996, as shown in Figure 1.5 (b), which would be more considerable when crew numbers are included.

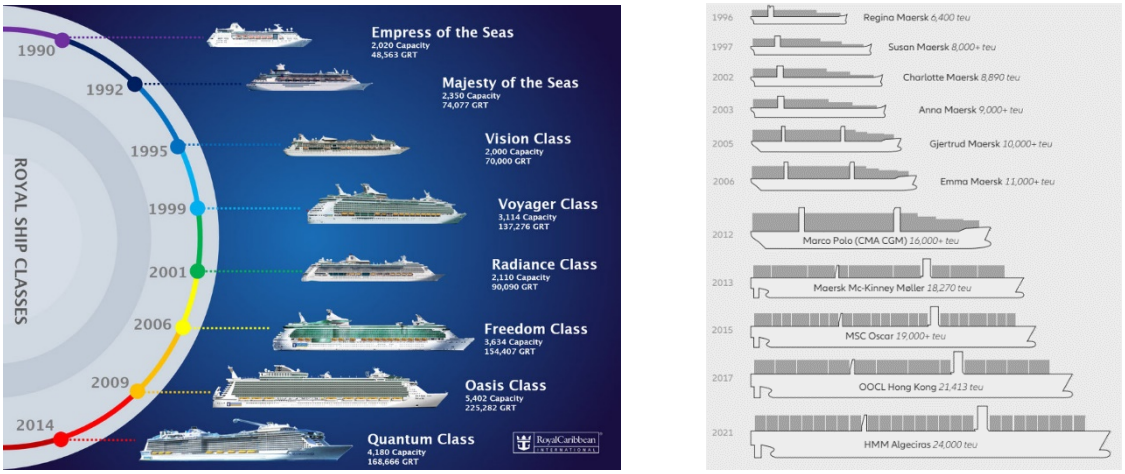

(a) (b)

Figure 1.4 (a) Evolution of ship sizes for the last two decades : (a) RCCL cruise ships and (b) Container ships

Therefore, the current trends of cruise ships can be summarised that lots of huge size of cruise ships are in operation more frequently than in the past, carrying four times more people (i.e., 6000-9000 people) on board. At the same time, there are a large number of high-speed ultra-large commercial vessels operating at sea. This means that thousands of persons on board are completely exposed to a far greater risk of fatality from a single accident, which may cause the worst catastrophe ever (AGCS, 2019).

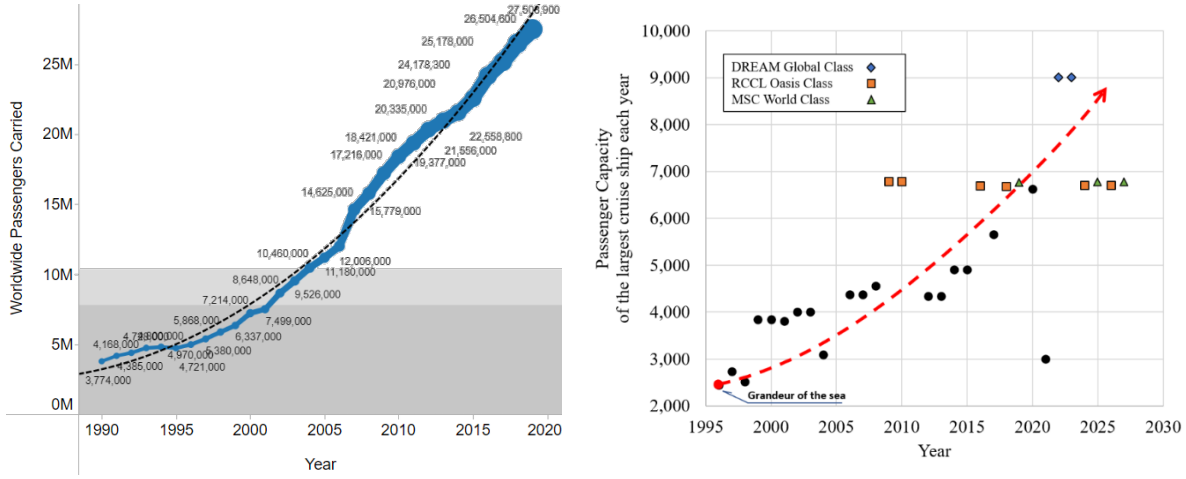

(a) (b)

Figure 1.5 (a) Growth of the ocean cruise line industry from 1990 to 2019 (Cruise Market Watch, 2022), (b) The maximum passenger capacity of the largest cruise ship of each year, including the vessels on order from 1999 to 2027

It should be noted that large vessels have higher unique risks than others. In particular, port facilities and salvage equipment to handle large ships are specialised and limited, which are also more expensive than other size vessels. Higher fatalities, in turn, may be expected if the evacuation of passengers or the initial emergency rescue is failed or delayed after casualties. Therefore, insurers may suffer from significant claims from fatalities, salvage, and vessel repair. In the case of the Costa Concordia, it remains one of the most expensive marine insurance losses at almost 2 billion USD in modern times (AGCS, 2021).

1.2 Evolution of Damage Stability

Since the Merchant Shipping Act 1854, known as the first legal requirement for ship safety concerning subdivision with watertight bulkheads, a number of regulatory provisions and treaties had been developed and adopted in the framework of national bodies until the sinking of the *Titanic* in 1912. It triggered the first International Convention for the Safety of Life at Sea (SOLAS) in London in 1914. Then, the first specific damage stability criterion on stability standards was established in SOLAS 1948, which was based on a deterministic approach such as maximum heeling angle and no margin line immersion at any damage cases by damage extents defined.

After the collision accident between *Andrea Doria* and *Stockholm1*with combined fatalities of 51 in 1956, the residual stability criterion with the requirement for a minimum residual GM of 0.05m was introduced at SOLAS 1960. It was the first specific attempt for a margin to

compensate for the upsetting environmental forces, making significant inroads into the following damage stability standards. A probabilistic method for damage stability was also adopted in 1973 as an alternative to the deterministic approach(IMO, 1973). In 1987, the *Herald of Free Enterprise* capsized due to bow waves and flooding, with the loss of 193 lives. It strongly influenced enhancements of damage stability requirements in SOLAS 1990. The probabilistic method of damage stability for cargo ships was adopted in SOLAS 1992, based on Res.A.265(8).

Another catastrophe, *the Estonia* accident, occurred in the Baltic Sea after the bow visor broke off in strong weather, and 852 lives were lost in 1994. After that, the regional agreement (so-called Stockholm Agreement) was adopted for Ro-Ro passenger vessels by the North West European Nations and later by the whole EU, Australia and Canada. *The Estonia* accident triggered a new damage stability framework proposed by the North West European Nations based on probabilistic methods to IMO in 1995. Then, the harmonization process was carried out to achieve unified rules for all types of vessels. A probabilistic framework was developed based on the EU project HARDER (2000-2003), "*Harmonization of Rules and Design Rationale*", and it was finally approved in SOLAS 2009.

In 2012, *the Costa Concordia* struck an underwater rock, capsized and sank in shallow waters by side grounding damage, and 32 persons on board lost their lives. Based on recommendations arising from the investigation into this accident, the substantive review of SOLAS 2009 has been made, focusing in particular on new passenger ships. In 2017, IMO adopted a set of amendments (IMO, 2017a)) to SOLAS chapter II-1, with an expected entry into force 1st of January 2020, amending, among other things, the regulations on the Required Subdivision of passenger ships to increase their safety, as well as regulations related to the stability information to be provided to a ship's master.

1.3 Problem Statement

The current SOLAS regulations for ship damage stability are insufficient to accommodate the current risks and to allow new safety designs as it was established from pre-determined probabilistic damage distributions based on past accident damage statistics.

1.3.1 Problem 1: Ship structural design and arrangements to be disregarded

The major premise of the current SOLAS requirements for damage stability is that floodings

have already taken place. This means that the collision resistance is not taken into account when assessing damage stability of vessels. In turn, crashworthy or strengthened side structures are treated in the same ways as single-hulled ships. What if the new materials, such as high-yield steel (i.e., HY-80/130) used for submarines, carbon nanotube or graphene in the aerospace industry, or even ultra-hard 30X cold-rolled stainless steel for Tesla's Cybertruck in Figure 1.6, would be applied to the outer shell of ships against ship collisions?

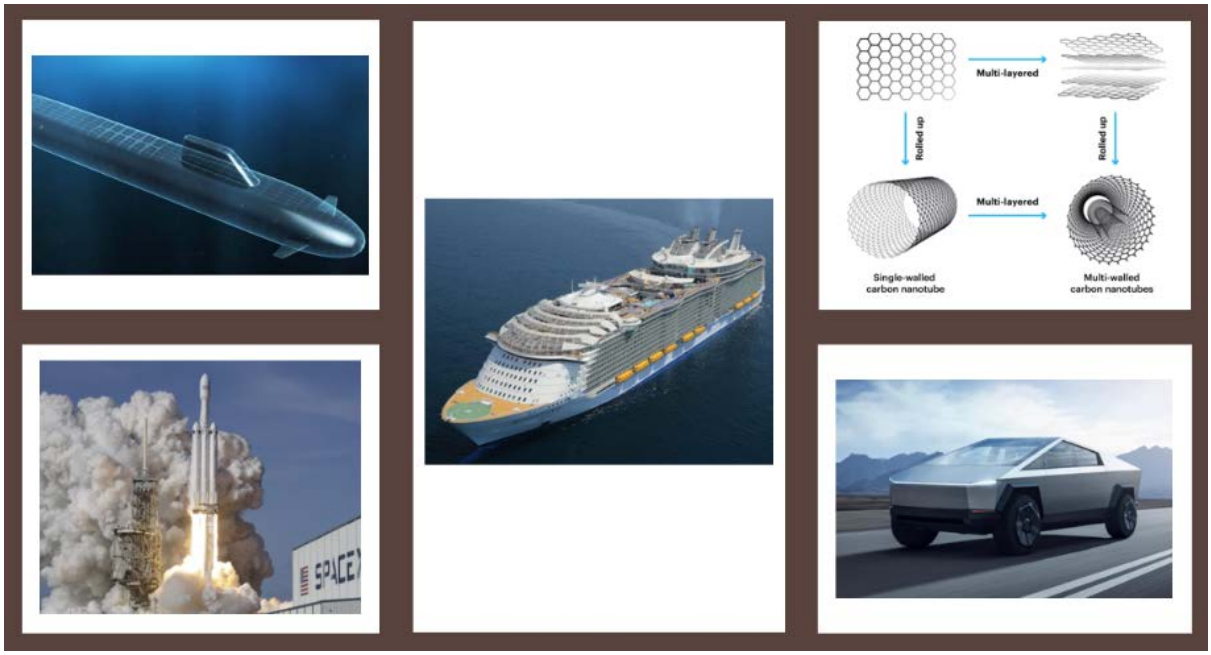

Figure 1.6 How can we evaluate ships made of new materials from the damage stability perspective?

Of course, IMO opens the door for innovative designs by providing alternative design processes such as "New Technology Qualification (NTQ)" procedures and the approval process of "Alternative Design and Arrangements (AD&A)". However, these assessment methods are too time-consuming and require expertise. Thus, it is not widely available in the market.

1.3.2 Problem 2: Limited solutions focusing solely on s −factors

To date, the shipbuilding industry has mainly focused on how to increase local s-factors (ship survivability at certain damage cases) to achieve a higher overall Attained Index A (i.e., A = $\sum(p \times s)$, see Section 2.2.2.2). Since SOLAS 2020 assumes that flooding takes place already for each damage case, there is no way to improve the p-factor (i.e., the probability of damage occurrence of a specific damage breach at a given location and side of the ship). Accordingly, only the s-factor is used to modify ship design by:

- Rearranging transverse watertight subdivisions for new ships and adding extra bulkheads, side tanks or side sponsons for existing ships (See Figure 1.7 (a))

- Decreasing vertical centre of gravity (KG) (See Figure 1.7 (b))
- Changing ship dimensions, such as increasing ship breadth and depth (See Figure 1.7 (c),(d) and (e))

These solutions are widely adopted as risk control options (RCOs) in many projects, including many research projects (FLARE, 2019-2022, EMSAIII, 2013-2016). Even though these solutions contribute to the local *s*-factor increase, it should be noted that they give rise to the following side effects.

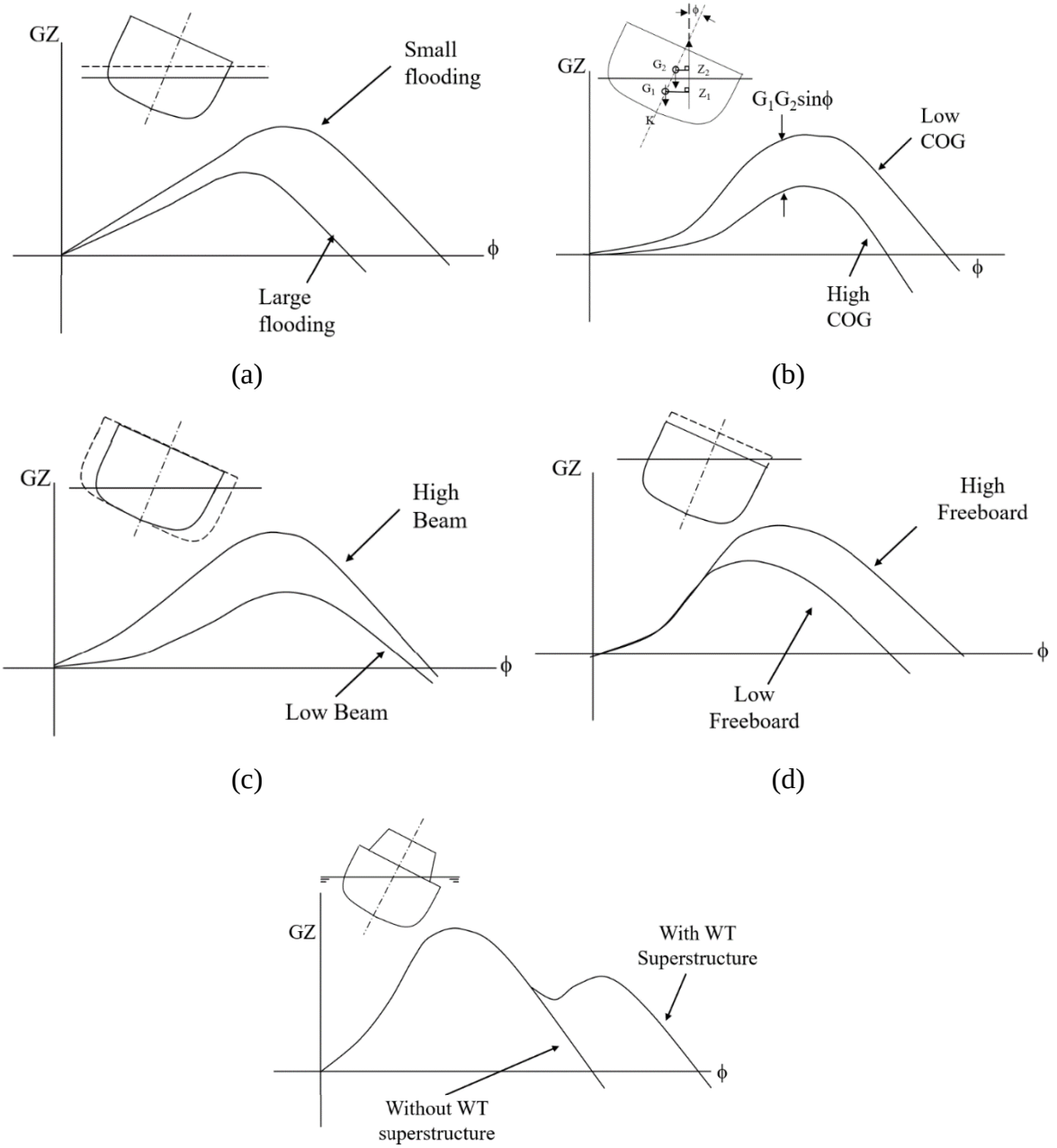

Figure 1.7 Typical righting arm curves depending on changes of (a) floodwater amount, (b) KG, (c) Breadth, (d) Depth and (e) additional watertight superstructure. [(b),(c),(d),(e) (Wilson, 2018a)]

Firstly, the installation of additional transverse watertight bulkheads helps the total flooding volume from damages to reduce. If flooding occurs symmetrically, a higher GZ curve will be obtained with high survivability (s factor), as shown in Figure 1.7(a). This measure is too expensive to improve only local s-factor since it requires not only material and labour for the manufacturing of new bulkheads but also the other associated systems and designs, such as fire insulations, additional dedicated HAVC, increased electric cables for power and lighting, penetrations fitting of pipe/cable/ducts, and additional access or escape route.

Secondly, reducing the vertical centre of gravity (VCG or KG) also provide benefits to increase ship survivability (i.e., s-factor) from a transverse metacentre height (GM_T) increase, as shown in Figure 1.7(b). However, in order to lower VCG, design (internal layout) changes cannot be avoided, and sometimes it requires high cost as well as design compromises. For example, for this VCG reduction, swimming pools on higher decks could be moved to lower decks. Or, the structural material of the upper superstructure also could be changed from mild steel to aluminium to make the upper part of the ship lighter for an overall VCG decrease. In this case, considerable costs should be taken into account, such as expensive aluminium materials, additional insulations, and extra labour costs related to the special welding for aluminium structures and for bimetals between aluminium parts and the rest of the hull.

Finally, a change in the ship's dimensions with a beam increase is the simplest solution to enhance overall ship survivability by a higher GZ from the higher BM_T (i.e., $GZ \approx GM \sin\theta$, GM=KB+BM-KG, BM = I / ∇, I is the second moment of waterplane area) as shown in Figure 1.7(c). Such a solution may affect the ship's overall performance due to the wide beam of the ship by decreasing ship speed or requiring high propulsion power for the equivalent speed. It will eventually lead to a surge in the overall cost of the ship.

1.3.3 Problem 3: Individual ships' characteristics to be disregarded

According to regulations, each damage length becomes non-dimensionalized by ship length and breadth to cover the different sizes of passenger ships, and identical damage distributions corresponding to the non-dimensional damage sizes are used for each damage case. The problem arises when these standardised damage distributions are applied to all passenger ships regardless of the ship's individual characteristics. This may lead to over- or under-estimation of the actual survivability of the ship design. Of course, this simplification may be reasonable for similar sizes of vessels in damage accident statistics, which is based on the current SOLAS regulation for damage stability. However, it is unrealistic for new ship designs, which are much

larger, more innovative, and very different from past vessel designs. For example, consider two cruise ships of different sizes, as shown in Figure 1.8. *Ship A* is a small expedition cruise ship with 142m in length and 18m in breadth, whereas *Ship B* is one of the largest cruise ships in the world with 294m in length and 47m in breadth. According to the current SOLAS regulations, the maximum damage extent of *ship A* is a longitudinal length of 60m and a penetration of 9 m, while *ship B* should consider 60m long and 23.5m penetration. That is, *Ship B* must take into account a more severe collision scenario with more damages by 14.5m than *Ship A.*

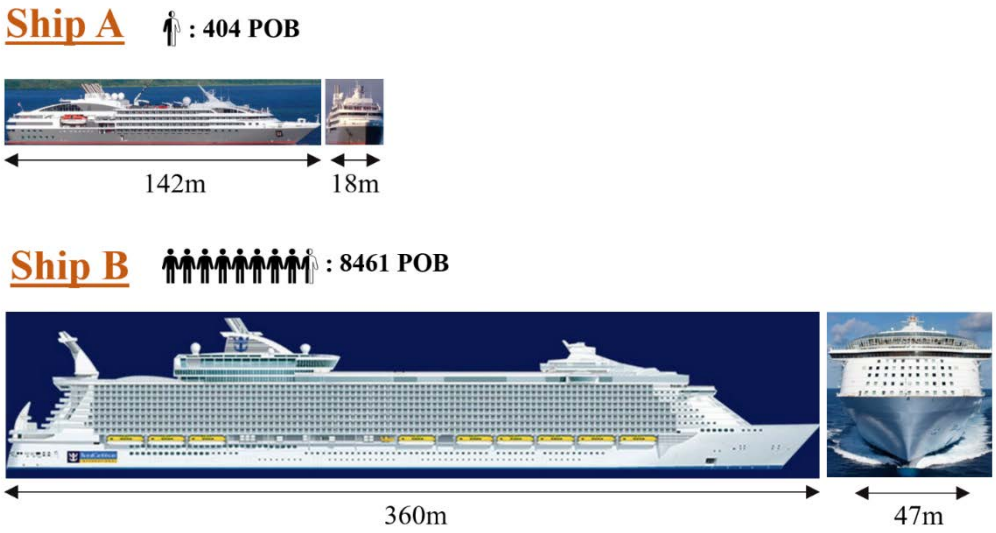

Figure 1.8 142m expedition cruise ship carrying 404 persons on board (Ship A) and 360m cruise ship carrying 8461 POB (Ship B)

Let us assume that two ships operate within the same area, which means they are naturally exposed to the same collision risk. If the majority of ships in the area are small- and medium-sized fishing vessels with low speeds, the damage to ship B from a collision with one of them would be minor, which means that *Ship B* may have a very excessive design. On the other hand, if the area where two ships operate is so busy with ultra-large container ships with high speeds, the damage from one of the container ships to ship B may be endurable based on the current safety requirement. Whereas a striking container ship to ship A may break through the entire breadth of the vessel, leading to possible ship loss with many fatalities after capsizing. In this case, *ship A* may have an insufficient design in terms of structural strength and damage stability from this kind of collision.

Therefore, a new methodology to evaluate the safety level of damage stability is sincerely required, which should be more realistic and specific, taking into account vessels' individual characteristics.

1.4 Objectives and Scope of Work

1.4.1 Aim and Objectives

In Section 1.3, this thesis points out the primary three current problems of SOLAS, namely:

- The damage stability framework ignores ship structural design and arrangements
- The current SOLAS solely open to s-factor for design solutions
- Individual ships' characteristics are disregarded for ship damage stability design

In order to address these problems conceptually, procedurally and methodologically, this thesis proposes a novel methodology of damage stability evaluation for new designs that utilises crashworthiness analysis, in this manner equivalent to the prevailing regulations.

The following objectives have been set forth to achieve the primary aim:

- **Comprehensive review for damage stability and crashworthiness:**
  From historical developments of damage stability, the fundamentals and direction of the regulatory framework can be understood and predicted the future development. For direct assessment, as one of the damage stability enhancement methods, the state of the art technics and the associated uncertainties of crashworthiness analyses can also be identified.
- **The development of a methodology**
  The Formal Safety Assessment (FSA) procedure defined by IMO is a great guideline for developing a new methodology in an official manner. Especially, emphasis in this methodology is on Quantitative Risk Assessment, which should focus on the crashworthiness analysis along with scenario selections. In particular, the application of the proposed methodology to a high-risk zone is recommended to achieve the most efficient outcomes based on the identification and classification of the local risks for each zone.
- **The proper application and verification of time-domain simulations for crashworthiness analyses**
  The proposed methodology adopts crashworthiness analyses, and reliable analysis results are essential. Therefore, standardised procedures and technics for time-domain simulations are required to be set up from a wide range of reviews of crashworthiness analysis research.

- **The methodology demonstration with the cost-benefit assessment**
  The case study should be presented to deliver the overall methodology concept, combining each step's methodology into integrated systematic procedures. Furthermore, in the demonstration, the cost-benefit assessment should be employed to select an optimum solution among RCOs.
- **The implementation of sensitivity study for various parameters**
  Variations always exist in any analysis with assumptions and simplifications. Therefore, it is also critical to investigate them for design margins and limitations of the methodology for future study.

1.4.2 Scope of Work

The following detailed scope of work has been devised to reach the thesis aim and objectives.

- Review of wide range of literature to understand both damage stability and crashworthiness and to identify the gaps and opportunities for their combinations.
- Development of the overall methodology for damage stability evaluation as a Quantitative Risk Assessment
- Assessment of damage stability based on the current regulations to identify risk status of a target ship and RCOs suggested
- Development of a methodology to classify vulnerable zones in order of highest risk
- Definition of a collision scenario case
- Execution of FE analyses with proper set-up using modern technics
- Development and implementation of risk control option designs
- Implementation of cost-benefit assessment
- Demonstration of a case study with the proposed methodology application
- Performance of sensitivity study in relation to variation of essential parameters employed in FE simulations

The primary aim is to offer a methodological approach to consider crashworthiness as a credible risk control option for damage stability enhancement in a Quantitative Risk Assessment framework.

1.4.3 Thesis Structure

Chapter 1, as the introductory chapter, outlines the potential risks of cruise ships due to economies of scale. Based on that, the main problems of SOLAS regulations are discussed, and the aim and objective of this thesis to be set forth are introduced.

Chapter 2 outlines key findings and observations made through extensive literature reviews for both damage stability and crashworthiness analysis. The historical developments are reviewed to fully understand the fundamentals and recent technics.

Chapter 3 suggests the overall concept of the proposed methodology to enable the evaluation of new structural designs, which focuses on collision accidents based on Quantitative Risk Assessment.

Chapter 4 describes the details of the nonlinear finite element method, including geometric model extent, finite elements type and size, material property modelling, structural failure criteria, contact and friction definition and external dynamic application for ship motions induced by the surrounding water. Verifications of FE analyses employed in this thesis are carried out using well-known experiments for collisions and groundings by ISSC. Furthermore, the results of a benchmark study for collisions (FLARE, 2019-2022).

Chapter 5 describes risk control options (RCOs) and cost-benefit analysis methods. A total of five types of RCOs, including four structural types and one non-structural type, are described. Structural type RCOs involve a single longitudinal subdivision (i.e., well-known as double-hull design), an internal safe space concept with two additional longitudinal watertight subdivisions, different hull thicknesses, and their combinations. The non-structural type RCO is to adopt the foam void-filling concept. In order to calculate the cost-effectiveness of each RCO, the cost-benefit assessment is employed, using the Gross Cost of Averting a Fatality (GCAF). The total cost of each RCO is estimated from the summation of capital expenditure (CAPAX) and operational cost (OPEX). The risk improvement of each RCO is obtained from potential loss of life (PPL), using the Attained Subdivision Index for each RCO calculated from damage stability assessment and risk models developed in GOALDS (2009-2012) and EMSAIII (2013-2016) projects.

Chapter 6 demonstrates a case study with the application of the proposed methodology using collision accidents between a 63,000 GT cruise ship and a 45,000 GT RoPax vessel. The vulnerability analysis and relative collision speed selection were initially carried out to identify

a target zone for RCOs application and a collision scenario. Then, 26 RCOs with five different types were applied to the target zone, and each collision simulation was conducted to obtain actual penetrations. The updated local p-factor distributions were reflected in the damage stability calculations, contributing to Attained Subdivision index improvement. Finally, optimum solutions were selected following the cost-benefit analyses.

Chapter 7 deals with a sensitivity study for uncertainties of time-domain simulations to identify design margins and future works. Four main parameters were investigated: structure failure criteria, rigid and deformable striking body, the definition of stress-strain material curves, and friction coefficient.

Chapter 8 discusses the proposed methodology results derived from the case study and sensitivity study from the damage stability and crashworthiness analysis perspectives. Based on them, the remaining challenges and further recommendations to develop for future works are described. Then, the conclusions of this thesis, with a summary of the work and contributions, were presented.

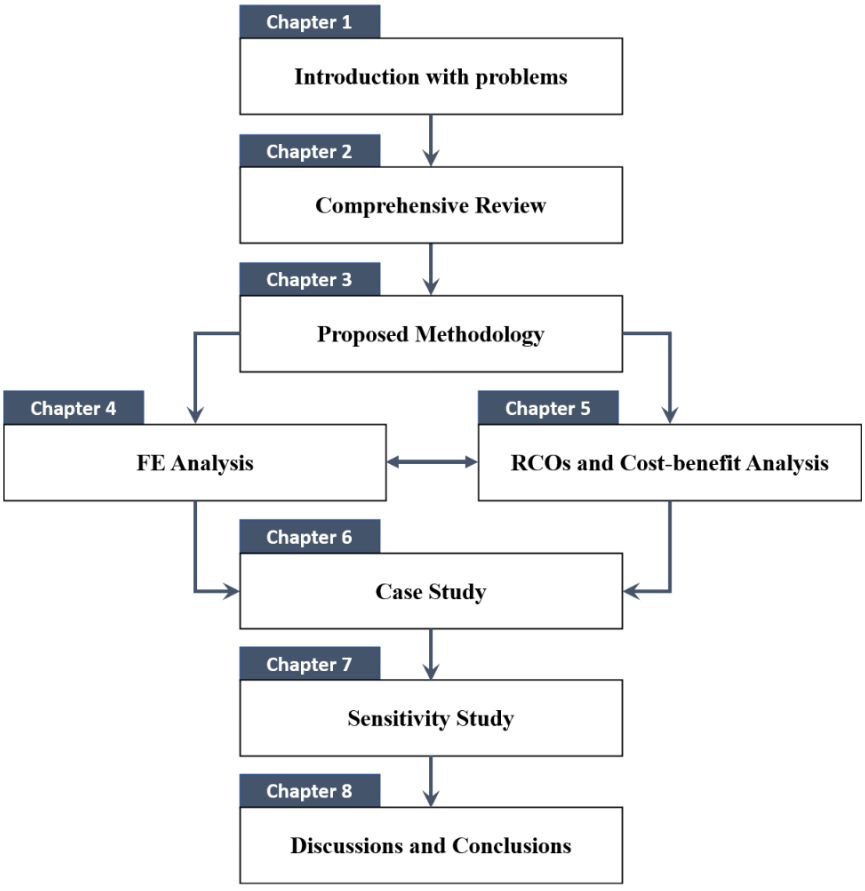

Figure 1.9 Thesis Structure

Chapter 2

Comprehensive Review

2 COMPREHENSIVE REVIEW

2.1 Preamble

In this chapter, methods and approaches that have been suggested and established in the past few decades for ship damage stability and crashworthiness analysis are summarised. In Section 2.2, historical developments of damage stability regulations in SOLAS are described for both deterministic and probabilistic approaches. Those provide insight into future developments based on the understanding of past and current regulations. In Section 0, an overview of crashworthiness analysis developments is provided. Particular focus is attributed to the material failure criteria for FE analysis as it is the most critical factor for numerical simulations. In Section 2.4, three previous studies that attempted to study the influence of crashworthiness analysis on ship damage stability are reviewed.

2.2 Ship Damage Stability

Ship damage stability can be assessed by probabilistic or deterministic methods. The first version of regulations-based assessment for ship damage stability was established in SOLAS 48 and applied to most international passenger ships for 60 years before SOLAS 2009 came into force. Knowledge and regulations slowly but steadily developed over these years by trial and error and on the basis of semi-empirical procedures following major maritime accidents (Francescutto and Papanikolaou, 2011). Even though the latest deterministic criteria encompassed in SOLAS 1990 for passenger ships are generally considered satisfactory, they are limited in terms of the number of damaged compartments. Furthermore, it has less design flexibility due to the regulations-based nature of the “pass” or “fail” concept. For example, whole damage stability designs would fail if there is at least one damage case not to fulfil the criteria. In order to address the above, a probabilistic method for damage stability for passenger ships was adopted at MSC80 in SOLAS 2009. A probabilistic approach for damage stability was firstly suggested by Wendel (1960) as an alternative to the deterministic requirements of SOLAS 1960, especially for RoPax with large holds below a bulkhead deck. Then, it was adopted in SOLAS 1974 as an alternative requirement. Interestingly, it was dry cargo ships that this probabilistic requirement was first applied by IMO (1990). This is the reason why the harmonisation process for the probabilistic requirements was needed for both passenger ships and cargo ships in SOLAS 2009. The probabilistic method considered all possible damage cases with the maximum longitudinal damage of 60m, transverse damage of B/2 and unlimited

vertical damage based on the zonal approach. On the other hand, the deterministic approach in SOLAS 90 defined the maximum longitudinal damage extent as 11m, transverse damage of B/5 and no limitation in vertical direction. Using the product of damage probability p_i and survivability s_i, the ship damage stability is accepted if the summation of the product for all damage cases (i.e., Attained Subdivision Index A) is greater or the same as the required value (i.e., Required Index of subdivision R). In other words, it allows some failure cases if the summation of the other cases satisfy the given criteria. Therefore, it shows more flexibility than the deterministic requirements from a ship design perspective.

Damage stability requirements utilising both deterministic and probabilistic methods are still used for different ship types with different rules and regulations, as indicated in Table 2.1.

Table 2.1 Overview of damage stability frameworks using probabilistic or deterministic methods

Regulatory Framework	Ship types	Application & Criteria	Approach
SOLAS2020 (Ch.II-1/Reg.6, 7,7-1,7-2,7-3)	Passenger ships Cargo ships	All damages : $A \geq R$ $A = \sum p_i \times s_i$	**Probabilistic**
SOLAS2020 (Ch.II-1/Reg.8, 9)	Passenger ships	Front Damages : $S_i = 1$ Side Damages : $S_i \geq 0.9$ Bottom damages : $S_i = 1$	**Deterministic**
The Stockholm agreement (2003/25/EC)	Ro-Pax	Same as SOLAS 90, but - water-on deck up to 0.5m on roro deck - Maximum B/5 penetration	**Deterministic**
SPS Code (Special purpose ships code) (Ch.2)	Special purpose ships	All damages : $A \geq R$ $A = \sum p_i \times s_i$ But, R is based on SOLAS2009	**Probabilistic**
1966 ICLL Convention (Reg.27)	Liquid cargo ships All other cargo ships	Single compartment damage - No progressive flooding - Maximum Heel ≤ 15 deg - Minimum GM > 0 - Freeboard ≤ Reg.28	**Deterministic**
MARPOL 2018 (Annex I/ Ch.IV/Reg.28)	Oil tanker	Side & Bottom Damages: - No progressive flooding - Maximum Heel ≤ 25 deg - Range ≤ 20 deg - Minimum GZ ≤ 0.1 m - Area ≤ 0.0175 m radian	**Deterministic**
IBC Code (International bulk chemical code) (Ch.2)	Chemical tankers	Same as MARPOL 2018	**Deterministic**
IGC Code (International liquefied gas carrier code) (Ch.2)	Liquefied gas carriers	Same as MARPOL 2018 except ; - Bottom damage extents - Maximum Heel ≤ 30 deg	**Deterministic**

2.2.1 Deterministic Approach

The first specific damage stability requirements in SOLAS 1948 assumed the maximum damage extent as follows: *" the longitudinal extent of 3.05 metres plus 3 per cent of the length of the ship, or 10.67 metres, whichever is the less, the transverse extent which is a distance of one-fifth of the breadth of the ship measured inboard from the ship's side, the vertical extent is a distance from the top of double bottom to margin line"*. Based on these damage extents, the final condition of the ship after damage should satisfy that the total heel shall not exceed seven degrees, and no margin line should be submerged in all damage cases. The rule assumes that asymmetrical flooding is kept at a minimum, and cross-flooding fittings may be acceptable depending on the Administration. It should be noted that there is no GM requirement in SOLAS 1948. In SOLAS 1960, vertical damage is assumed to extend from the baseline upwards without limit. It also introduced a GM criterion, namely a positive residual metacentric height of at least 50 millimetres (2 inches) as calculated by the constant displacement method in the case of symmetric flooding.

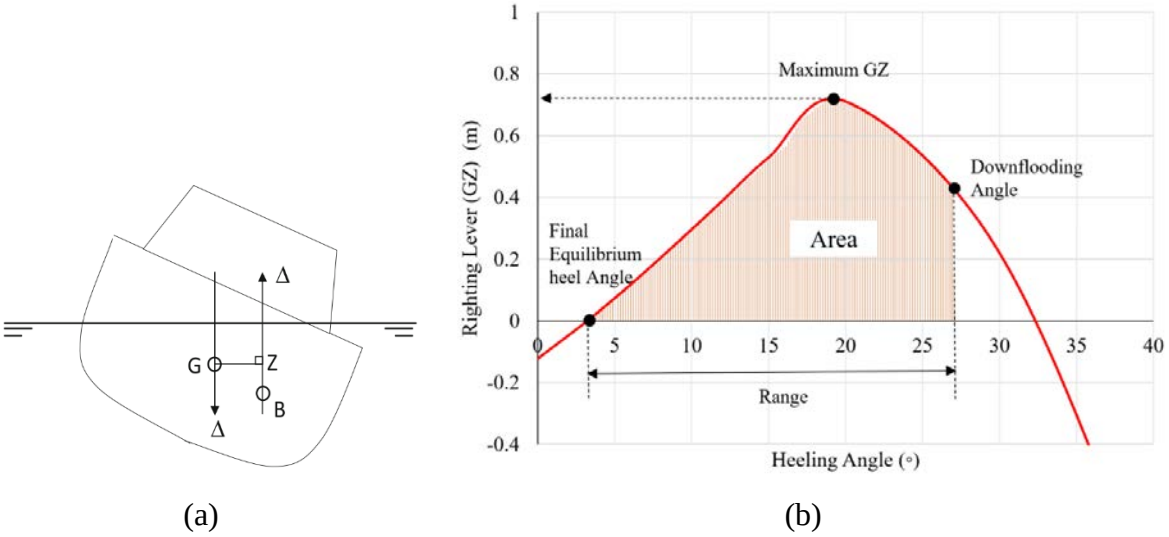

(a) (b)

Figure 2.1 (a)A heeled ship with righting moments in static condition (b) Typical Righting lever GZ-Curve for each damage case

In SOLAS 1990, additional requirements, such as range, area and the maximum right lever GZ (see Figure 2.1), were introduced depending on flooding stages for final and intermediate conditions after damage as follows :

- The maximum longitudinal damage extent was changed to the simple integer number, which is 3 metres plus 3 % of the length of the ship, or 11 metres, whichever is less.
- The maximum heel in the final condition after flooding is required separately for one-compartment and multi-compartment flooding with 7 degrees and 12 degrees,

respectively.

- For the final condition of flooding, the minimum range of 15 degrees beyond the angle of equilibrium is required in the positive residual righting lever curve, and the area under the righting lever curve shall be at least 0.015m-rad, measured from the angle of equilibrium to the lesser angle between progressive flooding angle and 22 degrees for one-compartment flooding or 27 degrees for multi-compartment. The maximum righting lever GZ in a residual righting lever curve shall be greater or the same as 0.1 to take into account the external heeling moments such as passenger crowding on one side, fully loaded survival craft launching on one side, or gust wind pressure.
- For the intermediate stages of flooding, a minimum of 0.05 m for the maximum righting lever GZ and a minimum of 7 degrees of the range are required.

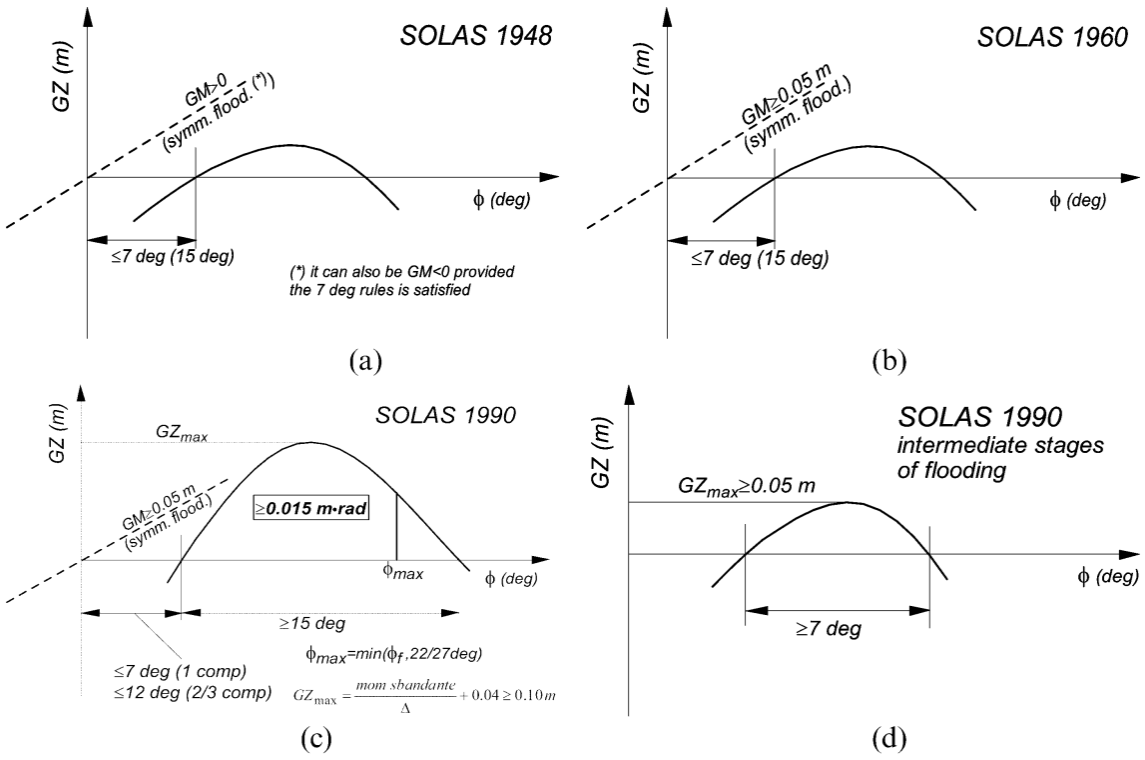

Figure 2.2 Evolution of Deterministic standards for passenger ships in SOLAS from SOLAS 1948 to SOLAS 1990 (Francescutto and Papanikolaou, 2011)

In SOLAS 1991/1992 amendment, these damage stability criteria are applied to all ro-ro passenger ships (Ro-Pax) constructed before SOLAS 1990 to enhance safety. In SOLAS 2009, the prime requirement for damage stability was completely changed from the deterministic approach to the probabilistic methods. However, the deterministic criteria still exist in the current SOLAS 2020 as additional damage requirements for minor damage cases such as front

and side damage collision and grounding. For example, in the case of head-on ship collisions as a striking ship, a survival probability S_i with front damage of 8% ship length should be 1. Additionally, a passenger ship carrying 36 or more persons should have capabilities to withstand damage along side shell and S_i of all damage cases shall be not less than 0.9. In the case of passenger ships intended to carry 400 or more persons, the longitudinal damage extent is defined as a damage length of 3% ship length but not less than 3m, in conjunction with a penetration inboard of B/10. This value should not be less than 0.75m, and the vertical extent of damage is to extend from the ship's moulded baseline to a position up to 12.5m above the position of the deepest subdivision draught. For the passenger ship with 36 persons on board (POB), the longitudinal extent is decreased from 3% to 1.5%, and the transverse damage is also defined as B/20 instead of B/10.

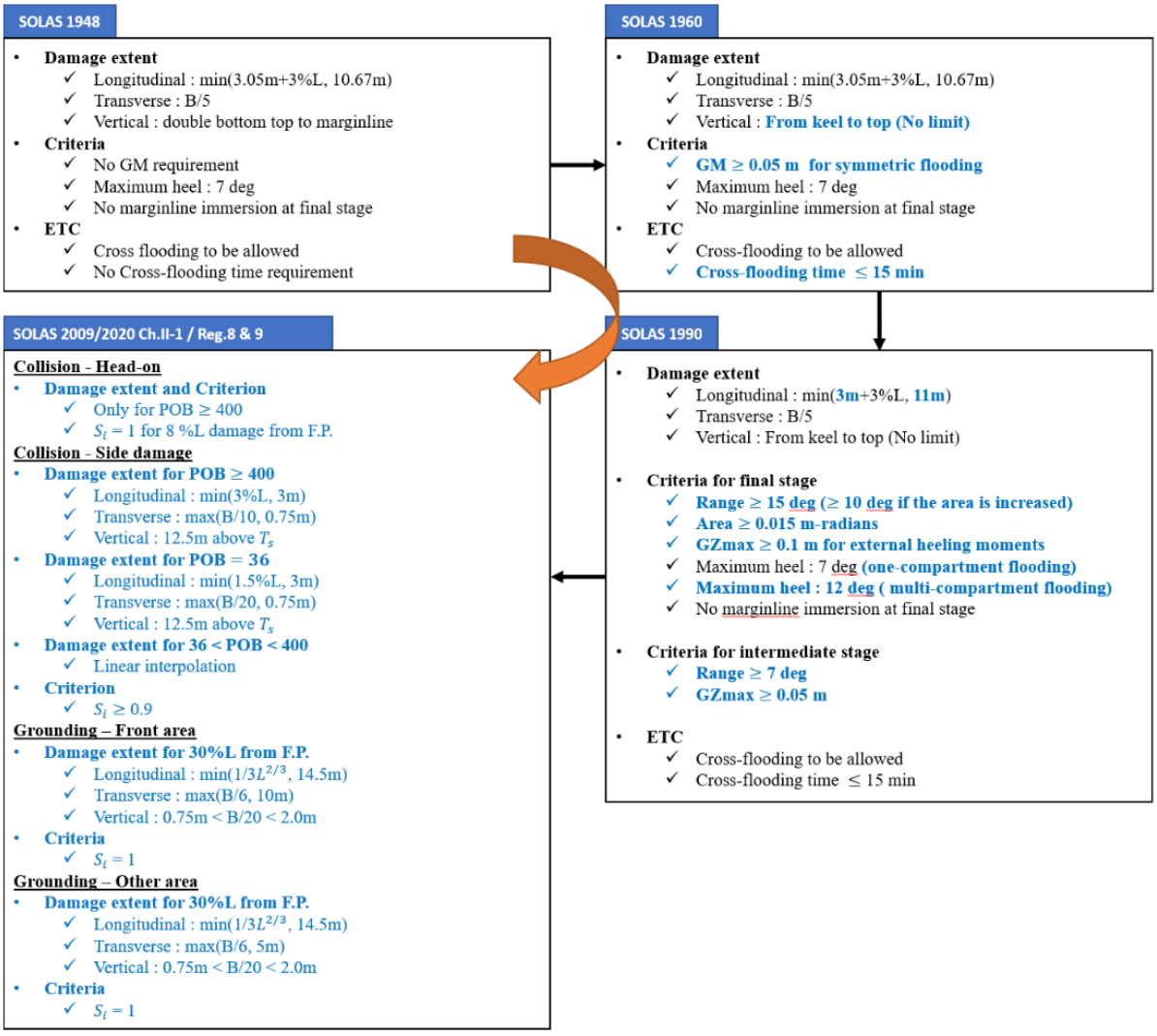

Figure 2.3 History of Deterministic requirement developments in SOLAS

Where more than 36, but fewer than 400 POB are carried, the values of damage length and penetration inboard, used in the determination of the assumed extent of damage, are to be obtained by linear interpolation between values of damage length and penetration. This regulation applies to ships carrying 36 persons to 400 persons. In addition to these minor collision criteria, deterministic requirements for bottom damage cases are also introduced in SOLAS 2009. Regardless of the number of persons, for passenger ships not to have a proper double-bottom arrangement, the regulations require S_i = 1 for that the ship is capable of withstanding bottom damages. Figure 2.3 describes the summary and the developments of deterministic requirements in SOLAS over time.

2.2.2 Probabilistic Approach

The probabilistic requirements are implemented by two factors. One is a Required Subdivision Index R, which is a "*safety factor"* defined based on past ship accident statistics and generally accepted as safe enough criteria, corresponding to ships' size and the number of people onboard exposed to collision hazards. The other factor is an Attained Subdivision Index A, representing the target ship's actual safety level depending on its design. Therefore, the Index A should be achieved with the same or greater than the Index R to show that the vessel has sufficient capability of safety against damage compared to the past ships with accidents.

$$A \geq R \tag{2.1}$$

2.2.2.1 Required Subdivision Index : R

The first probabilistic requirement for passenger ships in Resolution A.265(8) (IMO, 1973) was adopted in SOLAS 1974 as an alternative method instead of the deterministic approach for passenger ships' damage stability in SOLAS 1960. The initial subdivision Index R for passenger ships is determined from subdivision length, the total number of persons on board and lifeboats capability based on IMO accidental data from 1960s:

$$R = 1 - \frac{1000}{4L_s + N + 1500} \tag{2.2}$$

Where L_s indicates the subdivision ship length; N is a summation of N_1 and $2N_2$, N_1 is the number of persons for whom lifeboats are provided and N_2 is the number of persons, including officers and crew, that the ship is permitted to carry in excess of N_1.

When the probabilistic method was adopted in SOLAS 2009 as the main criteria for damage stability for passenger ships, the Required Subdivision Index R was enhanced as Equation (*2.3*) (Eliopoulou and Papanikolaou, 2004, IMO, 2005) based on the harmonisation research outcome from HARDER (2000-2003) project (see Figure 2.4).

$$R = 1 - \frac{5000}{L_s + 2.5N + 15225} \tag{2.3}$$

The damage distributions supporting the above were significantly updated with statistical samples of damage data up to the year 2000, along with additional damage data from numerical collision simulations.

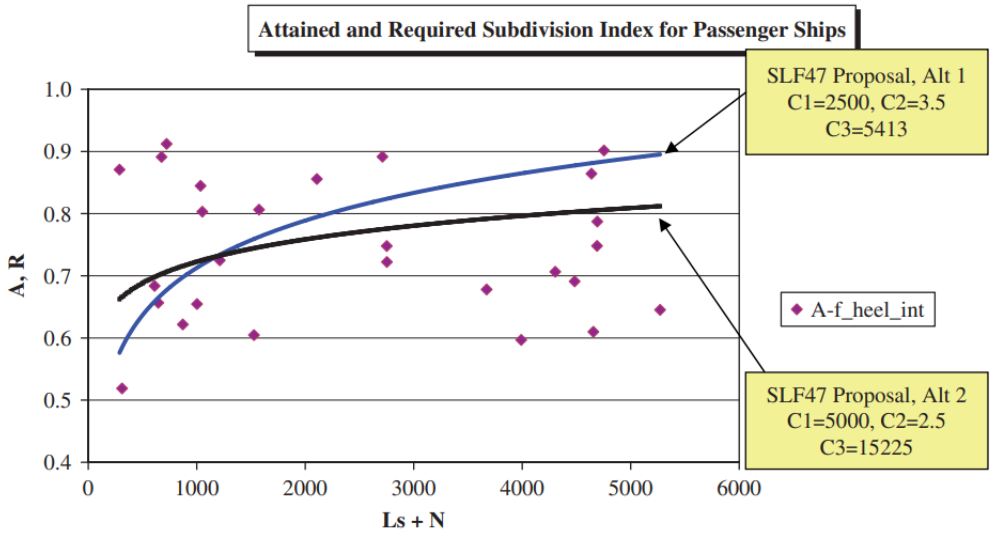

Figure 2.4 The subdivision required Index proposal in SLF47. Finally, Alt2 was adopted in SOLAS 2009

Vassalos and Jasionowski (2011) raised fundamental concerns as these probabilistic rules were initially developed based on cargo ship damage statistics of only 296 ship collisions occurring in the 1950s and 1960s. Under these circumstances, the damage stability research shifted towards large passenger ships (Vassalos, 2016). Consequently, a series of projects initiated GOALDS (2009-2012), EMSA(2009-2012), EMSAIII (2013-2016), eSAFE (2016-2018) and DGMOVE (2017-2019). A new Required Subdivision Index was approved under IMO Resolution MSC421(98) in SOLAS 2020 (IMO, 2017a), as shown in Figure 2.6:

$$\begin{aligned} R &= 0.722 && \text{for } N < 400 \\ R &= N / 7{,}850 + 0.66923 && \text{for } 400 \le N \le 1{,}350 \\ R &= 0.0369 \times Ln(N + 89.048) + 0.579 && \text{for } 1350 < N \le 6{,}000 \end{aligned} \tag{2.4}$$

$$R = 1 - \frac{(852.5 + 0.03875 \times N)}{(N + 5{,}000)} \qquad \text{for } N > 6{,}000$$

where, N is the total number of persons on board

However, the safety level was more relaxed than the initial proposal of the GOALDS project, which might be compensated for the political dictate or industrial requirements, as shown in Figure 2.5 and Figure 2.6.

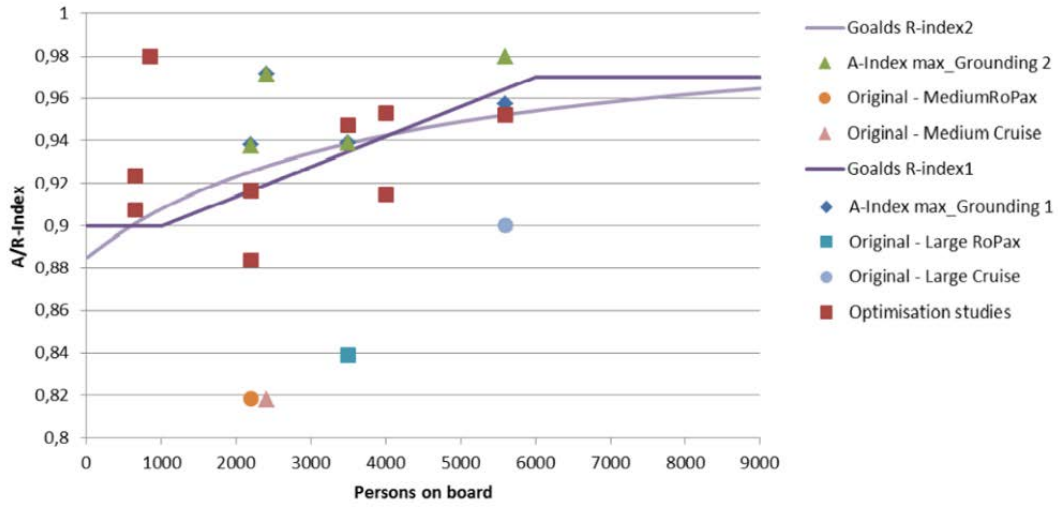

Figure 2.5 GOALDS Proposal for Required Subdivision Index R from risk model A

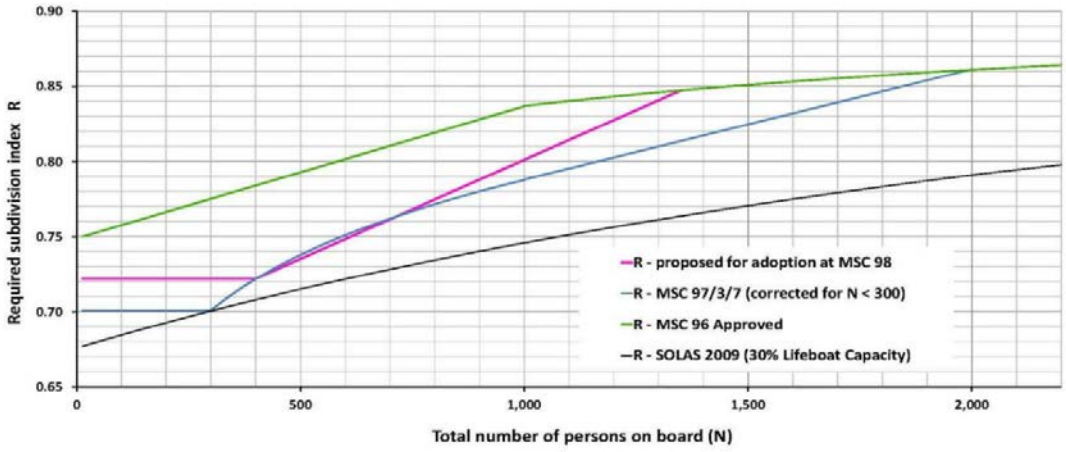

Figure 2.6 Accepted MSC98 proposal for Required Subdivision Index R for SOLAS2020 compared to other proposals. (MSC 98/3/3)

2.2.2.2 Attained Subdivision Index: *A*

The Attained Index A is a summation of contributions from all damage cases, using the product of the probability of damage occurrence (i.e., so-called p-factor) and the probability of ship

survival from the flooding by the damage (i.e., so-called s-factor) as:

$$A = \sum p_i \times s_i \tag{2.5}$$

where, i indicates the number of damage cases; p_i denotes the damage probability of each damage case, and it is generally named as p- factor; On the other hand, s_i accounts for survival probability when each compartment or group of compartments is flooded at each damage case and is generally named as s- factor.

The total Attained Subdivision Index A is calculated from the summation of three different indices weighted at different loading conditions, such as the deepest subdivision draught (d_s), a partial subdivision draught (d_p) and the lightest service draught (d_l) as follows:

$$A = 0.4\,A_s + \ 0.4\,A_p + \ 0.2A_l \tag{2.6}$$

where, A_s, A_p and A_l represent each Attained Index calculated for the draughts d_s, d_p and d_l, respectively.

In order to calculate Index A, the damage cases should be defined in advance. Thus, the target ship is divided into a fixed discrete number of zones in longitudinal, transverse and vertical directions having watertight integrity, as shown in Figure 2.7. This is known as the zonal approach. Primarily, a longitudinal zone, which is called simply *zone*, is defined as a longitudinal watertight subdivision interval of the ship within the subdivision length (IMO, 1991, Wilson, 2018b).

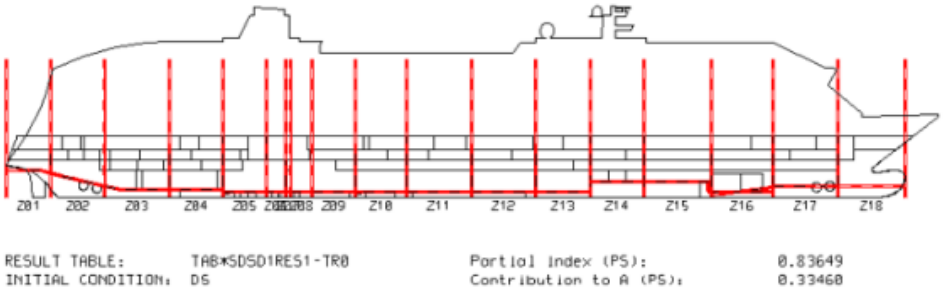

Figure 2.7 Typical ship subdivision

The p-factor of each damage case can be broken down to longitudinal (p), transverse (r), and vertical (v) damage occurrence probability as follows:

$$p_i = p \times r \times v \tag{2.7}$$

The detailed formulations for the probability of each direction are not dealt with in this section.

However, it is well presented in Chapter II-1 Regulation 7-1 in SOLAS 2020, and the overall concept is shown in Figure 2.8. According to SOLAS 2020, the maximum damage extents are defined as shown in Table 2.2.

Table 2.2 Maximum damage extent definition of SOLAS 2020 (Ch.II-1/Reg.7-1)

Direction	Maximum Damage extent
Longitudinal extent	60 m
Transverse extent	B / 2 (Distance from outer hull to ship centre)
Vertical extent	No limitation

It is up to designers how many adjacent zones are taken into account for the calculation. If all damage cases up to the maximum longitudinal damage extent of 60m and transverse damage extent of B/2 are considered, the summation of the probability of damage occurrence (p-factor) will be 1. The formulations for the p-factor defined in SOLAS 2009 have not changed in SOLAS2020.

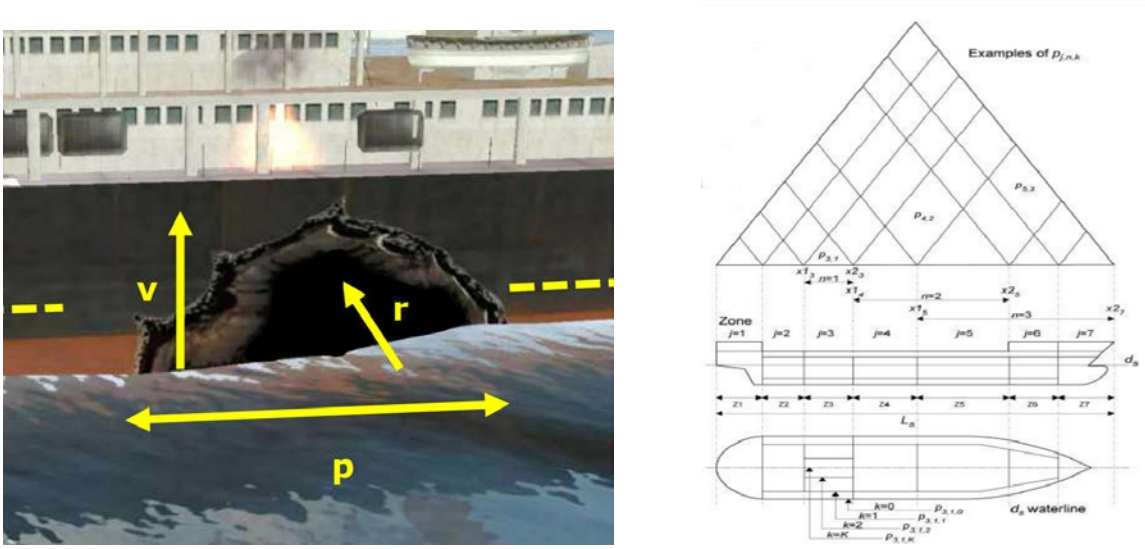

(a) (b)

Figure 2.8 (a) The probability of each direction at specific damage (NAPA, 2017) (b) Schematic diagram for s-factor calculation (IMO, 1991)

Figure 2.9 ~ 2.11 show the simplified probability distribution for each direction damage defined in SOLAS2020, which is assumed to have equal lengths of watertight compartments in a longitudinal, transverse and vertical direction in order to understand the overall shape of distribution easily. Then, they are compared to the HARDER database in 2000 and SOLAS 1992 for cargo ship probabilistic damage stability.

As indicated with a red dotted circle in Figure 2.9(c), the zones located in the middle show the

identical longitudinal probability p regardless of their locations in the ship, while a relatively high value shows in both end zones, especially for single-zone damage cases. Interestingly, two-compartment damage cases show the highest probability among all damage cases, and the sum of single- and two-compartment probabilities account for approximately 85% of total probability, as the damage lengths of them take about 60% (i.e., 18m × 2 zones / 60m) of the maximum longitudinal extent of 60 m as shown in Figure 2.9(d).

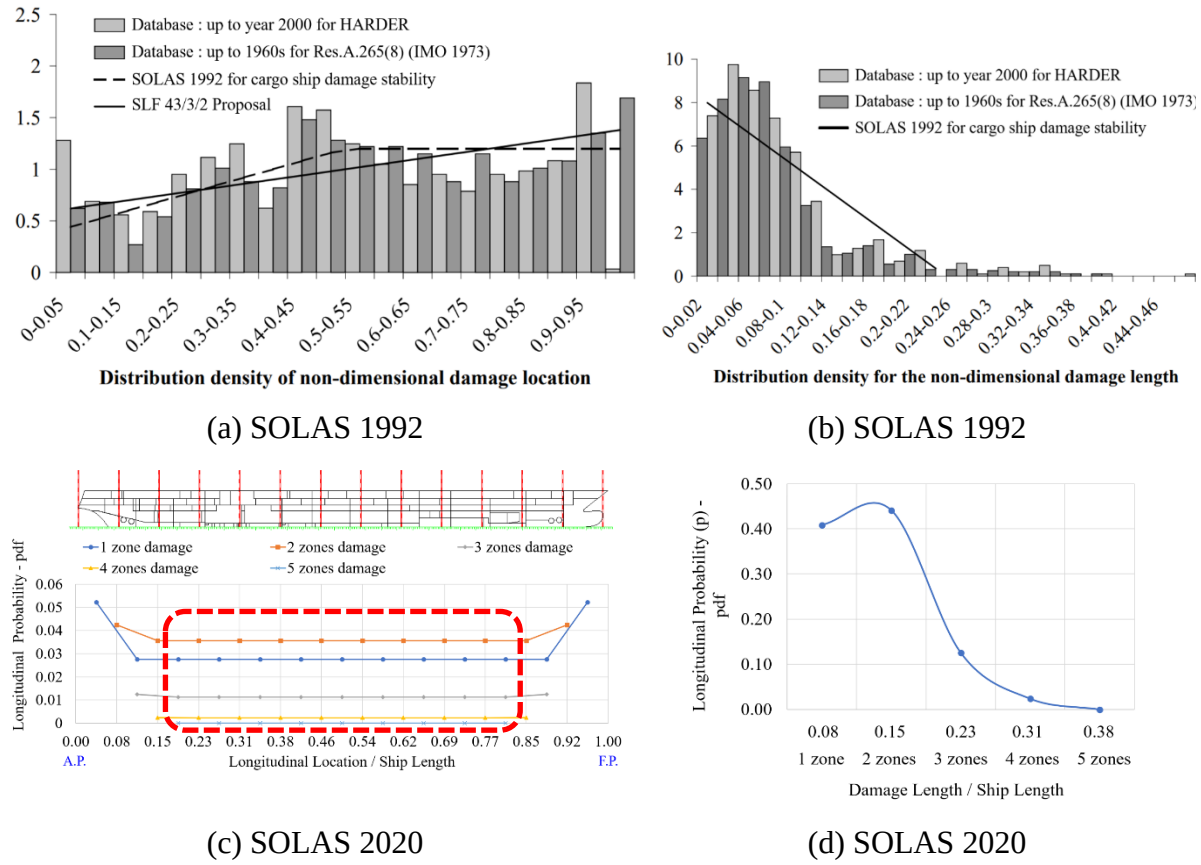

(a) SOLAS 1992 (b) SOLAS 1992

(c) SOLAS 2020 (d) SOLAS 2020

Figure 2.9 Longitudinal distribution density : (a,b) HARDER in 2000 and Res.A.265(8) in 1973 (Lützen, 2001) and (c,d) current SOLAS 2020 with equal subdivisions by 18m. (Left: Damage location, Right: Damage length)

The transverse probability r shows that damages close to the ship sides have a higher probability of damage, as shown in Figure 2.10. It decreases non-linearly until it converges to zero at the ship's centre line. The vertical probability v is only considered when horizontal subdivisions exist above the draught. Otherwise, it is regarded as 1. The probability of each horizontal subdivision above draught is decided proportionally depending on the heights. Therefore, the cumulative vertical probability linearly rises up to the distance of 7.8m from the draught, and it goes up with different slop until it converges 1 in Figure 2.11, based on the following formulae:

$$\begin{cases} v(h,d) = 0.8\dfrac{(H-d)}{7.8} & \textit{If } (H_m - d) \textit{ is less than or equal to 7.8m} \\ v(h,d) = 0.8 + 0.2\left[\dfrac{(H-d)-7.8}{4.7}\right] & \textit{In all other cases} \end{cases} \tag{2.8}$$

where, H indicates the height of each horizontal subdivision measured from a keel of a ship; d denotes the draught of the ship; H_m is the uppermost horizontal subdivision of the ship.

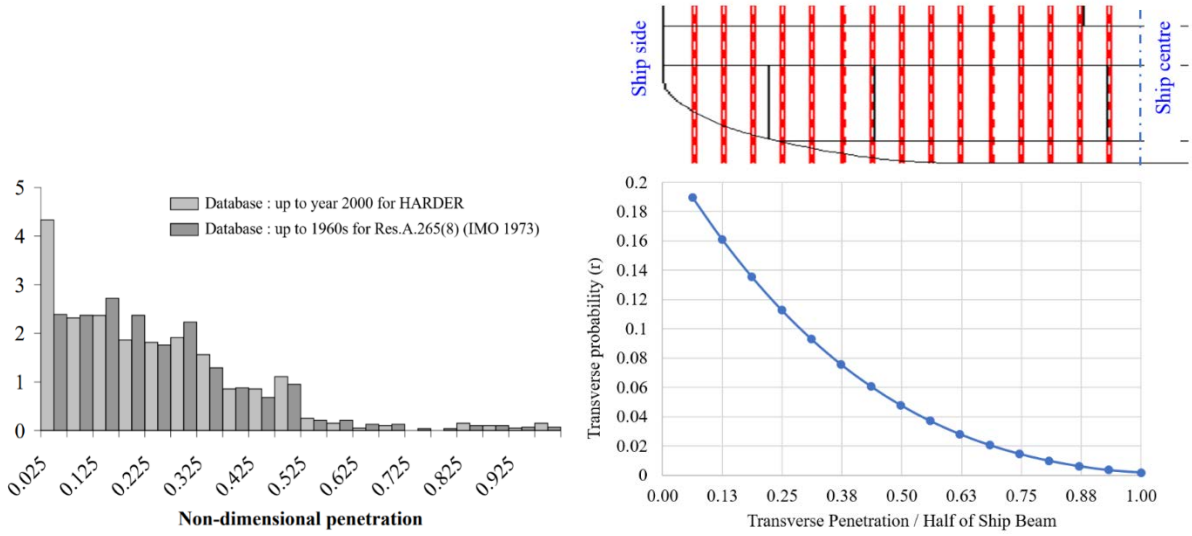

(a) Database (b) SOLAS 2020

Figure 2.10 Transverse distribution density : (a) HARDER in 2000 and Res.A.265(8) in 1973 (Lützen, 2001) and (b) current SOLAS 2020 with equal subdivisions by 1m

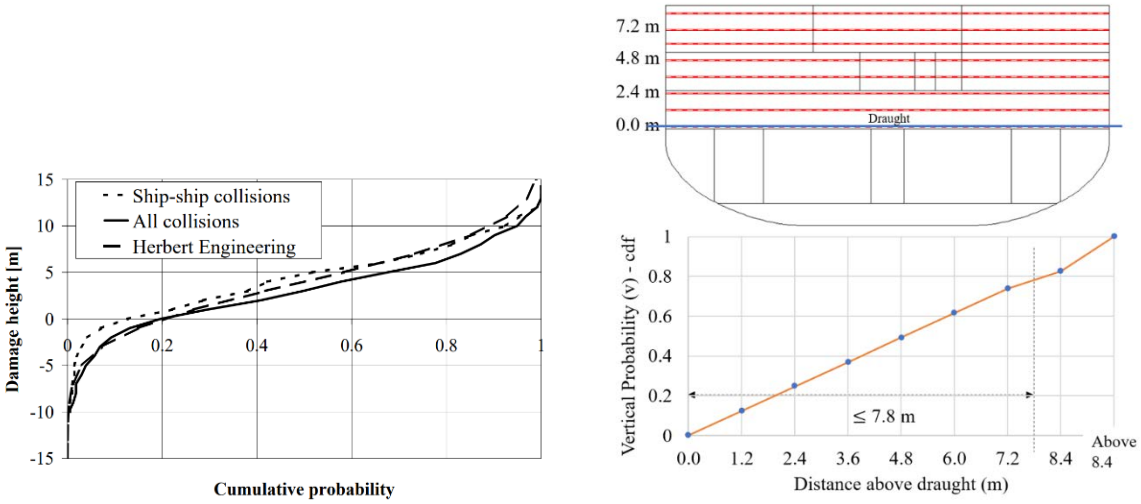

(a) Database (b) SOLAS 2020

Figure 2.11 Vertical cumulative distribution density of damage height :(a) HARDER database (Herbert Engineering, 2001) and (b) current SOLAS 2020 with equal subdivisions by 1.2m above draught

The s-factor is the survival probability of the ship remaining afloat after the damage occurs on the ship when flooding from the specific damage cases occurs. According to SOLAS2009, for determining the s-factor, three different heeling conditions require to be investigated. Those correspond to the intermediate $s_{intermediate\_i}$, final flooding stage s_{final_i} and the maximum heeling moment conditions s_{moment_i} as follows:

$$s_i = minimum\ (s_{intermediate_i}, s_{final_i}, s_{moment_i}) \tag{2.9}$$

$$s_{intermediate\_i} = [\frac{GZ_{max}}{0.05} \times \frac{Range}{7}]^{\frac{1}{4}} \tag{2.10}$$

$$s_{final\_i} = K \times [\frac{GZ_{max}}{0.12} \times \frac{Range}{16}]^{\frac{1}{4}} \tag{2.11}$$

$$s_{moment\_i} = \frac{(GZ_{max} - 0.04) \times Displacement}{M_{heel\_max}} \tag{2.12}$$

$$\begin{cases} K = 1 & \text{, If } \theta_e \leq \theta_{min} \\ K = \sqrt{\dfrac{\theta_{max} - \theta_e}{\theta_{max} - \theta_{min}}} & \text{, For passenger ships, } \theta_{min} = 7^{\circ}, \theta_{max} = 15^{\circ} \\ & \text{, For cargo ships, } \theta_{min} = 25^{\circ}, \theta_{max} = 30^{\circ} \\ K = 0 & \text{, If } \theta_e \geq \theta_{max} \end{cases} \tag{2.13}$$

where, GZ_{max} is the maximum GZ value of a right lever curve at a flooding condition of each damage case; $Range$ is heeling angle range ; M_{heel_max} is the maximum heeling moments and is selected as the maximum value from moments by passengers, wind or survival crafts; K is the coefficient associated with a final equilibrium angle (θ_e), a minimum (θ_{min}), and a maximum angle(θ_{max}).

$s_{intermediate\_i}$ is required only for passenger and cargo ships with cross-flooding devices. Otherwise, it will be 1. In this condition, the maximum GZ value shall not be taken as more than 0.05m and $Range$ as not more than 7°. If the intermediate heel angle exceeds 15° for passenger ships and 30° for cargo ships, the $s_{intermediate\_i}$ shall be zero. If cross-flooding fittings are required, the time for equalization shall not exceed 10 minutes. For final flooding stage s_{final_i}, GZ_{max} is not to be taken as more than 0.12m, and $Range$ is not to be taken as more than 16°. In SOLAS 2020, the s_{final_i} was replaced with the following definition:

$$s_{final\_i} = K \times [\frac{GZ_{max}}{TGZ_{max}} \times \frac{Range}{TRange}]^{\frac{1}{4}} \quad (2.14)$$

where, GZ_{max} is not to be taken as more than TGZ_{max}, and $Range$ is not to be taken as more than $TRange$; TGZ_{max} and $TRange$ are 0.20m and 20° respectively, for each damage case associated with a ro-ro space of Ro-Pax vessels; Otherwise, they are to be taken as 0.12m and 16°, respectively; K is the same as SOLAS 2009.

Figure 2.12 clearly shows how much SOLAS2020 becomes strict in comparison to previous requirements.

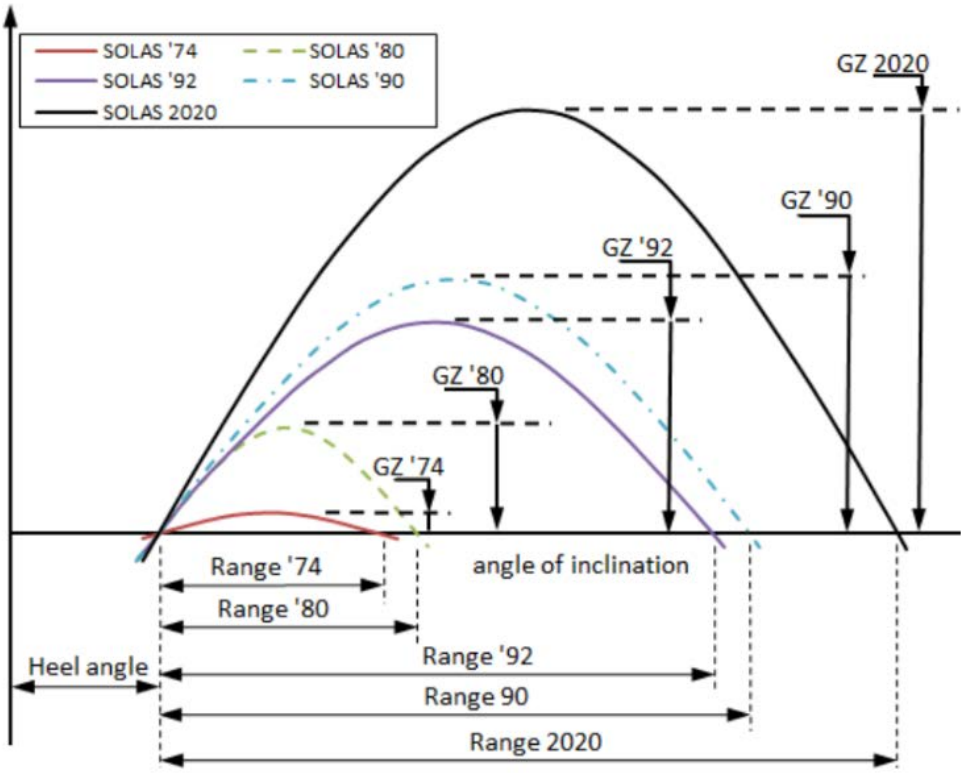

Figure 2.12 Evolution of damage stability requirements in righting lever curve for passenger ships until now (Hutchinson and Scott, 2016)

2.3 Crashworthiness Analysis

It is well known that ship collision dynamics consist of external dynamics and internal mechanics. External dynamics describe the rigid body motion of the ships and collision energy to be dissipated in the structures associated with the collision event. Internal mechanics focus on the local structural response based on the definition of strength or resistance for corresponding ship structures during an accident, as shown in Figure 2.13.

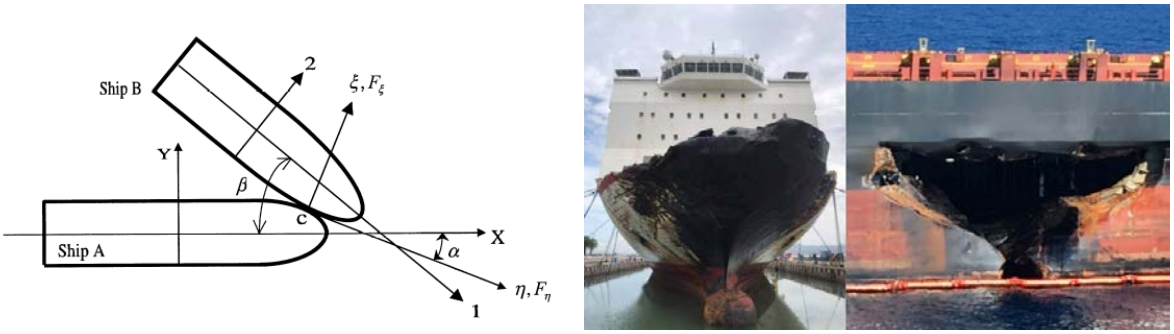

(a) (b)

Figure 2.13 (a) External dynamics (Zhang, 1999) and (b) Internal mechanics

For internal mechanics, four methods have been generally used to estimate structural response. They are classified as empirical, analytical, experimental and FE analysis methods. The key background of each of these methods is presented in the following sections.

2.3.1 Empirical and Analytical Methods

Minorsky (1959) first carried out ship collision research to protect the nuclear reactors in nuclear-powered ships against external collisions. He also proposed the empirical formulation given in Equations (2.15) and (2.16) based on 26 collision cases of actual ship accidents and gives good agreement for high-energy collision accidents (see Figure 2.14).

$$E = 47.2R_T + 32.7\ , (MJ) \tag{2.15}$$

$$R_T = \sum P_N L_N t_N + \sum P_n L_n t_n\ , (m^3) \tag{2.16}$$

where, E and R_T represent the absorbed energy in MJ and resistance factor in m^3 defined as the destroyed material volume of both a striking and a struck ship, respectively; P, L and t are depths, lengths and thickness of damage, respectively; N and n mean members of the striking ship and the struck ships, respectively.

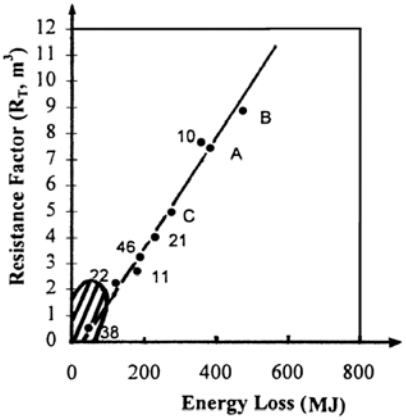

Figure 2.14 Absorbed Energy and resistance factor curve from Minorsky (Minorsky, 1959, Zhang, 1999)

Then, Haywood (1971), Vaughan (1978), Woisin (1979), Jones (1979), and Pedersen and Zhang (2000) developed a method based on the Minorsky formula.

In 1971, Haywood (1971) proposed the modification of Minorsky's formula obtained from the collision assessment in double-hull LNG carriers. He suggested the different constant values to take into account the type of stiffened outer shell as below;

$$E = 47.2R_T + b_1 + b_2\ (MJ) \tag{2.17}$$

where, E and R_T are the absorbed energy and resistance factor; b_1 is 32 for transversely stiffened outer shell or 96 for longitudinal stiffened one; b_2 is the same as b_1 if a longitudinal bulkhead exists, otherwise it is zero

Furthermore, Woisin (1979) developed the constant term using structural members' details based on experimental outputs. He proposed a function of the height of side-shell or longitudinal bulkhead and its plate thickness in 1979, as shown in Equation (2.18). Then, he modified this formula in 1986, considering the distance (d_s) between the nearest plate structure attached to the shell as follows;

$$E = 47.2R_T + 0.5\sum h_s {t_s}^2 \tag{2.18}$$

$$E = 47.2R_T + 0.19\sum d_s h_s t_s \tag{2.19}$$

where, h_s is the height of damaged longitudinal member; t_s is its thickness

On the other hand, Jones (1979) focused on low-energy collisions, as shown in the bottom corner of Figure 2.14. During this minor collision, he found that the membrane energy absorbed by the outer shell and decks is dominant. He considered a rigid perfectly plastic beam, and it

assumed fully clamped supports across a span of $2L_b$ with a concentrated load P_c at the mid span as shown in the following Equation (2.20). In 1983, his method was modified as indicated in Equation (2.21) and compared with the original Minorsky correlation, as shown in Figure 2.15.

$$E = 0.030288\sigma_s R_T (\frac{W_f}{L_b})^2 \tag{2.20}$$

$$E = 0.5\sigma_s R_T (\frac{2W_f}{L_b})^2 \tag{2.21}$$

where, R_T is the volume of side shell to be involved in the membrane mechanism; σ_s is the yield stress; W_f is the final deflection; L_b is a span

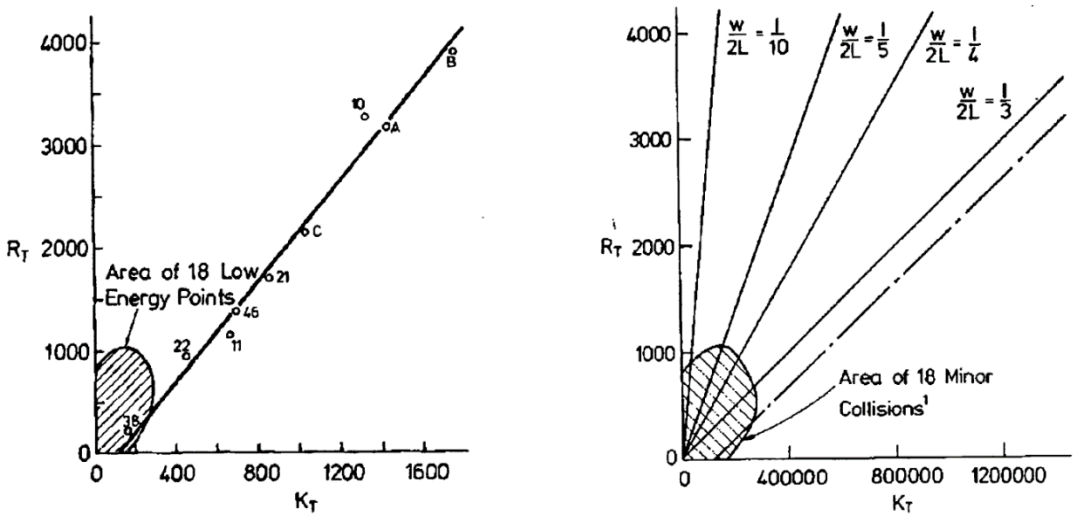

(a) (b)

Figure 2.15 (a) Original Minorsky correlation and (b) Modified Minorsky correlation with $\sigma_s = 207$ MPa by Jones and Wierzbicki (1993), K_t is absorbed energy in ton knot^2 and R_t is resistannce factor in ft^3,

More recently, Pedersen and Zhang (2000) revised the Minorsky method by considering the structural arrangement, the material properties and the different damage modes. In this method, he defined three different formulas of energy absorption depending on different energy absorption mechanisms, such as the plastic tension damage mode (E_1), the folding and crushing damage mode (E_2) and the tearing damage mode (E_3) as follows;

$$E_1 = 0.77\varepsilon_c \sigma_0 R_T \tag{2.22}$$

$$E_2 = 0.35(\frac{t}{b})^{0.67} \sigma_0 R_T \tag{2.23}$$

$$E_3 = 3.21(\frac{t}{l})^{0.6} \sigma_0 R_T \tag{2.24}$$

where, E and R_T are the same as Equation (2.15); $\varepsilon_c = 0.10(\varepsilon_f/0.32)$ and ε_f is the steel

material ductility obtained from a tensile test; σ_0 is the flow stress of the plate; t is the average thickness of the crushed plates; b is the average width of the plates in the crushed cross-section; l is equal to the tearing length; Side collision is E_1+E_2; Bow crushing to fixed wall is E_2; Grounding is E_3

As an analytical method, the detailed theoretical models of structure responses for different structural components were also investigated by various authors as follows:

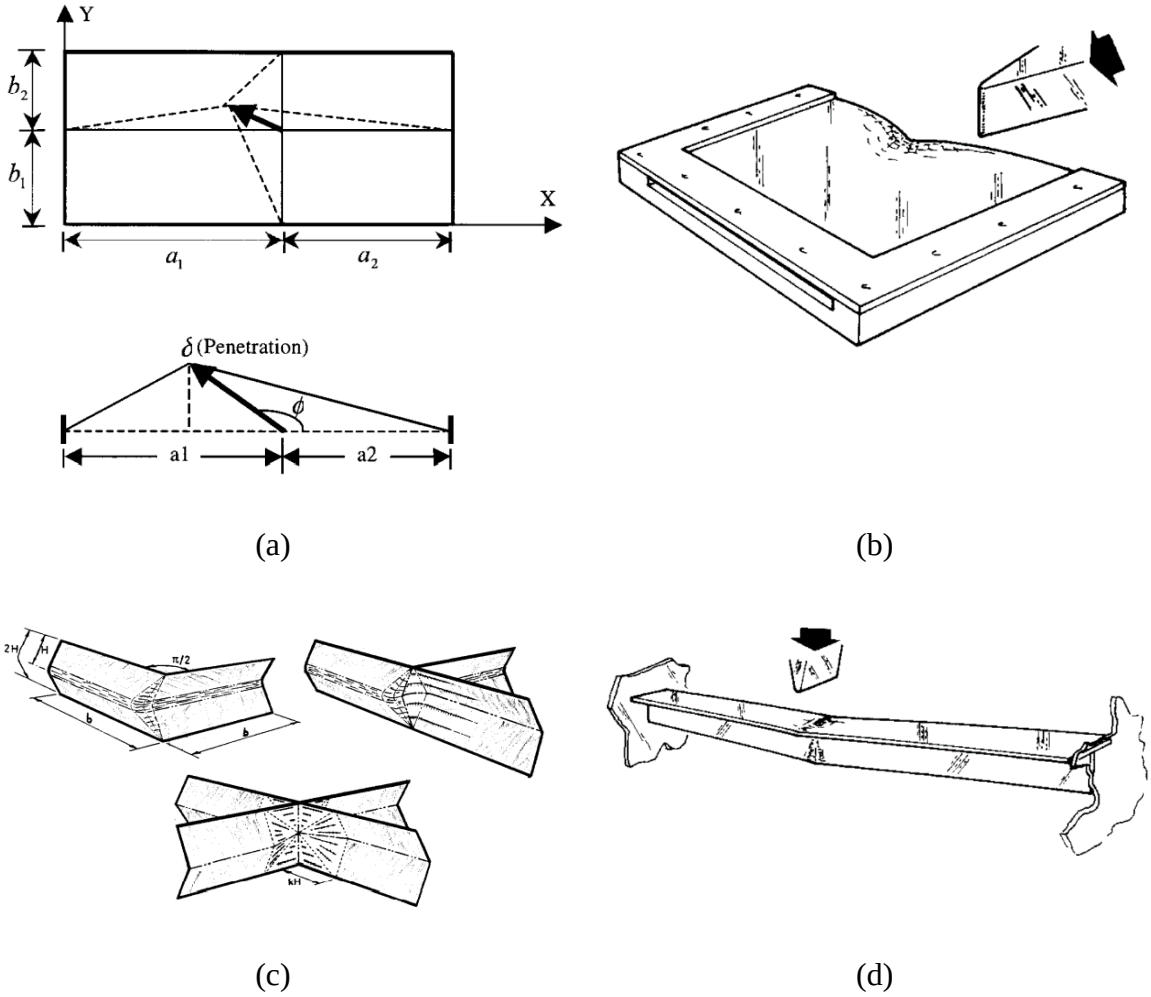

Figure 2.16 Various structural behaviours during collisions (a) lateral loading on shell plates (b) In-plane crushing and tearing of plates (c) crushing of intersecting structural elements (d) Lateral loading on beams

- <u>Lateral loading on shell plates</u>

  When an outer or inner hull is laterally loaded (see Figure 2.17) the plates will suffer bending, shearing and tension deformations at the beginning. However, the membrane forces dominate the deformation behaviour when large out-of-plane deflections occur. Therefore, only a large normal deflection of the shell plate is considered until it ruptures.

This structural behaviour was studied by Wierzbicki and Simonsen (1996), Wang and Ohtsubo (1997), Zhang (1999), Wang (2002). Buldgen et al. (2012) modified the resistance model of shell plates a plate simply supported on its four edges proposed by Wierzbicki and Simonsen (1996) and Zhang (1999). The lateral force F of plates with a certain angle ϕ is expressed by ;

$$F = \sum_{i=1}^{4} \frac{\dot{E}_{m\_i}}{\dot{\delta} sin\phi} \sqrt{1+\mu^2} \tag{2.25}$$

where, $\dot{E}_m$ is the rate of membrane energy, and it can be expressed based on the von Mises' criterion as $\dot{E}_m = \frac{2}{\sqrt{3}}\sigma_0 t \int \sqrt{\dot{\varepsilon_{xx}}^2 + \dot{\varepsilon_{yy}}^2 + \dot{\varepsilon_{xx}}\dot{\varepsilon_{yy}} + \dot{\varepsilon_{xy}}^2}$; $\varepsilon_{xx} = \frac{\partial w}{\partial x}\frac{\partial \dot{w}}{\partial x}$, $\varepsilon_{yy} = \frac{\partial w}{\partial y}\frac{\partial \dot{w}}{\partial y}$, $\varepsilon_{xy} = \frac{\partial w}{\partial x}\frac{\partial \dot{w}}{\partial y}$; $w(x,y) = \left(\frac{z}{a_1+\delta cos\emptyset}\right)^n \left(\frac{y}{b_1}\right)^n \delta sin\phi$; i indicates each surface consisting of the clamped plate; δ is the indentation; μ is the friction coefficient (see Figure 2.17). The plate rupture was assumed to occur when the effective plastic strain ε reaches a critical value of 0.1.

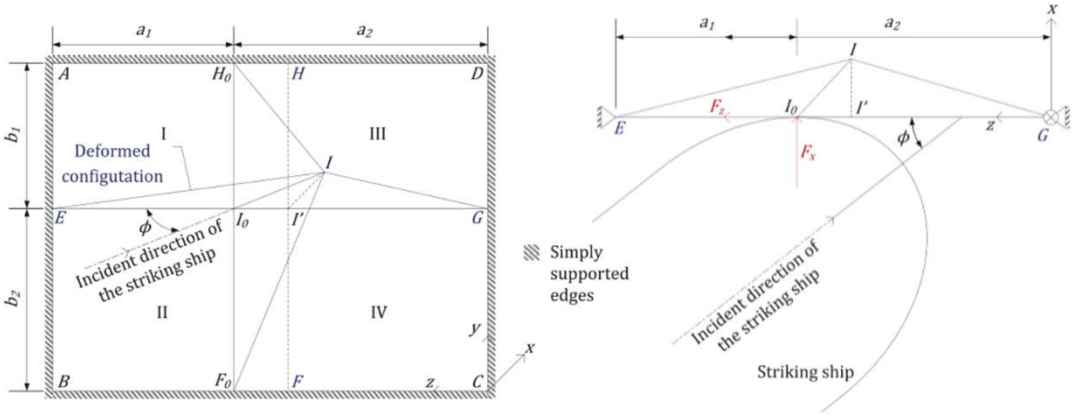

Figure 2.17 Model of an oblique collision on the clamped plate (Buldgen et al., 2012)

- In-Plane Crushing and Tearing of plates

When a deck is loaded by a point load, as shown in Figure 2.17 (b), it will first collapse plastically with folds extending to the nearest boundaries. After a certain penetration, the plate will fracture, and it will continue to fold up in front of the bow like a concertina. (Lützen, 2001). The former structural behaviour was investigated by McDermott et al. (1974), Wang (1995), Wierzbicki and Simonsen (1996) and Simonsen and Ocakli (1999). The following mean crushing force was proposed by Zhang (2002) when $b_1 = b_2 = b$ (see Figure 2.18):

$$F = 4.33\sigma_0 t^{1.67} b^{0.33} \tag{2.26}$$

where, σ_0 is flow stress; t is plate thickness; b is the length of the plate

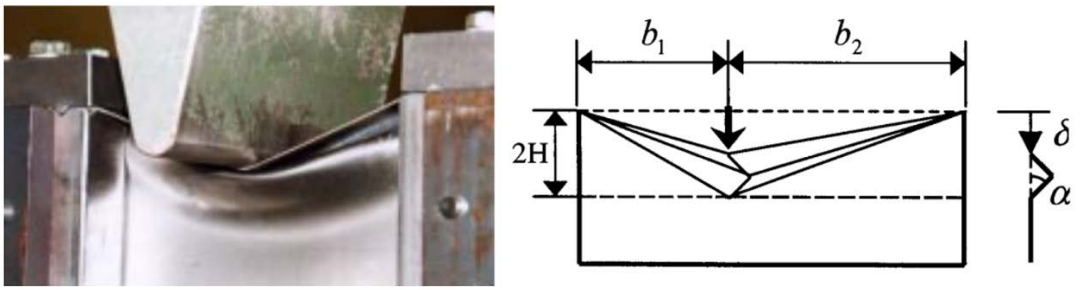

Figure 2.18 Experimental test and model of Web crushing (Zhang, 1999)

Then, Wierzbicki (1995) proposed the formulation for the later phenomena after rupture, which is the folding mode changes to concertina tearing. Additionally, cutting responses of a plate struck by a wedge were investigated based on a series of model tests by many researchers such as Jones and Jouri (1987), Lu and Calladine (1990), Wierzbicki and Thomas (1993) and Paik (1994). Wierzbicki (1995) suggested the mean load F of concertina tearing with the following expression:

$$F = \frac{3}{\lambda}\sigma_0 b^{0.33} t^{1.67} + \frac{2}{\lambda} Rt \tag{2.27}$$

where, σ_0 is flow stress; t is plate thickness; b is the width of the folded plate; λ is the factor for effective crushing length; R is a fracture parameter and ranges between 300 and 1000 N/mm (see Figure 2.19).

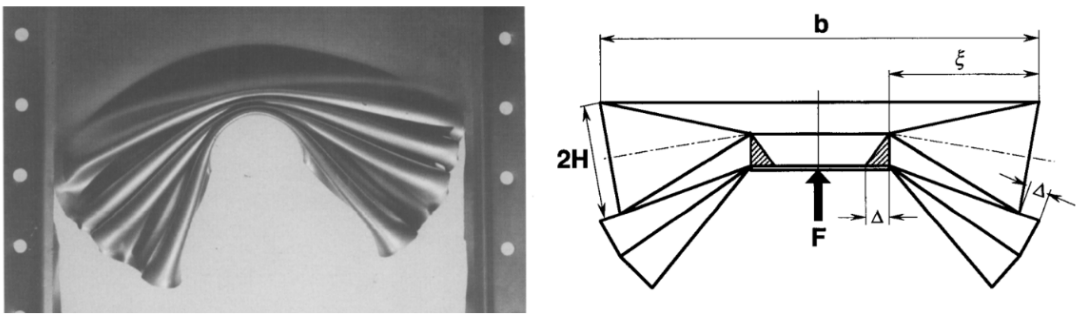

Figure 2.19 Experimental test and model of concertina tearing (Wierzbicki, 1995)

- Crushing of Intersections (L-, T-, and X-elements)

  When a deck is heavily stiffened or a region where a deck and transverse bulkhead are crossed, as shown in Figure 2.17 (c), completely different structural behaviours, such as folding, crushing and tension rupture, will show compared to the previous bare plate loading (Zhang, 1999). Amdahl (1983), Wierzbicki and Abramowicz (1983),

Kierkegaard (1993), Abramowicz (1994), Paik and Pedersen (1995), and Zhang (1999) investigated these axial crushing of basic elements, using theoretical and experimental methods. Zhang (1999) expressed the mean crushing force of the L-, T-, and X-sections as follows:

$$F_L = 2.3245\sigma_0 t^{1.5} c^{0.5} + (3N-2)2.025\sigma_0 t^2 \quad \text{for c=2b} \quad (2.28)$$

$$F_T = 2.8470\sigma_0 t^{1.5} c^{0.5} + (3N-2)3.036\sigma_0 t^2 \quad \text{for c=3b} \quad (2.29)$$

$$F_X = 3.2874\sigma_0 t^{1.5} c^{0.5} + (3N-2)4.048\sigma_0 t^2 \quad \text{for c=4b} \quad (2.30)$$

Where, σ_0 is flow stress; t is plate thickness; c is the total width of the folded plates; N is the number of a fold (seeFigure 2.20)

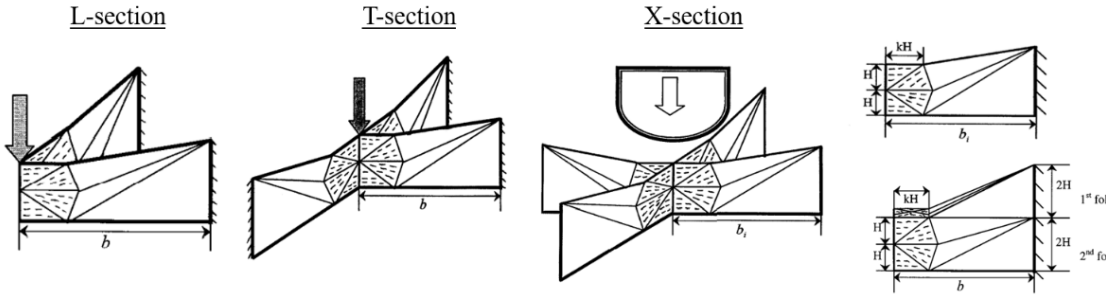

Figure 2.20 Model of crushing intersections (Zhang, 1999)

- Lateral loading on beams

  Lateral loading on the beams is the most common case for stiffeners, as shown in Figure 2.17 (d). During a collision of a clamped beam, a yield first occurs at the edges, and the plasticity progresses until fully developed hinges. Then, the bending moment at the loading point reaches yield, forming a hinge. The rupture happens when the deformation reaches a critical failure value. Therefore, in order to obtain a yield condition for a beam, it is necessary to find the combinations of the bending moment and the membrane force, which cause the cross-section of a perfectly plastic beam to become fully plastic (Jones, 1989b, Lützen, 2001, Buldgen et al., 2012). Lateral loading of beams with a specific angle ϕ is expressed with bending moment and the normal force N by Buldgen et al. (2012) as follows:

$$F = \frac{2M\left(\dot{\theta}_1 + \dot{\theta}_2\right) + N(\dot{\Delta}_1 + \dot{\Delta}_2)}{\dot{\delta} sin\phi} \quad (2.31)$$

where, M and N are the bending and axial capacities of the T cross-section; θ and Δ are beam rotations and the axial extensions of segment AI' and BI'; ϕ is collision angle

respectively (see Figure 2.21)

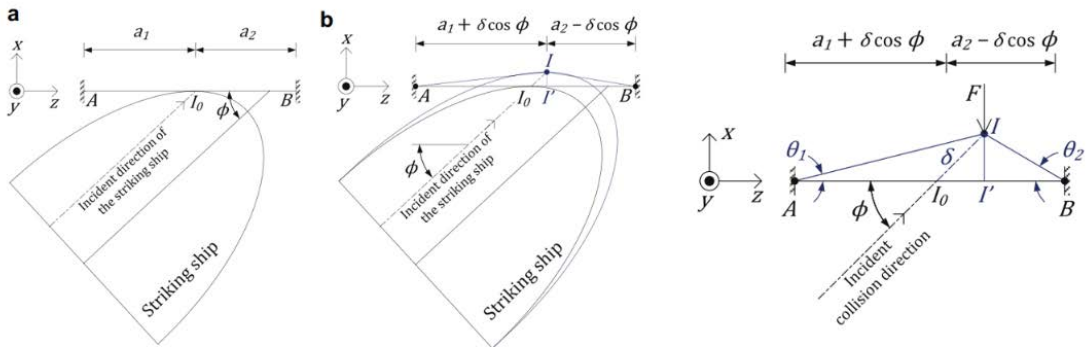

Figure 2.21 Model of lateral loading on beams(Buldgen et al., 2012)

These research outputs were the basis for analytical methods for internal ship mechanics during the collision, using upper-bound theorem, referred to as super-element solutions. Amdahl (1982), Lützen (2001), Buldgen et al. (2012) and Buldgen et al. (2012) contributed to the development of an analytical super-element method based on some assumptions from observations of accidental damages and experimental studies. Three major assumptions are based on this method. Firstly, if the work rate of a system of applied loads during any kinematically admissible collapse of the structure is equated to the corresponding internal energy dissipation rate, then that system of loads will casuse collapse of the structure. This is well know as “upper-bound theorme”. Secondly, each different structure member, such as side shell, decks, girders and stiffeners, contributes independently to the total collision resistance with no interaction with each other. Finally, the material is assumed to be perfectly plastic without strain hardening or softening. Solvers. Simply, it can be expressed as follows;

$$\dot{E}_{ext} = \dot{E}_{int} \tag{2.32}$$

$$\dot{E}_{ext} = F \cdot \dot{\delta} \tag{2.33}$$

$$\dot{E}_{int} = \dot{E}_b + \dot{E}_m \tag{2.34}$$

$$F \cdot \dot{\delta} = \sum_{i=1}^{k} \dot{E}_{b\_i} + \dot{E}_{m\_i} \tag{2.35}$$

where, $\dot{E}_{ext}$ and $\dot{E}_{int}$ are the external and internal energy rates; $\dot{E}_b$ and $\dot{E}_m$ are the bending and membrane energy rates; F is the external force; $\dot{\delta}$ is the velocity at the force action point; k is the number of damage modes associated with different structure members taken into account.

DAMAGE (Abramowicz and Sinmao, 1999, Simonsen, 1999), ALPS/SCOL(Paik and Pedersen, 1996), SHARP(Le Sourne, 2007, Le Sourne et al., 2012) and MarcolXMF(MARIN,

2021) were developed based on this super-element method for internal mechanics for ship collision calculations.

2.3.2 Full-and Large-scaled Experimental tests

Since 1960 many experimental tests for ship collisions have been carried out. In particular, in the 1960s and 1970s, large-scale model tests were performed in Italy, Germany and Japan for nuclear-powered ship designs to protect the nuclear reactor from collision damage, which was on the basis of the "Code of Safety for Nuclear Merchant Ships" by IMO (1982)

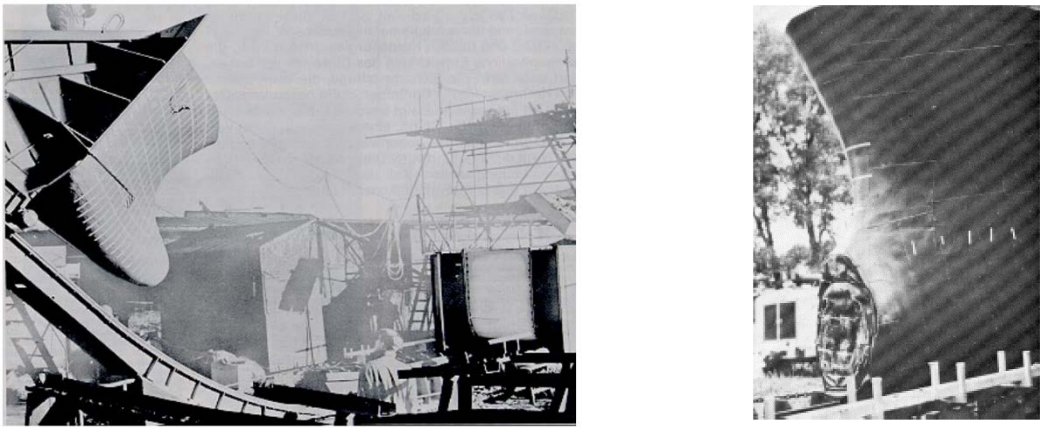

(a) (b)

Figure 2.22 Full-scale experiments in the 1960s and 1970s (a) Collision model test in Germany (Woisin, 1979) and (b) A damaged bulbous bow of a striking ship in Germany (Zhang, 1999)

In 1992, MARPOL adopted the double hull requirement (IMO, 1992) for tankers of 5,000 dwt and more after the disastrous oil pollution from the *EXXON VALDEZ* accident (Skinner, 1989). This triggered many experiments and numerical simulations for double-hull tanker design in the early 1990s. Examples are the Dutch-Japanese full-scale ship collision tests (Vredeveldt and Wevers, 1992, Lenselink, 1992, Ohtsubo et al., 1994), large-scale static failure tests for single- and double-bottom structures (Kuroiwa, 1992), large-scale static grounding test for a double bottom (Amdahl et al., 1992), large-scale dynamic and static collision tests for a double hull structure (Kuroiwa, 1993), large-scale dynamic collision tests (Qvist et al., 1995), large-scale collision test for VLCC side structure designs (Kitamura et al., 1998, Peschmann et al., 2002). The reference figures are shown in Figure 2.23 (a) – (f) in the order.

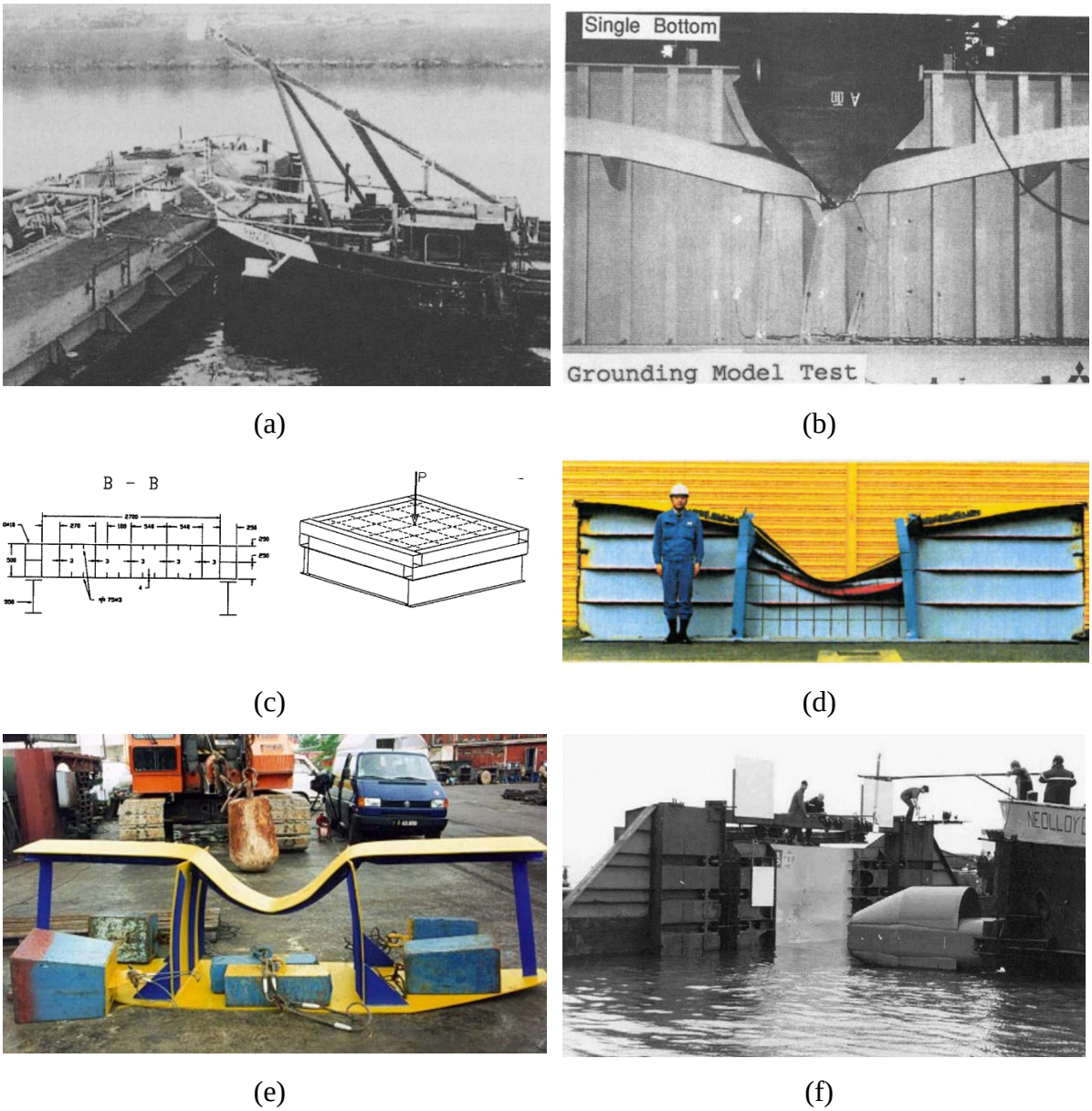

(a) (b)

(c) (d)

(e) (f)

Figure 2.23 Experiments in the 1990s

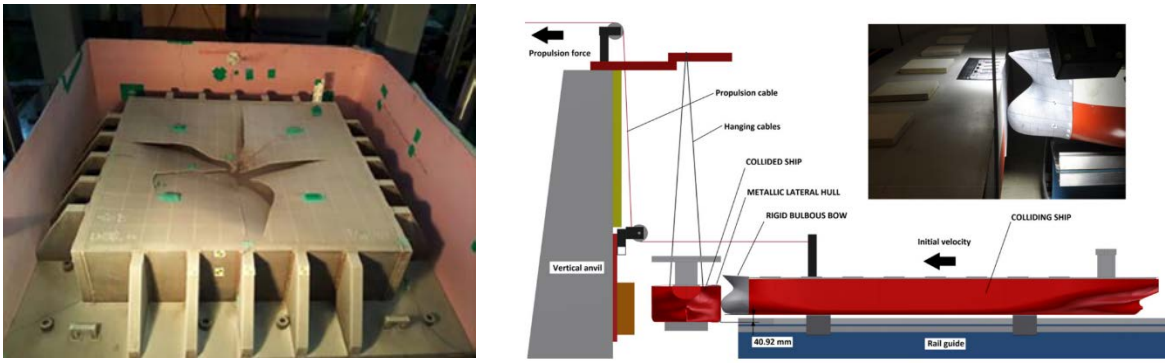

(a) (b)

Figure 2.24 Experimental tests for collisions after the 2000s

After the early 2000s, increased computing capability helped to focus on numerical simulations. However, experiments have still been carried out to validate the numerical simulation results, but it has been scaled down. Kim et al. (2016) and Calle et al. (2017) carried out small-scale experiments for impact responses of steel-plated structures in the arctic environment and 1:100 scaled ship-ship collision experiments (see Figure 2.24).

2.3.3 FE Analysis Method

Structural response of ship collisions and groundings involves highly non-linear structural mechanics associated with bending, bucking, crushing, plasticity and rupture. Thus, finite element analysis (FEA) has been widely employed for structural crashworthiness analysis. The reliability of non-linear FEM results depends on diverse factors such as proper geometric modelling, reasonable finite element size and types, realistic material property modelling, precise failure criteria, contact and friction during events, ship motions induced by the surrounding water, etc.

Ringsberg et al. (2018) performed a benchmark study on static non-linear FE simulation of a small-scale experiment of an indenter impact with a ship side-shell structure conducted by Karlsson et al. (2009). The same basic information for the benchmark study has been provided to all 13 participants, but each of them applied their own analysis approaches, such as different mesh sizes, different failure criteria and different damage models with a constitutive material model. The overall outcomes generally showed agreement with each other. However, discrepancies from some participants were also observed due to different analysis approaches. Ehlers et al. (2008) showed different numerical simulation results compared to experimental results in their benchmark study. Nine different analysis approaches, combinations of three different mesh sizes (i.e., 25mm, 50mm and 100mm) and three failure criteria (i.e., GL(Vredeveldt, 2001, Scharrer et al., 2002b), Perschmann (Peschmann and Kulzep, 2000) and RTCL (Tornqvist, 2003)), were applied to numerical simulations. The results indicated that the coarser meshes had more influence on forces than the fine meshes. However, there were still gaps among results from different failure criteria using the same fine mesh. Kõrgesaar et al. (2014) conducted ship collision simulations for two LNG tank carriers using different failure criteria and mesh sizes. Three mesh size (i.e., 50mm, 150mm and 300mm) and five failure criteria (i.e., Triax soft(Li and Wierzbicki, 2010), Triax sudden(Jones, 2013), GL(Vredeveldt, 2001, Scharrer et al., 2002b), DNV(Veritas, 2013), Barba(Barba, 1880)) were adopted for simulations. The discrepancies among simulation results were also observed, but validation

with full-scale experiments was not included. More recently, Kim et al. (2022) carried out a benchmark study for ship collisions between a 65,000 GT cruise ship and a 35,000GT Ro-Pax as a sub-work of the EU-funded project (FLARE, 2019-2022). Among the total four participants, two used FEM with explicit code and the others performed the analysis with their in house software developed based on superelement method. The differnet analysss approach has been used for each participant expcept the identical fractor stain of 0.1. For low speed perpendicular collision with low speed of 5 knots, the maximum penetration results show good agreement. However, for high-speed (i.g.10 knots) and oblique collisions, the result gaps between participants have been observed (See Section 4.4).

As described above, outcomes from FE analyses have still not provided high reliability since the analyses are subject to parameters' selection from different analysis approaches. A common conclusion is that the failure criteria, including the damage model and mesh size effects, are the most crucial factor in FE analysis to achieve reliable results.

2.3.4 Material Failure Criteria

2.3.4.1 Constant Failure strain: Shear Criterion

For this criterion, it is assumed that material failure occurs when material strain reaches a critical strain, such as damage initiation strain at the onset of necking or the equivalent plastic strain of fracture strain, which is one of the first used rupture criteria in FE analysis. It is also referred to as the "*Shear criterion*" as it relates to shear band localisation. This phenomenon involves a plastic localisation, which means there is a transition from a uniform to a non-uniform mode of deformation while the loading remains uniform, and then shear bands occur in the direction of maximum shear (Pineau and Pardoen, 2007), as shown in Figure 2.25. Generally, this fracture strain (ε_f) is easily identified from a material stress-strain curve experimentally measured from uniaxial tensile coupon tests, and other parameters associated with material failure processes (i.e., stress state) are disregarded. This is widely employed due to its simplicity as follows (Samuelides, 2011, Marinatos and Samuelides, 2015):

$$D_{SHEAR} = \frac{\int d\bar{\varepsilon}^p}{\varepsilon_{cr}} \tag{2.36}$$

where D_{SHEAR} is damage parameter, $d\bar{\varepsilon}^p$ denotes an increment of the true equivalent plastic strain, ε_{cr} is the critical equivalent true plastic strain. The shell element is deleted from the

modelling when the strain of the element becomes 1.

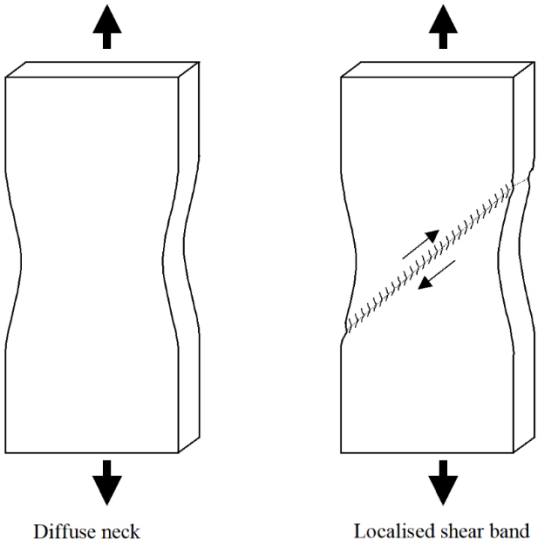

Figure 2.25 Diffuse neck and shear band localisation (Pineau and Pardoen, 2007)

Amdahl (1995) employed critical failure strain from 0.05 to 0.1 for his simplified analytical approach. However, those values were downscaled compared to his experimental results (i.e., from 0.2 to 0.35) from a mild steel tensile test (Amdahl et al. (1992) and Wen and Jones (1993)) to take into account scale effects and material imperfections in the assessment of full-scale collisions.

Servis and Samuelides (1999) used the maximum plastic strain of 0.18 for their collision simulation between two large RO-RO vessels as one of the sub-tasks of DEXTREMEL (1997). The material model employed was elastoplastic, including material hardening but did not account for strain rate effects. Simulation results showed overestimated deflections in comparison to the clamped model tests, but underestimations were observed for floating tests.

Kitamura (2002) used a failure strain of 0.2 for his FE collision simulations of VLCC colliding with a Suezmax tanker or a 6200TEU containership. He selected the value between the equivalent failure stain adopted in the simplified analytical approach in general (i.e., 0.05 ~ 0.15) and the one obtained from his standard uniaxial experimental test (i.e., 0.3). This value aimed to cope with geometrical stress concentration, multi-axial stress field, and plate and membrane bending stress for analysis with coarse mesh sizes.

Wiśniewski and Kołakowski (2003) employed two types of maximum plastic strains and two

different stress-strain material curves in collision simulations between a VLCC and a container ship using large finite element models: (1) a constant failure strain of 0.1, based on Technical University of Denmark (DTU) recommendation, and elastic-plastic material models without plastic hardening, and (2) a constant failure strain of 0.17, based on DNV Classification Rules, and experimental stress-strain curves with plastic hardening. Analysis results of the latter approach showed a greater resultant force but less bow penetration.

Yagi et al. (2009) set the failure criteria as the plastic strain of 0.2 for simulations between two LNG carriers. The elastic-plastic material model with hardening effect consideration was used, and the mesh sizes of two ships were 120 mm for a struck ship and 150mm for a striking ship, respectively.

Kõrgesaar et al. (2014) conducted a series of collision simulations using different failure criteria and mesh sizes. In this comparison analysis, he selected 0.1817 as a constant fracture strain based on the DNV rule(Veritas, 2013).

More recently, failure strains of 0.1 and 0.2 were used for explicit code-based simulations and numerical analysis with super elements, respectively, in a benchmark study (Le Sourne et al., 2021, Kim et al., 2021).

2.3.4.2 Element size-dependent Failure strain: Barba's Law

Many researchers have widely adopted the constant failure criterion in numerical analyses due to its simplicity, as described in the previous section. However, it is also well known that the failure strain is highly sensitive to simulation results as it is often used regardless of careful consideration of element size and damage model (Lehmann et al., 2001, Zhang et al., 2004, Yamada, 2007). Furthermore, the fracture strain differs depending on a measurement gauge's length on a specimen for a uniaxial tensile coupon test, as shown in Figure 2.26(b) (Ehlers and Varsta, 2009). Therefore, for these criteria, the equivalent size of mesh elements must be used as the gauge length of the experimental test for FEA to obtain precise results. However, taking every tensile test of different materials for each numerical analysis is impractical, and there is not enough information about the size of the gauge used for the test. The element size-dependent failure strain criterion, generally called "*Barba's law*", can address this problem by considering strain distribution on a measurement gauge length (i.e., mesh size). The concept of

this criterion is that the fracture strain ε_f is the summation of uniform strain ε_r and necking strain $\varepsilon_n$as shown in Figure 2.26 (a). Based on this principle, the fracture strain measured from a large gauge length will become smaller than that of a short gauge as the uniform strain ε_r region dominates strain measurement. However, the necking ε_n (local thinning) region is still the same (see Figure 2.26(c)).

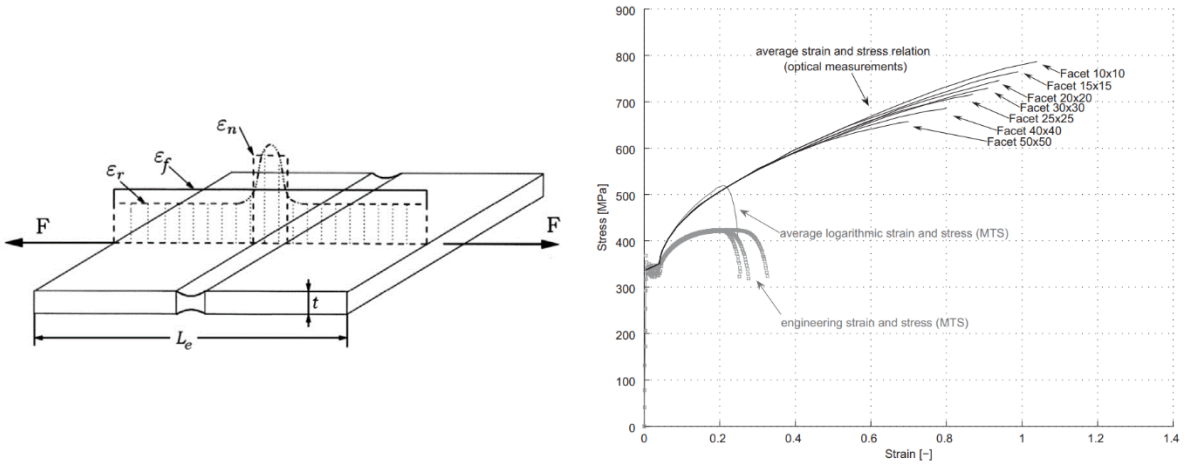

(a) (b)

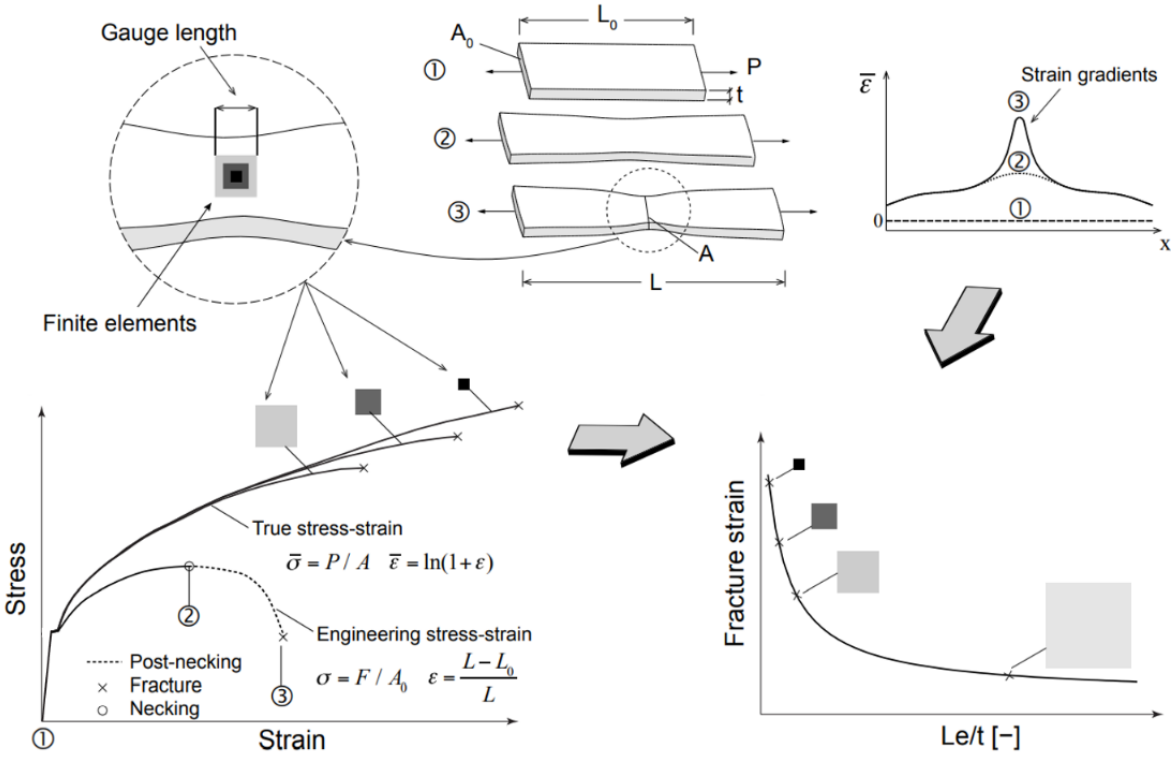

(c)

Figure 2.26 (a) Schematics of uniform strain (ε_r) and necking strain(ε_n) for failure strain(ε_f) calculation with a gauge length L_e; (b)The strain-stress curves showing different fracture strain points (Ehlers and Varsta, 2009); (c) Element size-dependent True Stress-strain (Kõrgesaar, 2015)

Barba (1880) initially presented the necking strain as the ratio between the gauge area and length by the following empirical formula:

$$\varepsilon_f = \varepsilon_u + \beta \frac{\sqrt{WT}}{L} \tag{2.37}$$

where, ε_f is engineering stain at rupture; ε_u is uniform engineering strain; β is a coefficient of proportionality; W and T denotes the gauge width and the thickness of the specimen.

Peschmann and Kulzep (2000) proposed the modified Barba's law derived from experimental results to evaluate the equivalent plastic strain. It expresses a necking term of the original formula with only plate thickness T and element length l_e as follows:

$$\varepsilon_f = \varepsilon_g + \alpha \frac{T}{l_e} \tag{2.38}$$

where ε_g denotes uniform strain, α is $\varepsilon_m(x_e/T)$, and ε_m and x_e are highly deformed strain in the necking area and the length of the necking, respectively; Both ε_g and α depend on thickness as follows:

$$\varepsilon_f = \begin{cases} 0.1 + 0.8 \frac{T}{l_e} & , if \ T \leq 12 \\ 0.08 + 0.65 \frac{T}{l_e} & , if \ T > 12 \end{cases} \tag{2.39}$$

Later, Lehmann and Peschmann (2002) updated the $\varepsilon_g$and α based on the experimental hull tanker collision tests using ship steel.

Yamada et al. (2005) also employed a failure stain from Barba's numerical collision analyses of a VLCC by another VLCC with a bulbous buffer bow. However, they converted the engineering failure value to true strain and multiplied the strain effects coefficient calculated from the Cowper-Symonds equation. In particular, the latter is a phenomenon that material behaviours under high strain rates (i.e., high-speed collision) show increased ultimate stress but decreased fracture strain (see Section 2.3.4.3). Based on a series of uniaxial tensile tests, the authors concluded that Barba's law showed a good agreement on test results with the uniform stain (ε_u) of 0.18 and Barba constant (β) of 0.5 for specimen dimensions W = 40mm and T = 22mm. Then, a failure stain of 0.2 (i.e., a true strain of 0.1823) was obtained based on the element length of 500–700mm as follows:

$$\varepsilon_f = ln(\varepsilon_u + \beta \frac{\sqrt{WT}}{L} + 1) \tag{2.40}$$

Considering strain rate effects for high collision speed greater than 15 knots, the authors multiplied the dynamic factor of 0.6 to the failure strain, and a fracture strain of 0.12 for simulations was finally obtained. For numerical validation, different simulation results with other failure values, such as 0.1, 0.12, 0.15 and 0.2, were conducted to identify the sensitivity, as shown in Figure 2.27 (b), but no experimental validation was presented.

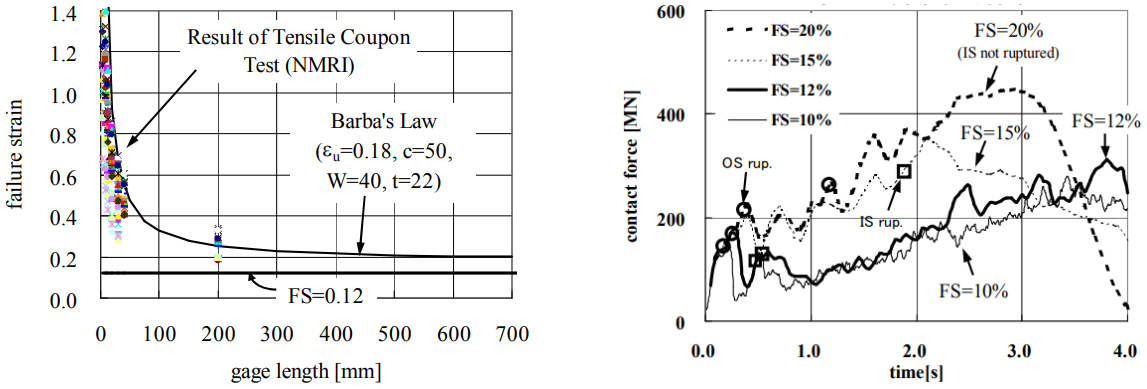

(a) (b)

Figure 2.27 (a) Experimental tensile results corresponding to Barba's Law and (b) simulation results with different failure strains (Yamada et al., 2005)

Hogström et al. (2009) also confirmed that Barba's law is valid for fracture strain estimation after necking from tensile tests of three different shipbuilding materials, namely Norske Veritas grade A (NVA) mild steel, high strength steel Domex 355 and aluminium NV5083. An optical strain measurement was used to observe accurate strain changes for the true stress-strain curve, and the following modified formula was suggested:

$$\varepsilon_f = ln(e^{\varepsilon_u} + \beta \frac{\sqrt{WT}}{L}) \tag{2.41}$$

where ε_u is 0.22, β is 0.93 , and W and T are 25mm and 4mm, respectively, for NVA mild steel.

Calle and Alves (2013) suggested ε_g=0.2823 and α=0.8627 in the modifed Barba's law of Peschmann and Kulzep (2000) as follows:

$$\varepsilon_f = 0.2823 + 0.8627 \frac{T}{l_e} \tag{2.42}$$

Similarly, Vredeveldt (2001) proposed the through-thickness strain criterion, which is well known as "GL criterion". The critical fracture strain ε_c was derived from empirial relations obtained from experimental measurements of the through-thickness strain ε_3 (i.e., the third principal strain or thinning strain) of damaged plates in actual ship structures engaged in ship collisions and groundings as follows:

$$\varepsilon_c = \varepsilon_g + \varepsilon_e \frac{t}{l_e} \tag{2.43}$$

where ε_c denotes critical fracture strain representing as $\varepsilon_{3f} = \varepsilon_c / (1 + \varepsilon_c)$, thinning strain ε_{3f} may be obtained from $\varepsilon_{3f} = -0.5(\varepsilon_1 + \varepsilon_2)$ based on the incompressibility condition with the Poisson ratio of 0.5; Uniform strain ε_g and necking strain ε_e are defined in Table 2.3 for different element types used in simulations.

Table 2.3 Uniform and necking strains depending on element types (Scharrer et al., 2002b)

Strain	1-Dimension Structure	2-Dimension Structure
ε_g	0.079	0.056
ε_e	0.760	0.540
Element Type	Beam, Truss	Shell, Plate

Figure 2.28 summarises fracture strain changes depending on element size and thickness ratio for each different formulation based on Barba's law.

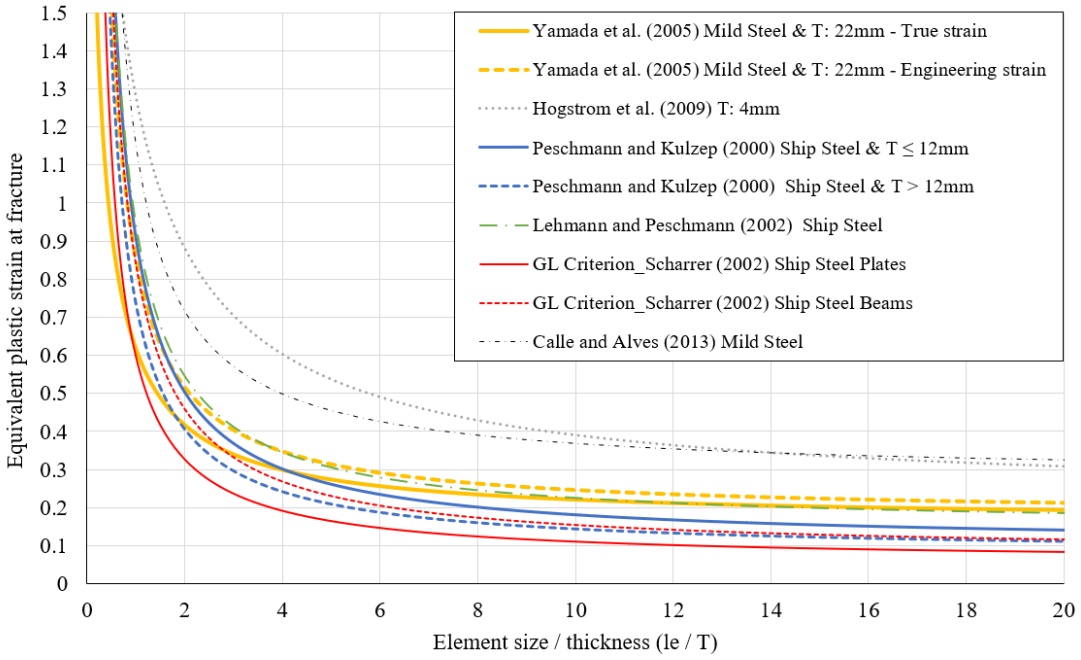

Figure 2.28 Comparisons of element size-dependent failure criteria

2.3.4.3 Strain state-based Failure criteria: FLD

In collisions and groundings, thin-plated ship structures experience tension, compression, or shear. Plate failures occur because of the combination of complex deformations. However, the previous two criteria, except GL criteria, are only based on one condition of deformation (i.e., a uniaxial tensile test), and the strain value at the onset of necking or the equivalent strain value at fracture is taken as a failure point to numerical simulations (see Figure 2.29 (a)), yielding unreliable results (Wierzbicki et al., 2005, Driemeier et al., 2015).

Some researchers attempted to adopt the "*Forming Limit Diagram (FLD)*" to consider all major strains from different loading conditions (see Keeler (1961) and Goodwin (1968)). Figure 2.29 (b) presents a graph on which the major strain values (ε_1) (i.e., the highest principal stain) at the onset of necking in sheet metal are plotted vertically, and the corresponding values of the minor strain (ε_2) (i.e., the smallest principal strain) are plotted horizontally. The onset of the failure line divides all possible strain combinations into two zones: the "safe" zone, where failure is not expected during forming, and the "failure" zone, where failure is expected. This FLD assumes proportional strain paths to plastic instability points (i.e., necking), for which the ratio between major and minor principal remains constant during deformation. However, loading paths in structural collision processes may not show linear behaviours due to material hardening, structure geometries, contact, etc.

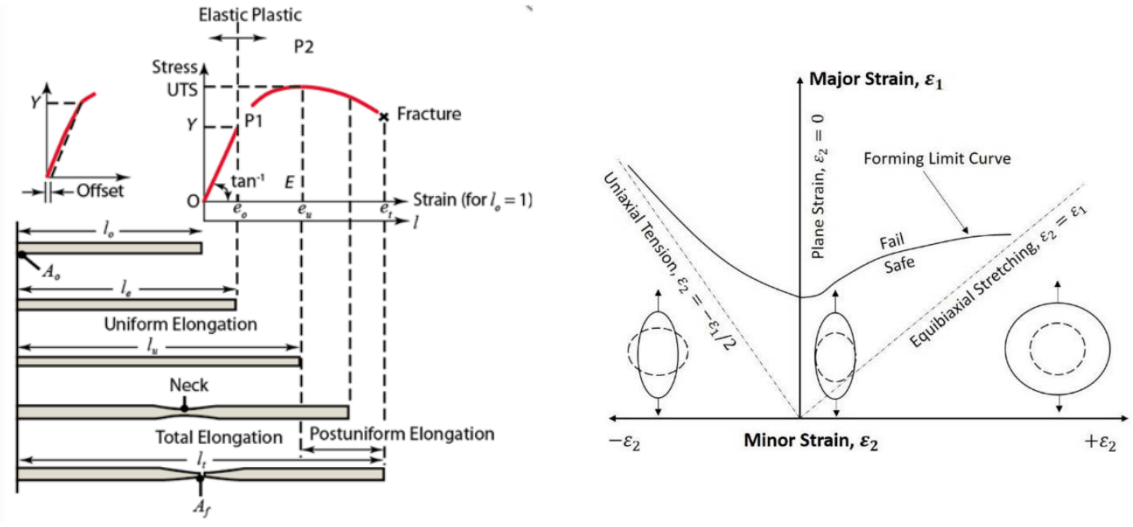

(a) (b)

Figure 2.29 (a) Typical engineering stress-strain curve from uniaxial tensile test and (b) Typical forming limit diagram (FLD) of necking initiation points (sentesoftware, 2018)

Stoughton (2000), (2001) and Stoughton and Zhu (2004) converted this original strain-based criterion to stress-based FLD criterion, which remains reasonably unaffected by strain path alterations.

Alsos et al. (2008) developed the stress-based FLD criterion, combining the shear stress criterion of Bressan and Williams (1983) and the local necking analysis in plates proposed by Hill (1952), to provide a simplified way to determine the onset of local necking in plates. Their method is widely known as the "*BWH criterion*".

$$\sigma_{1f} = \begin{cases} \frac{2K}{\sqrt{3}} \frac{1+\frac{1}{2}\beta}{\sqrt{\beta^2+\beta+1}} \left(\frac{2}{\sqrt{3}} \frac{\widehat{\varepsilon_1}}{1+\beta} \sqrt{\beta^2+\beta+1}\right)^n & if \quad \beta \leq 0 \ (Bressan\ and\ Williams) \\ \frac{2K}{\sqrt{3}} \frac{\left(\frac{2K}{\sqrt{3}} \widehat{\varepsilon_1}\right)^n}{\sqrt{1-\left(\frac{\beta}{2+\beta}\right)^2}} & otherwise\ (Hill) \end{cases} \tag{2.44}$$

where σ_{1f} denotes principal stress at the onset of necking, β is strain rate ratio ($\dot{\varepsilon}_1/\dot{\varepsilon}_2 \approx \varepsilon_1/\varepsilon_2$), which means the ratio between major and minor strain, K and n are the plastic hardening parameters from power law ($\sigma = K\varepsilon^n$) of material; Critical strain $\widehat{\varepsilon_1}$ can be assumed to be equal to the power-law coefficient n according to Hill's criterion (Hill, 1952).

The method can show good agreement for proportional and non-proportional strain paths as compared to experimental FLD data for aluminium Al 2008 T4, ARMCO iron and mild steel for three different test cases such as virgin, 10% uniaxial pre-straining, 15% biaxial pre-straining. Figure 2.30 shows the BWH criterion validation results for mild steel in comparison with FLDs acquired from experimental and analytical methods by Brunet and Morestin (2001).

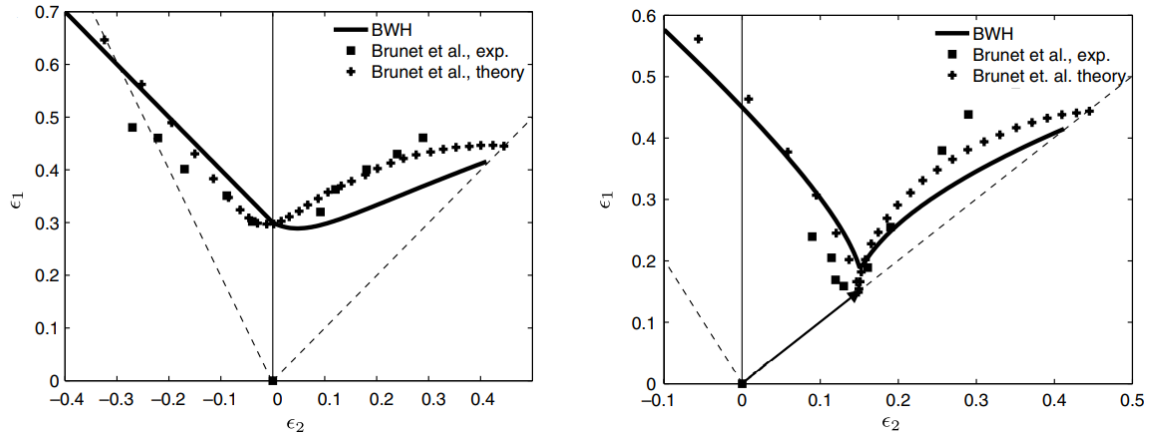

(a) (b)

Figure 2.30 BWH criterion validation results of FLD for mild steel (Alsos et al., 2008) compared with data provided by Brunet and Morestin (2001): (a) virgin material (b) 15% biaxial pre-straining

This BWH criterion is mesh-independent as it ignores the post-necking process. However, Alsos et al. (2009) suggested including mesh dependent term into the original formula in Equation (2.44), replacing $\hat{\varepsilon_1}$ with $\frac{n}{2}(\frac{T}{l_e}+1)$ for coarse meshes (i.e., l_e/T ratio between 3 and 8) that do not capture the actual local strain concentrations. This approach improves mesh scalability for stiffened panel structures, in which failure is typically initiated close to a stiffening member.

On the other hand, Jie et al. (2009) proposed FLD failure model with strain rate-dependent effects, and AbuBakar and Dow (2013) adopted this failure model as the simplified FLD failure model excluding strain rate effect for his FEA grounding simulations of a double bottom structure with 15mm element mesh size as follows:

$$\varepsilon_1 = \begin{cases} \dfrac{n}{1+r_\varepsilon} & if\ r_\varepsilon \le 0 \\ \dfrac{3{r_\varepsilon}^2 + n(2+r_\varepsilon)^2}{2(2+r_\varepsilon)({r_\varepsilon}^2 + r_\varepsilon + 1)} & if\ r_\varepsilon > 0 \end{cases} \tag{2.45}$$

where, $\varepsilon_1$denotes major principal strain, n is the power law exponent, r_ε is the principal strain ratio between major and minor strains ($\varepsilon_1/\varepsilon_2$).

This failure criterion was validated from FEA simulations using the ABAQUS damage evolution model (i.e., stress-strain curve with progressive damage degradation). Then, simulation results were compared to actual experimental data (Alsos and Amdahl, 2009, Alsos et al., 2009), as well as the other results from BWH(Alsos et al., 2008) and RTCL(Tornqvist, 2003), and acceptable agreement was obtained. It is notable that penetration forces obtained from grounding simulation showed a good correlation with results from Samuelides et al. (2007) and Zilakos et al. (2009).

2.3.4.4 Stress state-based Failure criteria: Stress Triaxiality

Hancock and Mackenzie (1976), Bao and Wierzbicki (2004), Barsoum and Faleskog (2007) corroborated that the triaxial stress state strongly affects fracture ductility based on experimental studies. The first attempt to consider the hydrostatic stresses in fracture criterion for naval and marine structure analysis was made by Lehmann and Yu (1998). They introduced a rupture Index I_R as a critical damage parameter based on continuum damage mechanics (CDM) model that governs material damage evolution until the rupture.

$$I_R = \varepsilon_V f(T)^{2n+1} \tag{2.46}$$

$$f(T) = \frac{2}{3}(1+\upsilon) + 3(1-2\upsilon)(T)^2 \tag{2.47}$$

where, ε_V and υ denotes the maximum effective strain and the Poisson coefficient, n is the power law exponent; T expresses triaxiality which is a ratio between mean and equivalent Von Mises stresses (i.e., T = $\sigma_m/\bar{\sigma}$); σ_m and $\bar{\sigma}$ are the mean and equivalent Von Mises stresses represented with principal stresses ($\sigma_1, \sigma_2, \sigma_3$) as follows:

$$\sigma_m = \frac{\sigma_1 + \sigma_2 + \sigma_3}{3} \tag{2.48}$$

$$\bar{\sigma} = \sqrt{\frac{1}{2}[(\sigma_1 - \sigma_2)^2 + (\sigma_2 - \sigma_3)^2 + (\sigma_3 - \sigma_1)^2]} \tag{2.49}$$

The critical value I_R can be derived from uniaxial tensile test simulation, and fracture is to be assumed to occur when it is exceeded.

Kitamura et al. (1998) suggested the use of a semi-empirical failure criteria for steel plates that consider time-domain damage evolution $D(t)$ via a pressure coefficient $f(T)$ as follows:

$$D(t) = \int_0^t f(T)\frac{1}{\varepsilon_f(t)}\frac{d\varepsilon_1(t)}{dt}dt \leq 1.0 \tag{2.50}$$

$$f(T) = min\left(\frac{tan^{-1}\left(-\frac{1}{T}\right)}{tan^{-1}\left(-\frac{1}{3}\right)}, 1.0 \right) \tag{2.51}$$

where, $\varepsilon_f(t)$ is Peschmann and kulzep criterion for equivalent strain over time presented as $\varepsilon_f(t) = \varepsilon_g + \varepsilon_m/l_e$; ε_g and ε_m were obtained from experiments in the time frame; $d\varepsilon_1(t)$ denotes the increment in the magnitude of the principal strain at time t; In this work, it is assumed that the local plate material will fracture when the cumulative $D(t)$ reaches 1.0 (Calle and Alves, 2015).

Tornqvist (2003) developed further this triaxial stress state failure criterion by combing different failure models based on Rice-Tracey and the Cockcroft-Latham criteria, which is well known as the "*RTCL criterion*". The former (Rice and Tracey, 1969) can yield reliable results

for shear-dominated damage caused due to void growth (i.e., a low triaxial stress range). On the other hand, the latter (Cockcroft and Latham, 1968) shows good predictions for tension-dominated damage (i.e., a high triaxial stress range). The damage D is defined as a damage indicator D_i :

$$D_i = \frac{1}{\varepsilon_0}\int f(T)\ d\varepsilon \tag{2.52}$$

$$f(T) = \begin{cases} 0 & for\ T \leq -\frac{1}{3} \quad \text{(Compression)} \\ \frac{2 + 2T\sqrt{12 - 27T^2}}{3T + \sqrt{12 - 27T^2}} & for\ -\frac{1}{3} < T \leq \frac{1}{3} \quad \text{(shear)} \\ \frac{1}{1.65} exp\left(\frac{3T}{2}\right) & for\ T \geq \frac{1}{3} \quad \text{(tension)} \end{cases} \tag{2.53}$$

where, ε_0 denotes critical fracture strain from uniaxial tensile conditions, and T is triaxiality. This criterion assumes that the material fracture occurs when the cumulative strain from different loadings (i.e., triaxial stress state) reaches the equivalent fracture strain (ε_0) from the uniaxial tension condition, which is D_{cr} = 1. Figure 2.31 shows the triaxiality function $f(T)$ curve of RTCL criterion compared with some of the earlier described criteria and models. Figure 2.31 (b) compares the triaxiality function for three different failure criteria described herein. The value of the triaxiality function greater than 1.0 means that fracture will occur earlier than the equivalent failure strain.

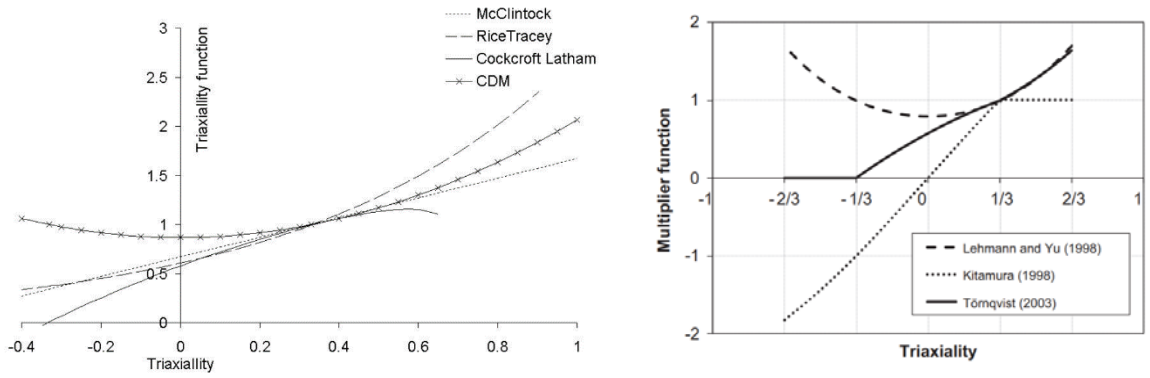

(a) (b)

Figure 2.31 (a) Triaxiality function f (T) of RTCL criteria (Tornqvist, 2003) (b) Multiplier function (Triaxiality function f (T)) for three different failure criteria (Calle and Alves, 2015)

The author validated this criterion using large-scale numerical simulations in ship collision and grounding and compared the results to experimental data for double hull stranding, a collision of ship's side with a bridge pier, ship grounding by NSWC, and ISSC benchmark of ship grounding and collision. It shows reasonably acceptable agreement compared with those from experiments.

2.3.4.5 Strain rate sensitivity failure strain

It is well known that strain rates influence material stress-strain curves (see Figure 2.32). Jones (1989a), (2006) firstly suggested strain rate-based failure criteria derived from the inverse of the Cowper-Symonds model (Cowper and Symonds, 1957) as follows:

$$\varepsilon_{fd} = \left[1 + (\frac{\dot{\varepsilon}}{C})^{1/q}\right]^{-1} \varepsilon_f \tag{2.54}$$

where ε_{fd} and ε_f are the fracture strains in the dynamic and static conditions, respectively; $\dot{\varepsilon}$ denotes strain rate; C and q are the constants for strain rate sensitivity of the Cowper-Symonds model (Cowper and Symonds, 1957).

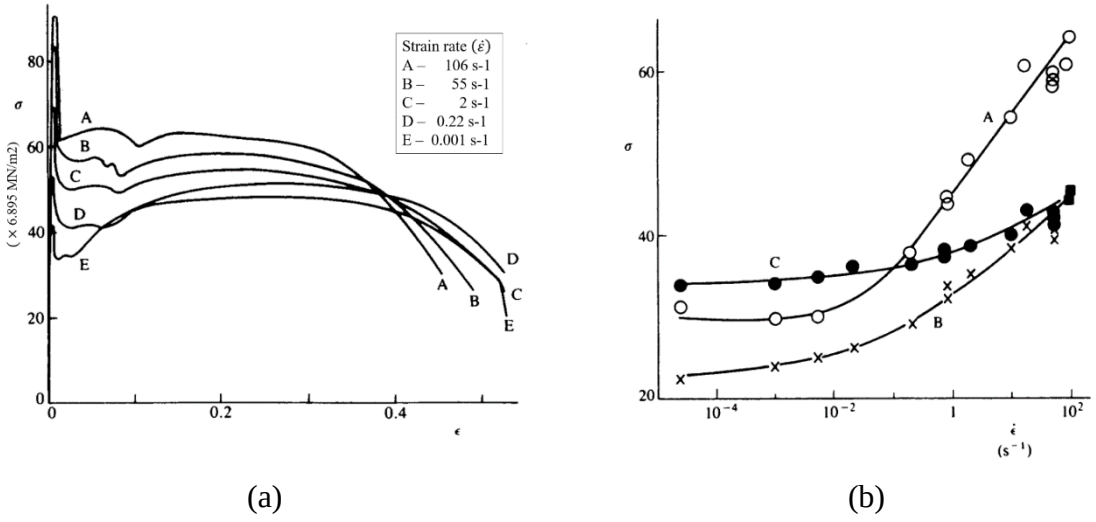

(a) (b)

Figure 2.32 (a) Stress-strain curves from dynamic uniaxial tensile tests on mild steel at various mean plastic strain rates (b) Strain rate-stress curve for A, B and C cases (COMPBELL and Cooper, 1966)

Paik (2007) derived a critical fracture strain from mesh size influences. The derivation was based on a series of tensile test simulations conducted with three different stress-strain curves. Model I used a true stress-strain curve defined up to the ultimate tensile stress only (i.e., before necking) after converting an engineering stress-strain curve obtained from a tensile test. Model II employed the whole true stress-strain curve up to the fracture strain, including strain

hardening and softening (i.e., necking) behaviour. Model III used the whole true stress-strain curve, but it was modified with a new approach called the knockdown factor.

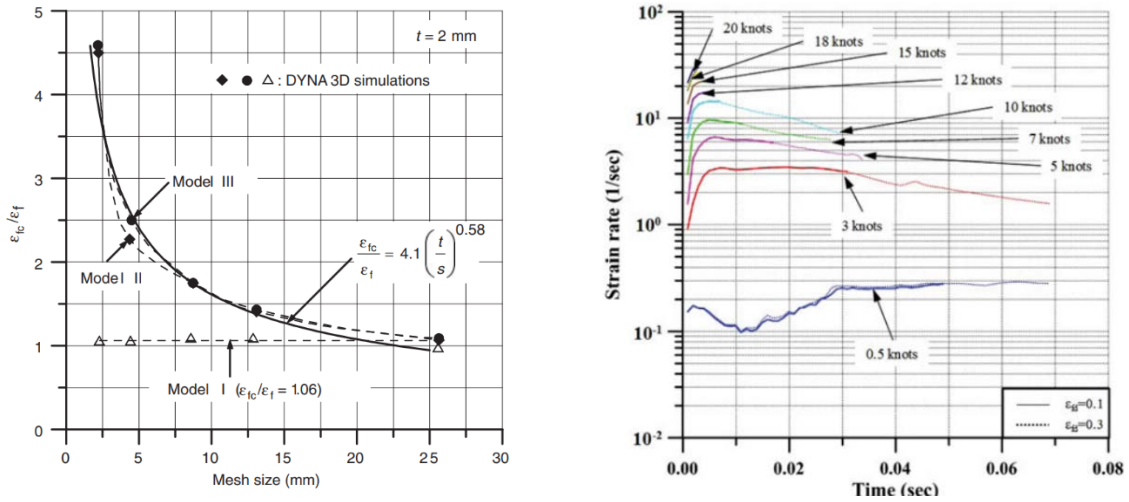

(a) (b)

Figure 2.33 (a) Critical fracture strain changes depending on mesh sizes in FEA at a quasi-static loading condition (Paik, 2007) (b) Variation of the Strain rates for different collision speeds (Ko et al., 2018b)

Simulations of Model I and Model II shown in Figure 2.33 (a) confirm the relationship between critical fracture strain ε_{fc} for FE simulations and static fracture strain ε_f obtained from experiements (Paik, 2007, 2018, 2020, Hughes and Paik, 2010) as follows:

$$\varepsilon_{fc} = \gamma d_1 (\frac{t}{s})^{d2} \varepsilon_f \tag{2.55}$$

where, t is the element thickness; d_1 and d_2 are coefficients of 4.1 and 0.58 respectively when t = 2mm for room temperature; γ is the correction (knock-down) factor associated with localised bending, which becomes more significant with increased element thickness, and 0.3~0.4 is recommended for the thicker shipbuilding material.

Regarding strain rate in Equation (2.54), Ko et al. (2018b) suggested the strain rates as a function of initial collision speed based on collision simulations between two VLCCs. The measurements were taken from the initial contact element of the struck ship, and the following empirical formula was expressed as:

$$\dot{\varepsilon} = 2.970 V_0 - 0.686 \; for \; V_0 \geq 0.231 \; m/s \tag{2.56}$$

where, $\dot{\varepsilon}$ is the maximum strain rate value, as shown in Figure 2.33 (b).

2.3.4.6 Failure strain based on Crack propagation

Crack propagation is another important aspect of structural behaviour in collisions and groundings. Various authors, such as Kitamura (2002) and Simonsen and Törnqvist (2004), attempted to include this crack propagation effect on the failure criteria by delaying or avoiding element removal during analysis. Recently, Kõrgesaar and Romanoff (2013) proposed fracture criteria for damage-induced softening for large-scale structural analysis by enabling the coupling between fracture criterion and material model that softens the stress-strain curve in two-stage. Stage 1 begins with the onset of necking and ends with fracture initiation (i.e., maximum fracture plastic strain for previous failure criteria). The 2nd stage is associated with fracture propagation, as indicated in Figure 2.34(a). Later, it was simplified with only one softening stage based on damage process results from parametric studies, as shown in Figure 2.34(b). Damage of this failure criterion and softening of the material model is defined as :

$$D = \int_0^{\bar{\bar{\varepsilon}}_f} \frac{d\bar{\bar{\varepsilon}}}{\bar{\varepsilon}_f(\eta_a)} \tag{2.57}$$

$$\tilde{\sigma} = \beta\bar{\sigma} \tag{2.58}$$

where $\bar{\varepsilon}_f(\eta_a)$ denotes the fracture locus in the space of equivalent plastic strain and average stress triaxiality η_a; $\tilde{\sigma}$ is the softened flow stress for the damage evolution beyond critical damage initiation; β is softening coefficient defined as $\beta = [(D_c - D)/(D_c - D_0)]^m$ (Li and Wierzbicki, 2010). Material deterioration begins at the onset of necking D_0 and $\beta = 1$, and fracture initiates when the normalised damage indicator D reaches the value of one, D =1 (i.e., the cumulative strain is equal to the equivalent plastic strain). Then, when $D = D_c$ and $\beta = 0$, the fracture propagation energy element is finally removed.

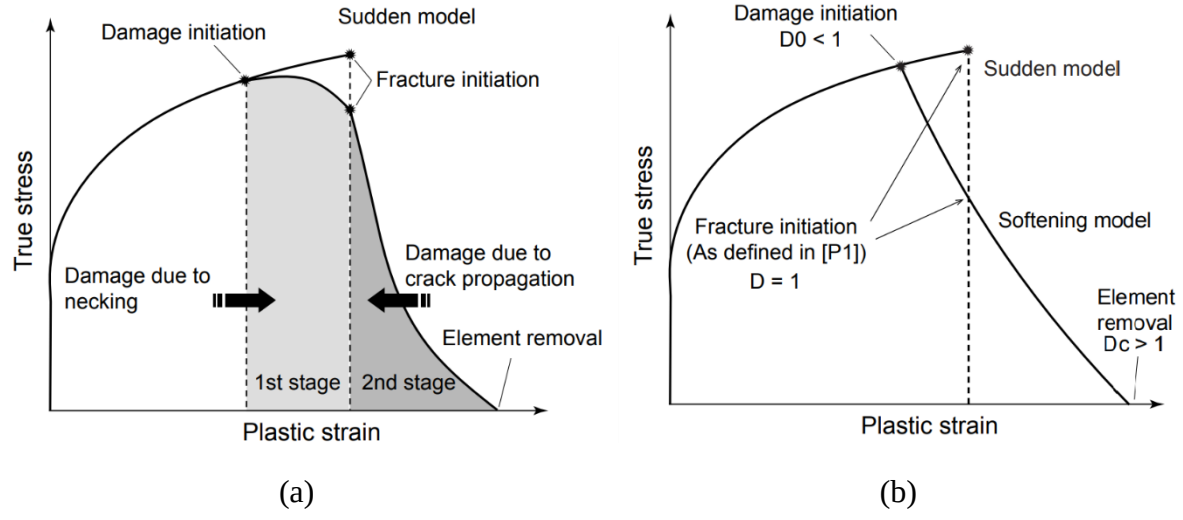

Figure 2.34 Damage crack propagation model (a) Two-stage softening model (b) One-stage softening model (Kõrgesaar, 2015)

2.4 Combination of Damage stability and Crashworthiness

Most crashworthiness analysis studies for ship collision and grounding have been only focused on structural responses to protect certain regions of interest against external forces, such as offshore structures (Storheim and Amdahl, 2014), LNG tankers (Wang et al., 2008), wind turbines (Biehl and Lehmann, 2006), bridges (Larsen, 1993), etc. Likewise, ship damage stability assumed that damages have already taken place for flooding calculation, with no significant consideration for the influence of actual damage extents. However, from a damage stability perspective, the direct assessment using crashworthiness analysis has been continuously investigated as one of the approaches for damage stability improvement.

2.4.1 Monte Carlo simulations

Lützen (2001) developed an analytical simulation program using the super-element method as described in Section 2.3.1. The method was validated for a Ro-Ro vessel collision case by comparing simulation results with calculation models from DNV(Hysing, 1995) and GL(Scharrer and Ostergaard, 1996). Additional comparisons for the case of double hull tanker collision against solvers DAMAGE, ALPS/SCOL and SIMCOL, were reasonable. Monte Carlo simulations were carried out for 15 different types and sizes of struck vessels, and they were compared to the actual collision accident data. In the same research, she proposed new formulations of p-, r- and v- factors for the Attained Subdivision Index calculation using a probabilistic approach for passenger ship damage stability. However, the results have been based on the ship accident database, not on simulation results, in which crashworthiness analysis was not completely involved in damage stability calculations.

2.4.2 Approval procedure concept for alternative arrangements: First Attempt

Germanischer Lloyd (IMO, 2003, Zhang et al., 2004) made the first attempt to adopt crashworthiness analysis in ship damage stability. A methodology was proposed to evaluate double hull structure designs using absorbed energies derived from crashworthiness analysis of ship collision within the scope of the EU-Project (CRASHCOASTER, 2000-2003). The project initially aimed to provide a standard for evaluation and approval of alternative solutions for the design and construction of cargo vessels between 80 and 100m in length with double hull structural arrangement. The concept of the proposed procedure was to compare the deformation energies between the original and strengthened structures from ship collisions. If

the deformation energy of the latter E_s is equivalent or greater than that of the original structure E_{ref}, it is deemed to satisfy the degree of safety required from SOLAS as the original structure complied with the damage stability requirement as shown in Figure 2.35 (a) and the equation:

$$E_s \geq E_{ref} \tag{2.59}$$

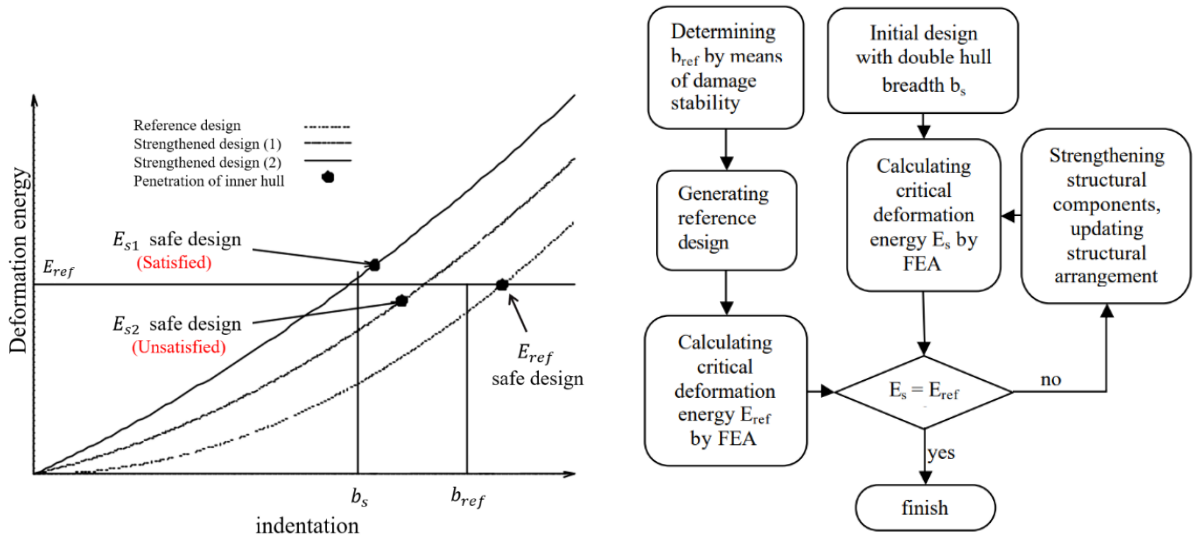

Figure 2.35 (a) Concept of the deformation energy comparison for reference and strengthened designs and (b) Proposed approval procedure for double hull structure alternative designs

GL recommended carrying out FE analysis for deformation energy calculation using recognised explicit finite element codes such as LS-DYNA, ABAQUS, PAM-CRASH, MSC/DYTRAN, etc. For a struck ship, a whole length of the target hold was modelled as a deformable body with 2D shell elements for most parts except stiffeners of the eccentric beam elements. The fine mesh was applied to the collision area, while the coarser mesh was used for other parts. It was recommended that the maximum mesh size in the collision areas should not be more than 200 mm. The transitional freedom was restricted for both ends of model boundaries. Two types of striking ships with and without bulbous bows were modelled as rigid bodies. For the material properties used for FEA, the following stress-strain curve defined by power-law was recommended based on tensile test results:

$$\sigma = C\,\varepsilon^n \tag{2.60}$$

where σ and ε denote the principal stress and strain, respectively; C is the hardening coefficient related to the ultimate tensile stress $R_m$defined as $C = R_m(e/n)^n$; n means a strain hardening exponent as $n = ln(1 + A_g)$, and A_g is the maximum uniform strain defined as $A_g =$

$1/\ (0.24 + 0.01395R_m)$.

In addition to this, for the failure criterion, the GL criterion (Scharrer et al., 2002b) was adopted with a recommendation of the element size and thickness ratio l_e/t of not less than 5. Regarding collision scenarios, perpendicular collisions were considered with a reasonable collision speed of the striking ship to a stationary struck ship. Four different relative vertical positions (i.e., draft differences) depending on the two ships' design and ballast drafts were considered. Based on these FE simulation set-ups, the following approval procedure was suggested (see Figure 2.35 (b)):

- Step1: Generation of an initial new structural design with a double hull breadth b_s
- Step2: Calculation of the reference double hull breadth b_{ref} in accordance with SOLAS Part B-1, Reg 25-3, 25-4 and 25-5 (SOLAS, 1997) considering reduction factor r for damage probability p of wing compartments fitted as:

  For J ≥ 0.2 b/B:

  $$r = \frac{b}{B}\left(2.3 + \frac{0.08}{J + 0.02}\right) + 0.1, \qquad if\ b/B\ \leq 0.2 \tag{2.61}$$

  $$r = \left(\frac{0.016}{J + 0.02} + \frac{b}{B} + 0.365\right), \qquad if\ \frac{b}{B} > 0.2 \tag{2.62}$$

  For J < 0.2 b/B:

  r to be determined by linear interpolation between r=1 for J=0 and r calculated from Equation (2.61) and (2.62) for J= 0.2 b/B (2.63)

  where J is the nondimensional length of a compartment defined as J = compartment length/subdivision length of the ship
- Step3: Generation of a correspondent reference structural design based on the reference double hull breadth b_{ref}
- Step4: Calculation of the critical deformation energy E_{ref} from the reference design
- Step5: Calculation of the deformation energy E_s from the new design
- Step6: Comparison of deformation energy between the reference and new design
- Step7: Iteration of the new design update with step5 and step 6 until $E_s\ \geq\ E_{ref}$

Unfortunately, the IMO proposal (IMO, 2003) containing this approval procedure has not been successfully accepted. Instead, the FE analysis method of this procedure for obtaining absorption energy before cargo tank rupture was adopted in the "*European Agreement*

concerning the International Carriage of Dangerous Goods by Inland Waterways" in 2008 (UN, 2008) and is simply known as ADN 2009. In this procedure, $Risk = P \times C$, where P is the probabilities of cargo tank rupture, and C is the consequences of cargo tank rupture by damage measurement. The probability P is calculated from a predefined function of energy absorption capacity (E) for various collision conditions such as three different collision draughts, three different locations, four different speeds with a maximum of 10m/s, two angles of 55° and 90° and two different bow shapes, while the consequence C is defined as the maximum capacity of the largest cargo tank in alternative and reference design.

2.4.3 Survival time based on damage openings

Schreuder et al. (2011) also investigated how the damage openings from ship collisions affect the damage stability in terms of flooding time to ship loss. The FE explicit code Abaqus (Systèmes, 2007) was employed to obtain damage openings for 179m Ro-Pax collision simulations. A partial geometry of a struck ship was modelled as a deformable body with 6 DOF restrictions, while a striking ship with a bulbous bow was a rigid body. The hull of the struck ship was assumed to be of NVA grade steel, and its material property was obtained from a uniaxial tensile test with Young's modulus of 210 Gpa and yield stress of 310 Mpa. The failure model took into account both damage initiation (necking) and a damage evolution developed by Hogström et al. (2009). Strain rate effects, residual stresses and welding effects were not considered in the simulations. A series of simulations were carried out by colliding one- or two-compartments of the stuck ship based on the damage scenarios according to SOLAS (1997) with various collision speeds from 2 knots to 10 knots. Based on the damage openings from the FE simulations, dynamic stability simulations of the damaged struck ship were performed in various sea states, such as the different significant wave heights and wave spectrums depending on the ship's headings.

Hogström and Ringsberg (2012) developed this methodology with a series of FE analyses for uncertainties. In this study, three different failure criteria, namely shear criterion, strain-based forming limit curve criterion (FLD) and stress-based forming limit curve criterion (FLSD), were investigated together with the bilinear criteria (Hogström et al., 2009) up to the point of fracture after necking point. Not only bow structure stiffness effects in collisions using rigid and deformable body, but also two collision speeds (i.e., 5 and 7 knots), three collision angle effects such as 45°, 60° and 90° and two friction coefficient effects for 0.1 and 0.3 were examined as shown in Figure 2.37. The time to capsize from each opening was simulated, and

a summary is given in Figure 2.38.

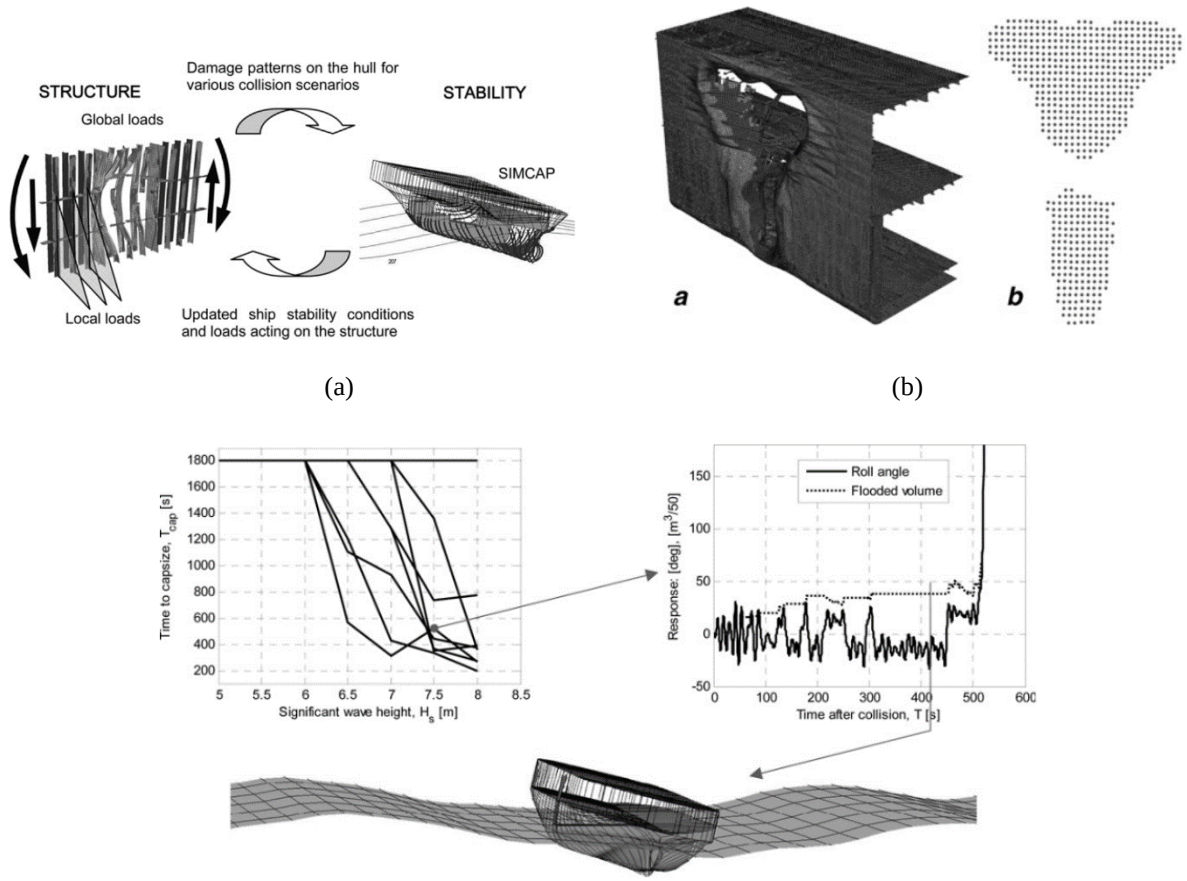

Figure 2.36 (a) Concept of the proposed methodology between (b) damage opening from FE simulations and (c) time to capsize using SIMCAP (Schreuder et al., 2011)

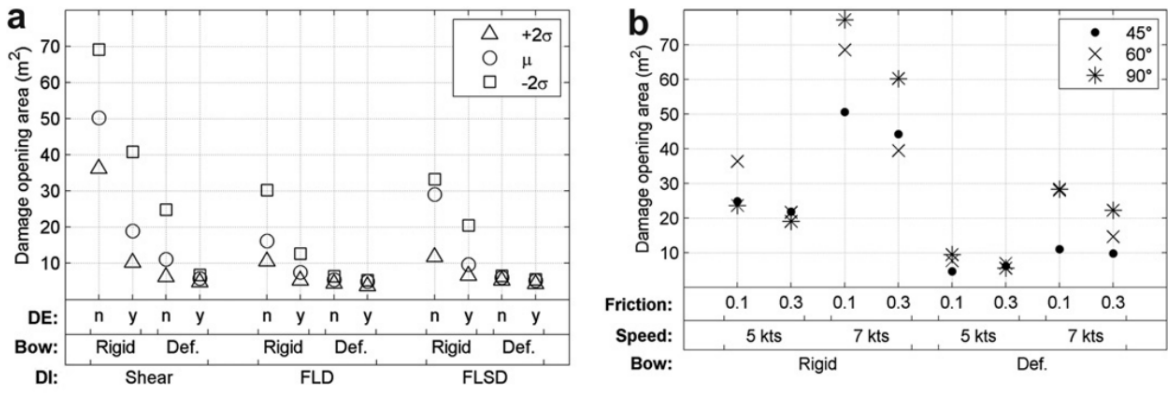

Figure 2.37 Simulation results of damage opening areas depending on various parameters, including failure criteria, bow structure stiffness, collision speeds, collision angles and friction coefficients (Hogström and Ringsberg, 2012)

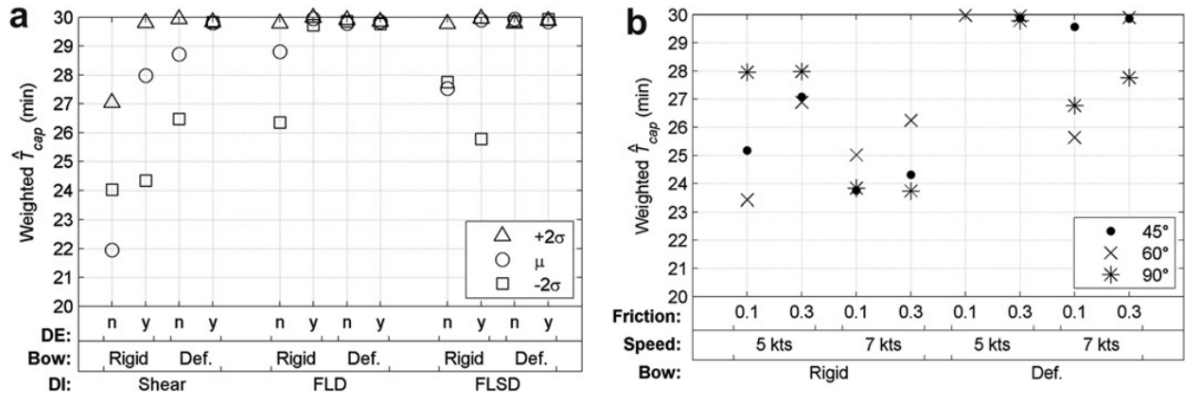

Figure 2.38 Capsize time simulation results from damage openings obtained from a series of simulations (Hogström and Ringsberg, 2012)

It is concluded that FE analysis with shear criteria, rigid striking body, perpendicular collision angle, low friction coefficient and no damage evolution give the most conservative results. However, no comparison against experiments was provided, and therefore it remains unclear which combinations of parameters result in the accurate openings from FE analysis.

In a similar method, Conti et al. (2022) carried out a number of crash simulations for a 45,000 GT cruise ship based on collision and grounding scenarios selected by the non-zonal Monte Carlo method. From the Super-element software SHARP, damage extents in box type were obtained and used for s-factor calculations for each damage case. The p-factor was defined as $P_k = 1/n$ instead of SOLAS regulations as below;

$$Attained\ Subdivision\ Index = \sum p_i \times s_i \tag{2.64}$$

$$s_i = f((ind_{side}, X_c, L_x, L_y, z_{UL}, z_{LL})_k) \tag{2.65}$$

where, n is the number of Monte Carlo scenario samples; ind_{side} is damage side such as port or starboard; X_c is longitudinal position of the centre of the damage; L_x is longitudinal damage extent; L_y is transverse damage extent (penetration); z_{UL} and z_{LL} are upper and lower limits of vertical damage extent, respectively.

The significant contribution of this method is to apply actual damage sizes to damage calculations based on their operational area using a non-zonal approach. For this approach, a number of collision samples are essential, and accurate damage results are critical. However, result accuracy from the super-element method is still in question for deformable bow collisions with various crash conditions, such as fraction strain criteria, oblique collisions, grounding, etc. On the other hand, collision simulations with a FE analysis tool would require too much cost.

Chapter 3

Methodology

3 METHODOLOGY

3.1 Preamble

Several disasters in the 80s, such as Herald of Free Enterprise(1987) with the loss of 193 lives, Piper Alpha(1988) with 167 fatalities and Exxon Valdez (1989), leading to severe oil pollution, provoked scepticism for the current prescriptive regime of relevance to maritime safety. In 1993, the UK Marine Safety Agency proposed the formal safety assessment (FSA) to the IMO. The method provides a rational and systematic procedure for a regulation-making process through risk analysis and cost-benefit assessment. *"Guidelines for FSA for use in the IMO regulation-making process"* were officially approved in MSC 74 in 2001 and MEPC 46 in 2002 and revised recently in 2018 (IMO, 2018). This FSA is consistent with the current IMO decision-making process in support of the regulation process and comprises the following five steps described in Figure 3.1.

- Step 1: Identification of hazards
- Step 2: Risk analysis
- Step 3: Risk Assessment for Risk control options
- Step 4: Cost-benefit analysis
- Step 5: Recommendations for decision making

The FSA is a standardized holistic approach for all kinds of accident hazards, including collision, fire and explosion, grounding and stranding, hull and machinery failure, foundering and severe flooding, and contact. The method is normally applied to groups of similar ships, such as cruise ships or RoPax, or indeed by grouping them all together into "passenger ships". On the other hand, Quantitative Risk Assessment focuses on a single ship. It accounts for its geometric and dynamic characteristics, operational profile, damage stability and survivability performance in this operational environment, as well as operational and emergency response in pertinent emergencies. It primarily uses direct assessments with first-principles tools which come under the umbrella of Quantitative Risk Assessment. The analysis steps are the same as IMO FSA, but the analysis and focus are different. This is normally referred to as the Safety Case.

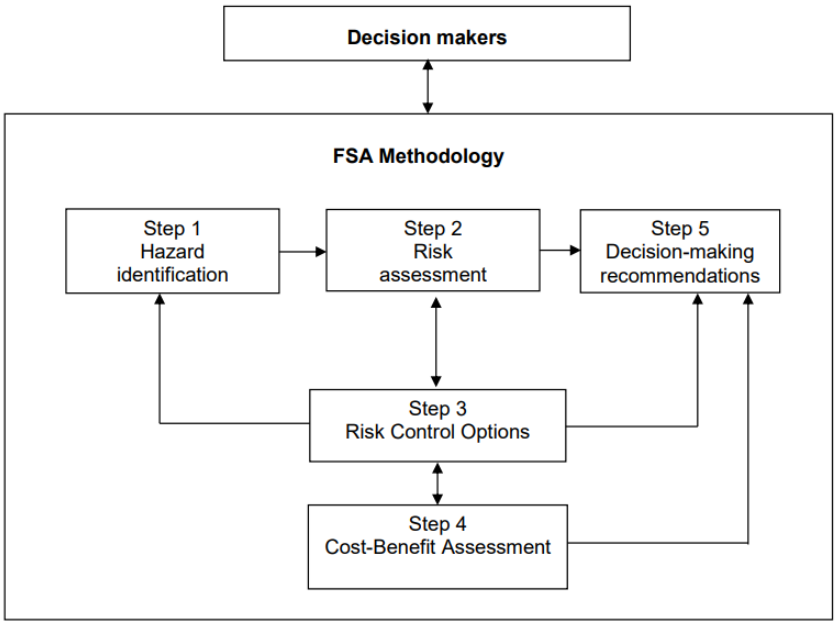

Figure 3.1 Flow Chart of the FSA Methodology (EU, 2003)

3.2 Proposed Methodology

Quantitative Risk Analysis to assess the damage stability of crashworthy arrangements in ship collisions can be divided into the following nine steps:

- **Step 1: Initial Damage Stability Assessment (SOLAS 2020)**

An initial damage stability assessment is carried out to identify the current risk profile of a target ship according to the current SOLAS regulations. The purpose is to identify how s-factors are distributed and contribute to the A-Index along the length of the ship. From this calculation, the current Required Subdivision and Attained Subdivision Indies can be obtained along with the s-factors and p-factors of each damage case.

- **Step 2: Vulnerable Zones Identification**

The second step is to identify vulnerable zones in which high risks exist using a vulnerability analysis. The risk level for each zone can be clearly classified from the highest risk zone to the least one. Then, one or two of the most high-risk zones are used for the development of alternative design solutions and ship overall risk improvement.

- **Step 3: Alternative Design Application (RCOs)**

Based on the previously quantified zonal vulnerability analysis, the third step of the process is

to apply alternative designs via the implementation of Risk Control Options - RCOs, to the target zones. Then, structural and non-structural passive types and their combinations of RCOs can be considered.

- **Step 4: Collision Scenario Selection**

The next step is to determine a proper collision scenario for structural crashworthiness analysis for the selected vulnerable zone with risk control options. Mainly four parameters influence ship collisions, such as striking ship, collision location, collision speed, collision angle and drafts.

- **Step 5: Structural Crashworthiness Analysis**

This step of the process aims to compute ship collision simulations for the target vulnerable zone with RCOs based on the determined collision scenario identified in the previous Step 4. The method used for simulations should account for nonlinear structural mechanics. In this thesis, the nonlinear finite element method (NLFEM) is employed. However, suitable versions of the super-element method could also be usefully implemented if it calculates reliable outcomes.

- **Step 6: Damage Distribution Update**

From the simulation results in Step 5, damage extents for each alternative design can be obtained. Then, transverse damage distributions can be modified by shifting the maximum penetration location point on the curve from B/2 to the actual penetration results measured from simulations, and the other points of the distribution should be moved proportionally.

- **Step 7: Damage Stability Re-assessment**

The damage stability of the target ship with RCOs and the updated transverse damage distribution on the target zone should be re-evaluated to identify how much improvement is practically achievable.

- **Step 8: Cost-benefit analysis for an optimum RCO selection**

Based on the type of RCO applied in Step 3 and damage stability results in Step7, a cost-benefit analysis should be performed to identify an optimum solution among RCOs. Consequently, the RCO that offers the highest risk reduction with the minimum cost and fewer design changes

will be selected.

- **Step 9: Decision making and AD&A process**

The RCO should be discussed by the relevant decision-makers on the basis of the Alternative Design and arrangement approval process (IMO, 2006, IMO, 2013). It is to be clarified that all the aforementioned steps are part of the approval process adopted by most IACS class societies for Alternative Design and Arrangements (AD&A).

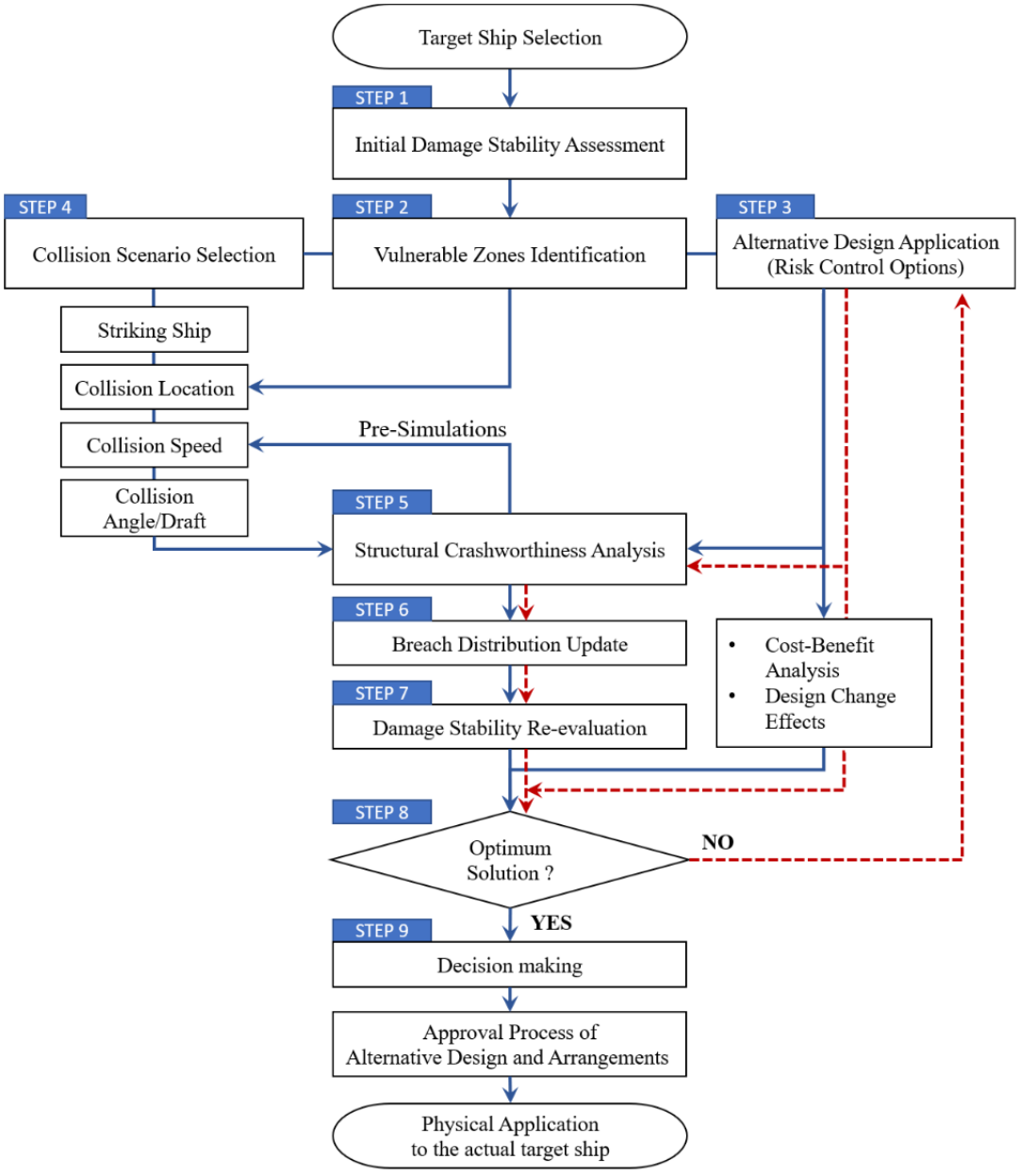

Figure 3.2 Schematic diagram of the proposed methodology in this thesis

3.3 STEP 1: Determination of the risk profile

An initial damage stability assessment needs to be undertaken to determine the distribution of risk assigned to different flooding scenarios of the target ship according to the probabilistic SOLAS 2020 damage stability regulations (see Section 2.2). The method comprises two parts that aim to evaluate the Required Subdivision Index R and the Attained Subdivision Index A. To fulfill a damage stability requirement, the Attained Index A of the target ship must be greater or the same as the Required Subdivision Index R. The Required Subdivision Index R indicates the level of safety of the target ship. Requirements pertaining to persons on board are summarised in Table 3.1.

Table 3.1 Required Subdivision Index formulations depending on POB

Persons on board	R
N(*) < 400	$R = 0.722$
400 ≤ N ≤ 1,350	$R = N / 7{,}850 + 0.66923$
1350 < N ≤ 6,000	$R = 0.0369 \times Ln(N + 89.048) + 0.579$
N > 6,000	$R = 1 - \frac{(852.5 + 0.03875 \times N)}{(N + 5{,}000)}$

(*) N is the total number of persons on board

Attained Subdivision Index A is obtained by the summation of the partial indices A_s, A_p and A_l, weighted, and Each partial Index is a summation of the product p-factor and s-factor as follows:

$$A = 0.4\,A_s + 0.4\,A_p + 0.2A_l \tag{3.1}$$

$$A = \sum p_i \times s_i \tag{3.2}$$

The p-factors are defined depending on the shape of the damage breach and probability derived from collision damage statistics, whilst s-factors are calculated from ship flooding conditions for each damage case (See Section 2.2.2.2). Figure 3.3 shows the overall s-factor results of each damage case indicating their values by colour. The green colour means the survivability of the damage case is more than 0.99, the red colour is less than 0.05, and yellow is the value between the two. On the other hand, the damage cases over the maximum damage length of 60m are indicated with white colour. This process is based on following the zonal approach in

damage stability calculations (Bae et al., 2021).

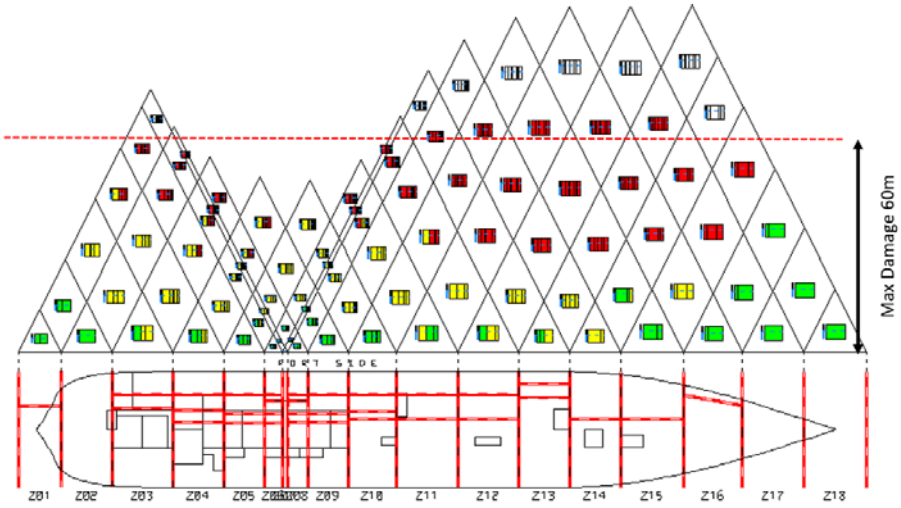

Figure 3.3 Example diagram for s-factor results

3.4 STEP 2: Risk Classification for Vulnerable Zones

3.4.1 General

The second step is vulnerability assessment to identify and classify individual zone risks based on the initial damage stability assessment of the target ship in Step 1. Since this thesis pursues a cost-effective optimum solution, minimum design changes are required for only one or two zones. It is, therefore, essential to classify zones where high risk is evident.

Figure 3.4 illustrates the local maximum and Attained Index in blue and red, respectively, for each damage case depending on their damage positions along the longitudinal x-axis. For one- or two-zone damages, most zones achieved almost their maximum Attained Index, whereas there are significant losses in local Attained Index at the forepart of the ship for three- and four-zone damages (see zones 12 to 17). If the definition of Attained Subdivision Index is recalled, it is simply the summation of the product of p-factors and s-factors for each breach/zone. Whilst the p-factor is a fixed value for a given damage zone, the s-factor changes depending on the consequence of flooding by the said damage. Therefore, these Index differences in Figure 3.4 are caused by low s-factor. Thus, in this thesis, it is defined as “Index Loss” (Bae et al., 2021), as follows:

$$Index\ Loss = \sum p_i \times (1 - s_i) \tag{3.3}$$

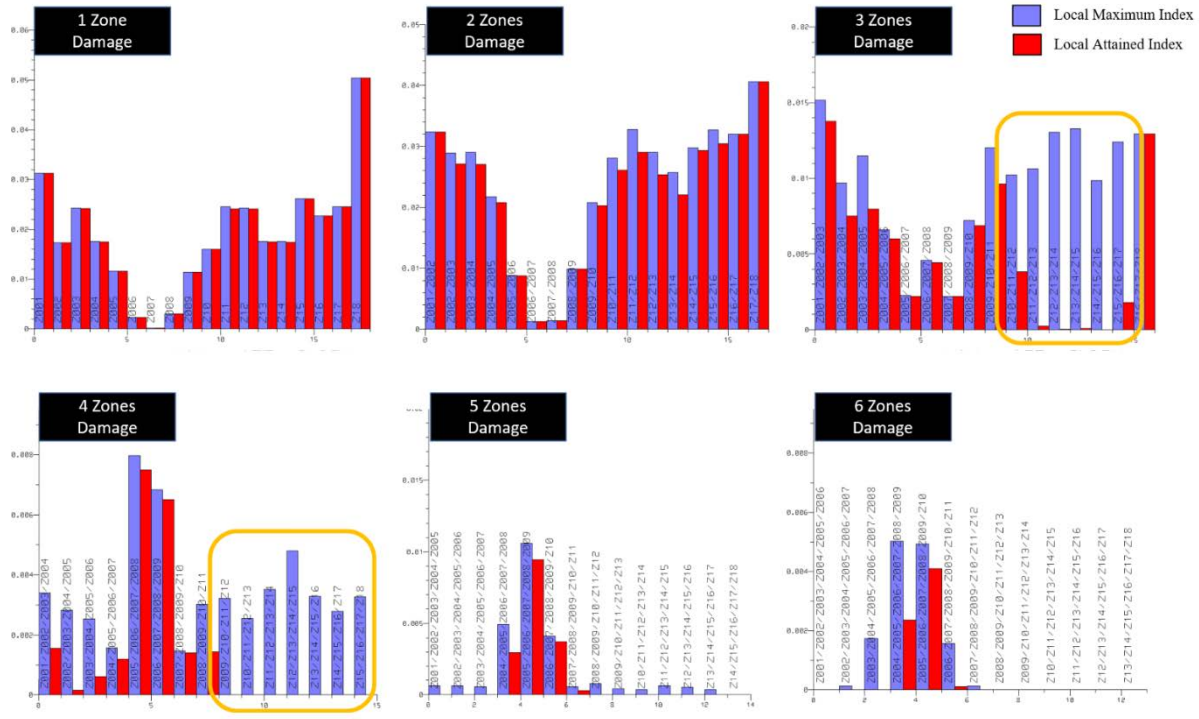

Figure 3.4 Comparision graphs between local maximum Index A and local Attained Index A for each zone damage cases

As shown in Figure 3.5, this "$p \times (1 - s)$" diagram has widely been used for flooding risk identification. This indicates each damage case risk showing all local Index loss (i.e., p × (1-s)) values from single-compartment damage to multi-compartment damages along with damage locations. From this graph, the damage case with the largest Index loss can be identified (e.g. 3-zone damage case at Zone16 in the graph), and most authors intend to focus on this zone for damage stability enhancement. However, the zone with the damage case with the highest damage loss will not always be the most vulnerable area in the target ship because the summation of local damage loss for other zones might have a larger total index loss. Hence, the local risk summation for each zone must be carried out. However, it is not simple to consider index loss for multi-zone damage cases as the damage occurs over zones. For example, let us assume that an Index loss of 0.003 is for a case of three-zone damages. How much Index loss do we consider for each zone? Dividing the index loss equally or depending on zone length? It is not clear.

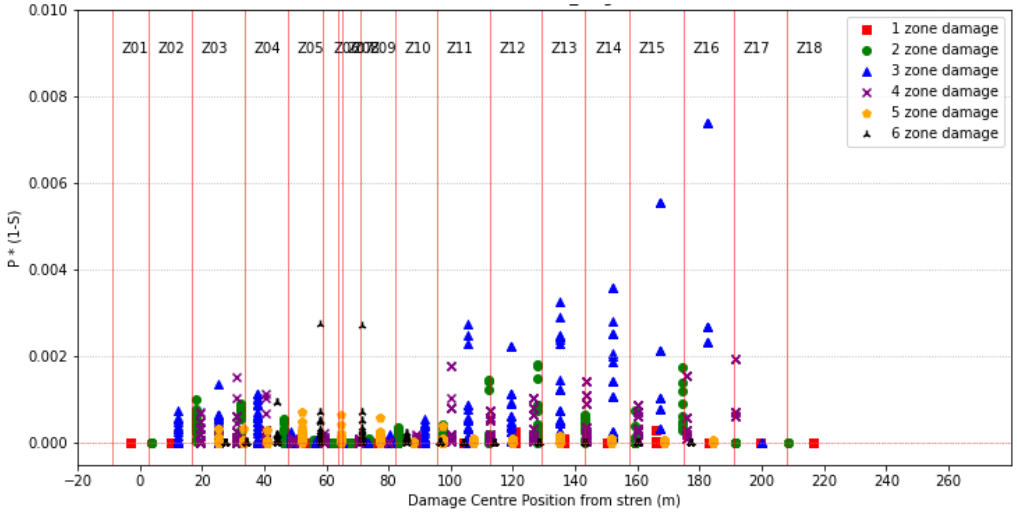

Figure 3.5 A typical example of Px(1-S) graph

3.4.2 Two Approaches for Vulnerability Analysis

Two different approaches are taken into account for assessing zone vulnerability. The first is to divide the Index loss among all related zones equally (Bae et al., 2021) (hereafter, it is termed an equality approach). The second method is that a zone where a damage centre locates takes all damage loss (hereafter, it is termed as a plurality approach).

3.4.2.1 Equality Approach

The first approach is based on an equality approach of Index loss to all zones associated with the corresponding damage case. For the example highlighted in Section 3.4.1, if there is an Index loss of 0.003 for a three-zone damage case from zone 11 to zone 13, an Index loss of 0.01 is equally assigned to each zone. Figure 3.6 illustrates how to calculate the Index loss of each zone using an Index loss equality assumption. The Index losses obtained from one-zone damage to six-zone damage cases are equally distributed to each corresponding zone, and summations are shown at the bottom of the table. It indicates the local risks of zones, enabling of classification of the vulnerability of zones in order of high risks. A summary of the results is presented in Table 3.2, with rankings of zones for vulnerability. Zone 15 was identified as the most vulnerable zone, as marked in red, and Zone 13 and 14 were followed as the second and third rankings, as shown in blue, respectively.

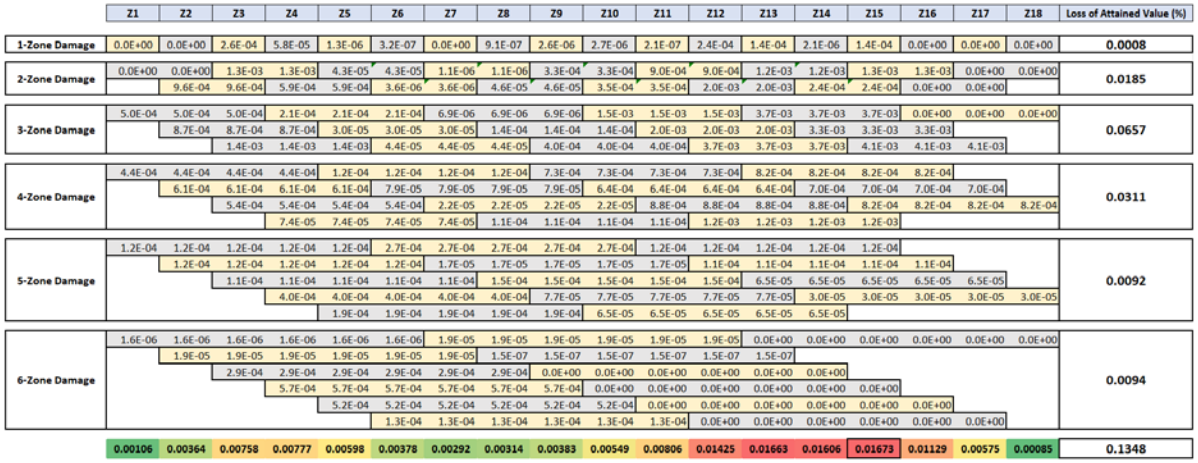

Figure 3.6 Example of vulnerability analysis using equality approach

Table 3.2 Detailed calculation for vulnerable zone assessment based on equality approach of Index loss assumption without distance factors

	1-zone damage	2-zone damage	3-zone damage	4-zone damage	5-zone damage	6-zone damage	Local A-Index	Risk ranking
Z1	0.0000	0.0000	0.0005	0.0004	0.0001	0.0000	**0.0011**	17
Z2	0.0000	0.0010	0.0014	0.0010	0.0002	0.0000	**0.0036**	14
Z3	0.0003	0.0023	0.0028	0.0016	0.0004	0.0003	**0.0076**	8
Z4	0.0001	0.0019	0.0025	0.0017	0.0008	0.0009	**0.0078**	7
Z5	0.0000	0.0006	0.0017	0.0013	0.0009	0.0014	**0.0060**	9
Z6	0.0000	0.0000	0.0003	0.0008	0.0011	0.0015	**0.0038**	13
Z7	0.0000	0.0000	0.0001	0.0003	0.0010	0.0016	**0.0029**	16
Z8	0.0000	0.0000	0.0002	0.0003	0.0010	0.0015	**0.0031**	15
Z9	0.0000	0.0004	0.0005	0.0009	0.0007	0.0012	**0.0038**	12
Z10	0.0000	0.0007	0.0020	0.0015	0.0006	0.0007	**0.0055**	11
Z11	0.0000	0.0012	0.0039	0.0024	0.0004	0.0002	**0.0081**	6
Z12	0.0002	0.0029	0.0071	0.0035	0.0005	0.0000	**0.0143**	**4**
Z13	0.0001	0.0032	0.0094	0.0035	0.0004	0.0000	**0.0166**	**2**
Z14	0.0000	0.0014	0.0107	0.0036	0.0004	0.0000	**0.0161**	**3**
Z15	0.0001	0.0016	0.0112	0.0035	0.0003	0.0000	**0.0167**	**1**
Z16	0.0000	0.0013	0.0074	0.0023	0.0002	0.0000	**0.0113**	**5**
Z17	0.0000	0.0000	0.0041	0.0015	0.0001	0.0000	**0.0057**	10
Z18	0.0000	0.0000	0.0000	0.0008	0.0000	0.0000	**0.0008**	18
Total Index Loss							**0.1348**	

(*) The red number means the first ranking, and the second and third rankings are shown in blue.

In addition to the equality approach, distance effects from the centre of ship gravity (COG) are also taken into account the distance from COG because flooding far from the COG worsens ship trim, negatively affecting ship damage stability such as early progressive floodings. The

detailed calculations are shown in Table 3.3. Distance factors ③ multiply by each index loss ④, then it scales up to have the identical sum of index loss ⑥. As a result of this approach, Zone 15 was identified as the zone where the highest risk exists.

Table 3.3 Detailed calculation for vulnerable zone assessment based on equality approach of Index loss assumption with distance factors

	Zone centre ①	Distance from COG ②= COG - ①	Distance factor ③=② / Lbp	Local Index loss ④	Modified Index loss ⑤=④ x③	Scaled Index loss ⑥=⑤x⑦/⑧	Risk ranking
Z1	-3.07	102.27	47%	0.0011	0.0005	0.0022	12
Z2	9.80	89.40	41%	0.0036	0.0015	0.0065	8
Z3	25.20	74.00	34%	0.0076	0.0026	0.0112	6
Z4	40.65	58.55	27%	0.0078	0.0021	0.0091	7
Z5	53.35	45.85	21%	0.0060	0.0013	0.0055	10
Z6	61.45	37.75	17%	0.0038	0.0007	0.0029	11
Z7	64.60	34.60	16%	0.0029	0.0005	0.0020	13
Z8	68.10	31.10	14%	0.0031	0.0005	0.0020	15
Z9	76.50	22.70	10%	0.0038	0.0004	0.0017	16
Z10	88.80	10.40	5%	0.0055	0.0003	0.0011	17
Z11	103.95	4.75	2%	0.0081	0.0002	0.0008	18
Z12	120.80	21.60	10%	0.0143	0.0014	0.0062	9
Z13	136.25	37.05	17%	0.0166	0.0028	**0.0123**	**4**
Z14	150.35	51.15	24%	0.0161	0.0038	**0.0164**	**3**
Z15	166.15	66.95	31%	0.0167	0.0052	**0.0224**	**1**
Z16	183.00	83.80	39%	0.0113	0.0044	**0.0189**	**2**
Z17	199.55	100.35	46%	0.0057	0.0027	**0.0115**	**5**
Z18	216.75	117.55	54%	0.0008	0.0005	0.0020	14
Total Index Loss				⑦ **0.1348**	⑧ **0.0311**	**0.1348**	

(*) The red number means the first ranking, and the second and third rankings are shown in blue.

3.4.2.2 Plurality Approach

The second approach is to assume a zone, where the damage centre locates, withstands all Index loss alone (sometimes, it is called "*winner-take-all*"). In the case of the previous example with a local Index loss of 0.003 for a three-zone damage case, the centre zone where a damage centre locates takes all of 0.003 is taken under consideration, and the others are assumed as no contribution to Index loss. Figure 3.6 illustrates an example of calculations. The local Index losses obtained from one-zone damage to six-zone damage cases are distributed to only one zone where the damage centre locates, and summations are shown at the bottom of the table. The summary of the results is presented in Table 3.4 with rankings of zones for vulnerability, and Table 3.5 shows the results with distance effects from the COG of the ship to the centre of

the zone.

	Z1	Z2	Z3	Z4	Z5	Z6	Z7	Z8	Z9	Z10	Z11	Z12	Z13	Z14	Z15	Z16	Z17	Z18	Loss of Attained Value (%)
1-Zone Damage	0.0E+00	0.0E+00	2.6E-04	5.8E-05	1.3E-06	3.2E-07	0.0E+00	9.1E-07	2.6E-06	2.7E-06	2.1E-07	2.4E-04	1.4E-04	2.1E-06	1.4E-04	0.0E+00	0.0E+00	0.0E+00	0.0008
2-Zone Damage	0.0E+00	0.0E+00	4.5E-03	1.2E-03	8.6E-05	7.2E-06	0.0E+00	2.1E-06	9.2E-05	6.7E-04	2.5E-03	4.0E-03	2.3E-03	0.0E+00	3.2E-03	0.0E+00	0.0E+00	0.0E+00	0.0185
3-Zone Damage	0.0E+00	1.5E-03	2.6E-03	4.2E-03	7.3E-04	0.0E+00	1.3E-04	0.0E+00	4.5E-04	1.2E-03	4.5E-03	5.9E-03	1.1E-02	1.1E-02	9.9E-03	1.2E-02	0.0E+00	0.0E+00	0.0657
4-Zone Damage	0.0E+00	0.0E+00	4.2E-03	2.2E-03	2.9E-04	4.7E-04	0.0E+00	3.2E-04	8.7E-05	4.5E-04	2.9E-03	6.1E-03	0.0E+00	4.8E-03	3.3E-03	2.8E-03	3.3E-03	0.0E+00	0.0311
5-Zone Damage	0.0E+00	0.0E+00	1.2E-03	5.5E-04	2.0E-03	0.0E+00	9.4E-04	0.0E+00	1.4E-03	8.4E-05	1.1E-03	3.3E-04	6.1E-04	5.3E-04	3.3E-04	1.5E-04	0.0E+00	0.0E+00	0.0092
6-Zone Damage	0.0E+00	0.0E+00	9.9E-06	1.9E-03	3.4E-03	0.0E+00	0.0E+00	0.0E+00	3.1E-03	8.0E-04	1.1E-04	0.0E+00	0.0E+00	0.0E+00	0.0E+00	0.0E+00	0.0E+00	0.0E+00	0.0094
	0.00000	0.00149	0.01285	0.01007	0.00655	0.00048	0.00107	0.00032	0.00513	0.00321	0.01116	0.01655	0.01403	0.01652	0.01676	0.01534	0.00328	0.00000	0.1348

Figure 3.7 Example of vulnerability analysis using plurality approach

Table 3.4 Detailed calculations for vulnerable zone assessment based on plurality approach of Index loss assumption without distance factors

	1-zone damage	2-zone damage	3-zone damage	4-zone damage	5-zone damage	6-zone damage	Local A-Index	Risk ranking
Z1	0.0000	0.0000	0.0000	0.0000	0.0000	0.0000	0.0000	17
Z2	0.0000	0.0000	0.0015	0.0000	0.0000	0.0000	0.0015	13
Z3	0.0003	0.0045	0.0026	0.0042	0.0012	0.0000	0.0128	6
Z4	0.0001	0.0012	0.0042	0.0022	0.0006	0.0019	0.0101	8
Z5	0.0000	0.0001	0.0007	0.0003	0.0020	0.0034	0.0065	9
Z6	0.0000	0.0000	0.0000	0.0005	0.0000	0.0000	0.0005	15
Z7	0.0000	0.0000	0.0001	0.0000	0.0009	0.0000	0.0011	14
Z8	0.0000	0.0000	0.0000	0.0003	0.0000	0.0000	0.0003	16
Z9	0.0000	0.0001	0.0004	0.0001	0.0014	0.0031	0.0051	10
Z10	0.0000	0.0007	0.0012	0.0005	0.0001	0.0008	0.0032	12
Z11	0.0000	0.0025	0.0045	0.0029	0.0011	0.0001	0.0112	7
Z12	0.0002	0.0040	0.0059	0.0061	0.0003	0.0000	**0.0166**	**2**
Z13	0.0001	0.0023	0.0110	0.0000	0.0006	0.0000	0.0140	5
Z14	0.0000	0.0000	0.0112	0.0048	0.0005	0.0000	**0.0165**	**3**
Z15	0.0001	0.0032	0.0099	0.0033	0.0003	0.0000	**0.0168**	**1**
Z16	0.0000	0.0000	0.0124	0.0028	0.0001	0.0000	0.0153	4
Z17	0.0000	0.0000	0.0000	0.0033	0.0000	0.0000	0.0033	11
Z18	0.0000	0.0000	0.0000	0.0000	0.0000	0.0000	0.0000	17
Total Index Loss							**0.1348**	

(*) The red number means the first ranking, and the second and third rankings are shown in blue.

Table 3.5 Detailed calculations for vulnerable zone assessment based on plurality approach of Index loss assumption with distance factors

	Zone centre ①	Distance from COG ②= COG - ①	Distance factor ③=② / Lbp	Local Index loss ④	Modified Index loss ⑤=④ x③	Scaled Index loss ⑥=⑤x⑦/⑧	Risk ranking
Z1	-3.07	102.27	47%	0.0000	0.0000	0.0000	17
Z2	9.80	89.40	41%	0.0015	0.0006	0.0027	10
Z3	25.20	74.00	34%	0.0128	0.0044	**0.0191**	**3**
Z4	40.65	58.55	27%	0.0101	0.0027	0.0119	5
Z5	53.35	45.85	21%	0.0065	0.0014	0.0060	9
Z6	61.45	37.75	17%	0.0005	0.0001	0.0004	15
Z7	64.60	34.60	16%	0.0011	0.0002	0.0007	13
Z8	68.10	31.10	14%	0.0003	0.0000	0.0002	16
Z9	76.50	22.70	10%	0.0051	0.0005	0.0023	11
Z10	88.80	10.40	5%	0.0032	0.0002	0.0007	14
Z11	103.95	4.75	2%	0.0112	0.0002	0.0011	12
Z12	120.80	21.60	10%	0.0166	0.0016	0.0072	7
Z13	136.25	37.05	17%	0.0140	0.0024	0.0105	6
Z14	150.35	51.15	24%	0.0165	0.0039	**0.0170**	**4**
Z15	166.15	66.95	31%	0.0168	0.0052	**0.0226**	**2**
Z16	183.00	83.80	39%	0.0153	0.0059	**0.0259**	**1**
Z17	199.55	100.35	46%	0.0033	0.0015	0.0066	8
Z18	216.75	117.55	54%	0.0000	0.0000	0.0000	17
Total Index Loss				**⑦ 0.1348**	**⑧ 0.0311**	**0.1348**	

(*) The red number means the first ranking, and the second and third rankings are shown in blue.

3.4.2.3 Adjacent Zones Consideration and Summary

Figure 3.8 summarises the vulnerability analysis results using two different approaches with and without distance factors. The plurality approach with distance factors (see Table 3.5) shows that Zone 16 is the highest risk, and Zone 3 and 4 are included in the top five highest-risk zones. Whereas Zone 15 is identified as the most vulnerable zone calculated from other approaches, and all top five vulnerable zones have been identified at the forepart of the ship (See also Table 3.2 ~ 3.4).

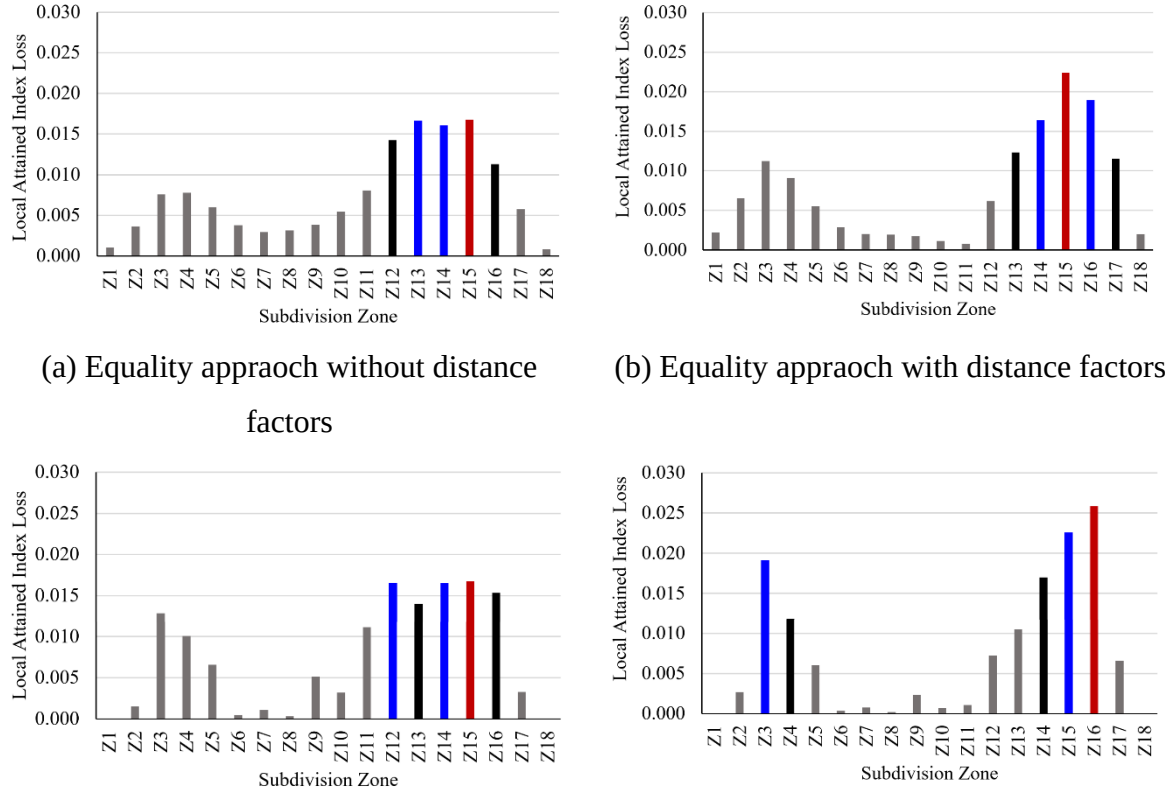

(a) Equality appraoch without distance factors

(b) Equality appraoch with distance factors

(c) Plurality approach without distance factors

(d) Plurality approach with distance factors

Figure 3.8 Vuneralbility analysis results derived from two different approaches with and without distance factors

A series of actual damage stability calculations have been carried out to identify how much Attained Index in each zone can be actually recovered. Each zone in question was assumed to be fully protected from damages and not flooded (i.e., the permeability of the zone was set as 0). Damage stability improvements from zone 12 to zone 16 have been compared to the vulnerability analysis results shown in Table 3.6.

Table 3.6 Comparision results between actual calculations and vulnerability analyses

Zones	Actual calculations (A Index recovery)	Vulnerability Analyses (Local Index A losses)			
		Equality approach without distance factors	Equality approach with distance factors	Plurality approach without distance factors	Plurality approach with distance factors
Zone 12	**4th (0.0380)**	4th (0.0143)	9th (0.0062)	2nd (0.0166)	7th (0.0072)
Zone 13	**3rd (0.0434)**	2nd (0.0166)	4th (0.0123)	5th (0.0140)	6th (0.0105)
Zone 14	**2nd (0.0444)**	3rd (0.0161)	3rd (0.0164)	3rd (0.0165)	4th (0.0170)
Zone 15	**1st (0.0457)**	**1st** (0.0167)	**1st** (0.0224)	**1st** (0.0168)	2nd (0.0226)
Zone 16	**5th (0.0319)**	5th (0.0113)	2nd (0.0189)	4th (0.0153)	**1st** (0.0259)
Zone 17	-	10th (0.0106)	5th (0.1150)	11th (0.0033)	8th (0.0066)

(*) The red number means the first ranking, and the second and third rankings are shown in blue.

From actual calculations with the permeability change of each zone, the improved Index A between 0.0319 and 0.0457 was obtained, which is approximately three times the local Index loss of each zone calculated from the proposed vulnerability analysis (i.e., 0.113~00167 in the case of equality approach results). This means that each zone improvement may affect other zones (see Figure 6.16). Therefore, it may be reasonable to consider adjacent zones for this vulnerability analysis. For example, the local Index-A loss of Zone 15 becomes 0.0441 when the equality approach is used. This is a summation of Zone 14, Zone 15 and Zone 16 (i.e., 0.0161 + 0.0167 +0.0113 = 0.0441). Table 3.7 presents results, taking into account adjacent zones, and Table 3.8 compares high-ranked zones. The plurality approach considering adjacent zones without distance factors shows almost identical results compared with the actual calculation results. In particular, the differences between Index A improvements and local Index loss for adjacent zones are in the range of 6.4 ~ 10.8 %. Therefore, the plurality approach to three adjacent zones is recommended for the vulnerability analysis to classify the risks of all subdivision zones.

Table 3.7 Detailed calculations for vulnerable zone assessment based on plurality approach of Index loss assumption with and without distance factors considering adjacent zones effects

	Equality approach without distance factors		Equality approach with distance factors		Plurality approach without distance factors		Plurality approach with distance factors	
	+ considering adjacent zones							
	Index Loss	Ranking	Index Loss	Ranking	Index Loss	Ranking	Index Loss	Ranking
Z1	0.0047	18	0.0087	13	0.0015	18	0.0027	17
Z2	0.0123	14	0.0199	8	0.0143	12	0.0217	8
Z3	0.0190	8	0.0268	6	0.0244	8	0.0335	6
Z4	0.0213	7	0.0258	7	0.0295	7	**0.0369**	**4**
Z5	0.0175	10	0.0174	10	0.0171	11	0.0182	10
Z6	0.0127	12	0.0104	12	0.0081	14	0.0071	12
Z7	0.0098	16	0.0068	15	0.0019	17	0.0013	18
Z8	0.0099	15	0.0057	16	0.0065	15	0.0033	15
Z9	0.0125	13	0.0048	17	0.0087	13	0.0032	16
Z10	0.0174	11	0.0036	18	0.0195	9	0.0041	14
Z11	0.0278	6	0.0081	14	0.0309	6	0.0089	11
Z12	**0.0389**	**4**	0.0193	9	**0.0417**	**4**	0.0186	9
Z13	**0.0469**	**2**	**0.0349**	**4**	**0.0471**	**3**	**0.0346**	**5**
Z14	**0.0494**	**1**	**0.0512**	**3**	**0.0473**	**2**	**0.0500**	**3**
Z15	**0.0441**	**3**	**0.0578**	**1**	**0.0486**	**1**	**0.0654**	**1**
Z16	**0.0338**	**5**	**0.0529**	**2**	**0.0354**	**5**	**0.0550**	**2**
Z17	0.0179	9	**0.0325**	**5**	0.0186	10	0.0325	7
Z18	0.0066	17	0.0135	11	0.0033	16	0.0066	13
Total Index Loss							**0.1348**	

(*) The red number means the first ranking, and the second and third rankings are shown in blue.

Table 3.8 Comparision results between actual calculations and vulnerability analyses considering adjacent zones effects

Zones	Actual calculations (A Index recovery)	Vulnerability Analysis **+ considering adjacent zones** (Local Index-A losses)			
		Equality approach without distance factors	Equality approach with distance factors	Plurality approach without distance factors	Plurality approach with distance factors
Zone 12	**4th (0.0380)**	4th (0.0389)	9th (0.0193)	**4th (0.0417)**	9th (0.0186)
Zone 13	**3rd (0.0434)**	2nd (0.0469)	4th (0.0349)	**3rd (0.0471)**	5th (0.0346)
Zone 14	**2nd (0.0444)**	3rd (0.0494)	3rd (0.0512)	**2nd (0.0473)**	3rd (0.0500)
Zone 15	**1st (0.0457)**	**1st (0.0441)**	**1st (0.0578)**	**1st (0.0486)**	**1st (0.0654)**
Zone 16	**5th (0.0319)**	5th (0.0338)	2nd (0.0529)	**5th (0.0354)**	**2nd** (0.0550)
Zone 17	-	9th (0.0179)	5th (0.0325)	10th (0.0186)	7th (0.0325)

(*) The red number means the first ranking, and the second and third rankings are shown in blue.

3.5 STEP 3: Alternative Design Application as RCOs

The third step is to apply alternative design solutions, risk control options (RCOs), to identified target zones to increase overall ship safety. Traditional solutions involve the rearrangement of ship subdivision, installation of additional buoyancy tanks and sponsons, and layout changes for reducing KG. However, in this thesis, the following simple crashworthy structural arrangements were employed for a minimum design change and high cost-effectiveness:

- **Double hull plates (Structural type RCO)**
  Two single longitudinal subdivisions at both sides with four different positions, such as at B/20, 2B/20, 3B/20 and 4B/20, were investigated.
- **Multi longitudinal plates (Structural type RCO)**
  The first longitudinal subdivision plays a role like the double hull plates, while the second subdivision will be installed just after a maximum penetration position, protecting an internal safe space.
- **Hull thickness change (Structural type RCO)**
  The measures with a strengthened hull were taken into account. Six kinds of different thickness changes were considered, such as:
  - 50% and 100% more thickened than the original hull
  - Identical hull thickness of 20T, 30T, 40T and 50T.
- **Combinations of RCOs (Structural type RCO)**
  More than two types of structural passive RCOs were applied simultaneously to find optimum solutions.
- **Foam void filling (Non-structural type RCO)**
  A high-expansion foam was used to fill the spaces between the external and internal plates with foam to protect against asymmetry during flooding, reduce permeability of the void space and enhance crashworthiness of the overall arrangement (i.e., wing compartments filled with foam).

The detailed descriptions of each RCO are presented in Chapter 5, and the results of implementing those are demonstrated in Chapter 6.

3.6 STEP 4: Collision Scenario Definition

Collision scenarios are the most critical factors for crashworthiness analysis of ship collisions. In particular, the following parameters associated with operating conditions and accident situations should be taken into account:

- Striking ship
- Collision speed
- Collision location
- Collision angle, draught and trim

Many authors suggested the methods of potential collision scenarios based on collision probability from AIS data (Ståhlberg et al., 2013, Zhang et al., 2021a) or actual accident databases (Paik et al., 2017). However, this thesis considers only a reasonable worst-case scenario based on SOLAS 2020 regulations to take into account maximum damage from collisions. However, it is recommended that the final collision scenario should be discussed with and approved by the Administration in a real case and should consider actual operating routes and profiles of the target ship.

3.6.1 Striking Ship

The striking ship is a vital parameter in ship collisions since it influences both external dynamics and internal mechanics of damages. External dynamics are mainly related to ship mass and collision speed of a striking ship :

$$Initial\ Kinetic\ Energy_{striking\ ship} = \frac{1}{2}mV^2 \qquad (3.4)$$

The fore part shape of the striking ship also influences internal mechanics and may result in different damage results, as shown in Figure 3.9. Therefore, it seems reasonable to select a striking ship with a high probability of encountering a target struck ship based on its actual operational profile history, such as AIS data (Zhang et al., 2021a, Zhang et al., 2021b) of the target ship. However, the proposed methodology assumes that a striking ship has been already designated, and it is out of the work scope of this thesis. Therefore, the final decision for the striking ship must be discussed with the associated Administration.

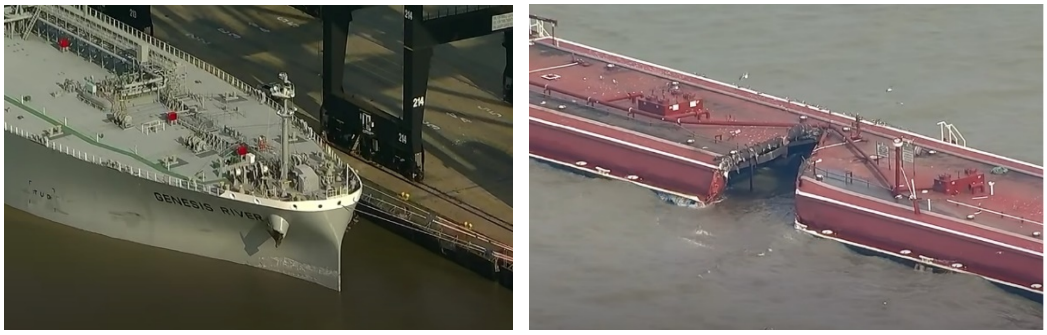

(a)

(b)

Figure 3.9 Different types of striking ships and collision results: (a) Striking ship with a plumb stem bow (ABC13, 2019) and (b) String ship with a raked stem and a bulbous bow (BEAmer, 2018)

3.6.2 **Collision Speed**

The collision speed of the striking ship mainly dominates initial collision kinetic energy, directly affecting damage extents, as shown in Equation (3.4). However, various range of collision speeds has been employed for large-scale ship collision simulations so far. For example, Schreuder et al. (2011) employed collision speeds of 2 ~ 10 knots for 179m RoPax vessel collision against the identical size of RoPax, while Hogström and Ringsberg (2012) adopted 5 and 7 knots collision speeds for the same RoPax vessel collisions. Paik et al. (2017) suggested a maximum 6.024 knots collision speed based on the collision database from 1991 to 2012 for collision simulations of a struck VLCC tanker against various types of vessels. More recently, Kim et al. (2021) performed collision simulations using 0.5 ~ 9.0 knots collision speeds for a 9,000 TEU container ship. Kim et al. (2022) employed collision speeds of 5 and 10 knots at full-scaled collision simulations between a cruise ship and a Ro-Pax for a benchmark study on an EU-funded project. On the other hand, some researchers adopted a higher speed for their simulations. Zheng et al. (2007) used 7, 14 and 18 knots for Aframax tanker collision simulations against the same type of vessel. Zhang et al. (2004) and Kõrgesaar

et al. (2014) carried out their simulations with 10 m/s (19.44 knots) for a 90m multi-purpose cargo ship and a 310m LNG carrier using a tanker bow shape and a bulbous bow shape indenter, respectively. Ehlers et al. (2008) also carried out collision simulations with a collision speed of 10 m/s for numerical validations between crashworthy structures and a bow shape indenter and compared them to experiments performed by TNO (the Netherlands Institute for applied physical research). It should be noted that the kinetic energy with 19.44 knots is 15 times larger than that with 5 knots, and the consequences of those simulations are entirely different. Therefore, a proper collision speed must be carefully selected for crashworthiness analysis.

Under these circumstances, this thesis proposes "*a relative collision speed*" to fulfil the current regulatory criteria and to avoid simulation errors from various simulation parameters. According to SOLAS (IMO, 2017b), the maximum transverse penetration for damage stability calculation is defined up to B/2 to consider the worst heeling moment condition. Therefore, an initial collision speed can be defined as a speed resulting in B/2 transverse penetration on a target stuck ship. Additionally, an identical collision speed may result in different simulation outcomes due to various simulation setups with different analysis approaches. However, this relative collision speed also helps simulations calibrate result gaps from different simulation settings (see Chapter 7 Sensitivity study). Therefore, a series of pre-simulations of collision analyses at various speeds are required to find a relative collision speed for a B/2 penetration. Figure 3.10 shows pre-simulations for a collision speed selection employed in the proposed methodology. For collision conditions, a speed of a struck ship is assumed to be in a static condition with zero speed.

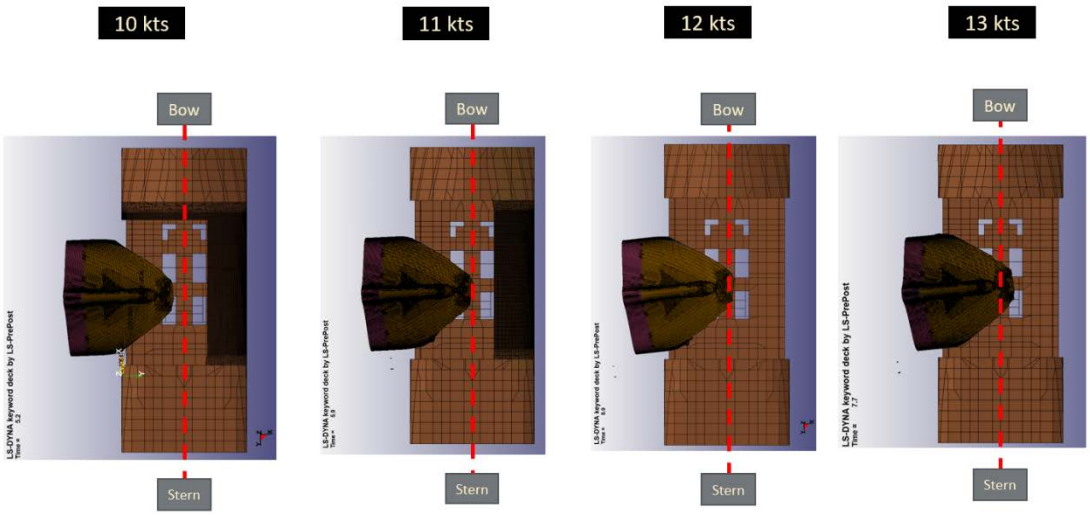

Figure 3.10 Example of pre-simulations for a collision speed selection

3.6.3 Collision Location

The collision location is defined as a centre of a selected vulnerable zone, where RCOs will be implemented for damage stability improvement, as previously described in Section 3.4.

3.6.4 Collision Angle

Collision angles between two ships also affect damage consequences, generating different damage extents. For a perpendicular collision (i.e., 90° collision angle), the initial kinetic energy in a transverse direction of a struck ship will impact the struck ship, while the penetration may be reduced in other angle collisions. Zhang (1999) carried out collision analyses for the case of two container vessels, and a collision at 120° gave the maximum energy. However, the collision condition was assumed that two container vessels move at 4.5 m/s speed (see Figure 3.11(a)). Brown (2002) also performed a series of collision simulations at a collision speed of 4.27 knots for two 150,000 dwt oil tankers and two 45,000 dwt oil tankers. In this case, the speed of struck ships was set to 2.49 knots. From the simulation results, the maximum penetrations occurred at 80 ~ 85°, as shown in Figure 3.11(b).

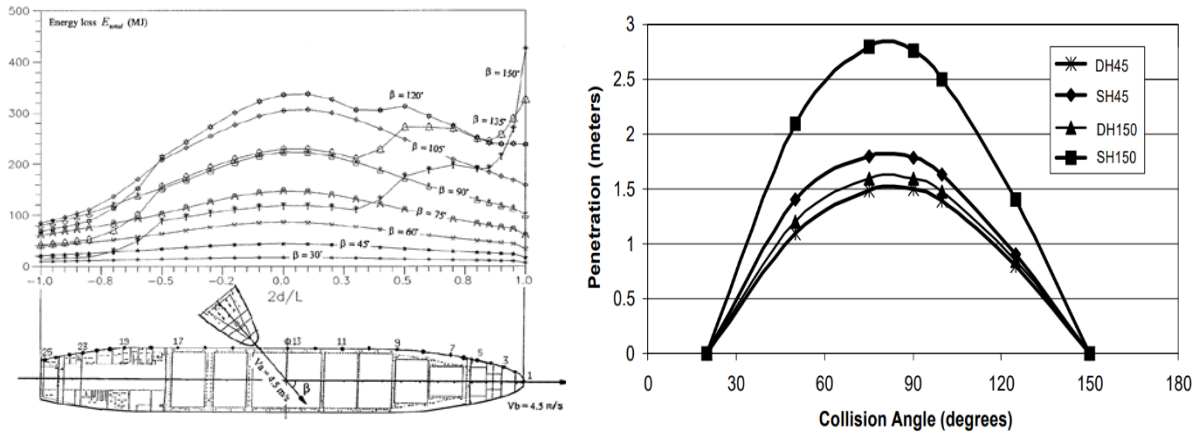

(a) (b)

Figure 3.11 Simulation results at the different angles (a) struck ship speed of 8.75 knots (4.5m/s) (Zhang, 1999) and (b) struck ship speed of 2.49 knots (Brown, 2002)

On the other hand, Zheng et al. (2007) assumed that the struck ship was in a static condition with zero speed in the Aframax tanker collision simulations. As a result, the maximum internal energy was obtained at 90° collision in Figure 3.12 (a). Hogström and Ringsberg (2012) also carried out a series of simulations for 179m RoPax collisions, and the struck ship speed was set to zero in the collision scenario. The results showed that 90° collisions showed the maximum damage openings, as indicated in Figure 3.12 (b).

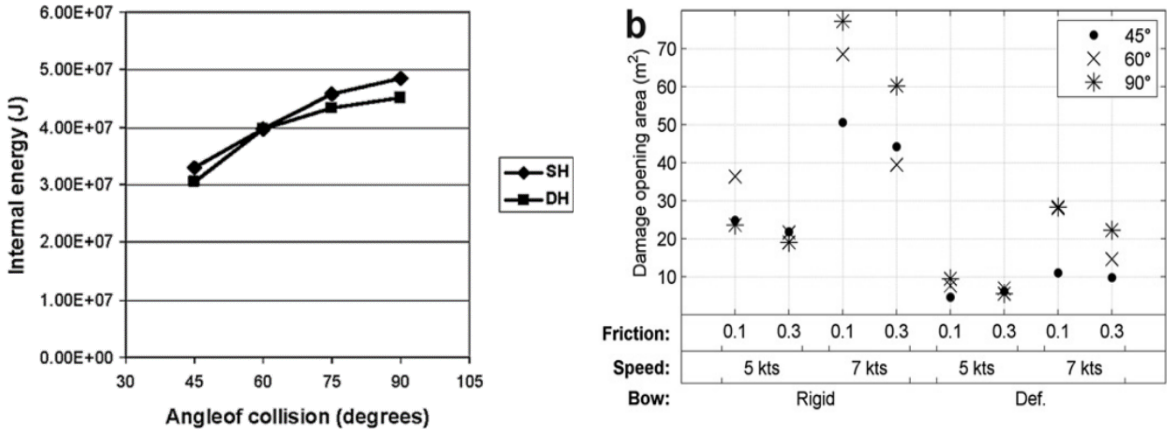

(a) (b)

Figure 3.12 Simulation results at the different angles with struck ship speed of 0 knots (a) by Zheng et al. (2007) and (b) by Hogström and Ringsberg (2012)

According to the previous Section 3.6.2, the speed of a struck ship is assumed zero. Therefore, the collision angle of this proposed methodology is set to 90° for maximum energy delivery in simulations.

3.6.5 Collision Draught and Trim

Collision draughts of both striking and stuck ships are associated with the corresponding displacements, affecting the initial kinetic energy of the striking ship, the dissipated energy for the struck ship and resulting in different damage consequences. Therefore, Zhang et al. (2004) suggested using four different draughts in collision simulations as follows:

$$\begin{cases} \Delta T_1 = T_{2max} - \dfrac{3T_{1min} + T_{1max}}{4} \\ \Delta T_2 = T_{2max} - \dfrac{T_{1min} + 3T_{1max}}{4} \\ \Delta T_3 = \dfrac{T_{2min} + 3T_{2max}}{4} - T_{1max} \\ \Delta T_4 = \dfrac{3T_{2min} + T_{2max}}{4} - T_{1max} \end{cases} \tag{3.5}$$

where, T_1 and T_2 are draughts of the striking and struck ship, respectively.

However, all requisite information is not always available, and various conditions make simulations complicated. Therefore, in this thesis, only design draughts of the two ships are

utilised for collision simulations between them.

3.7 STEP 5: Structural Crashworthiness Analysis

Structural crashworthiness analyses for alternative designs with RCOs are a core process in this proposed methodology. The aim is to obtain precise damage extents for damage probability updates of the target struck ship. For structural response during collisions as internal mechanics, various well-known numerical methods and tools have been utilised, such as LS-DYNA (Hallquist, 2007, Paik, 2020), ABAQUS(Simulia, 2008) and SHARP (Paboeuf et al., 2015). In addition, a fluid-structure interaction model such as MCOL (Le Sourne et al., 2003) has also been adopted to provide practical motions of both ships during collisions for external dynamics. In this thesis, crashworthiness analyses have been carried out using ANSYS LS-DYNA explicit code and MCOL solver for internal mechanics and external dynamics, respectively, in ship collisions. Furthermore, ANSYS AQWA(ANSYS, 2019) has also been employed for input data of MCOL, such as mass matrix, hydrostatic restoring matrix and added mass matrix. A more detailed methodology for this nonlinear finite element method is described in Chapter 4.

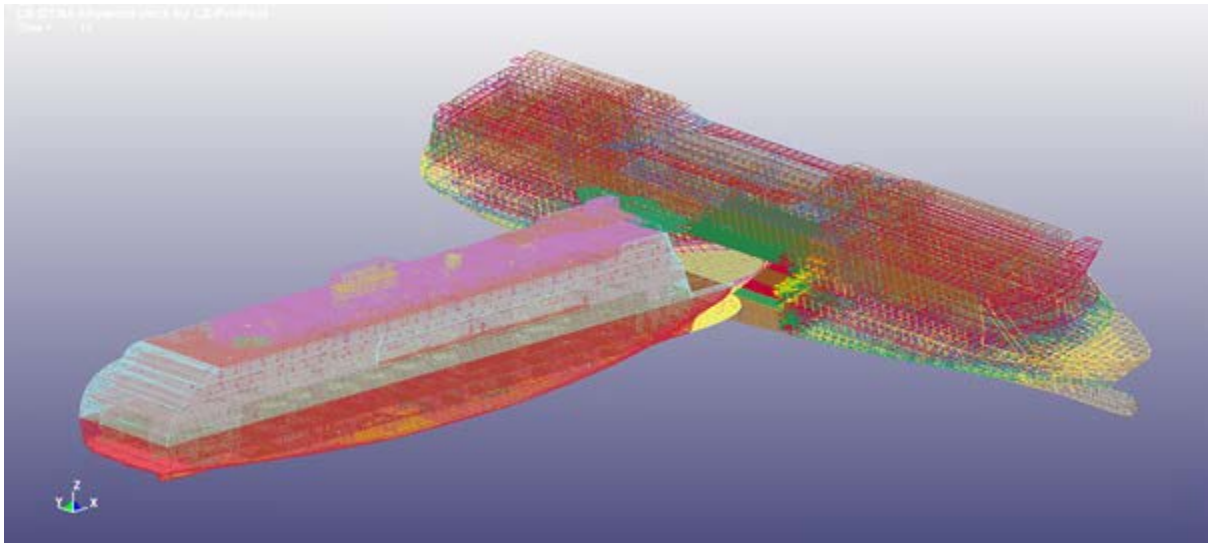

Figure 3.13 Example of structural crashworthiness analysis using LS-DYNA

3.8 STEP 6: Transverse Damage Breach Distribution Update

This step of the methodology aims to update the local damage breach distribution of the target zone. Local p-factors of each damage case can be improved as a result of maximum penetrations obtained from simulations. The target zone's cumulative distribution function (CDF) is proportionally adjusted from a pre-defined SOLAS CDF by the penetration reduction obtained from the collision simulations, as shown in Figure 3.14. Then, the corresponding PDF from SOLAS is replaced with a new probability density function (PDF) (Bae et al., 2021) (see Section 6.9)

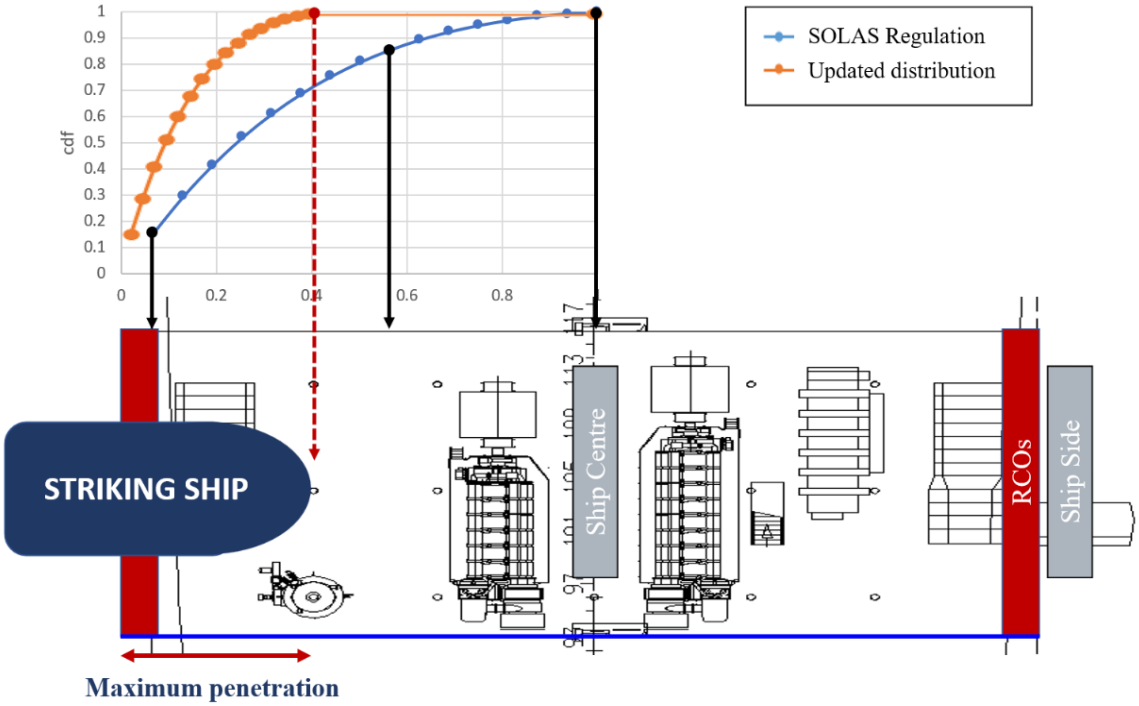

Figure 3.14 Example of a transverse damage distribution update based on collision simulation results

3.9 STEP 7: Re-evaluation of Damage Stability

This step aims to re-evaluate the damage stability of the vessel and identify how much the overall Index A has been improved by RCOs in Step 3 and the damage distributions updated in Step 6. Figure 3.15 shows the differences of s-factors for all damage cases between the original layout and a RCO with a double-hull plate application to the target zone (i.e., Zone 13); s-factors of some damage cases between zone 11 and 14 have been improved by the RCO on zone 13. The outer shell of the vessel and the double plates make wing compartments on both sides of the ship, contributing to overall s-factor improvement as buoyancy tanks.

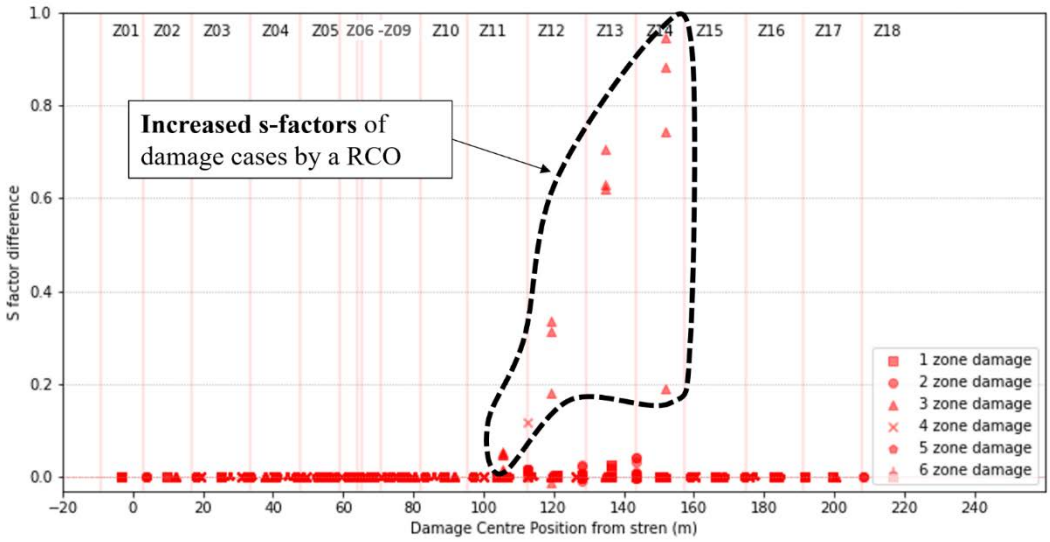

Figure 3.15 s-factor difference between the original layout and RCO (Double Hull) when RCO applied to Zone 13

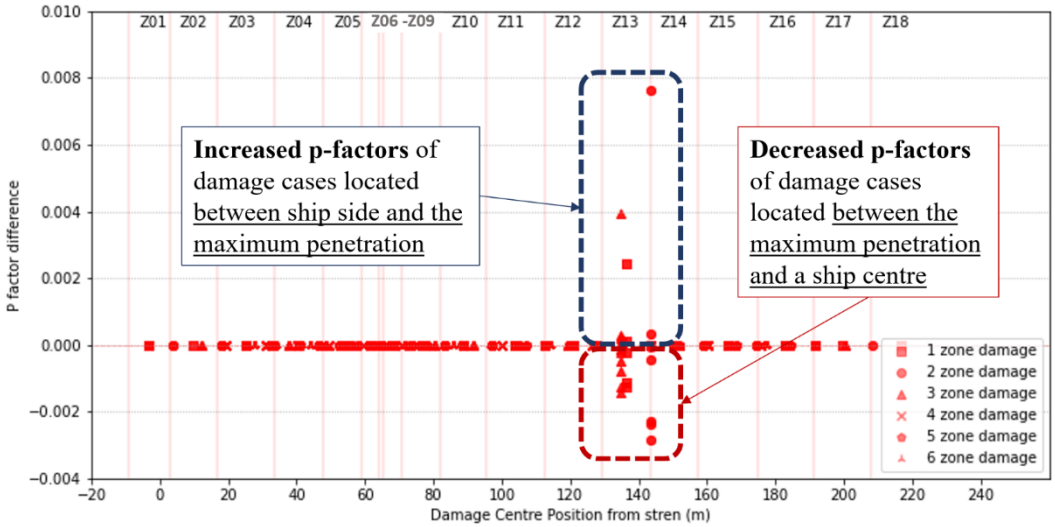

Figure 3.16 p-factor difference between original layout and RCO1 (Double Hull)

Figure 3.16 indicates how p-factors are affected by the updated damage distribution. The p-factors of damage cases located between the hull and the maximum penetration have risen compared to the original layout, while p-factor differences for some damage cases show negative values as those damage cases located between a ship centre and the maximum penetration have been excluded from the calculations as zero when the updated distribution is applied. Therefore, the overall subdivision Index A improvement from the RCO can be identified, as shown in Figure 3.17 (i.e., Subdivision Index A = $\sum s \times p$).

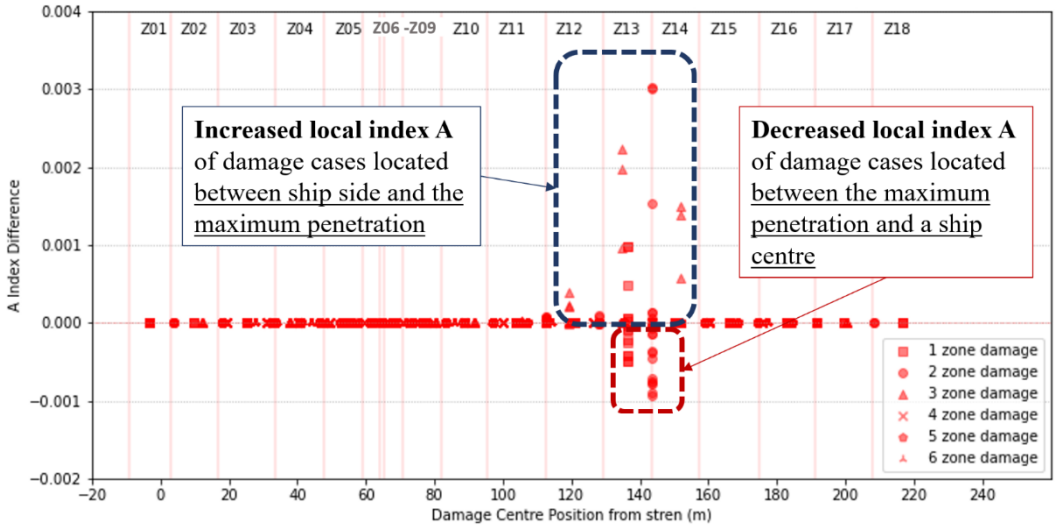

Figure 3.17 Index A difference between the original layout and RCO (double hull)

3.10 STEP 8: Cost-Benefit Analysis for an Optimum RCO Selection

3.10.1 Cost-Benefit Analysis

This step focuses on a cost-benefit analysis to identify an optimum solution among alternative designs (RCO). According to the current guidelines for formal safety assessment (FSA) adopted by IMO (2018), the Gross Cost of Averting a Fatality (GCAF) and Net Cost of Averting a Fatality (NCAF) are generally used as criteria to express the cost-effectiveness of each RCO as follows:

$$GCAF = \frac{\Delta Cost}{\Delta Risk} \tag{3.6}$$

$$NCAF = \frac{\Delta Cost - \Delta Benefit}{\Delta Risk} \tag{3.7}$$

where, $\Delta Cost$ is the cost of the RCO, $\Delta Benefit$ is the economic benefits of the RCO, $\Delta Risk$ is the risk reduction implied by the RCO in terms of potential loss of life (PPL).

However, IMO recommends mainly considering GCAF instead of NCAF as NCAF considers economic benefits from the RCOs and may be misused in some cases for pushing certain RCOs(IMO, 2018). Hence, in this methodology, only GCAF is adopted as a tool for cost-effectiveness analysis for each RCO.

3.10.2 Design Change Effects

New alternative designs or arrangements influence current designs, systems or even ship performances. For example, additional longitudinal bulkheads at a single subdivision divide a whole space into two rooms, leading to less flexible spaces for machinery arrangement or public spaces and requiring more HVAC and electric wiring systems. They may also increase overall ship weight, causing ship speed reduction and fuel consumption increase. In this context, the consequences of each RCO are considered as one of the critical criteria for an optimum solution.

3.11 STEP 9: Decision Making

Based on Step 8, the optimum RCOs will be provided to the relevant decision-makers, and they will determine the best solution among them, screening those which are not cost-effective or impractical. In particular, for alternative or novel solutions aiming at risk reduction, Class Societies advocate the Alternative Design and arrangement approval process (IMO, 2006, IMO, 2013), targeting approval of Novel Risk Control Options.

3.12 Chapter Summary

The FSA published by the IMO (2002b) aimed to prevent future disasters. This thesis proposes a detailed methodology for ship collisions using crashworthiness analysis to enhance the damage stability of a target ship. Figure 3.18 summarises the specific steps of the proposed quantitative risk assessment methodology for collision accidents within the context of standard IMO FSA procedures.

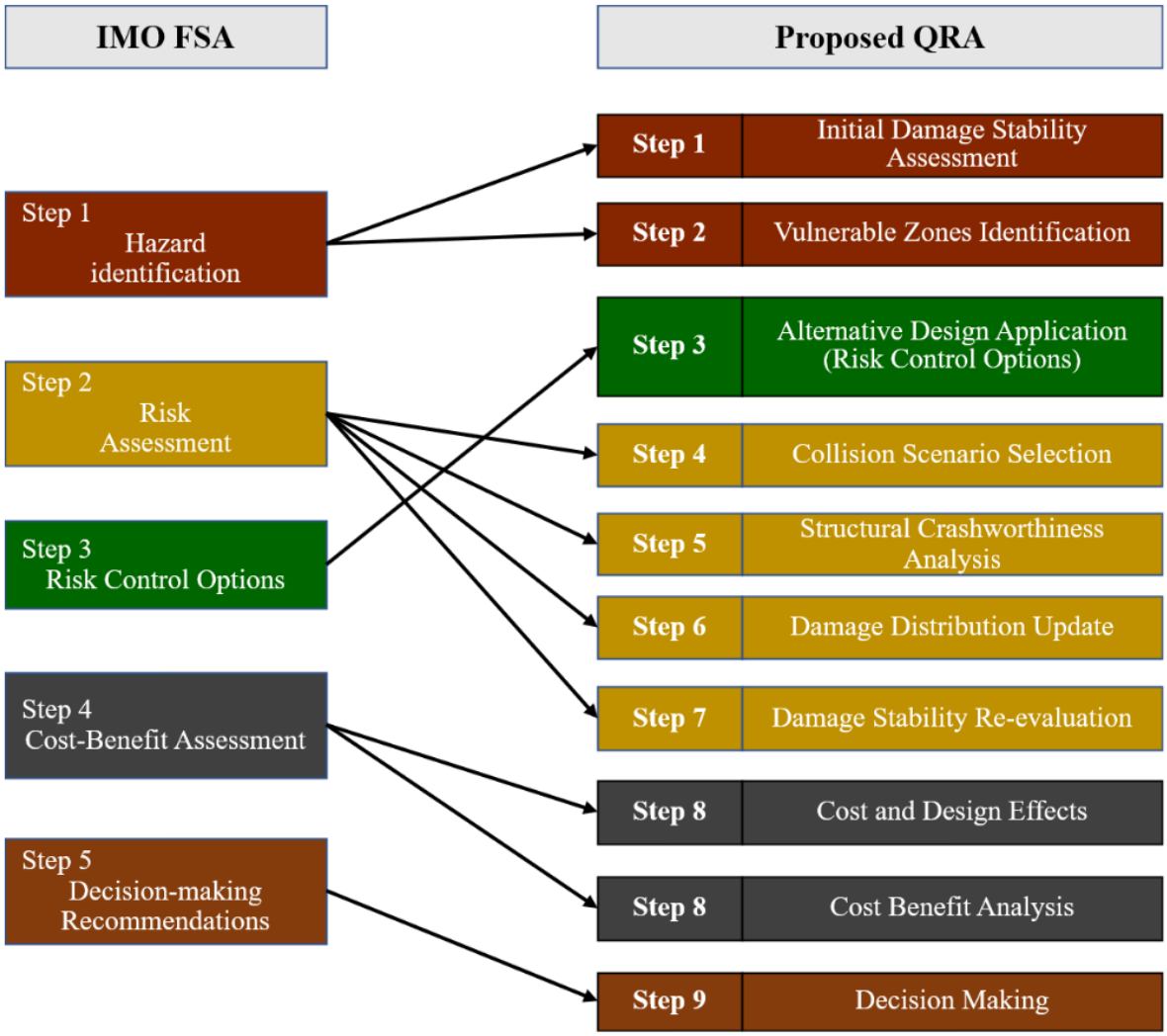

Figure 3.18 Proposed methodology employed in this thesis compared to IMO FSA methodology

Chapter 4

The Non-linear Finite Element Method

4 THE NON-LINEAR FINITE ELEMENT METHOD

4.1 Preamble

As briefly described in Section 3.7 STEP 5, this thesis aims to introduce the new methodology for the assessment of ship damage stability based on structural crashworthiness for collision protection. The method enables the evaluation of the effects of RCOs associated with crashworthy structures by measuring penetration differences between the original layout and modified arrangement with RCOs, which cannot be provided by the current SOLAS regulations. Therefore, the penetration estimation from collision simulations is critical. In this respect, this chapter describes the detailed methodology of numerical collision simulations using the non-linear finite element method.

4.2 Methodology

This section describes the detailed parameters, settings, assumptions, and techniques which have been applied to the collision simulation analysis. However, the simulation details presented herein may be required to be improved or updated for better results and calculation time. With regard to software used in this thesis, HYPER MESH was utilised for structural geometry modelling and finite mesh controls. Collision simulations are computed by the ANSYS/LS-DYNA NLFEM tool (Hallquist, 2007) along with the MCOL solver which enables external dynamics with practical ship motions between two ships during collisions. The input parameters for the MCOL solver for hydrodynamic ship motions were obtained from ANSYS AQWA (ANSYS, 2019).

4.2.1 Geometric Model Extents

The collision analysis begins with modelling geometries of both a struck and striking vessel. Analyzing crashworthiness with full geometric models of target vessels may be the best way to obtain the most accurate results. However, it requires high computational costs and time. In particular, cost-effective analyses should be crucial when a range of RCOs is required to be investigated. Therefore, the two different types of model extents have been explored in this thesis. For example, in the benchmark described in Section 4.4, partial models, a 90m midship part and a 30m bow structure for both struck and striking ships, respectively, have been used.

Whereas, for the case study displayed in Section 6, the full model of a struck ship and a 30 m partial model of a striking ship have been modelled. In particular, a bulwark has been included in the striking ship modelling since it is well structurally supported against ship slamming and green water with relatively high height (i.e., approximately 3.8m from a mooring deck in benchmark study, as shown in Figure 4.1).

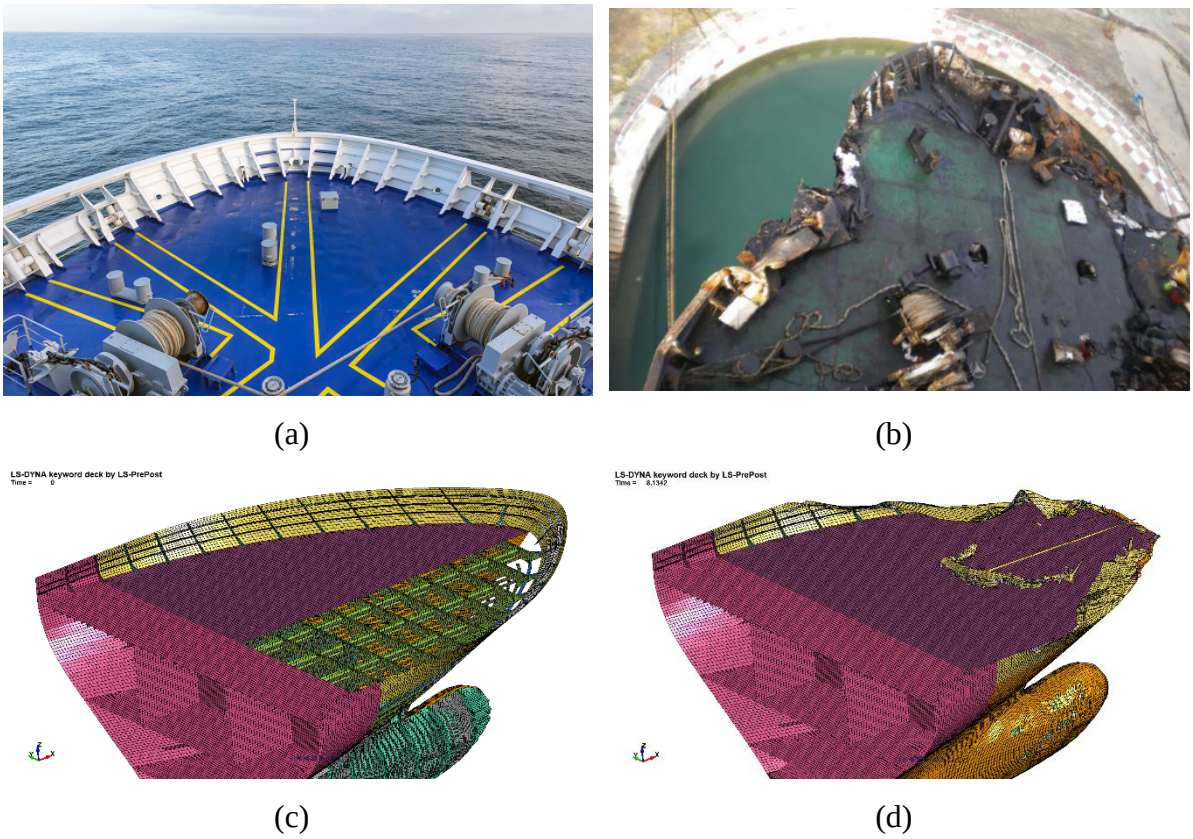

Figure 4.1 Geometric model of striking ship employed: (a) Typical bulwark of a vessel, (b) Damaged bulwark of Vessel ULYSSE after collision (BEAmer, 2018), (c) Geometric model of a striking ship and (d) Damaged bulwark after collision

4.2.2 Finite Element Type and Size

Figure 4.2 represents one of the geometric models of struck ships employed in collision analyses of this research. All structural plates and stiffeners greater than 200mm were modelled. However, all pillars, which were initially designed to support vertical loads from the top deck to the hull, were disregarded in the geometric modelling because they may not significantly affect the collision analysis and collision forces act transversely to the struck ship, not vertically. All finite elements of geometric models for both striking and struck ships were made of four

nodded quadrilateral Belytschko-Tsay shell elements with five integration points through their thickness (LSTC, 2019) (see Figure 4.3). This type of element formulation is based on Reissner-Mindlin kinematic (Timoshenko) assumption, describing displacements and rotations with shear deformation and being regarded as a highly effective formulation. It has been commonly employed for numerical analyses of crash mechanics for thin-walled structures (Naar et al., 2002, Tornqvist, 2003, Ehlers, 2010, Haris and Amdahl, 2013, Kim et al., 2022). Details of the formulas are given in Appendix A. The structural deformation of the striking ship was defined as deformable bodies in contact regions to capture the precise results of damage penetration (Ko et al., 2018a, Hogström and Ringsberg, 2012) in contrast to many authors (Kõrgesaar et al., 2014, Schreuder et al., 2011, Ehlers et al., 2008) who employed the rigid striking bow. The detailed comparison between deformable and rigid bows in ship collisions is described in Section 7.5 sensitivity study.

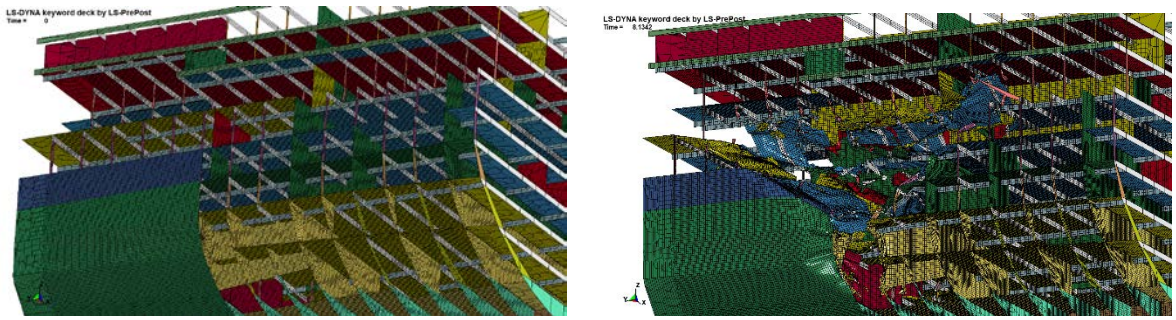

(a) (b)

Figure 4.2 Geometric models of striking ship employed: (a) Geometric model of a struck ship and (b) Damaged struck ship after collision

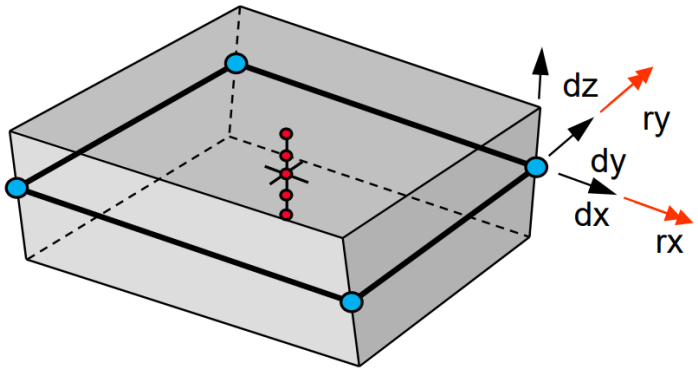

Figure 4.3 Schematic diagram of Belytschko--Lin-Tsay shell formulation

Regarding finite element size, Paik (2018) suggested the following updated guideline, initially based on Wierzbicki and Abramowicz (1983), to compute the structural crashworthiness of thin-walled structures when a rectangular type plate-shell element is used.

$$s \leq \frac{H}{8} = 0.1228 b^{2/3} t^{1/3} \tag{4.1}$$

where, s is the element size; H is the half-fold length; $b$is the plate breadth between support members (i.e., stiffeners, frames, and stringers), and t is the plate thickness.

However, it sometimes requires a relatively small mesh size for some cases (i.e., 60mm element size for 2800mm plate breadth with 15mm thickness for a cruise ship model), which demands high computational time and cost. Alternatively, the mesh convergency study has been conducted to find out the proper mesh size, which is employed by many authors such as Paik (2018) and Kim et al. (2022). However, complete convergence was not observed, as shown in Figure 4.4(a). Therefore, according to the recommendation of ADN 2009 (UN, 2008) (i.e., the guideline for mesh size for FEM, less than 200mm), the mesh sizes of 175mm and 200mm were determined considering frame spacings of a striking and struck ship, which are a quarter of frame spacings (i.e., 175mm = 700mm /4 and 200mm = 800mm / 4). These element sizes affect the determination of fracture strains of each structural member since element size and thickness ratio-dependent fracture criteria (i.e., GL criterion) is adopted in this thesis (see Figure 4.4 (b)).

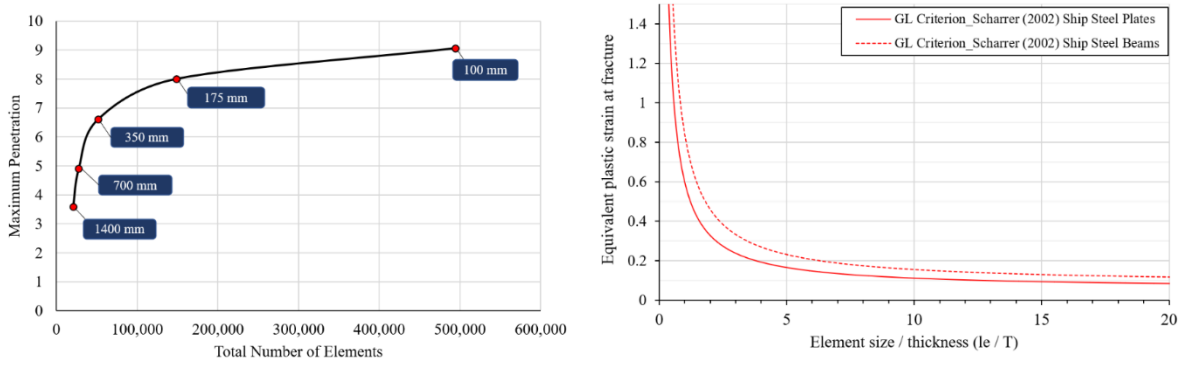

(a) (b)

Figure 4.4 (a) Mesh convergence study results and (b) GL Criteria (Vredeveldt, 2001, Scharrer et al., 2002a) for fracture strain

4.2.3 Material Property Modelling

As many authors (Vredeveldt and Wevers, 1992, Amdahl et al., 1992, Ehlers et al., 2008, Paik, 2018) proved, structural response in ship collisions shows highly non-linear structural mechanics with elastoplastic behaviours, including bending, bucking, crushing, plasticity and rupture. In this thesis, a modified true stress-true strain curve for the mild steel was employed in collision simulations of this thesis to capture actual structural behaviours, as shown in Figure 4.5. This allows for the consideration of actual mild steel behaviour, including the strain-hardening effect. The material curve was obtained from modifying an actual true stress-true strain curve (Paik, 2018) based on the material properties in Table 4.1.

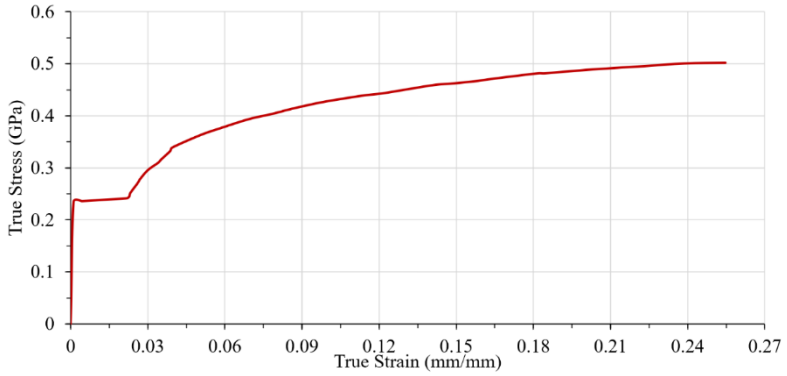

Figure 4.5 Modified True Stress True Strain curve employed at the simulation

Table 4.1 Typical material properties for mild steel

Parameters	values
Density, ρ (kg/m3)	7850
Young's modulus, E (MPa)	205,800
Poisson's ratio	0.3
Yield stress, σY (Mpa)	235
Ultimate tensile strength (Mpa)	400

It is widely known that materials respond differently depending on external loadings and environmental conditions. Especially, in high-speed dynamic loading conditions, the material tends to show relatively high yield strength (see Section 2.3.4.5). However, an earlier fracture is observed compared with results from static tensile coupon tests in quasi-static conditions. Cowper and Symonds (1957) suggested a constitutive equation in the relation between the dynamic yield stress and the strain rate sensitivity of the material:

$$\frac{\sigma_{Yd}}{\sigma_Y} = 1.0 + (\frac{\dot{\varepsilon}}{C})^{1/q} \quad (4.2)$$

Where σ_{Yd} and σ_Y are dynamic and static yield stresses, $\dot{\varepsilon}$ is strain rate, C and q are coefficients determined on the basis of test data.

In order to include this material dynamic phenomina, a "Material type 24 Piecewise Linear Isotropic Plasticity (LSTC, 2019)" from LS-DYNA material library has been employed at contact regions to take into account elastoplastic deformations to capature real structrual responses, whilst the rest of the area was defined as rigid (see Figure 4.6).

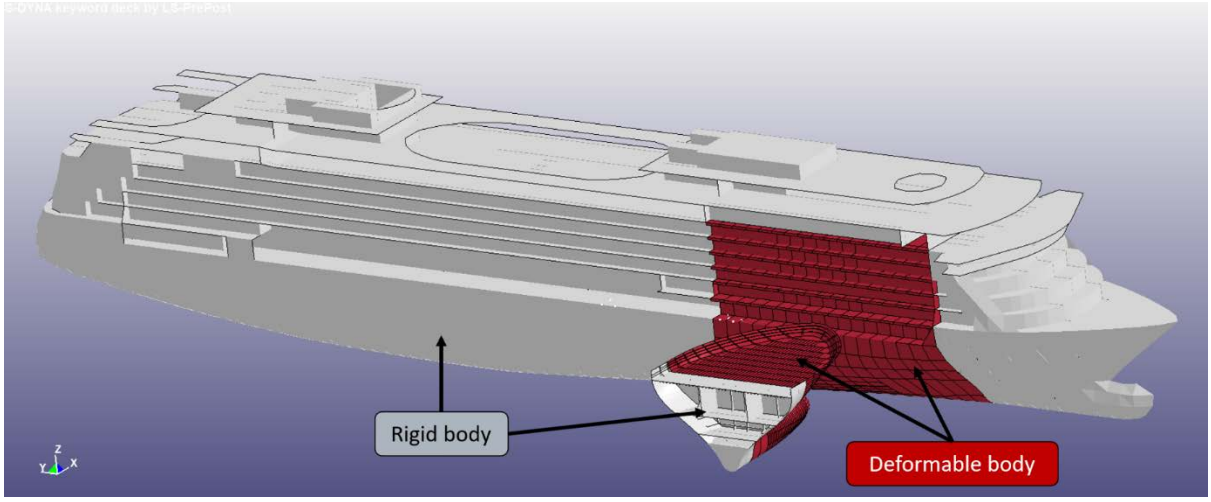

Figure 4.6 Model stiffness definition

4.2.4 Failure Criteria

The structural responses under impact loading show different behaviour depending on the mechanical properties of materials. Therefore, it is essential to set proper failure criteria in collision simulations. As previously discussed in Section 2.3.4, many authors proposed various failure criteria. Among them, this thesis adopted the GL criterion in collision simulations. Firstly, it is suitable for collision simulations with relatively large element sizes as it is element size-dependent. Secondly, it was officially adopted in one of the international rules named *"European Agreement concerning the International Carriage of Dangerous Goods by Inland Waterways (ADN)"*(UN, 2008) as failure criteria for collision simulations. It is also called as "through-thickness strain criterion" because the critical fracture strain ε_c was derived from empirial relations obtained from experimental measurements of the through-thickness strain ε_3 (i.e., the third principal strain or thinning strain) of damaged plates in actual ship structures

engaged in ship collisions and groundings as follows:

$$\varepsilon_c = \varepsilon_g + \varepsilon_e \frac{t}{l_e} \tag{4.3}$$

where, ε_g and ε_e are uniform strain and necking strain, respectively.

Scharrer et al. (2002a) suggested ε_g =0.056 and ε_e =0.54 for 2D shell elements based on experiements. He recommended for this criteria application that the ratio between element length and thickness l_e/T should be greater than 5 for numerical simulations (Scharrer et al., 2002a). In this respect, the current geometries satisfy it with a range of 5.83 ~ 35 (i.e., l_e/T =175/30 ~ 175/5).

In addition to the above criterion, the constant shear criterion of 0.1 (mm/mm) has also been employed for a benchmark study of EU funded FLARE project (See Section 4.4), which is generally used as the industry practice (Paik and Jeong, 1999, Sajdak and Brown, 2005, Jones, 2006).

4.2.5 Contact and Friction

Contact problems are always involved in nonlinear structural mechanics since individual thin walls are separated before folding and come into contact at a later stage as crushing continues (Paik, 2020). There are two types of contact, namely general contact and self-contact. The former means wall contacts among different structural components, while the latter occurs within structural components themselves, as shown in Figure 4.7. These two types of contact arise together in ship-ship crash simulations. General contact happens between striking and struck ship structures, and the self-contact manifests when internal structures of each ship are folded during collisions. LS-DYNA provides various contact types and a number of parameters to improve the contact performance for diverse cases for various contact situations such as beam-to-beam, beam-to-shell edge, beam-to-shell surface, shell edge-to-shell edge, shell segment-to-segment and shell edge-to-shell edge. The proper contact type for shell element models are Automatic_Suface_to_Surface and Automatic_Single_Surface (see Table 4.2). Furthermore, according to LSTC (2019) and Oasys (2020), a deformable model with edge contact problems Automatic_Singl_Surface is recommended. Therefore, in order to take into account both the self-contact and shell edge-to-edge contact functions in collision simulations, Automatic_Single_Surface is selected in the FE analyses of this thesis.

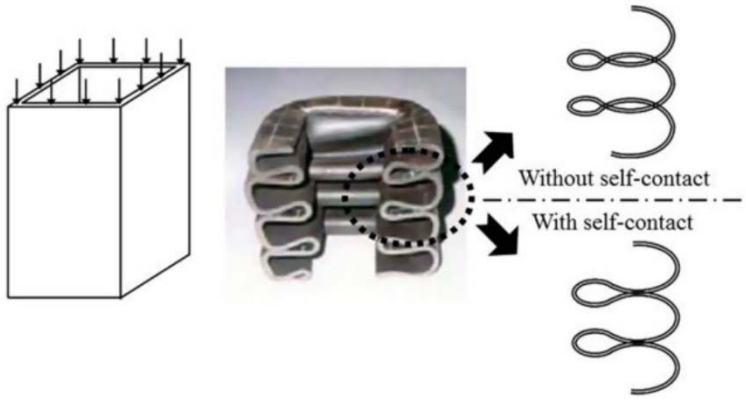

(a) Self-Contact phenomenon

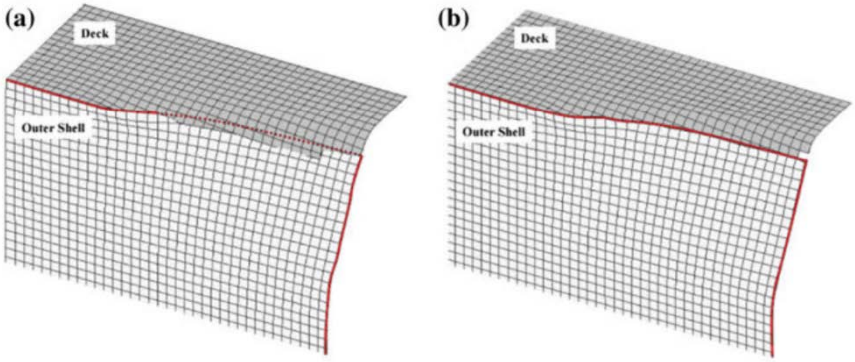

(b) Comparison of analysis results without (left) and with (right) self-contact function application

Figure 4.7 Self-Contact effects (Park and Samuelides, 2009)

Table 4.2 LS DYNA Contact types and Usage (Oasys, 2020)

Contact Type	**Beams**			**Shell**		
	Beam to beam	Beam to shell	Beam to surface	Edge to edge(*)	Segm. to Segm.	Edge to edge(**)
Automatic_General	O	O	O	O	O	X
Automatid_General_Interior	O	O	O	O	O	X
Automatic_surface_to Surface	X	X	X	O	O	O
Auomatic_single_surface	X	X	O	O	O	O
Automatic_beams_to_surface	X	O	O	X	X	X
Sigle_edge	X	X	X	O	X	X

O - Contact worked / X – Contact failed

(*) edge of a single shell

(**) edge formed by the connection of two shells

Friction occurs between two colliding bodies during a collision event. It is more critical for collisions generating force moment. When the striking body collides with the target zone of the stuck ship located far from COG, the moment by the collision force occurs and changes the collision angle over time. Therefore, the friction in those collision scenarios may be more dominant than the perpendicular collision on the midship. The friction coefficient is very critical since all initial collision energy except friction energy would involve in internal collision mechanics leading to deformations and ruptures of structures. The "NASA Reference Publication 1228: Fastener Design Manual (Barrett, 1990)" suggests a standard friction coefficient of 0.57 for non-lubricated mild steel against mild steel and 0.09-0.19 for lubricated surfaces. For ship structures, hull surfaces under the water are always wet and sometimes polluted by biofouling for old ships, while the hull above the waterline is dry. In ship collisions, both areas are always involved. The submerged bulbous of the striking ship collides with the wet hull of the struck ship, and the dry stem part contacts the upper dry hull and superstructure of the collided ship. Therefore, the above friction coefficient of 0.09 ~ 0.57 may be considered for ship collision analysis. In addition to this, many authors, such as Sajdak and Brown (2005) and Paik (2007), recommend dynamic friction coefficients of 0.3 to simplify problems, which is also reasonably included in the recommended values in the above Manual. Therefore, a value of 0.3 for the dynamic friction coefficient is adopted in this study.

4.2.6 Ship Motions induced by Surrounding Water

During ship collisions, the surrounding water around both striking and struck ships moves simultaneously. This is because of frictions between the hull and water that also affect ship motion as added mass. Therefore, Minorsky (1959) considered this surrounding water effect in ship collisions and proposed to use the added mass coefficient of 0.4 for the sway motion. Motora et al. (1971) found that the added mass coefficient for the sway motion ranged from 0.4 to 1.3 from a series of model tests and hydrodynamic analyses. Petersen (1982) suggested 0.85 and 0.70 of added mass coefficients for the same motion in the case of the constant and linear forces, respectively, based on several simulation results. Pedersen and Zhang (1998) suggested 0.0 5 for an added mass coefficient of the surge motion and 0.85 for the sway motion, as well as that of 0.21 for the yaw motion of the struck ship. In particular, the later coefficients have been widely adopted in simplified methods for added mass effects of two ships in collisions.

In collisions, the positions of two ships are continuously affected by hydrodynamic forces such

as restoring, wave damping and resistance. Therefore, internal collision mechanics must be coupled with external dynamics as global ship motions. Brown (2002) introduced this coupling mechanics in his solver (i.e., a Simplified Collision Model (SIMCOL)). MCOL solver (Ferry et al., 2002) also provides the coupling motions between two bodies floating on the water, which were initially developed by Mitsubishi and then embedded in LS-DYNA. In particular, it takes into account large rotational movements (i.e., rolling of the struck ship during the collision) from the collision force and hydrodynamic forces. Therefore, the MCOL solver enables precise calculations of ship motions during collision events, while the LS-DYNA solver performs internal collision mechanics, as shown in Figure 4.8. Therefore, in this thesis, the MCOL solver has been employed for the external ship motions of two vessels.

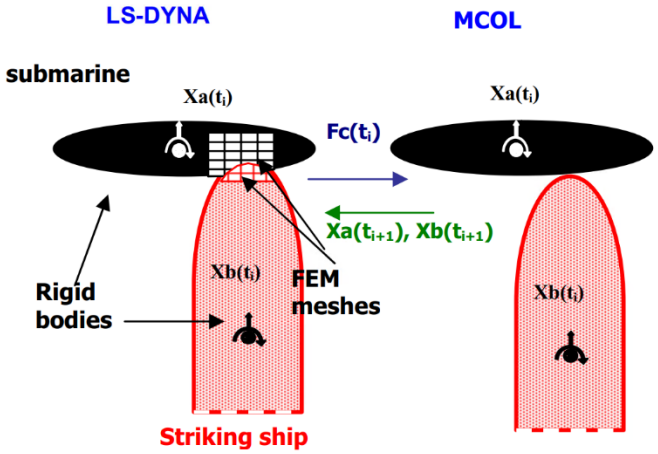

Figure 4.8 LS-DYNA and MCOL collision simulation system (Le Sourne et al., 2003)

The basic equation of MCOL used for ship motion calculations can be written in the body-fixed reference system in the following equation, and the detailed formulas are given in Appendix B:

$$[M_{RB} + M_A]\dot{\boldsymbol{y}} + [G_{RB} + G_A]\boldsymbol{y} = [F_W + F_H + F_V](\boldsymbol{y}, \boldsymbol{x}) + F_C \qquad (4.4)$$

where, M_{RB} is a structural mass of ship; M_A is constant added mass for infinite frequency; x denotes the earth-fixed position of the centre of ship mass, including three transitions and three rotations (i.e., $\boldsymbol{x} = (x_{0G}, y_{0G}, z_{0G}, \phi, \theta, \Psi)$); y is the body fixed components of the absolute velocity $\boldsymbol{v}$ of the centre df mass and of the angular velocity vector ω (i.e, $\boldsymbol{y} = (u, v, w, p, q, r) = (\boldsymbol{v}, \boldsymbol{\omega})$) in Figure 4.9; G is the gyroscopic matrix; F_W, F_H, F_V and F_C are the wave damping force, restoring force, viscous force and contact force, respectively.

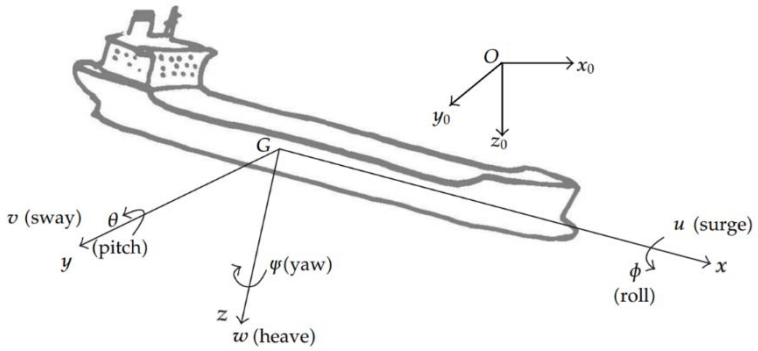

Figure 4.9 Coordinate system defined in MCOL

The input parameters for the MCOL solver were calculated from ANSYS AQWA (ANSYS, 2019). However, the wave damping forces F_W and viscous forces F_V were not taken into account as the influence of waves is minor to analysis results (Kim et al., 2021), but it increases the overall calculation time.

4.3 NLFEM Verification

The simulations for the following two experiments have been carried out, and these results are compared with actual experimental data.

4.3.1 ISSC Benchmark of Ship Collision

4.3.1.1 Description of Experiments

Kuroiwa (1993) carried out experiments to observe failure mechanisms and energy absorption capacity of structures using the side structure of a VLCC. A half-scale of a VLCC double hull structure and a half sphere-shaped indenter of 8.4 ton weight with a radius of 500mm as a bow model of a striking ship was used for the model tests, as shown in Figure 4.10. Static and dynamic experiments were conducted: The former was carried out by pressing the double hull model smoothly with the bow model indenter for a quasi-static condition. Due to the hydraulic piston capacity limitation, the indenter slowly pressed the side structure twice in a row by 450mm to achieve a total of 900 mm. On the other hand, for the dynamic test, the indenter was freely released at the height of 4.8m above the double hull model with an impact speed of 9.7 m/s for the dynamic experiments. These droppings were repeated three or four times until the penetration of 900mm was achieved. The bottom and side boundaries of the double hull model were fixed.

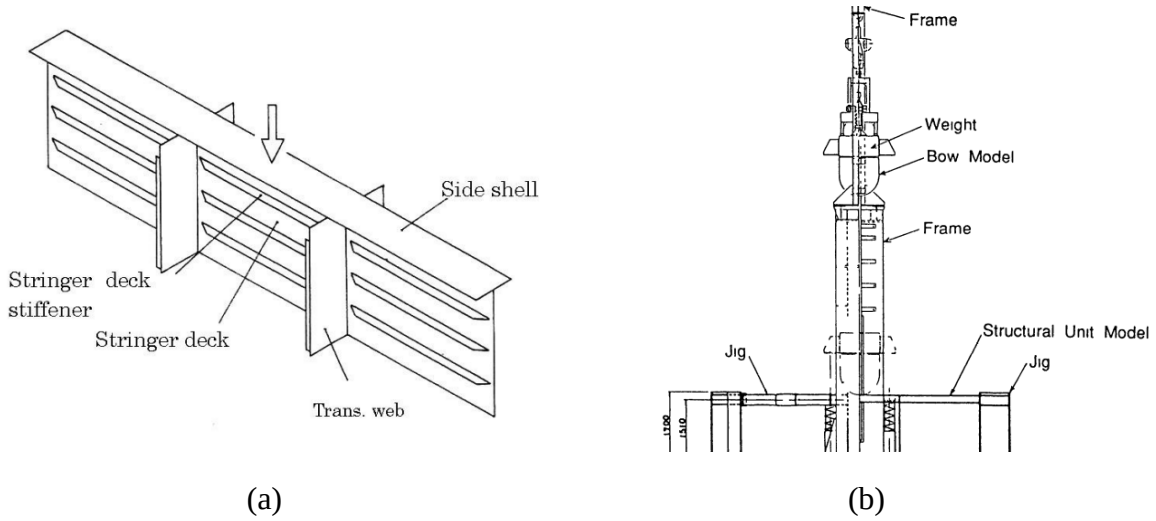

(a) (b)

Figure 4.10 (a) Schematic view of the experiments (b) Schematic view of dynamic tests setup

4.3.1.2 Finite Elements Simulation

Geometric modelling: A mesh size of 25mm was used for overall geometry. This mesh size corresponds to the ratio between element size and thickness l_e/T of 5 and is also smaller than the recommended mesh size of 40.6 mm (see Equation (4.1)). All elements for plates and stiffeners were made by Belytschko-Tsay shell elements (LSTC, 2019) with a 5/6 shear factor and five through shell thickness integration points.

Material model and Failure criteria: A material model of Piecewise Linear Isotropic Plasticity (Hodge et al., 1956, LSTC, 2019) was employed for the double bottom geometric modelling to observe the elastoplastic deformation from the collision, while the bow model was defined as rigid. Cowper-Symonds equation with C=3600 and q=5.5 was adopted for dynamic yield stress considering strain rate effects for the dynamic test simulation. Power-law material curves of each structural member and the critical damage strain derived by Tornqvist (2003) were employed (see Table 4.4). The Young's modulus of 210GPa and a Poison ratio of 0.3 were applied.

Table 4.3 Material properties of each component for a double bottom model (Tornqvist, 2003)

Components	Plate Thickness T (mm)	Yield Stress σ_Y (MPa)	Power Law Coefficients C(Mpa) , n	Critical damage strain
Deck / Stringer/ Web Stiffeners	7.0	314	800, 0.25	0.34
Web	8.0	324	800, 0.25	0.34
Side Shell	10	324	780, 0.25	0.41

Contact and Friction: Automatic_Single_Surface contact type was adopted to take into account both general and self-contacts with a friction coefficient of 0.3.

The static and dynamic simulations were conducted for the exact experiment procedures, imposing repeat loadings.

4.3.1.3 Results and Discussion

In the dynamic experiment, the first rupture occurred at the penetration of approximately 650 mm with the fillet weld failures between the stringer deck and transverse webs. At 750mm, the side shell region supported by transverse webs was ruptured, and a dramatic decrease in resultant force occurred. As shown in Figure 4.11, the first ruptures of elements in the FE simulation were also observed at the penetration of approximately 600 mm and 650 mm for static and dynamic tests, respectively and in between the stringer deck and transverse web. However, the rupture of the side shell at 750mm penetration did not take place in the simulations. This caused a constant increase in the resultant force after 750mm (see Figure 4.12 and Figure 4.13). It was assumed that the residual welding stresses of the side shell in the experiment led to this brittle fracture, which was not captured in FE simulations. Apart from the period after 750mm penetration, the results of simulations provided good correlations with the experimental result for both static and dynamic simulations.

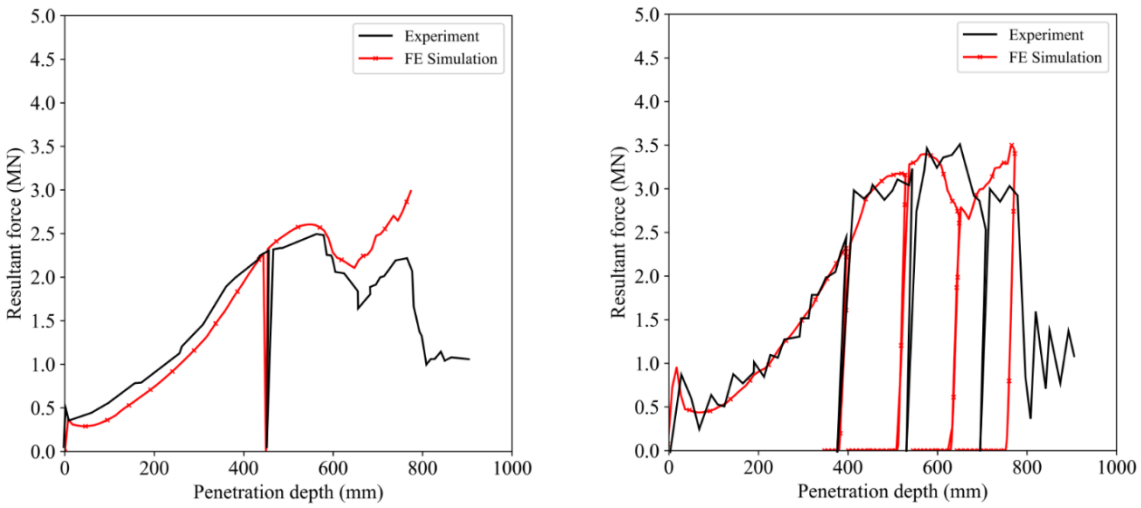

(a) Static test (b) Dynamic test

Figure 4.11 Comparison graphs of resultant forces in penetration depths between the experiment and FE simulation for (a) Static Test and (b) Dynamic Test

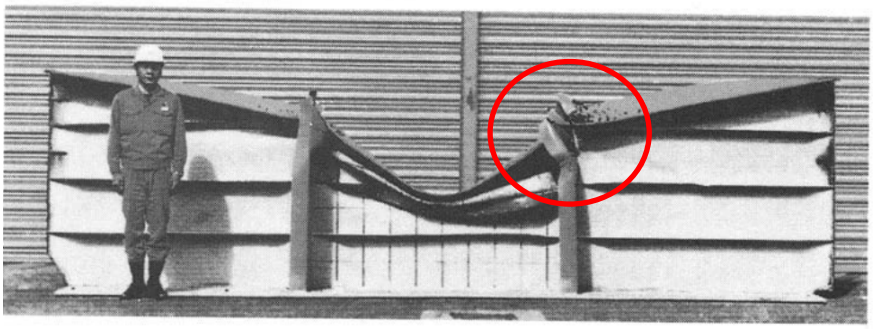

Static Test

(a)

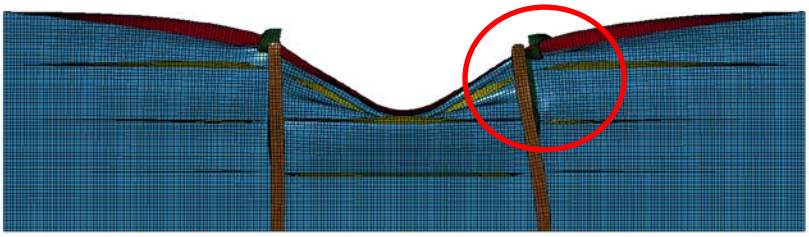

(b)

Figure 4.12 (a) Deformation after the static test (Ohtsubo et al., 1994) (b) Deformation after FE simulation in quasi-static condition

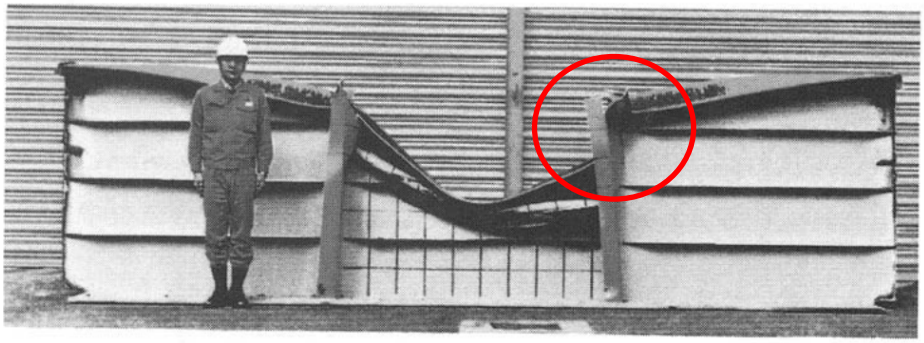

Dynamic Test

(a)

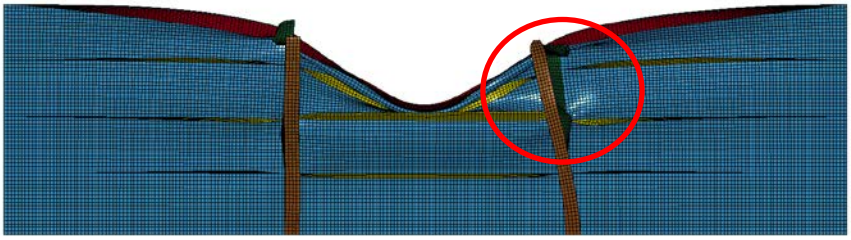

(b)

Figure 4.13 (a) Deformation after the dynamic test (Ohtsubo et al., 1994) (b) Deformation after FE simulation in dynamic condition

4.3.2 ISSC Benchmark of Ship Grounding

4.3.2.1 Description of Experiments

Kuroiwa (1992) conducted a model test to estimate the length of ruptured bottom from grounding accidents of VLCCs. A 1/3 scale of a VLCC double bottom structure and a wedge-shaped rigid model with a 90-degree tip angle as a rock were used for the model test, as shown in Figure 4.14. The bottom and side boundaries of the bottom model were fixed by a thick bottom plate and H-beams, respectively. The experiment was carried out by pressing the bottom model with the rock wedge at a velocity of 0.76 mm/s to ensure a quasi-static response from the test setup.

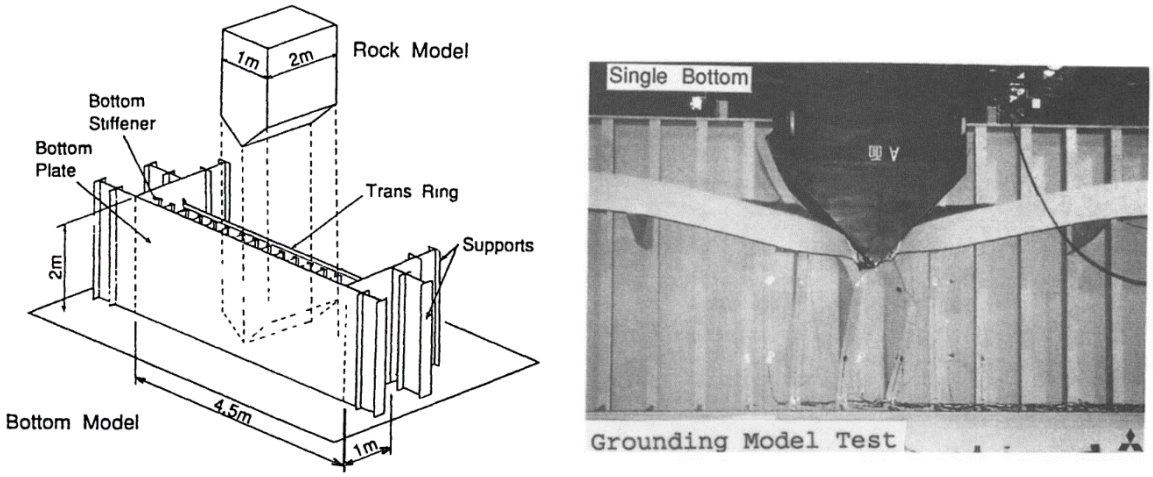

(a) (b)

Figure 4.14 (a) Schematic view of the experiments (b) view of experiments for a single bottom model (Ohtsubo et al., 1994)

4.3.2.2 Finite Elements Simulation

Geometric modelling: A mesh size of 25mm was used for overall geometry. This is the ratio between element size and thickness l_e/T of 5 and also smaller than the recommended mesh size (i.e., 53mm according to Equation (4.1)). All elements for plates and stiffeners were made by Belytschko-Tsay shell elements (LSTC, 2019) with a 5/6 shear factor and five through shell thickness integration points.

Material model and Failure criteria: A material model of Piecewise Linear Isotropic Plasticity (Hodge et al., 1956, LSTC, 2019) was employed for the double bottom geometric modelling to observe the elastoplastic deformation from the grounding, while the rock model was defined as rigid. No strain rate was considered due to the quasi-static loading condition. For the material curve, power-law curves of each structural member derived by Tornqvist (2003)

were employed. Those were derived from the true stress-strain curve based on material data in the experimental description indicated in Table 4.4. The same Young's modulus of 210 GPa and a Poison ratio of 0.3 were applied. The experimental failure criteria in Table 4.4 were used.

Table 4.4 Material properties of each component for a double bottom model (Tornqvist, 2003)

Components	Plate Thickness T (mm)	Yield Stress σ_Y (MPa)	Power Law Coefficients C(Mpa) , n	Fracture Strain (Experiment)
Longitudinal Stiffener Web & Floor stiffener	4.5	315	720,0.23	0.33
Floor plating	5.0	315	720, 0.23	0.33
Inner and outer bottom shell	7.0	295	720, 0.24	0.34
Longitudinal Stiffener Flange	7.0	295	780,0.24	0.34

Contact and Friction: Automatic_Single_Surface contact type was adopted to take into account both general and self-contacts with a friction coefficient of 0.3.

4.3.2.3 Results and Discussion

The simulation was conducted by compressing the rigid rock model to the double bottom model with a velocity of 1.4 m/s. The resultant force rose from the penetration depth of 400 mm up to 600 mm, where the first element fracture on the floor plating was initiated. Then, another peak was observed at the penetration of 760mm just before the floor plating was split entirely. The maximum force occurred at 914mm when the shoulder of the rock model approached the floor plating position, pushing the remaining plates to both sides.

The simulation showed a very good agreement with the experiment results, even though the first point of a steep increase in force at 400mm was slightly delayed.

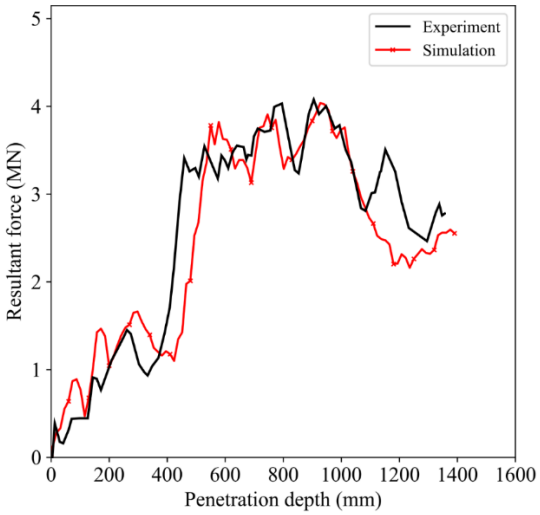

Figure 4.15 Comparison results of force and penetration depth depending on different failure criteria

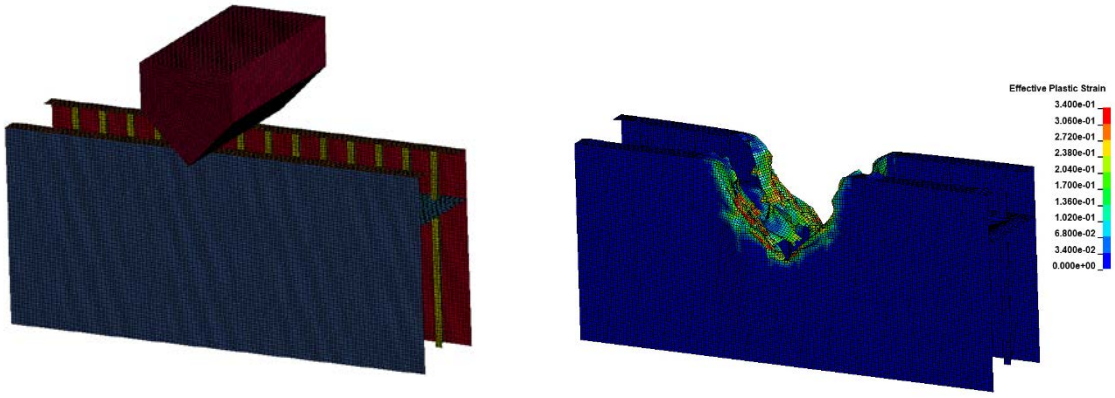

(a) (b)

Figure 4.16 (a) Geometric model setup for simulations (b) Maximum resultant force at the penetration depth of 927mm

4.4 FLARE Project: Benchmark Study

In addition to the verifications in the previous section, a benchmark study (Kim et al., 2022, Le Sourne et al., 2021), as a sub-project WP3 of the FLARE project, has been carried out for collisions. MSRC at the University of Strathclyde, Aalto University, BV, ICAM and MARIN have participated in this study to verify the SHARP software in collision and FLAGS software in grounding compared to other crashworthiness methods (i.e., finite element method). SHARP and FLAGS software were developed based on the modelling of the ship by very large-sized structural units (i.e., super-elements) for collision mechanism, which provides prompt calculation outcomes compared to the traditional FE method. The resistance of each individual super-element is calculated from the closed-form analytical expressions for collisions (Buldgen et al., 2012, Buldgen et al., 2013), which are based on experimental validations.

As shown in Table 4.5, BV and ICAM have jointly conducted collision simulations with SHARP program, while MSRC and Aalto University have adopted the FE method with LS-DYNA explicit code for dynamic structural analysis. MARIN has performed the study using in-house software based on the super-element method, which is a similar concept as SHARP, but it adopts different closed-form expressions derived by Simonsen and Ocakli (1999), Zhang (1999), and Buldgen et al. (2012).

Table 4.5 Numerical Tools employed by each participant for benchmark studies.

	Hydrodynamic simulation	Structural Analysis
MSRC	Hydrostar	LS-DYNA/MCOL
AALTO	Hydrostar	LS-DYNA/MCOL
BV/ICAM	Hydrostar	SHARP/MCOL
MARIN	MARIN XMF	

4.4.1 Target ships and Collision scenarios

A 63,000 GT cruise ship and a 45,000 GT RoPax ship, as a struck ship and a striking ship, respectively, were used with the following particulars in Table 4.6.

Table 4.6 Principal particulars of target ships

Parameter	Struck ship	Striking ship
Ship type	Cruise ship	Ro-Pax
Length of overall (m)	238.0	221.5
Breadth (m)	32.2	30.0
Design Draft (m)	7.2	6.9
Displacement (Tons)	35,367	31,250
Gross Tonnage (Tons)	63,000	45,000
Remark	FLOODSTAND SHIP B	D-ROPAX

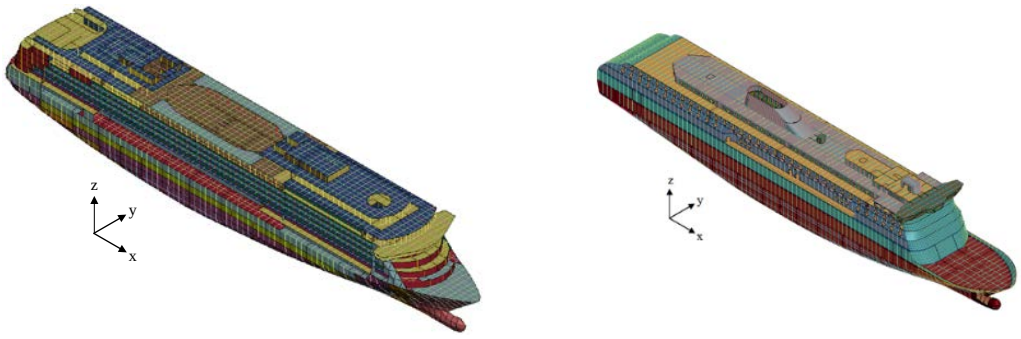

(a) Struck ship (b) Striking ship

Figure 4.17 Target vessels utilised in benchmark studies

Four different scenarios have been given to collision analyses, such as collision locations, speeds of the striking ship and collision angle, as shown in Table 4.7 and Figure 4.18. Scenario 1 was the base case of collision, in which the striking ship was assumed to collide perpendicularly to the centre of a watertight compartment located near the midship of the struck

ship with 5 knots. Scenario 2 is the same collision location as scenario 1, but with a 10 knots collision speed. Collision 3 was about an oblique collision between two ships at the same collision location and speed as scenario 1. Finally, scenario 4 was a perpendicular collision at the aft transverse bulkhead of the ship's watertight compartment with 5 knots. Especially, the collision speed of scenario 1 is adopted from the distributions, which are based on the ship accident database defined by Paik et al. (2017).

Table 4.7 Collision Scenarios

Scenario Number	Striking ship Speed (knot)	Struck ship Speed (knot)	Collision Angle (˚)	Collision Location from A.P. of a struck ship (m)
1	5	0	90	103.95m
2	10	0	90	103.95m
3	5	0	45	103.95m
4	5	0	90	95 m (at a transverse bulkhead)

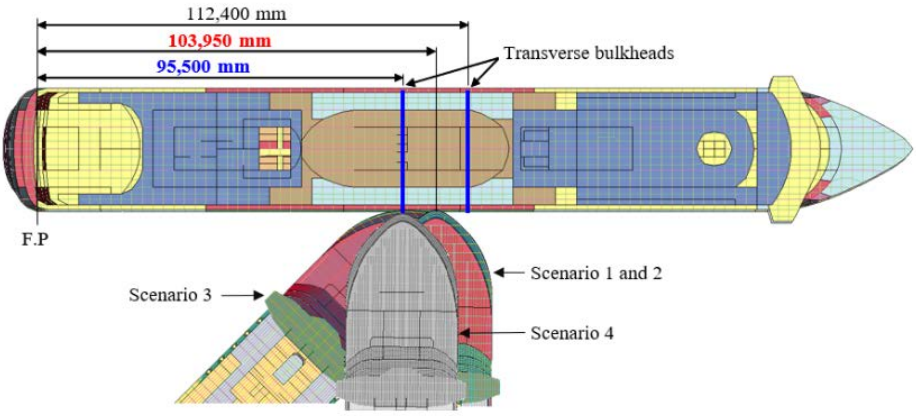

Figure 4.18 Collision Scenarios (Kim, 2020)

4.4.2 Geometric Model

Figure 4.19 shows the different types of geometric models adopted in the benchmark study by each participant. MSRC and Aalto university employed a deformable striking bow, while BV/ICAM and MARIN used a rigid body for the striking ship.

Regarding elements type of models, MSRC and AALTO used Belytschko-Tsay shell elements for the plated structure. Especially, MSRC adopted 2D shell elements for all geometries such as plates and stiffeners for both striking and struck bodies, while AALTO used 1 D beam elements defined by the Hughes-Lie cross-section integration model (LSTC, 2019). The geometries employed by BV/ICAM were modelled by very large-sized structural element units and a limited number of nodal points (i.e., so-called super-elements) in SHARP software (Le Sourne, 2007, Le Sourne et al., 2012). Similarly, MARIN also modelled their geometries using

super-elements. MSRC used elements size of 200mm for the striking model and 175mm for the struck model, which is based on a quarter of the frame spacing of both ships (i.e., 800mm and 700mm for the striking and struck ship, respectively). On the other hand, AALTO selected the element size of 150mm from a convergency study (Kim et al., 2021).

Regarding the structural extent of the model, MSRC and MARIN used partial models for both the striking and struck ship, while Aalto adopted full models. On the other hand, BV modelled only the hull part without the superstructure for the struck ship, and a partial model of the striking ship without a bulwark was adopted for their collision simulations. Table 4.8 summarises the extent of geometries adopted by each participant for simulations.

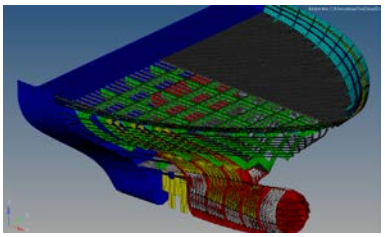

(a) Striking ship - MSRC (Deformable)

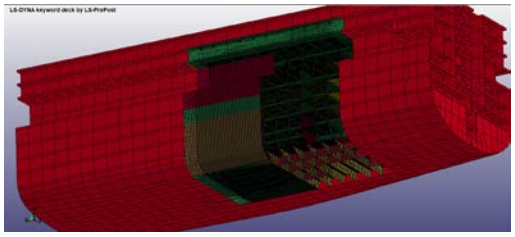

(b) Struck ship - MSRC

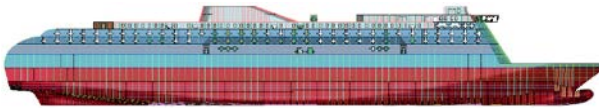

(c) Striking ship - AALTO

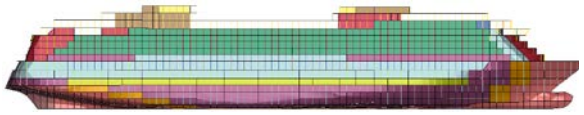

(d) Struck ship – AALTO

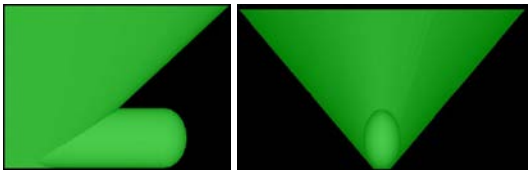

(e) Striking ship - BV/ICAM

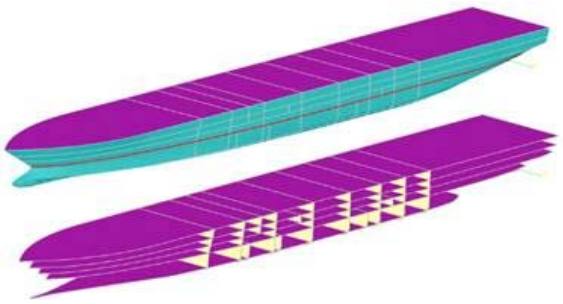

(f) Struck ship - BV/ICAM

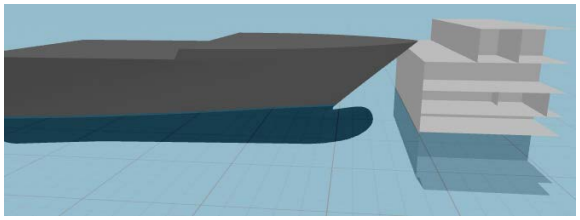

(g) Striking/struck ships - MARIN

Figure 4.19 Different types of Geometries employed by participants in each benchmark study

Table 4.8 Extent of geometries and structural body conditions in simulation

Participant	Striking ship	Struck ship
MSRC	Partial model: Deformable body – All 2D shell elements	Partial model: Deformable body – All 2D shell elements
Aalto	Full model : Deformable body – 2D shell (Plates) – 1D beam element (stiffeners)	Full model : Deformable body – 2D shell (Plates) – 1D beam element (stiffeners)
BV/ICAM	Full model: Rigid body – Super-elements	Partial model: Deformable body – Super-elements
MARIN	Partial model: Rigid body – Super-elements	Partial model: Deformable body – Super-elements

4.4.3 Assumptions for Structural Response

Mild steel accounts for the majority of the materials used for shipbuilding construction, even if a range of materials such as mild steel, high-tensile steel, aluminium or composite are practically used in shipbuilding. Therefore, in this benchmark study, only mild steel was taken into account to simplify the analysis of the material properties, as shown in Table 4.9.

While MSRC and AALTO adopted a linear elastic-perfectly plastic curve for their material behaviours, BV/ICAM and MARIN employed a rigid-perfectly plastic curve. Cowper-Symonds equation (c =40.4 and q=5 for mild steel) has been used by MSRC, AALTO and MARIN for the dynamic effect of material, which is originally derived for the upper yield stress. (Cowper and Symonds, 1957). Especially, all participants applied a plastic strain of 0.1 to a failure strain threshold for all collision scenarios.

Table 4.9 Material properties – Mild Steel

Description	MSRC	AALTO	BV/ICAM	MARIN
Material curve	Linear elastic-perfectly plastic (E_h=0)		Rigid-perfectly plastic (E_h=0)	
Density (kg/m^3)	7,850			
Young's modulus (MPa)	205,800			
Yield strength (MPa)	235			
Flow stress (MPa)	-	-	235	317.5
Dynamic effect	Cowper-Symonds (c = 40.4 and q = 5)		-	Cowper-Symonds (c = 40.4 and q = 5)
Fracture strain	0.1			
Frictional coefficient	0.3			

4.4.4 Ship Motions and Surrounding Water effects

In MSRC, AALTO and BV/ICAM collision analysis, hydrodynamic boundary conditions have been considered in their simulations using MCOL. This solver enables ships to move practically in the water, accounting for mass matrix, hydrodynamic restoring forces, water added mass, buoyancy parameters and wave damping forces (Le Sourne et al., 2003). The input parameters for the solver were calculated from Hydrosta (MARIN, 2021). Aalto and BV/ICAM calculated wave damping parameters in 20 frequency steps (0.1-2.0 rad/s) in infinite water depth at zero speed of the struck ship and a forward speed of 5 or 10 knots for the striking ship. Whereas MSRC did not take into account them in their simulation as their effects are minor (Kim et al., 2020). In contrast with other participants, MARIN employed their in-house solver, MarcolXMF (MARIN, 2021), which is based on a 6 DOF time-domain rigid body hydrodynamic solver (Baraff, 2001). Restoring forces were calculated from the integration of hull geometry pressure. Added mass and damping forces used in MarcolXMF are derived from MARIN MSCN (Verkerk, 1992), accounting for forward speed effects and the influence of hydrodynamic manoeuvring derivatives in the horizontal plane.

In addition to the above conditions of ship motions in the water, AALTO considered resistant forces of the stuck ship in sway direction and the striking ship in surge direction in their analyses, using STAR CCM+ based on Reynolds-Averaged-Navier-Stokes (RANS) solver.

Table 4.10 shows the main ship parameter used for ship motion calculation in water, and Table 4.11 summarises the ship motion conditions considered at the collision simulations of each participant.

Table 4.10 Basic ship parameters to calculate ship motions in the surrounding water

Parameters		Ship A	Ship B
Draft (m)		7.2	6.9
Mass (tonne)		33,923	30,114
KG (m)		15.14	13.96
Gyration of radius (m)	Roll	11	11
	Pitch	60	55
	Yaw	61	55

Table 4.11 Applied ship motion conditions considering surrounding water

Participant	Restoring force	Added mass	Wave damping force	Resistance force
MSRC	O (considered)	O	X (not considered)	X
AALTO	O	O	O	O
BV/ICAM	O	O	O	X
MARIN	O	O	O	X

4.4.5 Results and Discussion

Figure 4.20 ~ Figure 4.24 summarise analysis results for four collision scenarios of the benchmark study conducted by each participant. Penetration, internal energy, and resultant forces are presented over time and penetration. The penetrations were measured as a transverse distance between the foremost point of the striking body and the outer shell of the stuck ship. For the deformable striking body, the initial contact point to the outer shell of a struck ship may not be the same point of the striking ship at the maximum penetration because the striking body may be deformed, and the initial contact point may be squashed and folded, being pushed behind during collisions. Internal energy accounts for the dissipated energy, including deformed and fractured structures and sliding energy from friction and contact. Especially for the SHARP solver, virtual displacements are calculated by internal analytical closed-form expressions for structural resistance with plastic deformation and friction mechanisms at the same time (i.e., the plies and the plastic hinges formed in a concertina deformation mechanism of a deck or a bulkhead) (Le Sourne, 2007, Buldgen et al., 2012, Buldgen et al., 2013, Le Sourne et al., 2012)

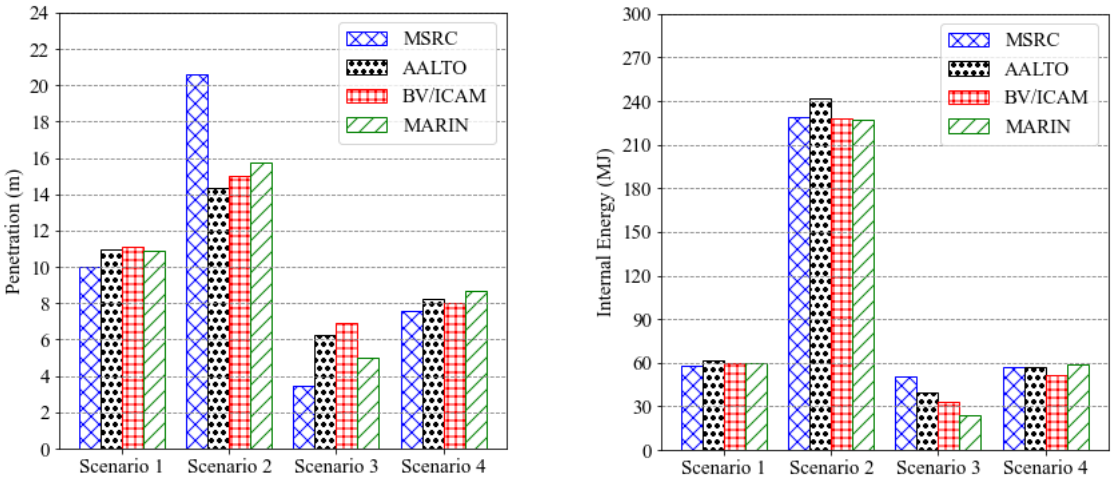

(a) Maximum penetration (b) Maximum dissipated energy

Figure 4.20 Comparison of maximum structural response in the collision benchmark study

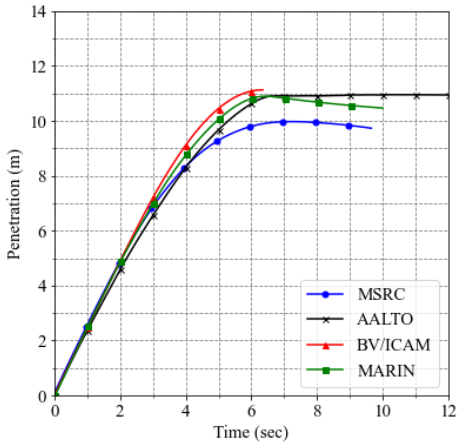

(a) Penetration - Time

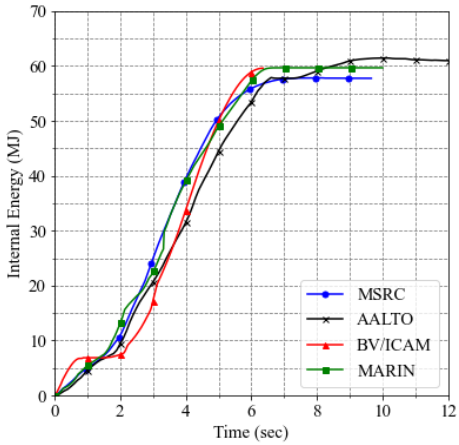

(b) Dissipated energy - Time

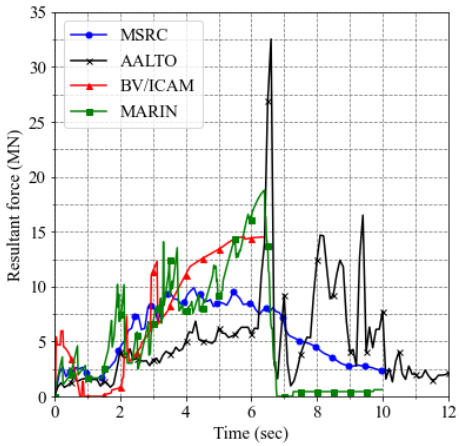

(c) Resultant force - Time

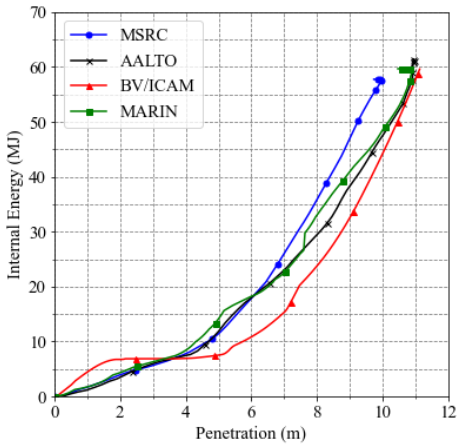

(d) Dissipated energy - Penetration

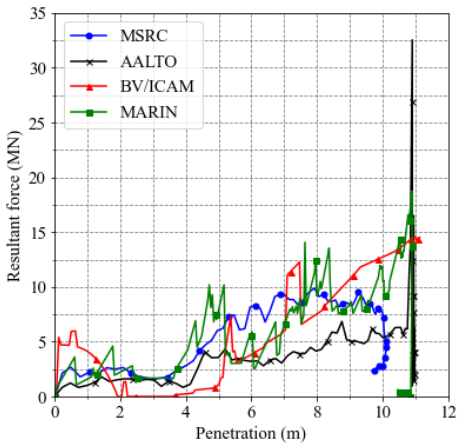

(e) Resultant force - Penetration

Figure 4.21: Scenario 1 Results: 5 knots perpendicular collision at the middle of WT compartment

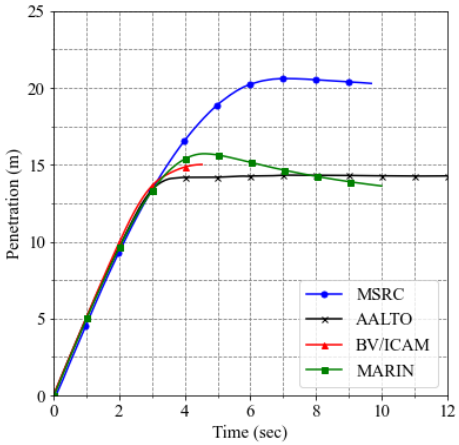

(a) Penetration - Time

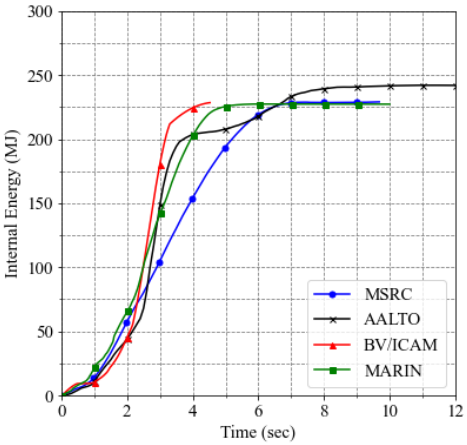

(b) Dissipated energy - Time

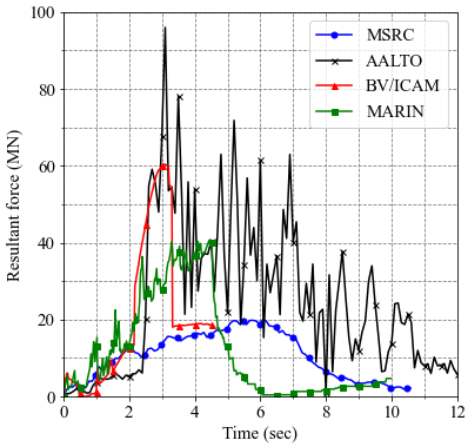

(c) Resultant force - Time

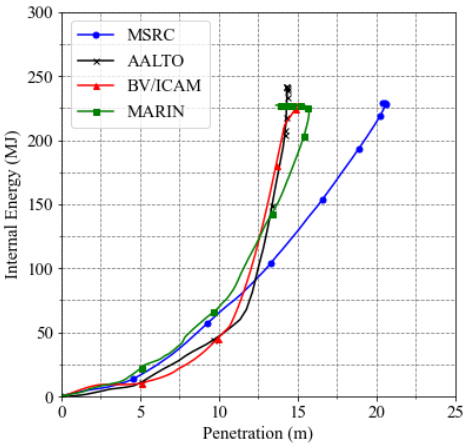

(d) Dissipated energy - Penetration

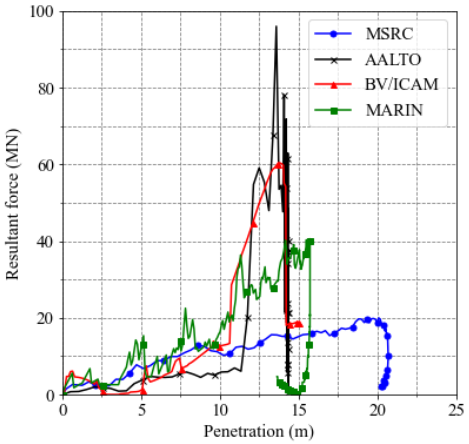

(e) Resultant force - Penetration

Figure 4.22 Scenario 2 Results: 10 knots perpendicular collision at the middle of WT compartment

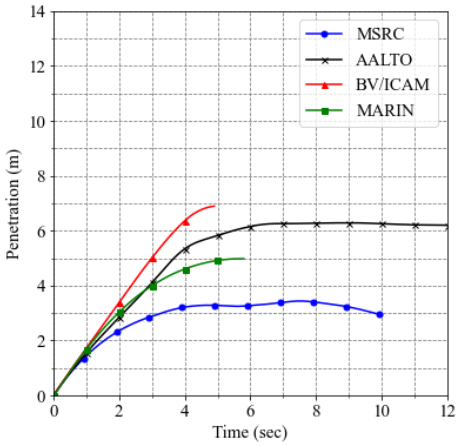

(a) Penetration - Time

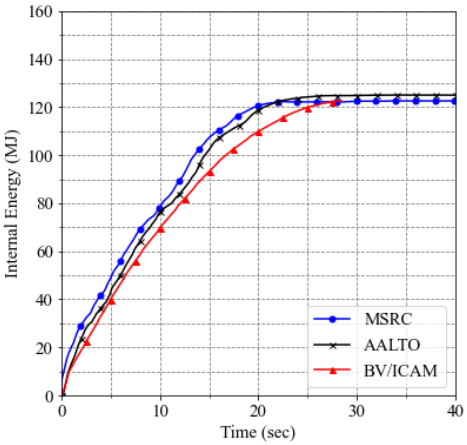

(b) Dissipated energy - Time

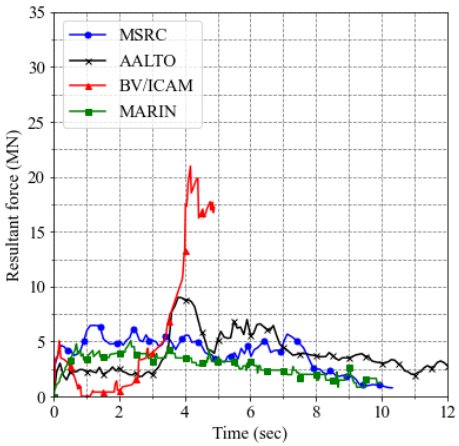

(c) Resultant force - Time

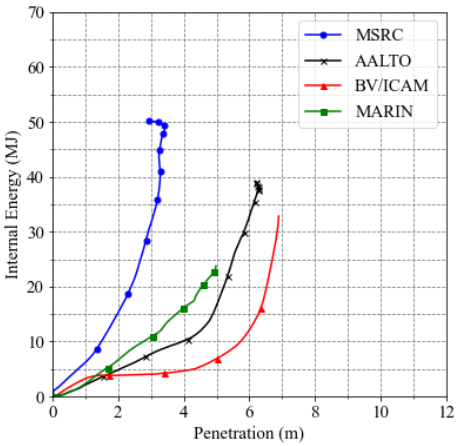

(d) Dissipated energy - Penetration

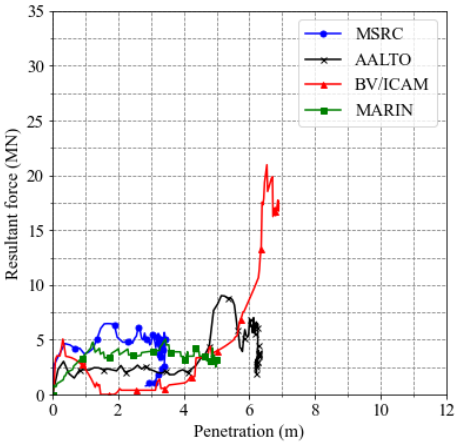

(e) Resultant force - Penetration

Figure 4.23 Scenario 3 Results: 5 knots oblique collision at the middle of WT compartment

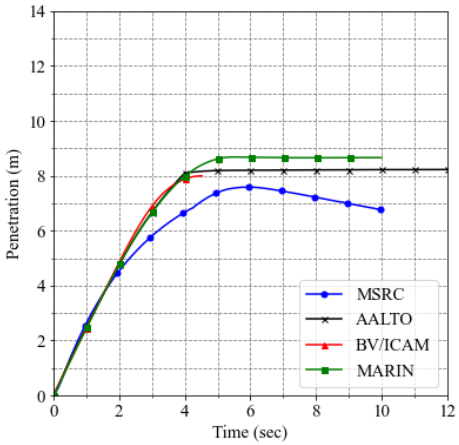

(a) Penetration - Time

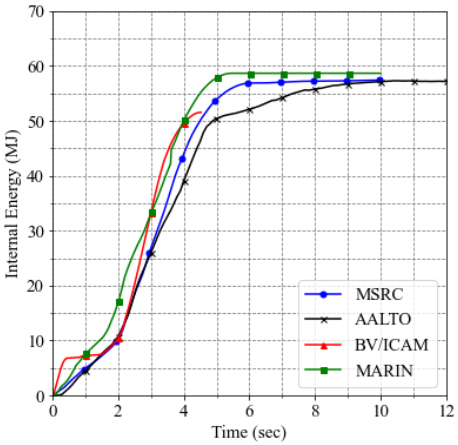

(b) Dissipated energy - Time

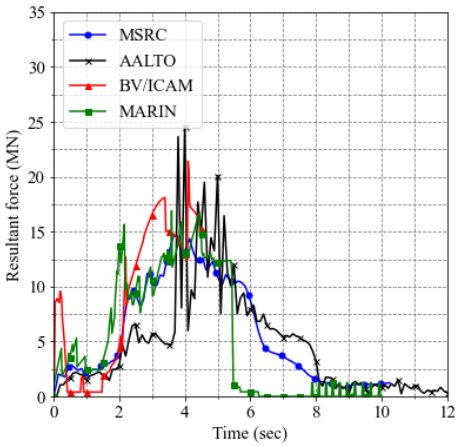

(c) Resultant force - Time

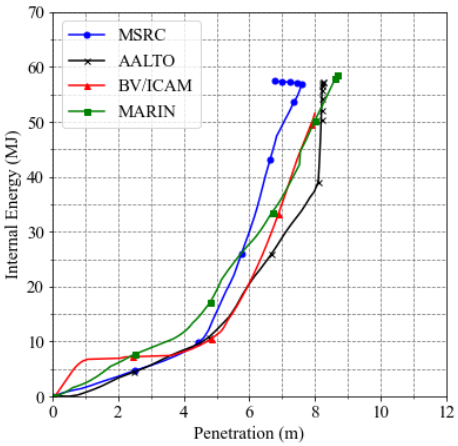

(d) Dissipated energy - Penetration

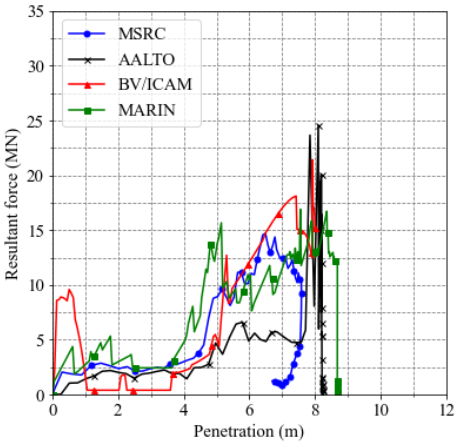

(e) Resultant force - Penetration

Figure 4.24 Scenario 4 Results: 5 knots perpendicular collision at WT bulkhead

MSRC results show good agreement for penetration and internal energy about the collision cases at low speed (i.e., scenario 1 and 4 with 5 knots collision speed) compared with other participants, as shown in Figure 4.20 ~ Figure 4.24. However, the deeper penetration is observed at the collision case with high collision speed (i.e., scenario 2 at 10 knots collision speed) in Figure 4.22, but the internal energy is similar to others. Furthermore, less penetration and high internal energy are shown in the case of oblique collision (i.e., scenario 3 in Figure 4.23). Compared to the results from AALTO, who use the same analysis technics using LS-DYNA explicit code, the results differences might come from the geometric model defined, such as applied finite element type (i.e., 1D beam and 2D shell elements), element size, etc.
Overall, all participant results are in good agreement for scenario 1 and 4 at low collision speed, while slightly different results are obtained for the oblique collision scenario. Therefore, the oblique collisions may need more investigation for further work.

4.5 Chapter Summary

The non-linear Finite Elements analysis for collision simulations with each RCO has been carried out using ANSYS/LS-DYNA explicit code for internal mechanics and MCOL solver for external dynamics.

The geometry of the reference ship was modelled with fine meshes for the contact area and defined as deformable regions, while the rest of the parts were made with coarse meshes and defined as rigid parts. For the striking ship, the fore part was only considered as the striking ship, and the forward part of 27.6m was modelled with fine meshes and defined as a deformable part, while the aft part was set to rigid. The element sizes of the fine meshes for the struck ship and the striking ship were selected as 175mm and 200 mm. This is a quarter of the frame spacing of each ship and, therefore, may reasonably capture the structural behaviour economically. Belytschko-tsay 2D shell elements (LSTC, 2019) with a 5/6 shear factor and five through shell thickness integration points have been applied to all geometries, in particular not only for plates but also for stiffeners. Both vessels were assumed to be constructed of mild steel. A material model of Piecewise Linear Isotropic Plasticity has been adopted in wat of the contact regions made of fine meshes for both ships to observe the elastoplastic deformation from collisions. Based on the given material property, a true stress true strain curve has been applied. The through-thickness strain criterion, which is well known as the "GL criterion" and element size-dependent, has been adopted for the collision simulations. Cowper and Symonds's formulation has been applied to reflect strain rate effects. The node-on-segment penalty method was adopted for contact definition. The "Automatic Single Surface" option in LS-DYNA for contact was used for the FE analysis setup, and a value of 0.3 was adopted for both static and dynamic friction coefficients.

Moreover, for the actual hydrodynamic boundary conditions for ship collisions, such as restoring forces associated with ship mass and buoyancy, added mass of both ships and wave damping forces, the MCOL solver embedded in LS-DYNA was employed to take into account those ship motions and added mass for FE analysis. The input parameters were calculated from ANSYS AQWA based on the reference ship characteristics.

Table 4.12 summarises the FE method adopted for crash simulations in this thesis.

Table 4.12 Summary of adopted FE Method

Parameter	Striking ship	Struck ship
Analysis tool	• Crashworthiness Analysis: ANSYS-LS DYNA • Ship motions: MCOL • Mesh control: HYPER MESH • Hydrodynamic coefficient calculation: ANSYS-AQWA	
Geometry Modeling	• Partial Geometry • Fore parts • With Bulwark geometry • Collision region: Deformable • Rest of collision region: Rigid	• Partial or full Geometry • At least Two Main Fire Zones (MFZ) • Collision region: Deformable • Rest of collision region: Rigid
Size of Finite element	• 175 mm for the struck ship and 200 mm for the striking ship • A quarter of frame spacing, which should be a reasonable size for the capture of structural response considering computation time	
Material Property	• Mat.024 Piecewise Linear Isotropic Plasticity • Modified True stress true strain material curve	
Fracture Strain	• GL Criteria (Case study in Chapter 6) • Constant fracture strain value of 0.1 (Collision Benchmark study in Section 4.4)	
Contact Condition	• Friction coefficient = 0.3 • Automatic Single Surface	
Dynamic Effect	• Cowper-Symonds Equation	
Hydrodynamic effect	• MCOL solver excluding wave damping and viscous forces	

Chapter 5

RCOs and Cost-Benefit Assessment

5 DESIGN OF RCOS AND COST-BENEFIT ASSESSMENT

5.1 Preamble

This Chapter deals with the risk control options (RCOs) and cost-benefit analysis (CBA) methods. A total of five types of RCOs are described in Section 5.2. The passive structural types involve a single longitudinal subdivision (well-known as double-hull design), an internal safe space concept with two additional longitudinal watertight subdivisions, different hull thicknesses, and combinations. Other RCOs consider adopting foam void filling (Paterson, 2020) introduced by Vassalos and Paterson under the University of Strathclyde's patent (Patent No.PCT/ GB2017/050681). In Section 5.3, the details of cost estimation and risk reduction calculation are presented for the Gross Cost of Averting a Fatality (GCAF) (i.e., $GCAF = Cost / Risk$). The total cost of each RCO can be estimated from the summation of capital expenditure (CAPAX) and operational cost (OPEX). The risk improvement of each RCO can be obtained from the potential loss of life (PPL). This is achieved by using the Attained Subdivision Index for each RCO calculated from damage stability assessment and risk models developed in GOALDS(IMO, 2012) and EMSAIII (EMSA, 2015) projects.

5.2 Risk Control Options

The RCOs aim to :

- Reduce accident frequency through improved design,
- Mitigate structural and associated failures,
- Alleviate circumstances where failures may happen, and
- Mitigate accident consequences.

Therefore, most of the proposed RCOs are usually based on the industry's best practice and accounts for cost-effective solutions for managing risks.

Table 5.1 summarises the RCOs adopted from previous FSAs of cruise ships (IMO, 2008, IMO, 2012, EMSA, 2015) related only to structural alternations. RCO no 1 and no 2 are measures to change the dimensions of ships and could increase overall ship survivability significantly. However, these measures directly affect overall ship cost and performance. RCO no 3 and no 4 enable ships to have additional buoyancy in flooding conditions, leading to survivability improvement. These RCOs are the most common solutions as simple and cost-effective measures to increase the s-factor. However, the loss of space due to additional subdivisions

cannot be avoided. In particular, the additional transverse subdivision (i.e., ROC no 4) may cause severe problems, such as pipe/duct/cable penetrations and additional watertight accesses (see Section 1.3.2). RCO no 5 is also one of the common solutions for the s-factor increase. On the other hand, a high cost may be required if lightweight material like aluminium is applied or it affects the original ship layout (e.g. a heavy-weight swimming pool moved from the top deck to the lower deck) (see also Section 1.3.2). RCO no 6 and no 7 are minor and cost-effective measures. While RCO no 6 is to increase the sill of the weathertight doors connecting the internal spaces, especially on the aft or fore wether deck area of the ships, RCO no 7 is to install cross-flooding pipes within the double bottom to avoid unsymmetric flooding.

Table 5.1 Risk Control Options investigated in the different projects

No.	Configuration (RCOs)	Project
1	Breadth increase by 0.5m ~2.0m	SAFEDOR(1), GOALDS(2), (3) ,EMSAIII(4),(5)
2	Freeboard increase by 0.5m~1.5m	SAFEDOR(1), GOALDS(2), (3) ,EMSAIII(4),(5)
3	Additional longitudinal subdivisions (Added Buoyancy compartments)	SAFEDOR(1)
4	Additional Transverse Subdivision	GOALDS(3) ,EMSAIII(4),(5)
5	Lightship KG decrease	GOALDS(3)
6	Sill increase of weathertight door	EMSAIII(5)
7	Added Cross flooding device	EMSAIII(5)

(1) SAFEDOR : The reference ship is a medium-sized cruise ship of 90,000 GT with 2,500 POB
(2) GOALDS : The reference ship is a large cruise ship of 125,000 GT with 5,600 POB
(3) GOALDS : The reference ship is a medium-sized cruise ship of 63,000 GT with 2,400 POB
(4) EMSA3 : The reference ship is a large cruise ship of 153,400 GT with 6,730 POB
(5) EMSA3 : The reference ship is a small-sized cruise ship of 34,000 GT with 478 POB

In this thesis, the emphasis is on proposing RCOs that are cost-effective and require the least and most economical design changes. Therefore, among those existing RCOs in Table 5.1, the measure with additional longitudinal subdivision (i.e., RCO no 3) is employed in the applied RCOs with other new types of measures. Other cost-effective RCOs, such as no 6 and no 7, have not been included in this study as they are minor measures. However, they can be applied later for additional ship survivability enhancements.

5.2.1 Structural Passive Risk Control Option

5.2.1.1 RCO Type 1: Single Longitudinal Subdivision

Single longitudinal subdivision, also known as the double hull concept, has been widely used in tankers and LNG carriers to protect the environment from oil spills by ship collisions. In this thesis, a single longitudinal plate on each ship side is considered one of the passive risk control option types. The plates are assumed to be extended from a double bottom deck (i.e., deck 1) to an embarkation deck (i.e., deck 5), as shown in Figure 5.2. They are made of mild steel with a thickness of 10mm without any stiffeners. No cross-flooding devices between two wing compartments on both ship sides are also taken into account.

Different plate positions, namely B/20, 2B/20, 3B/20 and 4B/20, displayed in Figure 5.1, have been investigated to identify collision reduction effects of this RCO depending on locations. B/20 is the distance required for the ship's double bottom height according to SOLAS (2020) and MARPOL(IMO, 2004). B/10 is the maximum transverse damage extent defined in SOLAS Reg.II-1/B-1/8. B/10(SOLAS, 2020) and SRtP (IMO, 2008b). B/5 is the criteria of damage penetration for Ro-Pax according to the Stockholm Agreement (EU, 2003). Finally, 3B/20, which is the centre position between B/10 and B/5, was added to compare position effects with others.

The single longitudinal subdivision creates a wing compartment on each side of the ship, providing the advantage of local s-factor increases due to additional buoyancies by these spaces. However, it should be noted that the original spaces should be divided into separate spaces, which is a disadvantage from the internal design and layout perspective.

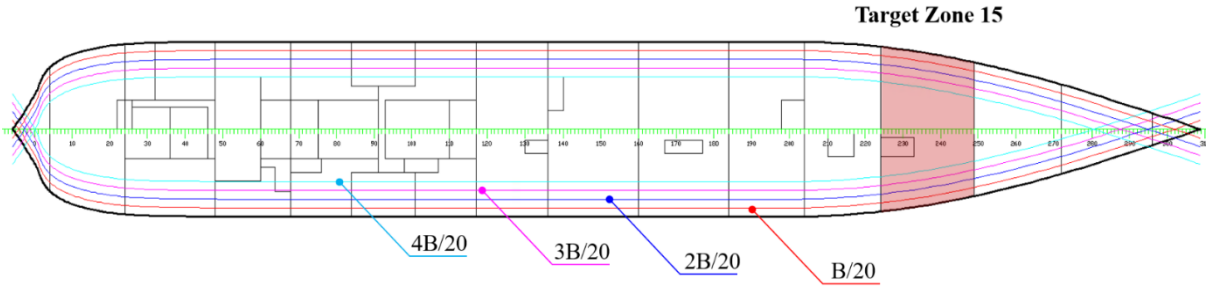

Figure 5.1 Locations of the longitudinal bulkhead at B/20, B/10, 3B/20 and B/5

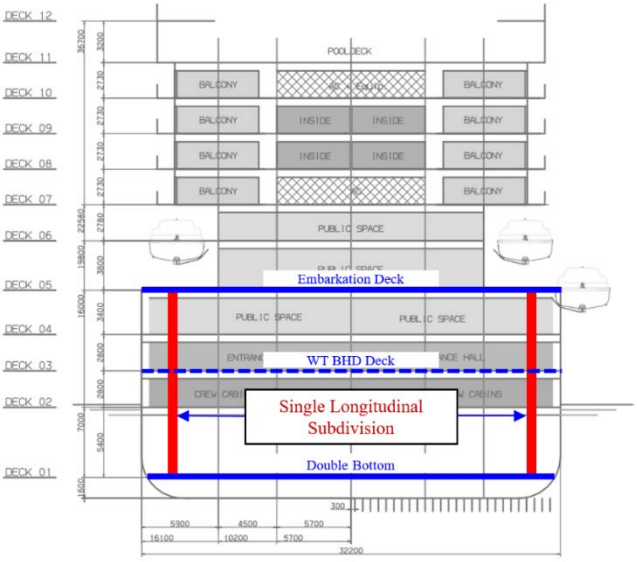

(a)

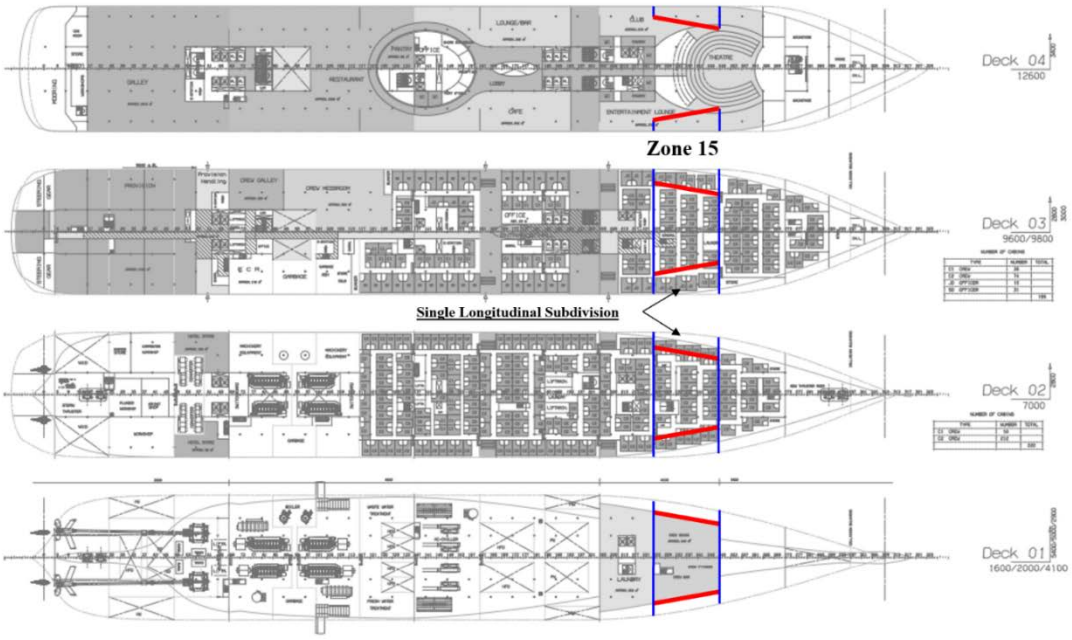

(b)

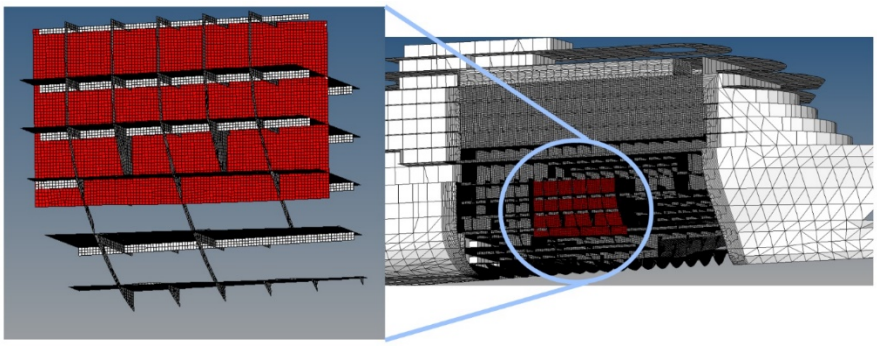

(c)

Figure 5.2. RCO type 1: Single Longitudinal Subdivisions : (a) Section view (b) Plan view, and (c) FEA modelling

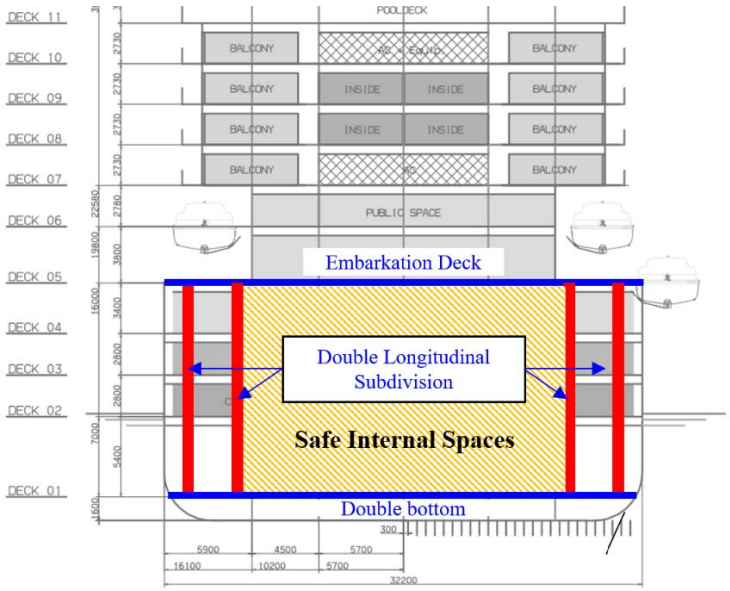

(a)

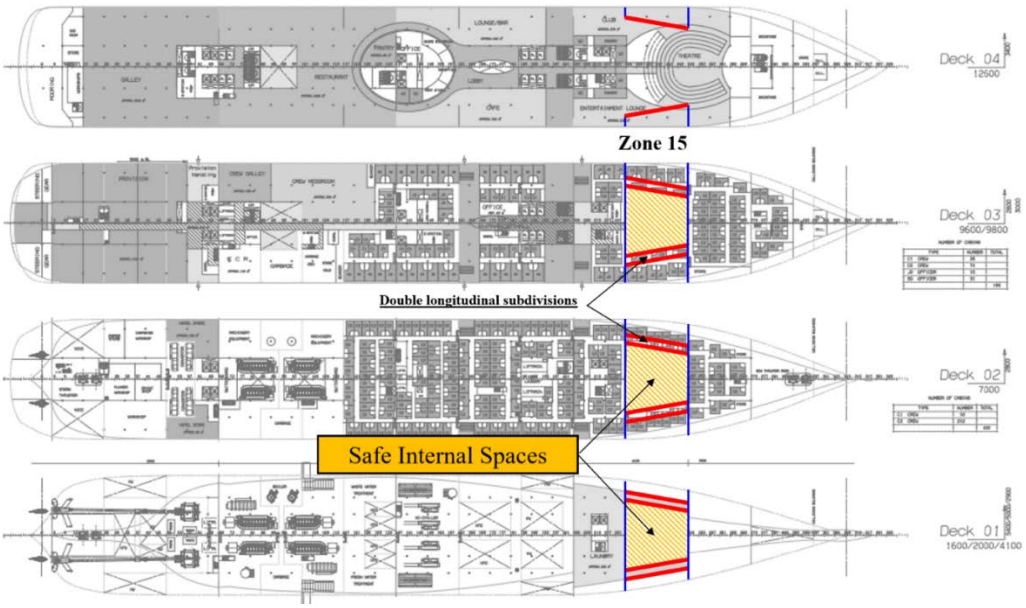

(b)

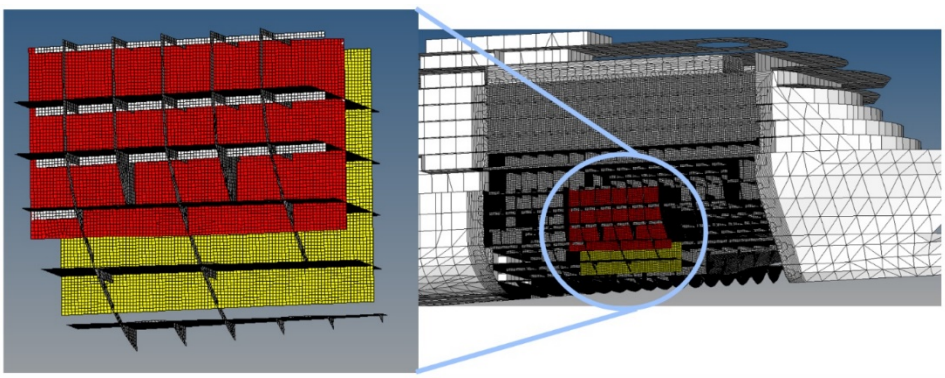

(c)

Figure 5.3 RCO Type 2: Double longitudinal Subdivision : (a) Section view (b) Plan view and (c) FEA modelling

5.2.1.2 RCO Type 2: Double Longitudinal Subdivision

The second RCO was to apply an additional longitudinal subdivision to RCO type 1, so there are two longitudinal subdivisions on each side of the target zone. The difference from RCO Type 1 is that the additional subdivision will be located just after the maximum penetration based on the crashworthiness analyses. Therefore, the first barrier may reduce the penetration from collisions, and the second subdivision protects the internal from flooding, forming "*safe internal spaces*". Since these safe spaces are not prone to flooding following the collision, their permeability can be assumed to be zero. No cross-flooding device was not also considered for wing compartments.

Four wing compartments, which are made by double subdivisions on each side of the ship, take advantage of local s-factor increases due to additional buoyancy, and the internal safe spaces may bring a large contribution to s-factor improvement. On the other hand, large spaces should be sacrificed for those compartments. This may lead to weight and cost increases.

5.2.1.3 RCO Type 3: Hull Plate Thickness change

Thickening the hull can reinforce structural crashworthiness against ship collisions. This approach does not affect original layouts, but it may lead to relatively high weight and cost increases depending on hull thicknesses. Nevertheless, it is worth investigating because a fairly enough thickness can protect the hull with no small opening in collisions, and the internal area can be considered as an "*unflooded zone*". As shown in Figure 5.4 , the concept can be applied to the hull of the target zone from the keel to deck 7.

A huge contribution to s-factor improvement is expected if no damage opening on the hull occurs by the RCO with enough thick hull. The improvement may be very limited for the RCO with less effective thickness, and the feasibility of implementation should be investigated on the basis of cost and weight increase.

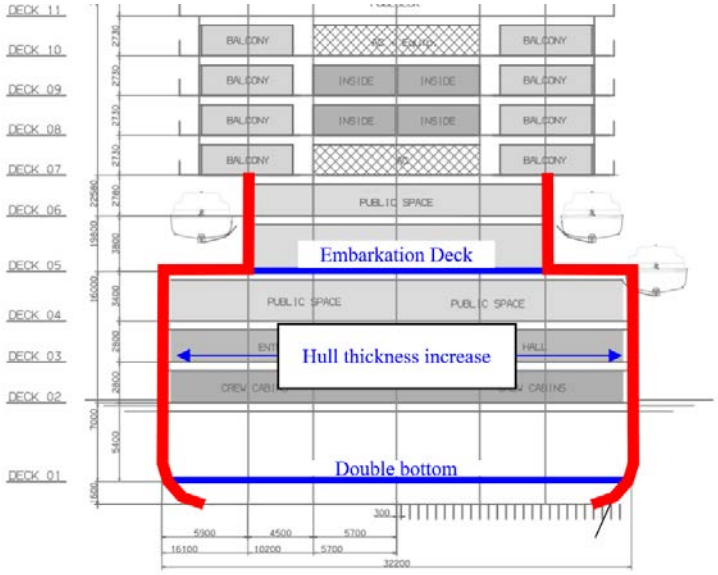

(a)

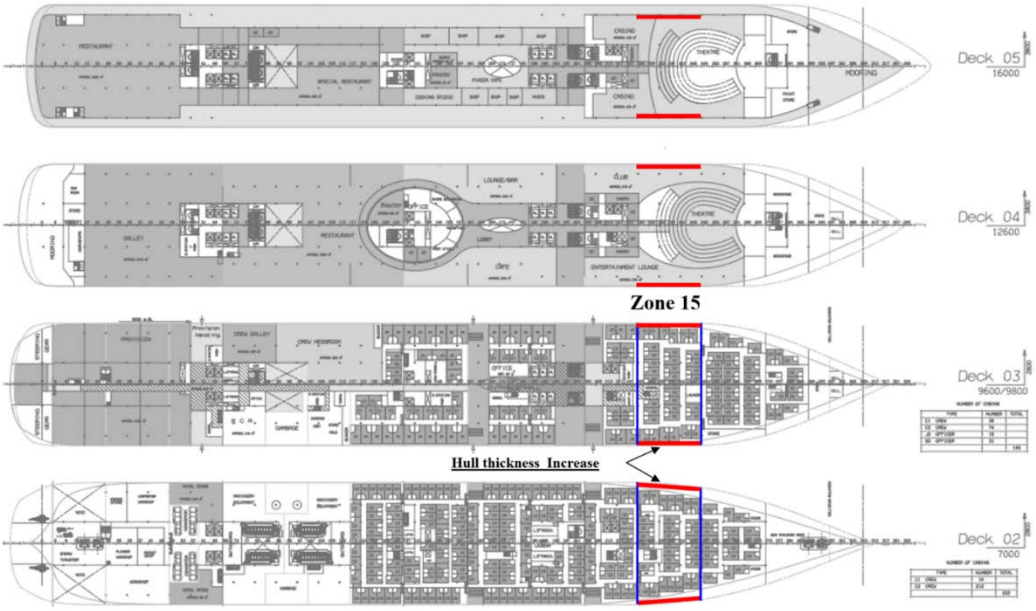

(b)

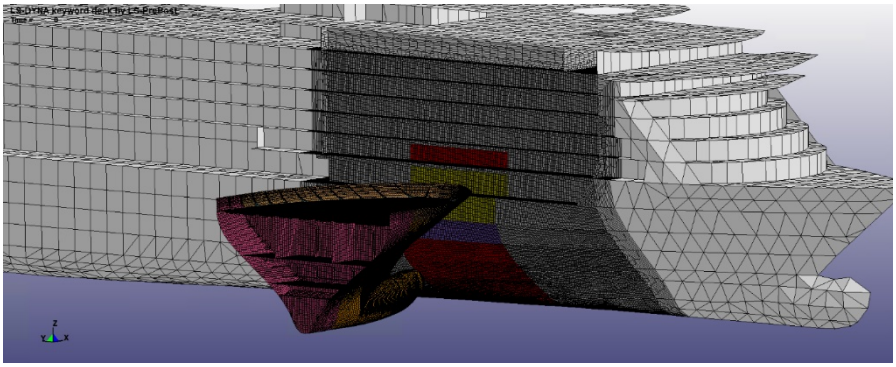

(c)

Figure 5.4 RCO Type 3: Hull Thickness Increase: (a) Section view (b) Plan view and (c) FEA modelling

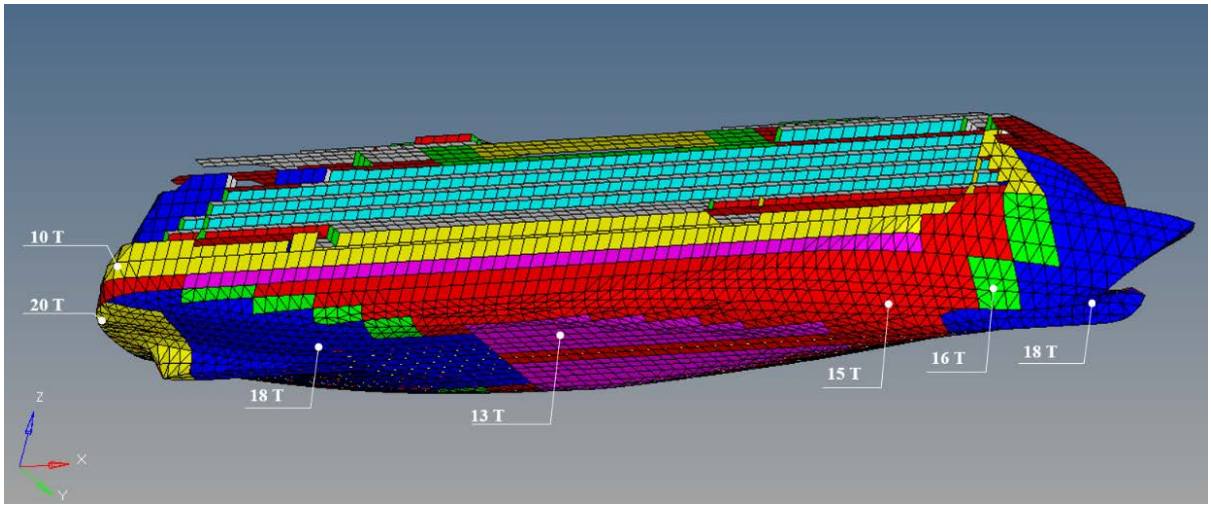

(a)

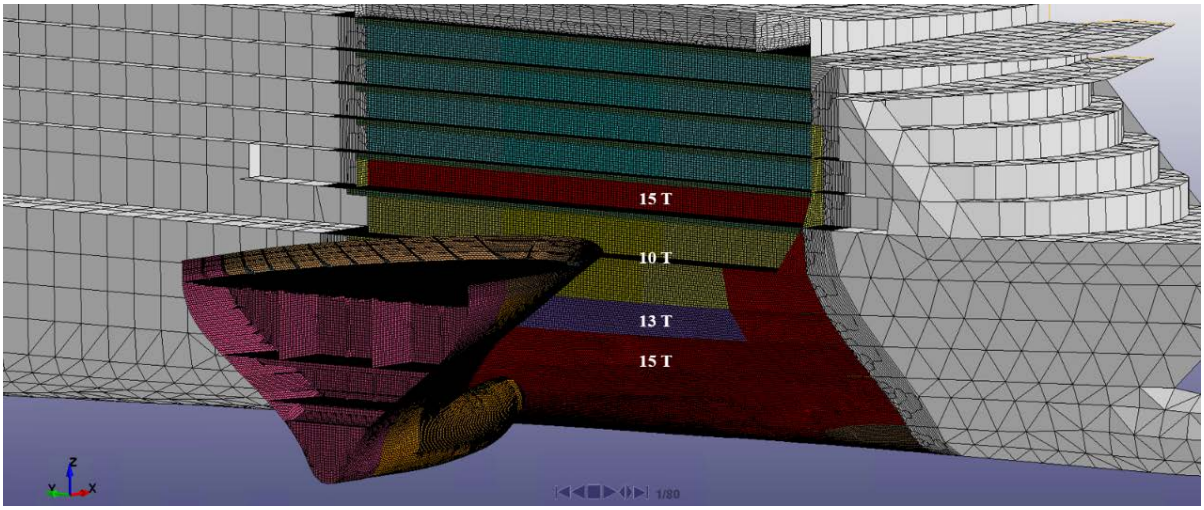

(b)

Figure 5.5 Hull plate thickness of a typical cruise ship for(a) a whole ship and (b) a target zone

Figure 5.5 illustrates the different hull-plate thicknesses depending on the positions of the ship. In general, the bow and stern part of a hull have a thicker plate than the midship section, and the bottom plate is thicker than the upper part. Therefore, several variations of type 3 RCO can be accounted for, changing thicknesses.

In this thesis, a total of 6 RCOs for type 3 have been investigated to identify the effects of hull thickness changes. The first two RCOs increased all hull shell thickness by the same proportion of 50% and 100%. The other four RCOs applied identical shell thicknesses from 20T to 50 T. The application area of this RCO, from the ship's bottom to the embarkation deck area, accounted for collision regions defined in pre-simulations in which the stuck ship was collied with the bulbous bow and uppermost part of the striking ship.

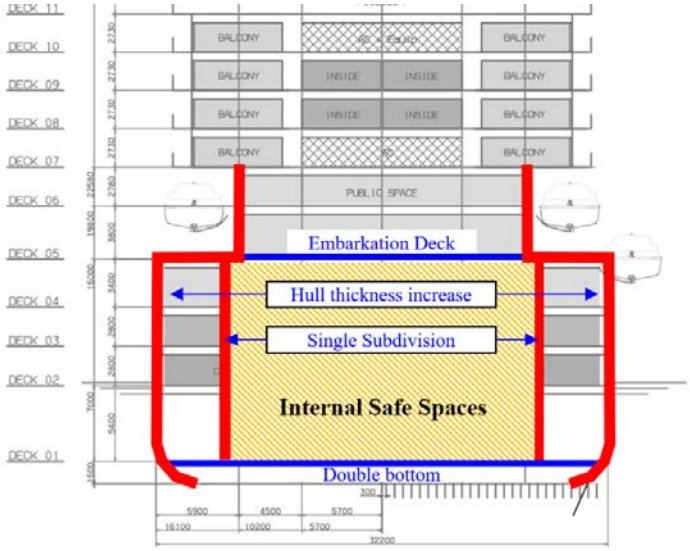

(a)

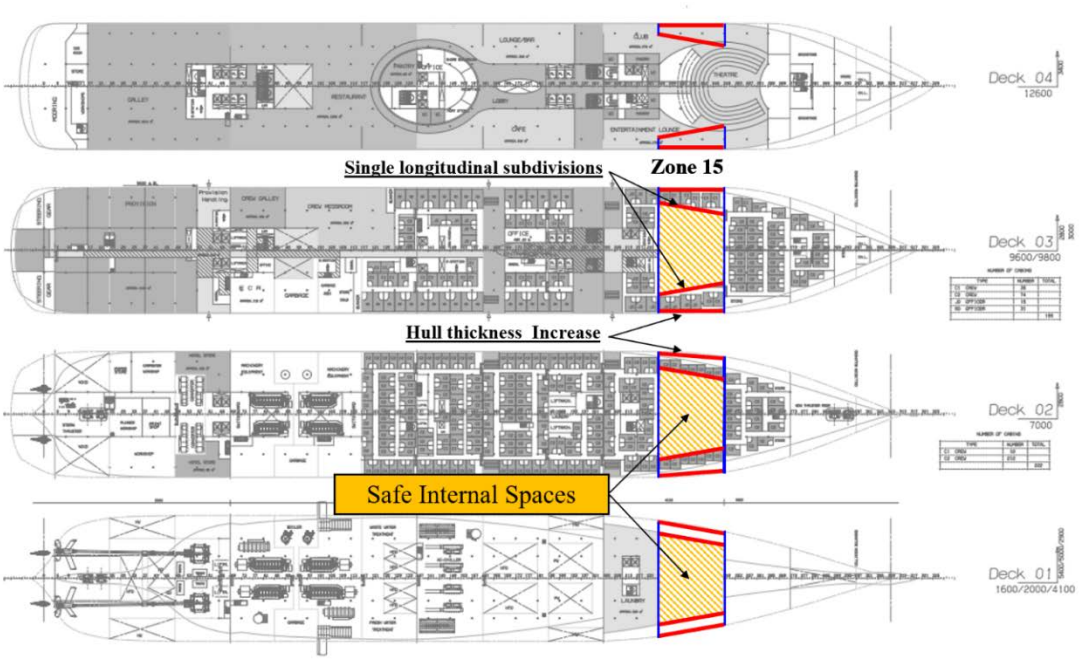

(b)

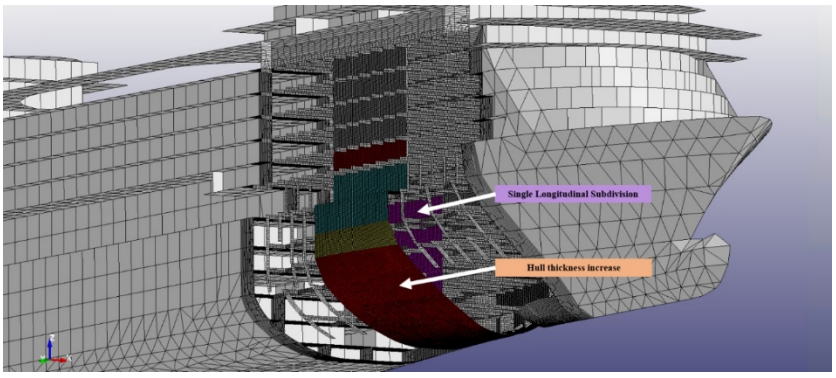

(c)

Figure 5.6 RCO type 4 : Combination of passive RCOs: (a) Section view (b) Plan view and (c) FEA modelling

5.2.1.4 RCO Type 4: Combination of two Passive RCOs

RCO type 4 is a measure to apply for both ROC type 1 and type 3 simultaneously to achieve the most effective advantages from the previous passive structural RCOs. In this RCO, firstly, the thickened hull (i.e., RCO type 3) reduces the original penetration from collisions. Secondly, the single subdivision (i.e., RCO type 1), which is considered to be located just after the maximum penetration, protects internal spaces similar to the second barrier of the RCO type 2. Implementation of this RCO also leads to a weight increase of about 161.55 tons for 30T hull thickness and a single subdivision on each side of the ship, which is reasonably acceptable as only 0.6% of the lightship weight based on the calculation in Section 6.11. Two wing compartments on the target zone of the struck ship are not cross-connected to include unsymmetrical heeling effects at this RCO.

The wing compartments and internal safe spaces directly improve the s-factors of the target due to additional buoyancy and zero permeability, respectively. Furthermore, the penetration reduction by thickened hull positively contributes to the p-factor improvement, leading to a local Index A increase.

5.2.2 Non-structural Risk Control Option

5.2.2.1 RCO Type 5: Foam Void Filling to RCO Type 4

This type of risk control option is to apply foam filling to the previous RCO type 4, especially for the case of double hull arrangement as suggested by Vassalos et al. (2016), Paterson (2020), and the University of Strathclyde Patent No.PCT/ GB2017/050681. This system can fill high-expansion foam to the target spaces with the aim of reducing flooding volume. It can also keep the vessel upright from the asymmetry-induced heeling moment, thus resulting in stability improvement. Additionally, the density of the foam is relatively lighter than other materials, with 25 kg/m3 (Paterson, 2020), which does not cause a significant increase in the lightweight of the ship.

Figure 5.7 shows that a foam filling applies to the wing compartments between the hull and a single longitudinal bulkhead on each side of the target ship. The permeability of side spaces with foam filling is 0.05, as proposed by Paterson (2020). Therefore, if this foam filling is used for wing compartments of the arrangement of RCO4 in Section 5.2.1.4, the permeability of wing compartments and internal safe spaces will have 0.05 and 0.00, respectively. This means that the target zone with this RCO will never be flooded after collisions as an "*unsinkable zone*".

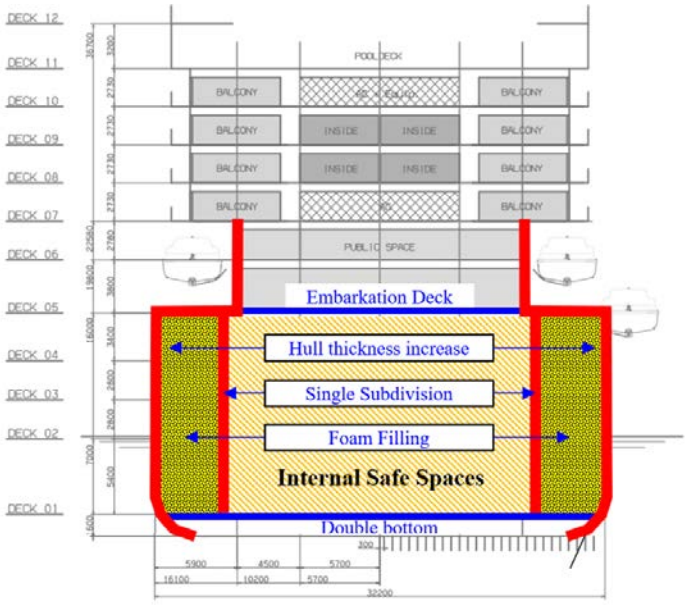

(a)

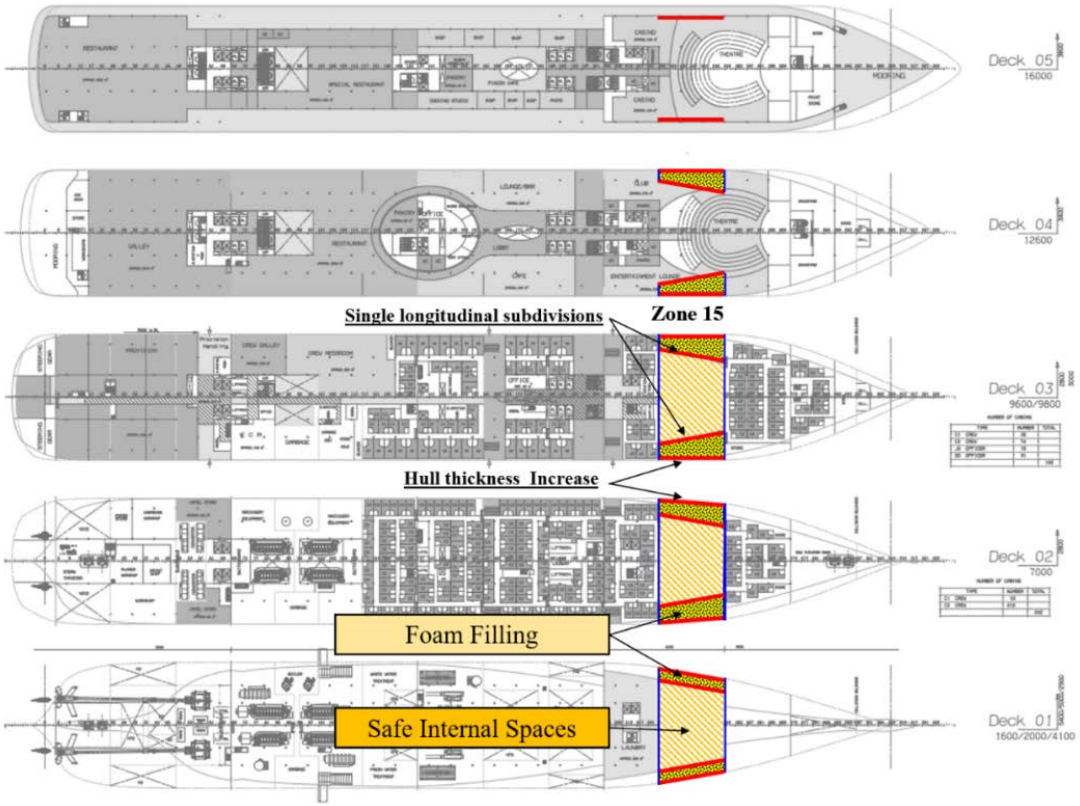

(b)

Figure 5.7 RCO Type5: passive RCOs with a Foam filling system: (a) Section view and (b) Plan view

5.3 Cost-Benefit Assessment

The guidelines for formal safety assessment (FSA) define the overall methodology of cost-benefit assessment as follows:

- Perform risk assessment for both accident frequencies and consequences to define the base case of risk levels of the situation;
- Propose feasible RCOs after reviewing the costs and benefits of each RCO
- Calculate and compare the cost-effectiveness of each RCO with the cost per unit risk reduction from the total net cost increase divided by the risk reduction achieved as a result of RCO adoption
- Screen the RCOs which are not cost-effective or impractical, and rank the rest of RCOs from a cost-benefit perspective to provide the decision-making recommendations

It is recommended that the cost of each RCO should be expressed in view of life cycle costs, including initial setup, operating, training, inspection, certification, decommission etc.

5.3.1 Cost Estimation of RCOs

5.3.1.1 Unit Cost of previous projects

Several investigations were carried out to find components of cost for RCO implementation and associated unit cost from previous FSA studies. In 2002, the "IACS Bulk Carrier FSA study-Fore end watertight integrity" (IMO, 2002a) was carried out for 44,000 dwt bulk carriers using structural RCOs such as watertight bulkhead replacement, double sie skin installation and hold frame replacement. Table 5.2 shows unit costs of associated components, such as material, labour, paint, blast, paintwork, facility and other incidental works for a new building and conversions. IMO (2008) conducted an additional FSA for a cruise ship and a Ro-Pax based on finding on the EC-funded Project (SAFEDOR, 2005-2009). In this analysis, 6,000 USD/Ton was used for steel cost. This includes both material and labour costs based on the assumption of 10 ~ 90 man-hours per ton of steel, the labour cost of 55 ~ 80 USD per hour and the hot rolled steel plate price of 737 USD per ton. It is not clear whether this unit cost includes paint, paintwork, and facility cost used at bulk carrier FSA.

In 2012, IMO (2012) performed another FSA for a passenger ship which was also financially supported by the EU (GOALDS, 2009-2012). The same unit cost(i.e., 6,000 USD/ton) was adopted for the cost estimation of each RCO.

Table 5.2 Unit Cost of RCO implementation for bulk carriers in 2001

Components of cost	For New Building	For W.T. Bhd Replace, Double side skin & Hold frame Replace	For Reinforcement of W.T. Bhd
Material [USD/Ton]	600	800	1,170
Work [USD/Ton]	300	1,850	3,690
Paint [USD/m^2]	2,883	Included in Material cost	
Blast [USD/m^2]	-		
Paint Work [USD/m^2]	4,272	Included in Work cost	
Incidental Work	1,961		
Facilities	-	19 [USD/day/1000GT]	
Total Sum (*)	**10,016**	**8,502**	**10,712**

(*) 44K GT Panamax bulk carrier and seven days works are assumed.

More recently, the EMSAIII project (EMSA, 2015) was also carried out further investigation for an increase in the Required Subdivision Index R. In line with this, the cost benefit assessment was conducted for two cruise ships and three RoPax vessels in case of new build ships, and following cost assumptions was adopted depending on ship size and shipyard:

- Steel weight, including piping, ducting, and painting 4500 ~ 6000 €/ton
- Public areas, including ducting, cabling etc. 2600 ~ 3000 €/m2
- Cabin areas, including ducting, cabling 2400 ~ 2500 €/m2
- Service areas, like gallery, laundry including ducting, cabling etc. 2500 ~ 5000 €/m2
- Additional installed power of main engines, taking into account any discrete step in engine size 380 €/kW
- Additional installed propulsion power 700 €/kW

5.3.1.2 Capital Expenditure (CAPEX)

The suggested RCOs of this research are primarily associated with internal construction (e.g. adding watertight subdivisions or enforcing the hull shell with thick plates), not affecting overall ship dimensions. Therefore, the steel cost and its associated labour should be considered for most of the total cost. Since the bulkhead divides one space into two rooms, watertight sliding doors on each deck for access are assumed. Thus, sliding doors and the relevant material/labour costs for cabling and ducting penetration were also considered. Regarding the engine size effects due to ship weight increase from each RCO implementation, it was assumed

to be neglected since the weight increase of each measure is relatively small. The increased weight by ROCs was calculated as less than 300 tons (i.e., 0.85% of target ship displacement), so it does not affect total ship resistance or lead to changes in engine size. However, the fuel oil consumption due to the weight increase was considered as an operational cost.

Since there is a discrepancy in unit cost between bulk carriers and passenger ships, this research adopted the cost assumptions employed for a Baltic cruise ferry during EMSAIII project (EMSAIII, 2013-2016). The exchange rate between Euro and US dollar currencies was about 1.1 in 2015. The same value was used to directly compare GCAF indices of proposed RCOs to those calculated at previous FSA projects. Thus, the inflation rate was not considered. The summary of cost assumptions employed in this research is shown in Table 5.3. For the foam filling as non-structural RCO, 600 € /m3 was considered (Paterson, 2020).

Table 5.3 Unit cost assumptions for cost-benefit assessment of this research (EMSAIII, 2013-2016)

Description	Unit Cost
Steel weight, including piping, ducting, painting	6,600 USD/ton
Public areas, including ducting, cabling etc	3,300 USD/m2
Cabin areas, including ducting, cabling	2,750 USD/ m2
Service areas, like gallery, laundry including ducting, cabling etc	2,750 USD/ m2
Additional Watertight Sliding Door, including cabling (*)	33,000 USD/pcs
Additional installed power of main engines, taking into account any discrete step in engine size	418 USD/kW
Foam void filling	660 USD/m3

(*)An additional 20% of the door cost is assumed for penetrations of ducting and cabling on the subdivision.

5.3.1.3 Operational Cost (OPEX)

The weight increase from each RCO requires more propulsion power due to the increased draught of the ship. In general, the skin frictional resistance is dominated by the wetted surface area and accounts for 60~70 % of total resistance depending on ship speeds. Therefore, for simplifying fuel oil estimation, it is assumed that the required propulsion power rises proportionally depending on the wetted surface area increase calculated from NAPA.

According to SAFEDOR FSA (IMO, 2008), the actual fuel consumption obtained from a cruise vessel of approximately 80,000 GT in 2006 was 40,143 tons per year. 2/3 of the fuel was used for propulsion, and the remaining 1/3 was used for other uses, such as hotel power. The same amount of fuel was assumed to be used for the target ship. This is because the size of the target

ship (i.e., 63,000 GT) is similar to this reference vessel (i.e., 80,000 GT).

The costs of fuel oil and fuel mix were based on the cost assumptions employed in the EMSAIII (2013-2016) project. The price of HFO and MGO is 600 and 900 USD/ton, respectively. These values were obtained from the average prices for 2013 and 2014 in Rotterdam using Clarkson Intelligence (Clarkson, 2014). As shown in Figure 5.8, the price of low sulphur HFO was derived from the summation of 20% of HFO and 80% of MGO price, which is 840 USD/ton (EMSA, 2015).

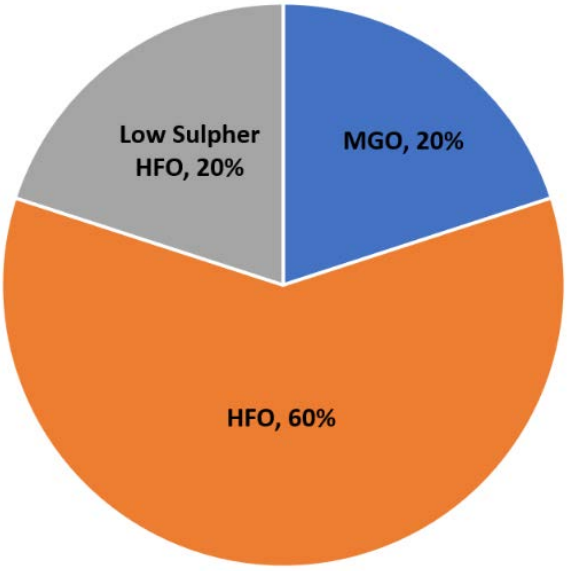

Figure 5.8 Distribution of fuel types (EMSAIII, 2013-2016)

The cost of fuel was calculated based on the assumption of 30 years ship life, using the Net Present Value (NPV) given by:

$$NPV = A + \frac{X}{(1+r)} + \frac{X}{(1+r)^2} + \frac{X}{(1+r)^3} + \cdots + \frac{X}{(1+r)^t} = A + \sum_{t=1}^{T} \frac{X}{(1+r)^t} \quad (5.1)$$

where, X is the cost of RCO any given year; A is the amount spent initially and the inflation rate r was assumed as 5%.

5.3.2 Risk of RCOs

The risk models for the cruise and RoPax ships and the definition of expected fatalities (i.e., ΔPLL) were also adopted from EMSAIII project (EMSA, 2015) to estimate risk reduction ($\Delta risk$) for *GCAF* calculation. The total PLL was defined as:

$$PLL_{total} = PLL_{collision} + PLL_{grounding/contact} + PLL_{fire/explosion} \tag{5.2}$$

The collision and grounding risk models for the cruise and RoPax ships are shown in Figure 5.9. The fire and explosion risk model was not included in this calculation as it was assumed that the proposed RCOs are not related to fire and explosion events. In order to consider the contribution of each RCO on the risk models, the updated Attained Subdivision Index A by each RCO (see Section 3.9) was used at the sinking probability in level 4, as indicated in the red dotted rectangles of Figure 5.9. The sum of the product between each probability of events and the pre-defined number of fatalities gave the $\mathrm{PLL_{collision}}$ per year. The final $\mathrm{PLL_{collision}}$ was determined for a ship lifetime of 30 years.

Similar to $\mathrm{PLL_{collision}}$, a risk model for grounding accidents of cruise ships proposed in EMSAIII was employed for $\mathrm{PLL_{grounding/contact}}$ calculation. A total of 8 level event sequences were defined for grounding accidents, and the updated Attained Index for grounding was applied to the probability of the vessel remaining afloat, as marked in the red dotted rectangles of Figure 5.10. In particular, two alternative empirical formulae proposed in GOALDS were used for the approximation of the grounding Attained Index A_{GR} based on the collision Attained Index A_{CN} (EMSA, 2014b) as follows:

$$\begin{aligned} A_{GR.GOALDS1} &= A_{CN} + 0.1\,(1 - A_{CN}) \\ A_{GR.GOALDS2} &= \begin{cases} A_{CN} + 0.1 & for\ A_{CN} \le 0.9 \\ 1 & for\ Others \end{cases} \end{aligned} \tag{5.3}$$

Since two different groundings Attained Index A_{GR} was used, two different results of $\mathrm{PLL_{grounding/contact}}$ were obtained, but, in the analysis, their average value was used for the final grounding PLL. Therefore, the final PLL reduction for 30 years can be achieved from the differences between PLL from the original layout and PLL with RCOs.

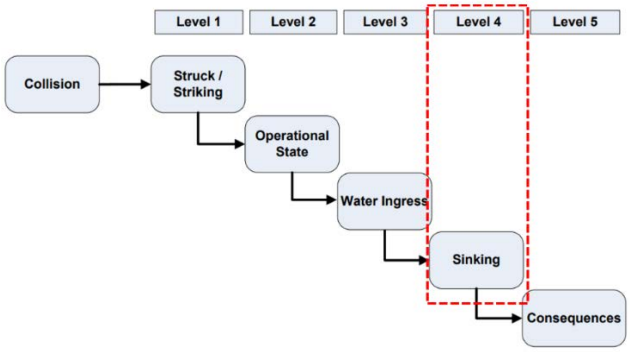

(a)

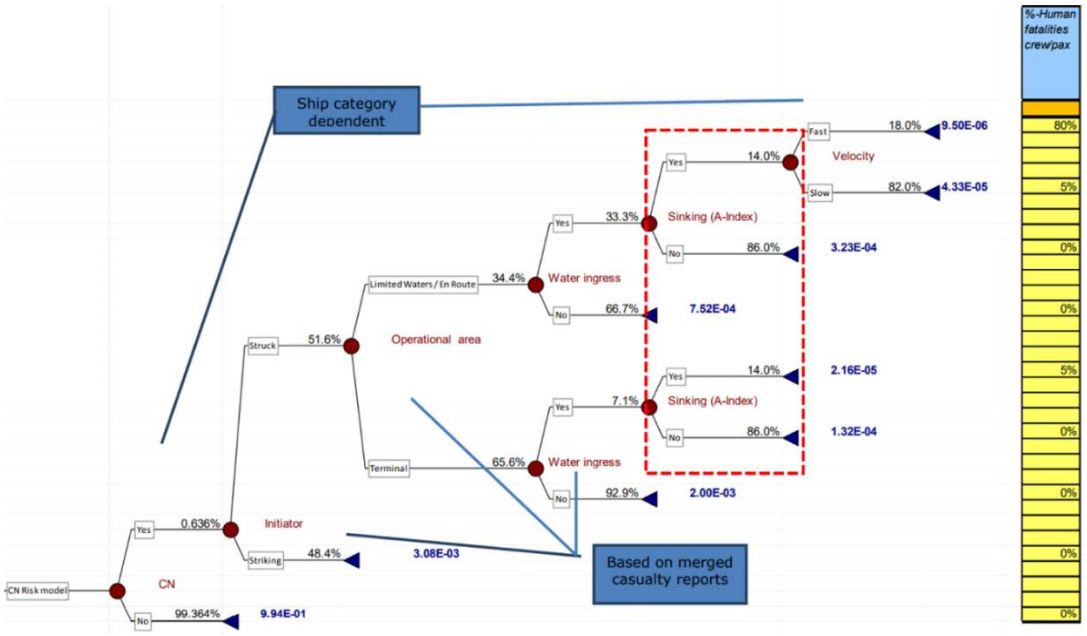

(b)

Figure 5.9 EMSAIII : (a) high-level event sequence,.and (b) collision risk model for cruise vessels in EMSAIII (EMSA, 2015) The Attained Subdivision Index calculated for each RCO is updated for level 4 sinking stages indicated with red dotted squares.

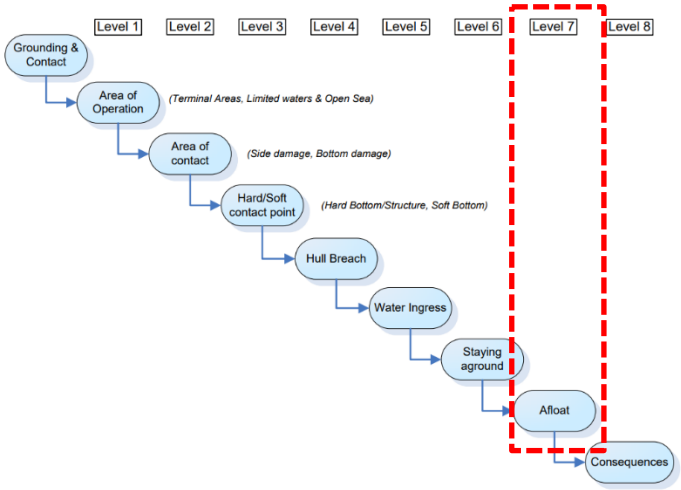

(a)

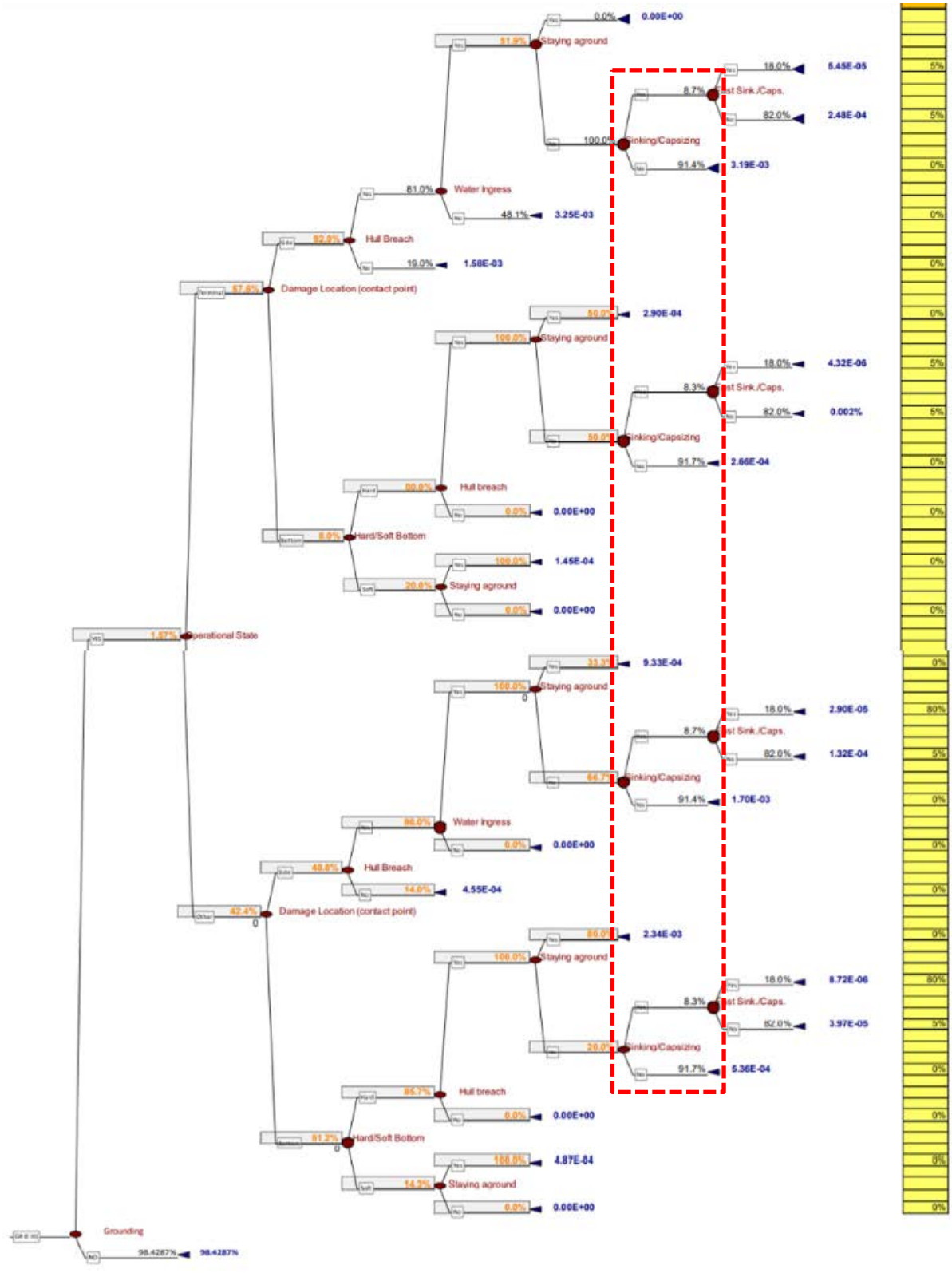

(b)

Figure 5.10 EMSAIII : (a) high-level event sequence, (b) Grounding risk model for cruise vessels(EMSA, 2015). The Attained Subdivision Index for grounding is updated for level 7 afloat stages indicated with red dotted squares.

5.4 Chapter summary

This chapter described the design alternatives (RCOs) applied to a target stuck ship and the methodology of the cost-benefit analysis.

Table 5.4 Summary of RCO types

RCO	Description
Type 1	To add a single longitudinal Subdivision on both sides of the target zone
Type 2	To add double longitudinal Subdivisions on both sides of the target zone
Type 3	To increase hull thickness of the target zone
Type 4	To combine all structural passive type RCOs (Especially RCO type 1 + type3)
Type 5	To apply foam filling on ROC type 4

Five types of RCOs were suggested, as summarised in Table 5.4. RCO type 1 adds a single longitudinal subdivision on each side of the ship. The measure has been widely used for tankers and LNG carriers and is well-known as “double-hull” or “double-side skin” used to protect oil spills from collisions with tankers. The single longitudinal subdivision may reduce the transverse penetration from collisions. The second type of passive RCO is to consider a second additional longitudinal bulkhead at the end of maximum penetration and aims to protect the internal space along with the first subdivision of the previous RCO. In this case, the first bulkhead reduces transverse penetration, and the second bulkhead forms and protects internal spaces, preventing flooding. The third type of RCO aims to increase hull thickness and hence reduce the maximum penetration following collisions. A huge contribution to s-factor improvement is expected if no damage opening on the hull occurs by the RCO with enough thick hull. The benefit may be very limited when the effective thickness is low. RCO type 4 combines all passive structural type RCOs. It is based on the idea that a thickened hull will resist penetration, and a single longitudinal subdivision will form internal safe spaces free from collisions. Consequently, the application of a foam filling system to wing compartments can help maximise ship survivability. In this way, almost maximum improvement can be possible for the target zone as internal safe spaces, and wing compartments with foam filling have a permeability of 0.00 and 0.05, respectively. RCO 4 essentially introduces the concept of an “*unsinkable zone” against collisions.*

Each ROC type can have variants depending on the locations of subdivisions or plate thicknesses. They are demonstrated in the case study of Chapter 6 and discussed the effects in

the discussion Section of Chapter 8.

The above RCOs were analysed to find an optimum solution in terms of cost increase and risk reduction, using cost-benefit assessment. For cost estimation, the cost of each RCO is divided into two parts, namely CAPEX and OPEX. In the CAPEX, the steel material and associated labour cost, as well as the cost of watertight sliding doors, including additional works for cabling and ducting routing and penetration on the additional bulkhead, were considered. Unit and fuel costs were based on the values proposed by EMSAIII project. For CAPEX, the required fuel amount increased by the additional weight of RCO was calculated based on the wetted surface area changes. The Net Present Value (NPV) concept for 30 years ship life was primarily employed for fuel oil cost estimation. Regarding the risk reduction for GCAF, the collision and grounding risk models for cruise ships developed in the EMSAIII project were utilised, and the updated Attained Subdivision Index for each RCO was used to estimate the probability of ship survival and to obtain PLL.

Chapter 6

Case Study- 63,000GT Cruise ship

6 CASE STUDY

6.1 Preamble

This chapter demonstrates a case study with the application of the proposed methodology using collision accidents between 63,000 GT cruise ship and 45,000 GT RoPax vessel, explaining overall systematic procedures. Collision simulations were carried out in way of zone 15, which was identified as the highest risk zone following vulnerability assessment. The relative collision speed was obtained from pre-stage simulations, which generate B/2 penetration based on the current SOLAS assumption. Based on regulation criteria for bulkhead positions and feasibility for hull thicknesses, four variations of each RCO type were initially selected. In addition to those cases, additional RCO variations from RCO type 3 and type 5 were added for more detailed investigations. Therefore, a total of 26 RCOs were determined; Four RCOs account for single longitudinal subdivisions positioned at different positions, four RCOs consider two longitudinal subdivisions, six RCOs account for different hull thickness, four RCOs are measures of the combination of two passive measures, and other RCOs considered the combination of a crashworthy structure with foam filling in double-hull applications. Then, cost-benefit analyses were carried out to find an optimum solution.

6.2 Target Structures

A 63,000 GT cruise ship and a 45,000 GT RoPax ship as a struck ship and a striking ship, respectively, were used for crashworthiness analysis of ship-ship collisions, as shown in Figure 6.1. The main particulars of the two ships are represented in Table 6.1.

Table 6.1. Main particulars of the struck and striking ship

	Struck ship (Reference)	Striking ship
Ship type	Cruise ship	RoPax
Length of overall (m)	238.0	221.5
Length between p.p. (m)	216.8	200.0
Moulded breadth (m)	32.2	30.0
Depth (m)	16.0	15.2
Design draft (m)	7.2	6.9
Displacement (tonne)	35,367	31,250
Number of persons onboard	2,400	-

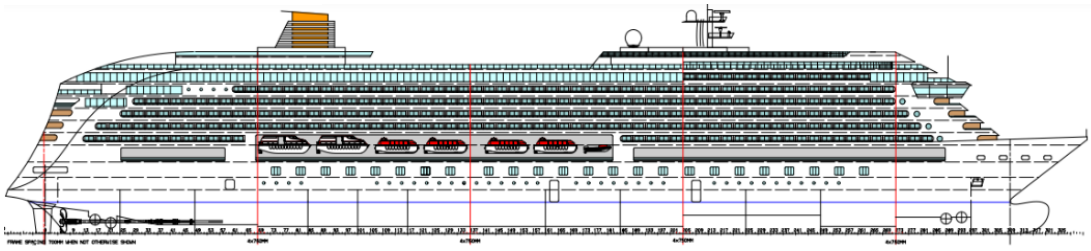

(a)

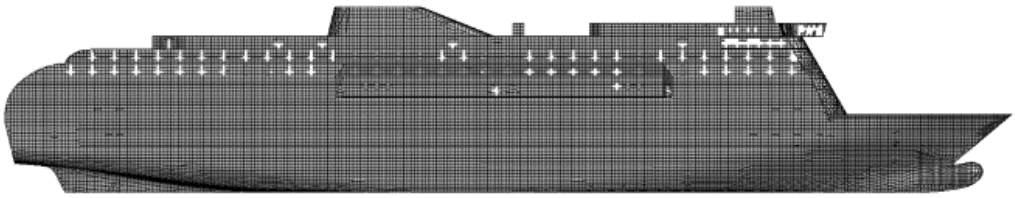

(b)

Figure 6.1 Target ships utilised in crashworthiness analysis (a) 63,000 GT cruise ship as a struck ship and (b) 45,000GT RoPax as a striking ship

6.3 STEP 1: Initial Damage Stability Assessment

As a first step, the damage stability assessment has been performed for the struck ship to identify the risk of the as-built design. Table 6.2, and Table 6.3 summarise the damage stability calculation results according to MSC.421(98) Reg.6 (SOLAS2020). The vessel achieved an Attained Subdivision Index of 0.8579, which fails to meet a Required Subdivision Index of 0.8676. This means that the current design of the struck ship cannot satisfy the SOLAS regulations and require ship survivability improvement.

Table 6.2. Calculation Results of Attained and Required Subdivision Index of the struck ship

Draught (m)		Trim (m)	GM (m)	Partial Indices		Weight coefficient	Attained Index A
Dl	6.890	0.120	2.670	Al	0.87787	0.2	0.1756
Dp	7.196	0.000	2.620	Ap	0.85723	0.4	0.3429
Ds	7.400	0.000	2.720	As	0.84853	0.4	0.3394
Attained Subdivision Index A							**0.8579**
Required Subdivision Index R							0.8676

Table 6.3 Attained Subdivision Index according to the number of damage zones

Number of Damaged zones	Calculated Attained Index
1	0.3416
2	0.3864
3	0.0879
4	0.0220
5	0.0158
6	0.0042
Attained Subdivision Index A	0.8579
Loss of Attained Subdivision Index A	**0.1348**

6.4 STEP 2: Vulnerability Analysis

Figure 6.2 illustrates the local Attained Indices of the total Attained Subdivision Index of 0.8579 compared to the maximum local Attained Index values. As shown in Figure 6.2 (c) and (d), the local attained indices for 3- and 4-zone damages were not fully achieved the maximum indices from zone 10 to zone 17, as indicated with dotted rectangles. This means that the vessel is exposed to high risks from damages associated with those zones.

As suggested in previous Section 3.4, the plurality approach for adjacent zones was used to identify the most vulnerable zone of the struck ship for the vulnerability analysis. It assumes that a zone, where the damage centre of each damage case is located, loses the total of associated local Attained losses at the damage case, and this loss affects the three adjacent zones.

Table 6.4 shows the calculation results of each local Attained Index loss depending on zones and the number of damage cases. The Index loss summation of damage cases for each zone is indicated as “Local Index Loss”, and the summation of “Local Index Loss” for adjacent zones is referred to as the “Adjacent Zones Index Loss”. For example, the “Adjacent Zones Index Loss” for Zone 15 is 0.0486 = 0.0165 at Zone 14 +0.168 at Zone 15 +0.0153 at Zone 16. As a result of “Adjacent Zones’ Index Loss”, in way of Zone 15 was identified as the most vulnerable zone.

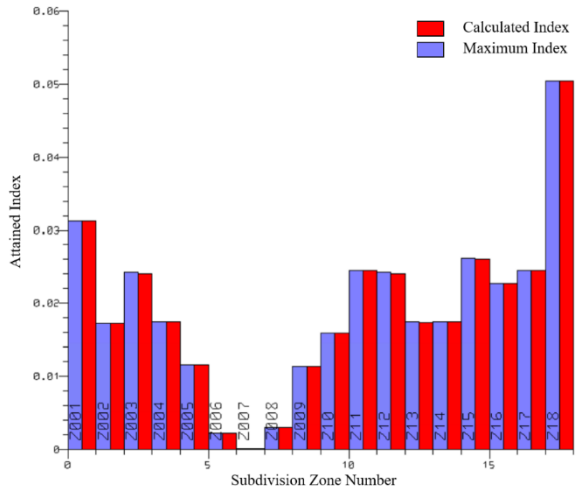

(a) 1-zone Damages

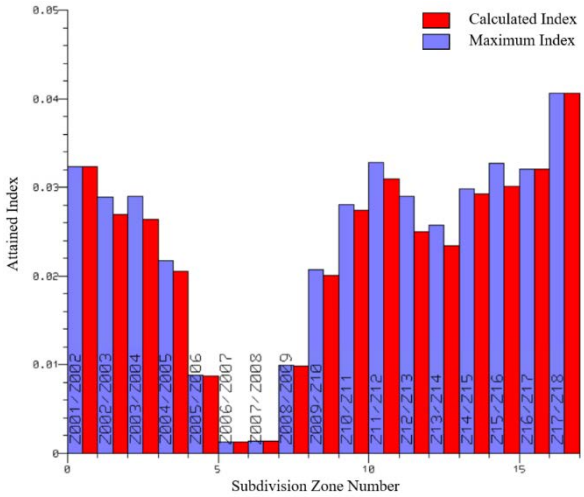

(b) 2-zone Damages

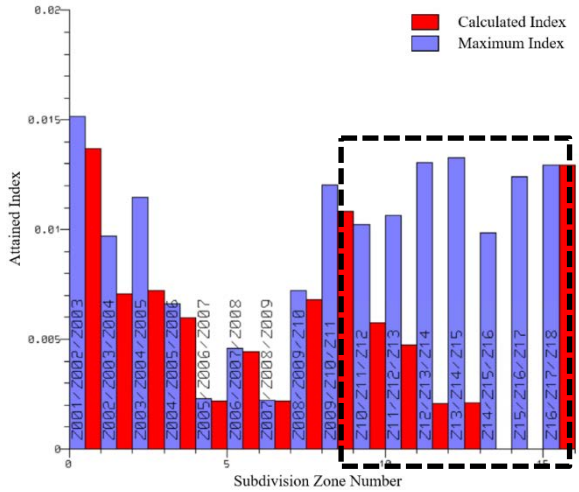

(c) 3-zone Damages

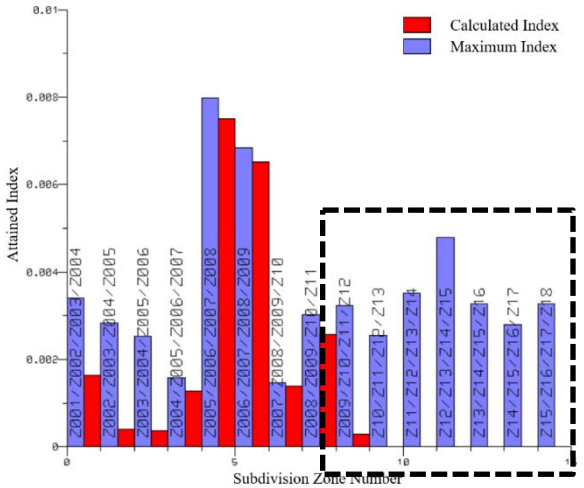

(d) 4-zone Damages

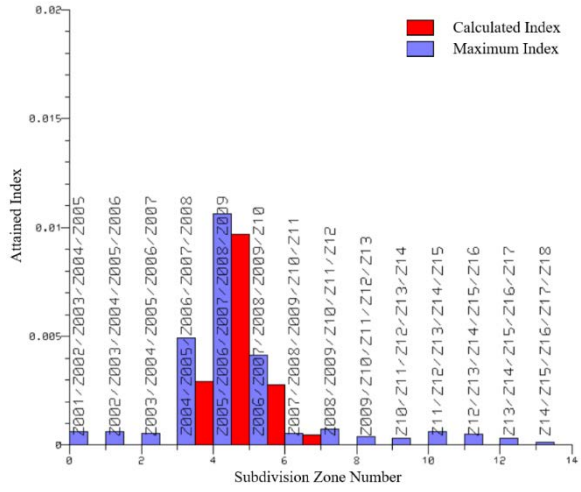

(e) 5-zone Damages

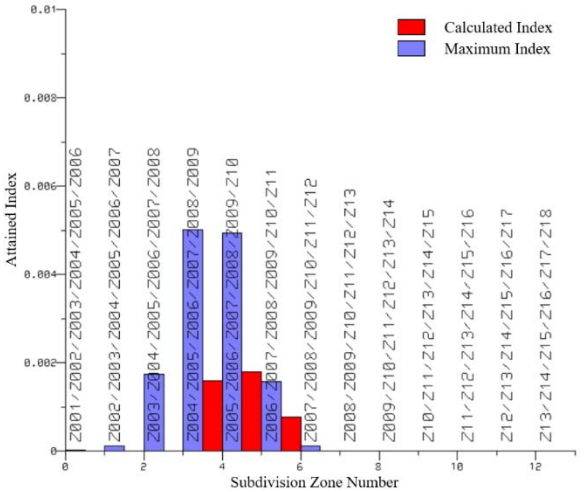

(f) 6-zone Damages

Figure 6.2 Local Attained Subdivision Index depending on the number of damage zones

Table 6.4 Results of vulnerability analysis using plurality approach for adjacent zones

	1-zone damage	2-zone damage	3-zone damage	4-zone damage	5-zone damage	6-zone damage	Local Index Loss	Adjacent Zones' Index Loss	Risk ranking
Z1	0.0000	0.0000	0.0000	0.0000	0.0000	0.0000	0.0000	0.0015	18
Z2	0.0000	0.0000	0.0015	0.0000	0.0000	0.0000	0.0015	0.0143	12
Z3	0.0003	0.0045	0.0026	0.0042	0.0012	0.0000	0.0128	0.0244	8
Z4	0.0001	0.0012	0.0042	0.0022	0.0006	0.0019	0.0101	0.0295	7
Z5	0.0000	0.0001	0.0007	0.0003	0.0020	0.0034	0.0065	0.0171	11
Z6	0.0000	0.0000	0.0000	0.0005	0.0000	0.0000	0.0005	0.0081	14
Z7	0.0000	0.0000	0.0001	0.0000	0.0009	0.0000	0.0011	0.0019	17
Z8	0.0000	0.0000	0.0000	0.0003	0.0000	0.0000	0.0003	0.0065	15
Z9	0.0000	0.0001	0.0004	0.0001	0.0014	0.0031	0.0051	0.0087	13
Z10	0.0000	0.0007	0.0012	0.0005	0.0001	0.0008	0.0032	0.0195	9
Z11	0.0000	0.0025	0.0045	0.0029	0.0011	0.0001	0.0112	0.0309	6
Z12	0.0002	0.0040	0.0059	0.0061	0.0003	0.0000	0.0166	0.0417	4
Z13	0.0001	0.0023	0.0110	0.0000	0.0006	0.0000	0.0140	0.0471	3
Z14	0.0000	0.0000	0.0112	0.0048	0.0005	0.0000	**0.0165**	0.0473	2
Z15	**0.0001**	**0.0032**	**0.0099**	**0.0033**	**0.0003**	**0.0000**	**0.0168**	**0.0486**	**1**
Z16	0.0000	0.0000	0.0124	0.0028	0.0001	0.0000	**0.0153**	0.0354	5
Z17	0.0000	0.0000	0.0000	0.0033	0.0000	0.0000	0.0033	0.0186	10
Z18	0.0000	0.0000	0.0000	0.0000	0.0000	0.0000	0.0000	0.0033	16
Total Index Loss							**0.1348**		

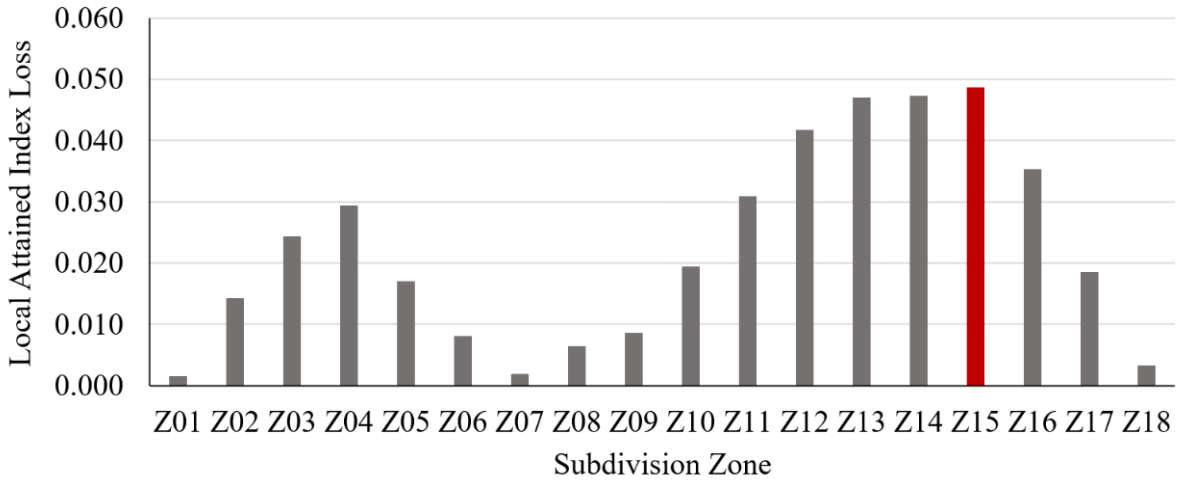

Figure 6.3 Local Attained Index Loss of adjacent zones for the struck ship

6.5 STEP 3: Risk Control Option Application

As summarised in Table 6.5, a total of 18 structural RCOs, including single and double longitudinal subdivisions, plate thickness changes, and combinations of different passive RCOs have been taken into account as structural crashworthy measures. In addition, six non-structural RCOs with a foam-filling application to those structural RCOs were investigated to find an optimum cost-effective solution. (see Section 5.2).

Table 6.5 Risk Control Options list to be applied to the case study

NO	Name	RCO Type	Description
1	RCO1	Single longitudinal subdivision	B/20 Longitudinal bulkhead (LBHD)
2	RCO2		2B/20 LBHD
3	RCO3		3B/20 LBHD
4	RCO4		4B/20 LBHD
5	RCO5	Double longitudinal subdivision	B/20 LBHD+ Another LBHD (10T) at 13.1m (*)
6	RCO6		2B/20 LBHD+ Another LBHD (10T) at 13.1m (*)
7	RCO7		3B/20 LBHD+ Another LBHD (10T) at 13.1m (*)
8	RCO8		4B/20 LBHD+ Another LBHD (10T) at 13.1m (*)
9	RCO9	Hull thickness change	50% Hull thickness increase
10	RCO10		100% Hull thickness increase
11	RCO11		20T Hull thickness
12	RCO12		30T Hull thickness
13	RCO13		40T Hull thickness
14	RCO14		50T Hull thickness
15	RCO15	Combination of single subdivision and hull thickness change	B/20_100% plate thickness increased
16	RCO16		2B/20_100% plate thickness increased
17	RCO17		20T hull + Single LBHD (10T) at 10.6m (*)
18	RCO18		30T hull + Single LBHD (10T) at 6.6m (*)
19	RCO1-F	Structural Crashworthiness RCOs + Foam RCO (Permanent Foam Filling)	RCO1 + Foam Filling of wing compartments
20	RCO2-F		RCO2 + Foam Filling of wing compartments
21	RCO3-F		RCO3 + Foam Filling of wing compartments
22	RCO4-F		RCO4 + Foam Filling of wing compartments
23	RCO6-F		RCO6 + Foam Filling of wing compartments
24	RCO8-F		RCO8 + Foam Filling of wing compartments
25	RCO17-F		RCO17 + Foam Filling of wing compartments
26	RCO18-F		RCO18 + Foam Filling of wing compartments

(*) The distance from the outer shell of the hull

6.6 STEP 4: Collision Scenario Definition

As described in Section 3.6.2, pre-collision simulations at various speeds have been carried out to find the speed resulting in B/2 penetration. This is the maximum transverse penetration for damage stability calculation defined in SOLAS2020 (IMO, 2017b) and causes the most significant heeling moment due to unsymmetric flooding from damages.

Figure 6.4 shows the penetration results at different speed collisions on a time base. The simulation with 10.14 knots collision speed generated 16.15 m penetration, almost the same as B/2 (16.1m), and it was selected as the relative collision speed in this case study. The selected speed also seems reasonable since 96% of collision accidents happen in limited waters and near terminals. (IMO, 2012) Furthermore, it is relatively high compared to the collision speeds of 5 ~10 knots employed in the benchmark study of the FLARE project (see Section 4.4) and the speeds of 1.6 ~ 6.0 knots in selected scenarios from a sampling method based on the actual accident database from 1991 to 2012 by Paik et al. (2017).

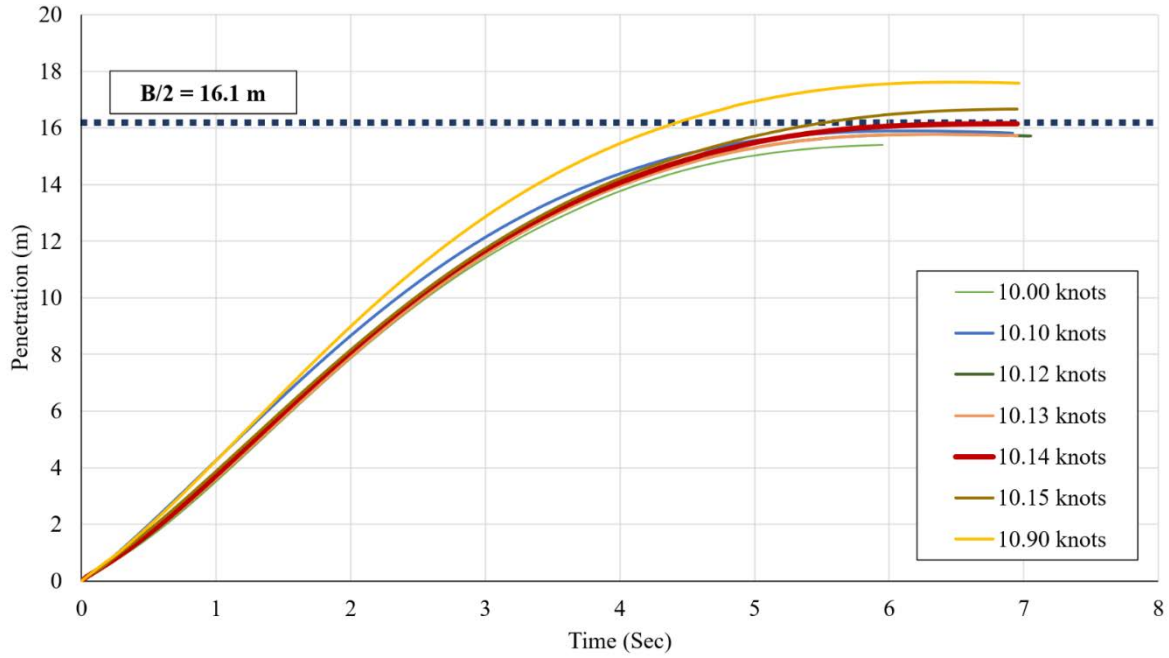

Figure 6.4 Penetration results depending on various speeds for relative collision speed finding

For a collision location, Zone 15 was identified as the most vulnerable zone in the previous Section 6.4. Simulations assumed that the longitudinal centre of Zone 15 collided with the striking ship. A perpendicular collision (i.e., 90 degrees) was taken into account to achieve the worst damage condition, as described in Section 3.6.4. Design draught and even trim conditions for both a struck and striking ship were assumed for the collision simulation. The collision scenario is summarised in Table 6.6.

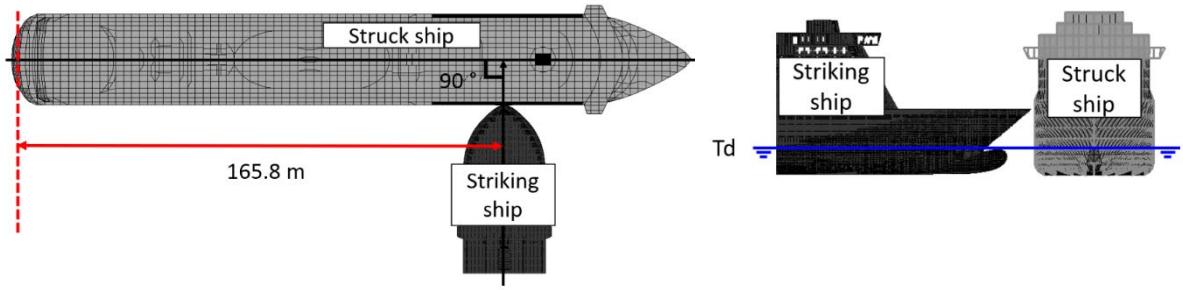

(a) (b)

Figure 6.5 Collision angle and draught for collision scenarios: (a) 90-degree collision and (b) design draught

Table 6.6 Summary of the collision scenario in the case study

Ships	speed (knots)	angle (˚)	From A.P. (m)	Draft (m)	Trim (m)
Struck ship	0	0	0	7.2	0
Striking ship	10.14	90	165.8(*)	6.9	0

(*) Longitudinal centre of Zone 15

6.7 STEP 5: Structural Crashworthiness Analysis

6.7.1 Geometric Modelling

The HYPER MESH software (Hyperworks, 2018) was used for finite mesh controls, and ANSYS/LS-DYNA NLFEM tool (LSTC, 2019) with MCOL solver(Ferry et al., 2002) has been employed for collision simulation analysis. The inputs of ship motions for MCOL were obtained from ANSYS-AQWA(ANSYS, 2019).

As shown in Figure 6.6(a), the entire ship geometry was modelled from zone1 to zone18. Fine meshes were used for the contact area for three watertight zones, and the target Zone 15 is located in the middle of those zones. The outside region of the fine mesh area was expected to be less impacted by collisions and therefore was modelled by coarser elements and a rigid body. For the struck ship, an approximate 30m forepart of the ship was utilised, including a bulwark on the weather deck. The first fore part of 27.6m was defined as a deformable part with fine mesh, while the aft part of 2.4 m was set to rigid. For more details for both struck and striking ship geometric modelling, see Section 4.2.

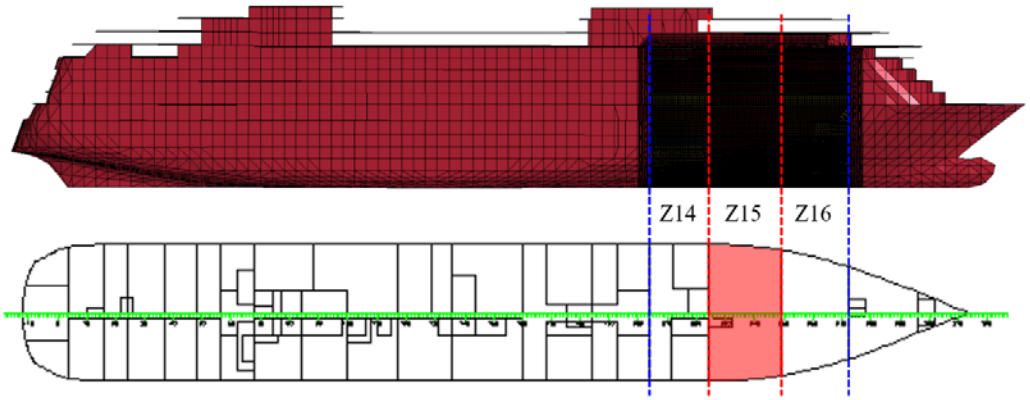

(a)

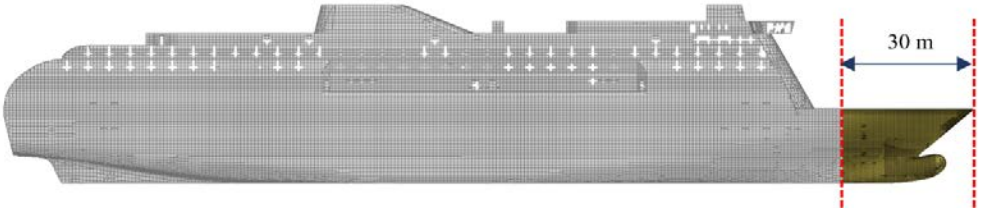

(b)

Figure 6.6 (a) Full geometric model for the struck ship and (b) partial geometric model for the striking ship

Regarding the element size, 200mm and 175mm of element sizes for both striking and struck ships, respectively, were determined for fine mesh area, which is a quarter of the frame spacing of each ship (e.g., 800mm for the striking ship and 700mm for the struck ship) and may reasonably capture the structural damage of the ship. All elements for plates and stiffeners within deformable parts for both ships were made by Belytschko-Tsay shell elements (LSTC, 2019), as shown in Figure 6.7, with a 5/6 shear factor and five through shell thickness integration points.

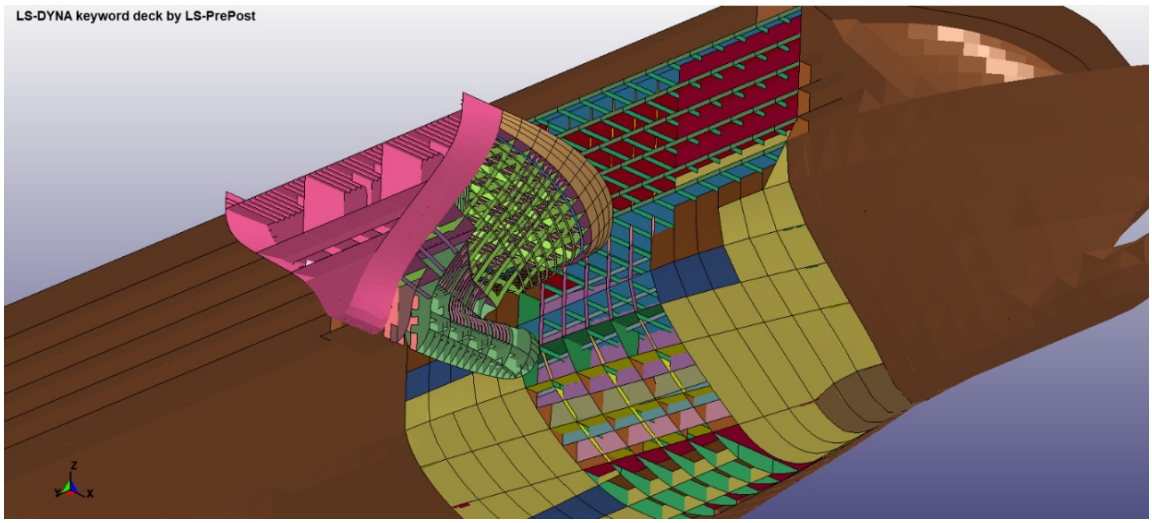

Figure 6.7 2D shell elements applied to all plates and beams for both ships

6.7.2 Material Properties

A material model of Piecewise Linear Isotropic Plasticity (Hodge et al., 1956, LSTC, 2019) was employed on the contact regions for both ships to capture the elastoplastic deformations during the collision. Notably, the modified true stress-true strain curve for the mild steel in Figure 4.5 in Section 4.2.3 was applied in these simulations. This allowed for the actual mild steel behaviour, including the strain-hardening effect. This modified material curve was reformed from the actual true stress-true strain curve introduced (Paik, 2018) based on the material properties given in Table 4.1 of Section 4.2.3.

6.7.3 Dynamic Effects and Fracture Strain

As described in detail in Section 4.2, the Cowper-Symonds model (Cowper and Symonds, 1957) was adopted for the dynamic yield strength. The *GL criterion* (i.e., the through-thickness strain criterion) proposed by Vredeveldt (2001) and Scharrer et al. (2002b) was used for fracture strain definition. The fracture strain values used in this case study were 0.0671 ~ 0.1004 for the stuck ship and 0.0723 ~ 0.1169 for the striking ship, depending on the various thickness of plates and different mesh sizes for both ships involved in the collision (see Table 6.7).

Table 6.7 Fracture strains depending on steel plate thickness for the struck and striking ships

Struck ship		Striking ship	
thickness (mm)	Fracture strain	thickness (mm)	Fracture strain
5	0.0671	8	0.0723
6	0.0693	10	0.0763
7	0.0715	11.5	0.0794
8	0.0737	12	0.0804
10	0.0782	13.5	0.0834
12	0.0826	15	0.0865
13	0.0848	19.5	0.0956
14	0.0871	20	0.0966
15	0.0893	25	0.1068
20	0.1004	30	0.1169

6.7.4 Contact and Friction Effects

Two types of contacts, namely general- and self-contact, were used to idealise contact and friction effects. General contact implies wall contact among different structural components. Self-contact occurs within the structural components themselves. In order to include both contacts, the "*Automatic Single Surface*" option in LS-DYNA for contact was considered for

the analyses since it covers both general contact and self-contact. During ship collisions, friction between two colliding bodies occurs, which can absorb the kinetic energy due to collision impact. In this study, a friction coefficient of 0.3 was adopted, as discussed in Section 4.2.5.

6.7.5 Hydrodynamic Boundary Conditions

The hydrodynamic boundary conditions around ships may significantly contribute to the ship motions during the collision. Based on the computational model developed by Ferry et al. (2002), the MCOL solver in LS-DYNA provides the effects of the surrounding water of both ships, such as hydrodynamic restoring forces, water added mass and buoyancy. The input parameters for the solver were obtained from ANSYS AQWA (ANSYS, 2019) using the ship characteristics displayed in Table 6.8.

Table 6.8. Ship Characteristics for ANSYS AQWA calculation

Parameters		Struck ship	Striking ship
Draft (m)		7.2	6.9
Displacement (tonne)		35,367	31,250
LCG (m)		99.29	85
KG (m)		15	14
Gyration radius (m)	x-direction (Surge)	10.95	11
	y-direction (Sway)	54.20	55
	z-direction (Heave)	56.37	55

6.8 Crashworthiness Analysis Result

6.8.1 General- Orignal layout vs RCO11 example

A series of structural crashworthiness analyses were carried out for ship collisions at Zone 15 with 24 RCOs based on the pre-defined scenario in Section 6.6. Among them, the simulation results of RCO11 are presented in this Section as an example case, and they are compared with the simulation results before RCO application (hereafter, the initial layout with no RCO is termed the original layout.). Figure 6.8 illustrates the effective plastic strain status of the original layout computed by LS-DYNA when the B/2 penetration occurred. While the striking geometry from the stem of the ship to the weather deck was somewhat damaged with squashed and torn bulwarks, the bulbous bow was less damaged, keeping the overall shape due to robust inner structures. On the other hand, large damages on the struck ship were observed by the striking ship with deeper penetration to the ship centre.

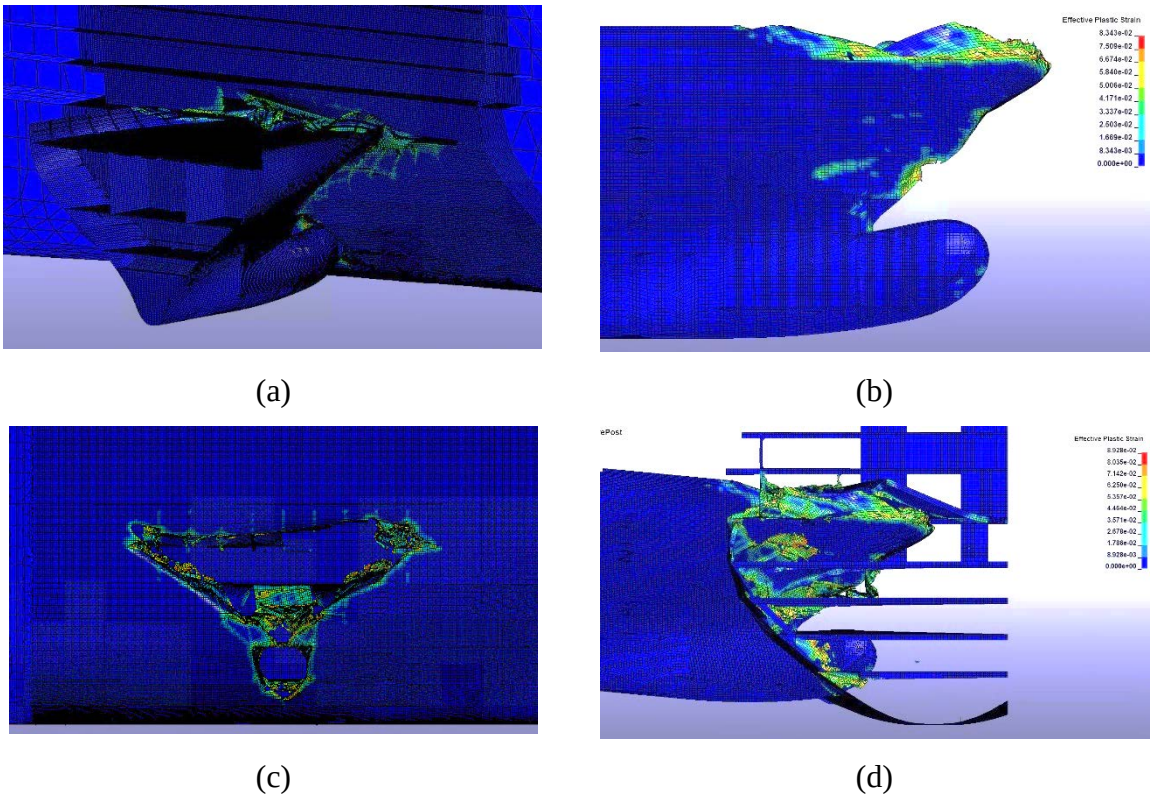

Figure 6.8 FE simulation results of original layout resulting in B/2 penetration: (a) ISO view, (b) Damaged striking ship, (c) Damaged struck ship and (d) Section view

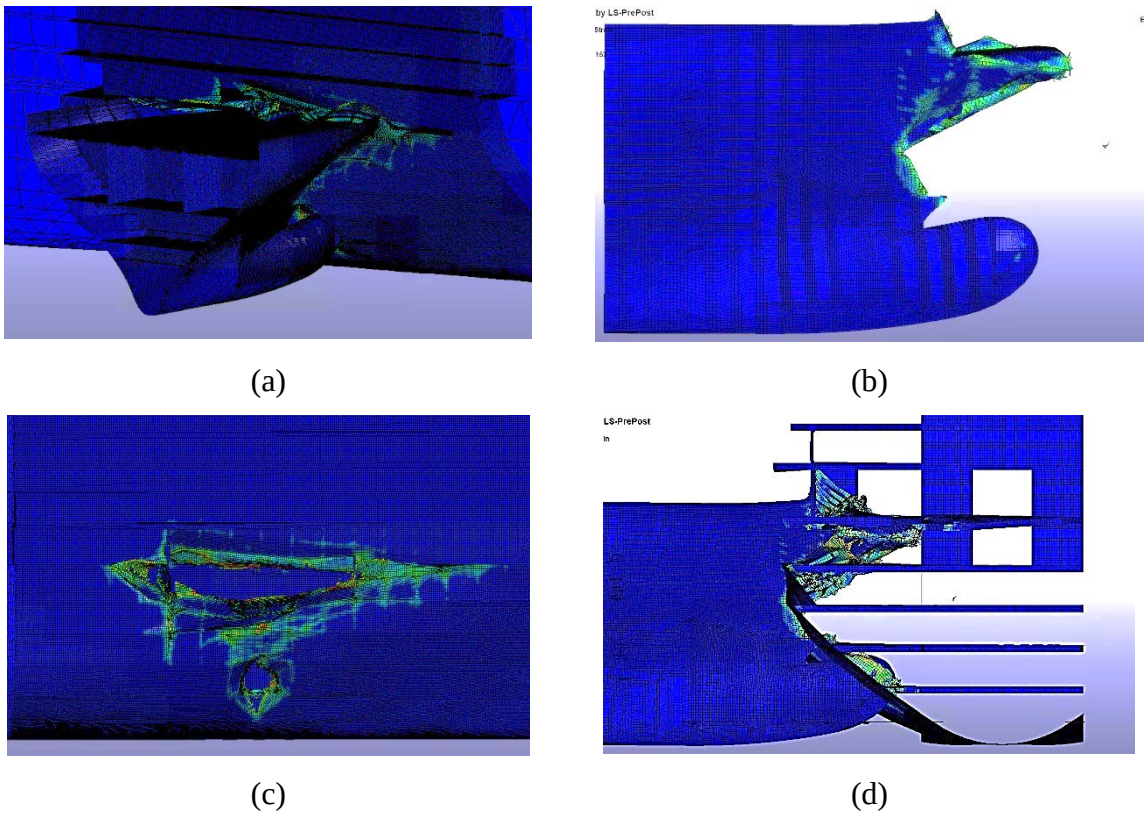

Figure 6.9 FE simulation results of RCO 11 (20T hull thickness): (a) ISO view, (b) Damaged striking ship, (c) Damaged struck ship and (d) Section view

Figure 6.9 shows the simulation results of RCO11. The overall outer shell was thickened to 20 T. Due to increased resistance by the thick hull of the struck ship, more damage occurred on the stem part of the striking ship, and less penetration was observed.

As shown in Figure 6.10 (a) and (b), the maximum dissipated energy, including internal energy and sliding energy, between the original layout and RCO11 showed similar results as the initial energy of two collision cases are the same due to the same collision speed. In particular, the emphasis of this simulation analysis is on maximum penetration. The collision simulation with the RCO11 (i.e., 20T thickness hull) showed a maximum transversal penetration of 10.46m, which was reduced by 5.69m compared to the simulation with the original layout (i.e., 16.15m of penetration), as indicated in Figure 6.10 (c) and Figure 6.11. This proves that the contributions of crashworthy structures can be quantified.

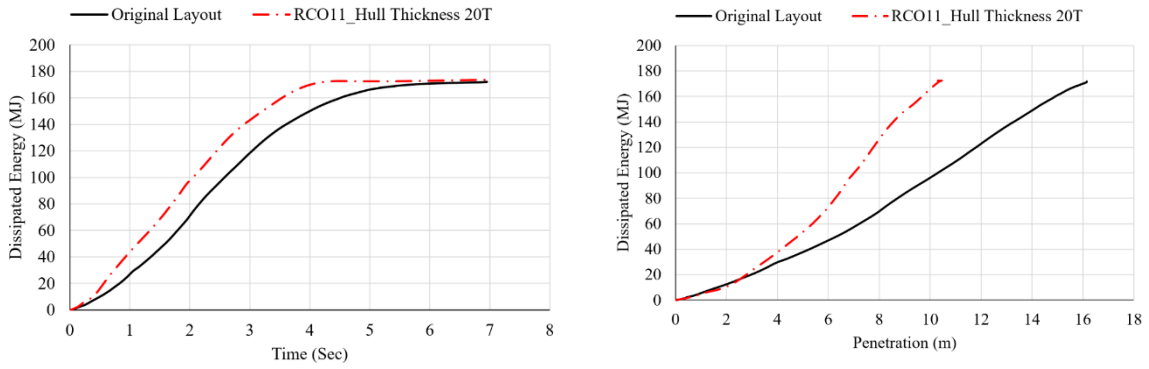

(a)

(b)

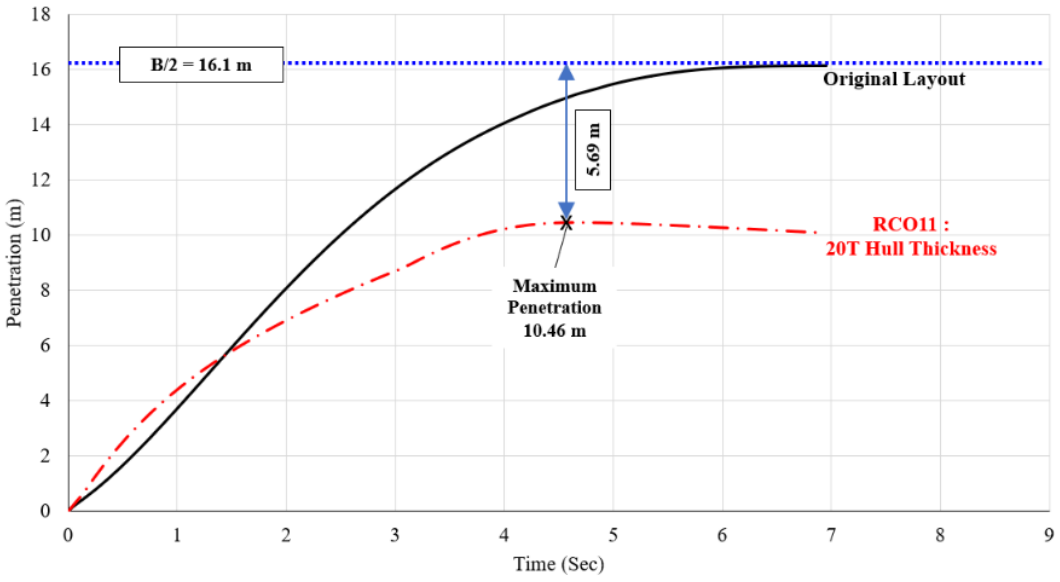

(c)

Figure 6.10 Comparison graphs between original layout and RCO11 for (a) internal energy changes over time, (b) internal energy over penetration and (c) penetration over time

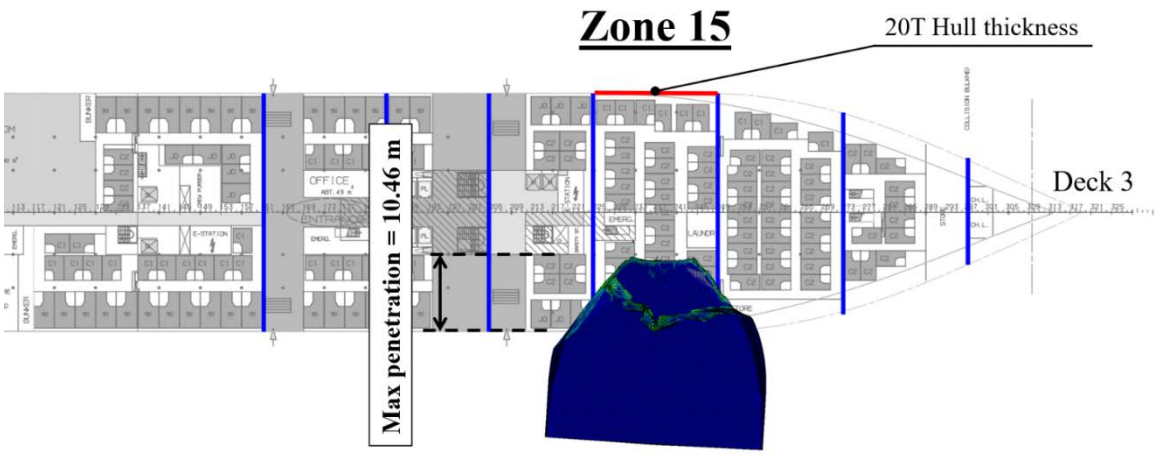

Figure 6.11. Striking ship position at the maximum penetration for RCO11

More detailed damage processes can be identified from the resultant force graph over penetration (see Figure 6.12). Overall, the resultant forces of RCO11 are higher than that from the original layout due to the increased resistance from the thickened hull.

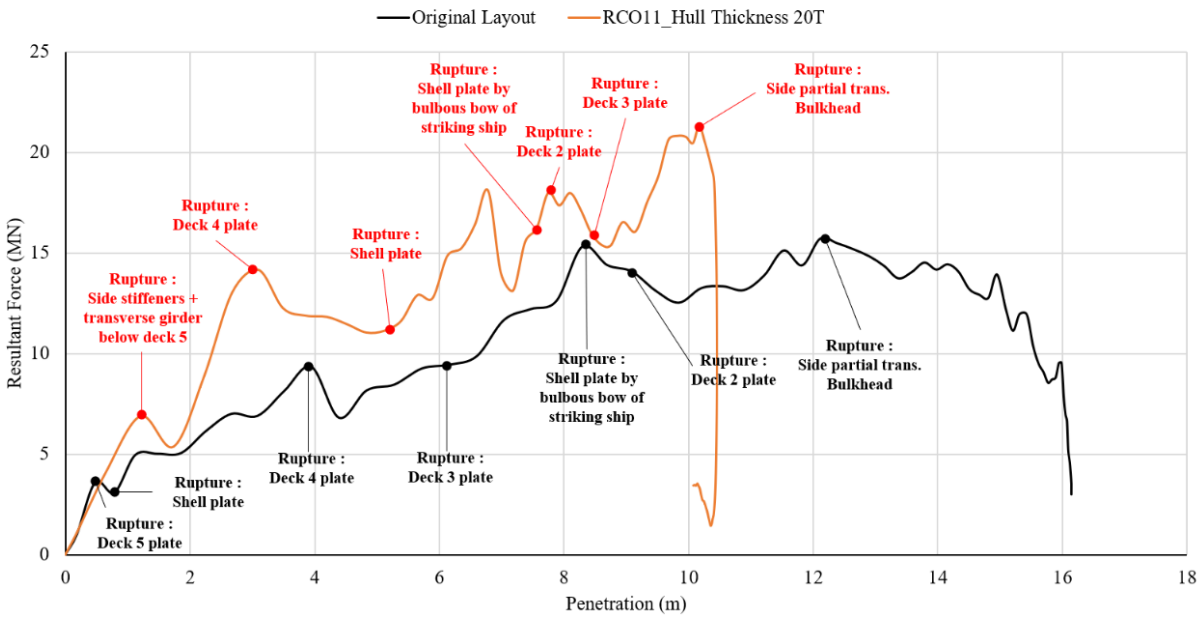

Figure 6.12 Resultant Force changes for original layout and RCO11 with specific rupture points

6.8.2 Penetration Results of all RCOs

Table 6.9 and Figure 6.13 summarise the penetration results of each RCO following crashworthiness analysis. Interestingly, there is no penetration observed for RCO14 which has a 50T hull thickness.

Table 6.9 Crashworthiness Analysis results of all RCOs

NO	Name	Description	Max Penetration (m)	Penetration Decrease (m)
		Original Layout	16.15	0
1	RCO1	Single LBHD at B/20	13.13	3.02
2	RCO2	Single LBHD at 2B/20	13.03	3.12
3	RCO3	Single LBHD at 3B/20	11.82	4.33
4	RCO4	Single LBHD at 4B/20	12.51	3.64
5	RCO5	1st LBHD at B/20 + 2nd LBHD (10T) at 13.1m (*)	13.13	3.02
6	RCO6	1st LBHD at 2B/20 + 2nd LBHD (10T) at 13.1m (*)	13.03	3.12
7	RCO7	1st LBHD at3 B/20 + 2nd LBHD (10T) at 13.1m (*)	11.82	4.33
8	RCO8	1st LBHD at 4B/20 + 2nd LBHD (10T) at 13.1m (*)	12.51	3.64
9	RCO9	50% Hull thickness increase	11.72	4.43
10	RCO10	100% Hull thickness increase	8.22	7.93
11	RCO11	20T Hull thickness	10.46	5.69
12	RCO12	30T Hull thickness	6.58	9.57
13	RCO13	40T Hull thickness	6.64	9.51
14	RCO14	50T Hull thickness	0.00	16.15
15	RCO15	B/20_100% plate thickness increased	10.14	6.01
16	RCO16	2B/20_100% plate thickness increased	10.31	5.84
17	RCO17	20T hull + Single LBHD (10T) at 10.6m (*)	10.46	5.69
18	RCO18	30T hull + Single LBHD (10T) at 6.6m (*)	6.58	9.57
19	RCO1-F	RCO1 + Foam Filling of wing compartments	13.13	3.02
20	RCO2-F	RCO2 + Foam Filling of wing compartments	13.03	3.12
21	RCO3-F	RCO3 + Foam Filling of wing compartments	11.82	4.33
22	RCO4-F	RCO4 + Foam Filling of wing compartments	12.51	3.64
23	RCO6-F	RCO6 + Foam Filling of wing compartments	13.03	3.12
24	RCO8-F	RCO8 + Foam Filling of wing compartments	12.51	3.64
25	RCO17-F	RCO17 + Foam Filling of wing compartments	10.46	5.69
26	RCO18-F	RCO18 + Foam Filling of wing compartments	6.58	9.57

(*) The distance from the outer shell of the hull

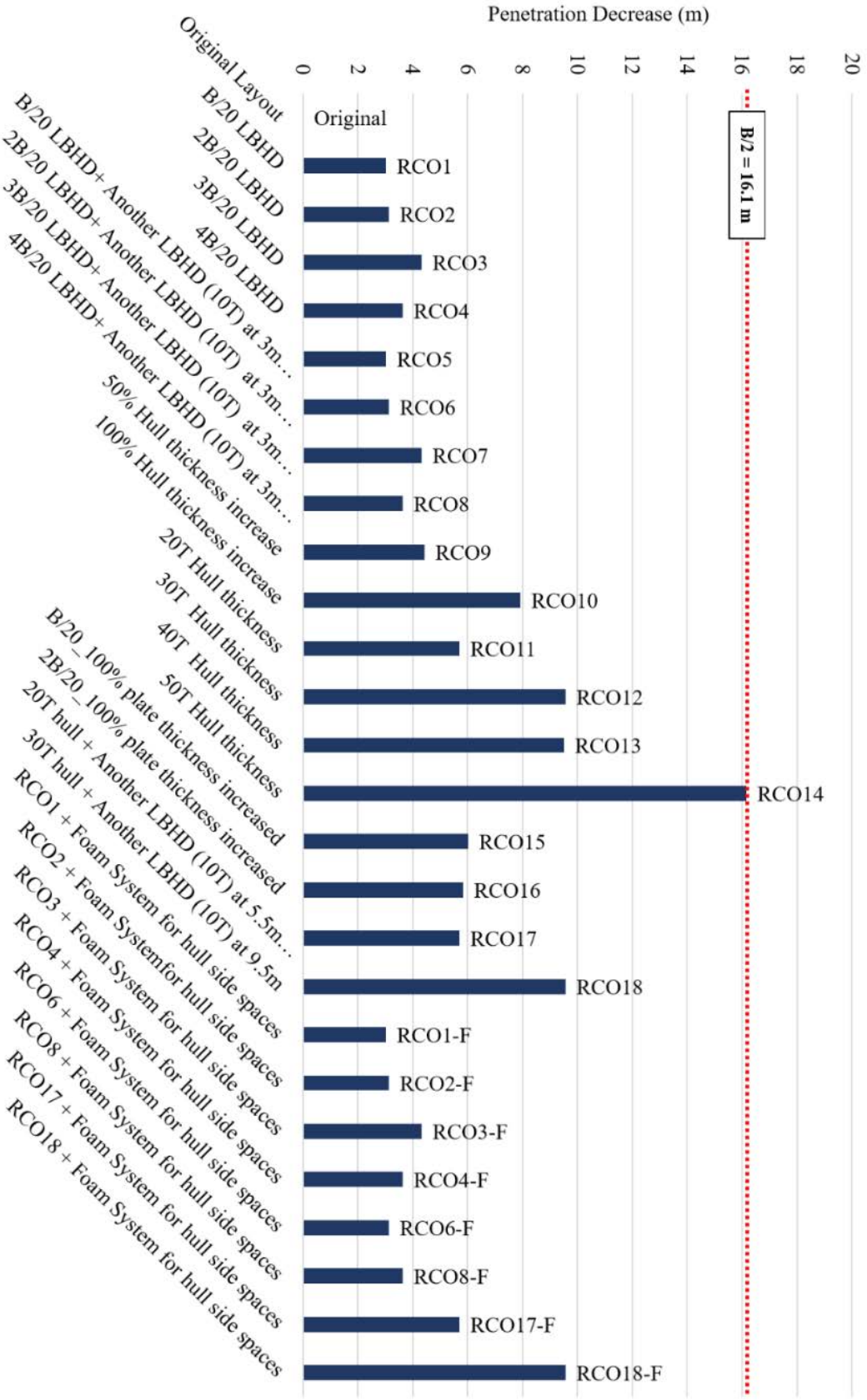

Figure 6.13 Penetration Decrease of each RCO based on the crashworthiness analyses

6.9 STEP 6: Transverse Damage Distribution update

Figure 6.14 indicates the current SOLAS and the updated cumulative density function (CDF) and probability density function (PDF) for RCO18-F. The updated CDF was obtained with proportional adjustment of SOLAS CDF by shifting the maximum penetration point from 16.1m (i.e., B/2) to 6.58m measured from the outer shell of the stuck ship hull. The PDF was derived from the difference between two points of the modified CDF. Consequently, the p-factors of damage cases associated with Zone 15 have been modified. As a result, the damage case located within 0~6.58m penetration displayed higher p-factors than that defined in SOLAS, while those located between 6.58m and ship centre of 16.1m were disregarded since no damage occurred in this area.

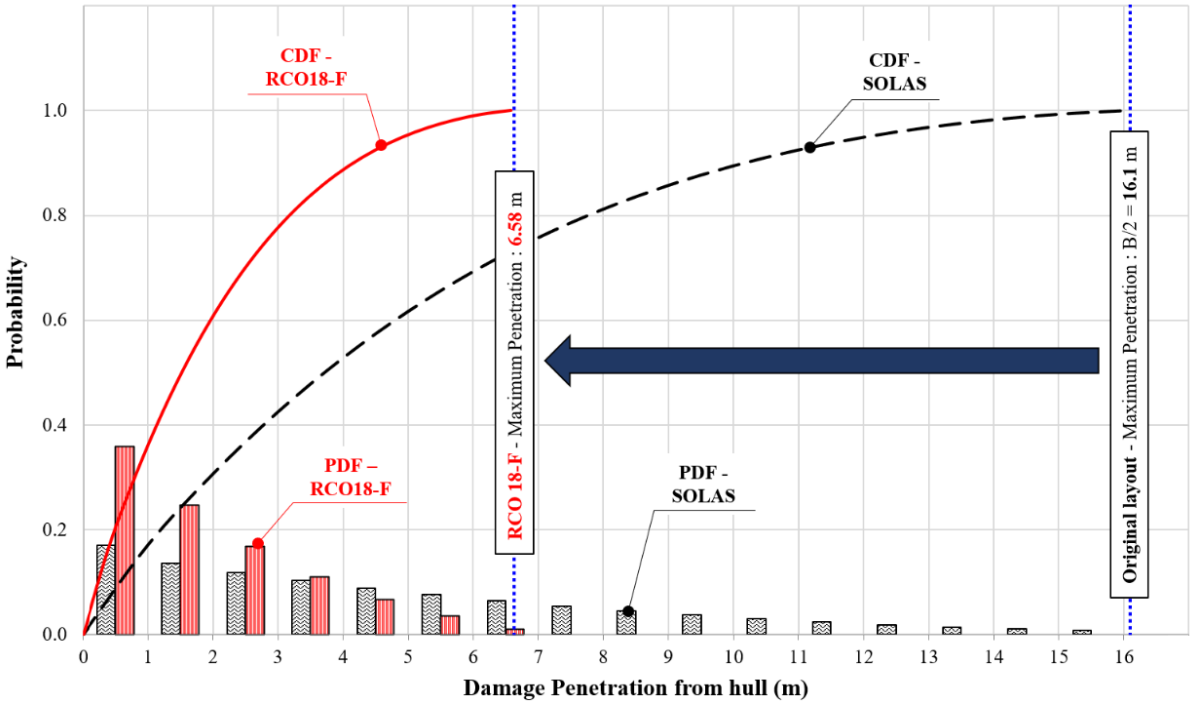

Figure 6.14 Updated transverse damage distribution for RCO18-F

After re-calculating damage stability with each RCO, the revised transverse damage distributions have been applied manually to Zone 15 as the current NAPA software does not provide a function of local distribution changes.

6.10 STEP 7: Damage Stability Re-assessments

6.10.1 Damage Stability Re-evaluation

Based on the previous updates by RCOs, the damage stability was re-evaluated for each RCO with modified layouts. Figure 6.15 illustrates a new layout of RCO18-F in which additional longitudinal bulkheads at 9.6m from the ship centre on both ship sides were installed to the original layout. Since the maximum penetration of RCO18-F from collision simulation was 6.58m from the outer shell (i.e., 9.57m from the ship centre), the longitudinal bulkheads at 9.5m can protect the inner spaces as safe internal areas. Therefore, the permeability value of these inner areas was defined as zero for the calculation. Additionally, two wing compartments between the outer shell and the longitudinal bulkhead at 9.5m would be protected from foam filling. The permeability of these spaces was set to 0.05, as shown in Table 6.10.

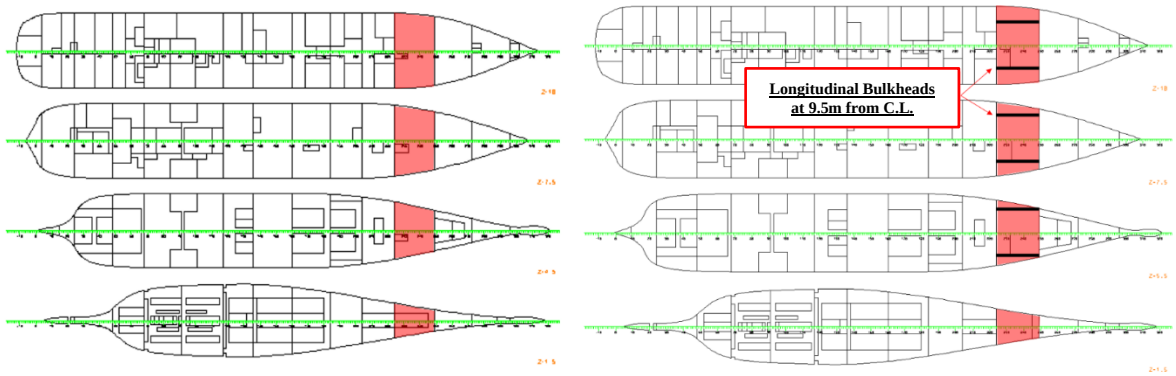

(a) (b)

Figure 6.15 Layout update of RCO18-F for re-assessment of damage stability (a) original layout and (b) RCO18-F layout

Table 6.10 Permeability applied to RCO18-F

Spaces	Permeability
Appropriated to stores	0.60
Occupied by accommodation	0.95
Occupied by machinery	0.85
Void Spaces	0.95
Intended for liquids	0 or 0.95
Safe inner Area	**0.00**
Spaces protected from foam filling	**0.05**

6.10.2 Results

Table 6.11 summarises re-calculated local Subdivision Attained Indices for five different RCOs, and the results of the other RCOs are indicated in Appendix C and D. Compared to the original layout, the total Attained Index increased from 0.1 % to 5.0%. Notably, even though such RCOs were applied to only a single zone, namely Zone 15, they influenced other adjacent zones from zone 14 to zone 17 (see Figure 6.16). This means that the new arrangement from RCOs, such as additional buoyancy side spaces or permeability change of spaces in Zone 15, also affected not only the zone applied but also the adjacent zones.

Table 6.11. Results of the Subdivision Attained and improvement comparison for selected RCOs

Subdivision Zones	Original Layout	RCO4	RCO11	RCO14	RCO17-F	RCO18-F
		4B/20 LBHD	20T Hull thickness	50T Hull thickness	20T Hull + LBHD+Foam	30T Hull + LBHD+Foam
Z01	0.0312	0.0312	0.0312	0.0312	0.0312	0.0312
Z02	0.0633	0.0633	0.0633	0.0633	0.0633	0.0633
Z03	0.0865	0.0865	0.0865	0.0865	0.0865	0.0865
Z04	0.0456	0.0456	0.0456	0.0456	0.0456	0.0456
Z05	0.0343	0.0343	0.0343	0.0343	0.0343	0.0343
Z06	0.0111	0.0111	0.0111	0.0111	0.0111	0.0111
Z07	0.0143	0.0143	0.0143	0.0143	0.0143	0.0143
Z08	0.0109	0.0109	0.0109	0.0109	0.0109	0.0109
Z09	0.0361	0.0361	0.0361	0.0361	0.0361	0.0361
Z10	0.0507	0.0507	0.0507	0.0507	0.0507	0.0507
Z11	0.0890	0.0890	0.0890	0.0890	0.0890	0.0890
Z12	0.0538	0.0538	0.0538	0.0538	0.0538	0.0538
Z13	0.0429	0.0429	0.0429	0.0429	0.0429	0.0429
Z14	0.0196	0.0206	0.0196	0.0312	0.0300	0.0301
Z15	0.0854	0.0922	0.0862	0.1000	0.1003	0.1006
Z16	0.0227	0.0285	0.0227	0.0362	0.0356	0.0364
Z17	0.0695	0.0707	0.0695	0.0727	0.0728	0.0728
Z18	0.0910	0.0910	0.0910	0.0910	0.0910	0.0910
Attained Index A	**0.8579**	**0.8727**	**0.8587**	**0.9008**	**0.8993**	**0.9005**
Improvement		*1.72%*	*0.10%*	*5.00%*	*4.82%*	*4.97%*
Loss of Index A	**0.1348**	**0.1200**	**0.1340**	**0.0919**	**0.0934**	**0.0922**
Improvement		*10.96%*	*0.60%*	*31.82%*	*30.70%*	*31.61%*

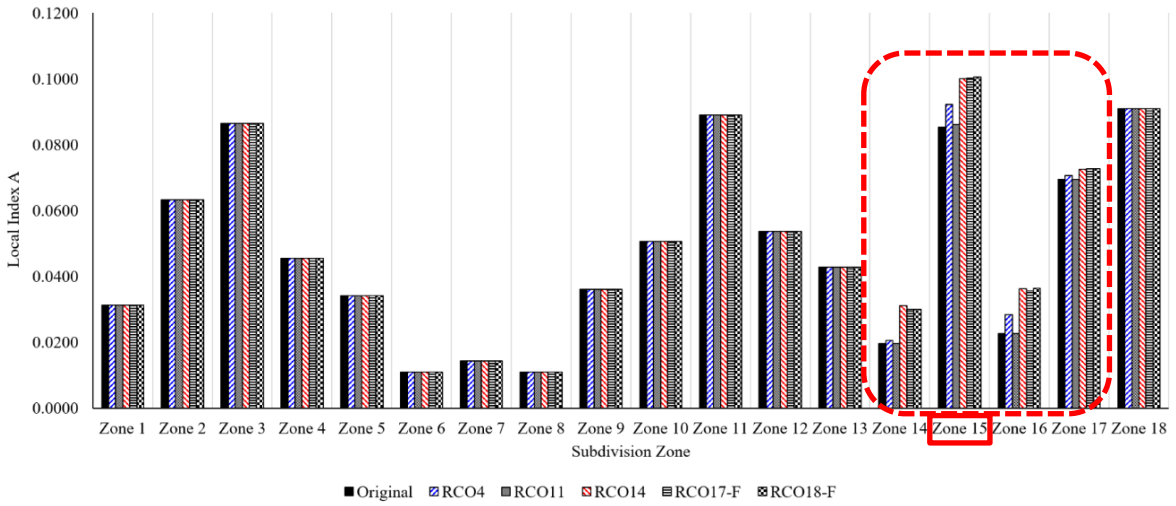

Figure 6.16 Local Attained Index improvement by zones for selected RCOs

In particular, the overall improvement attributed to each RCO can be separated into each individual measure's contribution. Table 6.12 ~ Table 6.16 show the individual contribution of each measure for RCO18-F, RCO17-F, RCO 14, RCO 11 and RCO 4. For example, in the case of RCO18-F in Table 6.12, the first measure with hull thickness increases of 30T shows no improvement for Attained Index A. This proves the crashworthy structure cannot be evaluated from current damage stability regulation. However, when the additional longitudinal bulkheads, as the second measure, were installed at the position of 9.5m from the ship centre, the Attained Subdivision Index A significantly increased by 0.0344. This is because the inner spaces between the additional longitudinal bulkheads were considered as "Safe internal spaces" and the permeability of 0 was applied. These spaces decreased huge amounts of floodwater, increasing s-factors of the damage cases associated with Zone 15. The 3rd measure, foam filling applied to side spaces, also contributed to Index A improvement by 0.007. Finally, the updated transverse distribution, the 4th measure, enhanced Index A by 0.0011 (see Table 6.12).

Table 6.12. Individual contribution of each measure for RCO18-F

Measure	Effects of Measures	Index A	Improvement	Contributions
0	**Original Layout**	**0.8579**	-	-
1st	+ Hull thickness increase to 30T	0.8579	0.0000$^{(*)}$	0.00 %
2nd	+ Additional longitudinal bulkheads	0.8923	0.0344	4.01 %
3rd	+ Foam Filling application to side spaces	0.8993	0.0070	0.82 %
4th	+ Revised transverse distribution application	0.9005	0.0011	0.13 %
	Total	**0.9005**	**0.0426**	**4.97 %**

(*) A penetration occurred during the simulation, so the current SOLAS was applied, which assumes that flooding takes place regardless of structural crashworthiness.

Table 6.13. Individual contribution of each measure for RCO17-F

Measure	Effects of Measures	Index A	Improvement	Contributions
0	**Original Layout**	0.8579		
1st	+ Hull thickness increase to 20T	0.8579	0.0000(*)	
2nd	+ Additional longitudinal bulkheads	0.8808	0.0229	2.67%
3rd	+ Foam Filling application to side spaces	0.8984	0.0176	2.06%
4th	+ Revised transverse distribution application	0.8993	0.0008	0.10%
	Total	**0.8993**	**0.0414**	**4.82%**

(*) A penetration occurred during the simulation, so the current SOLAS was applied, which assumes that flooding takes place regardless of structural crashworthiness.

Table 6.14. Individual contributions of each measure for RCO14

Measure	Effects of Measures	Index A	Improvement	Contributions
0	**Original Layout**	0.8579	-	-
1st	+ Hull thickness increase to 50T	0.9008	0.0429(*)	5.00%
	Total	**0.9008**	**0.0429**	**5.00%**

(*) No opening was observed on the hull. Therefore, zero permeability was applied to the target zone.

Table 6.15. Individual contribution of each measure for RCO11

Measure	Effects of Measures	Index A	Improvement	Contributions
0	**Original Layout**	0.8579	-	-
1st	+ Hull thickness increase to 20T	0.8579	0.0000(*)	0.00%
2nd	+ Revised transverse distribution application	0.8587	0.0008	0.09%
	Total	**0.8587**	**0.0008**	**0.09%**

(*) A penetration occurred during the simulation, so the current SOLAS was applied, which assumes that flooding takes place regardless of structural crashworthiness.

Table 6.16. Individual contribution of each measure for RCO4

Measure	Effects of Measures	Index A	Improvement	Contributions
0	**Original Layout**	**0.8579**	-	**-**
1st	+ Additional longitudinal bulkheads	0.8693	0.0114	1.33 %
2nd	+ Revised transverse distribution application	0.8727	0.0034	0.39 %
	Total	**0.8727**	**0.0148**	**1.72 %**

6.11 STEP 8: Cost-Benefit Analysis

The cost-benefit analysis has been performed for all 26 RCOs. Table 6.17 and Table 6.18 show the Gross Cost of Averting a Fatality (GCAF) of each RCO with the maximum penetrations, weight increase, cost, and final Subdivision Attained Index. The GCAF of each RCO was calculated based on risk reduction in terms of change in the Attained Index instead of potential loss of life (PLL). The results vary from 0.86 millionUSD/PPL for RCO4 to 51.47 millionUSD/PPL for RCO13. In particular, the RCOs related to a hull thickness change, from RCO9 to RCO13, show high GCAF values due to the low Attained Index improvement by the insufficient current rules and regulations for crashworthy structures. However, when it was combined with other measures, such as an additional single longitudinal subdivision and foam filling system, the outcomes were maximised.

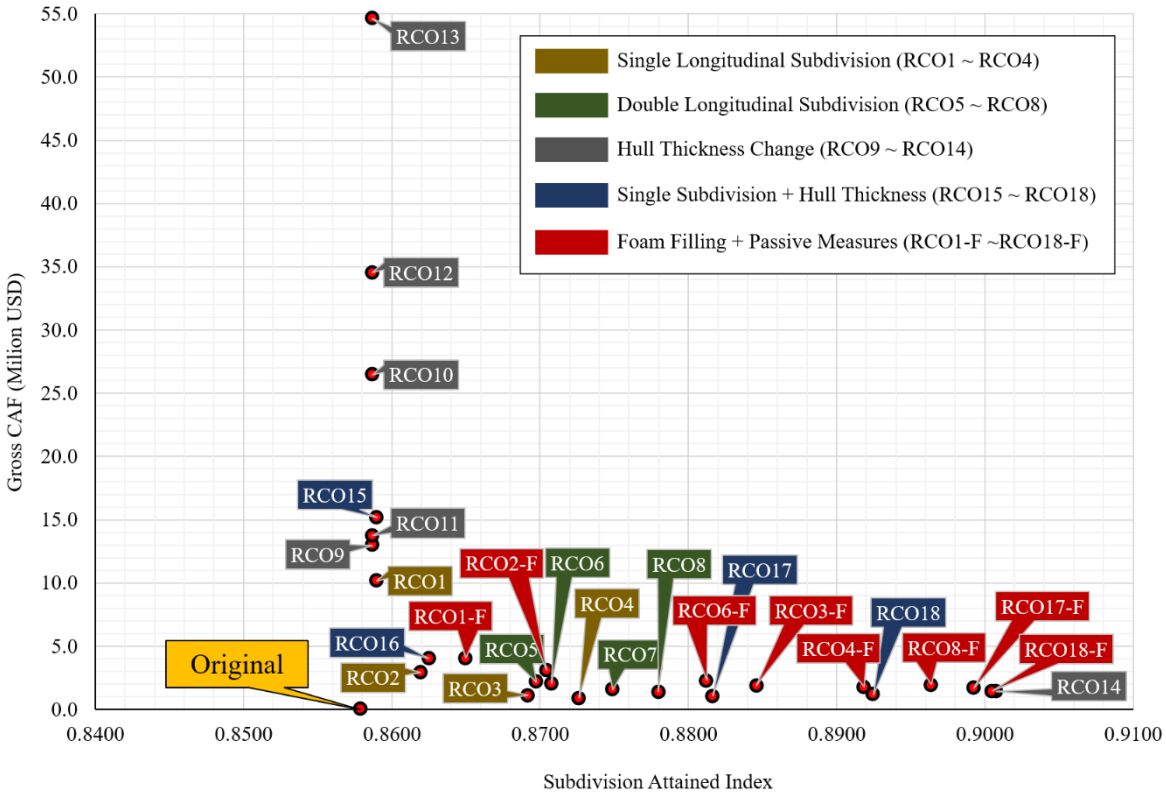

Figure 6.17 Gross CAF results of each RCO compared to the Original layout

Based on the GCAF results in Figure 6.17, the optimum solution might be RCO14 with 50T hull thickness, as it achieved the maximum risk improvement with a reasonable cost, and it is expected to have less maintenance cost, providing the maximum internal spaces. However, there are potential risks of this single-hull being damaged by structural defects such as corrosion, and then the target zone cannot avoid being flooded.

RCO18-F seems to be another optimum RCO that combines the benefits of foam filling to structural RCO (i.e., 30T hull thickness and a single longitudinal subdivision at 9.5m from ship centre). It shows a GCAF of 1.40 million USD / PPL, improving the Subdivision Attained Index to 0.9005 with a cost of 2.90 million USD. For the same reason, the only structural measure RCO18 may be a good alternative, which also shows significant improvement in ship survivability with Attained Subdivision Index of 0.8925 and 1.84 million USD cost, resulting in a GCAF of 1.09. In particular, from the latter two measures, the safe internal areas with 19m breadth (i.e., $9.5 \text{ m} \times 2$) were achieved. This means that wider safe internal areas can be achieved if these ROCs also apply to the adjacent zones, and those spaces can be used for innovative and flexible design.

Table 6.17 Detailed Cost results for each RCO compared to the original layout

NO	RCO	RCO Type	Description	Weight increase (Ton)	CAPEX increase (Mil USD)	WSA increase (%)	Fuel Consumption increase (Ton/year)	OPEX Increase (NPV for 30 years, Mil USD)	Total Cost (Mil USD)
	Original		**Original Layout**	**0.0000**	**-**	**0.00%**	**-**	-	-
1	RCO1	Single longitudinal Subdivision	Single LBHD at B/20	28.14	0.17	**0.03%**	**9.13**	0.10	0.55
2	RCO2		Single LBHD at 2B/20	31.58	0.45	**0.04%**	**10.25**	0.11	0.58
3	RCO3		Single LBHD at 3B/20	34.67	0.47	**0.04%**	**11.25**	0.12	0.62
4	**RCO4**		**Single LBHD at 4B/20**	**37.42**	**0.49**	**0.05%**	**12.14**	**0.13**	**0.64**
5	RCO5	Double longitudinal Subdivision	1st LBHD at B/20 + 2nd LBHD (10T) at 13.1m (*)	70.36	0.69	**0.09%**	**23.28**	0.25	1.25
6	RCO6		1st LBHD at 2B/20 + 2nd LBHD (10T) at 13.1m (*)	73.80	0.97	**0.09%**	**24.58**	0.27	1.28
7	RCO7		1st LBHD at3 B/20 + 2nd LBHD (10T) at 13.1m (*)	76.88	0.99	**0.10%**	**25.75**	0.28	1.32
8	RCO8		1st LBHD at 4B/20 + 2nd LBHD (10T) at 13.1m (*)	79.63	1.01	**0.10%**	**26.79**	0.29	1.35
9	RCO9	Hull thickness Increase	50% Hull thickness increase	49.51	0.30	**0.06%**	**16.07**	0.17	0.50
10	RCO10		100% Hull thickness increase	99.03	0.59	**0.13%**	**34.13**	0.37	1.03
11	**RCO11**		**20T Hull thickness**	**52.58**	**0.32**	**0.06%**	**17.06**	**0.19**	**0.53**
12	RCO12		30T Hull thickness	128.38	0.77	**0.17%**	**45.03**	0.49	1.34
13	RCO13		40T Hull thickness	204.18	1.23	**0.26%**	**70.54**	0.77	2.12
14	**RCO14**		**50T Hull thickness**	**279.98**	**1.68**	**0.36%**	**97.52**	**1.06**	**2.91**
15	RCO15	Combination (Thickness increase + single LBHD)	B/20_100% plate thickness increased	56.29	0.34	**0.07%**	**18.27**	0.20	0.83
16	RCO16		2B/20_100% plate thickness increased	63.17	0.64	**0.08%**	**20.55**	0.22	0.90
17	RCO17		20T hull + Single LBHD (10T) at 10.6m (*)	92.15	0.82	**0.12%**	**31.53**	0.34	1.22
18	RCO18		30T hull + Single LBHD (10T) at 6.6m (*)	**161.55**	1.23	**0.21%**	**55.78**	0.61	1.94
19	RCO1-F	Structural Crashworthiness RCOs + Foam RCO (Permant Foam Void Filling)	RCO1 + Foam Filling of wing compartments	56.73	0.92	**0.07%**	**18.41**	0.20	1.40
20	RCO2-F		RCO2 + Foam Filling of wing compartments	75.51	1.61	**0.09%**	**25.23**	0.27	1.91
21	RCO3-F		RCO3 + Foam Filling of wing compartments	95.18	2.07	**0.12%**	**32.68**	0.36	2.45
22	RCO4-F		RCO4 + Foam Filling of wing compartments	114.59	2.53	**0.15%**	**40.03**	0.44	2.98
23	RCO6-F		RCO6 + Foam Filling of wing compartments	117.73	2.13	**0.15%**	**41.21**	0.45	2.62
24	RCO8-F		RCO8 + Foam Filling of wing compartments	156.81	3.04	**0.20%**	**54.24**	0.59	3.68
25	**RCO17-F**		**RCO17 + Foam Filling of wing compartments**	**162.75**	**2.68**	**0.21%**	**56.17**	**0.61**	**3.35**
26	**RCO18-F**		**RCO18 + Foam Filling of wing compartments**	**196.62**	**2.16**	**0.25%**	**67.68**	**0.74**	**2.99**

Table 6.18 Gross CAF results for each RCO compared to the original layout

NO	RCO	RCO Type	Description	Penetration (m)	Penetration Decrease (m)	Attained Index	Attained Index Increase	Δ PPL (GOALDS)	Δ PPL (EMSAIII)	Gross CAF (EMSAIII)
	Original		**Original Layout**	**16.15**	**-**	**0.8579**	**-**	**-**	**-**	**-**
1	RCO1	Single longitudinal Subdivision	Single LBHD at B/20	13.13	3.02	0.8590	0.0011	0.06	0.05	10.15
2	RCO2		Single LBHD at 2B/20	13.03	3.12	0.8619	0.0041	0.24	0.20	2.94
3	RCO3		Single LBHD at 3B/20	11.82	4.33	0.8692	0.0113	0.66	0.55	1.11
4	**RCO4**		**Single LBHD at 4B/20**	**12.51**	**3.64**	**0.8727**	**0.0148**	**0.86**	**0.72**	**0.89**
5	RCO5	Double longitudinal Subdivision (Safety Zone)	1st LBHD at B/20 + 2nd LBHD (10T) at 13.1m (*)	13.13	3.02	0.8698	0.0119	0.69	0.58	2.14
6	RCO6		1st LBHD at 2B/20 + 2nd LBHD (10T) at 13.1m (*)	13.03	3.12	0.8708	0.0129	0.75	0.63	2.03
7	RCO7		1st LBHD at3 B/20 + 2nd LBHD (10T) at 13.1m (*)	11.82	4.33	0.8749	0.0170	0.99	0.83	1.58
8	RCO8		1st LBHD at 4B/20 + 2nd LBHD (10T) at 13.1m (*)	12.51	3.64	0.8780	0.0201	1.17	0.98	1.37
9	RCO9	Hull thickness Increase	50% Hull thickness increase	11.72	4.43	0.8587	0.0008	0.05	0.04	12.96
10	RCO10		100% Hull thickness increase	8.22	7.93	0.8587	0.0008	0.05	0.04	26.48
11	**RCO11**		**20T Hull thickness**	**10.46**	**5.69**	**0.8587**	**0.0008**	**0.05**	**0.04**	**13.76**
12	RCO12		30T Hull thickness	6.58	9.57	0.8587	0.0008	0.05	0.04	34.54
13	RCO13		40T Hull thickness	6.64	9.51	0.8587	0.0008	0.05	0.04	54.64
14	**RCO14**		**50T Hull thickness**	**0**	**16.15**	**0.9008**	**0.0429**	**2.49**	**2.08**	**1.40**
15	RCO15	Combination (Thickness increase + single LBHD)	B/20_100% plate thickness increased	10.14	6.01	0.8590	0.0011	0.07	0.06	15.16
16	RCO16		2B/20_100% plate thickness increased	10.31	5.84	0.8625	0.0046	0.27	0.23	4.02
17	RCO17		20T hull + Single LBHD (10T) at 10.6m (*)	10.46	5.69	0.8816	0.0238	1.38	1.16	1.04
18	RCO18		30T hull + Single LBHD (10T) at 6.6m (*)	6.58	9.57	0.8925	0.0346	2.01	1.69	1.14
19	RCO1-F	Structural Crashworthiness RCOs + Foam RCO (Permant Foam Void Filling)	RCO1 + Foam Filling of wing compartments	13.13	3.02	0.8650	0.0071	0.41	0.35	4.05
20	RCO2-F		RCO2 + Foam Filling of wing compartments	13.03	3.12	0.8704	0.0126	0.73	0.61	3.10
21	RCO3-F		RCO3 + Foam Filling of wing compartments	11.82	4.33	0.8846	0.0267	1.55	1.31	1.87
22	RCO4-F		RCO4 + Foam Filling of wing compartments	12.51	3.64	0.8919	0.0340	1.97	1.66	1.79
23	RCO6-F		RCO6 + Foam Filling of wing compartments	13.03	3.12	0.8812	0.0234	1.36	1.14	2.30
24	RCO8-F		RCO8 + Foam Filling of wing compartments	12.51	3.64	0.8964	0.0385	2.23	1.88	1.95
25	**RCO17-F**		**RCO17 + Foam Filling of wing compartments**	**10.46**	**5.69**	**0.8993**	**0.0414**	**2.40**	**2.03**	**1.65**
26	**RCO18-F**		**RCO18 + Foam Filling of wing compartments**	**6.58**	**9.57**	**0.9005**	**0.0426**	**2.47**	**2.07**	**1.44**

(*) The distance from the outer shell of the hull

6.12 Chapter Summary

The case study demonstrated how the proposed methodology improves ship survivability using crashworthiness analysis. A 65,000 GT medium size cruise ship was utilised for this study as a target struck ship whom a 45,000 GT Ro-Pax vessel assumes to collide with. As a first step, initial damage stability was assessed to identify the current risk status. A vulnerability assessment was followed to classify the risk of subdivision zones. Zone 15, located at the forepart of the ship, was identified as the most vulnerable zone for the target zone for this case study. For collision scenario definition, a series of pre-simulations for collisions were carried out to find a collision speed resulting in B/2 penetration, and 10.14 knots was determined for the collision speed. Total 26 RCOs were examined in the target zone. The 18 RCOs out of them were structural measures with four categories: namely, a single longitudinal subdivision, double longitudinal subdivisions, hull thickness change, and combinations of structural measures. The other eight RCOs were to apply foam filling to the crashworthy RCOs. Following crashworthiness analyses for those 26 RCOs, the maximum penetrations were obtained. Based on these results, for the RCOs aiming to have safe internal spaces (i.e., RCO5~RCO8, RCO17, RCO18 and ROC6-F~ ROC18-F), the transverse positions of longitudinal bulkheads were determined to the end of damaged areas. Then, re-evaluations of damage stability for each RCO were carried out with the following three updates; new layout by RCOs, permeability change (i.e., zero permeability for safe internal spaces and permeability of 0.05 for foam-filled spaces), and revised transversal damage distributions based on the maximum penetration. Finally, the cost-benefit analysis for each RCO was conducted to find an optimum solution. Each RCO showed a penetration reduction from 3.02m for RCO1 to 16.15m for RCO14 compared to the original penetration of B/2. Notably, RCO14, 50T hull thickness on Zone 15, showed no penetration. The updated Subdivision Attained Indices were improved from 0.008 to 0.0429.

From cost-benefit analyses for a total of 26 RCOs, the Gross CAF ranged from 0.86 to 51.47 MilUSD / PPL was calculated. Finally, three RCOs among all RCOs, namely RCO14, RCO18 and ROC18-F, were identified as optimum solutions: the single-hull type with 50T hull thickness, double-hull type with 30T hull and single subdivision at 6.6m, permanent foam filling application to ROC18, respectively. The final decision would be made by the associated decision-makers, and the "approval process of alternative design and arrangement (AD&A)" would be followed for the actual implementation of the final RCO.

In particular, for RCO 18 and RCO18-F as a double-hull concept, more flexible and spacious internal spaces can be achieved if those RCOs apply to the adjacent zones. Then, it may provide significant design innovations for ships in the future.

Chapter 7

Sensitivity Study

7 SENSITIVITY ANALYSIS

7.1 Preamble

In the case study in Chapter 6, the proposed QRA methodology proved effective for evaluating crashworthy structures' contribution to ship damage stability by comparing changes in the maximum penetrations with the original layout in the same scenario. However, many researchers have pointed out that various parameters employed are susceptible to simulation results due to their uncertainties (see Section 2.3.3), such as;

- Failure strain criteria associated with mesh sizes
- Material property curve
- Friction coefficient
- Geometry deformation definition (rigid or deformable)
- Element type of geometries (shell or beam)
- The extent of geometries (full or partial model)

Thus, unidentical penetration results might be obtained when different analysis assumptions are applied to collision simulations.

This chapter focuses on the proposed methodology's reliability for simulation results when different analysis assumptions are employed. For this purpose, the most critical four parameters were investigated: fracture strain criteria, material curves, friction coefficients and rigidity definition of striking bow body. Firstly, as a traditional analysis, simulations with different parameters were carried out using an identical collision speed employed at the original simulation. Then, those results were compared with the original simulation to identify the effects of each parameter. Next, the same simulations were conducted based on the proposed analysis approach. In these simulations, different collision speeds (i.e., resulting in B/2) by the different parameters were used. Additional simulations of four different arrangements were also conducted to identify the methodology reliability of design influences (see Table 7.1).

Table 7.1 RCOs used for sensitivity study

RCO	Description
Original Layout	Original layout with no RCO
RCO4 (RCO8, RCO4-F)	Original layout with a single longitudinal bulkhead at 4B/20
RCO11 (RCO17, RCO17-F)	Original layout with the hull of 20T
RCO12 (RCO18, RCO18-F)	Original layout with the hull of 30T
RCO14	Original layout with the hull of 50T

RCO4 is the arrangement with a single longitudinal subdivision located at B/5 of the ship, which is a typical example of a double hull design. The other three RCOs, such as RCO11, RCO12 and RCO14, are related to the hull thickness increase measures, which were proven as the most effective measures from the case study in Chapter 6. In particular, RCO14 shows no penetration on the hull of the stuck ship in the original collision simulation.

7.2 Effects of Fracture strains

7.2.1 Analysis Description

Firstly, a sensitivity study was conducted for fracture strain parameters. In the original simulation, the *GL criterion* (Vredeveldt, 2001, Scharrer et al., 2002b) was adopted for fracture stain, and the fracture strain of approximately 0.1 (hereafter, it is termed FS≈0.1 or Original failure strain) was employed based on geometric models' mesh sizes and plate thicknesses(see Section 6.7.3). However, as shown in Figure 7.1, other formulas suggested by various authors are also feasible. According to the GL recommendation (Scharrer et al., 2002a), the ratio of element length and thickness (l_e/T) should be higher than 5 for the numerical simulations. Thus, based on a minimum ratio of 6.67 (i.e., l_e/T =200/30) for the current FE models, the feasible fracture strain ranges from 0.1 to 0.4. Therefore, three other constant failure strains, such as 0.2, 0.3 and 0.4 (hereafter, they are termed FS=0.2, FS=0.3 and FS=0.4) were selected for failure strain effects on simulations.

As a first step, initial simulations with three different failure strains were performed based on the same collision speed employed in the original simulation for the purpose of identifying fracture strain effects. Then, for the proposed analysis approach, a series of pre-simulations with different fracture stains were repeatedly carried out to find the collision speeds resulting in the penetration length of B/2 for each case. Figure 7.2 shows the results of pre-simulations for FS=0.2, FS=0.3 and FS=0.4, including the original simulation results (i.e., FS≈0.1) in the study case for the comparison purpose. The collision speeds resulting in B/2 penetration were 19 knots for FS=0.2, 25 knots for FS=0.3 and 28 knots for FS04 compared to 10.14 knots from the original calculation FS01.

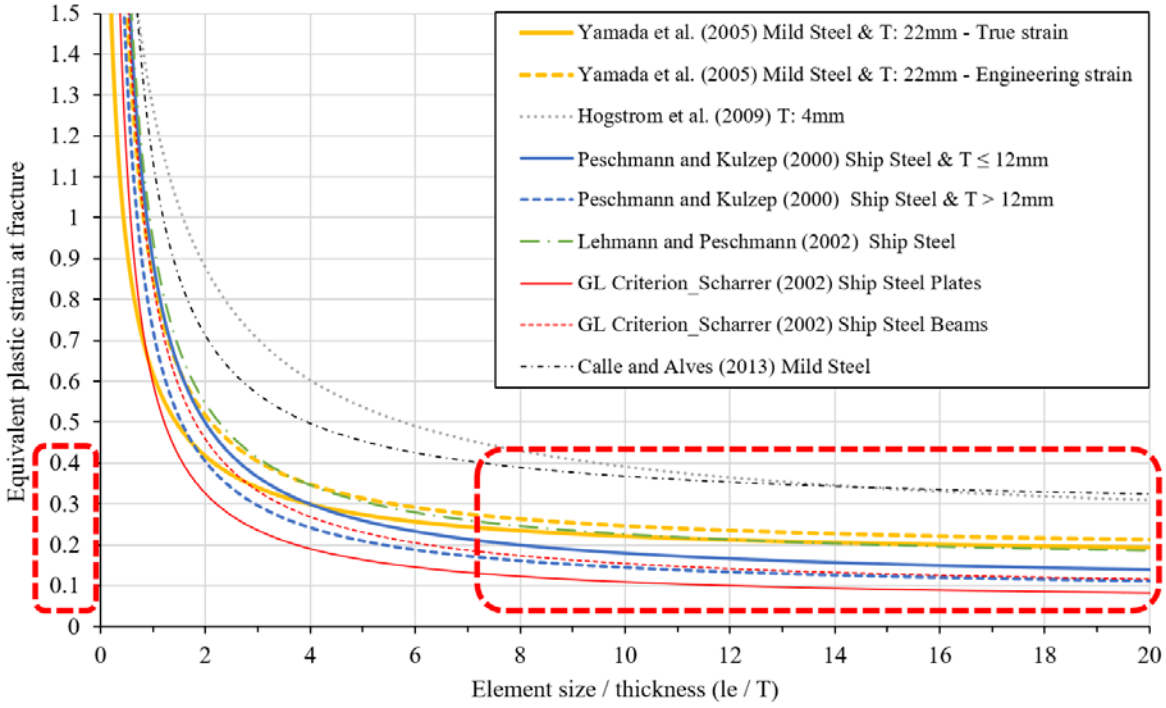

Figure 7.1 Various element size-dependent failure criteria based on Barba's law

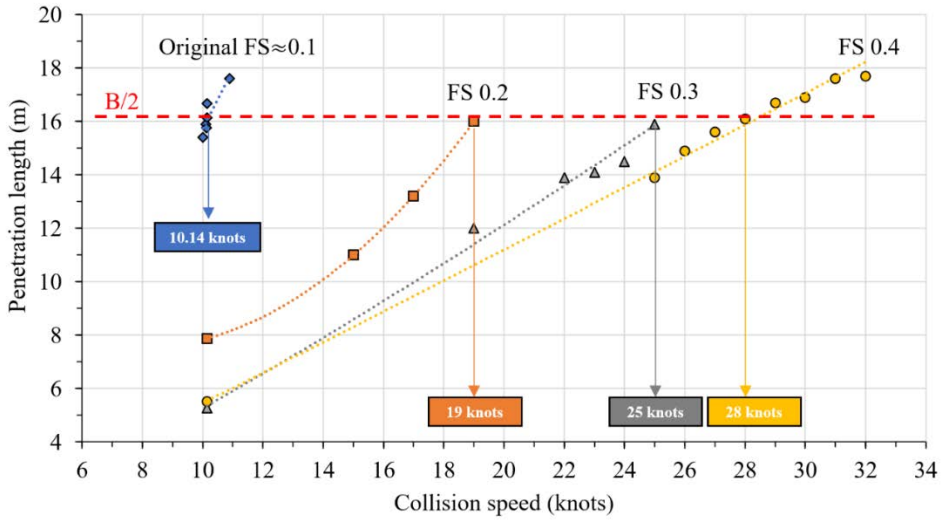

Figure 7.2 Pre-simulation results for collision speed findings with four different fracture criteria

Figure 7.3 shows the dissipated energy and the resultant forces depending on penetration changes of four simulations with four different fracture strains at the selected collision speeds. It clearly indicates that the collision with high initial speed dissipated much more energy absorbed by the structures (i.e., FS = 0.4), while structures absorbed the low energy for a low-speed collision case (i.e., FS≈0.1). However, those simulations resulted in the same penetration due to the different fracture strains used.

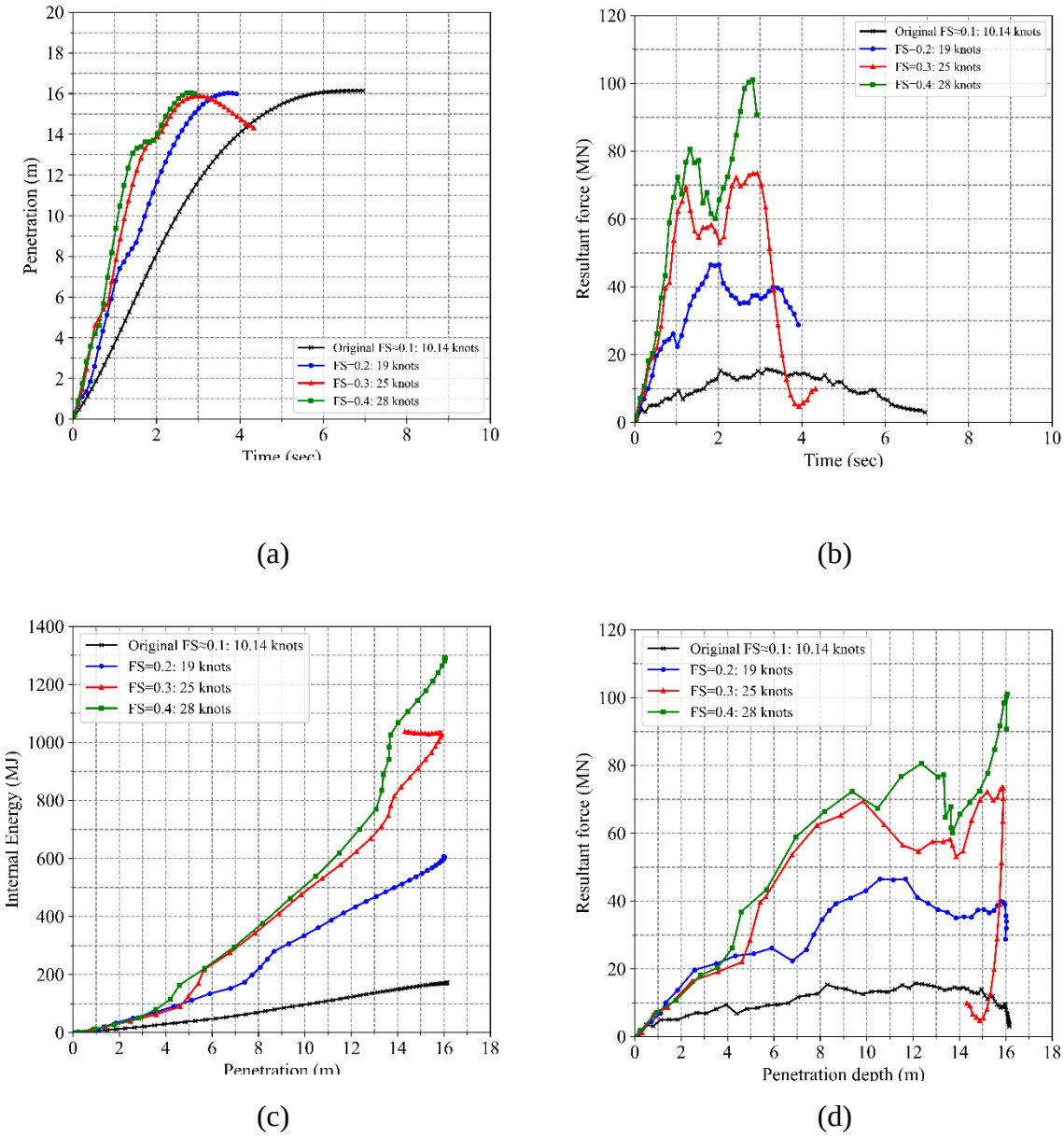

Figure 7.3 Simulation results for the different collision speeds resulting in B/2 penetration: (a) Penetration vs time, (b)Resultant force vs time, (c) Internal energy vs Penetration graph and (d) Resultant force vs penetration graph at corresponding collision speeds

7.2.2 Results and Discussion

Figure 7.2 shows the results of different failure strains employed for simulations, in which the same collision speed of 10.14 knots was used. Compared to the original penetration of 16.15m, significant changes in penetrations by 8.27 ~ 10.64 m were observed. This confirms the effects of failure criteria. These results imply that outcomes from simulations with a direct approach

may be unreliable depending on the simulation assumptions.

Table 7.2 Penetration results at the different fracture strain values – using the same collision speed

Layout	Maximum Penetration (m)				Average (m)	Standard Deviation (m)	Coefficient of Variation
	Original FS≈0.1 (m)	FS=0.2 (m)	FS=0.3 (m)	FS=0.4 (m)			
	Collision speed of 10.14 knots						
Original Layout	**16.15**	7.88	5.28	5.51	8.71	5.10	59%

Table 7.3 and Figure 7.4 summarise the results of the simulations obtained from the proposed analysis approach. The relative speeds resulting in B/2 with each different failure criteria were applied to the different simulations (See Figure 7.2). However, the same maximum penetrations (i.e. B/2) were obtained from the simulations of the original layout. In order to identify the methodology reliability and design influences, the same simulations were carried out for additional simulations of four ROCs. The results for RCO4 showed a substantial level of agreement with the original failure strain case (i.e., FS≈0.1). On the other hand, the results from RCO11, RCO12 and RCO14 showed quite different penetrations from those of FS≈01.

Table 7.3 Penetration results at the different fracture stain values– using the different collision speeds resulting in B/2 penetration

Layout	Maximum Penetration (m)				Average (m)	Standard Deviation (m)	Coefficient of Variation
	Original FS≈0.1 (m)	FS=0.2 (m)	FS=0.3 (m)	FS=0.4 (m)			
	10.14 knots(*)	19 knots(*)	25 knots(*)	28 knots(*)			
Original Layout	**16.15**	16.02	15.89	16.05	16.03	0.11	1%
RCO4	**12.51**	12.95	12.67	13.15	12.82	0.29	2%
RCO11	**10.46**	12.53	14.05	10.93	11.99	1.63	14%
RCO12	**6.61**	12.12	10.19	0.00(*)	7.23	5.33	74%
RCO14	**0.00 (**)**	9.48	0.00(**)	0.00(**)	2.37	4.74	200%

(*) Collision speeds resulting in B/2 transverse penetration

(**) No penetration on the outer hull occurred, with only indentation

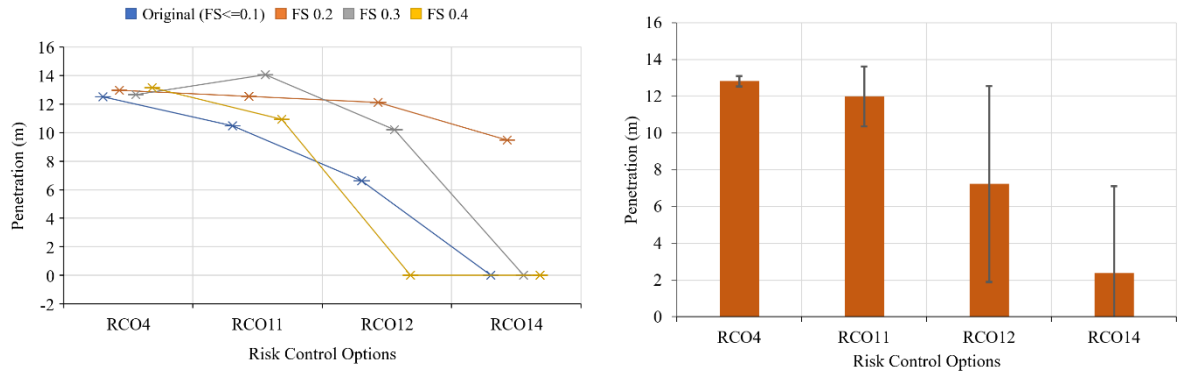

Figure 7.4 Failure criteria effects of each RCO: Simulation results for (a) all cases and (b) mean values and standard deviations

The combination effects of RCO type and failure strain might affect these results. While RCO4 had no change in the hull, the other RCOs had hull thickness increases. Due to the strengthened hull, the striking ship required more force to break through the hull of the struck ship. At the same time, the striking ship's body was continuously damaged until the local element strains reached the higher fracture strain employed. Therefore, the striking body was severely deformed at the early stage of the simulations, and it continued to affect the rest of the process, causing fluctuating results. The deformed shape of the striking ship between the beginning and final stages of each simulation is almost identical (See Figure 7.5). On the other hand, in the case of RCO4, relatively less deformation occurred on the striking body when breaking through the hull, and it continuously deformed during overall simulations (See Figure 7.6). As a result, it showed reliable outcomes for the different fracture strains. Interestingly, the deformation effect of the striking body was also observed in this case. As shown in Figure 7.6, the maximum penetration point of the striking ship was the foremost of the stem for FS01, whereas the other cases for FS=0.2, FS=0.3 and FS=0.4 happened at the bulbous bow since the stem was totally damaged and pushed back. In particular, the sudden penetration of 9.48m for RCO14 with FS=0.2 is attributed to the fact that the struck ship was defined as having penetration, instead of just deep indentation, due to an opening on the hull at a final stage (Figure 7.7).

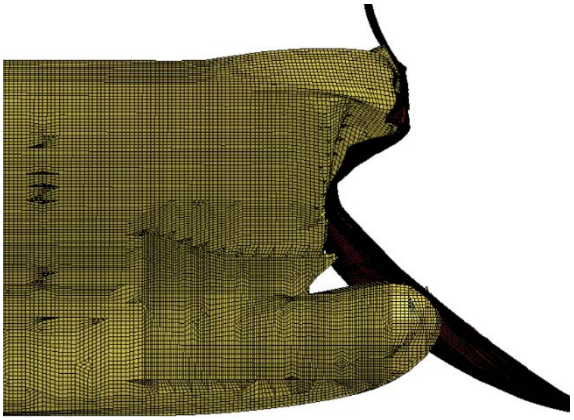

(a1) RCO12/FS=0.1- Beginning stage

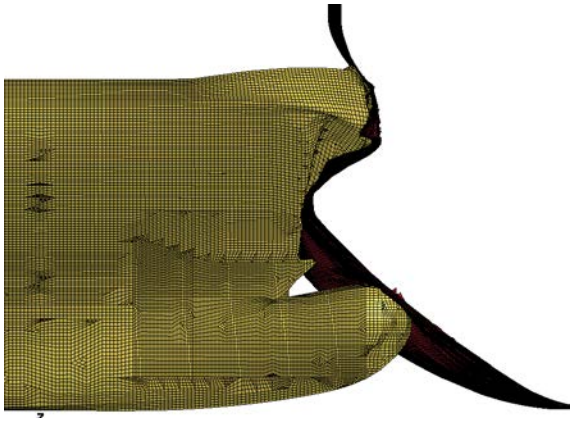

(a2) RCO12/FS=0.1- Final stage

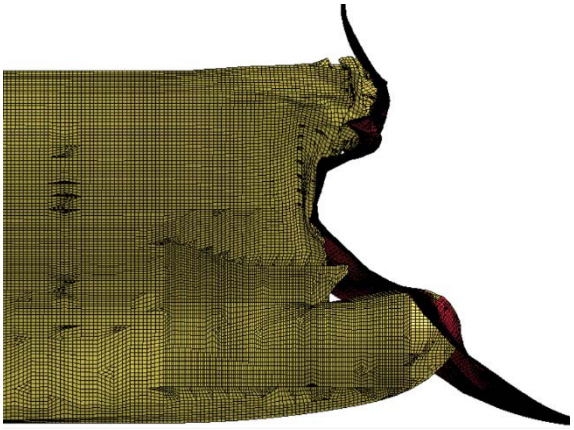

(b1) RCO12/FS=0.2- Beginning stage

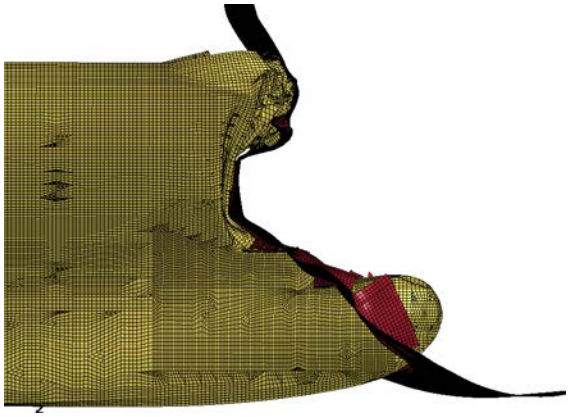

(b2) RCO12/FS=0.2- Final stage

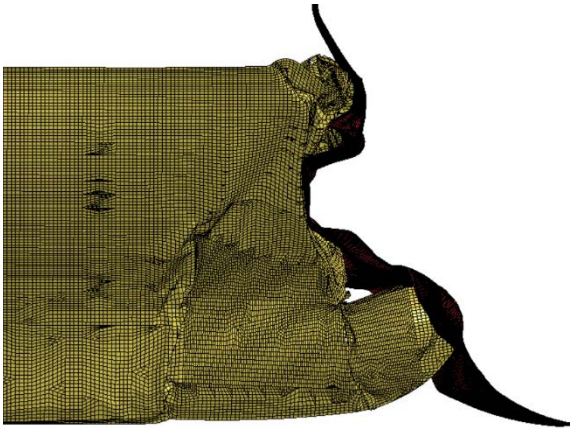

(c1) RCO12/FS=0.3- Beginning stage

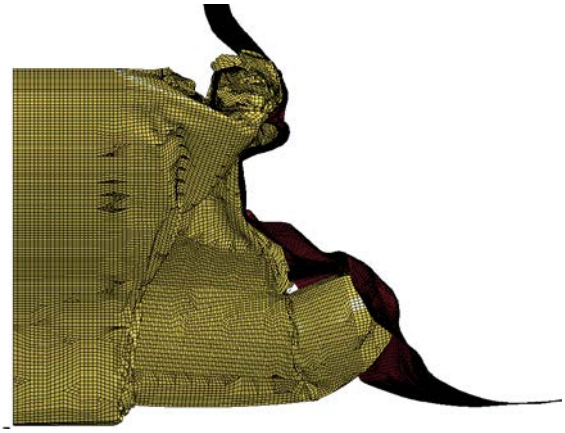

(c2) RCO12/FS=0.3- Final stage

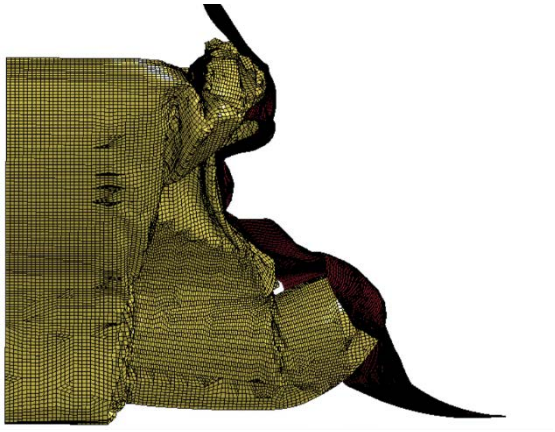

(d1) RCO12/FS=0.4- Beginning stage

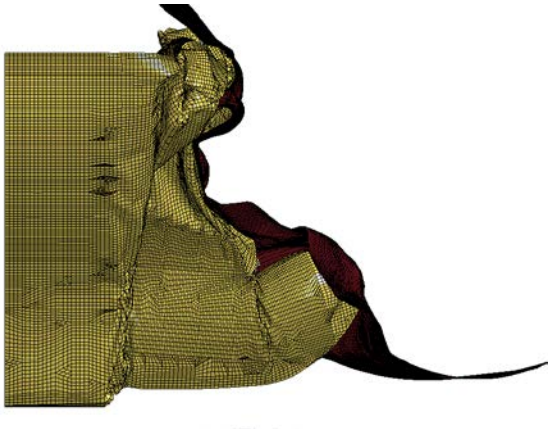

(d2) RCO12/FS=0.4- Final stage

Figure 7.5 RCO12 simulation results for the different failure strains based on the different collision speeds resulting in B/2 penetration

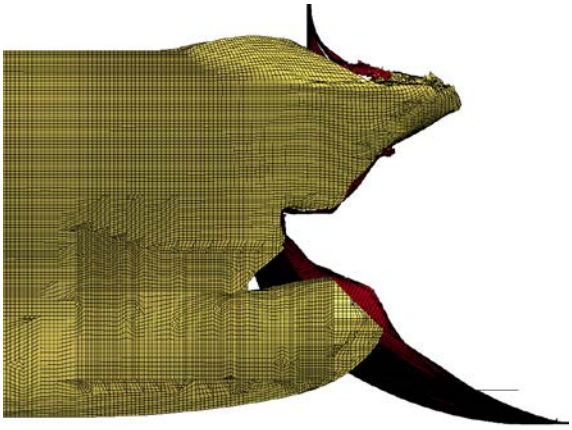

(a1) RCO4/FS=0.1- Beginning stage

(a2) RCO4/FS=0.1- Final stage

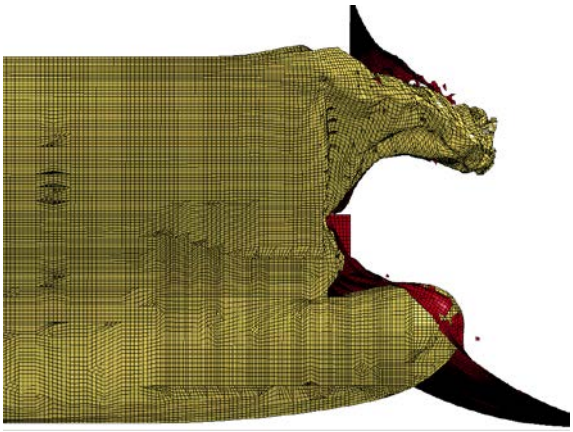

(b1) RCO4/FS=0.2- Beginning stage

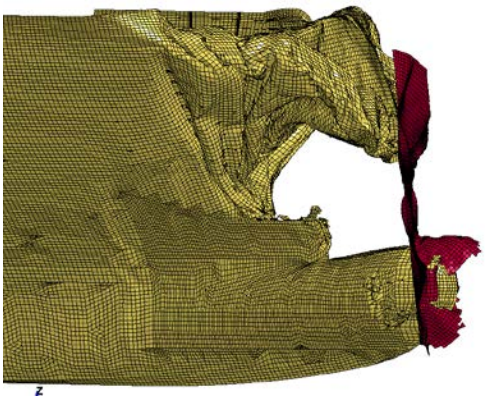

(b2) RCO4/FS=0.2- Final stage

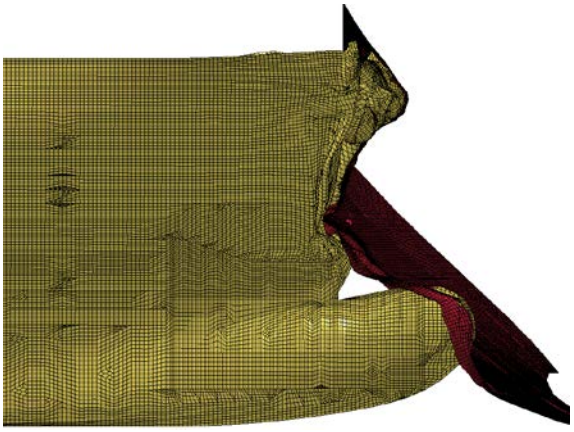

(c1) RCO4/FS=0.3- Beginning stage

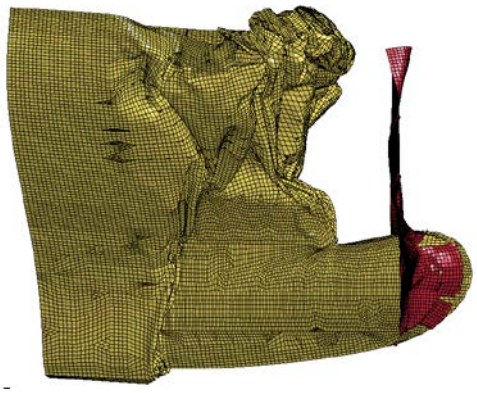

(c2) RCO4/FS=0.3- Final stage

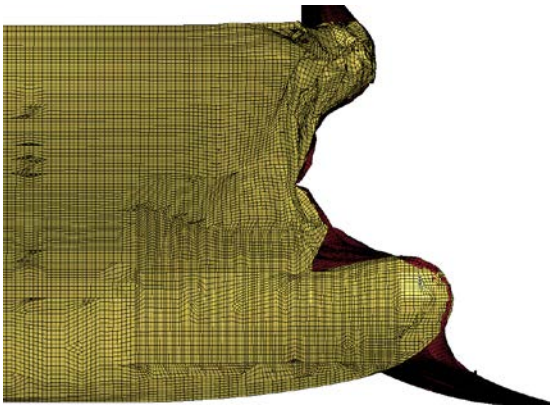

(d1) RCO4/FS=0.4- Beginning stage

(d2) RCO4/FS=0.4- Final stage

Figure 7.6 RCO4 simulation results for the different failure strains based on the different collision speeds resulting in B/2 penetration

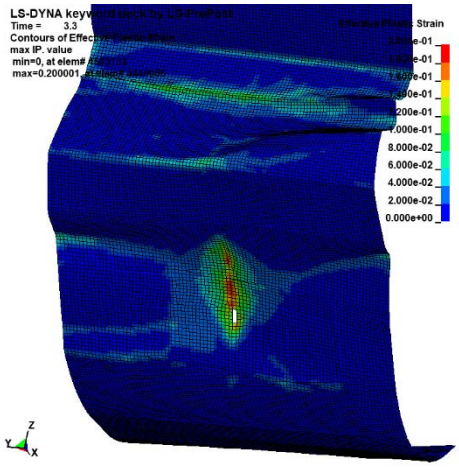

(a) RCO14/ FS=0.2

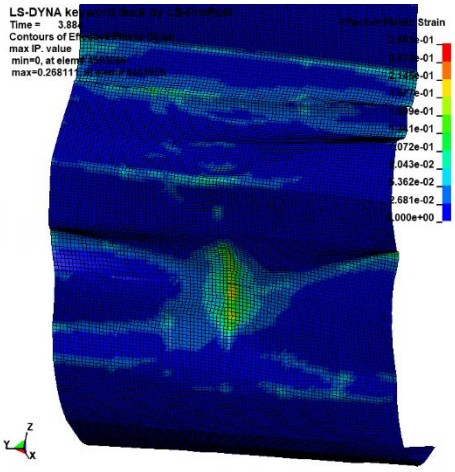

(b) RCO14/ FS=0.4

Figure 7.7 RCO14 penetration results for the different failure strains based on the different collision speeds resulting in B/2 penetration

7.3 Effects of Stress-strain curves

7.3.1 Analysis Description

The stress-strain material curve is another key parameter that controls material behaviour in the relationship between stresses and strains until the fracture strain occurs. Three different stress-strain curves, including the original material curve, were investigated to identify the sensitivity of material curves (See
Table 7.4 and Figure 7.8). The first model is the original result obtained from the modified true stress-true strain curve (hereafter, it is MTSS and see Section 4.2.3). The second model behaves in a linear elastic-perfectly plastic manner (hereafter, it is termed LEPP). Accordingly, stress is proportional to the elastic constant E (i.e., Young's modulus) up to the yield point and remains constant for the plastic region. Thus, the plastic hardening and softening (i.e., necking) are disregarded in this model. The third model is a material curve expressed as a power-law equation (hereafter, it is termed Power law):

$$\sigma_{true} = K(\varepsilon_{true})^n \qquad (7.1)$$

where, K denotes the hardening coefficient, and n is a strain hardening exponent; For this sensitivity study, K=770 Mpa and n=0.2 are used, which is derived from the tensile simulation by Tornqvist (2003) for the mild steel with E=210Gpa and σ_y = 250 Mpa.

Firstly, simulations with the two material curves above were carried out at the same collision speed of 10.14 knots employed at the original simulation and compared to the original result obtained from MTSS to identify the effects of material curves on FE simulations.

Table 7.4 Stress-Strain material curve models for a sensitivity study

Material curve	Stress-Strain Model	Material Property	Remark
Original - MTSS	Modified true stress-true strain curve (MTSS)	σ_y = 235 Mpa σ_U = 400 Mpa E = 205.8 Gpa Poisson ratio = 0.3	-
LEPP	Linear Elastic- perfectly plastic Model (LEPP)		-
Power law	Power law curve		K =770 Mpa, n = 0.2

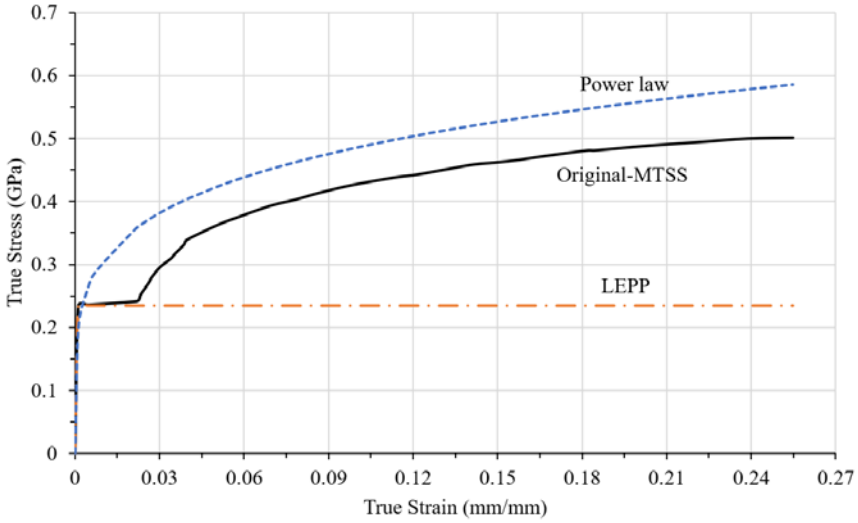

Figure 7.8 Three different true stress-true strain material curves

As the second step, based on the proposed analysis approach, a series of pre-simulations with different fracture stains were repeatedly carried out to find the collision speeds resulting in the penetration length of B/2 for each case. Figure 7.9 shows the results of pre-simulations with three different material curves, including the original simulation results in the study case for comparison purposes. 8.5 knots and 10.4 knots were identified as the collision speeds generating B/2 penetration in simulations with LEPP and Power-law, respectively. It means that lower energy (i.e, lower collision speed) is required for LEPP to make certain damage compared with the original simulation with MTSS, whereas the simulation with a power-law curve needed more energy (i.e, higher collision speed) for the same damage, as shown in Figure 7.10.

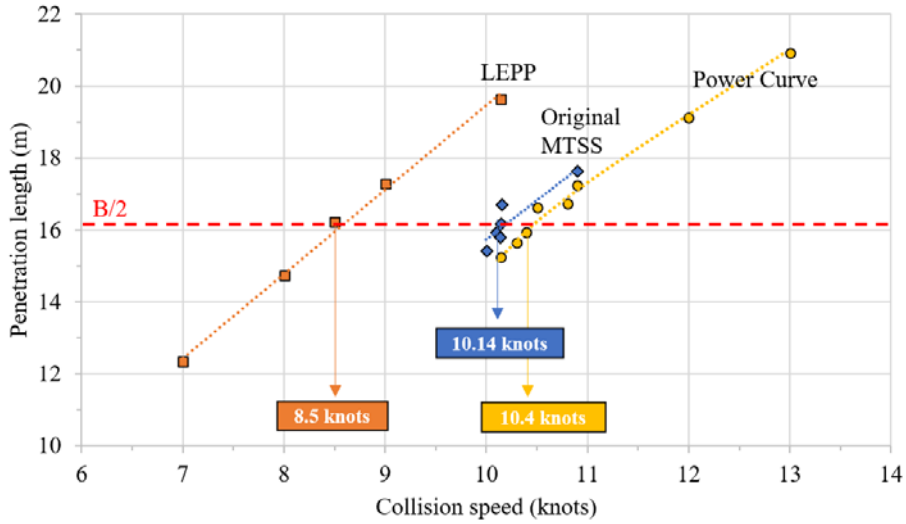

Figure 7.9 Pre-simulation results for collision speed findings with three different material curves

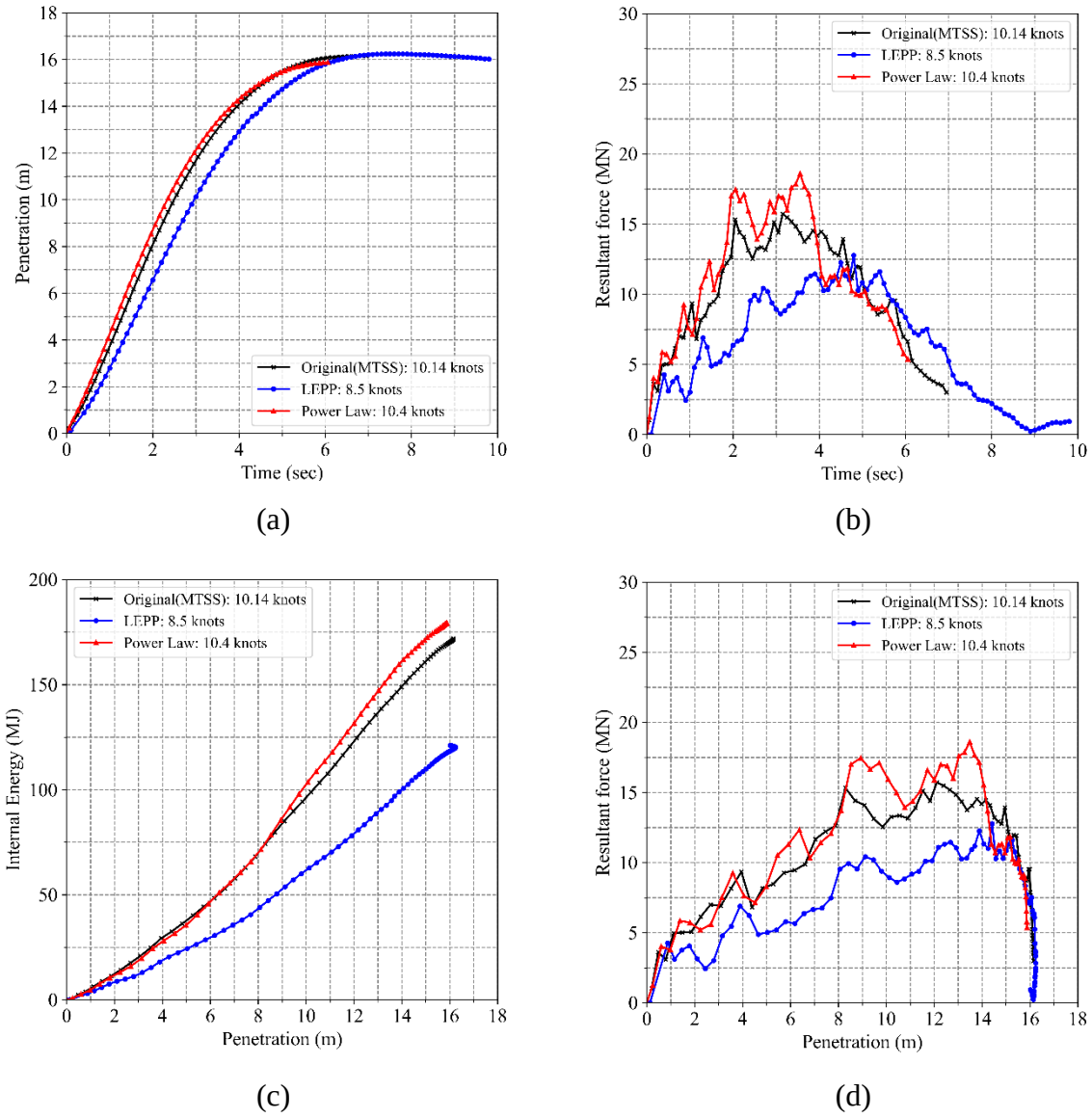

Figure 7.10 Simulation results for the different collision speeds resulting in B/2 penetration: (a) Penetration vs time, (b)Resultant force vs time, (c) Internal energy vs Penetration graph and (d) Resultant force vs penetration graph at corresponding collision speeds

7.3.2 Results and Discussion

Table 7.5 shows the results of different material curves employed for simulations at the same collision speed of 10.14 knots. The effects of stress-strain curves were also clearly observed with changes in penetrations by -0.83 ~ 3.45 m.

On the other hand, Table 7.6 and Figure 7.11 summarised the simulation results based on the proposed analysis approach with the relative collision speeds. The simulations for RCO4 gave 13.6 m penetration for LEPP and 10.40 m penetration for Power-law, which deviated slightly from the penetration with MTSS. However, they are reasonably acceptable based on the 13%

variation coefficient with an average penetration of 12.17m and a standard deviation of 1.63m. The simulation results of RCO 11 and RCO 12 were more consistent with penetration differences of less than 1 m. The average penetrations of the two cases were 10.28 m and 6.7m, which were almost identical to the original results. For RCO14, which is the simulation with a hull of 50 mm thickness, no opening was observed for all material curves.

Table 7.5 Penetration results at three different material stress-strain curves– using the same collision speed

Layout	Maximum Penetration (m)			Average (m)	Standard Deviation (m)	Coefficient of Variation
	Original MTSS	LEPP	Power law			
	Collision speed of 10.14 knots					
Original Layout	**16.15**	19.6	15.20	16.98	2.32	14%

Table 7.6 Penetration results at three different material stress-strain curves using collision speeds resulting in B/2 penetration

Layout	Maximum Penetration (m)			Average (m)	Standard Deviation (m)	Coefficient of Variation
	Original MTSS	LEPP	Power law			
	10.14 knots(*)	8.5 knots(*)	10.4 knots(*)			
Original Layout	**16.15**	16.24	15.9	16.10	0.18	1%
RCO4	**12.51**	13.60	10.40	12.17	1.63	13%
RCO11	**10.46**	10.90	9.48	10.28	0.73	7%
RCO12	**6.61**	7.13	6.36	6.70	0.39	6%
RCO14	**0.00** (*)	0.00 (*)	0.00 (*)	0.00	0.00	0%

(*) Collision speeds resulting in B/2 transverse penetration

(**) No penetration on the outer hull occurred, with only indentation

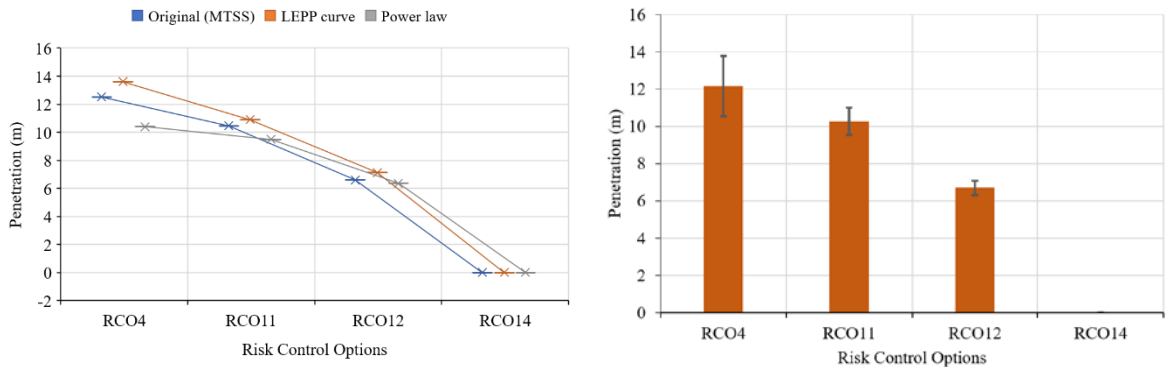

Figure 7.11 Material curve effects of each RCO: Simulation results for (a) all cases and (b) mean values and standard deviations

Thus, in general, the simulations conducted based on the proposed methodology were in good agreement with the original simulation for the different material curves, showing a variation coefficient of 0 ~ 13 %. This implies that the proposed methodology compensates for simulation results from different material curves.

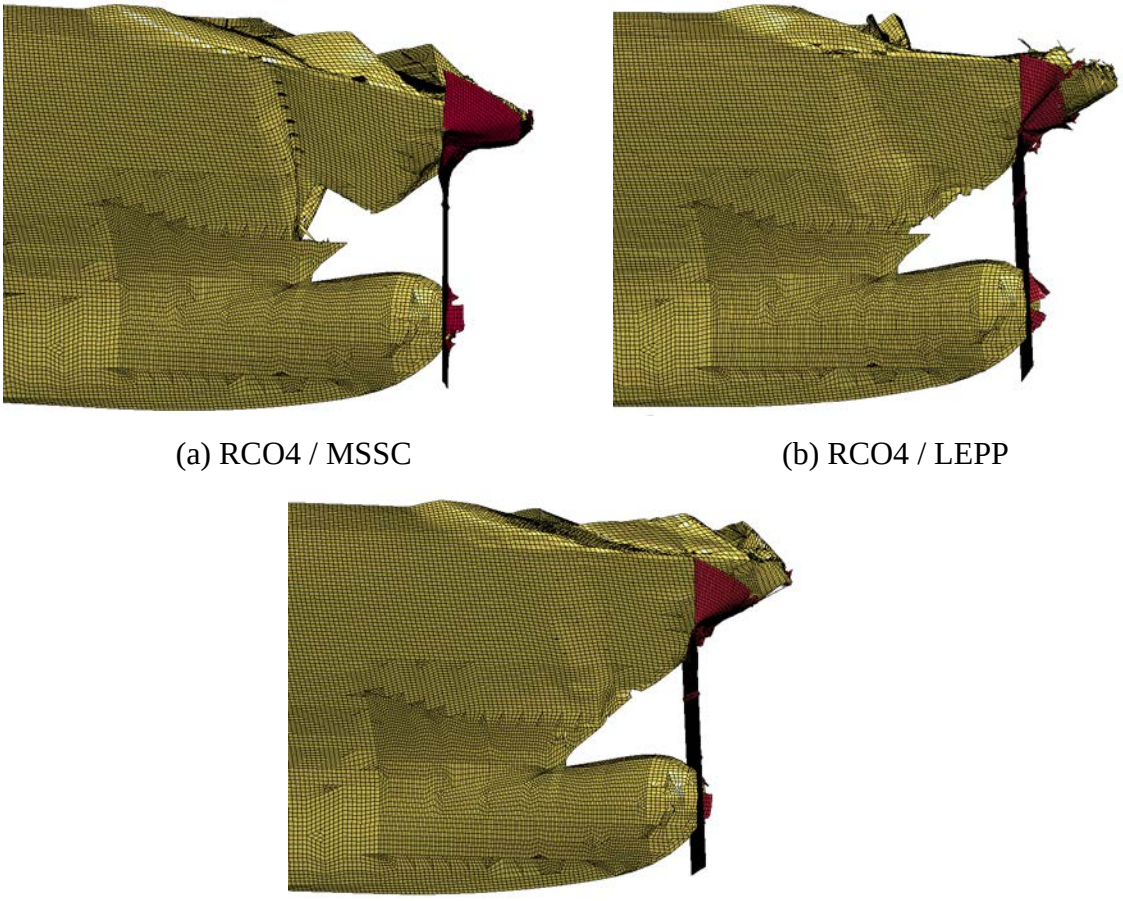

(a) RCO4 / MSSC (b) RCO4 / LEPP

(c) RCO4 / Power-law

Figure 7.12 RCO4 simulation results for the different material curves based on the different collision speeds resulting in B/2 penetration

7.4 Effects of friction coefficients

7.4.1 Analysis Description

Friction is another challenge of collision simulations. As discussed in Section 4.2.5, a friction coefficient of 0.3 was employed in the present thesis, which is the common value of a dynamic friction coefficient for analyses of ship collisions (Paik, 2007). This takes into account the characteristics of the steel material used for the shipbuilding, especially in the hull condition

polluted by bio-fouling. However, a friction coefficient of 0.09-0.19 for lubricated surfaces is also recommended in NASA Reference Publication 1228: Fastener Design Manual (Barrett, 1990). Furthermore, according to experiments by Karlsson et al. (2009), they obtained a low kinetic coefficient of friction, such as 0.23 $\pm$ 0.01 for the 240 steel grade material, 0.22 $\pm$ 0.01 for the 355 steel grade material, and 0.15 $\pm$ 0.01 for the 700 steel grade material from a series of friction tests. This means that a friction coefficient of lower than 0.3 is reasonably feasible for collision simulations. Thus, a simulation with a friction coefficient of 0.1 (hereafter, it is termed FR=0.1) has been carried out to investigate friction effects, and they are compared to the original simulation results with a friction coefficient of 0.3 (hereafter, it is termed FR=0.3). In this simulation, the same collision speed of 10.14 knots employed used in the original simulation. As the second step, using the proposed analysis approach, a series of pre-simulations with different fracture stains were repeatedly carried out to find the collision speeds resulting in the penetration length of B/2 for each case. Figure 7.13 shows the results of pre-simulations with a friction coefficient of 0.1 and 0.3. The collision speed of 8.5 knots was achieved for FR=0.1 compared to 10.14 knots from the original calculation (i.e., FR=0.3). Due to the low friction coefficient of 0.1 for FR=0.1, less energy was dissipated from the sliding energy, whilst more energy was focused on the internal structure mechanism, generating more significant damages than the simulation with FR=0.3 at the same collision speed. This means that less collision energy (i.e., low collision speed) resulted in B/2 penetration easily for the simulation with a low friction coefficient, as shown in Figure 7.14.

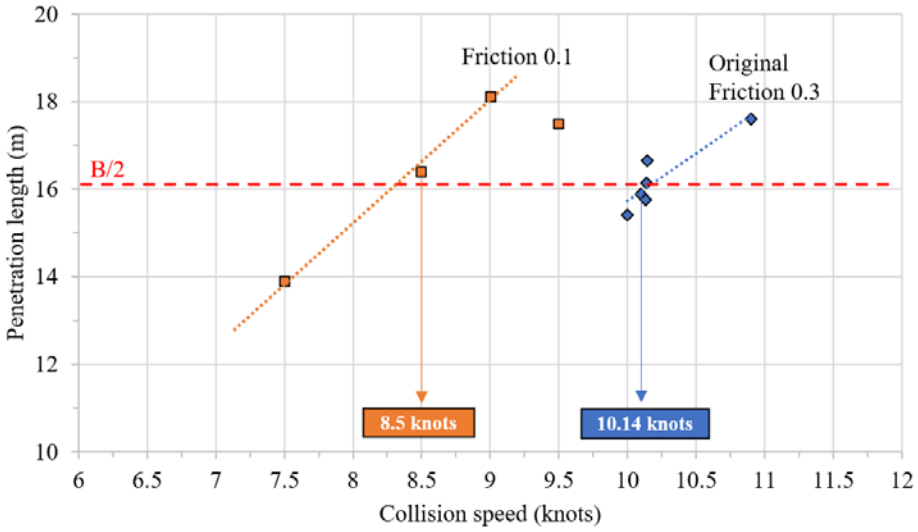

Figure 7.13 Pre-simulation results for collision speed findings with two different friction coefficients

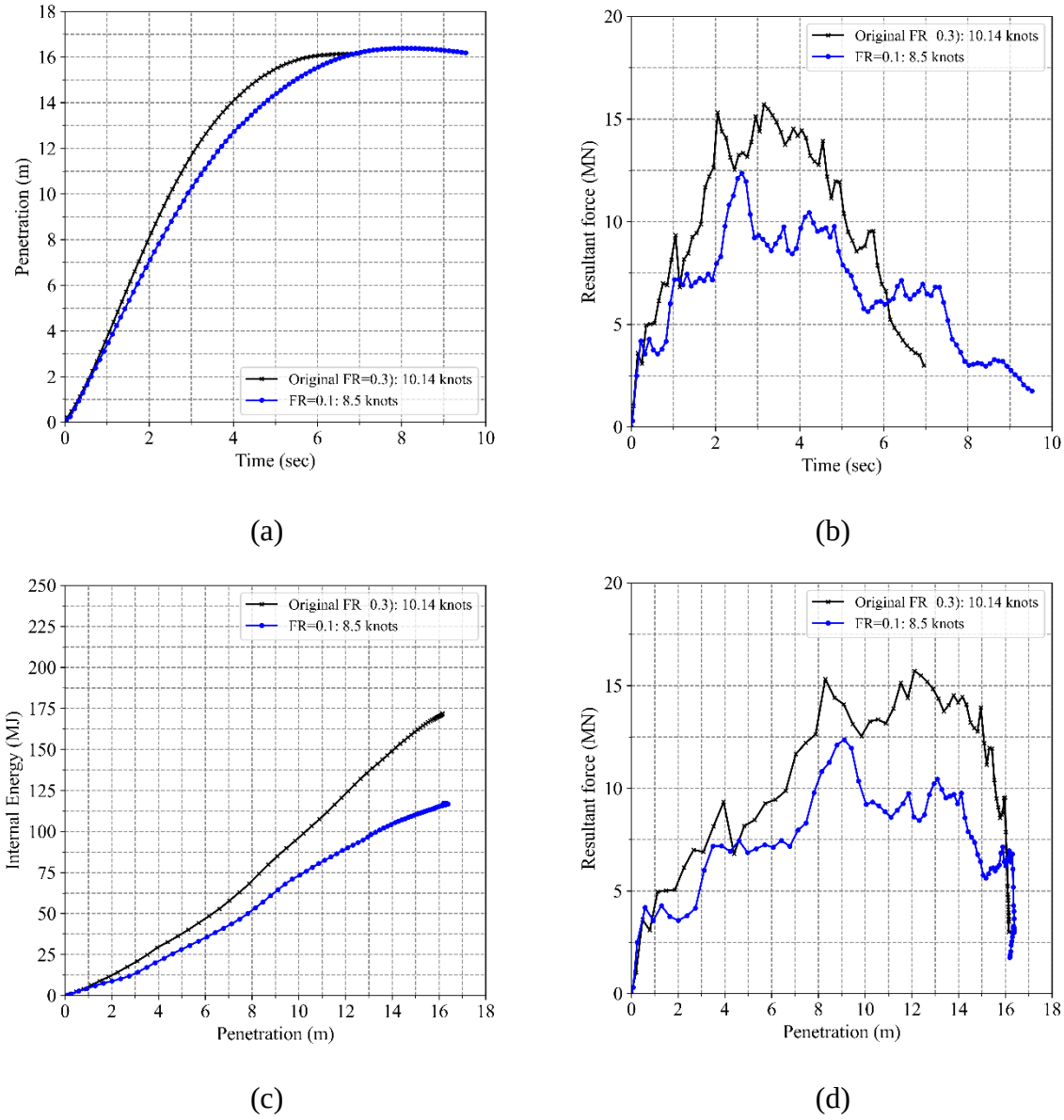

Figure 7.14 Simulation results for the different collision speeds resulting in B/2 penetration : (a) Penetration vs time, (b)Resultant force vs time, (c) Internal energy vs Penetration graph and (d) Resultant force vs penetration graph at corresponding collision speeds

7.4.2 Results and Discussion

Table 7.7 shows the first simulation results of the different friction coefficients at the same collision speed of 10.14 knots. The deeper penetration by 4.25 m was observed for FR=0.1 compared to FR=0.3. This clearly shows the effect of the friction coefficient on the collision simulations. On the other hand, Table 7.8 and Figure 7.15 summarise the simulation results for each RCO obtained from the proposed analysis approach using different collision speeds resulting in B/2 penetration. The simulations for RCO4 and RCO12 showed almost the same results as the original calculation with only 0.3 ~ 0.4 m differences, which is relatively small

when the element size of 0.175 m for the struck ship is considered. The simulation results for RCO11 with FR=0.1 showed less penetration than FR=0.3 by 1.5m, but it seems to be reasonably acceptable because the coefficient of variation was only 11 %. Regarding RCO14, which is the simulation with a hull of 50 mm thickness, no opening was observed for all RCO14 cases.

Table 7.7 Penetration results at three different material stress-strain curves– using the same collision speed

Layout	Maximum Penetration (m)		Average (m)	Standard Deviation (m)	Coefficient of Variation
	Original FR = 0.3	FR = 0.1			
	Collision speed of 10.14 knots				
Original Layout	**16.15**	20.40	18.28	3.01	16%

Table 7.8 Penetration results at two different friction coefficients – using collision speeds resulting in B/2 penetration

Layout	Maximum Penetration (m)		Average (m)	Standard Deviation (m)	Coefficient of Variation
	Original FR = 0.3	FR = 0.1			
	10.14 knots(*)	8.5 knots(*)			
Original Layout	**16.15**	16.40	16.28	0.18	1%
RCO4	**12.51**	12.90	12.71	0.28	2%
RCO11	**10.46**	8.93	9.70	1.08	11%
RCO12	**6.61**	6.31	6.46	0.21	3%
RCO14	**0.00** (*)	0.00 (*)	0.00	0.00	0%

(*) Collision speeds resulting in B/2 transverse penetration

(**) No penetration on the outer hull occurred with only indentation

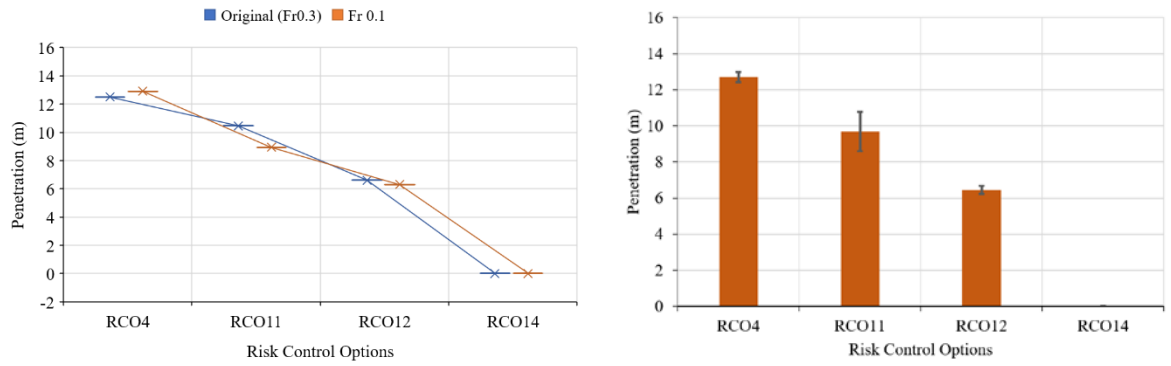

(a) (b)

Figure 7.15 Friction coefficients effects of each RCO: simulation results for (a) all cases and (b) mean values and standard deviations

In general, the simulation results based on the proposed approach gave excellent consistency to each other, showing variation coefficients between 0 and 11 % for simulations of the different layouts. This also proves that the proposed methodology compensates for the traditional direct analysis approach and generates reliable results for different friction coefficients.

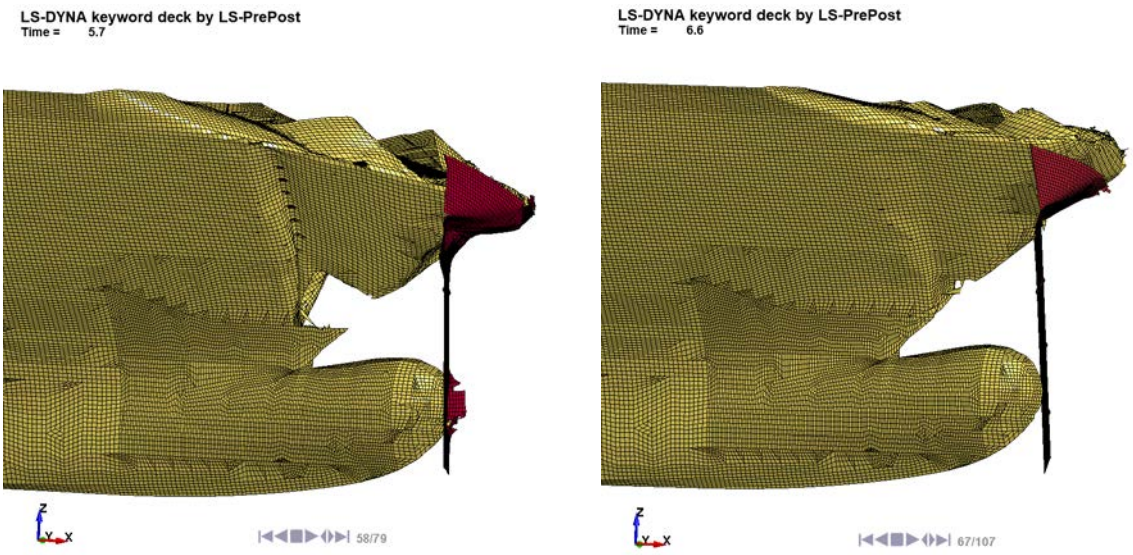

(a) ROC4 / FR=0.3 (b) ROC4 / FR=0.1

Figure 7.16 RCO4 penetration results for the different friction coefficients based on the different collision speeds resulting in B/2

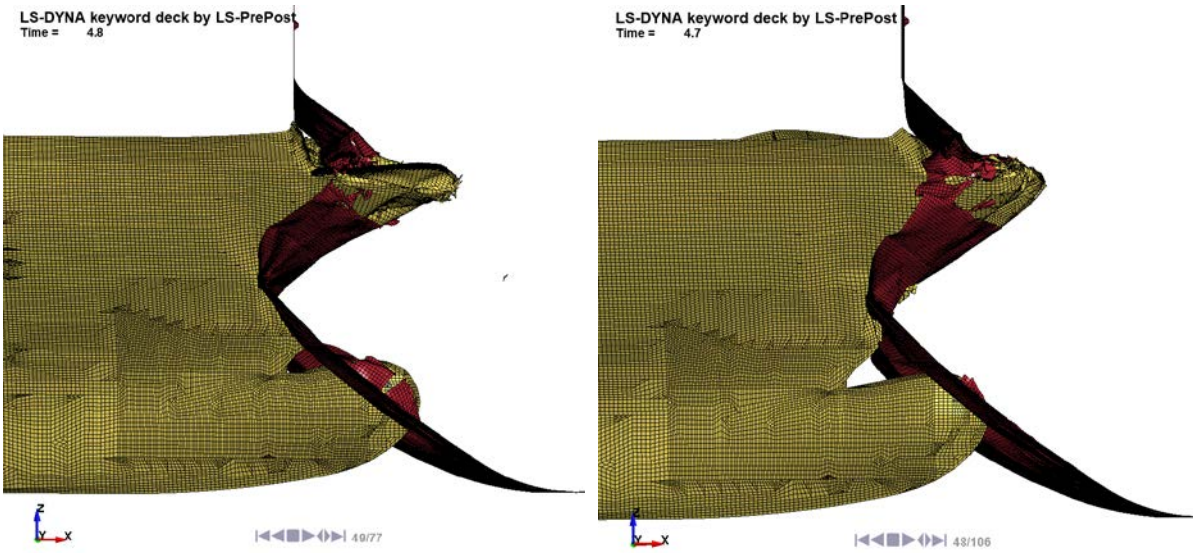

(a) RCO11 / FR=0.3 (b) RCO11 / FR=0.1

Figure 7.17 RCO11 penetration results for the different friction coefficients based on the different collision speeds resulting in B/2

7.5 Effects of Rigid striking bodies

7.5.1 Analysis Description

For most crash simulations, a striking ship is generally treated as a rigid body due to its robust structure, but penetration results by the rigid body are relatively higher than a deformable body. In particular, at high collision speeds, the foremost part above a bulbous bow of the deformable striking body has significant damage, leading to reduced transverse penetration. Therefore, the deepest penetration point may be a ship's foremost point or a bulbous bow's tip, depending on the damages of the striking ship by collision speeds or material model definition, as previously observed in Figure 7.6.

Thus, for the effects of the rigid body, the identical collision simulations in the different fracture strains in Section 7.2 were carried out using a rigid striking bow. Firstly, simulations for the original layout were performed again to find a collision speed because the previous original collision speed of 10.14 knots was obtained by the deformable striking bow. Then, using that collision speed, additional simulations were conducted for each different failure strain to identify the effects of rigid body bow on collision analysis. As the second step, the simulations based on the proposed analysis methodology were followed by finding collision speeds for each case. A series of pre-simulations with different fracture stains were repeatedly carried out to find each collision speed resulting in the penetration depth of B/2.

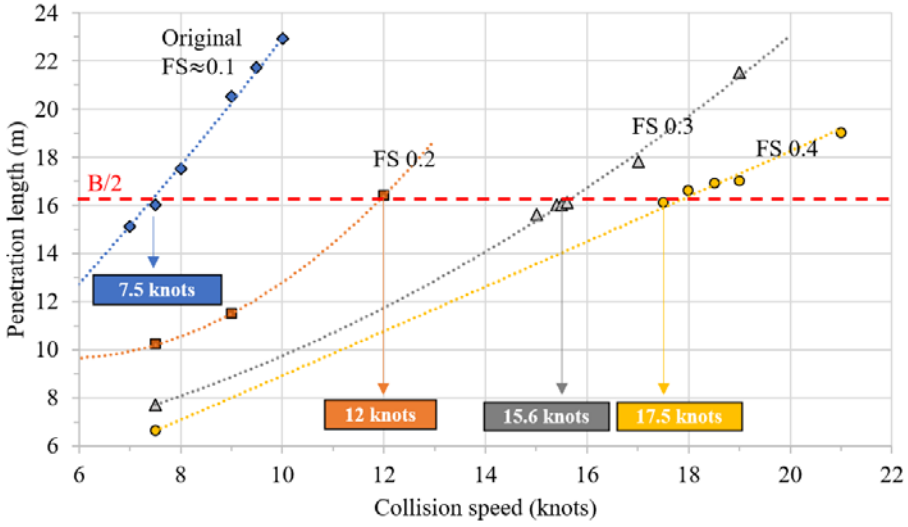

Figure 7.18 Rigid bow: Pre-simulation results for collision speed findings with four different fracture criteria

Figure 7.18 shows the results of pre-simulations for four different failure strains. The collision speed of 7.5 knots was obtained from the simulations for the original layout, while the collision simulation with FS=0.2 required 12 knots for half-breadth damage. The collision speeds of

15.6 knots and 17.5 knots were also obtained for simulations with FS=0.3 and FS=0.4, respectively. Compared to the collision speeds of the deformable striking bow, relatively low speeds were observed for the B/2 penetration (See Figure 7.2). Since the struck ship is solely absorbed the total collision energy during collisions with the rigid striking bow, much more structures in the struck ship are damaged by the concentrated energy. This means that less collision energy (i.e., low collision speed) is required for B/2 penetration at the simulation with a rigid striking bow, as shown Figure 7.19.

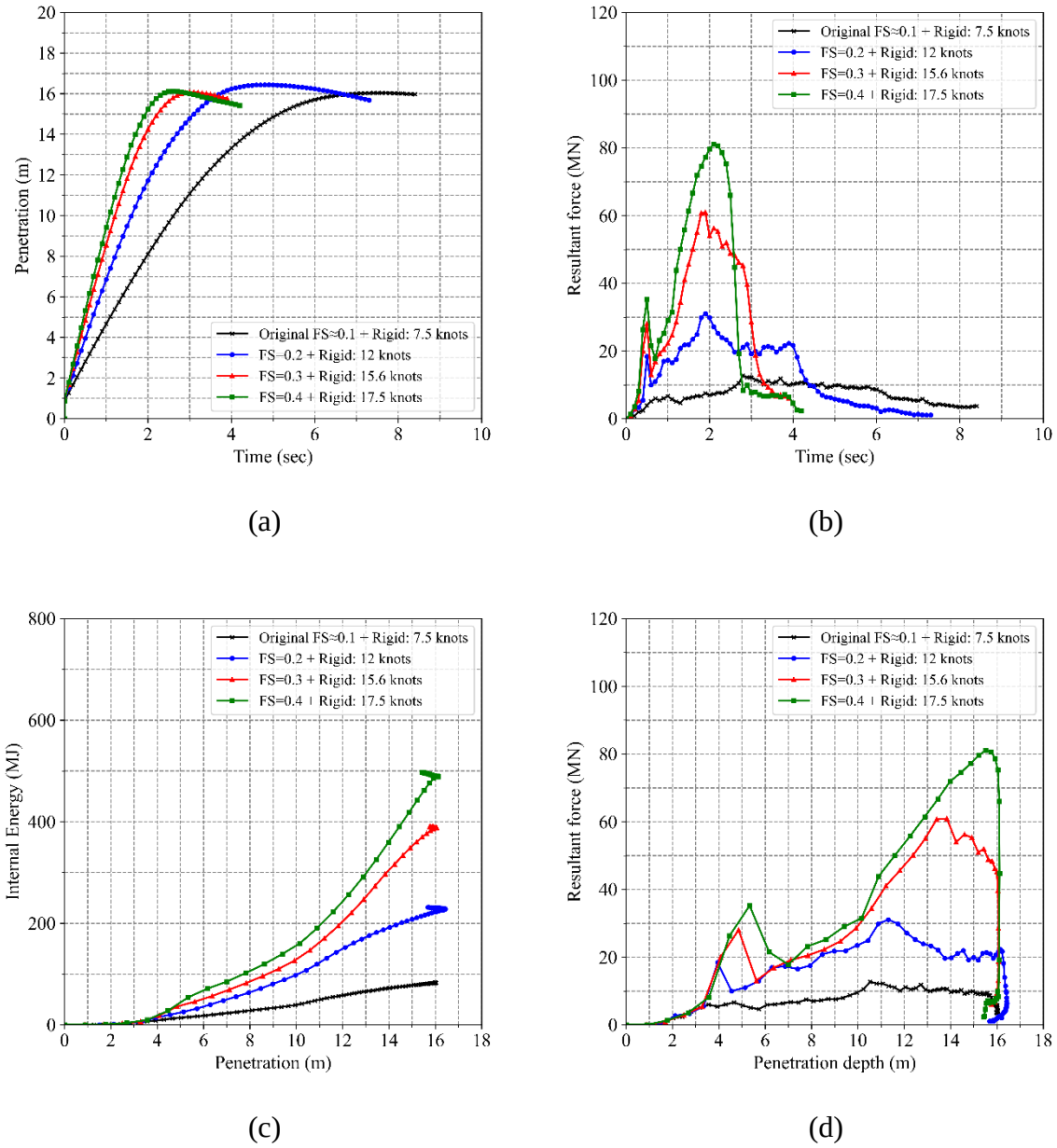

Figure 7.19 Simulation results for the different collision speeds resulting in B/2 penetration : (a) Penetration vs time, (b)Resultant force vs time, (c) Internal energy vs Penetration graph and (d) Resultant force vs penetration graph at corresponding collision speeds

7.5.2 Results and Discussion

Table 7.9 shows the penetration results achieved from the simulations of the different failure strains using the same collision speed of 7.5 knots. Compared to the original penetration of 16.00 m, significant changes in penetrations by 5.8 ~ 9.39 m were observed. This confirms the effects of failure criteria. These results also imply that outcomes from simulations with a direct approach may be unreliable depending on the simulation assumptions.

Table 7.9 Rigid bow: Penetration results– using the same collision speed of 7.5 knots

Layout	Maximum Penetration (m)				Average (m)	Standard Deviation (m)	Coefficient of Variation
	Original FS≈0.1	FS=0.2	FS=0.3	FS=0.4			
	Collision speed of 7.5 knots						
Original Layout	**16.00**	10.20	7.70	6.61	10.13	4.19	41%

Table 7.10 summarises the results of collision simulations with a rigid striking bow calculated based on the proposed analysis approach. RCO4 showed almost identical results to each other with only a coefficient of variation of 1%. The simulation results for RCO11 and RCO12 were also in good agreement with each other, presenting low standard deviations and low coefficient of variations. Overall, the simulation results with a rigid bow gave reliable outcomes, showing similar trends from RCO4 to RCO14 for each fracture strain, as shown in Figure 7.20 (a) and (b) with small variation coefficients.

Table 7.10 Rigid bow: Penetration results – using the different collision speeds for each simulation with the different fracture strain

Layout	Maximum Penetration (m)				Average (m)	Standard Deviation (m)	Coefficient of Variation
	Original FS≈0.1	FS0.2	FS0.3	FS0.4			
	7.5 knots(*)	12 knots(*)	15.6 knots(*)	17.5 knots(*)			
Original Layout	**16.00**	16.40	16.07	16.03	**16.13**	**0.19**	**1%**
RCO4	**15.60**	15.80	16.00	16.01	15.85	0.19	1%
RCO11	**11.20**	12.50	13.50	13.40	12.65	1.07	8%
RCO12	**9.72**	11.10	12.00	11.40	11.06	0.97	9%
RCO14	**0.00 (*)**	0.00 (*)	0.00 (*)	0.00 (*)	0.00	0.00	0%

(*) Collision speeds resulting in B/2 transverse penetration

(**) No penetration on the outer hull occurred with only indentation

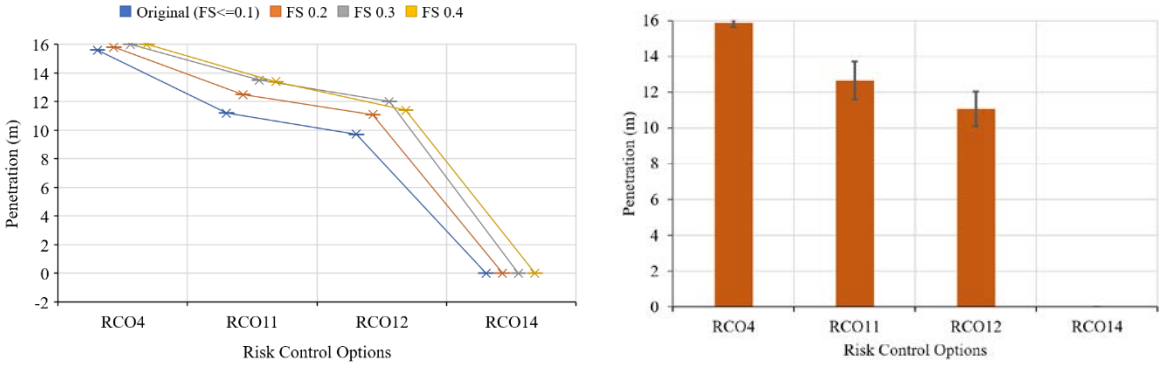

(a) (b)

Figure 7.20 Rigid bow effects of each RCO: simulation results for (a) all cases and (b) mean values and standard deviations

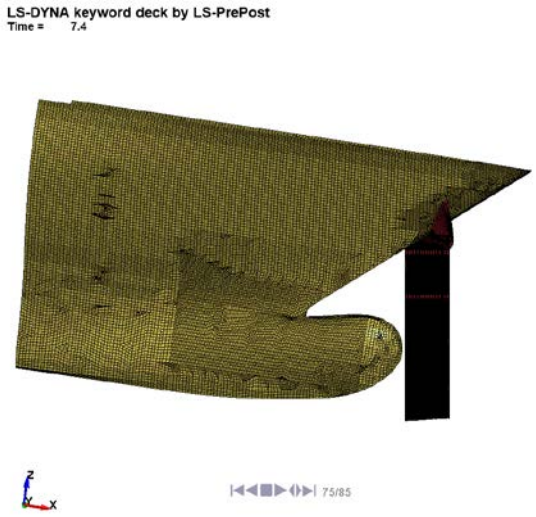

(a) RCO4 / FS=0.1

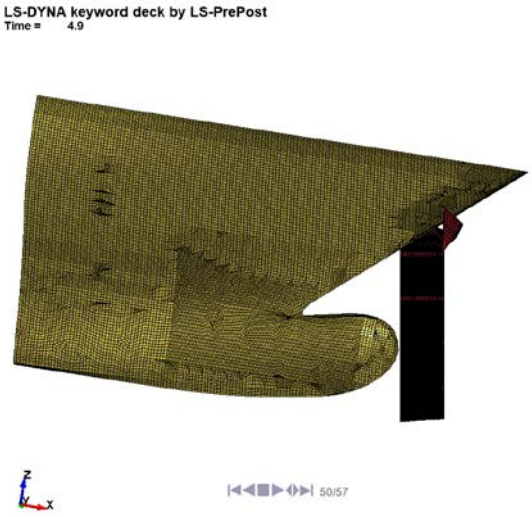

(b) RCO4 / FS=0.2

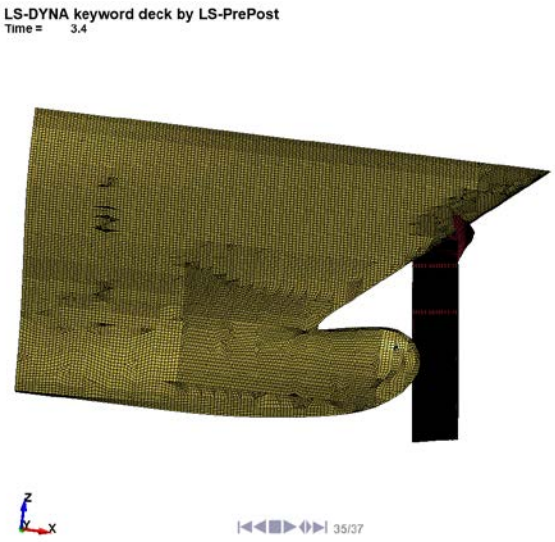

(c) RCO4 / FS=0.3

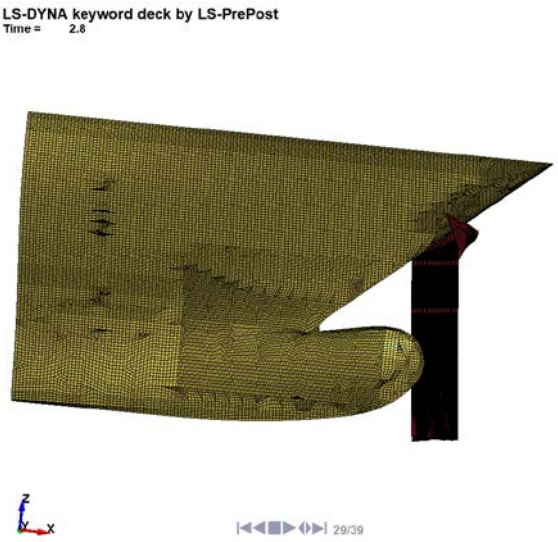

(d) RCO4 / FS=0.4

Figure 7.21 RCO4 penetration results with a rigid striking bow based on the different collision speeds

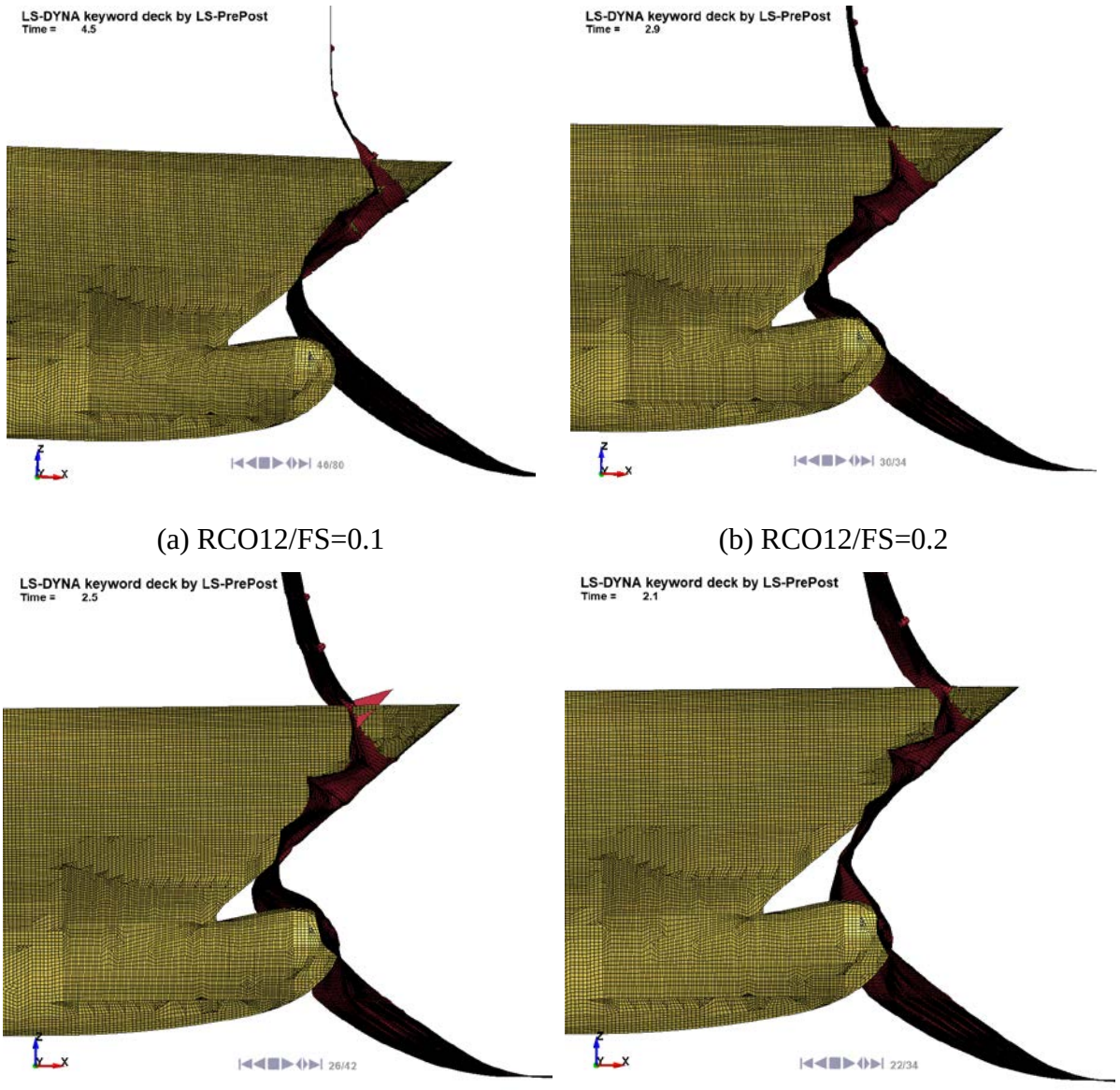

(a) RCO12/FS=0.1 (b) RCO12/FS=0.2

(c) RCO12/FS=0.3 (d) RCO12/FS=0.4

Figure 7.22 RCO12 penetration results with a rigid striking bow based on the different collision speeds

However, as shown in Figure 7.21 for RCO4 simulations, the rigid striking bow damaged only the upper part of the B/5 bulkhead, but the rest parts remained undamaged. Additionally, regarding simulation results for RCO11 and RCO12, the penetration reduction effect by hull thickness increase from RCO11 to RCO12 (i.e., from 20T hull to 30T hull) seemed to be underestimated compared with the results from the deformable bow in Section 7.2. Figure 7.22 shows that similar damage patterns among different fracture strains were observed. Therefore, the deformable and rigid bow application should be carefully investigated for the present proposed methodology. A detailed discussion between deformable and rigid body bow simulations was

given in the next Section 7.5.3.

7.5.3 Comparison between Deformable and Rigid Bow

Generally, the rigid striking bow is more often adopted in collision simulations as it saves calculation time and provides more conservative results. However, recent research (Hogström and Ringsberg, 2012, Ko et al., 2018a) show significant gaps between the deformable and rigid collision in terms of penetrations. It was also observed in pre-simulation results from the sensitivity study, as shown in Figure 7.23. While the deformable bow penetrated 16.15m at the simulation with FS≈0.1 and 10.14 knots collision speed, the rigid bow simulation with FS≈0.1 resulted in 23m penetration at the same speed. Similarly, for simulations with FS=0.2, 8m penetration was obtained from the deformable bow collision at 10.14 knots, whilst the rigid bow collision was estimated at approximately 13m. These calculation results were clearly distinguished when the same collision speeds were employed in the simulations. However, from the simulations based on the proposed analysis approach, the difference between the deformable and rigid bow simulations is not explicitly distinguished because the relative collision speeds, resulting in B/2 penetration, compensate for result gaps from various parameters. Therefore, several analysis data and graphs, such as the comparison results, resultant force and penetration graph, and actual simulation figures, were used to find out the effects of rigid and deformable bows.

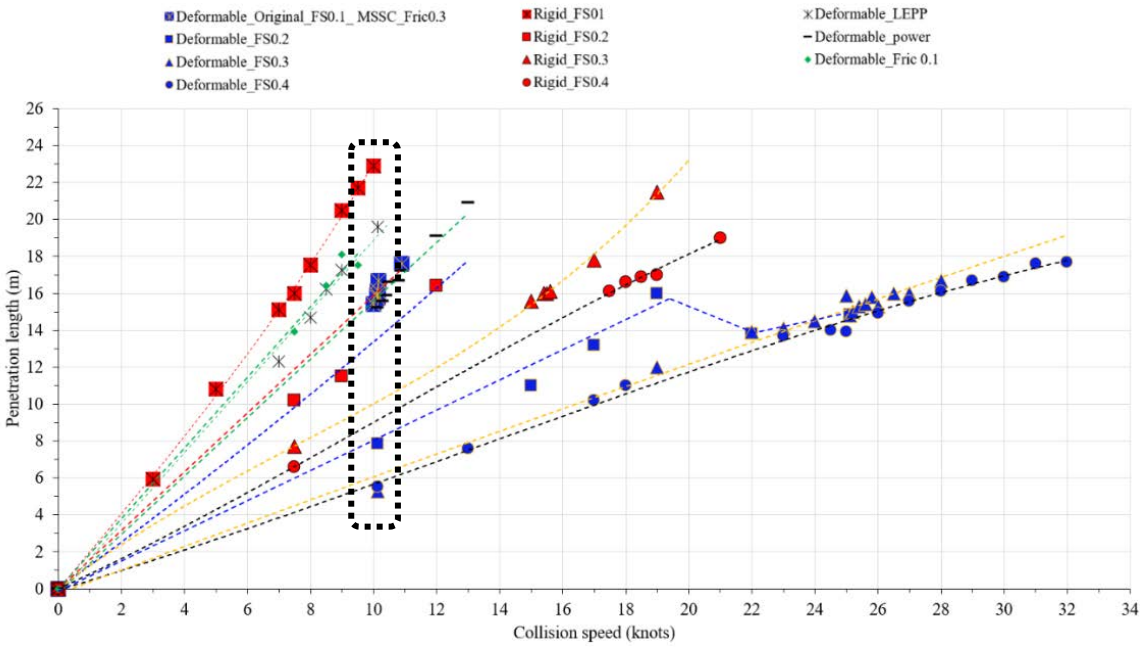

Figure 7.23 Simulation results of collision speed selections for the sensitivity study

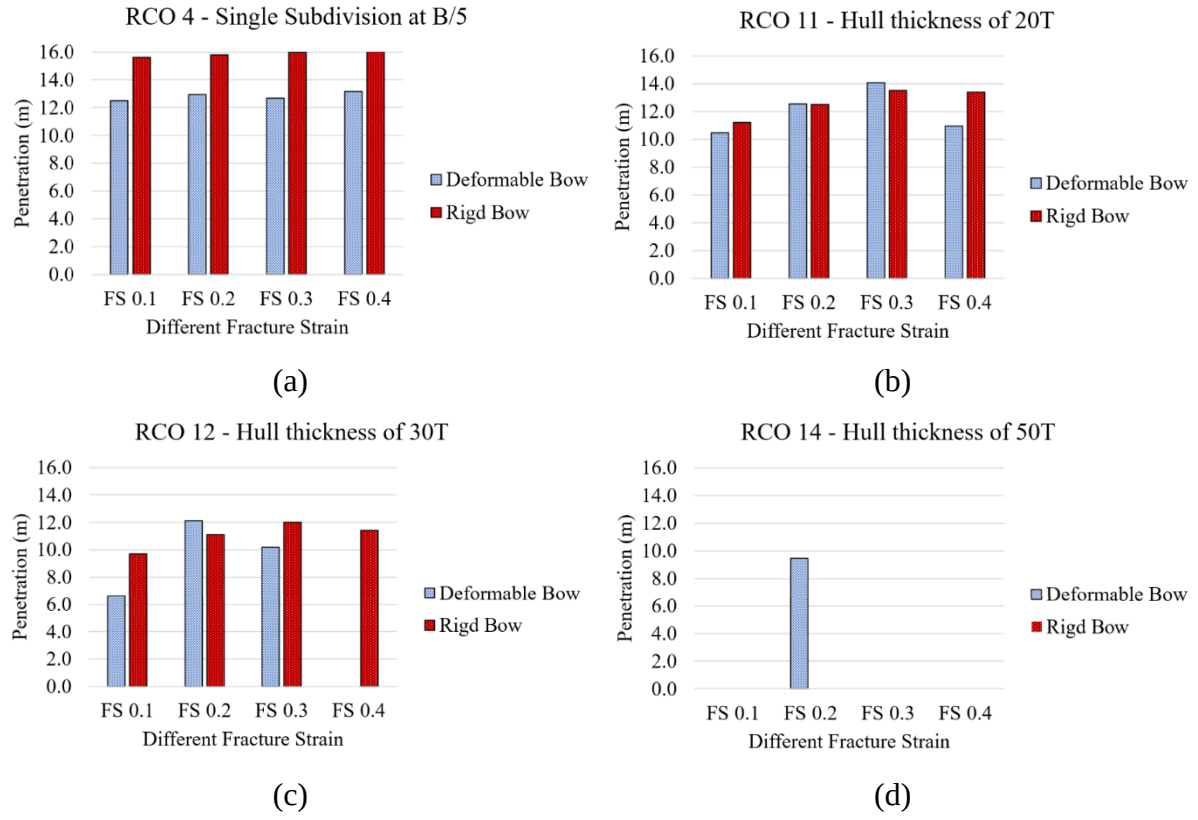

Figure 7.24 Penetration comparison depending on the different fracture strains for each RCO: (a) RCO4, (b) RCO11, (c) RCO12 and (d) RCO14

Figure 7.24 summarises the overall penetration results for the different fracture strains and RCOs, and the penetrations by the deformable bow are compared with those by the rigid body. Generally, rigid bow simulations show linear and predictable results, while some abnormal outcomes are observed in the deformable simulations. For more detailed comparisons, the resultant forces-penetration graphs in Figure 7.25 are used for the simulation results of the original arrangement with a deformable and a rigid bow. For the rigid bow simulation with FS = 0.2, which is indicated as the dotted blue line in the graph, the first hull fracture occurred on the upper part of the hull when the bow penetrated by 4.0m into the struck ship (See Figure 7.25(a)). Then, the bulbous bow collided with the lower outer hull at total penetration of 10.4 m after a further 6.4m penetration from the first hull fracture (i.e., 10.4m – 4m =6.4m), as shown in Figure 7.25 (b). This is the exact distance between the foremost tip of the striking ship and its bulbous bow (See in Figure 7.26). Then, the tip of the stem reached B/2 after further penetration of 5.8m. This collision procedure with the rigid bow is very clear and predictable. Similar collision procedures were also observed in other rigid simulations for FS=0.1, FS=0.3 and FS=0.4, but the first hull damage initiations were delayed with longer penetrations when the fracture strain values were increased, which means the hull structures were stretched more

due to higher fracture strain values.

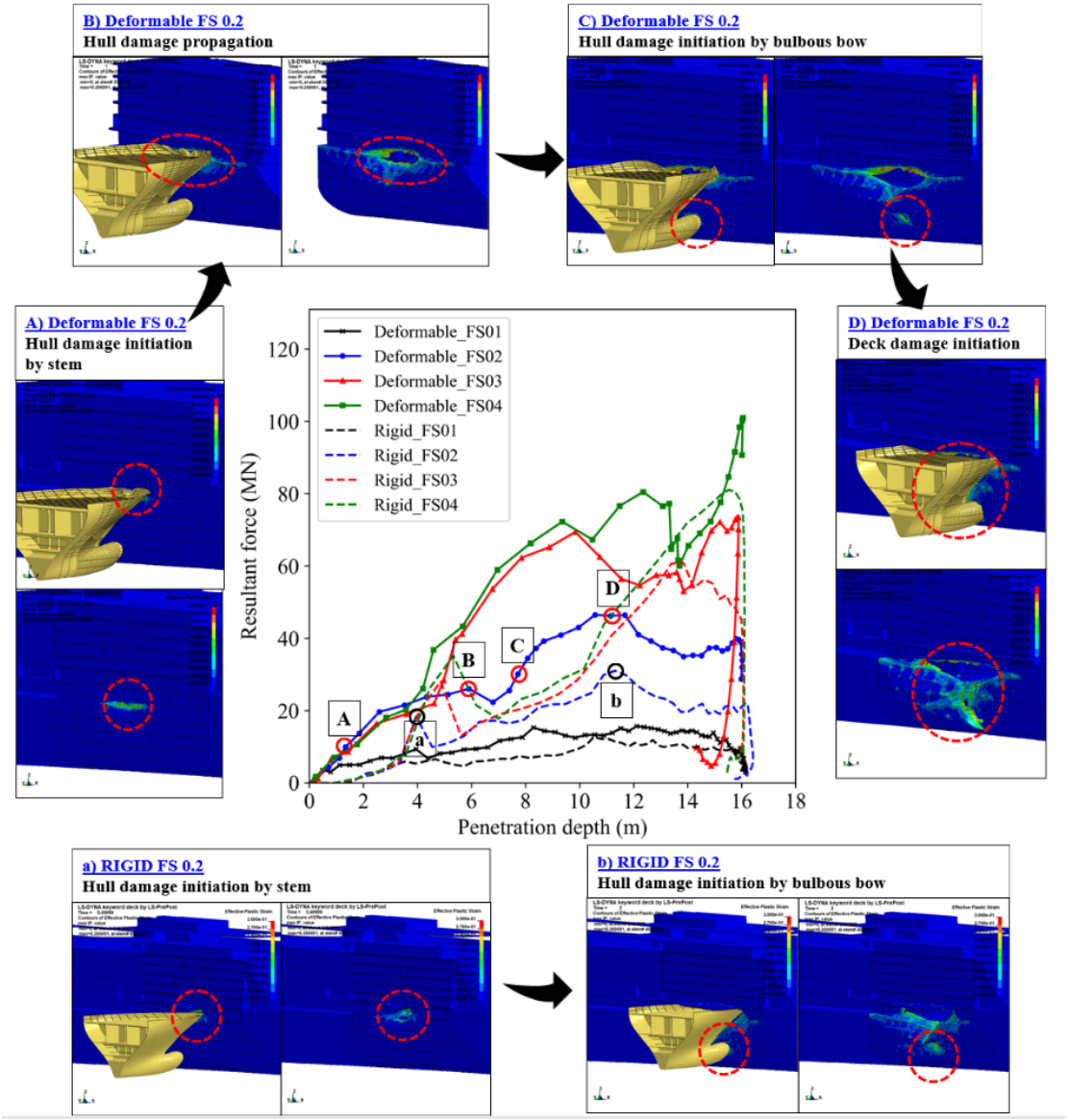

Figure 7.25 The relation of Resultant forces and penetration for the original layout with simulation status

On the other hand, the collision with the deformable bow showed the unpredictable process due to deformations of both striking and struck bodies. The deformable striking bow damaged the upper part of the outer shell of the hull at 2.6m penetration, as shown in Figure 7.25 (A). Then, the bulbous bow of the striking ship collided with the struck hull when the total penetration of the striking ship was 8m (See Figure 7.25 (C)). This is 2.4m earlier than the rigid bow penetration of 10.4m because the tip of the stem part of the deformable bow was squashed and pushed behind during the collision. So, the deeper maximum penetration could not be achieved. After that, the resultant force of the deformable collision reached the peak at 11.5m penetration in Figure 7.25 (D), and all decks at collision regions were finally broken up. This

means the deformed bow part required more energy to damage all decks after the bulbous bow collision, whilst the maximum resultant force of the rigid bow was when the bulbous bow broke through the hull because the stem of the rigid bow damaged all decks at the same time. Interestingly, due to the deformation effects, the maximum penetrations were observed at the tip of the bulbous bow for a deformable bow collision, in contrast to the rigid collision in which the foremost point of the stem part made the maximum penetration, as shown in Figure 7.27.

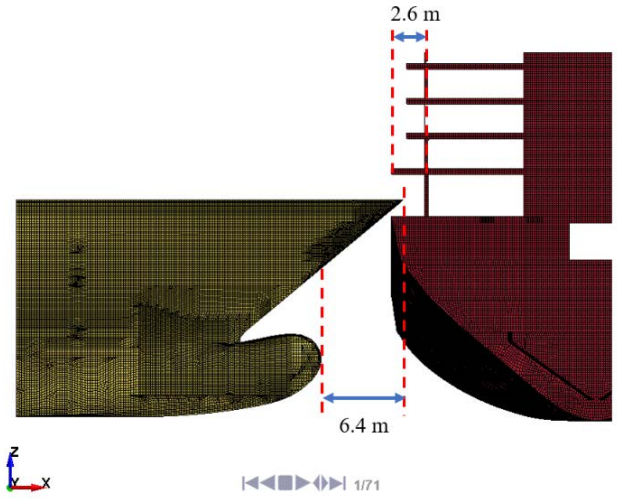

Figure 7.26 Striking and stuck ship geometries

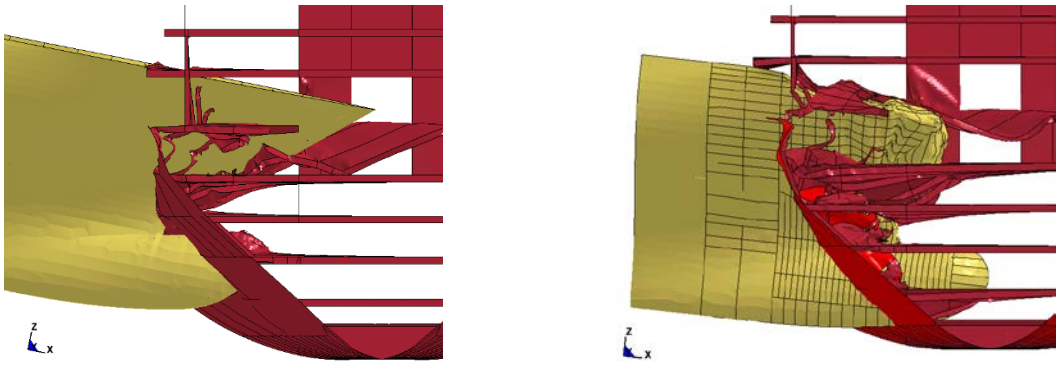

(a) (b)

Figure 7.27 The moment of the maximum penetration of B/2 from (a)rigid bow and (b) deformable bow collisions at the initial layout with 0.2 fracture strain

The resultant force-penetration graphs in Figure 7.28 more clearly show the differences between the rigid and deformable bow collisions. It compares resultant force graphs for the original layout and RCO11 arrangement (i.e., longitudinal subdivisions added at B/5 of the original). The resultant forces from deformable bow collisions dramatically increased when the bow started to strike the B/5 bulkhead until the bulbous bow made openings on the hull. It was marked with shadows in black for FS=0.1, blue for FS=0.2 and red for FS=0.3 in Figure

7.28(b), representing the period of the deformable bow collision with the B/5 bulkhead. On the other hand, the rigid forces in dotted lines show no significant difference between the original and RCO11. This proves that the simulations with a rigid bow cannot properly capture the collision phenomena with the B/5 longitudinal bulkhead, as discussed in Section 7.5.2 and Figure 7.21.

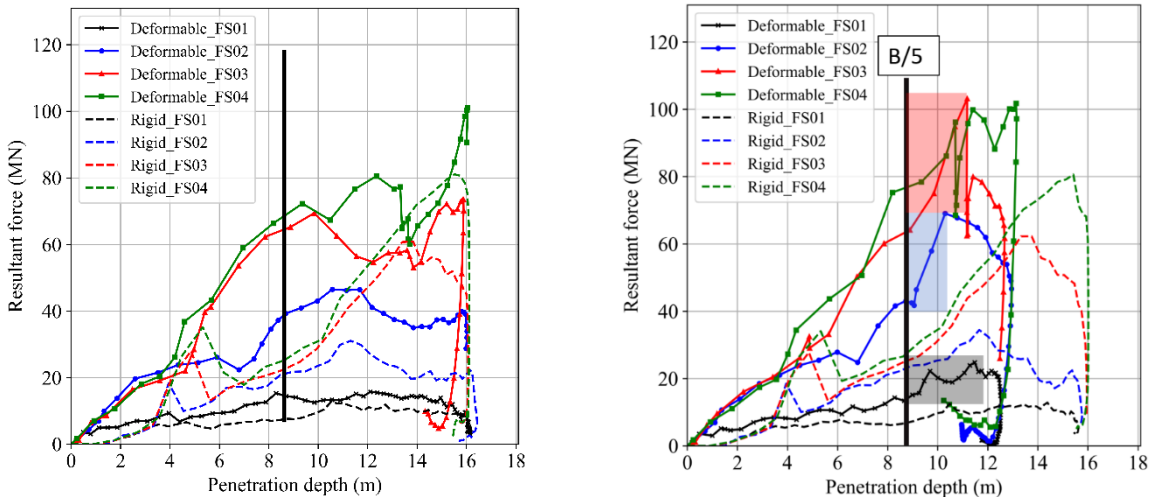

(a) Original (b) RCO4

Figure 7.28 The differences between deformable and rigid bow effects for RCO4 (B/5 Subdivision)

Figure 7.29 illustrates the graphs of resultant forces between the original layout and RCO11/12/14 arrangement (i.e., hull thicknesses increased to 20T, 30T and 50T, respectively, compared to the original). As soon as the deformable striking bow collided with the outer shell of the struck ship hull, the resultant forces of deformable bow collisions dramatically increased (See the solid lines in blue shadow in Figure 7.29(b),(c), and (d)). On the other hand, the resultant forces from the rigid bow, as marked in red shadow in dotted lines, show no significant increase compared to the original, but only small rises were observed.

Based on the above analyses, the following recommendations and conclusions can be drawn. Firstly, if the rigid striking bow is adopted for collision simulations, the locations of longitudinal subdivisions and their contributions to the collisions should be carefully investigated. Otherwise, it is recommended to employ the deformable bow even though it may give a few fluctuated results. Secondly, for collision simulations employing a hull thickness measure, rigid bow simulations are likely to underestimate the effects of structural hull strength. Therefore, it is recommended to adopt a deformable bow for those collision simulations for more precise results.

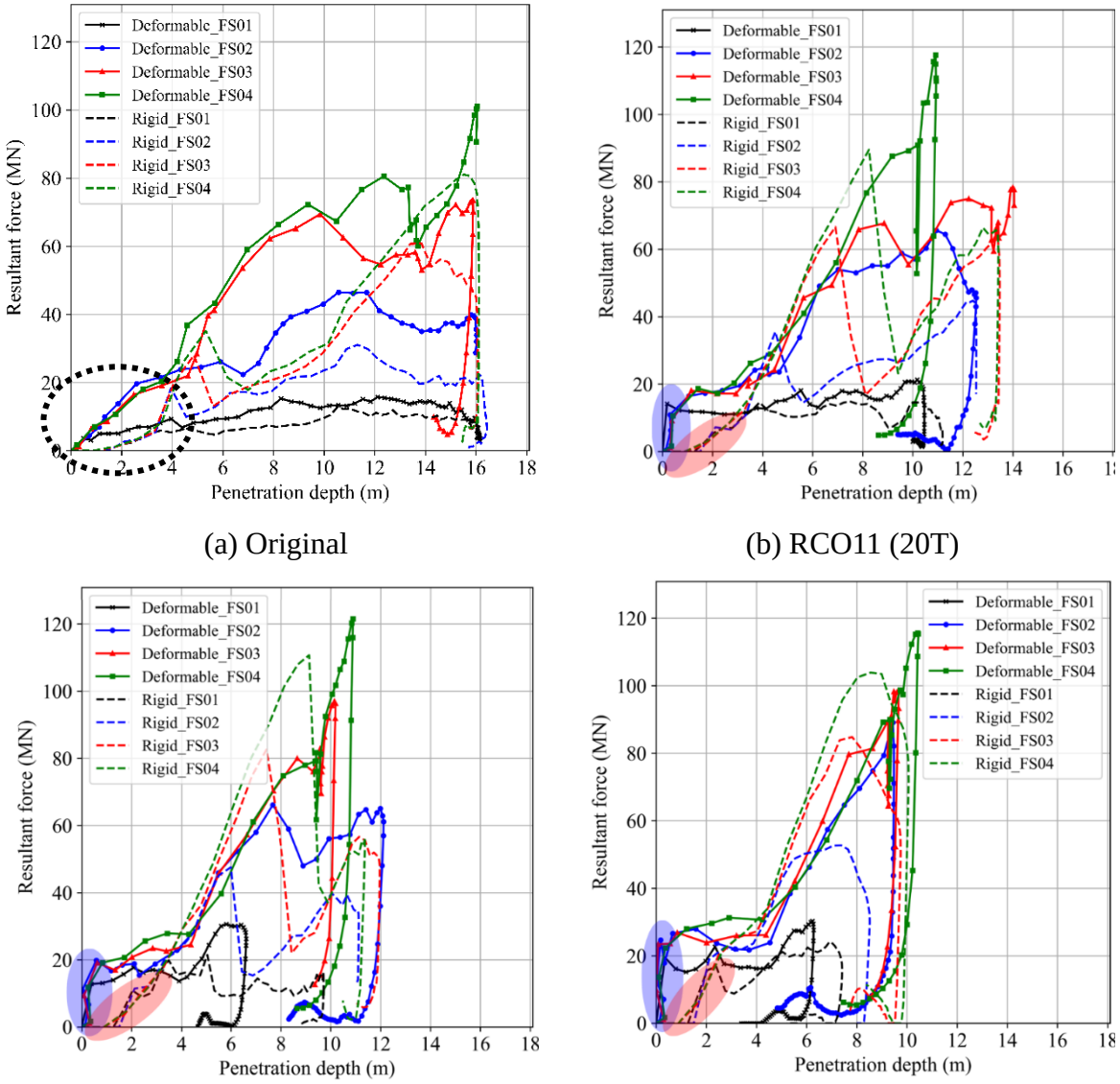

(a) Original

(b) RCO11 (20T)

(c) RCO12 (30T)

(d) RCO14 (50T)

Figure 7.29 The differences between deformable and rigid bow effects for RCO11 (B/5 Subdivision)

In conclusion, the resultant detailed force-penetration graphs proved that the deformable body collisions more accurately capture the structural behaviours during collisions than the rigid bow collisions, especially for the different RCO arrangements. Therefore, adopting the deformable bow for the proposed methodology is strongly recommended.

7.6 Overall Sensitive Parameter Results

Table 7.11 and Table 7.12 summarise all results calculated from the traditional and the proposed analysis approach (i.e. identical collision speed vs relative collision speed) for the simulations with the different parameters in the previous sections. From them, the reliability of the proposed

analysis approach can be relatively compared to others, identifying the gaps as the design margins. When the identical collision speed was used for the simulations as the traditional analysis approach, the average penetration deviated from the original result by 5.3 m. In contrast, the differences between the original and the average penetrations are below 1.8 m.

Table 7.11 All penetration results calculated based on the traditional analysis approach for collision simulations when the different parameters are applied

Layout	Maximum Penetration (m)											Average (except original result) (m)	Difference from Original (m)
	Deformable Bow							Rigid Bow					
	Original FS =0.1	FS =0.2	FS =0.3	FS =0.4	LEPP curve	Power law	FR =0.1	FS =0.1	FS =0.2	FS =0.3	FS =0.4		
	Collision speed of 10.14 knots												
Original Layout	**16.2**	7.9	5.3	5.5	15.2	19.6	20.4	10.2	7.7	6.6	10.1	**10.85**	**-5.3**

Table 7.12 All penetration results calculated based on the proposed analysis approach for collision simulations when the different parameters are applied

Layout	Maximum Penetration (m)											Average (except original result)	Diff. from Original (m)
	Deformable Bow							Rigid Bow					
	Original FS =0.1	FS =0.2	FS =0.3	FS =0.4	LEPP curve	Power law	FR =0.1	FS =0.1	FS =0.2	FS =0.3	FS =0.4		
	10.1 kn(*)	19.0 kn(*)	25.0 kn(*)	28.0 kn(*)	8.5 kn(*)	10.4 kn(*)	8.5 kn(*)	7.5 kn(*)	12.0 kn(*)	15.6 kn(*)	17.5 kn(*)		
Original Layout	**16.2**	16.0	15.9	16.1	16.2	15.9	16.4	16.0	16.4	16.1	16.0	**16.1**	**0.2**
RCO4	**12.5**	13.0	12.7	13.2	13.6	10.4	12.9	15.6	15.8	16.0	16.0	**13.8**	**1.3**
RCO11	**10.5**	12.5	14.1	10.9	10.9	9.5	8.9	11.2	12.5	13.5	13.4	**11.6**	**1.1**
RCO12	**6.6**	12.1	10.2	0.0	7.1	6.4	6.3	9.7	11.1	12.0	11.4	**8.4**	**1.8**
RCO14	**0.0**	9.5	0.0	0.0	0.0	0.0	0.0	0.0	0.0	0.0	0.0	**0.9**	**0.9**

(*) Collision speeds in knots resulting in B/2 transverse penetration

As described in previous Section 7.5, rigid bow simulations have not enough captured the crashworthy structural responses compared to those using a deformable bow. Therefore, it would be reasonable to eliminate those results from the overall evaluations. Additionally, the modified trimmed mean method (Arulmozhi, 2009) is employed for data filtering to obtain reliable data. In this method, also called the Olympic average (Peterson, 2012), the highest and the lowest figures are taken out, and the remaining values from the data are used to achieve a

more robust average, as shown in Figure 7.3, as marked with dotted red circles.

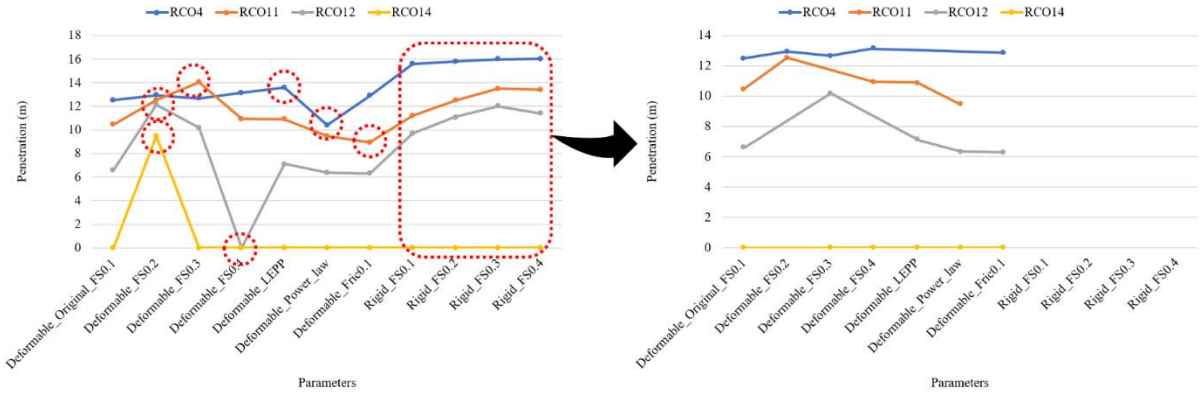

Figure 7.30 Data filtering for the reliable results

Table 7.13 All penetration results calculated based on the traditional analysis approach for collision simulations when the different parameters are applied

Layout	Maximum Penetration (m)											Average (except original result) (m)	Diff. from Original (m)
	Deformable Bow							Rigid Bow					
	Original FS =0.1	FS =0.2	FS =0.3	FS =0.4	LEPP curve	Power law	FR =0.1	FS =0.1	FS =0.2	FS =0.3	FS =0.4		
	Collision speed of 10.14 knots												
Original Layout	**16.2**	7.9	-	5.5	15.2	19.6	-	-	-	-	-	**12.05**	**-4.1**

Table 7.14 All penetration results calculated based on the proposed analysis approach for collision simulations when the different parameters are applied

Layout	Maximum Penetration (m)											Average (except original result)	Diff. from Original (m)
	Deformable Bow							Rigid Bow					
	Original FS =0.1	FS =0.2	FS =0.3	FS =0.4	LEPP curve	Power law	FR =0.1	FS =0.1	FS =0.2	FS =0.3	FS =0.4		
	10.1 kn(*)	19.0 kn(*)	25.0 kn(*)	28.0 kn(*)	8.5 kn(*)	10.4 kn(*)	8.5 kn(*)	7.5 kn(*)	12.0 kn(*)	15.6 kn(*)	17.5 kn(*)		
Original Layout	**16.2**	16.0	-	16.1	16.2	15.9	-					**16.1**	**0.1**
RCO4	**12.5**	13.0	12.7	13.2	-	-	12.9	-	-	-	-	**12.9**	**0.4**
RCO11	**10.5**	12.5	-	10.9	10.9	9.5	-	-	-	-	-	**11.0**	**0.5**
RCO12	**6.6**	-	10.2	-	7.1	6.4	6.3	-	-	-	-	**7.5**	**0.9**
RCO14	**0.0**	-	0.0	0.0	0.0	0.0	0.0	-	-	-	-	**0.0**	**0.0**

(*) Collision speeds in knots resulting in B/2 transverse penetration

Table 7.13 and Table 7.14 show the trimmed data. The differences between the original and the modified average penetration results now become more practical and smooth, indicating a more realistic picture. Regarding the trimmed data of the proposed analysis approach, the RCO4, RCO11 and RCO14 show high consistency with a below 0.5m gap. RCO12 with a 30T hull thickness increase also gives good agreement with the original penetration, showing only a 0.9 m difference (See Table 7.14). On the other hand, in the case of trimmed data achieved from the identical collision speed, as shown in Table 7.13, a significant difference in penetration with 4.1m is still observed.

Overall, the simulation results obtained from the proposed analysis approach show more reliable outcomes compared to the traditional method in terms of maximum penetration. However, for consideration of design effects, approximately a 5% design margin is recommended for RCOs with the longitudinal bulkheads, whilst a 10% design margin seems to be reasonable for RCOs associated with hull thickness increase. In particular, for the latter, more careful attention should be given to its structural behaviours due to deformable bow effects.

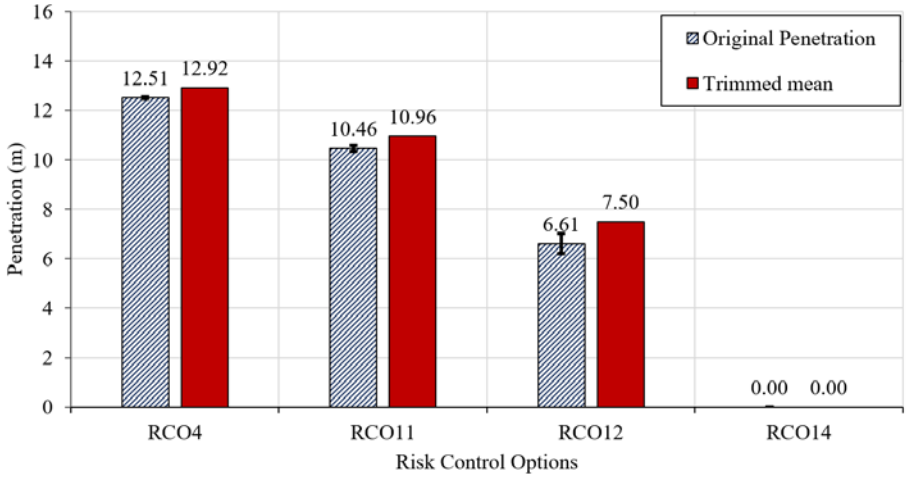

Figure 7.31 Summary of penetration differences between the original and the trimmed mean penetrations

7.7 Chapter Summary

This chapter addressed sensitivity studies for four different parameters: fracture strains effects, material curve effects, friction coefficient effects and striking bow rigidity effects. Additionally, four RCOs, such as RCO4, RCO11, RCO12 and RCO14, were adopted for the simulations to identify different structural arrangement effects. Firstly, as a traditional direct analysis, simulations with different parameters were carried out using an identical collision speed employed in the original simulation to identify parameter effects on simulations. Next, for the proposed analysis approach, a series of pre-simulations with the different parameters were repeatedly carried out to determine each collision speed resulting in the penetration length of B/2. Then, the same simulations were conducted based on the proposed analysis approach. The results were compared to the simulations from the traditional approach for parameter effects and to the original simulations to identify the reliability of this proposed method.

In the sensitivity study for fracture strain effects, the results for RCO4 by the proposed analysis approach showed a substantial level of agreement with the original failure strain case (i.e., FS≈0.1). On the other hand, the results of RCO11, RCO12 and RCO14 showed quite fluctuated outcomes. It is because the early damage on the striking body by the high-speed collisions affected the rest of the simulations. In particular, the sudden penetration for RCO14 with FS=0.2 was attributed to an opening on the hull at the final simulation stage instead of deep indentation.

Regarding the effects of the stress-strain material curve, the overall simulations from the relative collision speed demonstrated good consistency with the original penetration showing a variation coefficient of less than 13 %, whereas the simulation with the LEPP curve at the identical collision speed clearly showed the effects of the material curve on simulations with significant penetration difference by 3.45 m.

For friction coefficient effects, the simulation results gave an excellent consistency compared to the original, showing a less than 11 % variation coefficient when the simulations were carried out based on the proposed analysis approach. The simulation results from the different parameters for RCO 11 and RCO 12 were consistent with each other, resulting in penetration differences were less than 1m. For RCO14 with 50 mm hull thickness, no opening was observed for all material curves.

The simulation results with a rigid bow generally gave reliable outcomes. In particular, the penetrations from RCO4 to RCO14 showed similar trends with each other. However, from the detailed analysis, two problems were found: Firstly, it did not capture the structure behaviour adequately for RCOs with longitudinal bulkheads. It is because the robust fore part of the rigid striking ship damaged most of the upper part of the stuck ship. This caused the ship position changes between the colliding bodies, resulting in minor damage only on the upper part of the bulkhead. Secondly, for collision simulations employing a hull thickness measure, rigid bow simulations are likely to underestimate the effects of structural hull strength.

Finally, the overall results obtained from this sensitivity study were summarised and discussed for the reliability of the simulation results from the proposed analysis approach with the relative collision speed. After filtering data with the trimmed mean, the penetration outcomes obtained from the proposed analysis approach showed higher reliability than those from the traditional approach. This implies that the proposed methodology compensates for simulation result gaps from various parameters. Even though the results were reasonably acceptable, it was recommended to have a 5% design margin for RCOs with longitudinal additions and a 10% design margin for ROCs related to hull thickness increase to take into account the different parameter effects.

Chapter 8

Discussions and Conclusions

8 DISCUSSIONS AND CONCLUSIONS

8.1 Preamble

In this chapter, the proposed quantitative risk assessment methodology is revisited and discussed in detail based on the simulation outcomes demonstrated in the case study with the following questions.

- Is the proposed QRA methodology a suitable tool for evaluating new structural designs and arrangements in relation to damage stability?
- What aspects should we bear in mind to determine relative collision speeds ?
- Which RCOs are more effective, and what limitations do other RCOs have ?
- What aspects should we consider to design RCOs ?
- Can the QRA methodology widely apply to all kinds of vessels?

Then, further works identified from them are suggested for the future development of the present methodology. Finally, conclusions and contributions of this thesis are followed.

8.2 Discussions

8.2.1 Direct assessment methods

This research proposed QRA methodology using direct assessment of ship collisions for ship damage stability. A core concept is to perform FE analysis in a defined collision scenario and to apply modified breach distributions to damage stability calculation with updated local p-factors (i.e., r-factor, which is a transverse damage distribution) based on simulation results. Therefore, the method enables the evaluation of crashworthy designs and arrangements. In the case study, the QRAs for 26 RCOs have been carried out, and the contributions of those structural RCOs have been successfully quantified by means of the Gross Cost of Averting a Fatality (GCAF) based on an Attained Subdivision Index and cost. In particular, RCOs associated with hull thickness (i.e., RCO9 ~ RCO14) can be good examples of the advantage of this proposed methodology. Those analyses successfully captured the contributions of hull thickness effects with the total Attained Index improvement of 0.0008 (seeTable 8.1). However, if the current regulatory framework of SOLAS is applied to these RCOs, there is no change in damage stability. Similarly, for other RCOs, the crashworthy structure contributes to reducing overall penetration and updating local breach distribution, leading to overall Attained Subdivision Index improvement. Depending on the type of measures and application positions, the contributions were various (see Table 6.12 ~ Table 6.16 and Table 6.18).

Table 8.1 Attained Index improvements by transverse distribution update

Name	Description	Penetration (m)	Index A Before update	Index A After update	Index A Improvement
RCO11	20T Hull	10.46	0.8579	0.8587	**0.0008**
RCO12	30T Hull	6.58	0.8579	0.8587	**0.0008**
RCO13	40T Hull	6.64	0.8579	0.8587	**0.0008**

Additionally, this thesis introduces the plurality approach for a cost-effective solution by applying RCOs to high-risk zones. It considers all damage cases related to each zone and focuses on the total improvement of a ship when RCOs apply to a target zone. In contrast, the conventional approach focuses on eliminating the highest individual risk from a risk graph (i.e., Risk = p x (1-s)). The problem is that a zone having the highest individual risk is not always the most vulnerable zone. Thus, the application of RCOs to that zone does not guarantee maximum improvement. Therefore, from the proposed approach, the total improvements of each zone from various RCOs can be precisely estimated in advance, saving calculation time. Therefore, this proposed methodology can be concluded as a convenient and reliable tool to evaluate the crashworthy structure capabilities and its contributions.

8.2.2 Collision Speed Selection

High speeds may generate deeper penetrations and underestimate RCO benefits, while low speeds may not capture actual collision phenomena and likely ignore potential risks. Thus, determining collision speeds for the simulations is critical because it directly influences penetration outcomes. Additionally, as observed in Chapter 7, u in the simulation set-ups also significantly affect simulation outcomes. For example, as shown in Figure 7.23, collision simulations at 10 knots show various penetration results from 5m to 23 m due to different simulation set-up parameters. These results are totally unreliable in evaluating collision analysis. Therefore, this thesis proposed how to determine collision speeds for reliable simulation outcomes and suggested the concept of relative collision speed resulting in B/2 penetration. The sensitivity study proves that the average penetrations at the relative collision speeds for different parameter set-ups were less than 0.9m compared to the original calculations (see Table 7.14). This means that the use of the relative collision speed helps to adjust simulation result gaps by stimulation parameter differences.

However, the speed should be carefully selected. Figure 8.1 summarises all pre-simulation results from different parameter cases. The simulation outcomes by a rigid bow, as indicated in

red, show almost linear for collision speeds, which is very predictable and reliable. However, the deformable striking bow simulations show non-linearity, especially in black dotted circles in Figure 8.1. This could be attributed to the striking body being severely deformed at the early stage, affecting the rest of the simulations. Therefore, for simulations by a deformable bow at high speeds, a wide range of simulations is recommended to select the proper collision speeds. Interestingly, a special relationship for selected collision speeds between the deformable and rigid bow was observed, as shown in Table 8.2 and Figure 8.2. Collision speeds for simulations with the deformable bow are approximately 1.35 ~ 1.60 times faster than those from the rigid body collisions. Even though there is a limited database, it may be helpful to estimate a proper range of collision speeds for pre-simulations by the deformable bow, saving calculation times.

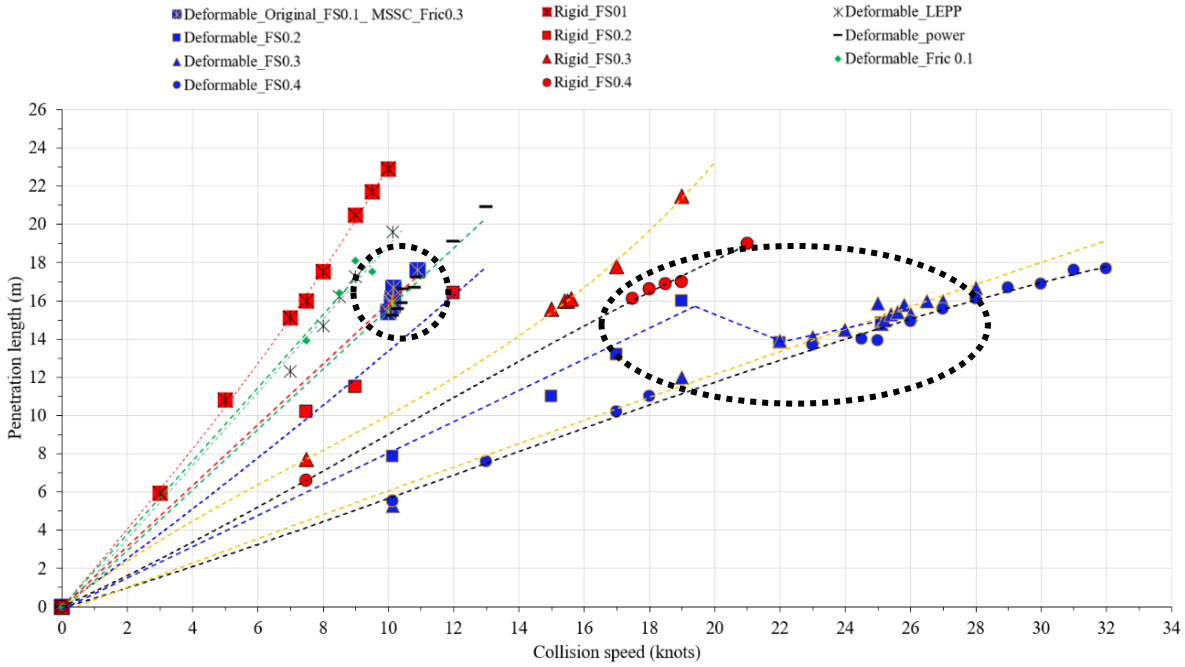

Figure 8.1 Simulation results of collision speed selections for the sensitivity study

Table 8.2 A relation between collision speeds from deformable and rigid bow collisions

		FS0.1	FS0.2	FS0.3	FS0.4
Deformable bow	Collision Speed	10.14 knots	19.00 knots	25.00 knots	28.00 knots
	Per cent of FS0.1	-	187%	247%	276%
Rigid bow	Collision Speed	7.50 knots	12.00 knots	15.60 knots	17.50 knots
	Per cent of FS0.1	-	160%	208%	233%
Collision speeds ratio between Deformable and Rigid bow		**1.35**	**1.58**	**1.60**	**1.60**

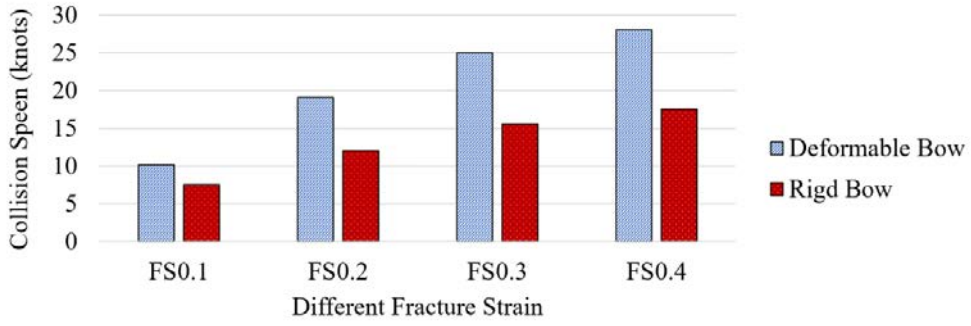

Figure 8.2 Summary of Collision speeds of deformable and rigid bow simulations for different fracture stains

8.2.3 Limitation of Transverse Damage Distribution update

Table 8.3 compares the total Attained Index improvements for two different types of RCOs. The first RCO group from RCO1 to RCO4 are associated with longitudinal subdivisions, and the other group from RCO11 to RCO13 are the measures with hull thickness increases. The former group shows that Attained Index increases when the longitudinal bulkhead is closer to the ship centre because improved s-factors and updated local p-factors resulted in an overall Attained Index A improvement (see Figure 3.15, Figure 3.16 and Figure 8.3(a)/(b)).

Table 8.3 Attained Index improvements by transverse distribution update

Name	Description	Penetration (m)	Index A Before update	Index A After update	Index A Improvement
RCO1	B/20 LBHD	13.13	0.8589	0.8590	**0.0001**
RCO2	2B/20 LBHD	13.03	0.8610	0.8619	**0.0009**
RCO3	3B/20 LBHD	11.82	0.8659	0.8692	**0.0033**
RCO4	4B/20 LBHD	12.51	0.8693	0.8727	**0.0034**
RCO11	20T Hull	10.46	0.8579	0.8587	**0.0008**
RCO12	30T Hull	6.58	0.8579	0.8587	**0.0008**
RCO13	40T Hull	6.64	0.8579	0.8587	**0.0008**

On the other hand, there is no difference between the second RCO group regardless of hull thickness increase as long as penetrations occur (i.e., see Table 8.5 for the case with no penetration on the hull). This is because the hull thickness measure does not contribute to any Index improvement based on the current SOLAS. However, the only improvement of 0.0008 shown in Table 8.3 is attributed to the local transverse breach distribution updated (see Figure 8.3(c2)) : The p-factors in Zone 15 were updated based on the simulation results, but s-factors

remain identical, as shown in Figure 8.3(c1). This means that the updated distribution did not effectively influence the overall Index due to no s-factors improvement. Therefore, it can be concluded that the transverse damage breach distribution updates are more effective when RCOs leading to s-factor improvements are employed (see Figure 8.3(a) and (b)).

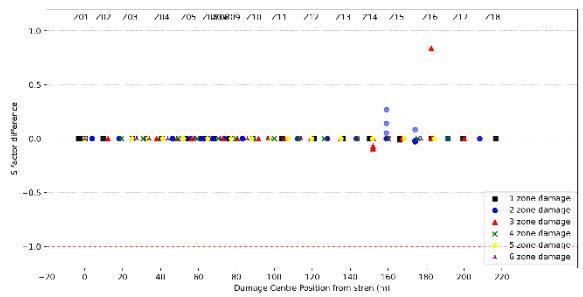

(a1) RCO1 – s-factor Changes

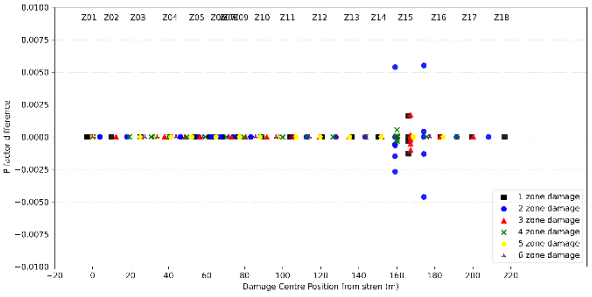

(a2) RCO1 – p-factor Changes

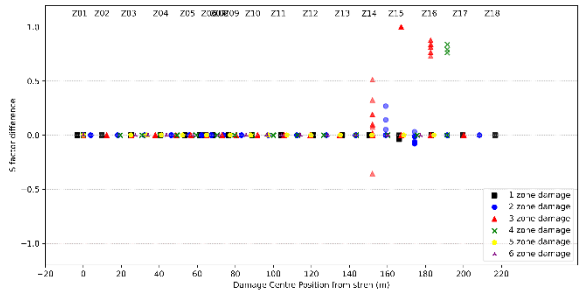

(b1) RCO4 – s-factor Changes

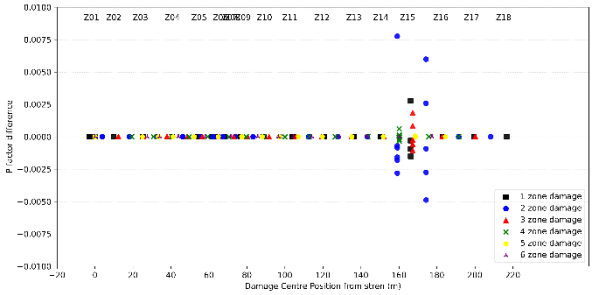

(b2) RCO4 – p-factor Changes

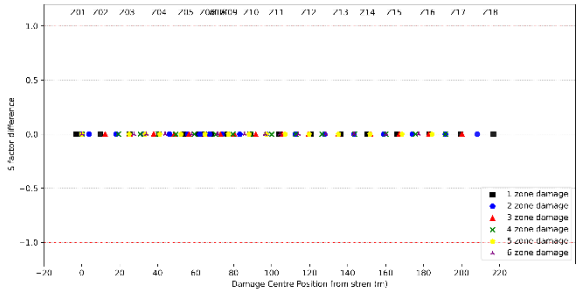

(c1) RCO12 – s-factor Changes

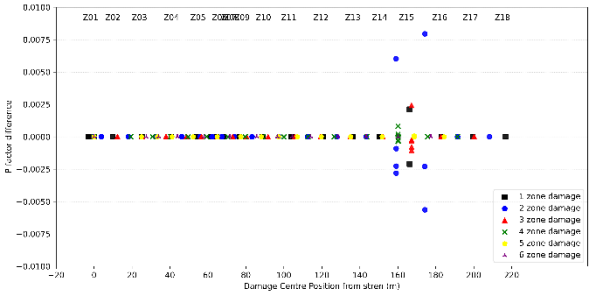

(c2) RCO12 – p-factor Changes

Figure 8.3 Changes in s- and p- factors of RCO1, RCO4 and RCO12 compared with those of the original layout

8.2.4 Design effects of RCOs

In this thesis, two different types of RCO design are used in terms of a structural measure, such as the addition of longitudinal bulkheads and hull thickness increase.

First, Table 8.4 summarises the analysis outcomes from RCOs with single longitudinal subdivisions at different locations. The penetrations tend to decrease when the longitudinal locations are closer to the ship centre, but the penetration differences between them are within the recommended design margin (i.e., 5%), as mentioned in the previous Section 7.6. Therefore, the penetration effects due to bulkhead locations can be neglected. In terms of damage stability improvements, RCO4, which has the closest LBHD to the ship centre, achieved the higher Attained Index (i.e., $\sum p \times s$) in comparision to other RCOs. This is because damage cases associated with RCO4 contributed to the higher survivability with increased s-factors and the updated p-factors made synergy with them (see Figure 8.3(a) and (b)). Even though RCO4 has the highest GCAF of 0.86 among those RCOs, it should be noted that the longitudinal subdivisions locate far inward and deteriorate internal spaces' efficiency. It may also cause to increase in steel weight depending on hull shape. Therefore, the design effects of each RCO should always be taken into account independently for optimum solution decisions

Table 8.4 Summary of results for RCOs with single longitudinal subdivisions at the different locations

Name	RCO1	RCO2	RCO3	RCO4
Location of LBHD	B/20	2B/20	3B/20	4B/20
Penetration (m)	**13.13**	**13.03**	**11.82**	**12.51**
Reduction (m)	3.02	3.12	4.33	3.64
ΔWeight (Ton)	**28.14**	**31.58**	**34.67**	**37.42**
ΔCost (Mil USD)	0.27	0.57	0.59	0.62
ΔA-Index	**0.0011**	**0.0041**	**0.0113**	**0.0148**
ΔPPL	0.05	0.20	0.55	0.72
GCAF	**4.96**	**2.84**	**1.07**	**0.86**

Table 8.5 summarises RCOs pertaining to different hull thicknesses, such as RCO9 ~ RCO14. The penetrations clearly decreased when the thickness increased. Special attention should be given to RCO12, RCO13 and RCO14 results. The penetration of 6.64m for RCO13 is almost similar to RCO12, and there were no openings observed on the hull for ROC14 but only an indentation of 6.25m. This means that the presence of an opening on the hull at the final

simulation stage decides whether it is penetration or an indentation, as shown in Figure 8.4. Therefore, simulation results for RCOs related to hull thickness should be carefully checked hull openings. In terms of damage stability, RCO14 achieved a significant enhancement on Attained Index due to permeability changed to zero by no penetration on the hull. On the other hand, there is no big improvement for other RCOs except the small improvement by the updated breach distribution (see Section 8.2.3). Therefore, if this type of RCO is used as a sole measure, it is only effective when enough hull thickness resulting in no openings on the hull is considered. Additionally, a feasibility study for maximum thickness application should be followed in terms of a manufacturing point of view. However, if this RCO is applied together with other measures, such as longitudinal subdivision or foam filling application, it contributes to penetration reduction. Then, it results in the improvement of breach distribution from the updated p-factors.

Table 8.5 Summary of results for RCOs associated with different hull thicknesses

Name	RCO9	RCO10	RCO11	RCO12	RCO13	RCO14
Hull Thickness (mm)	50%	100%	20T	30T	40T	50T
Penetration (m)	**11.72**	**8.22**	**10.46**	**6.58**	**6.64**	**0 (6.25(*))**
Reduction (m)	4.43	7.93	5.69	9.57	9.51	16.15
ΔWeight (Ton)	49.51	99.03	52.58	128.38	204.18	279.98
ΔCost (Mil USD)	0.47	0.97	0.50	1.26	1.99	2.74
ΔA-Index	**0.0008**	**0.0008**	**0.0008**	**0.0008**	**0.0008**	**0.04289**
ΔPPL	0.04	0.04	0.04	0.04	0.04	2.08
GCAF	**12.19**	**24.94**	**12.95**	**32.55**	**51.47**	**1.32**

(*) indentation length without no openings

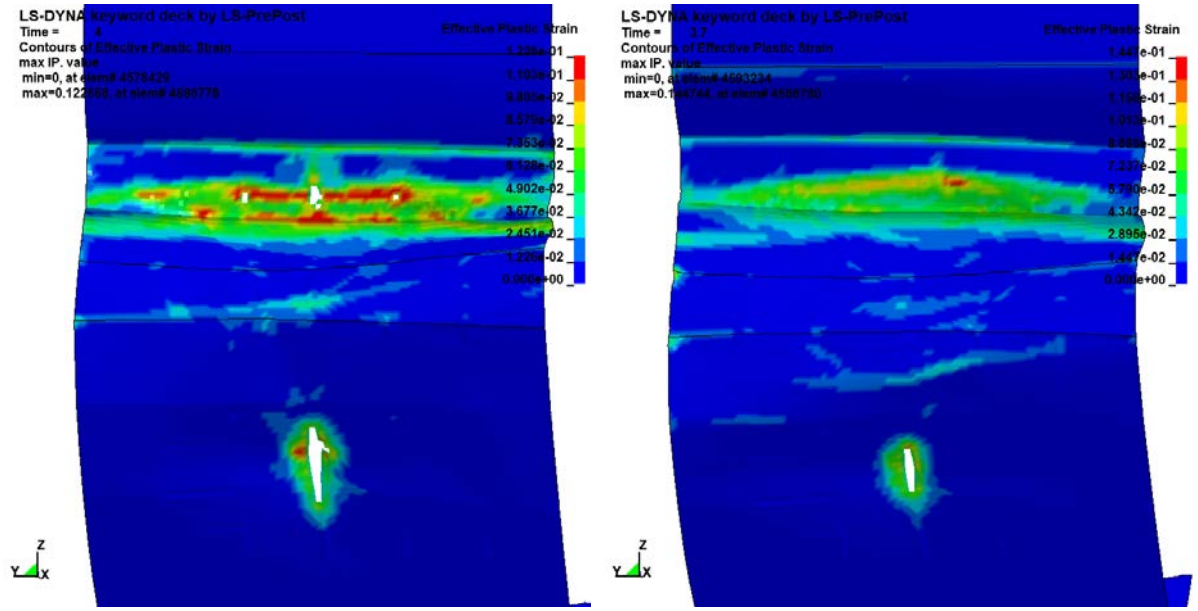

(a) RCO12 (30T) (b) RCO13 (40T)

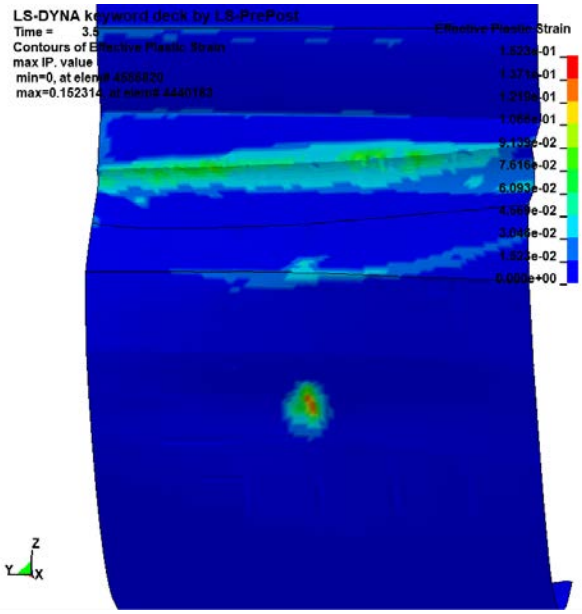

(c) RCO 14 (50T)

Figure 8.4 Hull damages of (a) RCO12 with 30T hull thickness, (b) RCO13 with 40T hull thickness and (c) RCO14 with 50T hull thickness

8.2.5 Generalisation to all kinds of ships

The key method is to adopt the damage extent criterion of B/2 penetration from SOLAS for collision speed selection at crashworthiness analysis, and it enables relative comparisons between original and new layouts within criteria requirements, minimising uncertainties from

simulation set-up differences. Therefore, if there are specific criteria regarding damage extent or required distances (i.g., B/20 for double bottom damage, B/5 for side damage of RoPax and B/10 for system installation) for other types of vessels or design requirements, the proposed QRA can be directly applied. For example, there are double hull arrangement (i.e., secondary plates) criteria with 1 ~ 2m for tankers according to MARPOL (IMO, 2004) and with 0.8 ~ 2.0m for gas carriers according to IGC code (IMO, 2014). Furthermore, damage stability for tankers and gas carriers is in compliance with cargo ships regulations in the current SOLAS, using the same maximum transverse damage extent of B/2 as passenger ships. Therefore, the corresponding collision speeds can be determined in compliance with those specific damage extent requirements. In the same manner, the contributions of each RCO can be analysed from the penetration results and cost increase from collision simulations and cost-benefit analysis within the current existing regulatory framework.

8.3 Recommendations for Future Work

8.3.1 Standardisation of FE Analysis and set-up

This thesis illustrated that the collision simulations resulted in various outcomes depending on the collision scenarios and simulation setups. It was also observed that collision speed selection was crucial for crashworthiness analysis. Therefore, the relative speed selection methodology was suggested in compliance with the current SOLAS regulation to calibrate simulation result gaps due to different simulation setups. This proposed relative approach is expected to be a very useful tool for evaluating certain crashworthy measures with different simulation set-ups. However, the further aim of this thesis is to design customised damage stability for all ships depending on their operational route and operational profile. Actual damage extent would become more important than the comparison of damage results since the rules and regulations might no longer be required. For this goal, a standardisation of FE analysis and set-ups for accurate and direct results from given scenarios must be achieved, such as fracture failure criteria with proper mesh sizes, material curves, static and dynamic friction coefficient, contact method, and precise ship motions with surrounding water effects. In order to achieve those goals, large-scale experiments also must be carried out to validate the numerical simulations.

8.3.2 Extended RCOs to Multi Zones

One of the simulation assumptions in this thesis is that RCOs are applied to a single zone (i.e., the most vulnerable zone), and collisions occur in the middle of the target compartment. However, collision results from multi-zones may differ from that of a single zone. Additionally, collisions may happen at various positions and directions, affecting the structural conditions of each RCO. Therefore, extending RCOs to multi-zones is required to be investigated by further study with different collision positions, angles and different draughts to identify how they affect new structural arrangements. Then, the multi-zonal application of RCOs may create more spacious internal spaces, which may be one of the good attractions to designers or stakeholders.

8.3.3 Rapid Analysis Tool

It is well known that FE analysis provides relatively high accuracy than empirical or analytical methods. However, computational time and cost are always primary problems. Notably, at an initial design stage, various alternatives should be investigated in a limited time. Therefore, a rapid analysis tool is required. That is why the simplified tools based on super-element methods such as DAMAGE (Abramowicz and Sinmao, 1999, Simonsen, 1999), ALPS/SCOL(Paik and Pedersen, 1996), SHARP((Le Sourne, 2007, Le Sourne et al., 2012) and MarcolXMF(MARIN, 2021) were developed. They show reliable results on some specific conditions. However, general accuracy cannot be guaranteed compared to FE analysis. In particular, all those tools adopt a rigid body striking bow for their calculations, which should be carefully used for high-speed collision, as discussed in Section 7.5. Therefore, it is worth investigating how to reduce the calculation time using the current FE analysis tool along with a deformable bow, such as finite element sizes or using partial models.

8.3.4 Grounding and Flooding Weight Effects

This thesis focused on the FE simulations of collision accidents since they have higher risks than groundings. This is attributed to the fact that a double bottom arrangement is mandatory for all passenger ships to avoid risks from groundings. However, as witnessed in the *Costa Concordia* grounding accident (MIT, 2012), it may generate severe consequences due to its higher occurrences and potential risks. Therefore, the proposed methodology also needs to be applied to grounding accidents, taking into account flooding weight effects during a relatively long accident time than collisions.

In Summary, the following future works were suggested.

- Investigating and developing standardisations of FE analysis with optimum simulation setups for accurate direct results along with validation from large-scale experiments,
- Applying the proposed methodology to multi-zones at various collision positions, angles and trims,
- Investigating how to improve calculation time based on the current FE analysis tool with a deformable bow, and
- Applying the proposed methodology to grounding accidents considering flooding water effects over time.

8.4 Conclusions

This thesis was motivated by three main problems with the current SOLAS regulations as follows:

- The damage stability framework adopted by SOLAS ignores ship structural design and arrangements in damage stability
- The current regulations are solely open to s-factor for design solutions, leading to saturated solutions in damage stability design improvements.
- Individual ships' operational features are disregarded for designs of damage stability.

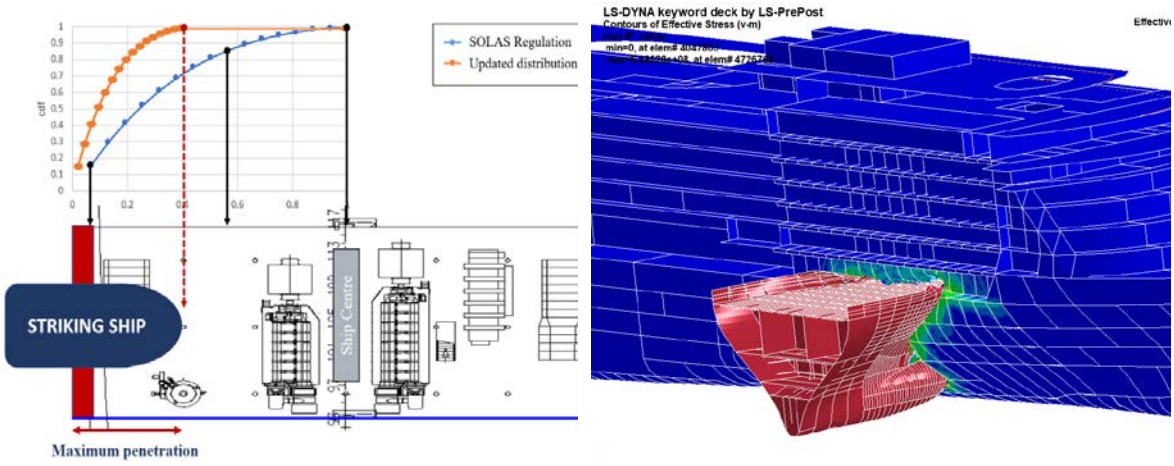

Figure 8.5 The concept of transverse breach distribution update (Left) based on crashworthiness results (Right)

Furthermore, the currently available "New Technology Qualification (NTQ)" procedures and approval process of "Alternative Design and Arrangements (AD&A)" are too time-consuming as well as require expertise that is not widely available in the market, thus stifling developments

in this area. Therefore, this thesis aims to provide a quantitative risk assessment platform to facilitate and nurture developments in damage stability using an innovative approach by addressing these problems.

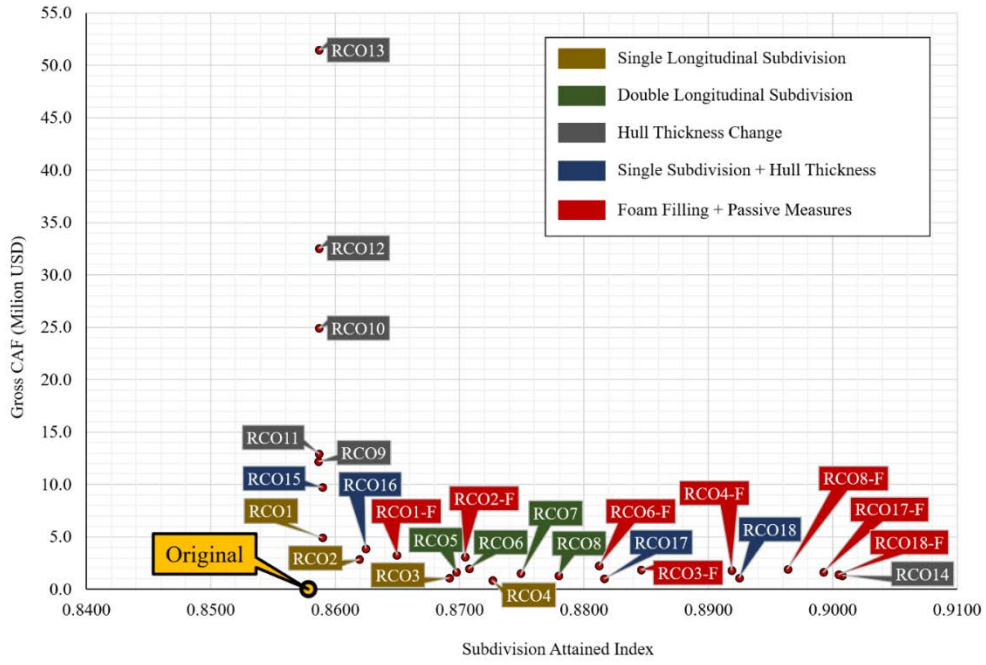

Figure 8.6 Summary of Gross CAF results for each RCO

The proposed methodology focuses on vulnerable areas where improved crashworthiness (i.e., RCOs and update of the p-factor) will lead to enhanced survivability using crashworthy structural design alternatives independent of loss modality (i.e., covering only the vulnerable area extent). Structural crashworthiness analysis using FE method leads to new damage breach distributions at the local area of application and the impact on ship survivability under specific flooding scenarios. Risk reduction (i.e., improved survivability) and cost of this Risk Control Option will support a cost-benefit analysis using the Gross Cost of Averting a Fatality (GCAF) for identifying optimum solutions. Improvement in survivability is significant depending on the protected area, and this is further enhanced by filling side void compartments with high-expansion foam, reducing asymmetry and keeping buoyancy. Based on all the aforementioned processes as a part of Alternative Design and Arrangements (AD&A), the final approval for optimum RCOs will be made by the International Association of Classification Societies (IACS). The proposed QRA has been demonstrated for a 65,000 GT cruise ship as a case study. A total of 26 RCOs for risk control or mitigation purposes were investigated, and the final three RCOs of, RCO14, RCO18 and ROC18-F among them, have been identified as optimum solutions, which are the single-hull type with 50T hull thickness, double hull type with 30T

hull and single subdivision at 6.6m, permanent foam filling application to ROC18, respectively. A sensitivity study has been performed to identify the reliability of the proposed methodology against various uncertainties of parameters about four different parameters: fracture strain, material curve, friction coefficient, and striking bow rigidity. Based on the study results, design margins of 5~10% were recommended for crashworthiness analysis depending on the RCO type.

8.5 Novelty

This thesis attempted to provide an innovative quantitative risk assessment for damage stability enhancement using collision crashworthiness analysis that the current SOLAS cannot cover. Although the demonstrations in this thesis have been carried out only for a part of the ship (i.e., the highest risk zone) for a cost-effective measure, the final goal of this research is to apply it to the ship overall, completely changing internal arrangements with innovative designs. If this methodology is widely accepted by the maritime industry in the future, this customised approach can be possible for all ships depending on their operating area and profiles for the individual vessels' characteristics. This would allow a rethinking of the structural arrangement with bigger internal spaces for passengers or cargo. Therefore, better ergonomics, more functionality, lower cost, better ship performances, and real safety are expected. Then, the shipbuilding industry may have new ship design paradigms.

8.6 Long-term Contributions

As a result of this research, many benefits may arise, mainly to society, stakeholders and the shipbuilding industry. Firstly, society, including all passengers and crew, would become safer than in the past, not only for new ships with enhanced safety but also for existing ships that do not comply with the current SOLAS. Even though existing ships are currently exempted from new safety regulations due to the huge costs and design changes, IMO would force them to enhance their safety by applying the cost-effective crashworthy measures suggested in this thesis. It would also save resources by upgrading and reusing older vessels, rather than scrapping due to a lack of safety, and eventually reducing CO2 emissions. Next, for stakeholders such as ship owners, operators and insurance companies, the proposed methodology can reduce the risk of ship property, saving insurance costs. Or, improved ship designs would attract more passengers, saving operating costs. Then, it would reinvest in other

vessels with higher levels of safety in a virtuous cycle. Finally, a variety of alternative design solutions would be available to the shipbuilding industry, including engineering companies and shipyards. The proposed methodology may provide more flexible design ideas to address ship survivability problems they may have. It is also compatible with new marine technologies, including digital-twin ship and ship emergency response systems, and could be widely used in the future.

Chapter 9

References

9 REFERENCES

ABC13 2019. WATCH LIVE: Barge and vessel collide in Houston Ship channel. ABC13 Houston: Youtube.

ABRAMOWICZ, W. 1994. Crushing resistance of T, Y, and X sections. *Joint MIT-Industry Project on Tanker Safety, Report,* 24.

ABRAMOWICZ, W. & SINMAO, M. 1999. User's Manual and Modeling Guide for the Program DAMAGE, Joint MIT-Industry Program on Tanker Safety. Report.

ABUBAKAR, A. & DOW, R. 2013. Simulation of ship grounding damage using the finite element method. *International Journal of Solids and Structures,* 50**,** 623-636.

AGCS 2019. Safety and Shipping Review 2019 : An annual review of trends and developments in shipping losses and safety. Munich, Germany.

AGCS 2021. Safety and Shipping Review 2021 : An annual review of trends and developments in shipping losses and safety. Munich, Germany.

ALSOS, H. S. & AMDAHL, J. 2009. On the resistance to penetration of stiffened plates, Part I–Experiments. *International Journal of Impact Engineering,* 36**,** 799-807.

ALSOS, H. S., AMDAHL, J. & HOPPERSTAD, O. S. 2009. On the resistance to penetration of stiffened plates, Part II: Numerical analysis. *International Journal of Impact Engineering,* 36**,** 875-887.

ALSOS, H. S., HOPPERSTAD, O. S., TÖRNQVIST, R. & AMDAHL, J. 2008. Analytical and numerical analysis of sheet metal instability using a stress based criterion. *International Journal of Solids and Structures,* 45**,** 2042-2055.

AMDAHL, J. 1982. *Energy absorption in ship-platform impacts.* PhD, Norweigian Institute of Technology.

AMDAHL, J. 1983. Energy absorption in ship-platform impacts.

AMDAHL, J. 1995. Side collision. *22nd WEGEmT Graduate School, Technical University of Denmark.*

AMDAHL, J., KAVLIE, D. & ASTRUP, O. 1992. Experimental and Numerical Simulation of Double Hull Stranding DNV-MIT Workshop on Mechanics of Ship Collision and Grounding. *DNV Høvik, Oslo*.

ANSYS 2019. User's manual for ANSYS AQWA version 18. *In:* INC., A. (ed.). PA, USA.

ARULMOZHI, G. 2009. *Statistics For Mgmt, 2E,* McGraw-Hill Education (India) Pvt Limited.

BAE, H., VASSALOS, D., PATERSON, D., MUJEEB-AHMED, M. & BOULOUGOURIS, E. 2021. The Effectiveness of Crashworthiness as a Damage Stability Risk Control Option. *Conference: 1st International Conference on the Stability and Safety of Ships and*

Ocean Vehicles (STAB&S 2021). Glasgow, UK.

BAO, Y. & WIERZBICKI, T. 2004. On fracture locus in the equivalent strain and stress triaxiality space. *International Journal of Mechanical Sciences,* 46**,** 81-98.

BARAFF, D. 2001. Physically based modeling: Rigid body simulation. *SIGGRAPH Course Notes, ACM SIGGRAPH,* 2**,** 2-1.

BARBA, M. 1880. Mémoires de la Société des Ingénieurs Civils. *Memoirs of the Society of Civil Engineers,* 22.

BARRETT, R. 1990. NASA Reference Publication 1228: Fastener Design Manual. *NASA Scientific and Technical Information Division: Hampton, VA, USA.*

BARSOUM, I. & FALESKOG, J. 2007. Rupture mechanisms in combined tension and shear—Experiments. *International journal of solids and structures,* 44**,** 1768-1786.

BEAMER 2018. Marine investigation report_Collision CSL VIRGINIA struck by ULYSSE on 7 October 2018, off cap Corse. France.

BELYTSCHKO, T. & HSIEH, B. 1973. Non-linear transient finite element analysis with convected co-ordinates. *International journal for numerical methods in engineering,* 7**,** 255-271.

BELYTSCHKO, T., LIN, J. I. & CHEN-SHYH, T. 1984. Explicit algorithms for the nonlinear dynamics of shells. *Computer methods in applied mechanics and engineering,* 42**,** 225-251.

BELYTSCHKO, T. & TSAY, C. S. 1983. A stabilization procedure for the quadrilateral plate element with one-point quadrature. *International Journal for Numerical Methods in Engineering,* 19**,** 405-419.

BIEHL, F. & LEHMANN, E. 2006. Collisions of ships with offshore wind turbines: Calculation and risk evaluation. *Offshore Wind Energy.* Springer.

BRESSAN, J. & WILLIAMS, J. 1983. The use of a shear instability criterion to predict local necking in sheet metal deformation. *International Journal of Mechanical Sciences,* 25**,** 155-168.

BROWN, A. J. 2002. Collision scenarios and probabilistic collision damage. *Marine Structures,* 15**,** 335-364.

BRUNET, M. & MORESTIN, F. 2001. Experimental and analytical necking studies of anisotropic sheet metals. *Journal of Materials Processing Technology,* 112**,** 214-226.

BULDGEN, L., LE SOURNE, H., BESNARD, N. & RIGO, P. 2012. Extension of the super-elements method to the analysis of oblique collision between two ships. *Marine Structures,* 29**,** 22-57.

BULDGEN, L., LE SOURNE, H. & RIGO, P. 2013. A simplified analytical method for estimating the crushing resistance of an inclined ship side. *Marine structures,* 33**,** 265-

296.

CALLE, M. & ALVES, M. An inverse methodology for tuning material parameters in numerical modeling of mechanical structures. International Symposium of Solid Mechanics, Porto Alegre, Brazil, 2013.

CALLE, M. & ALVES, M. 2015. A review-analysis on material failure modeling in ship collision. *Ocean Engineering,* 106**,** 20-38.

CALLE, M., OSHIRO, R. & ALVES, M. 2017. Ship collision and grounding: Scaled experiments and numerical analysis. *International journal of impact engineering,* 103**,** 195-210.

CLARKSON 2014. Shipping Intelligence Network. UK: Clarkson Research Service Limited.

COCKCROFT, M. G. & LATHAM, D. J. 1968. Ductility and workability of metals. *J. of Metals.,* 96**,** 2444.

COMPBELL, J. & COOPER, R. 1966. Yield and flow of low-carbon steel at medium strain rates.

CONTI, F., LE SOURNE, H., VASSALOS, D., KUJALA, P., LINDROTH, D., KIM, S. J. & HIRDARIS, S. 2022. A comparative method for scaling SOLAS collision damage distributions based on ship crashworthiness–application to probabilistic damage stability analysis of a passenger ship. *Ships and Offshore Structures,* 17**,** 1498-1514.

COWPER, G. R. & SYMONDS, P. S. 1957. Strain-hardening and strain-rate effects in the impact loading of cantilever beams. Brown Univ Providence Ri.

CRASHCOASTER 2000-2003. Crashworthy Side Structures for Improved Collision Damage Survivability of Coasters and Medium Size Ro Ro Cargo Ships. G3RD-CT-2000-00253.

CRUISE MARKET WATCH, L. 2022. *Growth of the Ocean Cruise Line Industry* [Online]. Available: https://cruisemarketwatch.com/growth/ [Accessed 10 Feb 2022 2022].

DEXTREMEL 1997. Design for Structural Safety under Extreme Loads. contract BRPR-CT97-0513.

DGMOVE 2017-2019. Assessment of Specific EU Stability Requirements for Ro-Ro Passenger Ships.

DRIEMEIER, L., MOURA, R. T., MACHADO, I. F. & ALVES, M. 2015. A bifailure specimen for accessing failure criteria performance. *International Journal of Plasticity,* 71**,** 62-86.

EHLERS, S. 2010. A procedure to optimize ship side structures for crashworthiness. *Proceedings of the Institution of Mechanical Engineers, Part M: Journal of Engineering for the Maritime Environment,* 224**,** 1-11.

EHLERS, S., BROEKHUIJSEN, J., ALSOS, H. S., BIEHL, F. & TABRI, K. 2008. Simulating the collision response of ship side structures: a failure criteria benchmark study.

International Shipbuilding Progress, 55**,** 127-144.

EHLERS, S. & VARSTA, P. 2009. Strain and stress relation for non-linear finite element simulations. *Thin-Walled Structures,* 47**,** 1203-1217.

ELIOPOULOU, E. & PAPANIKOLAOU, A. 2004. Final analysis of results of ISCGSLF47 proposal. Dry Cargo and Passenger ships contribution to IMO SLF 47/3/2 and 47/3/3.

EMSA 2014a. Annual overview of marine casualties and incidents 2014. Lisbon: European Maritime Safety Agency.

EMSA 2014b. Evaluation of risk from raking damages due to grounding, Interim report.

EMSA 2015. Risk Acceptance Criteria and Risk Based Damage Stability, Final Report, Part 2: Formal Safety Assessment.

EMSA 2021a. Annual overview of marine casualties and incidents 2021. Lisbon: European Maritime Safety Agency.

EMSA 2021b. Preliminary Annual Overview of Marine Casualties and Incidents 2014-2020. Lisbon: European Maritime Safety Agency.

EMSAIII 2013-2016. Study assessing the acceptable and practicable risk level of passenger ships related to damage stability ("EMSA 3"), undertaken by DNVGL. EMSA/OP/10/2013, http://emsa.europa.eu/damage-stability-study.html.

ESAFE 2016-2018. Damage Stability of Cruise Ships (eSAFE). Joint Industry Project, Cruise Ship Safety Forum.

EU 2003. THE EUROPEAN PARLIAMENT AND OF THE COUNCIL of 14 April 2003 on specific stability requirements for ro-ro passenger ships. *DIRECTIVE 2003/25/EC.* Official Journal of the European Union.

FERRY, M., SOURNE, H. L. & BESNIER, F. 2002. MCOL-theoretical manual. French Shipbuilding Research Institute, Nantes, France.

FLARE 2019-2022. FLooding Accident REsopnse. https://cordis.europa.eu/project/id/814753.

FRANCESCUTTO, A. & PAPANIKOLAOU, A. 2011. Buoyancy, stability, and subdivision: from Archimedes to SOLAS 2009 and the way ahead. *Proceedings of the Institution of Mechanical Engineers, Part M: Journal of Engineering for the Maritime Environment,* 225**,** 17-32.

GOALDS 2009-2012. Goal-Based Damage Stability of Passenger Ships. FP7-SST-2008-RTD-1-233876, http://www.goalds.org/.

GOODWIN, G. M. 1968. Application of strain analysis to sheet metal forming problems in the press shop. *Sae Transactions***,** 380-387.

HALLQUIST, J. O. 2007. LS-DYNA keyword user's manual. *Livermore Software Technology Corporation,* 970**,** 299-800.

HANCOCK, J. & MACKENZIE, A. 1976. On the mechanisms of ductile failure in high-strength steels subjected to multi-axial stress-states. *Journal of the Mechanics and Physics of Solids,* 24**,** 147-160.

HARDER 2000-2003. Harmonisation of Rules and Design Rationale. EC Contact No. GDRB-CT-1998-00028, Final Technical Report.

HARIS, S. & AMDAHL, J. 2013. Analysis of ship–ship collision damage accounting for bow and side deformation interaction. *Marine Structures,* 32**,** 18-48.

HAYWOOD, J. 1971. A note on collision estimate for LNG carriers, NCRE Report, Naval Construction Research Establisment, St. *Leonard Hill, Dunfermline, Scotland*.

HERBERT ENGINEERING, C. 2001. Vertical extent of damage, Technical report, report prepared for Commandant (G-MSE-2) US Coast Guard Headquaters. Washington D.C.

HILL, R. 1952. On discontinuous plastic states, with special reference to localized necking in thin sheets. *Journal of the Mechanics and Physics of Solids,* 1**,** 19-30.

HODGE, P., HOPKINS, H. & LEE, E. 1956. The theory of piecewise linear isotropic plasticity. *Deformation and Flow of Solids/Verformung und Fliessen des Festkörpers.* Springer.

HOGSTRÖM, P., RINGSBERG, J. & JOHNSON, E. 2009. An experimental and numerical study of the effects of length scale and strain state on the necking and fracture behaviours in sheet metals. *International Journal of Impact Engineering,* 36**,** 1194-1203.

HOGSTRÖM, P. & RINGSBERG, J. W. 2012. An extensive study of a ship's survivability after collision–a parameter study of material characteristics, non-linear FEA and damage stability analyses. *Marine structures,* 27**,** 1-28.

HUGHES, O. F. & PAIK, J. G. 2010. Ship structural analysis and design. *Published by: The Society of Naval Architects and Marine Engineers, SNAMNE, New Jersey, ISBN: 978-0-939773-78-3*.

HUTCHINSON, K. W. & SCOTT, A. L. 2016. Passenger Ro-Ro Ferry Damage Stability: Status and Development of International Regulations. *Design & Operation of Ferries & Ro-Pax Vessels.* London, UK: RINA.

HYPERWORKS, A. HyperMesh User's Manual. Ito, S., Koishikura, T. and Suzuki, D.(2010). Modeling and analysis techniques for suspension rubber bushings. 2010 SIMULIA Customer Conf., Providence, RI, USA, 2018.

IMLAY, F. H. 1961. The complete expressions for added mass of a rigid body moving in an ideal fluid. DAVID TAYLOR MODEL BASIN WASHINGTON DC.

IMO 1973. Regulation on subdivision and stability of passenger ships as an equvalent to Part B of Chapter II of the international convention for the safety of life at sea,1960. *Res.A.265(8).* International Maritime Organisation, London, UK.

IMO 1982. Code of Safety for Nuclear Merchant Ships. *Res.A.491(XII).* International Maritime

Organisation, London, UK.

IMO 1990. Adoption of amendments to the international convention for the safety of life at sea, 1974. *Res.MSC 19(58).* Maritime Safety Committee, International Maritime Organisation, London, UK.

IMO 1991. Expanatory notes to the SOLAS regulation on subdivision and damage stability of Cargo ships of 100 meters in length and over. *Res.A.684(17).* the Assembly, International Maritime Organisation, London, UK.

IMO 1992. Amendments to the Annex of the Protocol of 1978 relating to the International Convention for the Prevention of Pollution From Ships, 1973 (New regulations 13F and 13G and related amendments to Annex I of MARPOL 73/78). *Res.MEPC.52(32).* Marine Environment Protection Committee, International Maritime Organisation, London, UK.

IMO 2002a. BULK CARRIER SAFETY- Report on FSA Study on Bulk Carrier Safety submitted by Japan. *In:* 75/5/2, M. (ed.) *Maritime Safety Committee & Marine Environmental Protection Committee, International Maritime Organisation, London, UK.*

IMO 2002b. Guidelines for Formal Safety Assessment (FSA) for use in the IMO Rule Making Process. *In:* MSC/CIRC.1023 , M. C. (ed.) *Maritime Safety Committee & Marine Environmental Protection Committee, International Maritime Organisation, London, UK.*

IMO 2003. DEVELOPMENT OF EXPLANATORY NOTES FOR HARMONIZED SOLAS CHAPTER II-1, Approval procedure concept for alternative arrangements, Submitted by Germany. *SLF 46/INF.10.* SUB-COMMITTEE ON STABILITY AND LOAD LINES AND ON FISHING VESSELS SAFETY, International Maritime Organisation, London, UK.

IMO 2004. Amendments to the Annex of the Protocol of 1978 relating to the International Convention for the Prevention of Pollution From Ships, 1973. *Res.MEPC.117(52) Reg.19 & 20.* Marine Environment Protection Committee, International Maritime Organisation, London, UK.

IMO 2005. Adoption of Amendments to the International Convention for the Safety Of Life At Sea, 1974, as amended. *Res.MSC.194(80) : ANNEX 2 CH II-1 Reg. 9.* Maritime Safety Committee, International Maritime Organisation, London, UK.

IMO 2006. Guidelines on alternative design and arrangements for SOLAS Chapters II-1 and II-2. *MSC.1/Circ.1212.* Maritime Safety Committee, International Maritime Organisation, London, UK.

IMO 2008. FORMAL SAFETY ASSESSMENT - Cruise ships _Details of the Formal Safety Assessement. *MSC 85/INF.2.* Maritime Safety Committee, International Maritime Organisation, London, UK.

IMO 2012. The GOAL based Damage Stability project (GOALDS) - Development of a new risk-based damage stability requirement for passenger ships based on Cost-Benefit

Assessment. *In:* IMO (ed.) *SLF55/INF.9.* Maritime Safety Committee, International Maritime Organisation, London, UK.

IMO 2013. Guidelines for the approval of alternatives and equivalents as provided for in various IMO instruments. *MSC.1/Circ.1455.* Maritime Safety Committee, International Maritime Organisation, London, UK.

IMO 2014. Amendments to the International Code for the Construction and Equipment of Ships Carrying Liquefied Gases in Bulk: IGC Code. *In:* IMO (ed.) *MSC.370(93).* Maritime Safety Committee, International Maritime Organisation, London, UK.

IMO 2017a. Amendments to the International Convention for the Safety Of Life At Sea, 1974, as amended. *Res.MSC.421(98) : ANNEX Part B-2 Reg. 9.* Maritime Safety Committee, International Maritime Organisation, London, UK.

IMO 2017b. AMENDMENTS TO THE INTERNATIONAL CONVENTION FOR THE SAFETY OF LIFE AT SEA, 1974, AS AMENDED. *Res.MSC.421(98).* Maritime Safety Committee, International Maritime Organisation, London, UK.

IMO 2018. Revised Guidelines for Formal Safety Assessment (FSA) for use in the IMO Rule Making Process. *In:* 2, M.-M. C. R. (ed.) *Maritime Safety Committee & Marine Environmental Protection Committee, International Maritime Organisation, London, UK.*

JIE, M., CHENG, C., CHAN, L. C. & CHOW, C. 2009. Forming limit diagrams of strain-rate-dependent sheet metals. *International Journal of Mechanical Sciences,* 51**,** 269-275.

JONES, N. 1979. A literature survey on the collision and grounding protection of ships, Ship Structure Committee, Report No. *SSC-283.*

JONES, N. 1989a. On the dynamic inelastic failure of beams. *Structural failure,* 133-159.

JONES, N. 1989b. *Structural impact,* Cambridge university press.

JONES, N. 2006. Some recent developments in the dynamic inelastic behaviour of structures. *Ships and Offshore Structures,* 1**,** 37-44.

JONES, N. 2013. The credibility of predictions for structural designs subjected to large dynamic loadings causing inelastic behaviour. *International Journal of Impact Engineering,* 53**,** 106-114.

JONES, N. & JOURI, W. 1987. A study of plate tearing for ship collision and grounding damage. *Journal of Ship Research,* 31**,** 253-268.

JONES, N. & WIERZBICKI, T. 1993. International Symposium on Structural Crashworthiness and Failure (3rd) Held in Liverpool, United Kingdom on April 14-16, 1993. Volume 13, Number 2. Special Issue. PERGAMON PRESS INC ELMSFORD NY.

KARLSSON, U. B., RINGSBERG, J. W., JOHNSON, E., HOSEINI, M. & ULFVARSON, A. 2009. Experimental and numerical investigation of bulb impact with a ship side-shell structure. *Marine Technology and SNAME News,* 46**,** 16-26.

KEELER, S. P. 1961. *Plastic instability and fracture in sheets stretched over rigid punches.* Massachusetts Institute of Technology.

KIERKEGAARD, H. 1993. Ship Collision with Icebergs (Ph. D. thesis). *Department of Ocean Engineering, Technical University of Denmark, Lyngby, Denmark.*

KIM, K. J., LEE, J. H., PARK, D. K., JUNG, B. G., HAN, X. & PAIK, J. K. 2016. An experimental and numerical study on nonlinear impact responses of steel-plated structures in an Arctic environment. *International Journal of Impact Engineering,* 93**,** 99-115.

KIM, S.-J., KÕRGERSAAR, M., TAIMURI, G., KUJALA, P. & HIRDARIS, S. A Quasi-Dynamic Approach for the Evaluation of Structural Response in Ship Collisions and Groundings. The 30th International Ocean and Polar Engineering Conference, 2020. International Society of Offshore and Polar Engineers.

KIM, S. J., KORGERSAAR, M., AHMADI, N., TAIMURI, G., KUJALA, P. & HIRDARIS, S. 2021. The influence of fluid structure interaction modelling on the dynamic response of ships subject to collision and grounding. *Marine Structures,* 75**,** 102875.

KIM, S. J., TAIMURI, G., KUJALA, P., CONTI, F., LE SOURNE, H., PINEAU, J.-P., LOOTEN, T., BAE, H., MUJEEB-AHMED, M. & VASSALOS, D. 2022. Comparison of numerical approaches for structural response analysis of passenger ships in collisions and groundings. *Marine Structures,* 81**,** 103125.

KITAMURA, O. 2002. FEM approach to the simulation of collision and grounding damage. *Marine Structures,* 15**,** 403-428.

KITAMURA, O., KUROIWA, T., KAWAMOTO, Y. & KANEKO, E. A study on the improved tanker structure against collision and grounding damage. The Seventh International Symposium on Practical Design of Ships and mobile Units, PRADS, 1998.

KO, Y. G., KIM, S. J. & PAIK, J. K. 2018a. Effects of a deformable striking ship's bow on the structural crashworthiness in ship–ship collisions. *Ships and Offshore Structures,* 13**,** 228-250.

KO, Y. G., KIM, S. J., SOHN, J. M. & PAIK, J. K. 2018b. A practical method to determine the dynamic fracture strain for the nonlinear finite element analysis of structural crashworthiness in ship–ship collisions. *Ships and Offshore Structures,* 13**,** 412-422.

KÕRGESAAR, M. 2015. Modeling ductile fracture in ship structures with shell elements.

KÕRGESAAR, M. & ROMANOFF, J. 2013. Influence of softening on fracture propagation in large-scale shell structures. *International Journal of Solids and Structures,* 50**,** 3911-3921.

KÕRGESAAR, M., TABRI, K., NAAR, H. & REINHOLD, E. Ship collision simulations using different fracture criteria and mesh size. International Conference on Offshore Mechanics and Arctic Engineering, 2014. American Society of Mechanical Engineers, V04AT02A045.

KUROIWA, T. Study on damage of ship bottom structures due to grounding. First Joint Conference on Marine Fafety and Environment/Ship Production, 1992.

KUROIWA, T. Dynamic experiments and numerical simulations of failure of ship's side structure. Procedings of the Conference on Prediction Methodology of Tanker Structural Failure and Consequential Oil Spill, 1993.

LARSEN, O. D. 1993. *Ship collision with bridges: The interaction between vessel traffic and bridge structures*, IABSE.

LE SOURNE, H. A ship CollisionAnalysis Program Based on Super-Element Method Coupled with Large Rotational Ship Movement Analysis. 4th International Conference on Collision and Grounding of Ships, 2007. 131-138.

LE SOURNE, H., BESNARD, N., CHEYLAN, C. & BUANNIC, N. 2012. A ship collision analysis program based on upper bound solutions and coupled with a large rotational ship movement analysis tool. *Journal of Applied Mathematics,* 2012.

LE SOURNE, H., COUTY, N., BESNIER, F., KAMMERER, C. & LEGAVRE, H. 2003. LS-DYNA application in Shipbuilding. *Proceedings of 4th European LS-DYNA Conference*.

LE SOURNE, H., PINEAU, J., KIM, S., CONTI, F., KAYDIHAN, L., BAE, H., VASSALOS, D., KUJALA, P. & HIRDARIS, S. A comparison of crashworthiness methods for the assessment of ship damage extents. 1st International Conference on the Stability and Safety of Ships and Ocean Vehicles, 2021.

LEHMANN, E., EGGE, E., SCHARRER, M. & ZHANG, L. Calculation of collision with the aid of linear FE models, 8th Int. Symp. on Practical Design of Ships and Other Floating Structures (PRADS), Shanghai, 2001. 1293-1300.

LEHMANN, E. & PESCHMANN, J. 2002. Energy absorption by the steel structure of ships in the event of collisions. *Marine Structures,* 15**,** 429-441.

LEHMANN, E. & YU, X. On ductile rupture criteria for structural tear in the case of ship collision and grounding. International Symposium on Practical Designs of Ships and Floating Structures (PRADS), 1998.

LENSELINK, H. Numerical simulations of the Dutch-Japanese full scale ship collision tests. The Conference on" Prediction Methodology of Tanker Structural Failure"(1992), 1992.

LI, Y. & WIERZBICKI, T. 2010. Prediction of plane strain fracture of AHSS sheets with post-initiation softening. *International Journal of Solids and Structures,* 47**,** 2316-2327.

LSTC 2019. LS-DYNA keyword user's manual. *In:* CORPORATION, L. S. T. (ed.). California, USA.

LU, G. & CALLADINE, C. 1990. On the cutting of a plate by a wedge. *International Journal of Mechanical Sciences,* 32**,** 293-313.

LÜTZEN, M. 2001. Ship collision damage [Ph. D. thesis]. *Technical University of Denmark, Department of Mechanical Engineering*.

MARIN 2021. MarcolXMF theoretical manual. *MARIN Research Institute Netherlands, Wageningen, Netherlands.*

MARINATOS, J. & SAMUELIDES, M. 2015. Towards a unified methodology for the simulation of rupture in collision and grounding of ships. *Marine Structures,* 42**,** 1-32.

MCDERMOTT, J. F., KLINE, R. G., JONES, E., MANIAR, N. M. & CHIANG, W. P. 1974. Tanker structural analysis for minor collisions.

MINDLIN, R. 1951. Influence of rotatory inertia and shear on flexural motions of isotropic, elastic plates.

MINORSKY, V. 1959. An analysis of ship collision with refereene to protection of nuclear power ships. *Journal of Ship Research,* 3**,** 208-214.

MIT 2012. Report on the safety technical investigation for Cruise Ship : COSTA CONCORDIA, Marin casualty on January 13, 2012. Italy.

MOTORA, S., FUJINO, M., SUGIURA, M. & SUGITA, M. 1971. Equivalent added mass of ships in collisions. *Selected Papers, J of Soc of Naval Arch of Japan,* 7.

NAAR, H., KUJALA, P., SIMONSEN, B. C. & LUDOLPHY, H. 2002. Comparison of the crashworthiness of various bottom and side structures. *Marine Structures,* 15**,** 443-460.

NAPA 2017. SOLAS Probabilistic Damage Stability – Past, Present and the Future. NAPA.

OASYS 2020. Webinar: LS-DYNA Introduction to contacts - Oasys software. Jan. 2020 ed. UK: Oasys LS-DYNA Environment.

OHTSUBO, H., KAWAMOTO, Y. & KUROIWA, T. 1994. Experimental and numerical research on ship collision and grounding of oil tankers. *Nuclear engineering and design,* 150**,** 385-396.

PABOEUF, S., LE SOURNE, H., BROCHARD, K. & BESNARD, N. 2015. A damage assessment tool in ship collisions. *Proceedings of Damaged Ship III–The Royal Institution of Naval Architects***,** 25-26.

PAIK, J. 2007. Practical techniques for finite element modeling to simulate structural crashworthiness in ship collisions and grounding (Part I: Theory). *Ships and Offshore Structures,* 2**,** 69-80.

PAIK, J. G. & JEONG, J. Y. 1999. A basic study on static and dynamic crushing behavior of a stiffened tube. *Transactions of the Korean Society of Automotive Engineers,* 7**,** 219-219.

PAIK, J. K. 1994. Cutting of a longitudinally stiffened plate by a wedge. *Journal of ship research,* 38**,** 340-348.

PAIK, J. K. 2018. *Ultimate limit state analysis and design of plated structures,* Wiley Online Library.

PAIK, J. K. 2020. Computational Models for Structural Crashworthiness Analysis in Collisions

and Grounding. *Advanced Structural Safety Studies.* Springer.

PAIK, J. K., KIM, S. J., KO, Y. K. & YOUSSEF, S. A. Collision risk assessment of a VLCC class tanker. SNAME Maritime Convention, 23-28 October 2017 2017 Houston, USA. The Society of Naval Architects and Marine Engineers.

PAIK, J. K. & PEDERSEN, P. T. 1995. Ultimate and crushing strength of plated structures. *Journal of ship research,* 39**,** 250-261.

PAIK, J. K. & PEDERSEN, P. T. 1996. Modelling of the internal mechanics in ship collisions. *Ocean Engineering,* 23**,** 107-142.

PARK, J. H. & SAMUELIDES, E. 2009. Collision-accidental limit states performance of double-hull oil tanker structures: pre-CSR versus CSR designs. *Marine Technology and SNAME News,* 46**,** 183-191.

PATERSON, D. 2020. *Reconfiguring the ship environment for damage stability enhancement.* University of Strathclyde.

PEDERSEN, P. T. & ZHANG, S. 1998. On impact mechanics in ship collisions. *Marine Structures,* 11**,** 429-449.

PEDERSEN, P. T. & ZHANG, S. 2000. Absorbed energy in ship collisions and grounding: Revising Minorsky's empirical method.

PESCHMANN, J. & KULZEP, A. 2000. Side collision of double skin ships. *BMBF report, Tech. Univ. Hamburg.*

PESCHMANN, J., KULZEP, A. & LEHMANN, E. 2002. Structural behaviour of double-hull ships in collision and grounding. *Ship Technology Research,* 49**,** 105-113.

PETERSEN, M. J. 1982. Dynamics of ship collisions. *Ocean Engineering,* 9**,** 295-329.

PETERSON, P. 2012. Lessons from LIBOR. *farmdoc daily,* 2.

PINEAU, A. & PARDOEN, T. 2007. Failure mechanisms of metals. *Comprehensive structural integrity encyclopedia,* 2**,** 687-783.

QVIST, S., NIELSEN, K. B., SCHMIDT, M. H. & MADSEN, S. H. Ship collision-Experimental and numerical analysis of double hull models. Proceedings of the 9th DYMAT Technical Conference Material and structural modelling in collision research, 1995.

RICE, J. R. & TRACEY, D. M. 1969. On the ductile enlargement of voids in triaxial stress fields∗. *Journal of the Mechanics and Physics of Solids,* 17**,** 201-217.

RINGSBERG, J. W., AMDAHL, J., CHEN, B. Q., CHO, S.-R., EHLERS, S., HU, Z., KUBICZEK, J. M., KÕRGESAAR, M., LIU, B. & MARINATOS, J. N. 2018. MARSTRUCT benchmark study on nonlinear FE simulation of an experiment of an indenter impact with a ship side-shell structure. *Marine Structures,* 59**,** 142-157.

SAFEDOR 2005-2009. Design, Operation and Regulation for Safety. Integrated Project, FP6_2 Contract TIP4-CT-2005-516278, www.safedor.org.

SAJDAK, J. & BROWN, A. 2005. Modeling longitudinal damage in ship collisions. *SSC-437, Ship Structure Committee*.

SAMUELIDES, M. 2011. Designing for protection against collision.

SAMUELIDES, M. S., VOUDOURIS, G., TOULIOS, M., AMDAHL, J. & DOW, R. Simulation of the behaviour of double bottoms subjected to grounding actions. International Conference on Collision and Grounding of Ships; International Conference for Collision and Groundings ICCGS2007, September 2007, 2007.

SCHARRER, M., ZHANG, L. & EGGE, E. 2002a. Kollisionsberechnungen in schiffbaulichen Entwurfssystemen (Collision calculation in naval design systems). *Bericht ESS*.

SCHARRER, M., ZHANG, L. & EGGE, E. 2002b. Kollisionsberechnungen in schiffbaulichen entwurfssystemen (collision calculation in naval design systems). Bericht ESS 2002.183. *Germanischer Lloyd*.

SCHREUDER, M., HOGSTRÖM, P., RINGSBERG, J. W., JOHNSON, E. & JANSON, C. E. 2011. A method for assessment of the survival time of a ship damaged by collision. *Journal of ship research,* 55**,** 86-99.

SENTESOFTWARE 2018. Forming Limit Curve (FLC) and Forming Limit Diagram (FLD).

SERVIS, D. & SAMUELIDES, M. Ship collision analysis using finite elements. 1999. Citeseer.

SIMONSEN, B. C. 1999. Theory and validation for the collision module.

SIMONSEN, B. C. & OCAKLI, H. 1999. Experiments and theory on deck and girder crushing. *Thin-walled structures,* 34**,** 195-216.

SIMONSEN, B. C. & TÖRNQVIST, R. 2004. Experimental and numerical modelling of ductile crack propagation in large-scale shell structures. *Marine Structures,* 17**,** 1-27.

SIMULIA 2008. ABAQUS Analysis User's Manual ver. 6.8.

SKINNER, S. K. 1989. *The Exxon Valdez oil spill: A report to the president,* US Environmental Protection Agency.

SOLAS 1997. International Convention for the Safety of Life At Sea. *In:* IMO (ed.) *Chapter II-1, Part B, Subdivision and Stability.*

SOLAS 2020. International Convention for the Safety of Life At Sea. *In:* IMO (ed.) *Chapter II, Part B-1, Subdivision and Damage Stability of Cargo ships.*

STÅHLBERG, K., GOERLANDT, F., EHLERS, S. & KUJALA, P. 2013. Impact scenario models for probabilistic risk-based design for ship–ship collision. *Marine Structures,* 33**,** 238-264.

STORHEIM, M. & AMDAHL, J. 2014. Design of offshore structures against accidental ship collisions. *Marine Structures,* 37**,** 135-172.

STOUGHTON, T. B. 2000. A general forming limit criterion for sheet metal forming. *International Journal of Mechanical Sciences,* 42**,** 1-27.

STOUGHTON, T. B. 2001. Stress-based forming limits in sheet-metal forming. *J. Eng. Mater. Technol.,* 123**,** 417-422.

STOUGHTON, T. B. & ZHU, X. 2004. Review of theoretical models of the strain-based FLD and their relevance to the stress-based FLD. *International Journal of plasticity,* 20**,** 1463-1486.

SYSTÈMES, D. 2007. Abaqus version 6.7 documentation. Analysis user's manual, section 19.2. *Vélizy Villacoublay (France): ABAQUS Incorp*.

TORNQVIST, R. 2003. *Design of Crashworthy Ship Structures.* PhD, Technical University of Denmark.

UN 2008. European Agreement concerning the international Carriage of Dangerous Goods by Inland Waterways (ADN). *ECE/TRANS/203 (Vol.I).* United Nations, New York and Geneva.

VASSALOS, D. 2016. Damage survivability of cruise ships–Evidence and conjecture. *Ocean Engineering,* 121**,** 89-97.

VASSALOS, D., BOULOUGOURIS, E. & PATERSON, D. An alternative system for damage stability enhancement. 15th International Ship Stability Workshop, 2016. 1-6.

VASSALOS, D. & JASIONOWSKI, A. 2011. SOLAS 2009–raising the alarm. *Contemporary Ideas on Ship Stability and Capsizing in Waves.* Springer.

VAUGHAN, H. 1978. Bending and tearing of plate with application to ship-bottom damage. *The Naval Architect***,** 97-99.

VERITAS, D. N. 2013. DNV-RP-C208: Determination of structural capacity by non-linear FE analysis methods. *Det Norske Veritas*.

VERKERK, F. S. 1992. Voorstudie mathematisch model van de scheepsmanoeuvreerbaarheid. *MARIN, Postbus 28, 6700 AA Wageningen, Rapport 010955-1-PP, MSCN*.

VREDEVELDT, A., FEENSTRA E 2001. Crashworthy side structures for improved collision damage survivability of coasters and medium sized Ro-Ro cargo ships.

VREDEVELDT, A. & WEVERS, L. 1992. *Full scale ship collision tests results: version 03*, TNO Building and Construction Research, Centre for Mechanical Engineering.

WANG, B., YU, H.-C. & BASU, R. 2008. Ship and ice collision modeling and strength evaluation of LNG ship structure. *ASME 2008 27th International Conference on Offshore Mechanics and Arctic Engineering.* American Society of Mechanical Engineers Digital Collection.

WANG, G. 1995. Structural analysis of ship collision and grounding. *University of Tokyo, Tokyo, Japan*.

WANG, G. 2002. Some recent studies on plastic behavior of plates subjected to large impact loads. *J. Offshore Mech. Arct. Eng.,* 124**,** 125-131.

WANG, G. & OHTSUBO, H. Deformation of ship plate subjected to very large load. proceedings of the international conference on offshore mechanics and arctic engineering, 1997. American Society of Mechanical Engineers, 173-180.

WEN, H.-M. & JONES, N. 1993. Experimental investigation of the scaling laws for metal plates struck by large masses. *International journal of impact engineering,* 13**,** 485-505.

WENDEL, K. 1960. Die Wahrscheinlichkeit des Uberstehens von Verletzungen. *Schiffstechnik,* 7.

WIERZBICKI, T. 1995. Concertina tearing of metal plates. *International Journal of Solids and Structures,* 32**,** 2923-2943.

WIERZBICKI, T. & ABRAMOWICZ, W. 1983. On the crushing mechanics of thin-walled structures.

WIERZBICKI, T., BAO, Y., LEE, Y.-W. & BAI, Y. 2005. Calibration and evaluation of seven fracture models. *International Journal of Mechanical Sciences,* 47**,** 719-743.

WIERZBICKI, T. & SIMONSEN, B. C. 1996. Global structural model of bow indentation into ship side. *Technical Report 2.* MIT.

WIERZBICKI, T. & THOMAS, P. 1993. Closed-form solution for wedge cutting force through thin metal sheets. *International Journal of Mechanical Sciences,* 35**,** 209-229.

WILSON, P. A. 2018a. *Basic Naval Architecture,* Springer.

WILSON, P. A. 2018b. Stability Assessment Methods (Deterministic and Probabilistic). *Basic Naval Architecture.* Springer.

WIŚNIEWSKI, K. & KOŁAKOWSKI, P. 2003. The effect of selected parameters on ship collision results by dynamic FE simulations. *Finite elements in analysis and design,* 39**,** 985-1006.

WOISIN, G. 1979. Design against collision. *Advances in Marine Technology***,** 309-336.

YAGI, S., KUMAMOTO, H., MURAGISHI, O., TAKAOKA, Y. & SHIMODA, T. 2009. A study on collision buffer characteristic of sharp entrance angle bow structure. *Marine structures,* 22**,** 12-23.

YAMADA, Y. 2007. *Bulbous Buffer Bows: A Measure to Reduce Oil Spill in Tanker Collisions: PhD Thesis*, Technical University of Denmark, Section of Coastal, Maritime and Structural ….

YAMADA, Y., PEDERSEN, P. T. & ENDO, H. Numerical study on the effect of buffer bow

structure in ship-ship collision. The Fifteenth International Offshore and Polar Engineering Conference, 2005. OnePetro.

ZHANG, L., EGGE, E.-D. & BRUHNS, H. 2004. *Approval procedure concept for alternative arrangements*, Germanischer Lloyd.

ZHANG, M., CONTI, F., LE SOURNE, H., VASSALOS, D., KUJALA, P., LINDROTH, D. & HIRDARIS, S. 2021a. A method for the direct assessment of ship collision damage and flooding risk in real conditions. *Ocean Engineering,* 237**,** 109605.

ZHANG, M., MONTEWKA, J., MANDERBACKA, T., KUJALA, P. & HIRDARIS, S. 2021b. A big data analytics method for the evaluation of ship-ship collision risk reflecting hydrometeorological conditions. *Reliability Engineering & System Safety,* 213**,** 107674.

ZHANG, S. 1999. *The Mechanics of Ship Collision. Technical University of Denmark.* Doctoral Dissertation.

ZHANG, S. 2002. Plate tearing and bottom damage in ship grounding. *Marine Structures,* 15**,** 101-117.

ZHENG, Y., AKSU, S., VASSALOS, D. & TUZCU, C. 2007. Study on side structure resistance to ship-ship collisions. *Ships and Offshore Structures,* 2**,** 273-293.

ZILAKOS, I., TOULIOS, M., SAMUELIDES, M., NGUYEN, T.-H. & AMDAHL, J. 2009. Simulation of the response of double bottoms under grounding actions using finite elements. *Analysis and Design of Marine Structures.* CRC Press.

Appendix A

LS-DYNA

FINITE ELEMENT METHOD

APPENDIX A. LS-DYNA FINITE ELEMENT METHOD

A.1 Governing Equations

The explicit code adopted in LS-DYNA was originally developed and used to solve dynamic problems involving deformable bodies. Explicit only works when there is an acceleration of mass (dynamic), whereas an implicit approach can solve the problem without mass. Therefore, the explicit finite element equations can be expressed by the governing equilibrium (Belytschko and Hsieh, 1973, Belytschko et al., 1984):

$$M\ddot{u}^{(i)} + {f_{int}}^{(i)} = {f_{ext}}^{(i)} \tag{A.1}$$

where, f_{int} and f_{ext} are internal and external forces at a specific time i; M is the mass matrix ; $\ddot{u}^{(i)}$ is the nodal acceleration.

Furthermore, based on the central difference method, velocity and displacement at a particular point in time can be written by:

$$\dot{u}^{(i+\frac{1}{2})} = \dot{u}^{(i-\frac{1}{2})} + \frac{\Delta t^{(i+1)} + \Delta t^{(i)}}{2}\ddot{u}^{(i)} \tag{A.2}$$

$$u^{(i+1)} = u^{(i)} + \Delta t^{(i+1)}\dot{u}^{(i+\frac{1}{2})} \tag{A.3}$$

where, $\dot{u}^{(i)}$ and $u^{(i)}$ are the velocity and displacement at a specific time i; $\Delta t^{(i)}$ is the time step.

From Equation (A.1), (A.2) and (A.3), the displacement $u^{(i+1)}$ at the next time $i+1$ can be calculated since all other terms of previous history values, such as M, ${f_{int}}^{(\mathrm{i})}$, ${f_{\mathrm{ext}}}^{(\mathrm{i})}$, $\ddot{u}^{(i)}$, $\dot{u}^{(i+\frac{1}{2})}$, $u^{(i)}$, are known from previous calculations.

From this displacement $u^{(i+1)}$, internal force ${f_{int}}^{(\mathrm{i+1})}$, including velocity strain (rate of deformation), resulting stress and resultant forces and moments, can be calculated based on the Belytschko-Lin-Tsay element shell formation (See section A.2). Then, together with known external force ${f_{\mathrm{ext}}}^{(\mathrm{i+1})}$, acceleration $\ddot{u}^{(i+1)}$at time $i+1$ can be calculated. Then, it is again used for the calculation of the next time step's displacement $u^{(i+2)}$.

A.2 Internal forces

The Belystscho-Lin-Tsay shell element (Belytschko and Tsay, 1983, Belytschko et al., 1984) is based on a combined co-rotational and velocity-strain formulation. The efficiency of the element is obtained from the mathematical simplifications that result from these two kinematical assumptions.

The midsurface of the quadrilateral shell element, or reference surface, is defined by the location of the element's four corner nodes. An embedded element coordinate system, as shown in Figure A.0.1, that deforms with the element is defined in terms of these nodal coordinates.

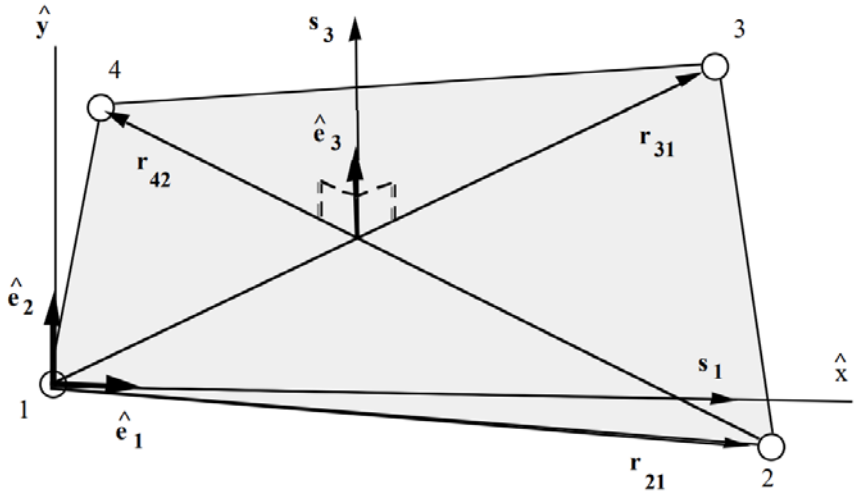

Figure A.0.1 Element coordinate system

Then, the procedure for constructing the co-rotational coordinate system begins by calculating a unit vector normal e_3 to the main diagonal of the element. The vectors tangent to the midplane are e_1 and e_2, and the unit vector in the thickness direction is e_3:

$$e_3 = e_1 \times e_2 \tag{A.4}$$

And the angle between the unit vector in thickness direction f (i.e., this vector is initially coincident with e_3) and e_3 is assumed to remain small:

$$|e_3 \cdot f - 1| < \delta \tag{A.5}$$

where, the magnitude of δ depends on the magnitude of the strains. Most engineering application's acceptable values of δ are on the order of 10^{-2} and if the condition expressed in Equation (A.5) is met, then the difference between the rotation of the co-rotational coordinates

e and the material rotation should be small.

In the Mindlin theory (Mindlin, 1951) of plates and shells, the velocity of a point in the shell is defined by the velocity of the midplane v^m and the angular velocity vector θ by:

$$v = vm - ze3 \times \theta \tag{A.6}$$

where the superscript caret($\widehat{\ }$) indicates the local element coordinate system.

The corotational components of the velocity strain, or rate of deformation, d are expressed as:

$$\hat{d}_{ij} = \frac{1}{2}\left(\frac{\partial \hat{v}_i}{\partial \hat{x}_j} + \frac{\partial \hat{v}_j}{\partial x_i}\right) \tag{A.7}$$

Substitution Equation (A.6) into (A.7) gives the following equations for the velocity strain:

$$\hat{d}_x = \frac{\partial \hat{v}_x{}^m}{\partial \hat{x}} + \hat{z}\frac{\partial \hat{\theta}_y}{\partial \hat{x}} \tag{A.8}$$

$$\hat{d}_y = \frac{\partial v_y{}^m}{\partial \hat{y}} - \hat{z}\frac{\partial \hat{\theta}_x}{\partial y}$$

$$2\hat{d}_{xy} = \frac{\partial \hat{v}_x{}^m}{\partial \hat{y}} + \frac{\partial v_y{}^m}{\partial \hat{x}} + \hat{z}\left(\frac{\partial \hat{\theta}_y}{\partial \hat{y}} - \frac{\partial \hat{\theta}_x}{\partial x}\right)$$

$$2\hat{d}_{yz} = \frac{\partial \hat{v}_z{}^m}{\partial \hat{y}} - \hat{\theta}_x$$

$$2\hat{d}_{xz} = \frac{\partial \hat{v}_z{}^m}{\partial \hat{x}} + \hat{\theta}_y$$

The above velocity-strain relations need to be evaluated at the quadrature points within the shell. Standard bilinear nodal interpolation is used to define the midsurface velocity, angular velocity, and the element's coordinates (isoparametric representation), which are expressed as:

$$\mathrm{v}^m = N_1(\xi,\eta)\mathrm{v}_I \tag{A.9}$$

$$\theta^m = N_1(\xi,\eta)\theta_I$$

$$\mathrm{x}^m = N_1(\xi,\eta)\mathrm{x}_I$$

where the subscript I is summed over all the element's nodes and the nodal velocities are obtained by differentiating the nodal coordinates with respect to time; (ξ,η) is a local coordinate system in midsurface and $(\xi,\eta)= (0,0)$ at the centre of the element.

The bilinear shape functions are as follows:

$$N_1 = \frac{1}{4}(1-\xi)(1-\eta) \tag{A.10}$$

$$N_2 = \frac{1}{4}(1+\xi)(1-\eta)$$

$$N_3 = \frac{1}{4}(1+\xi)(1+\eta)$$

$$N_4 = \frac{1}{4}(1-\xi)(1+\eta)$$

The velocity strains in Equation(B.8) at the centre of the element are developed using Equation(B.9) and (B.10):

$$\hat{d}_x = B_{1I}\hat{v}_{xI} + \hat{z}B_{1I}\hat{\theta}_{yI} \tag{A.11}$$

$$\hat{d}_y = B_{2I}\hat{v}_{yI} - \hat{z}B_{2I}\hat{\theta}_{xI}$$

$$2\hat{d}_{xy} = B_{2I}\hat{v}_{xI} + B_{1I}\hat{v}_{yI} + \hat{z}\left(B_{2I}\hat{\theta}_{yI} - B_{1I}\hat{\theta}_{xI}\right)$$

$$2\hat{d}_{xz} = B_{1I}\hat{v}_{zI} + N_1\hat{\theta}_{yI}$$

$$2\hat{d}_{yz} = B_{2I}\hat{v}_{zI} - N_1\hat{\theta}_{xI}$$

where,

$$B_{1I} = \frac{\sigma N_I}{\sigma\hat{x}} \tag{A.12}$$

$$B_{2I} = \frac{\sigma N_I}{\sigma\hat{y}}$$

After suitable constative evaluations using the above velocity strains, the resulting stresses are integrated through the thickness of the shell to obtain local resultant forces and moments. The integration formulae for the results are expressed as:

$$\hat{f}_{\alpha\beta}{}^{R} = \int \hat{\sigma}_{\alpha\beta}\, d\hat{z} \tag{A.13}$$

$$\hat{m}_{\alpha\beta}{}^{R} = -\int \hat{z}\hat{\sigma}_{\alpha\beta}\, d\hat{z}$$

where the superscript R means a resultant force or moment, and the Greek subscripts emphasize the limited range of the indices for plane stress plasticity.

The above element-centred stiffness force and moment resultants are related to the local nodal forces and moments by invoking the principle of virtual power and performing a one-point

quadrature. The relations obtained in this manner are:

$$\hat{f}_{xI} = A\left(B_{1I}\hat{f}_{xx}{}^{R} + B_{2I}\hat{f}_{xy}{}^{R}\right) \tag{B.14}$$

$$\hat{f}_{yI} = A\left(B_{2I}\hat{f}_{yy}{}^{R} + B_{1I}\hat{f}_{xy}{}^{R}\right)$$

$$\hat{f}_{zI} = Ak\left(B_{1I}\hat{f}_{xz}{}^{R} + B_{2I}\hat{f}_{yz}{}^{R}\right)$$

$$\hat{m}_{xI} = A\left(B_{2I}\hat{m}_{yy}{}^{R} + B_{1I}\hat{m}_{xy}{}^{R} - \frac{k}{4}\hat{f}_{yz}{}^{R}\right)$$

$$\hat{m}_{yI} = -A\left(B_{1I}\hat{m}_{xx}{}^{R} + B_{2I}\hat{m}_{xy}{}^{R} - \frac{k}{4}\hat{f}_{xz}{}^{R}\right)$$

$$\hat{m}_{zI} = 0$$

Then, these local nodal forces and moments are transformed into the global coordinate system. The global nodal forces and moments are then appropriately summed over all the nodes:

$$\hat{f}_{int} = \begin{Bmatrix} \hat{f}_{xI} \\ \hat{f}_{yI} \\ \hat{f}_{zI} \\ \hat{m}_{xI} \\ \hat{m}_{yI} \end{Bmatrix} \tag{B.15}$$

Based on the nodal accelerations in Equation(B.16), which is obtained from the governing equation (A.1), the global equations of motion are solved for the next increment $u^{(i+1)}$ (see Equation (A.2) and (A.3))

$$\ddot{u}^{(i)} = M^{-1}\left(f_{int}{}^{(i)} - f_{ext}{}^{(i)}\right) \tag{B.16}$$

Appendix B

Basic Equations of MCOL

APPENDIX B. BASIC EQUATIONS OF MCOL SOLVER

The basic equation of MCOL used for ship motion calculations can be written in the body-fixed reference system as follows:

$$[M_{RB} + M_A]\dot{\boldsymbol{y}} + [G_{RB} + G_A]\boldsymbol{y} = [F_W + F_H + F_V](\boldsymbol{y}, \boldsymbol{x}) + F_C \quad \text{(B.1)}$$

where, M_{RB} is a structural mass of ship; M_A is constant added mass for infinite frequency; x denotes the earth-fixed position of the centre of ship mass, including three transitions and three rotations (i.e., $\boldsymbol{x} = (x_{0G}, y_{0G}, z_{0G}, \phi, \theta, \Psi)$); y is the body fixed components of the absolute velocity $\boldsymbol{v}$ of the centre of mass and of the angular velocity vector ω (i.e., $\boldsymbol{y} = (u, v, w, p, q, r) = (\boldsymbol{v}, \omega)$) in Figure 4.9; G is the gyroscopic matrix; F_W, F_H, F_V and F_C are the wave damping force, restoring force, viscous force and contact force, respectively.

In addition to them, the body-fixed components of the forces and moments relative to the centre of mass acting on the body can be expressed as:

$$\boldsymbol{f} = (X, Y, Z, K, M, N) \quad \text{(B.2)}$$

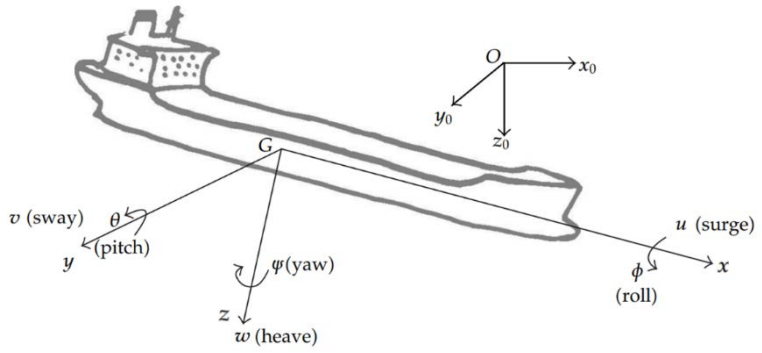

Figure B.0.1 Coordinate system defined in MCOL

An orthogonal matrix R with a positive determinant can describe the orientation of a rigid body, rotating freely in space. Based on Eulerian angles, the rotation matrix from the body-fixed frame to the earth-fixed frame can be defined as:

$$R = \begin{bmatrix} cos\theta cos\Psi & sin\phi sin\theta cos\Psi - cos\phi sin\Psi & cos\phi sin\theta cos\Psi + sin\phi sin\Psi \\ cos\theta cos\Psi & sin\phi sin\theta sin\Psi + cos\phi cos\Psi & cos\phi sin\theta sin\Psi - sin\phi cos\Psi \\ -sin\theta & sin\phi cos\theta & cos\phi cos\theta \end{bmatrix} \quad \text{(B.3)}$$

This matrix is obtained from three consecutive rotations. The first rotation is around $\vec{z}_0$-axis

and transforms the $(\vec{x}_0, \vec{y}_0, \vec{z}_0)$ earth-fixed frame into $(\vec{n}, \vec{t}, \vec{z}_0)$. The second rotation is applied around the new vector $\vec{t}$. It becomes $(\vec{x}\,', \vec{t}, \vec{z}_1)$. The last rotation is applied around $\vec{x}$ and transforms it into the body-fixed frame $(\vec{x}\,', \vec{y}, \vec{z}\,')$:

$$\begin{aligned} \vec{t} &= -\sin\psi\ \vec{x}_0 + \cos\psi\ \vec{y}_0 & \vec{x} &= \cos\theta\ \vec{n} - \sin\theta\ \vec{z}_0 \\ \vec{n} &= \cos\psi\ \vec{x}_0 + \sin\psi\ \vec{y}_0 & \vec{y} &= \cos\varphi\ \vec{t} + \sin\varphi\ \vec{z}_1 \\ \vec{z}_1 &= \sin\theta\ \vec{n} + \cos\theta\ \vec{z}_0 & \vec{z}\,' &= -\sin\varphi\ \vec{t} + \cos\varphi\ \vec{z}_1 \end{aligned} \tag{B.4}$$

Then, the angular velocity vector can be expressed as :

$$\vec{\omega} = \dot{\psi}\,\vec{z}_0 + \dot{\theta}\vec{t} + \dot{\varphi}\vec{x} \tag{B.5}$$

This leads to a nonlinear transformation between the body-fixed velocity components and the time derivatives of the position and the Eulerian angles:

$$\dot{\boldsymbol{x}} = \boldsymbol{J}\boldsymbol{y} \tag{B.6}$$

where, $\boldsymbol{J}$ is the transformation matrix defined by:

$$\boldsymbol{J} = \begin{bmatrix} \boldsymbol{R} & \boldsymbol{0} \\ \boldsymbol{0} & \boldsymbol{Q} \end{bmatrix} \qquad \text{with} \qquad \boldsymbol{Q} = \begin{bmatrix} 1 & \sin\varphi\tan\theta & \cos\varphi\tan\theta \\ 0 & \cos\varphi & -\sin\varphi \\ 0 & \sin\varphi\sec\theta & \cos\varphi\sec\theta \end{bmatrix} \tag{B.7}$$

B.1 RIGID-BODY DYNAMICS

According to Newton's law, the rigid body motion of the mass centre in a body-fixed rotating reference frame can be expressed as:

$$m\left[\ \dot{\vec{v}}_G + \vec{\omega} \times \vec{v}_G\ \right] = \vec{f}_{RG} \tag{B.8}$$

$$\boldsymbol{I}_G\dot{\vec{\omega}} + \ \vec{\omega} \times (\boldsymbol{I}_G\vec{\omega}) = \vec{m}_{RG} \tag{B.9}$$

where, m is the mass of the rigid body; $\vec{v}_G$ is the sway with respect to the centre of mass G;$\boldsymbol{I}_G$ is the inertia tensor at G in the body-fixed reference frame; $\vec{f}_{RG}$ and $\vec{m}_{RG}$ are the forces and moments applied to the rigid body with respect to G.

Then, the general form of rigid body motion in the body-fixed frame can be defined as:

$$M_{RB}\ \dot{\boldsymbol{y}} + \ G_{RB}\ \boldsymbol{y} = F_{RB} \tag{B.10}$$

$$M_{RB} = \begin{bmatrix} m & 0 & 0 & 0 & 0 & 0 \\ 0 & m & 0 & 0 & 0 & 0 \\ 0 & 0 & m & 0 & 0 & 0 \\ 0 & 0 & 0 & I_{xx} & -I_{xy} & -I_{xz} \\ 0 & 0 & 0 & -I_{xy} & I_{yy} & -I_{yz} \\ 0 & 0 & 0 & -I_{xz} & -I_{yz} & I_{zz} \end{bmatrix} \tag{B.11}$$

$$G_{RB} = \begin{bmatrix} 0 & 0 & 0 & 0 & mw & -mv \\ 0 & 0 & 0 & -mw & 0 & mu \\ 0 & 0 & 0 & mv & -mu & 0 \\ 0 & mw & -mv & 0 & -I_3 & I_2 \\ -mw & 0 & mu & I_3 & 0 & -I_1 \\ mv & -mu & 0 & -I_2 & I_1 & 0 \end{bmatrix} \tag{B.12}$$

Where, M_{RB} is the constant and positive rigid body inertia matrix; I_{xx}, I_{yy}, I_{zz} are the moments of inertia with respect to the x-, y- , and z- axes of the body-fixed frame; I_{xy}, I_{xz}, I_{yz} are the product of inertia; G_{RB} is the skew-symmetrical gyroscopic matrix; $I_1 = -I_{xx}p + I_{xy}q + I_{xz}r$; $I_2 = I_{xy}p - I_{yy}q + I_{yz}r$; $I_3 = I_{xz}p + I_{yz}q - I_{zz}r$

B.2 HYDRODYNAMIC MODEL – Added Inertia

Since the rigid body is afloat on water, the surrounding water moves together with the rigid body, and the inertia of fluid generates acceleration inertia forces. Imlay (1961) proposed the added masses as the inertial hydrodynamic forces for an arbitrarily shaped body, and he expressed it in the body-fixed frame as:

$$F_A = -M_A\ \dot{\boldsymbol{y}} - \ G_A\ \boldsymbol{y} \tag{B.13}$$

where, M_A is the added inertia matrix.

For a surface ship, M_A varies depending on the radiated wave frequency. Thus, M_A should be taken at infinite frequency $M(\infty)$ and can be expressed as :

$$\boldsymbol{M}_A = -\begin{bmatrix} X_{\dot{u}} & X_{\dot{v}} & X_{\dot{w}} & | & X_{\dot{p}} & X_{\dot{q}} & X_{\dot{r}} \\ Y_{\dot{u}} & Y_{\dot{v}} & Y_{\dot{w}} & | & Y_{\dot{p}} & Y_{\dot{q}} & Y_{\dot{r}} \\ Z_{\dot{u}} & Z_{\dot{v}} & Z_{\dot{w}} & | & Z_{\dot{p}} & Z_{\dot{q}} & Z_{\dot{r}} \\ \overline{K_{\dot{u}}} & \overline{K_{\dot{v}}} & \overline{K_{\dot{w}}} & | & \overline{K_{\dot{p}}} & \overline{K_{\dot{q}}} & \overline{K_{\dot{r}}} \\ M_{\dot{u}} & M_{\dot{v}} & M_{\dot{w}} & | & M_{\dot{p}} & M_{\dot{q}} & M_{\dot{r}} \\ N_{\dot{u}} & N_{\dot{v}} & N_{\dot{w}} & | & N_{\dot{p}} & N_{\dot{q}} & N_{\dot{r}} \end{bmatrix} = \begin{bmatrix} \boldsymbol{A}_{11} & \boldsymbol{A}_{12} \\ \boldsymbol{A}_{21} & \boldsymbol{A}_{22} \end{bmatrix} \tag{B.14}$$

Additionally, the gyroscopic matrix G_A can be written in component form as:

$$\boldsymbol{G}_A = \begin{bmatrix} 0 & 0 & 0 & 0 & -a_3 & a_2 \\ 0 & 0 & 0 & a_3 & 0 & -a_1 \\ 0 & 0 & 0 & -a_2 & a_1 & 0 \\ 0 & -a_3 & a_2 & 0 & -a_6 & a_5 \\ a_3 & 0 & -a_1 & a_6 & 0 & -a_4 \\ -a_2 & a_1 & 0 & -a_5 & a_4 & 0 \end{bmatrix} \tag{B.15}$$

Where,

$$\begin{cases} a_1 = X_{\dot{u}}u + X_{\dot{v}}v + X_{\dot{w}}w + X_{\dot{p}}p + X_{\dot{q}}q + X_{\dot{r}}r \\ a_2 = Y_{\dot{u}}u + Y_{\dot{v}}v + Y_{\dot{w}}w + Y_{\dot{p}}p + Y_{\dot{q}}q + Y_{\dot{r}}r \\ a_3 = Z_{\dot{u}}u + Z_{\dot{v}}v + Z_{\dot{w}}w + Z_{\dot{p}}p + Z_{\dot{q}}q + Z_{\dot{r}}r \\ a_4 = K_{\dot{u}}u + K_{\dot{v}}v + K_{\dot{w}}w + K_{\dot{p}}p + K_{\dot{q}}q + K_{\dot{r}}r \\ a_5 = M_{\dot{u}}u + M_{\dot{v}}v + M_{\dot{w}}w + M_{\dot{p}}p + M_{\dot{q}}q + M_{\dot{r}}r \\ a_6 = N_{\dot{u}}u + N_{\dot{v}}v + N_{\dot{w}}w + N_{\dot{p}}p + N_{\dot{q}}q + N_{\dot{r}}r \end{cases} \tag{B.16}$$

B.2 HYDRODYNAMIC MODEL – Restoring Forces and Moments

The gravitational and buoyancy can be simply expressed as:

$$\begin{aligned} W &= mg \\ B &= \rho g \nabla \\ \boldsymbol{F}_H &= W - B \end{aligned} \tag{B.17}$$

Where,g is the gravitational acceleration; ρ is the density of water; ∇ is the volume of the rigid body below water. They act along the z_0-axis of the earth fixed reference frame through the centres of gravity and buoyancy. Thus, the restoring forces and moments of the rigid body with respect to the body-fixed reference frame can be defined as:

$$\boldsymbol{F}_H = \begin{bmatrix} -\sin\theta\,(W-B) \\ \sin\phi\cos\theta\,(W-B) \\ \cos\phi\cos\theta\,(W-B) \\ (z_B\sin\phi\cos\theta - y_B\cos\phi\cos\theta)\;B \\ (x_B\cos\phi\cos\theta + z_B\sin\theta)\;B \\ (-y_B\sin\theta - x_B\sin\phi\cos\theta)\;B \end{bmatrix} \tag{B.18}$$

where, x_B, y_B and z_B are the centre of buoyancy in the body-fixed reference frame.

However, this $\boldsymbol{F}_H$ keeps changing depending on the earth-fixed vertical position $\boldsymbol{z}_{0G}$, the roll angle ϕ and the trim angle θ for the surface ship. Thus, They can be expressed as a linear function of displacements relative to a given reference position and attitude $\boldsymbol{x_{ref}}$:

$$\boldsymbol{F}_H = -\begin{bmatrix} \boldsymbol{R}^{*T} & \boldsymbol{0} \\ \boldsymbol{0} & \boldsymbol{R}^{*T} \end{bmatrix} \boldsymbol{K}\left(\boldsymbol{x} - \boldsymbol{x}_{ref}\right) + \boldsymbol{F}_{Href} \tag{B.19}$$

where,$R^*$is the rotation matrix from the reference waterplane fixed frame; $\boldsymbol{K}$ is a stiffness matrix in the earth-fixed frame;$\boldsymbol{F}_{Href}$is the restoring forces and moments in the body-fixed frame corresponding to the reference position.

$$\boldsymbol{K} = \rho g \begin{bmatrix} 0 & 0 & 0 & 0 & 0 & 0 \\ 0 & 0 & 0 & 0 & 0 & 0 \\ 0 & 0 & A_W & A_W y_W & -A_W x_W & 0 \\ 0 & 0 & A_W y_W & J_{Wx} & -J_{Wxy} & 0 \\ 0 & 0 & -A_W x_W & -J_{Wxy} & J_{Wy} & 0 \\ 0 & 0 & 0 & 0 & 0 & 0 \end{bmatrix} \tag{B.20}$$

$$\boldsymbol{R}^* = \begin{bmatrix} \cos\theta_{ref} & \sin\varphi_{ref}\sin\theta_{ref} & \cos\varphi_{ref}\sin\theta_{ref} \\ 0 & \cos\varphi_{ref} & -\sin\varphi_{ref} \\ -\sin\theta_{ref} & \sin\varphi_{ref}\cos\theta_{ref} & \cos\varphi_{ref}\cos\theta_{ref} \end{bmatrix} \tag{B.21}$$

where, A_W is the water plane area of the ship; x_W and y_W are the centre of water plane in the body-fixed frame; J_{Wx}, J_{Wy}, and J_{Wxy} are inertia componets of this area.

B.3 HYDRODYNAMIC MODEL – Other forces

As mentioned in Section 4.2.6, the wave damping forces $\boldsymbol{F_W}$and viscous forces $\boldsymbol{F_V}$were not taken into account as the influence of waves is minor to analysis results(Kim et al., 2021), but it causes to increase in the overall calculation time. The contact forces $\boldsymbol{F_c}$ can be obtained from LS-DYNA during the nemerical simulations.

Appendix C

Damage Stability Results of Case Study

APPENDIX C. DAMAGE STABILITY RESULTS

C.1 Final Damage Stability Results for RCOs in Case Study

Table C.1 ~ C.6 summarise re-calculated Subdivision Attained Indices for all 24 RCOs.

Table C.1 Results of the Subdivision Attained and improvement comparison for RCOs with single longitudinal subdivisions

Subdivision Zones	Original Layout	RCO1	RCO2	RCO3	RCO4
		1B/20 LBHD	2B/20 LBHD	3B/20 LBHD	4B/20 LBHD
Z01	0.0524	0.0312	0.0312	0.0312	0.0312
Z02	0.0544	0.0633	0.0633	0.0633	0.0633
Z03	0.0606	0.0865	0.0865	0.0865	0.0865
Z04	0.0495	0.0456	0.0456	0.0456	0.0456
Z05	0.0368	0.0343	0.0343	0.0343	0.0343
Z06	0.0192	0.0111	0.0111	0.0111	0.0111
Z07	0.0125	0.0143	0.0143	0.0143	0.0143
Z08	0.0214	0.0109	0.0109	0.0109	0.0109
Z09	0.0389	0.0361	0.0361	0.0361	0.0361
Z10	0.0496	0.0507	0.0507	0.0507	0.0507
Z11	0.0618	0.0890	0.0890	0.0890	0.0890
Z12	0.0563	0.0538	0.0538	0.0538	0.0538
Z13	0.0446	0.0429	0.0429	0.0429	0.0429
Z14	0.0453	0.0192	0.0199	0.0205	0.0206
Z15	0.0564	0.0852	0.0864	0.0908	0.0922
Z16	0.0581	0.0244	0.0252	0.0269	0.0285
Z17	0.0652	0.0695	0.0698	0.0703	0.0707
Z18	0.0750	0.0910	0.0910	0.0910	0.0910
Attained Index A	**0.8579**	**0.8590**	**0.8619**	**0.8692**	**0.8727**
Improvement		0.13%	0.47%	1.32%	1.72%
Loss of Index A	**0.1348**	**0.1337**	**0.1307**	**0.1235**	**0.1200**
Improvement		0.82%	3.01%	8.39%	10.96%
Total Index Sum	***0.9927***	***0.9927***	***0.9927***	***0.9927***	***0.9927***

Table C.2 Results of the Subdivision Attained and improvement comparison for RCOs with double longitudinal subdivisions

Subdivision Zones	Original Layout	RCO5	RCO6	RCO7	RCO8
		1B/20 LBHD + Another LBHD	2B/20 LBHD + Another LBHD	3B/20 LBHD + Another LBHD	4B/20 LBHD + Another LBHD
Z01	0.0524	0.0312	0.0312	0.0312	0.0312
Z02	0.0544	0.0633	0.0633	0.0633	0.0633
Z03	0.0606	0.0865	0.0865	0.0865	0.0865
Z04	0.0495	0.0456	0.0456	0.0456	0.0456
Z05	0.0368	0.0343	0.0343	0.0343	0.0343
Z06	0.0192	0.0111	0.0111	0.0111	0.0111
Z07	0.0125	0.0143	0.0143	0.0143	0.0143
Z08	0.0214	0.0109	0.0109	0.0109	0.0109
Z09	0.0389	0.0361	0.0361	0.0361	0.0361
Z10	0.0496	0.0507	0.0507	0.0507	0.0507
Z11	0.0618	0.0890	0.0890	0.0890	0.0890
Z12	0.0563	0.0538	0.0538	0.0538	0.0538
Z13	0.0446	0.0429	0.0429	0.0429	0.0429
Z14	0.0453	0.0217	0.0214	0.0212	0.0207
Z15	0.0564	0.0883	0.0891	0.0923	0.0932
Z16	0.0581	0.0291	0.0294	0.0302	0.0325
Z17	0.0652	0.0701	0.0702	0.0707	0.0710
Z18	0.0750	0.0910	0.0910	0.0910	0.0910
Attained Index A	**0.8579**	**0.8698**	**0.8708**	**0.8749**	**0.8780**
Improvement		1.38%	1.50%	1.99%	2.35%
Loss of Index A	**0.1348**	**0.1229**	**0.1219**	**0.1178**	**0.1147**
Improvement		8.81%	9.56%	12.65%	14.92%
Total Index Sum	***0.9927***	***0.9927***	***0.9927***	***0.9927***	***0.9927***

Table C.3 Results of the Subdivision Attained and improvement comparison for RCOs with hull thickness changes

Subdivision Zones	Original Layout	RCO9	RCO10	RCO11	RCO12	RCO13	RCO14
		50% Hull thickness increase	100% Hull thickness increase	20T Hull thickness	30T Hull thickness	40T Hull thickness	50T Hull thickness
Z01	0.0524	0.0312	0.0312	0.0312	0.0312	0.0312	0.0312
Z02	0.0544	0.0633	0.0633	0.0633	0.0633	0.0633	0.0633
Z03	0.0606	0.0865	0.0865	0.0865	0.0865	0.0865	0.0865
Z04	0.0495	0.0456	0.0456	0.0456	0.0456	0.0456	0.0456
Z05	0.0368	0.0343	0.0343	0.0343	0.0343	0.0343	0.0343
Z06	0.0192	0.0111	0.0111	0.0111	0.0111	0.0111	0.0111
Z07	0.0125	0.0143	0.0143	0.0143	0.0143	0.0143	0.0143
Z08	0.0214	0.0109	0.0109	0.0109	0.0109	0.0109	0.0109
Z09	0.0389	0.0361	0.0361	0.0361	0.0361	0.0361	0.0361
Z10	0.0496	0.0507	0.0507	0.0507	0.0507	0.0507	0.0507
Z11	0.0618	0.0890	0.0890	0.0890	0.0890	0.0890	0.0890
Z12	0.0563	0.0538	0.0538	0.0538	0.0538	0.0538	0.0538
Z13	0.0446	0.0429	0.0429	0.0429	0.0429	0.0429	0.0429
Z14	0.0453	0.0196	0.0196	0.0196	0.0196	0.0196	0.0312
Z15	0.0564	0.0862	0.0862	0.0862	0.0862	0.0862	0.1000
Z16	0.0581	0.0227	0.0227	0.0227	0.0227	0.0227	0.0362
Z17	0.0652	0.0695	0.0695	0.0695	0.0695	0.0695	0.0727
Z18	0.0750	0.0910	0.0910	0.0910	0.0910	0.0910	0.0910
Attained Index A	**0.8579**	**0.8587**	**0.8587**	**0.8587**	**0.8587**	**0.8587**	**0.9008**
Improvement		0.09%	0.09%	0.09%	0.09%	0.09%	5.00%
Loss of Index A	**0.1348**	**0.1340**	**0.1340**	**0.1340**	**0.1340**	**0.1340**	**0.0919**
Improvement		0.59%	0.60%	0.60%	0.60%	0.60%	31.82%
Total Index Sum	***0.9927***	***0.9927***	***0.9927***	***0.9927***	***0.9927***	***0.9927***	***0.9927***

Table C.4 Results of the Subdivision Attained and improvement comparison for RCOs with passive measure combinations

Subdivision Zones	Original Layout	RCO15	RCO16	RCO17	RCO18
		100% hull thickness increase + 1B/20 LBHD	100% hull thickness increase + 2B/20 LBHD	20T hull + Another LBHD at 10.6m	30T hull + Another LBHD at 6.6m
Z01	0.0524	0.0312	0.0312	0.0312	0.0312
Z02	0.0544	0.0633	0.0633	0.0633	0.0633
Z03	0.0606	0.0865	0.0865	0.0865	0.0865
Z04	0.0495	0.0456	0.0456	0.0456	0.0456
Z05	0.0368	0.0343	0.0343	0.0343	0.0343
Z06	0.0192	0.0111	0.0111	0.0111	0.0111
Z07	0.0125	0.0143	0.0143	0.0143	0.0143
Z08	0.0214	0.0109	0.0109	0.0109	0.0109
Z09	0.0389	0.0361	0.0361	0.0361	0.0361
Z10	0.0496	0.0507	0.0507	0.0507	0.0507
Z11	0.0618	0.0890	0.0890	0.0890	0.0890
Z12	0.0563	0.0538	0.0538	0.0538	0.0538
Z13	0.0446	0.0429	0.0429	0.0429	0.0429
Z14	0.0453	0.0192	0.0199	0.0214	0.0263
Z15	0.0564	0.0852	0.0870	0.0933	0.0977
Z16	0.0581	0.0244	0.0252	0.0349	0.0351
Z17	0.0652	0.0695	0.0698	0.0714	0.0728
Z18	0.0750	0.0910	0.0910	0.0910	0.0910
Attained Index A	**0.8579**	**0.8590**	**0.8625**	**0.8817**	**0.8925**
Improvement		0.13%	0.54%	2.77%	4.04%
Loss of Index A	**0.1348**	**0.1337**	**0.1302**	**0.1110**	**0.1002**
Improvement		0.83%	3.41%	17.63%	25.68%
Total Index Sum	***0.9927***	***0.9927***	***0.9927***	***0.9927***	***0.9927***

Table C.5 Results of the Subdivision Attained and improvement comparison for RCOs with structural RCOs + non-structural RCO (Foam filling system)

Subdivision Zones	Original Layout	RCO1-F	RCO2-F	RCO3-F	RCO4-F
		1B/20 LBHD + Foam Filling System	2B/20 LBHD + Foam Filling System	3B/20 LBHD + Foam Filling System	4B/20 LBHD + Foam Filling System
Z01	0.0524	0.0312	0.0312	0.0312	0.0312
Z02	0.0544	0.0633	0.0633	0.0633	0.0633
Z03	0.0606	0.0865	0.0865	0.0865	0.0865
Z04	0.0495	0.0456	0.0456	0.0456	0.0456
Z05	0.0368	0.0343	0.0343	0.0343	0.0343
Z06	0.0192	0.0111	0.0111	0.0111	0.0111
Z07	0.0125	0.0143	0.0143	0.0143	0.0143
Z08	0.0214	0.0109	0.0109	0.0109	0.0109
Z09	0.0389	0.0361	0.0361	0.0361	0.0361
Z10	0.0496	0.0507	0.0507	0.0507	0.0507
Z11	0.0618	0.0890	0.0890	0.0890	0.0890
Z12	0.0563	0.0538	0.0538	0.0538	0.0538
Z13	0.0446	0.0429	0.0429	0.0429	0.0429
Z14	0.0453	0.0237	0.0251	0.0272	0.0290
Z15	0.0564	0.0865	0.0890	0.0957	0.0975
Z16	0.0581	0.0245	0.0259	0.0303	0.0336
Z17	0.0652	0.0695	0.0698	0.0707	0.0711
Z18	0.0750	0.0910	0.0910	0.0910	0.0910
Attained Index A	**0.8579**	**0.8649**	**0.8705**	**0.8846**	**0.8919**
Improvement		0.82%	1.47%	3.11%	3.96%
Loss of Index A	**0.1348**	**0.1278**	**0.1222**	**0.1081**	**0.1008**
Improvement		5.22%	9.32%	19.81%	25.21%
Total Index Sum	***0.9927***	***0.9927***	***0.9927***	***0.9927***	***0.9927***

Table C.6 Results of the Subdivision Attained and improvement comparison for RCOs with passive RCOs + non-structural RCO (Foam filling system)

Subdivision Zones	Original Layout	RCO6-F	RCO8-F	RCO17-F	RCO18-F
		2B/20 LBHD + Another LBHD at 13.1m + Foam Filling System	4B/20 LBHD + Another LBHD at 13.1m + Foam Filling System	20T hull thickness + Another LBHD at 10.6m + Foam Filling System	30T hull thickness + Another LBHD at 6.6m + Foam Filling System
Z01	0.0524	0.0312	0.0312	0.0312	0.0312
Z02	0.0544	0.0633	0.0633	0.0633	0.0633
Z03	0.0606	0.0865	0.0865	0.0865	0.0865
Z04	0.0495	0.0456	0.0456	0.0456	0.0456
Z05	0.0368	0.0343	0.0343	0.0343	0.0343
Z06	0.0192	0.0111	0.0111	0.0111	0.0111
Z07	0.0125	0.0143	0.0143	0.0143	0.0143
Z08	0.0214	0.0109	0.0109	0.0109	0.0109
Z09	0.0389	0.0361	0.0361	0.0361	0.0361
Z10	0.0496	0.0507	0.0507	0.0507	0.0507
Z11	0.0618	0.0890	0.0890	0.0890	0.0890
Z12	0.0563	0.0538	0.0538	0.0538	0.0538
Z13	0.0446	0.0429	0.0429	0.0429	0.0429
Z14	0.0453	0.0289	0.0304	0.0300	0.0301
Z15	0.0564	0.0912	0.0988	0.1003	0.1006
Z16	0.0581	0.0301	0.0346	0.0356	0.0364
Z17	0.0652	0.0703	0.0719	0.0728	0.0728
Z18	0.0750	0.0910	0.0910	0.0910	0.0910
Attained Index A	**0.8579**	**0.8812**	**0.8964**	**0.8993**	**0.9005**
Improvement		2.72%	4.49%	4.82%	4.97%
Loss of Index A	**0.1348**	**0.1114**	**0.0963**	**0.0934**	**0.0922**
Improvement		17.33%	28.55%	30.70%	31.61%
Total Index Sum	***0.9927***	***0.9927***	***0.9927***	***0.9927***	***0.9927***

C.2 p×(1-s) and Attained index graphs for RCOs in Case Study

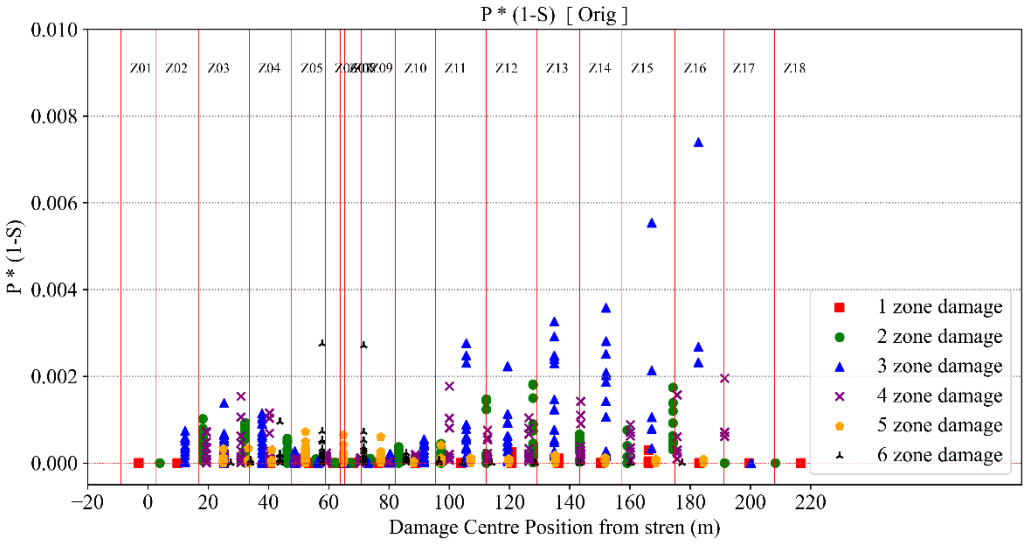

(a)

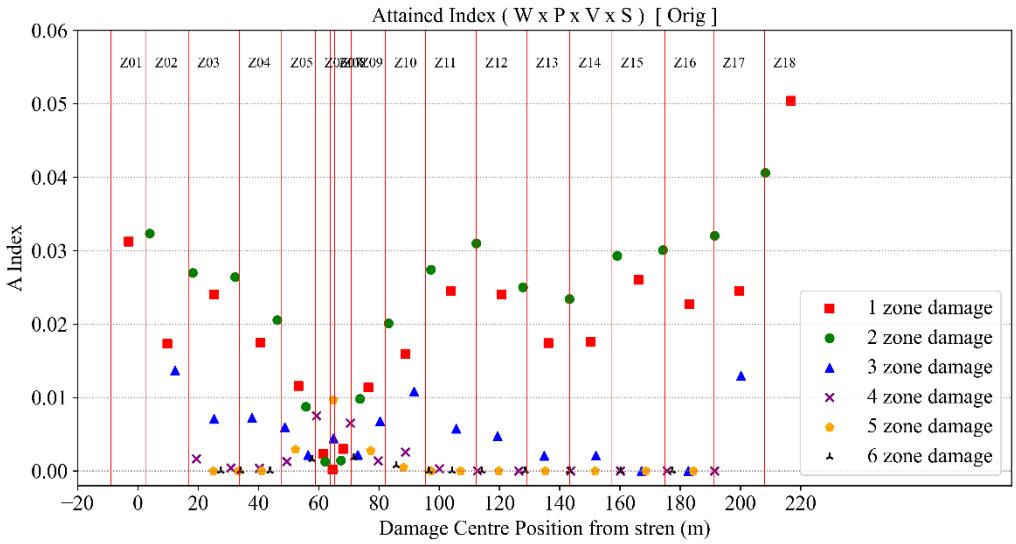

(b)

Figure C.1 Original : Summary of Damage Stablility (a) P (1-S) graph and (c) local Attained Index sub sum graph

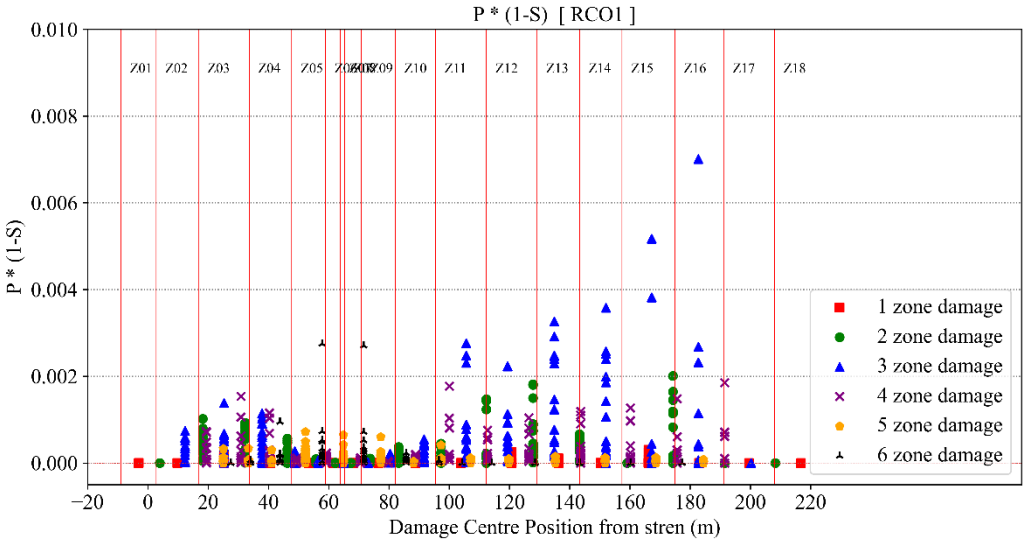

(a)

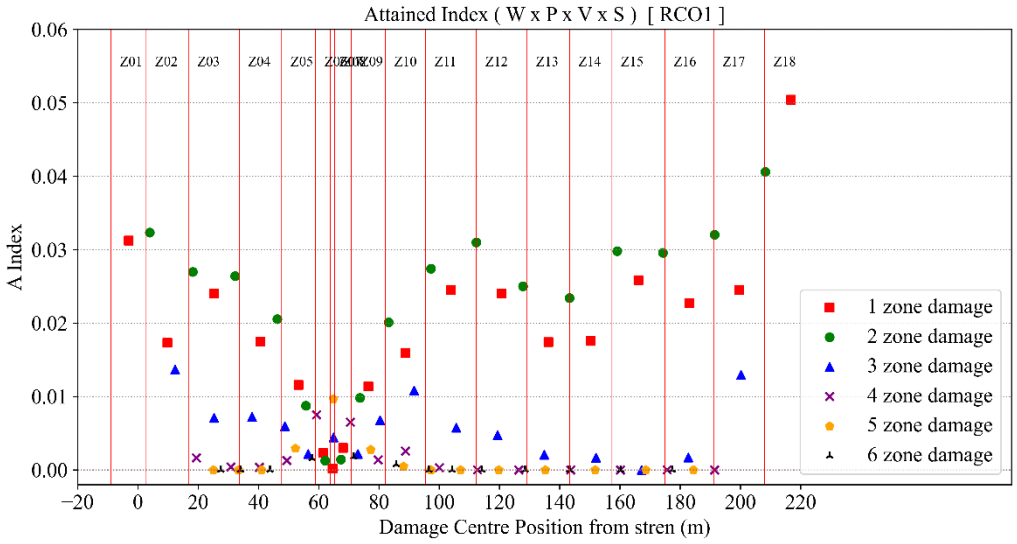

(b)

Figure C.2 RCO1: Summary of Damage Stablility (a) P (1-S) graph and (c) local Attained Index sub sum graph

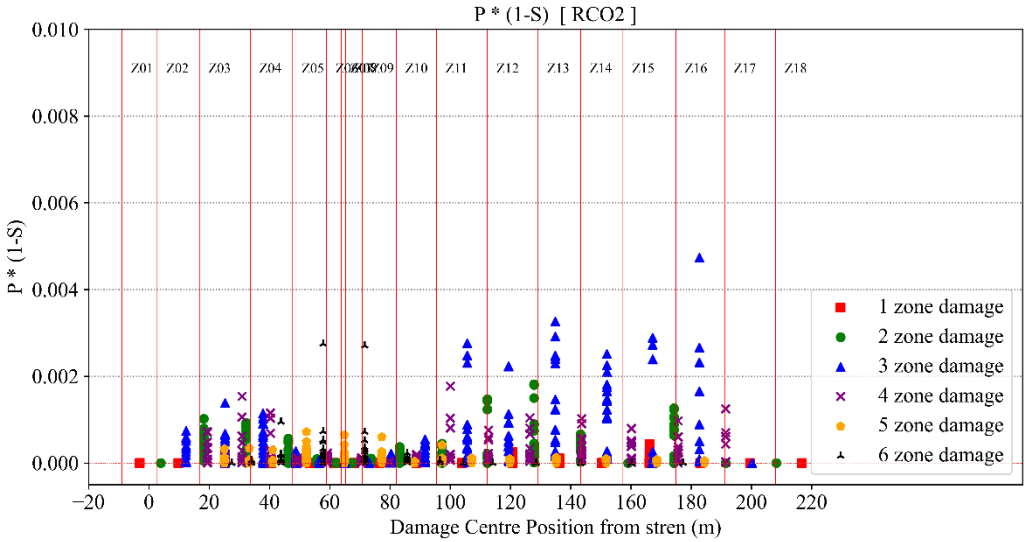

(a)

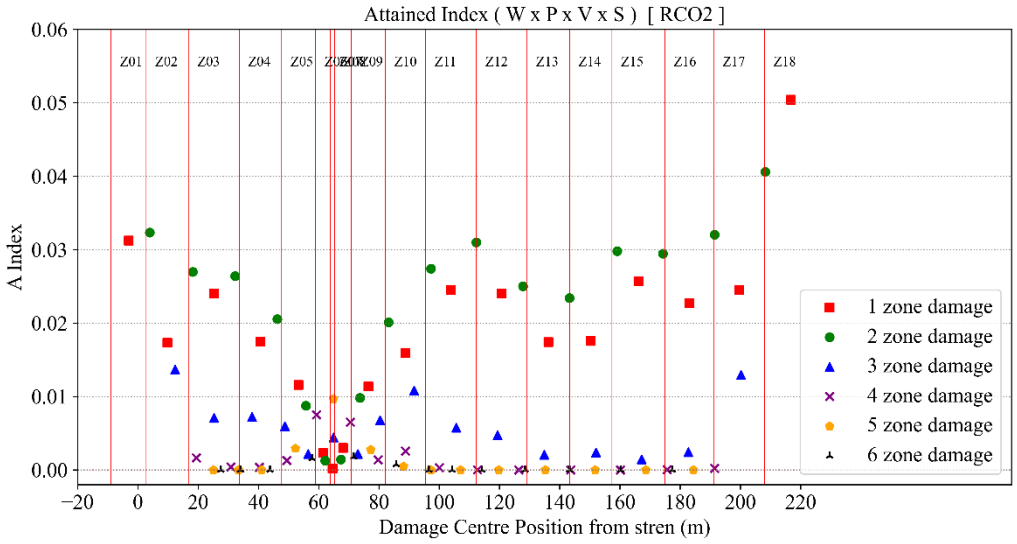

(b)

Figure C.3 RCO2: Summary of Damage Stablility (a) P (1-S) graph and (c) local Attained Index sub sum graph

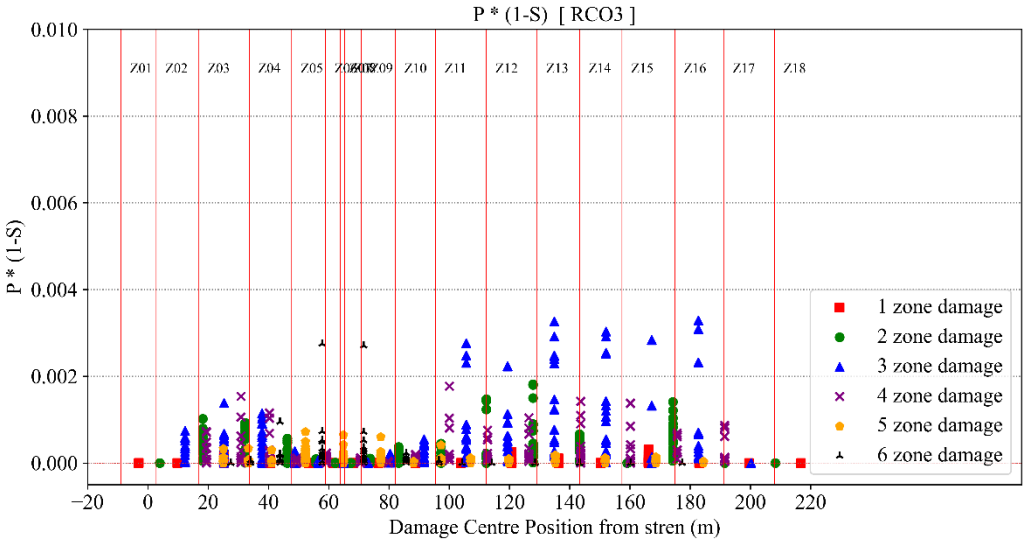

(a)

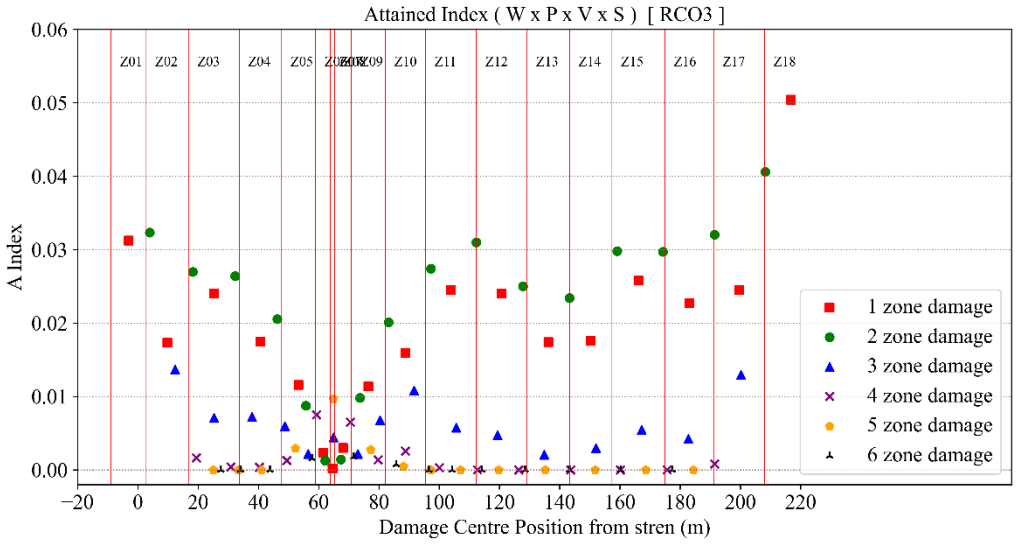

(b)

Figure C.4 RCO3: Summary of Damage Stablility (a) P (1-S) graph and (c) local Attained Index sub sum graph

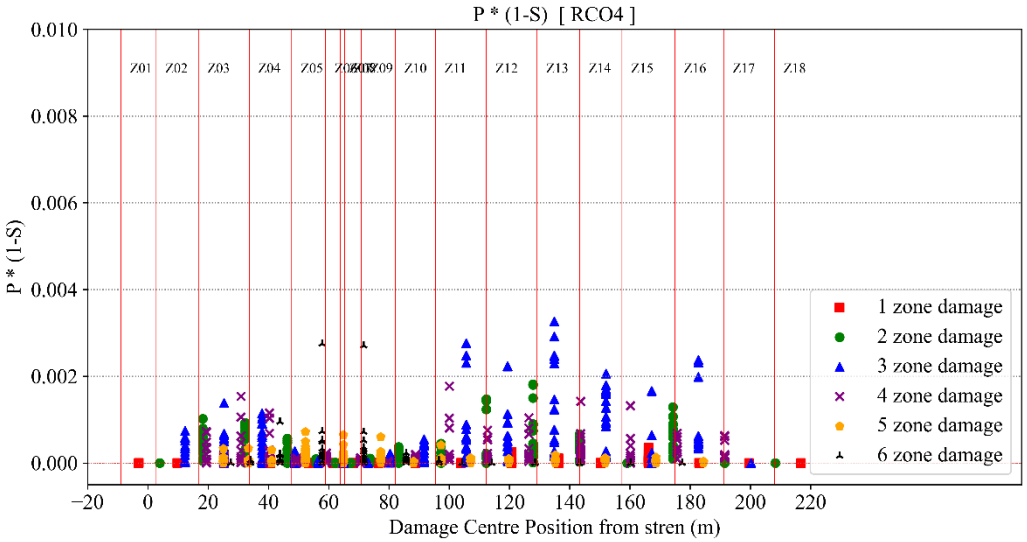

(a)

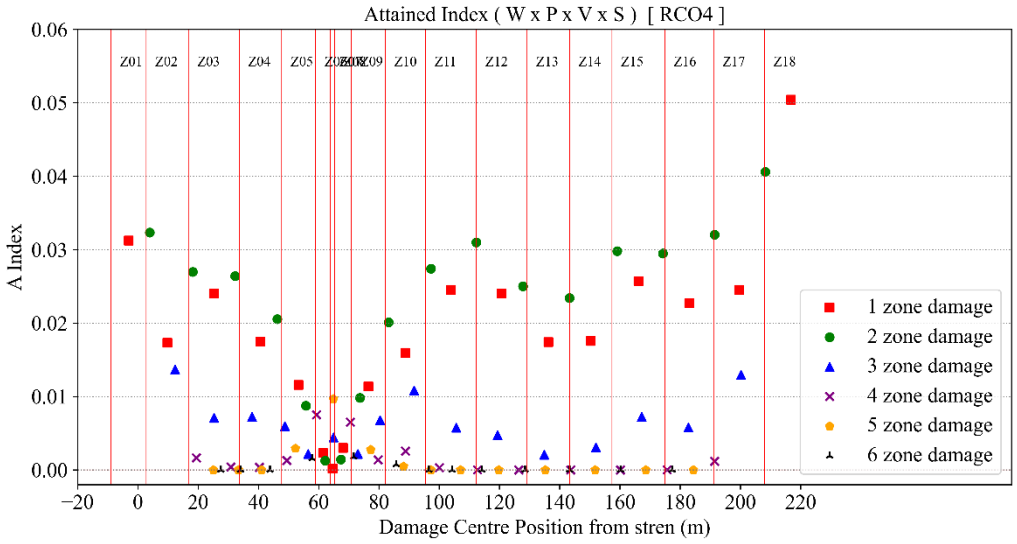

(b)

Figure C.5 RCO4: Summary of Damage Stablility (a) P (1-S) graph and (c) local Attained Index sub sum graph

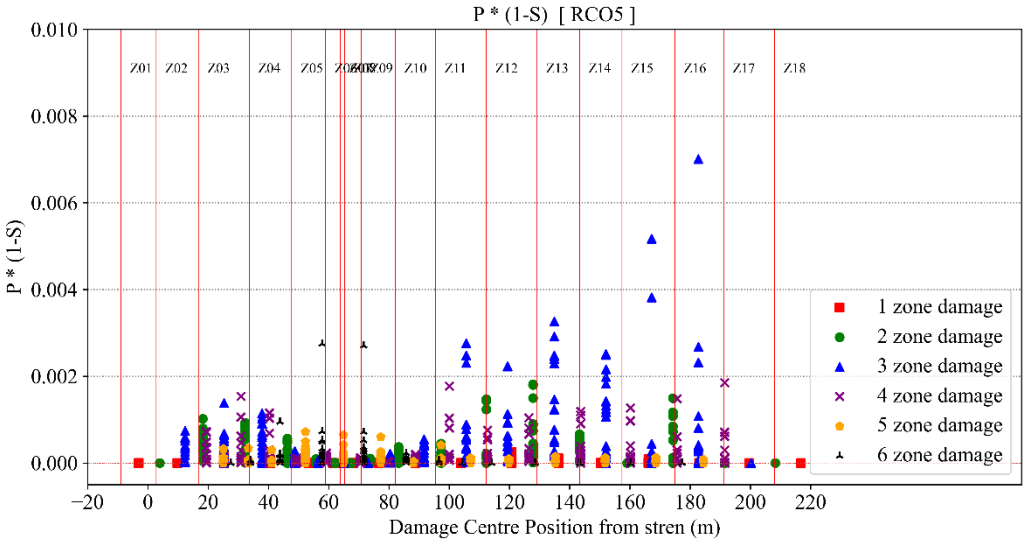

(a)

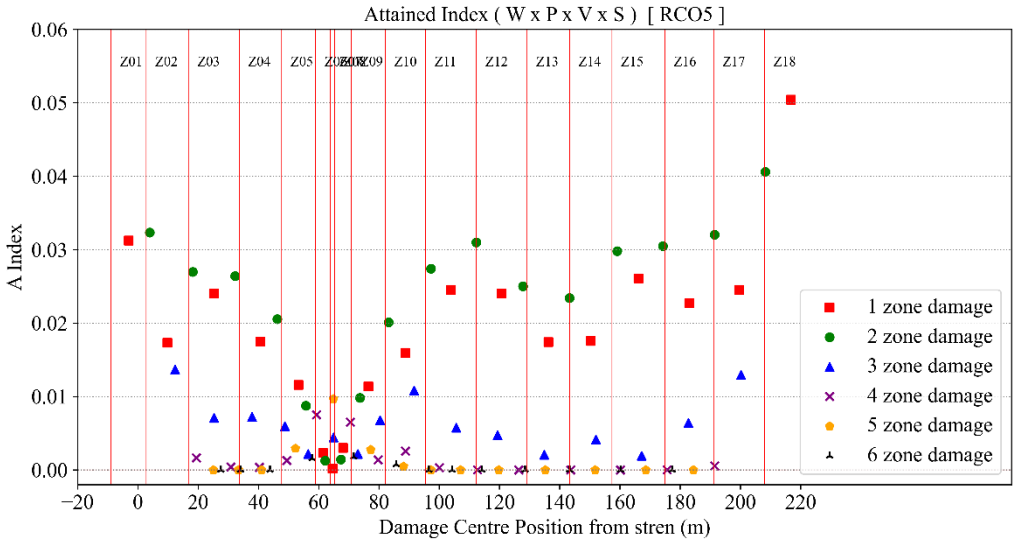

(b)

Figure C.6 RCO5: Summary of Damage Stablility (a) P (1-S) graph and (c) local Attained Index sub sum graph

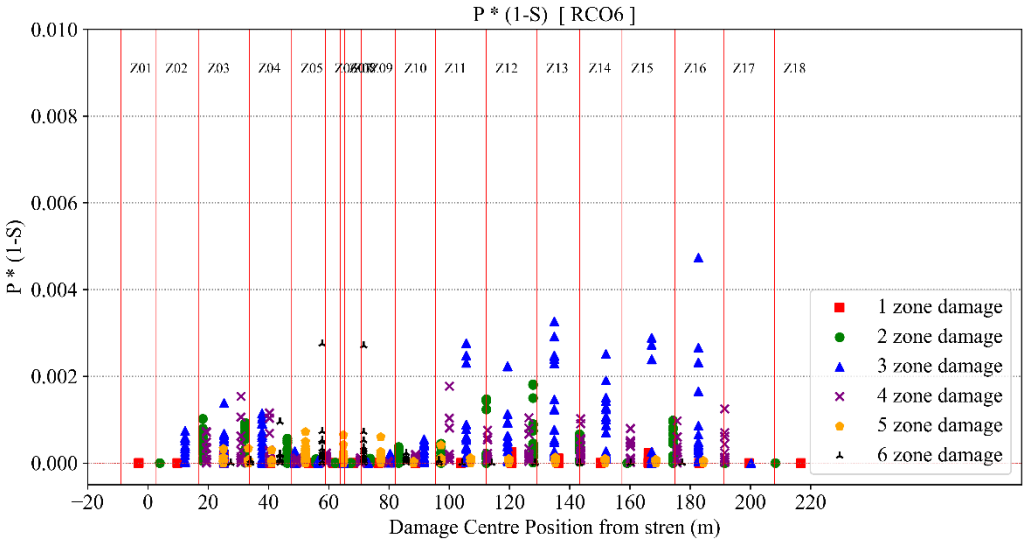

(a)

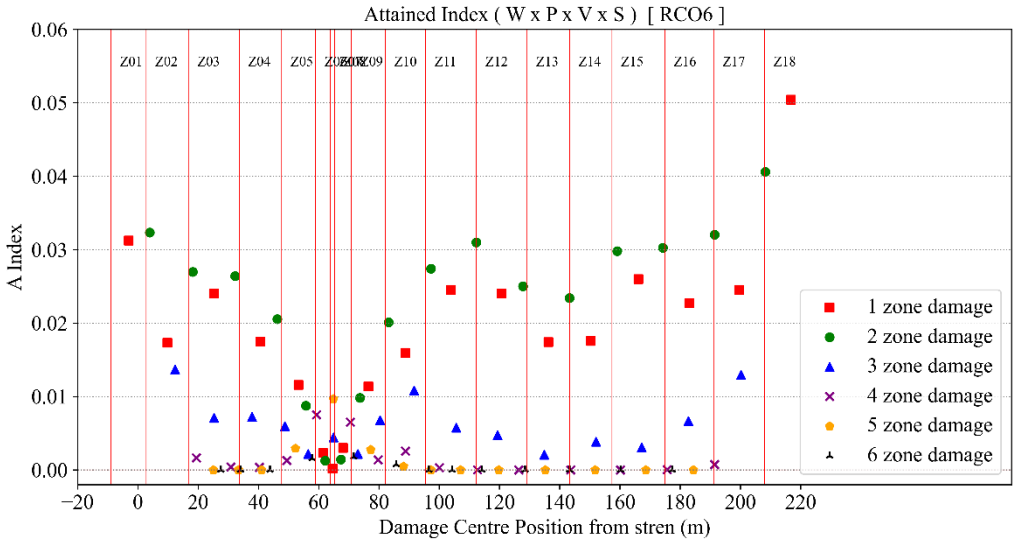

(b)

Figure C.7 RCO6: Summary of Damage Stablility (a) P (1-S) graph and (c) local Attained Index sub sum graph

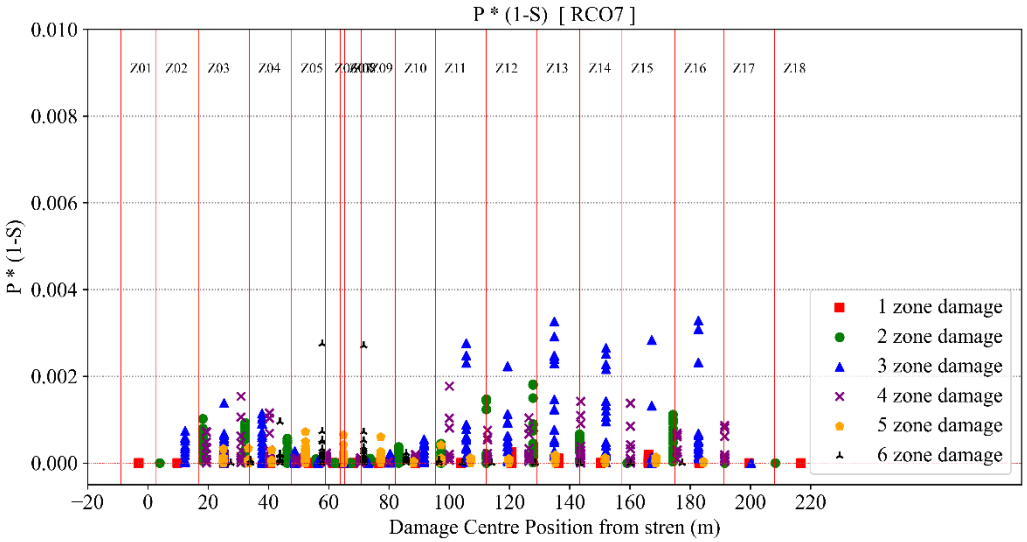

(a)

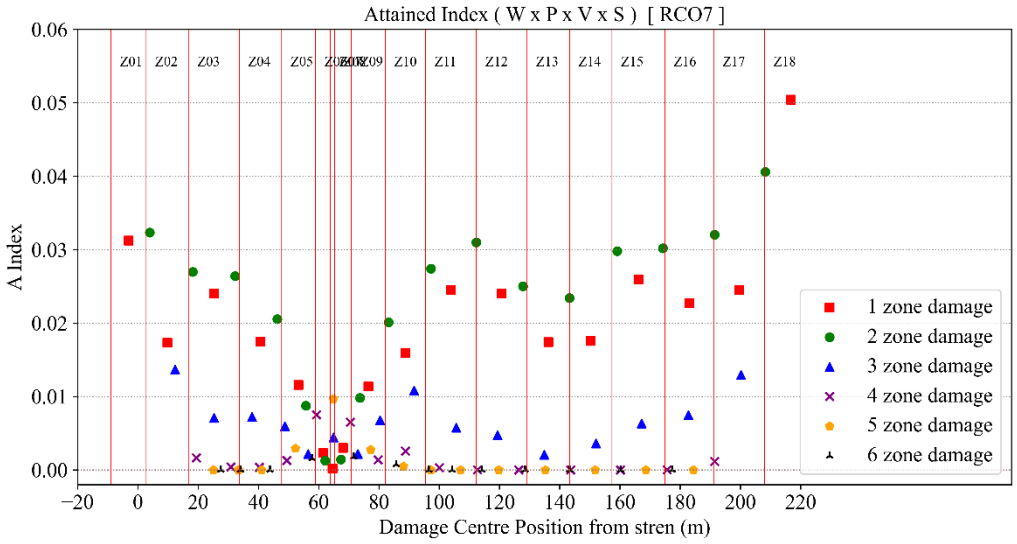

(b)

Figure C.8 RCO7: Summary of Damage Stablility (a) P (1-S) graph and (c) local Attained Index sub sum graph

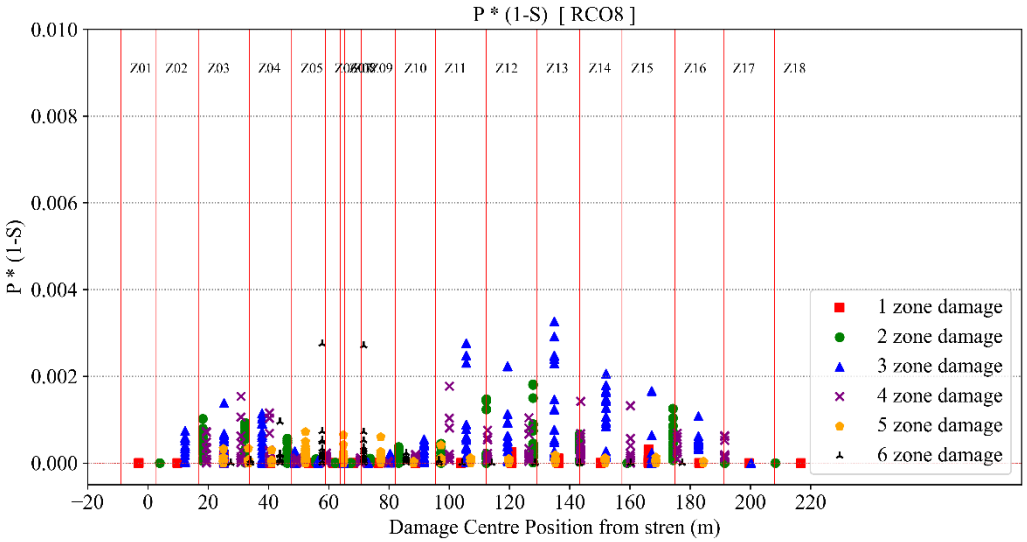

(a)

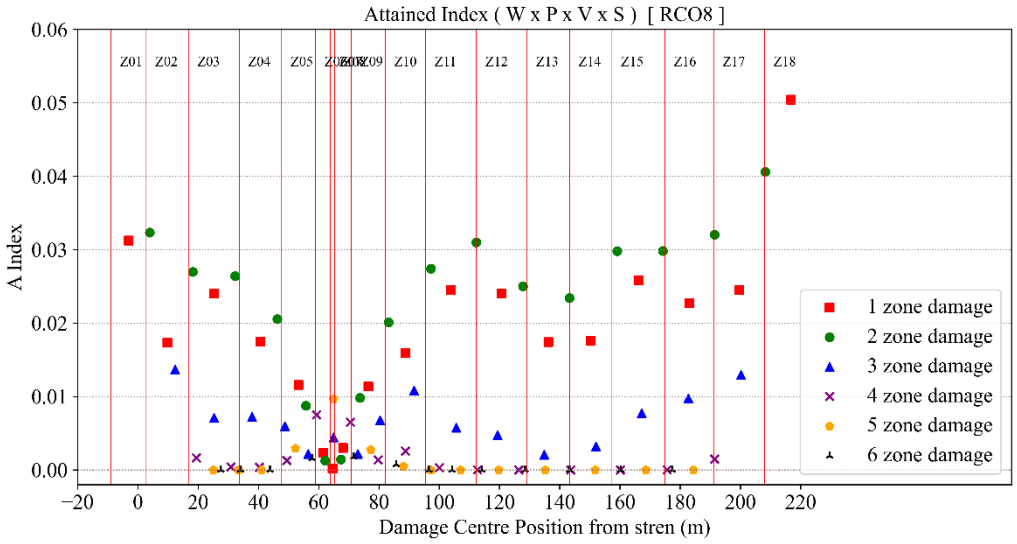

(b)

Figure C.9 RCO8: Summary of Damage Stablility (a) P (1-S) graph and (c) local Attained Index sub sum graph

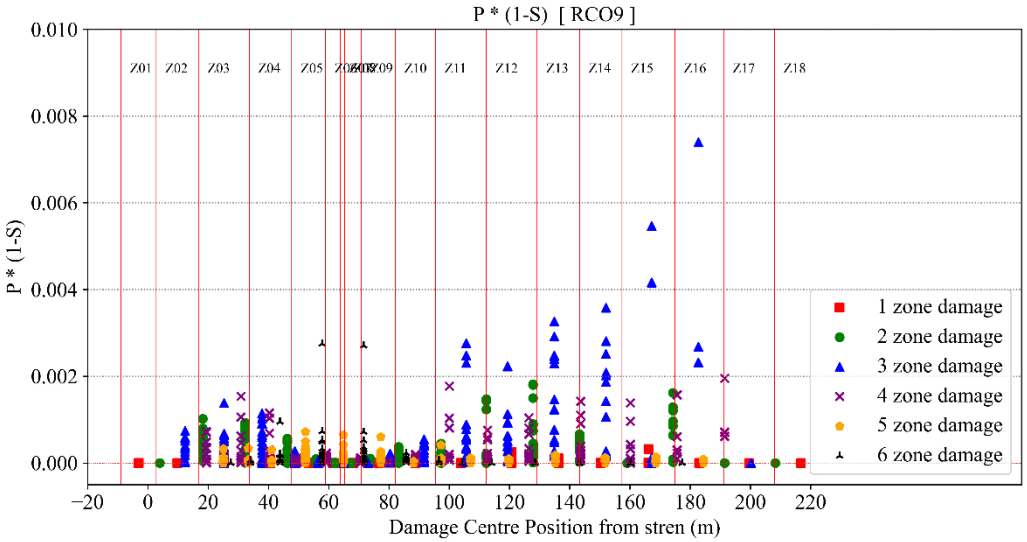

(a)

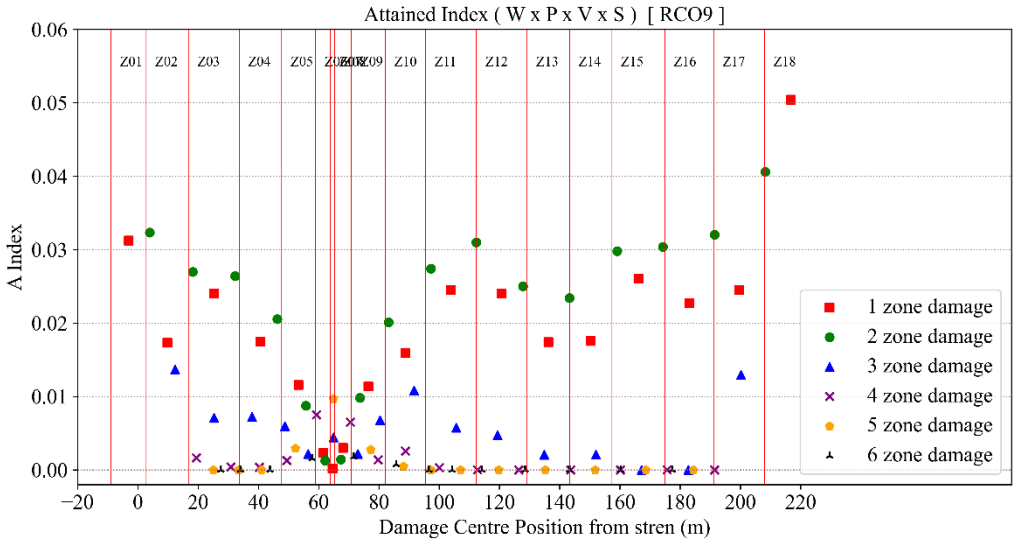

(b)

Figure C.10 RCO9~13: Summary of Damage Stablility (a) P (1-S) graph and (c) local Attained Index sub sum graph

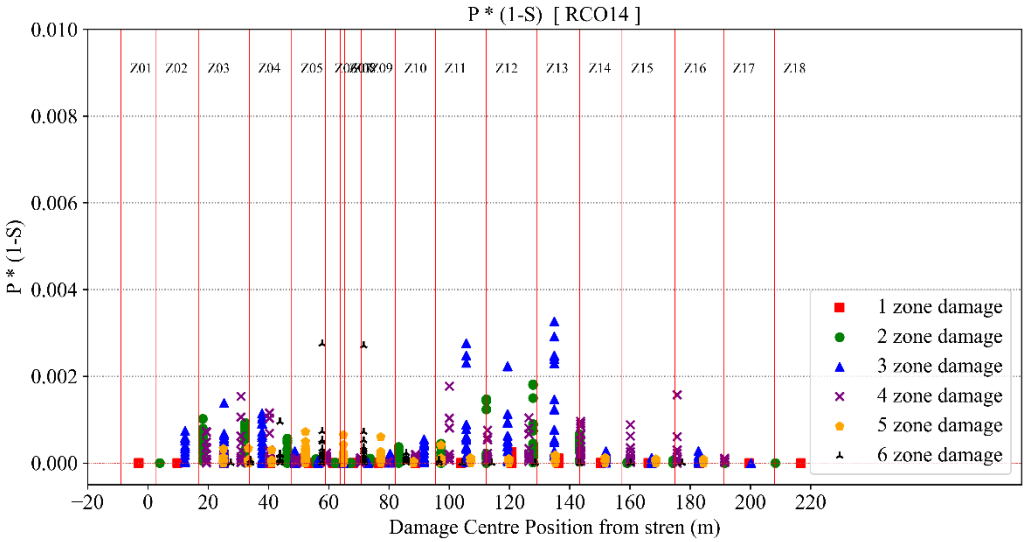

(a)

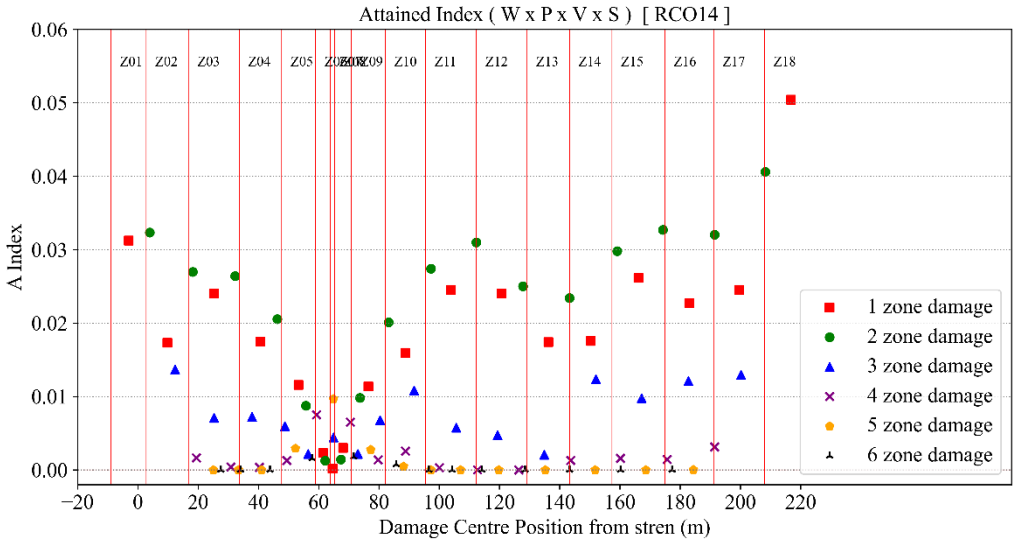

(b)

Figure C.11 RCO14: Summary of Damage Stablility (a) P (1-S) graph and (c) local Attained Index sub sum graph

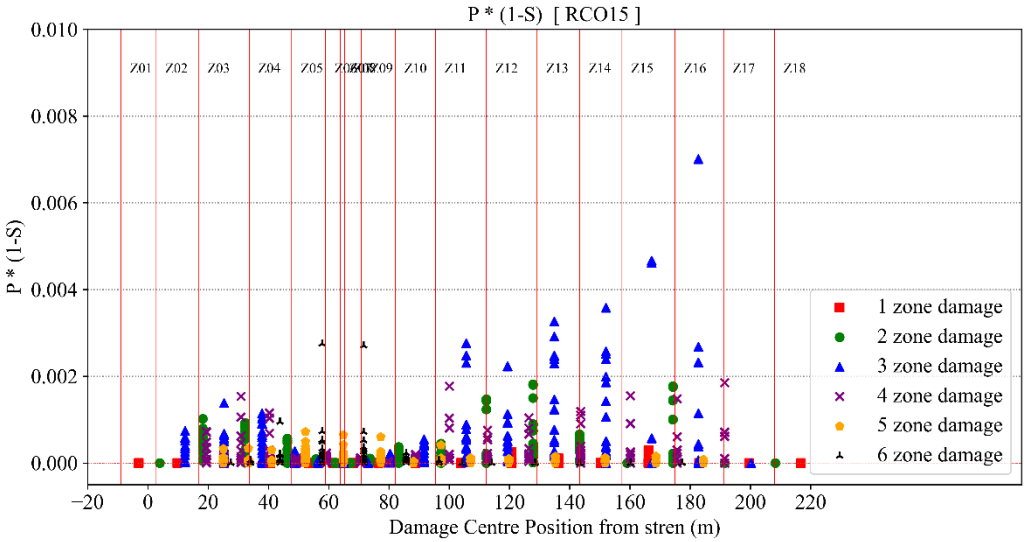

(a)

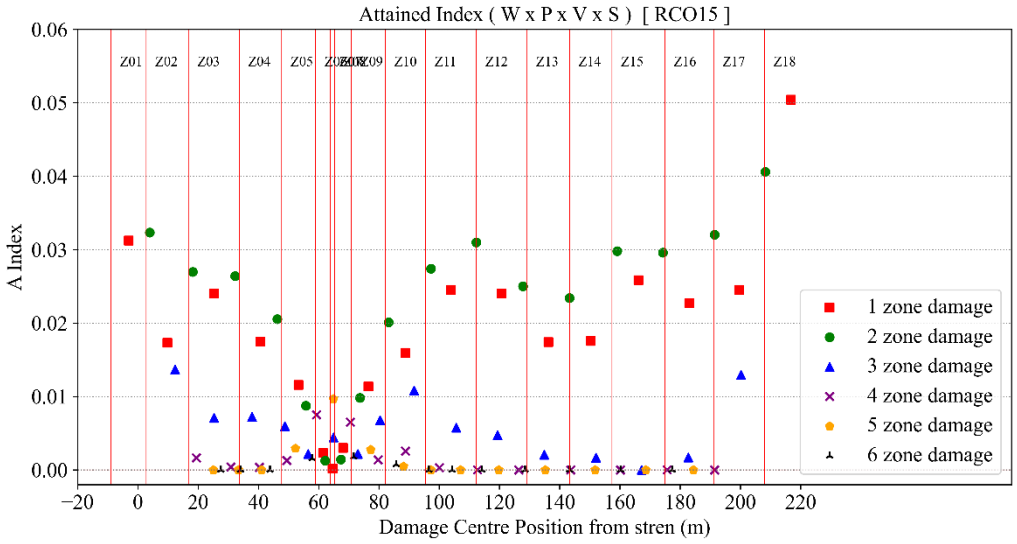

(b)

Figure C.12 RCO15: Summary of Damage Stablility (a) P (1-S) graph and (c) local Attained Index sub sum graph

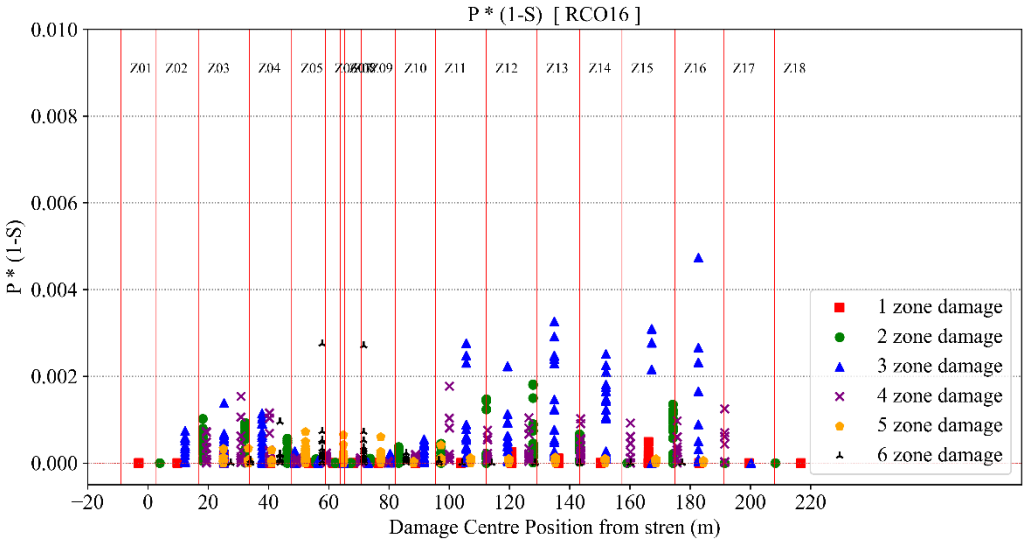

(a)

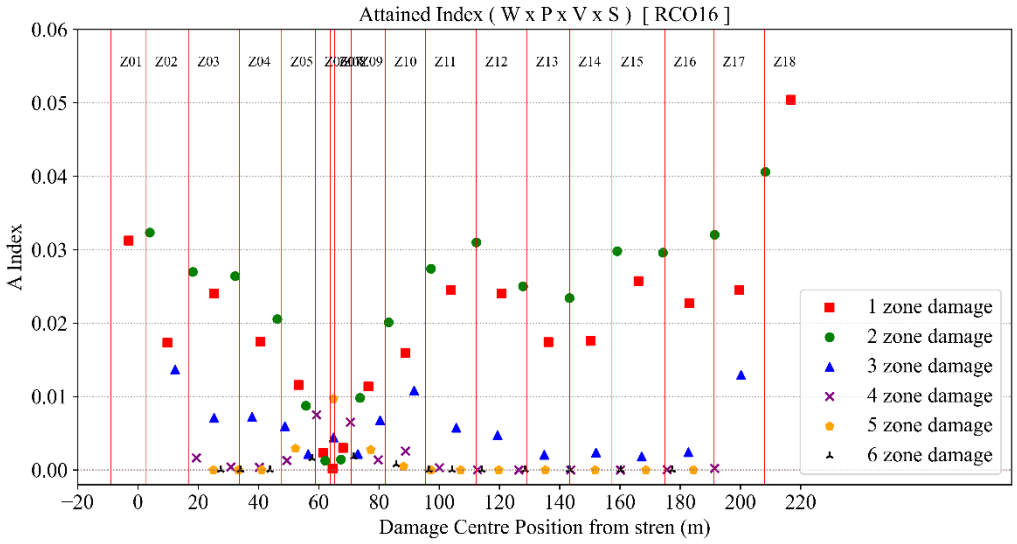

(b)

Figure C.13 RCO16: Summary of Damage Stablility (a) P (1-S) graph and (c) local Attained Index sub sum graph

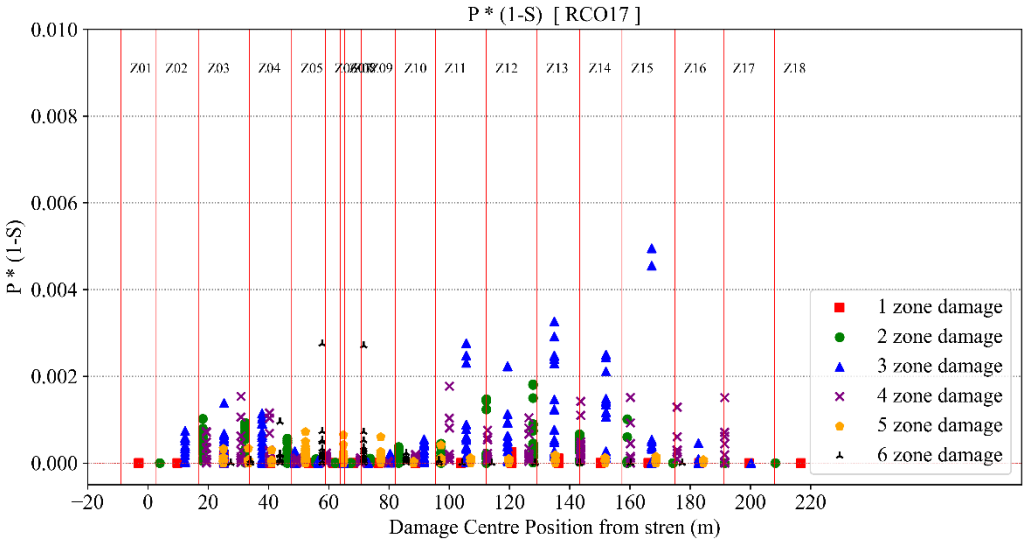

(a)

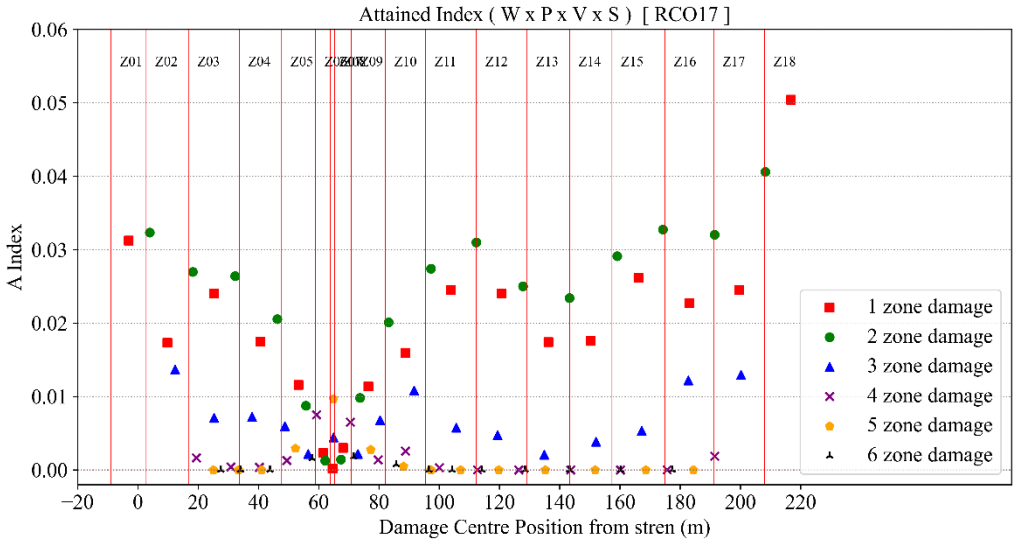

(b)

Figure C.14 RCO17: Summary of Damage Stablility (a) P (1-S) graph and (c) local Attained Index sub sum graph

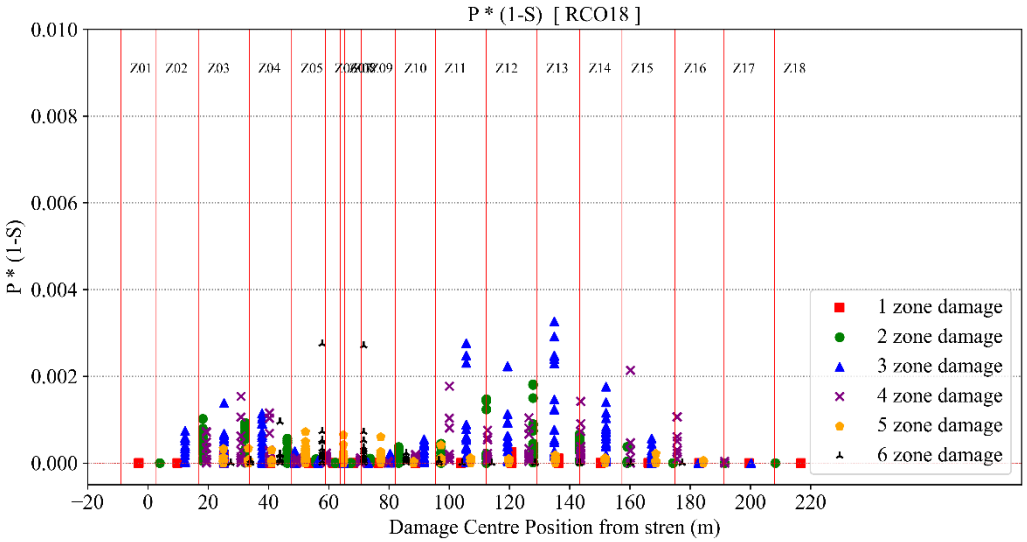

(a)

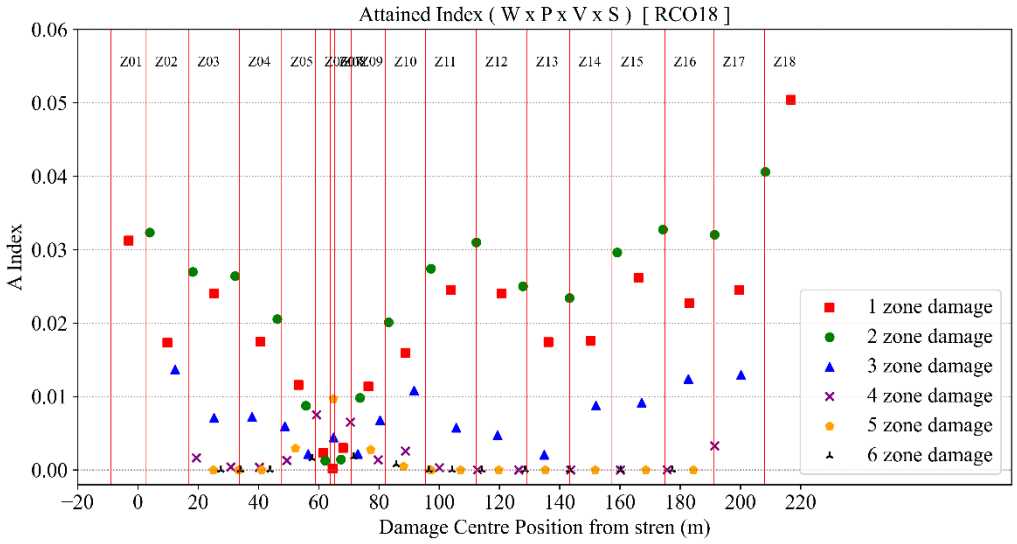

(b)

Figure C.15 RCO18: Summary of Damage Stablility (a) P (1-S) graph and (c) local Attained Index sub sum graph

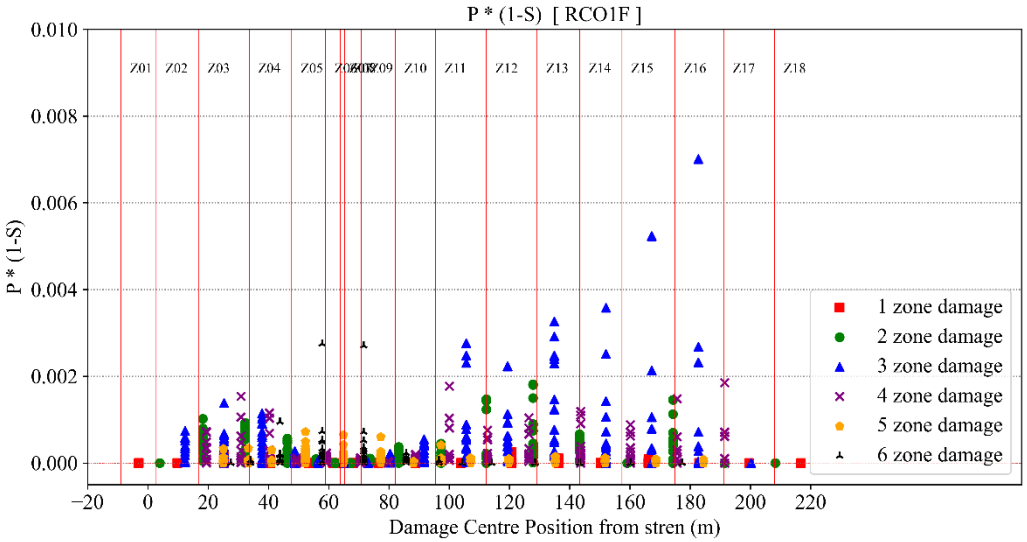

(a)

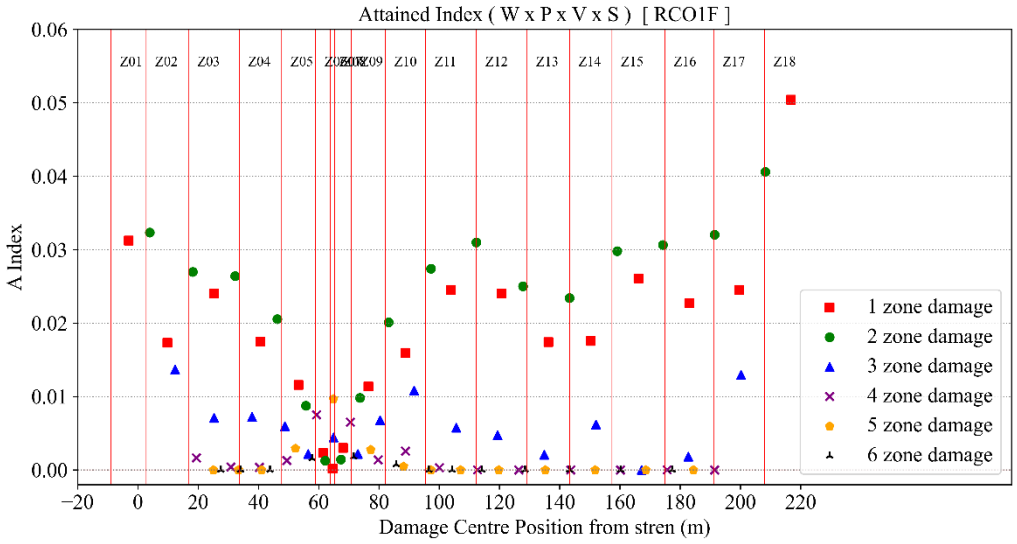

(b)

Figure C.16 RCO1-F: Summary of Damage Stablility (a) P (1-S) graph and (c) local Attained Index sub sum graph

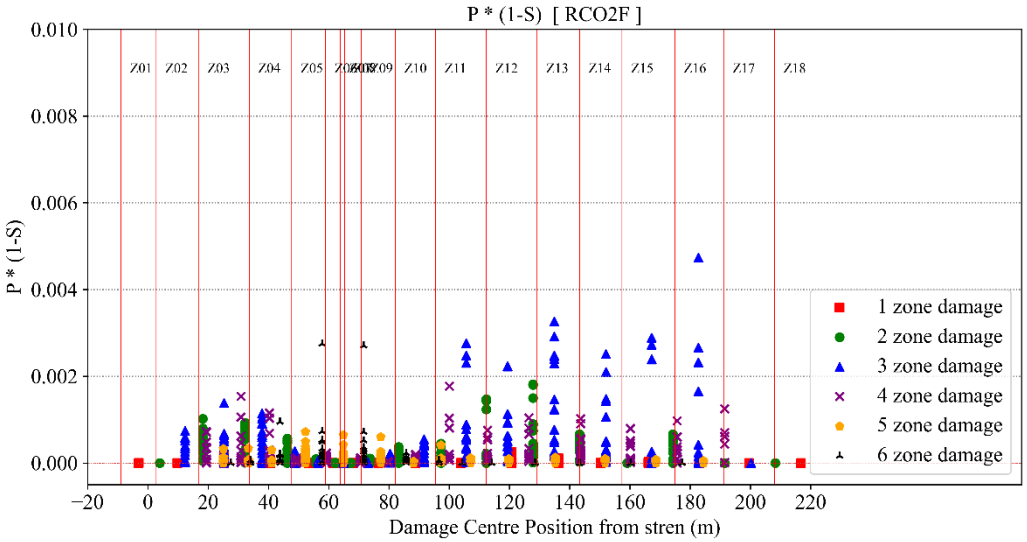

(a)

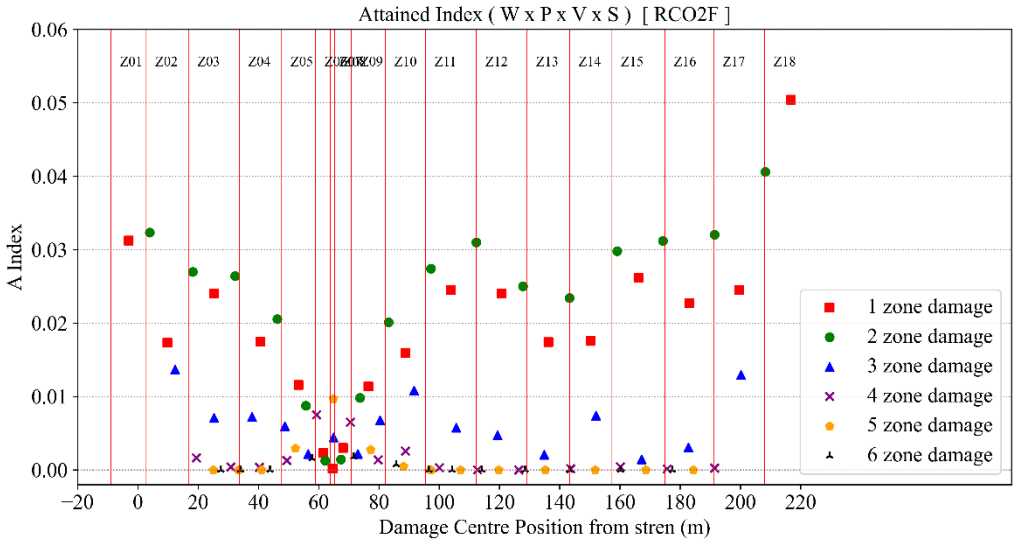

(b)

Figure C.17 RCO2-F: Summary of Damage Stablility (a) P (1-S) graph and (c) local Attained Index sub sum graph

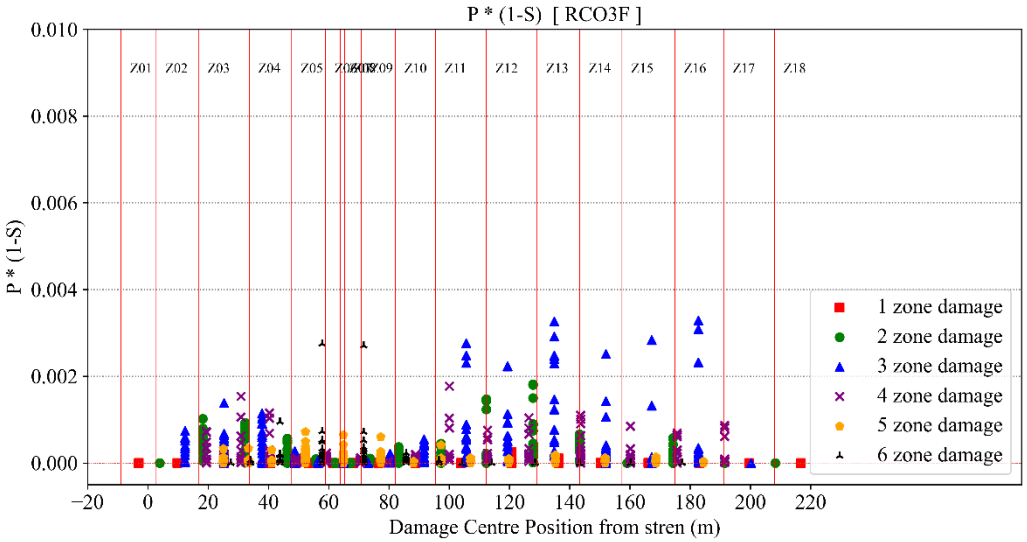

(a)

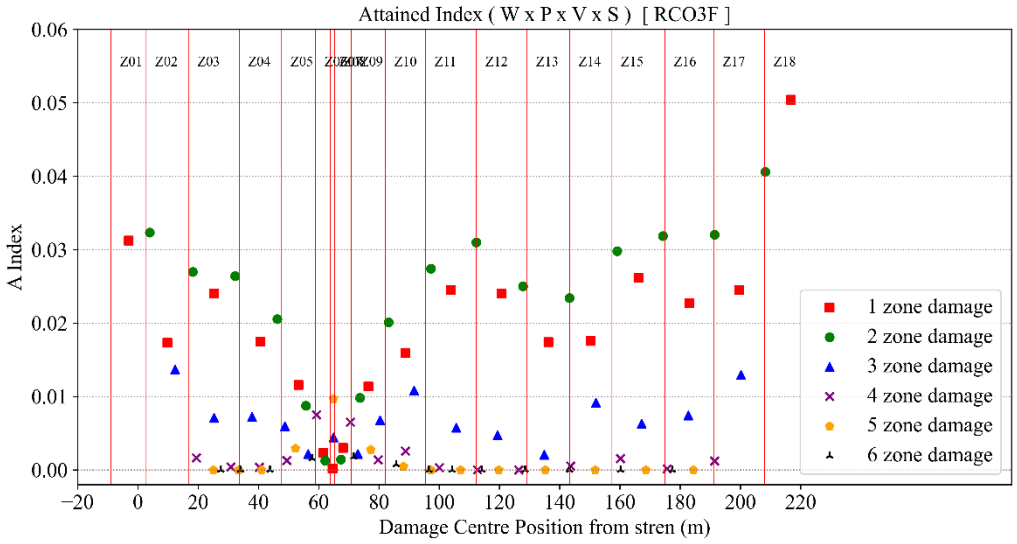

(b)

Figure C.18 RCO3-F: Summary of Damage Stablility (a) P (1-S) graph and (c) local Attained Index sub sum graph

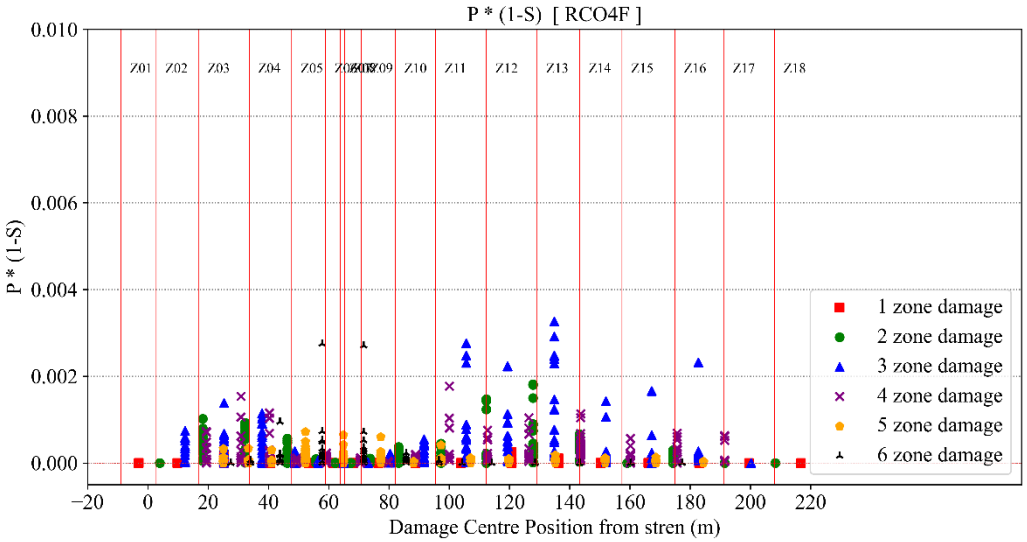

(a)

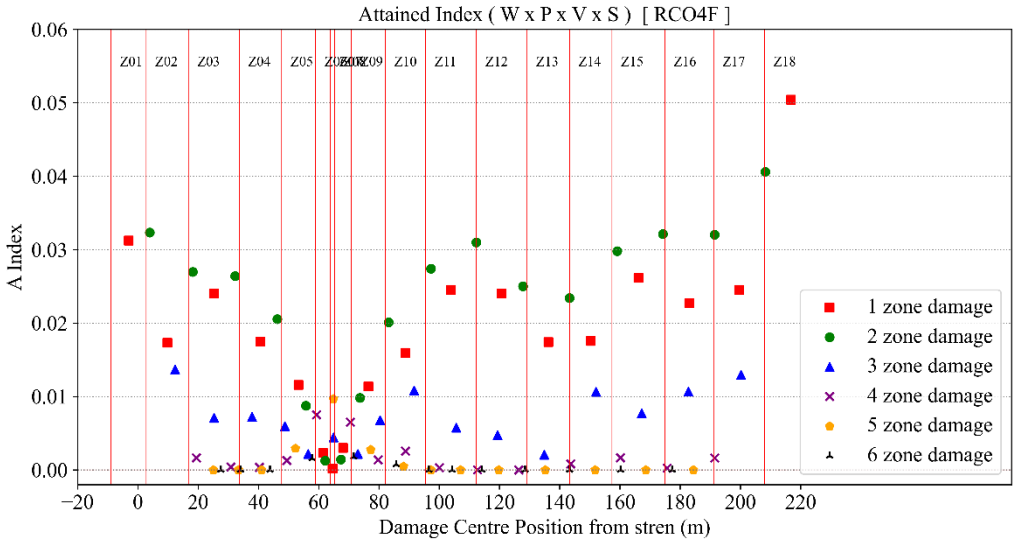

(b)

Figure C.19 RCO4-F: Summary of Damage Stablility (a) P (1-S) graph and (c) local Attained Index sub sum graph

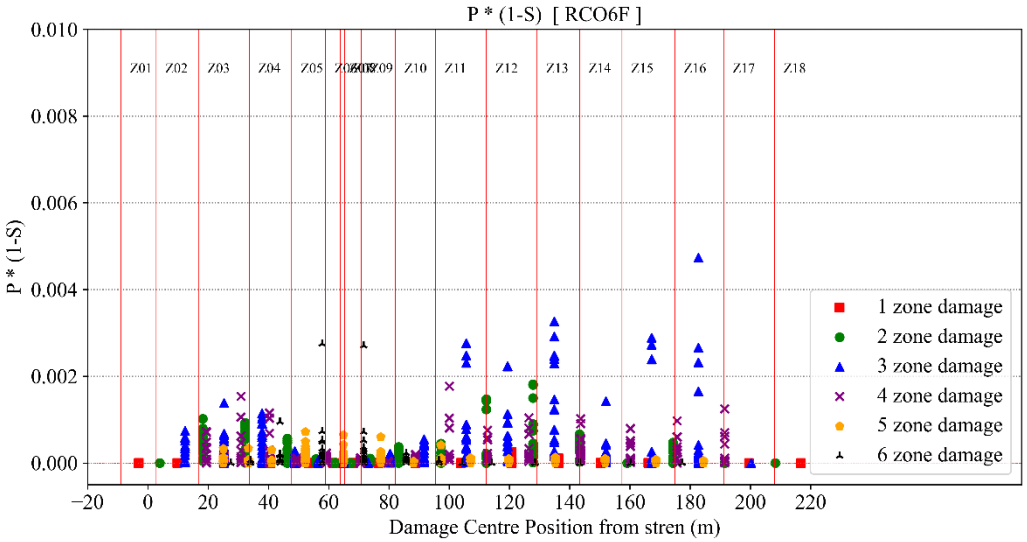

(a)

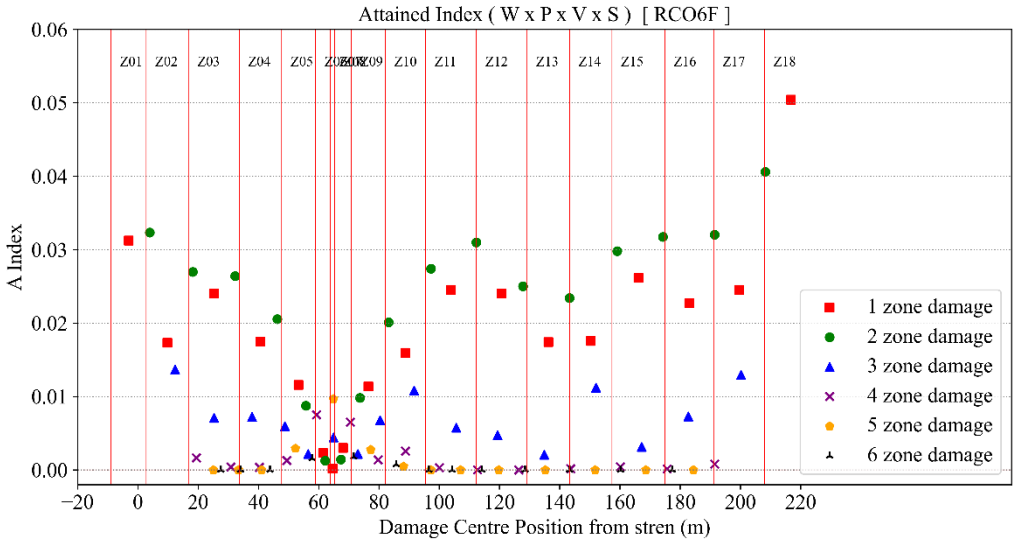

(b)

Figure C.20 RCO6-F: Summary of Damage Stablility (a) P (1-S) graph and (c) local Attained Index sub sum graph

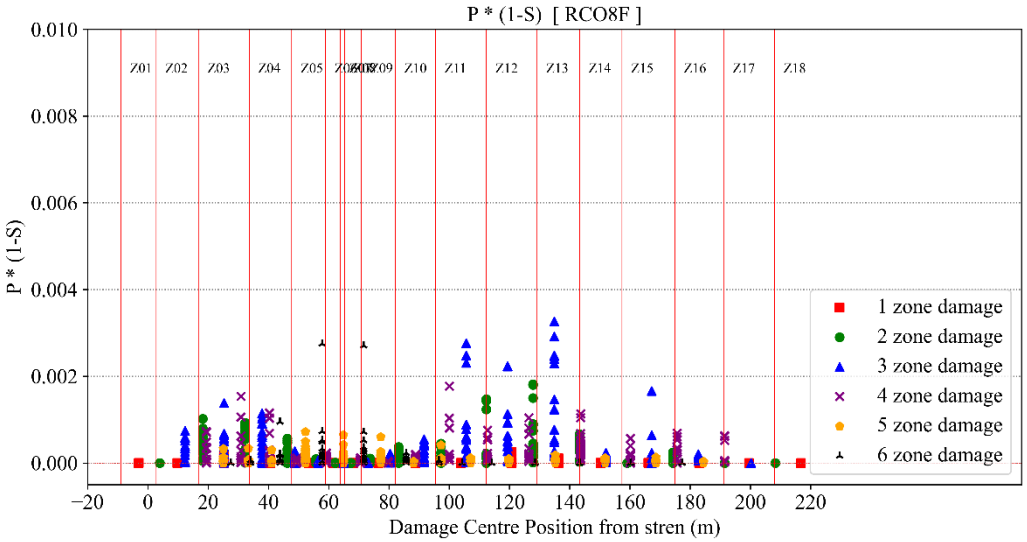

(a)

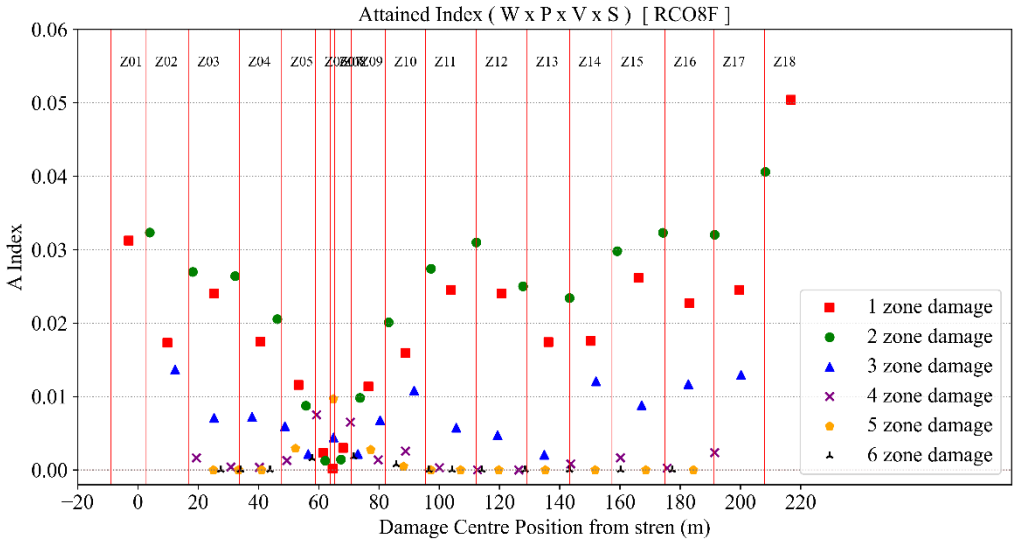

(b)

Figure C.21 RCO8-F: Summary of Damage Stablility (a) P (1-S) graph and (c) local Attained Index sub sum graph

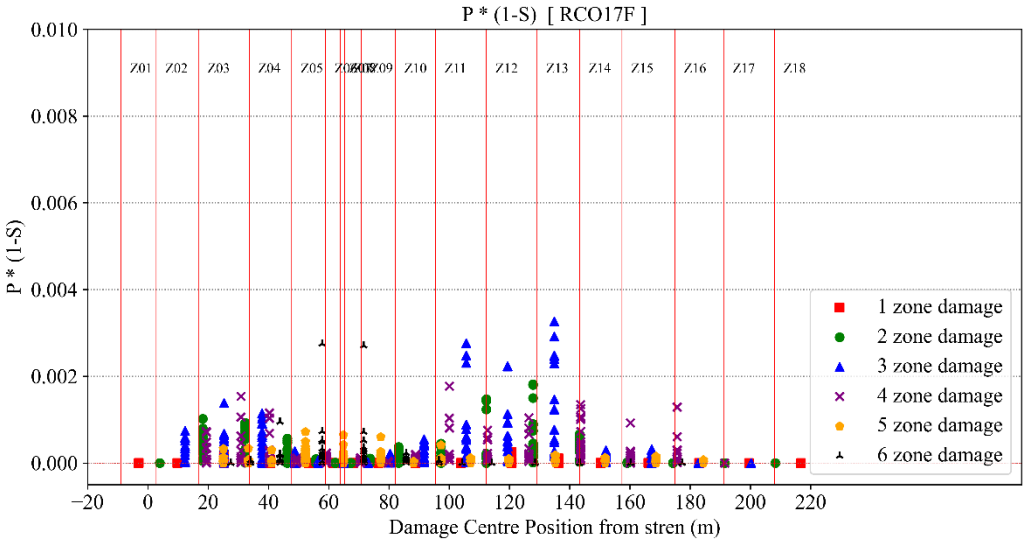

(a)

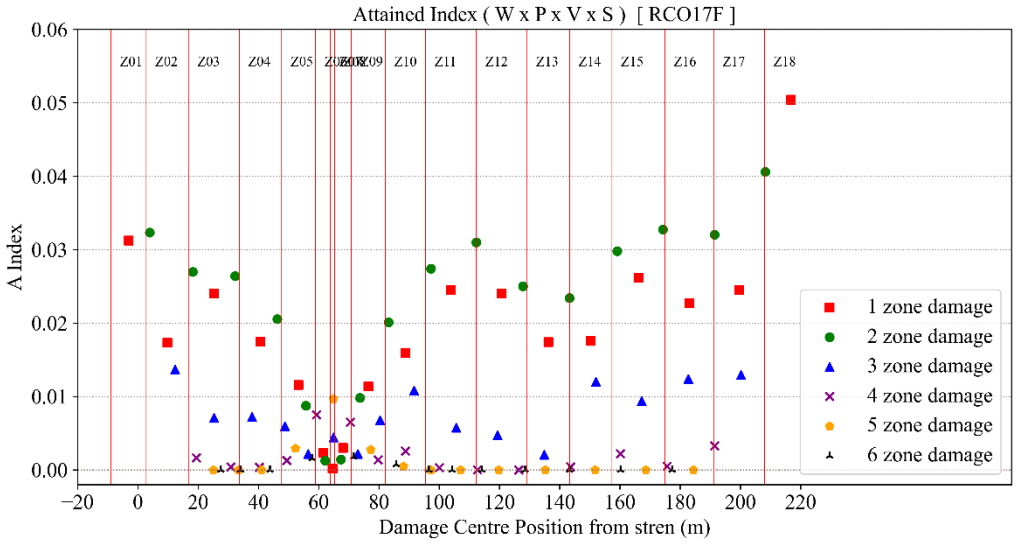

(b)

Figure C.22 RCO17-F: Summary of Damage Stablility (a) P (1-S) graph and (c) local Attained Index sub sum graph

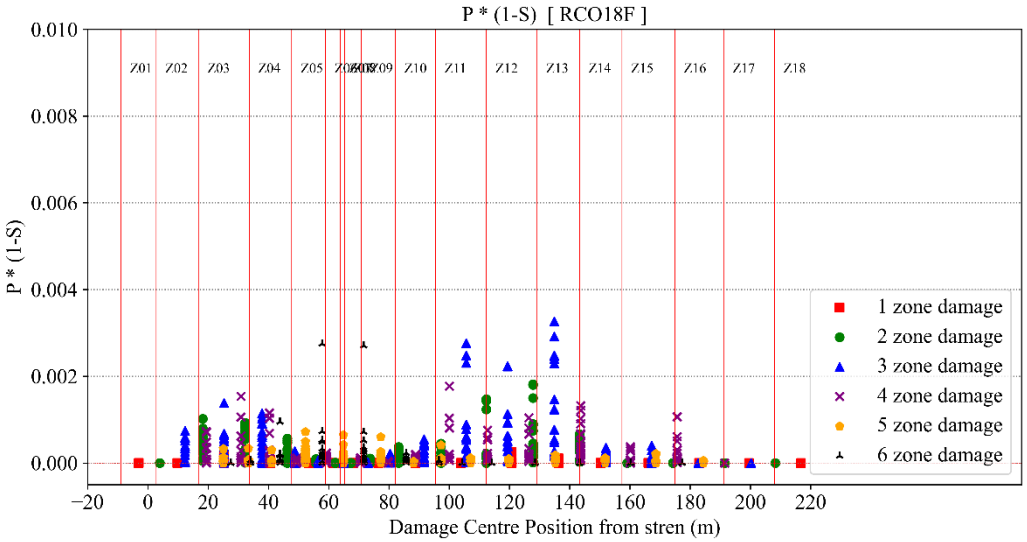

(a)

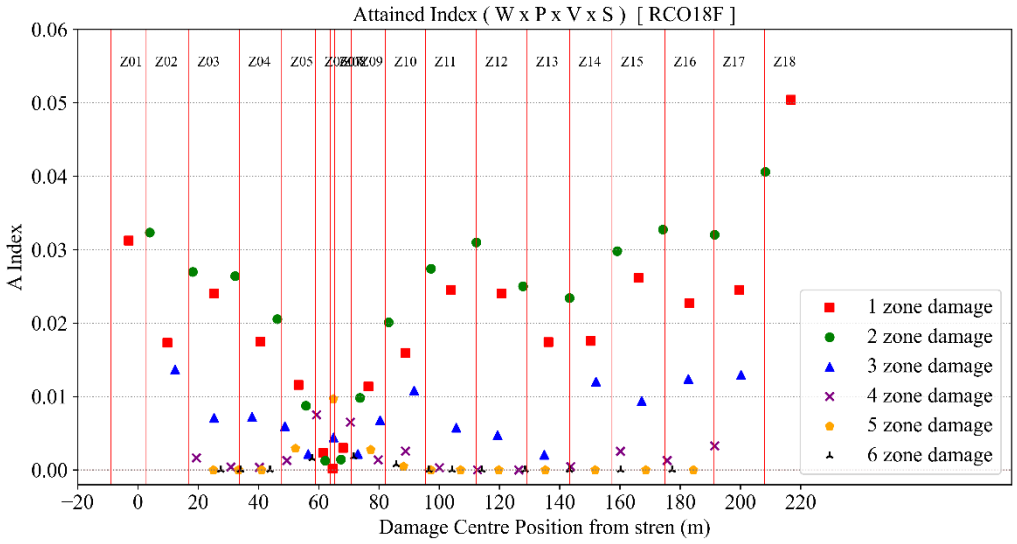

(b)

Figure C.23 RCO18-F: Summary of Damage Stablility (a) P (1-S) graph and (c) local Attained Index sub sum graph

Appendix D

FE Simulation Results

APPENDIX D. FE SIMULATION RESULTS

D.1 Crashworthiness analysis results in Case Study

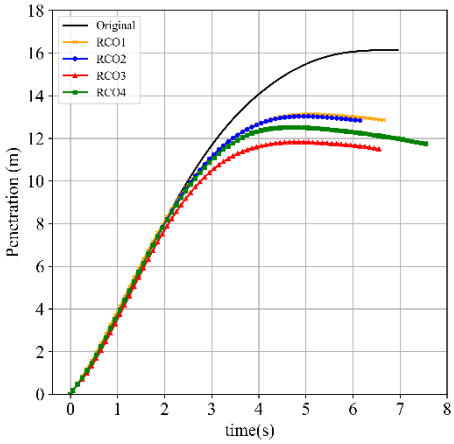

(a) Penetration - Time

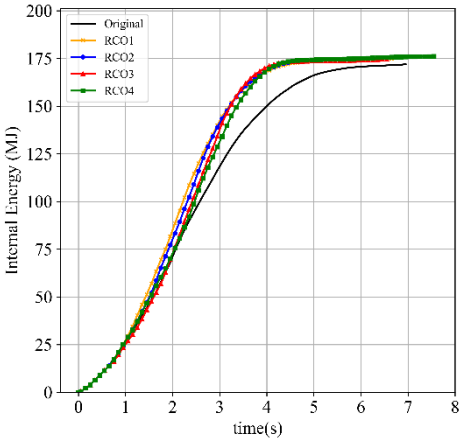

(b) Dissipated energy - Time

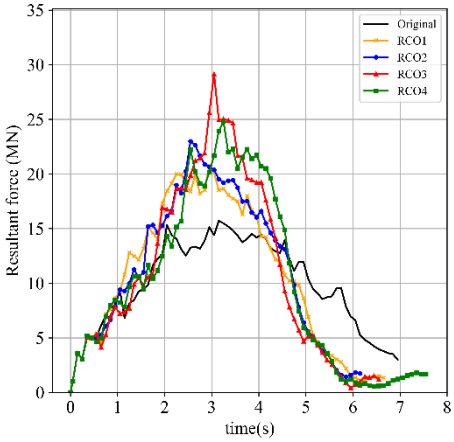

(c) Resultant force - Time

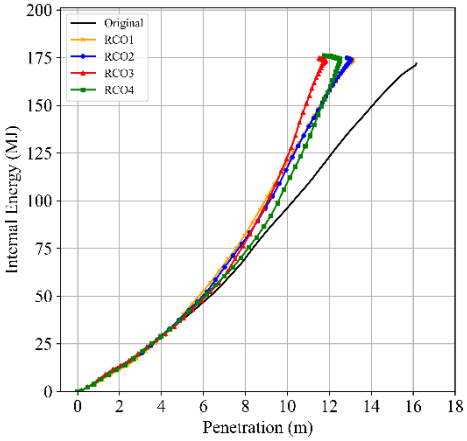

(d) Dissipated energy - Penetration

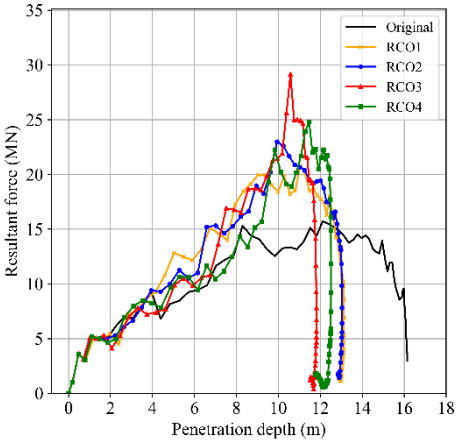

(e) Resultant force - Penetration

Figure D.1 RCOs with single longitudinal subdivisions

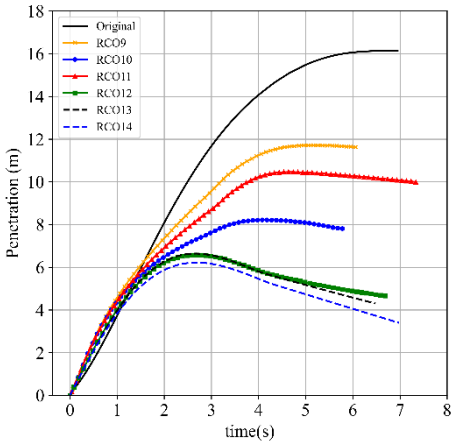

(a) Penetration - Time

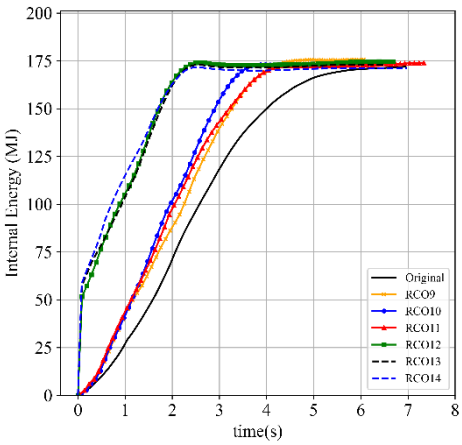

(b) Dissipated energy - Time

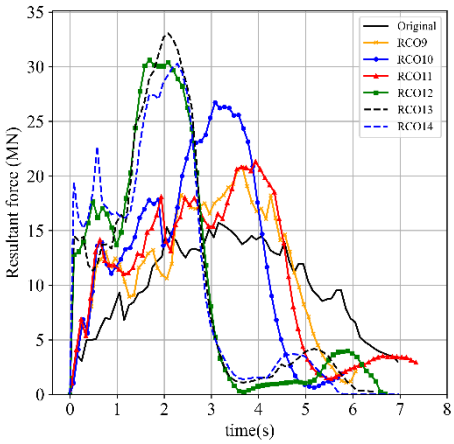

(c) Resultant force - Time

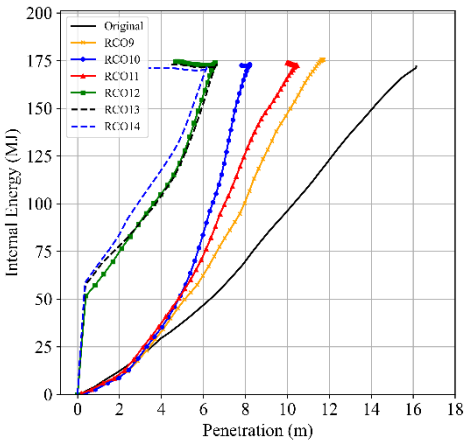

(d) Dissipated energy - Penetration

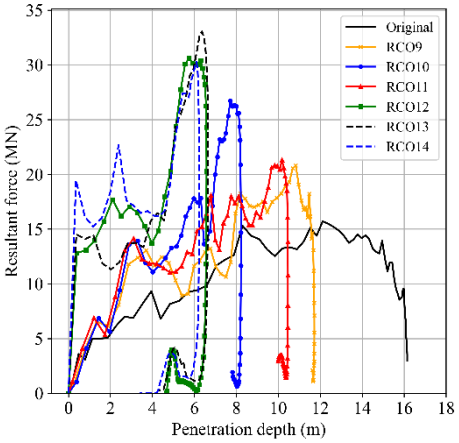

(e) Resultant force - Penetration

Figure D.2 RCOs with Hull thickness Change

D.2 Crashworthiness analysis results in Sensitivity Study-Failure Strain Effects

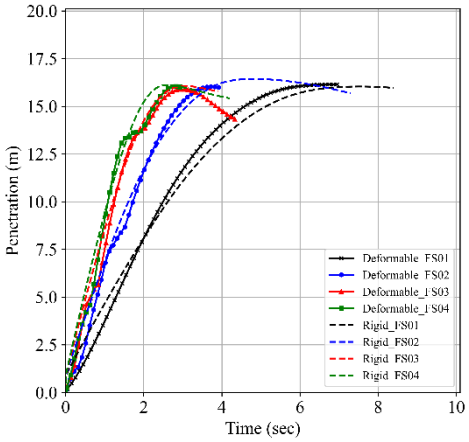

(a) Penetration - Time

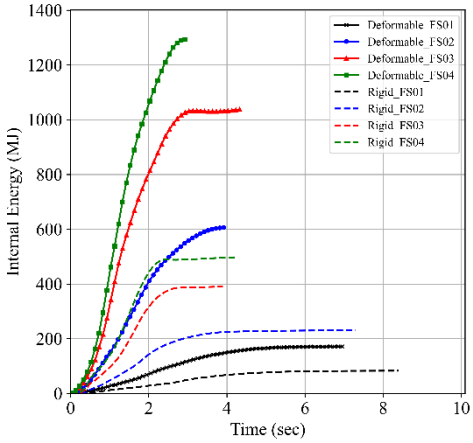

(b) Dissipated energy - Time

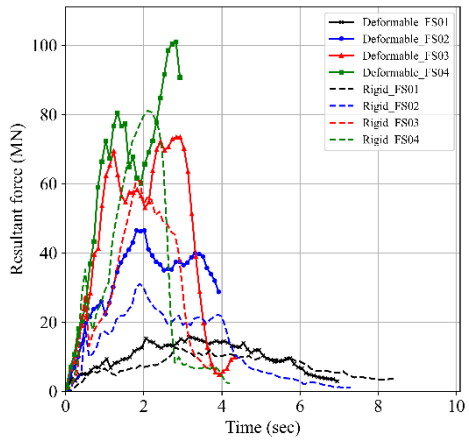

(c) Resultant force - Time

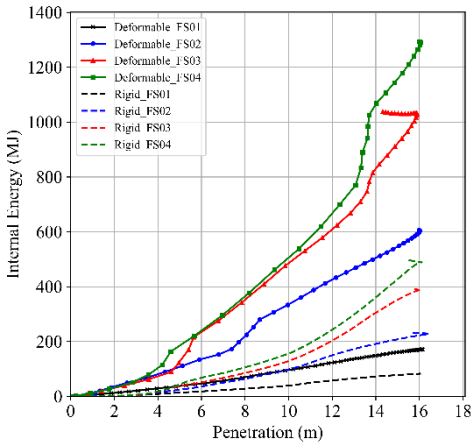

(d) Dissipated energy - Penetration

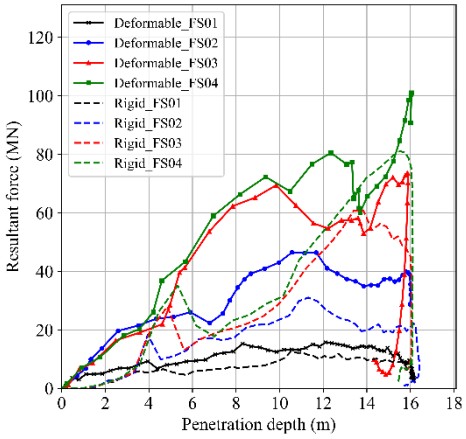

(e) Resultant force - Penetration

Figure D.3 Original for failure criteria effects with deformable and rigid bow

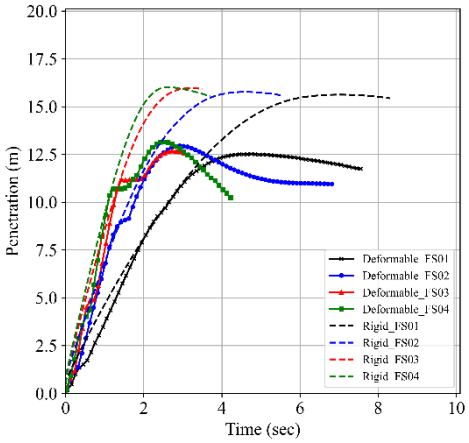

(a) Penetration - Time

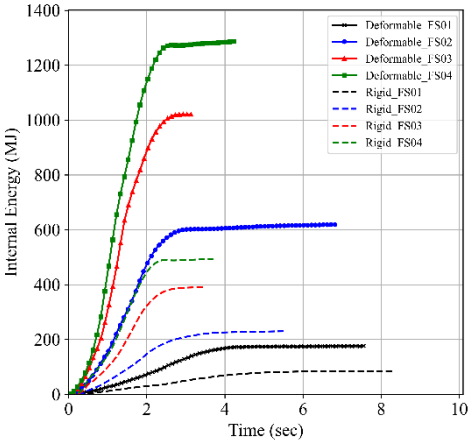

(b) Dissipated energy - Time

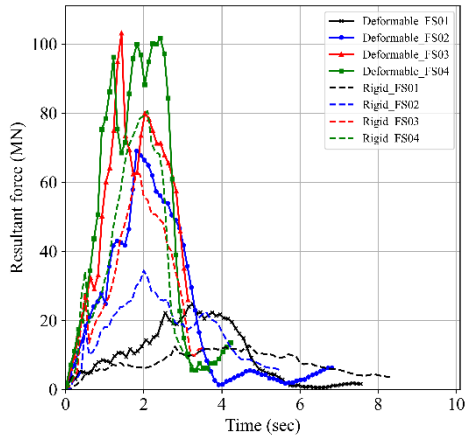

(c) Resultant force - Time

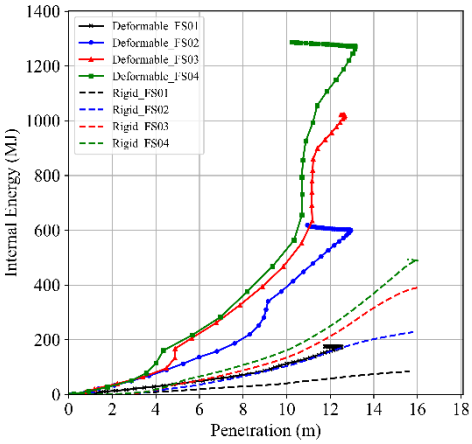

(d) Dissipated energy - Penetration

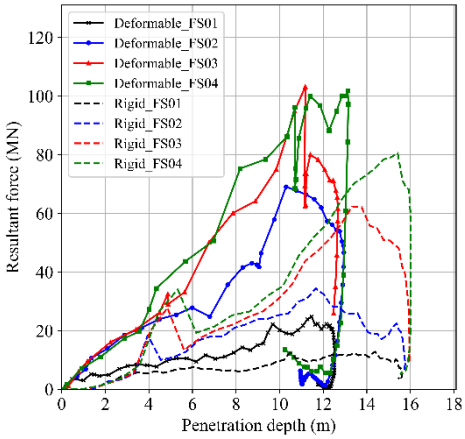

(e) Resultant force - Penetration

Figure D.4 RCO4 for failure criteria effects with deformable and rigid bow

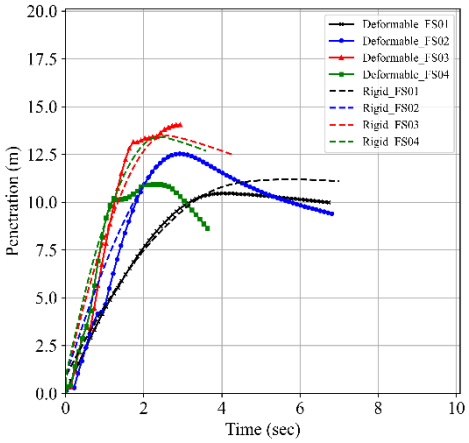

(a) Penetration - Time

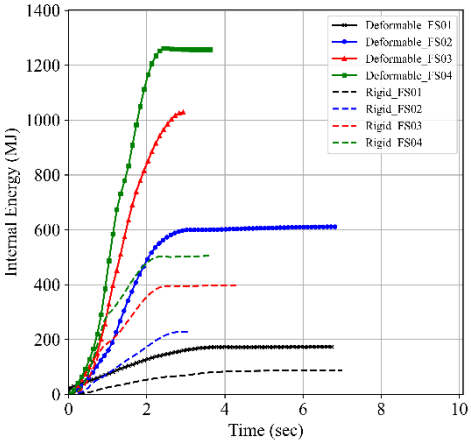

(b) Dissipated energy - Time

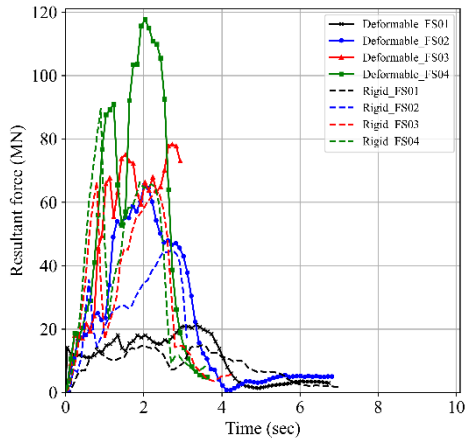

(c) Resultant force - Time

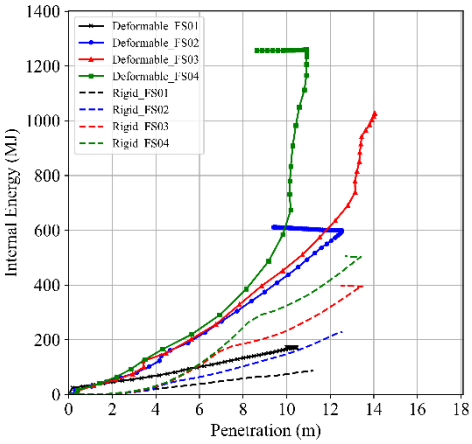

(d) Dissipated energy - Penetration

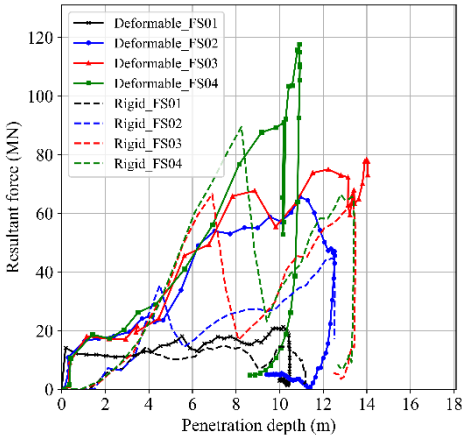

(e) Resultant force - Penetration

Figure D.5 RCO11 for failure criteria effects with deformable and rigid bow

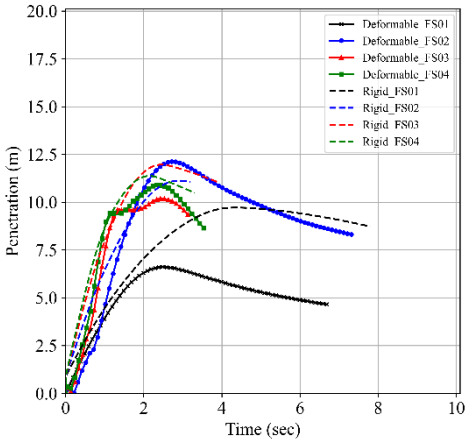

(a) Penetration - Time

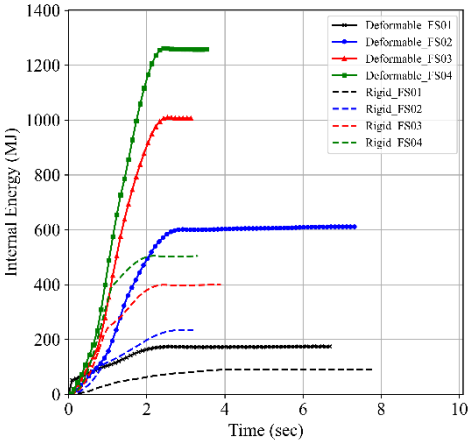

(b) Dissipated energy - Time

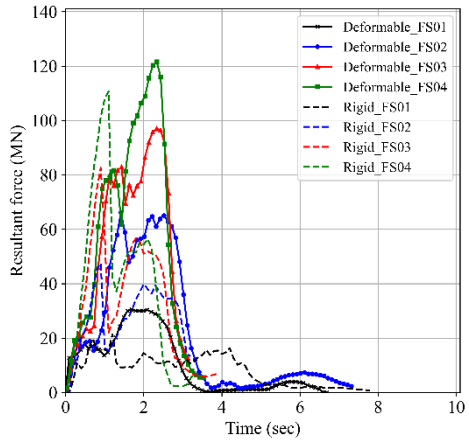

(c) Resultant force - Time

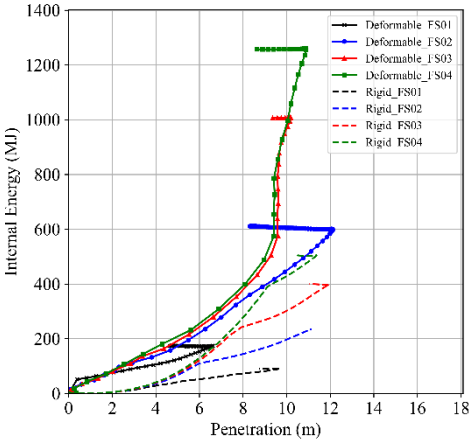

(d) Dissipated energy - Penetration

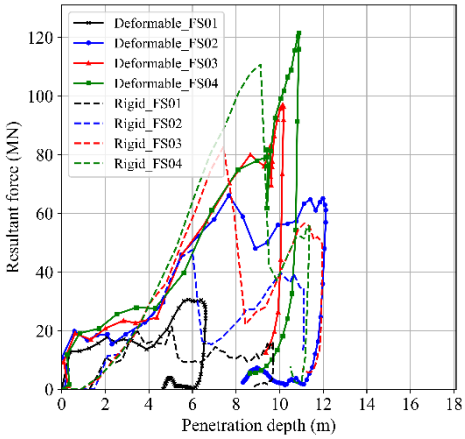

(e) Resultant force - Penetration

Figure D.6 RCO12 for failure criteria effects with deformable and rigid bow

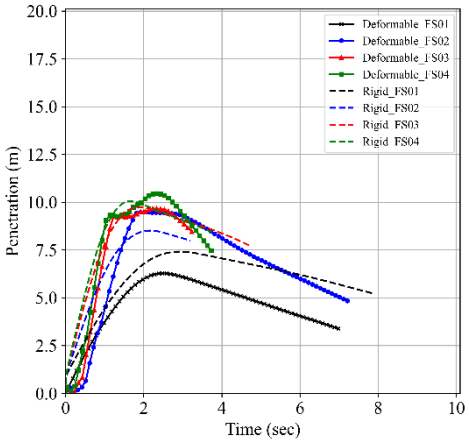

(a) Penetration - Time

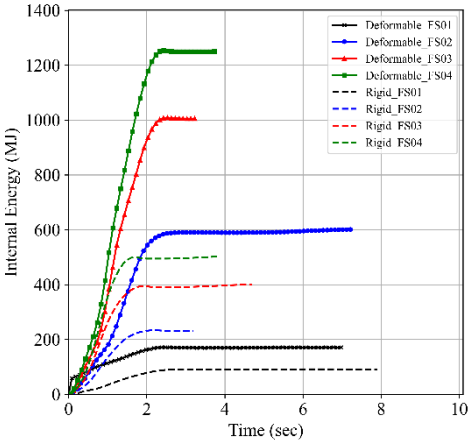

(b) Dissipated energy - Time

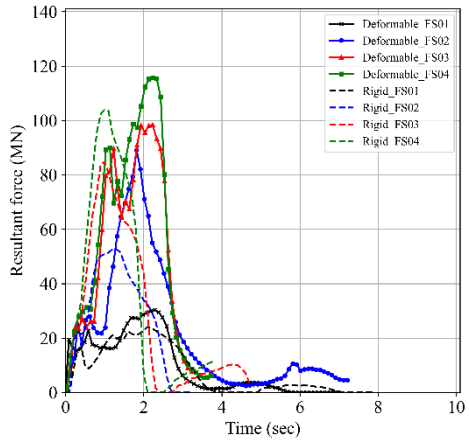

(c) Resultant force - Time

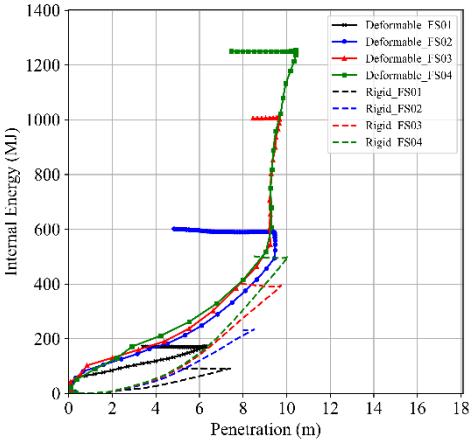

(d) Dissipated energy - Penetration

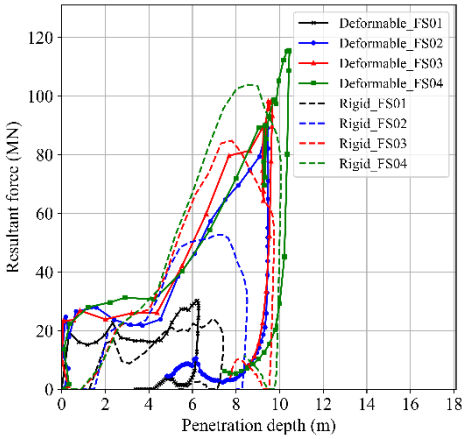

(e) Resultant force - Penetration

Figure D.7 RCO14 for failure criteria effects with deformable and rigid bow

D.3 Crashworthiness analysis results in Sensitivity Study-Material Curve Effects

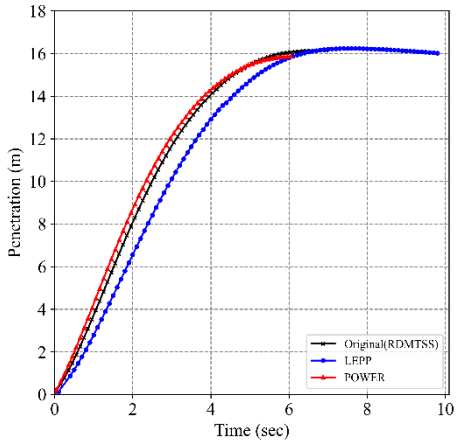

(a) Penetration - Time

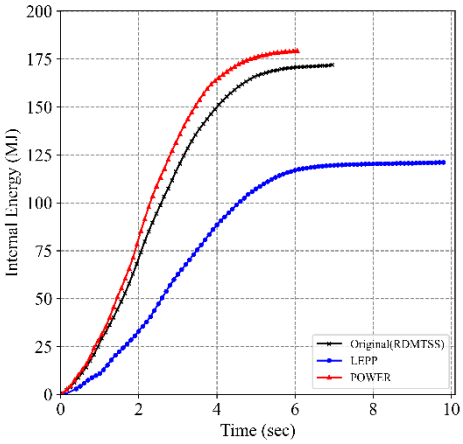

(b) Dissipated energy - Time

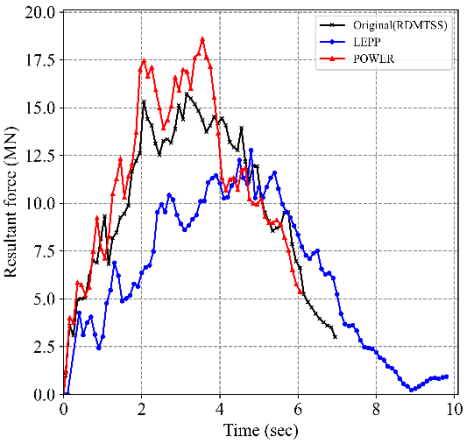

(c) Resultant force - Time

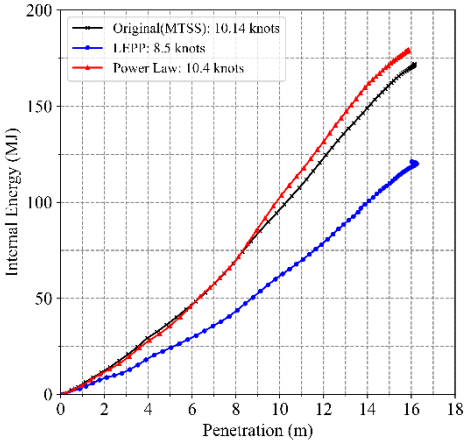

(d) Dissipated energy - Penetration

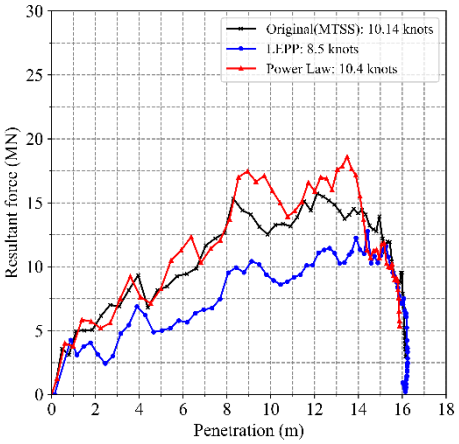

(e) Resultant force - Penetration

Figure D.8 Original for material curve effects

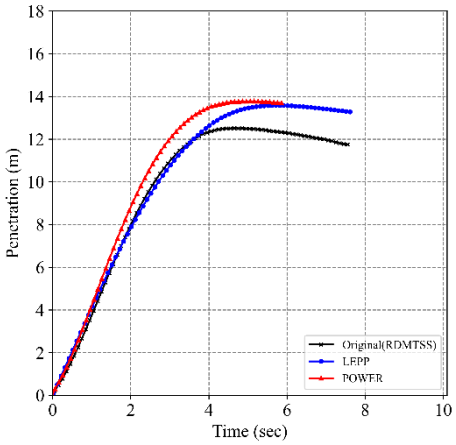

(a) Penetration - Time

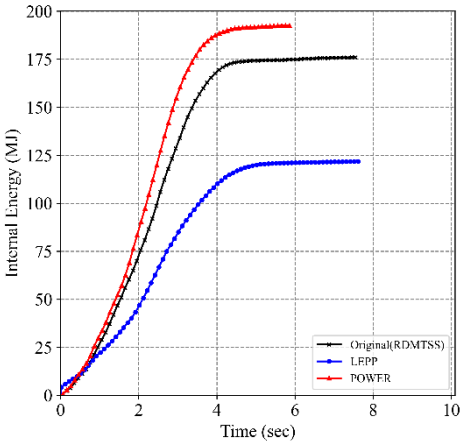

(b) Dissipated energy - Time

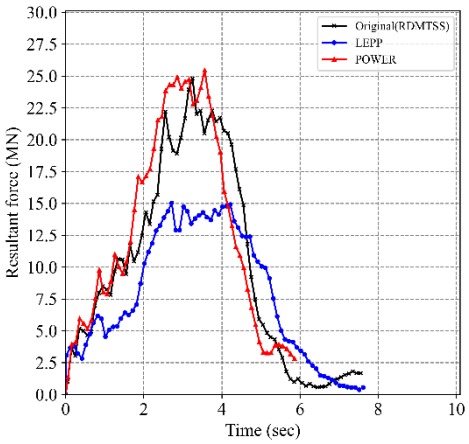

(c) Resultant force - Time

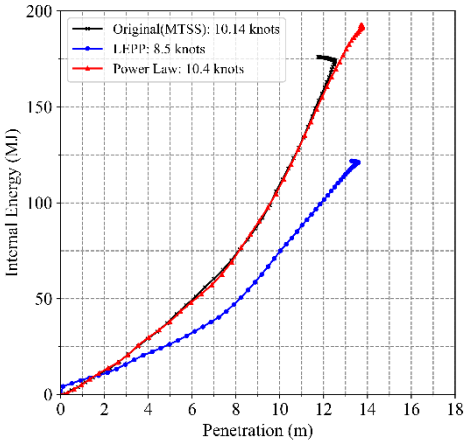

(d) Dissipated energy - Penetration

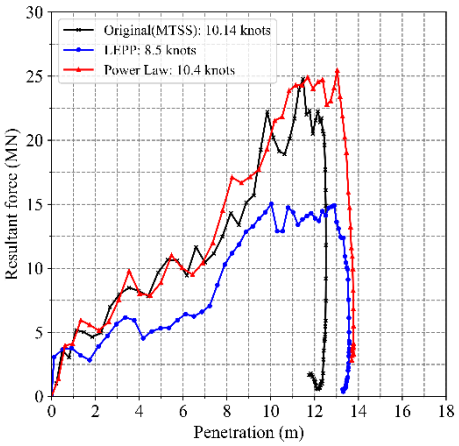

(e) Resultant force - Penetration

Figure D.9 RCO4 for material curve effects

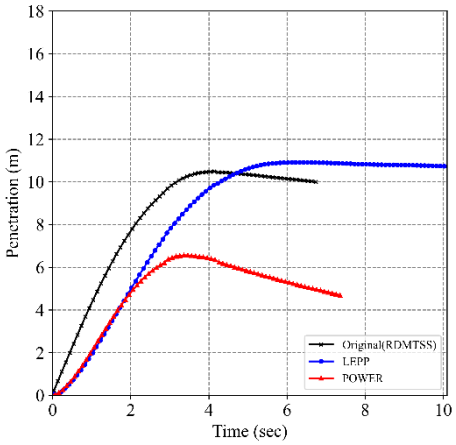

(a) Penetration - Time

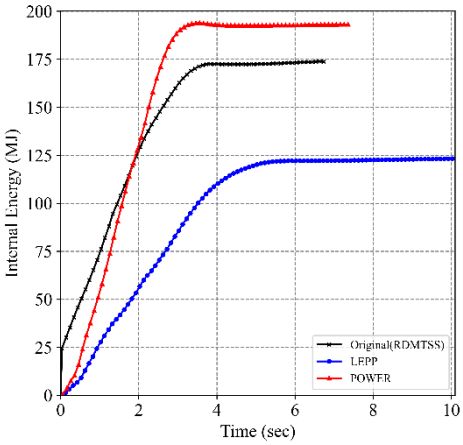

(b) Dissipated energy - Time

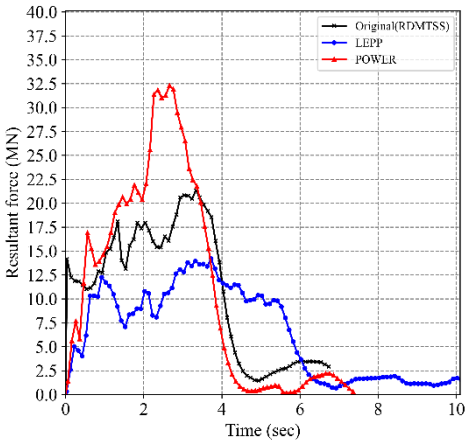

(c) Resultant force - Time

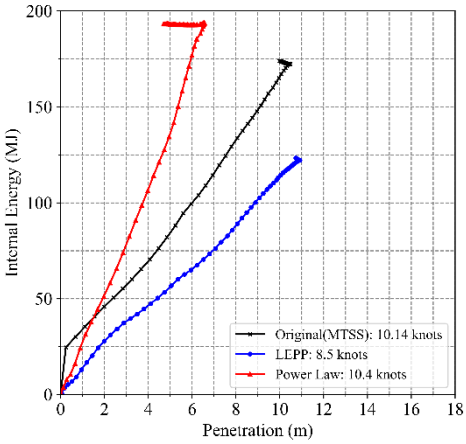

(d) Dissipated energy - Penetration

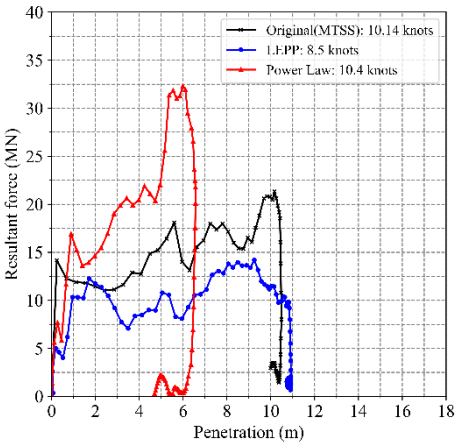

(e) Resultant force - Penetration

Figure D.10 RCO11 for material curve effects

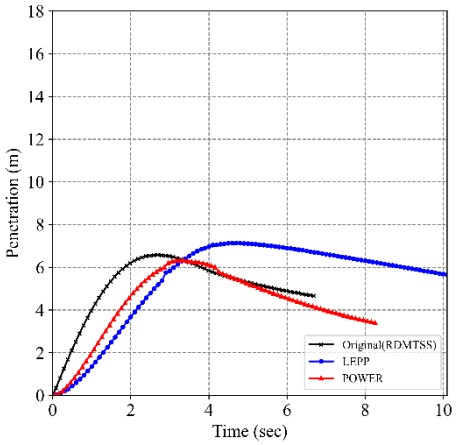

(a) Penetration - Time

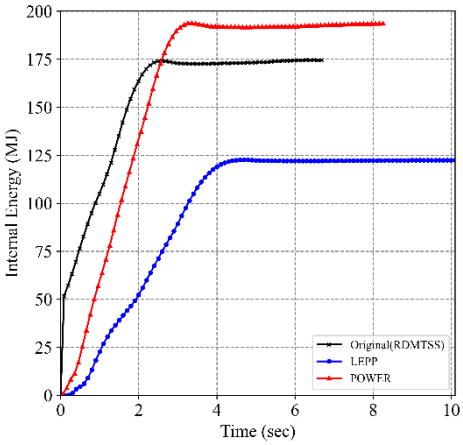

(b) Dissipated energy - Time

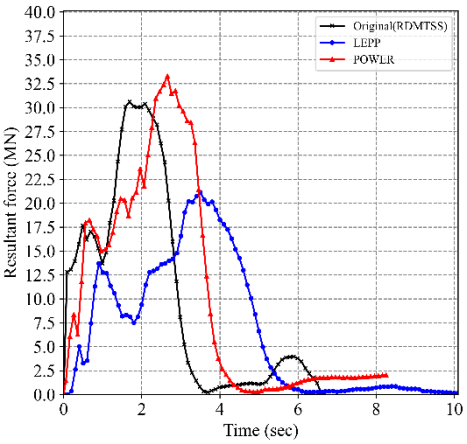

(c) Resultant force - Time

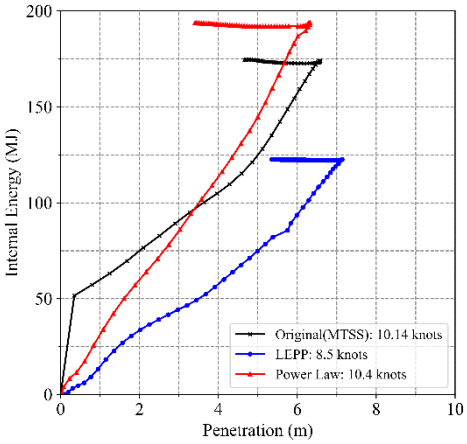

(d) Dissipated energy - Penetration

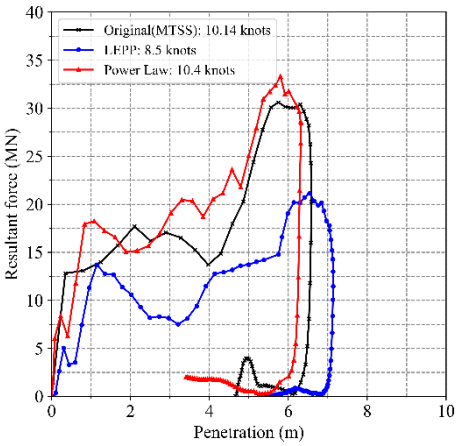

(e) Resultant force - Penetration

Figure D.11 RCO12 for material curve effects

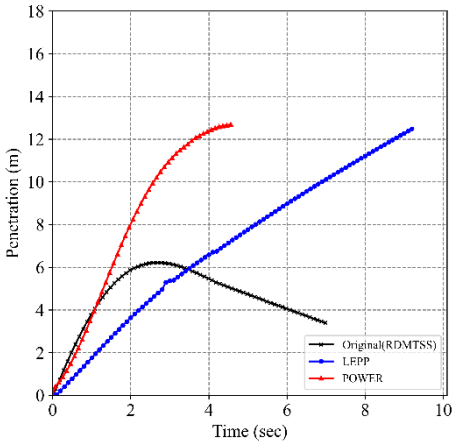

(a) Penetration - Time

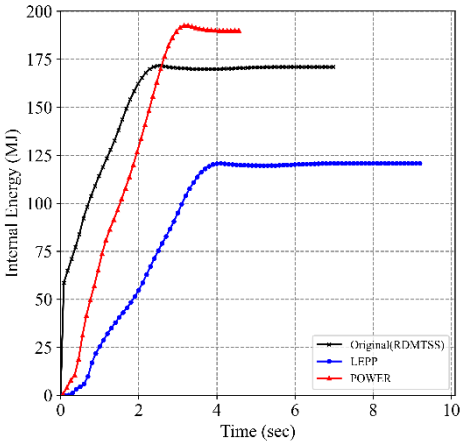

(b) Dissipated energy - Time

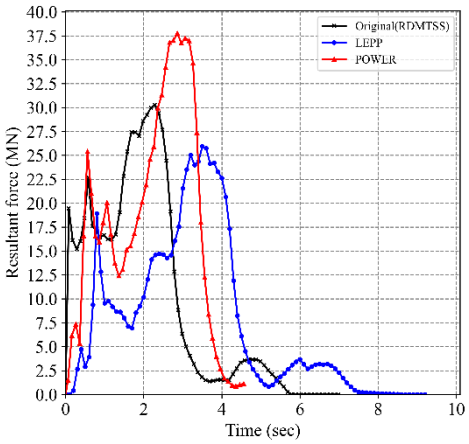

(c) Resultant force - Time

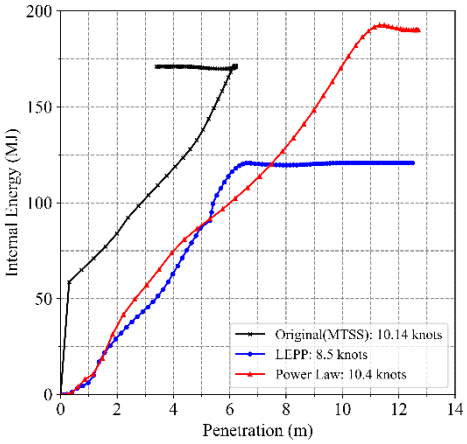

(d) Dissipated energy - Penetration

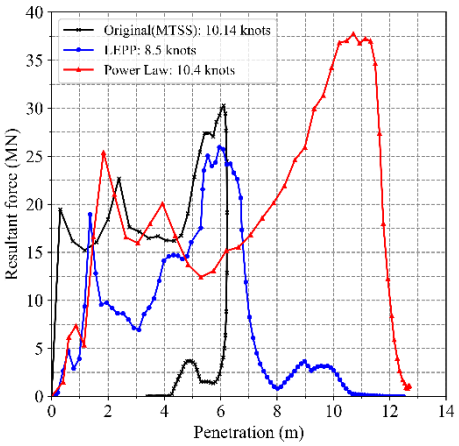

(e) Resultant force - Penetration

Figure D.12 RCO14 for material curve effects

D.4 Crashworthiness analysis results in Sensitivity Study-Friction Coefficient Effects

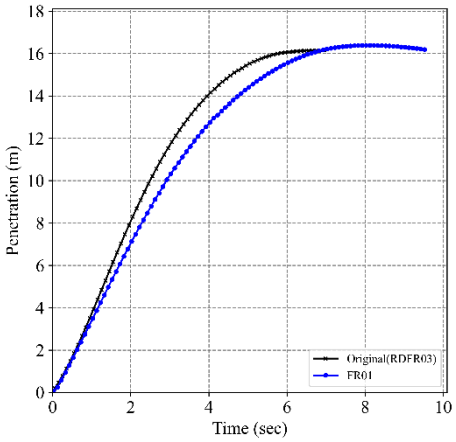

(a) Penetration - Time

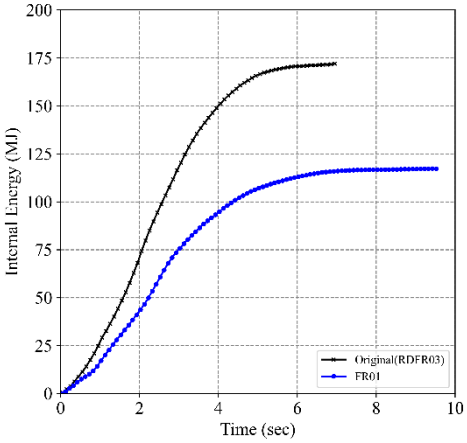

(b) Dissipated energy - Time

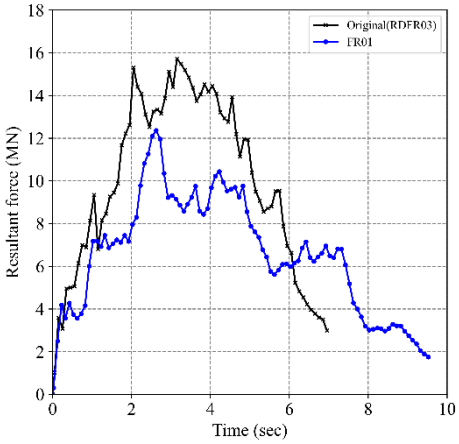

(c) Resultant force - Time

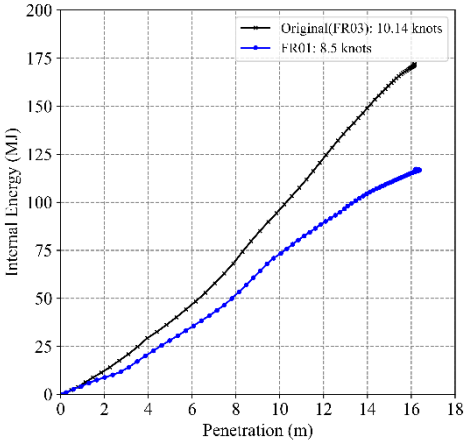

(d) Dissipated energy - Penetration

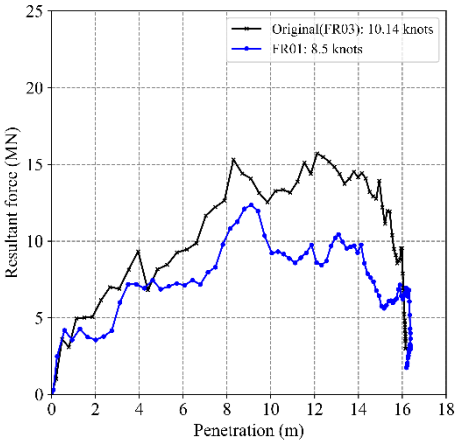

(e) Resultant force - Penetration

Figure D.13 Original for friction coefficient effects

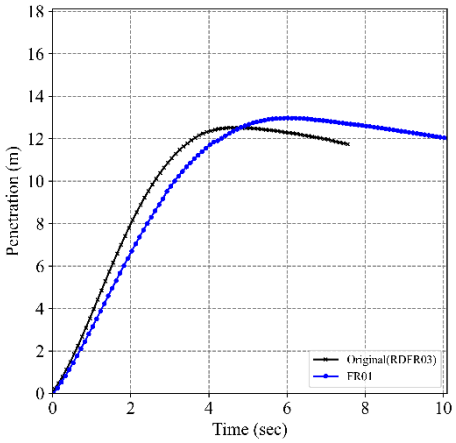

(a) Penetration - Time

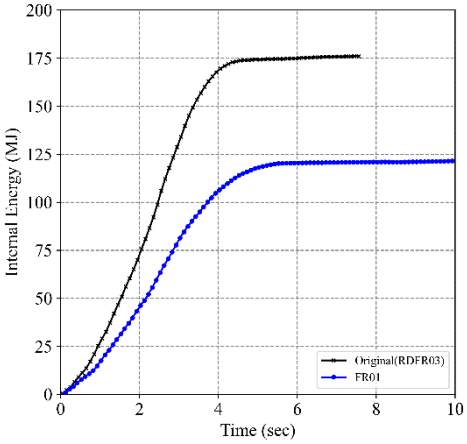

(b) Dissipated energy - Time

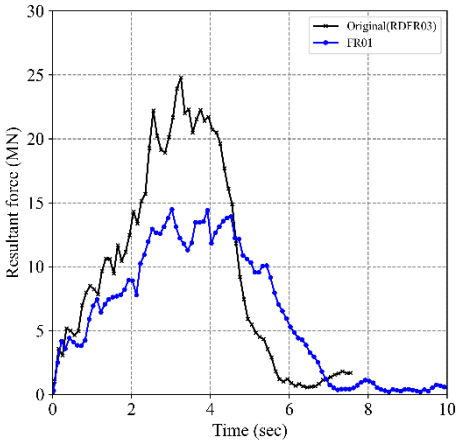

(c) Resultant force - Time

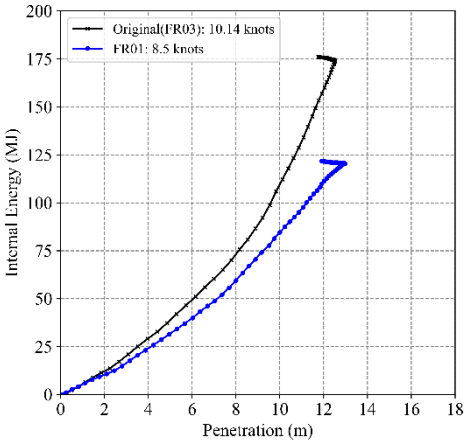

(d) Dissipated energy - Penetration

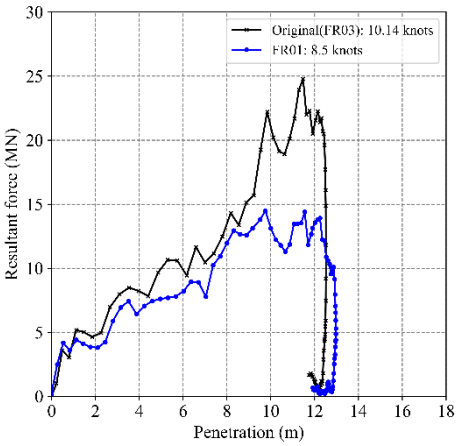

(e) Resultant force - Penetration

Figure D.14 RCO4 for friction coefficient effects

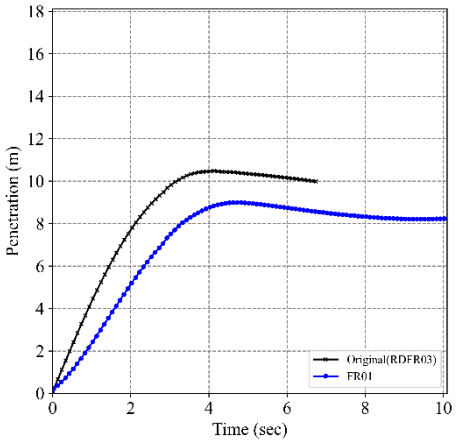

(a) Penetration - Time

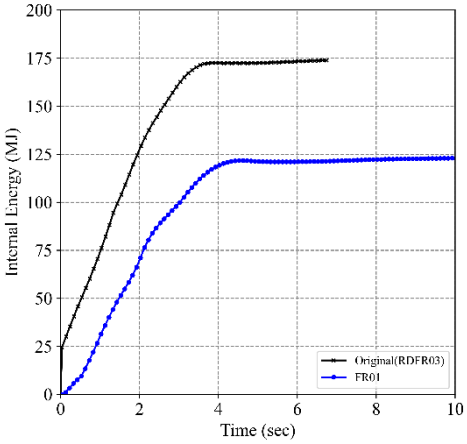

(b) Dissipated energy - Time

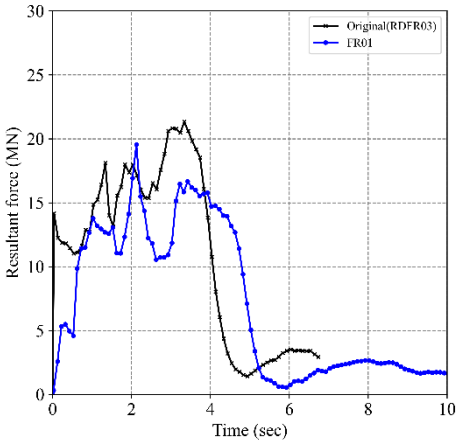

(c) Resultant force - Time

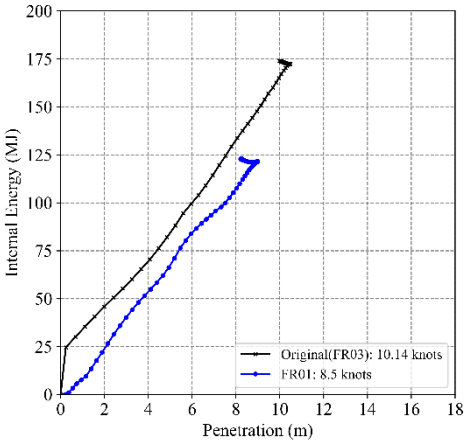

(d) Dissipated energy - Penetration

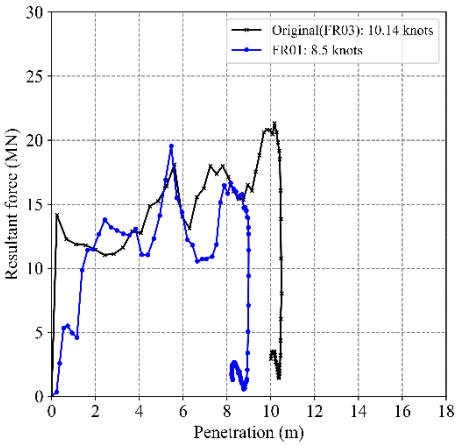

(e) Resultant force - Penetration

Figure D.15 RCO11 for friction coefficient effects

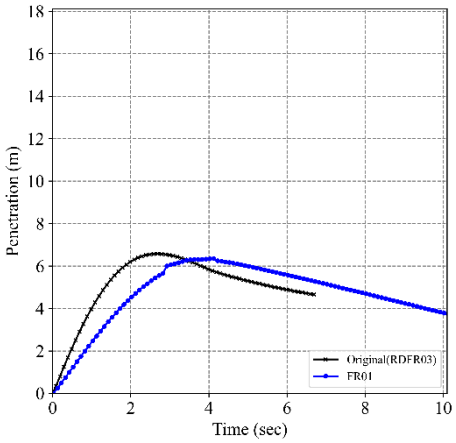

(a) Penetration - Time

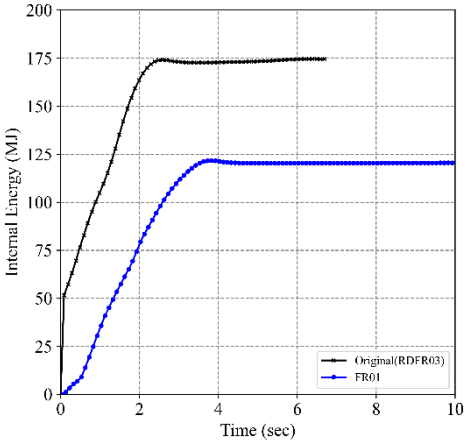

(b) Dissipated energy - Time

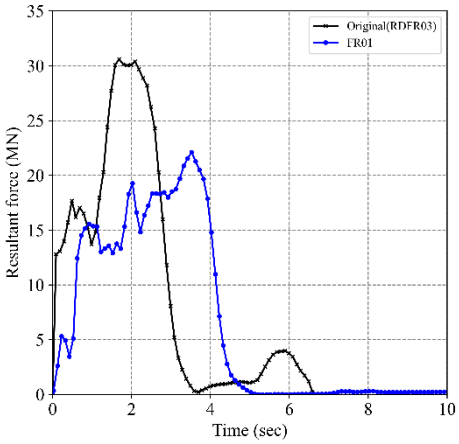

(c) Resultant force - Time

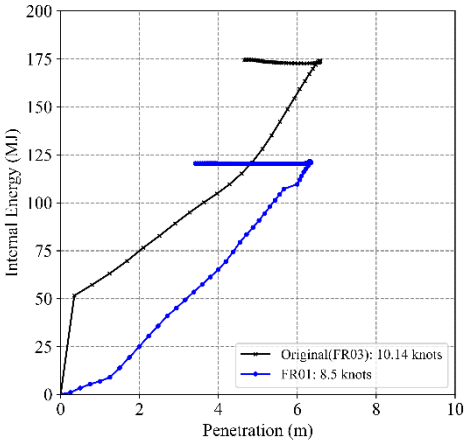

(d) Dissipated energy - Penetration

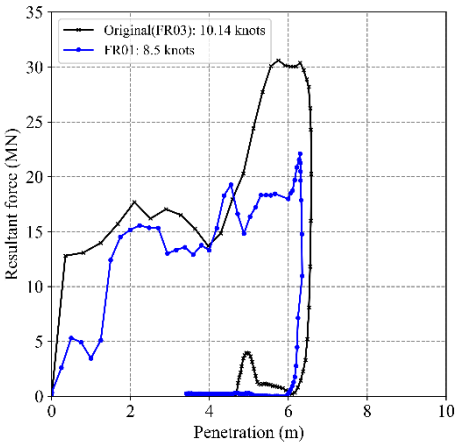

(e) Resultant force - Penetration

Figure D.16 RCO12 for friction coefficient effects

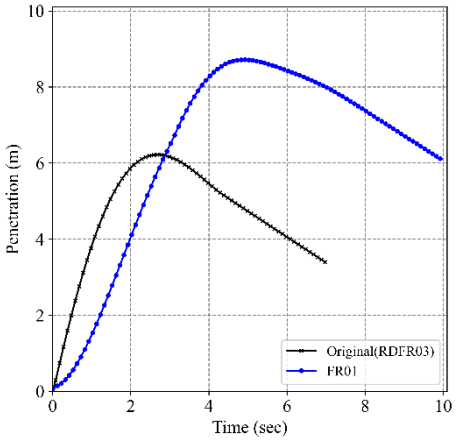

(a) Penetration - Time

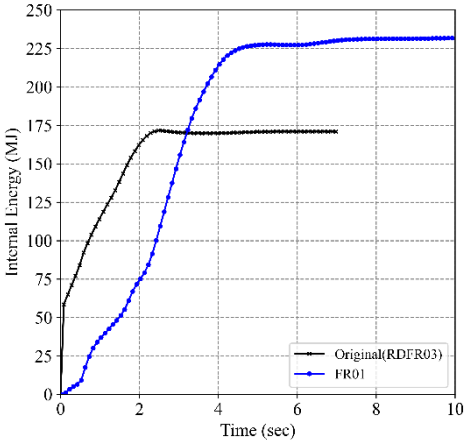

(b) Dissipated energy - Time

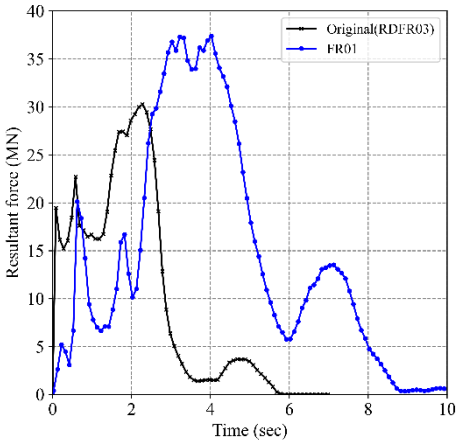

(c) Resultant force - Time

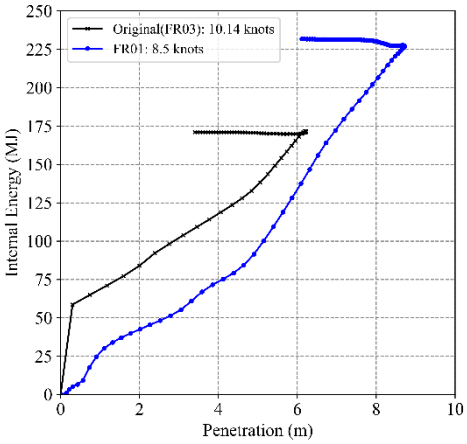

(d) Dissipated energy - Penetration

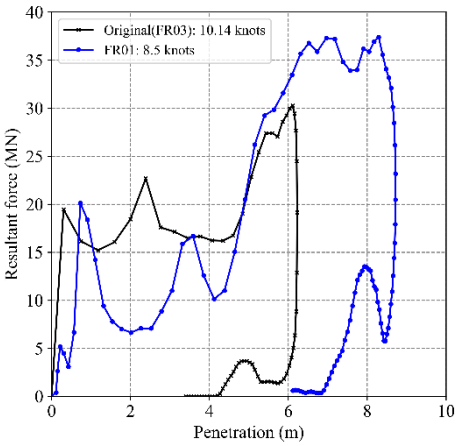

(e) Resultant force - Penetration

Figure D.17 RCO14 for friction coefficient effects

Appendix E

MCOL Code

APPENDIX E. MCOL INPUT DATA

E.1 MCOL Code- Struck ship

002$rigid body mass matrix (Mrb)
3.5367E+07 0.0000E+00 0.0000E+00 0.0000E+00 0.0000E+00 0.0000E+00
0.0000E+00 3.5367E+07 0.0000E+00 0.0000E+00 0.0000E+00 0.0000E+00
0.0000E+00 0.0000E+00 3.5367E+07 0.0000E+00 0.0000E+00 0.0000E+00
0.0000E+00 0.0000E+00 0.0000E+00 4.2794E+09 0.0000E+00 8.8418E+08
0.0000E+00 0.0000E+00 0.0000E+00 0.0000E+00 1.2732E+11 0.0000E+00
0.0000E+00 0.0000E+00 0.0000E+00 8.8418E+08 0.0000E+00 1.3160E+11
003$hydrostatic restoring matrix (Ks)
0.0000E+00 0.0000E+00 0.0000E+00 0.0000E+00 0.0000E+00 0.0000E+00
0.0000E+00 0.0000E+00 0.0000E+00 0.0000E+00 0.0000E+00 0.0000E+00
0.0000E+00 0.0000E+00 6.2495E+07 0.0000E+00 1.5953E+08 0.0000E+00
0.0000E+00 0.0000E+00 0.0000E+00 4.7642E+09 0.0000E+00 0.0000E+00
0.0000E+00 0.0000E+00 1.5953E+08 0.0000E+00 1.9046E+11 0.0000E+00
0.0000E+00 0.0000E+00 0.0000E+00 0.0000E+00 0.0000E+00 0.0000E+00
004$buoyancy parameters (xb,yb,zb,W=m*g,B=rho*g*displ,ZGref,PHIref,TETAref)
0.0000E+00 0.0000E+00 1.1000E+01 3.4695E+08 3.4695E+08 0.0000E+00 0.0000E+00 0.0000E+00
005$added mass matrix (Ma)
3.9990E+05 0.0000E+00 7.4090E+05 0.0000E+00 2.1639E+08 0.0000E+00
0.0000E+00 8.2640E+06 0.0000E+00 3.5063E+06 0.0000E+00 1.0640E+08
7.2753E+05 0.0000E+00 7.1953E+07 0.0000E+00 4.6024E+08 0.0000E+00
0.0000E+00 3.2945E+06 0.0000E+00 1.1321E+09 0.0000E+00 1.2099E+09
2.1526E+08 0.0000E+00 4.6298E+08 0.0000E+00 1.5023E+11 0.0000E+00
0.0000E+00 1.0629E+08 0.0000E+00 1.2180E+09 0.0000E+00 3.2693E+10
007$parameter for checking convergence (gosa0,accl)
0.1000E-03 0.1000E+01

E.1 MCOL Code- String ship

002$rigid body mass matrix (Mrb)
3.0114E+07 0.0000E+00 0.0000E+00 0.0000E+00 0.0000E+00 0.0000E+00
0.0000E+00 3.0114E+07 0.0000E+00 0.0000E+00 0.0000E+00 0.0000E+00
0.0000E+00 0.0000E+00 3.0114E+07 0.0000E+00 0.0000E+00 0.0000E+00
0.0000E+00 0.0000E+00 0.0000E+00 3.6438E+09 0.0000E+00 0.0000E+00
0.0000E+00 0.0000E+00 0.0000E+00 0.0000E+00 9.1094E+10 0.0000E+00
0.0000E+00 0.0000E+00 0.0000E+00 0.0000E+00 0.0000E+00 9.1094E+10
003$hydrostatic restoring matrix (Ks)
0.0000E+00 0.0000E+00 0.0000E+00 0.0000E+00 0.0000E+00 0.0000E+00
0.0000E+00 0.0000E+00 0.0000E+00 0.0000E+00 0.0000E+00 0.0000E+00
0.0000E+00 0.0000E+00 5.5380E+07 0.0000E+00 3.9302E+08 0.0000E+00
0.0000E+00 0.0000E+00 0.0000E+00 3.7847E+09 0.0000E+00 0.0000E+00
0.0000E+00 0.0000E+00 3.9302E+08 0.0000E+00 1.6438E+11 0.0000E+00
0.0000E+00 0.0000E+00 0.0000E+00 0.0000E+00 0.0000E+00 0.0000E+00
004$buoyancy parameters (xb,yb,zb,W=m*g,B=rho*g*displ,ZGref,PHIref,TETAref)
0.0000E+00 0.0000E+00 1.0134E+01 2.9542E+08 2.9542E+08 0.0000E+00 0.0000E+00 0.0000E+00
005$added mass matrix (Ma)
3.6631E+05 0.0000E+00 8.6433E+05 0.0000E+00 1.9734E+08 0.0000E+00
0.0000E+00 6.7481E+06 0.0000E+00 3.0540E+06 0.0000E+00 6.4773E+07
8.5624E+05 0.0000E+00 6.4687E+07 0.0000E+00 5.5397E+08 0.0000E+00
0.0000E+00 2.8351E+06 0.0000E+00 9.9657E+08 0.0000E+00 8.7912E+08
1.9663E+08 0.0000E+00 5.5443E+08 0.0000E+00 1.3573E+11 0.0000E+00
0.0000E+00 6.4774E+07 0.0000E+00 8.8231E+08 0.0000E+00 2.1422E+10
007$parameter for checking convergence (gosa0,accl)
0.1000E-03 0.1000E+01